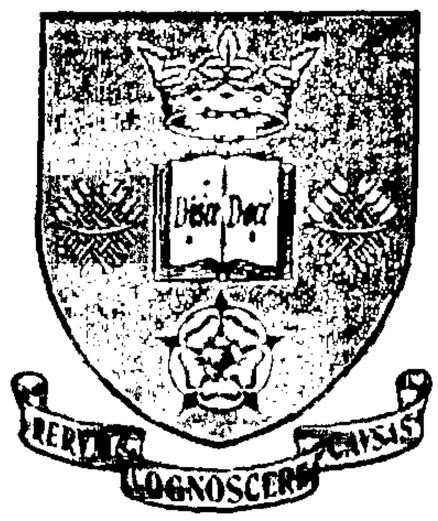

DEPARTMENT OF CIVIL AND STRUCTURAL ENGINEERING

UNIVERSITY OF SHEFFIELD

LIQUEFACTION OF SAND-TYRE CHIP MIXTURES

VOLUME 2

by

PANU PROMPUTTHANGKOON

A THESIS SUBMITTED TO THE UNIVERSITY OF SHEFFIELD

FOR THE DEGREE OF DOCTOR OF PHILOSOPHY

JULY 2009

CHAPTER 5

UNDRAINED MONOTONIC TRIAXIAL TESTS

5.1 Introduction

The undrained triaxial test with the measurement of pore water pressure was chosen to investigate the monotonic stress-strain behaviour and the pore water pressure characteristics of the sand as well as sand mixed with tyre chips. Both compression and extension tests were conducted using a consolidation pressure of 100kPa, which was the same as for the undrained cyclic triaxial test.

A total of 25 compression and 25 extension tests were performed. Each series of which comprised one pure sand specimen and 24 sand-tyre chip mixtures. Four different sizes of tyre chips were mixed with the sand; the sand to rubber ratios were 95:5, 90:10, 80:20, 70:30, 60:40, and 50:50. The stress-strain characteristics, pore water pressure behaviour, and stress paths are presented and discussed.

5.2 Results and Discussion

The undrained monotonic triaxial compression test results are summarised and shown in Table 5.1. It presents (1) group of specimens, (2) mixture, (3) test number, (4) sand to rubber ratio, (5) initial void ratio e_o, (6) consolidated void ratio e, (7) deviator stress at failure q_f, (8) mean effective normal stress at failure p'_f, and (9) pore water pressure coefficient at failure A_f. For the undrained monotonic triaxial extension tests, the test results are summarised and shown in Table 5.2. According to ASTM D4767-95 (1996a), q_f for the compression test was obtained from the peak deviator stress or the deviator stress at 15% axial strain, whichever was the maximum.

Under a consolidation pressure of 100kPa it was anticipated that the test sand could not be crushed. This was evident when considering the void ratios before and after the consolidation, i.e., e_o = 0.676 and e = 0.668; e_o = 0.675 and e = 0.668, corresponding to the compression and extension tests, indicating that only slight change occurred.

The initial void ratio averaged from the compression and extension tests shown in Table 5.1 and Table 5.2, respectively, for SA having rubber content of 5% was 0.676 ([0.673+0.678]/2) . It slightly increased to 0.680 ([0.688+0.672]/2) when the rubber was increased to 10%, and continued to increase to 0.700 ([0.699+0.700] /2) and 0.748 ([0.753+0.742]/2) corresponding to the increase of rubber of 20% and 30%, respectively. When the rubber was increased to 40% and 50%, the averaged values of e_o were 0.761 ([0.763+0.758]/2) and 0.748 ([0.755+0.741]/2), respectively (see Figure 5.1). This non-proportional change of void ratio with respect to rubber content may owe to the moderate difference in size between the sand and the rubber, i.e., D_{50} of sand = 0.7mm, D_{50} of CT0515 = 1.2mm. Note that the void ratio of composite materials having different sizes such as sand mixed with gravel was also found to vary with varying mixtures (Evans and Zhou, 1995).

When SA mixtures having 5% and 10% rubber contents were consolidated, it was observed that the consolidated void ratios decreased just slightly from the initial state, as illustrated by Figure 5.2, indicating a small effect of the rubber in the sand-rubber matrix on the consolidated void ratio. In other words, the behaviour of the mixtures was still governed by the sand. For SA containing 20% rubber it was observed that the change of void ratio before and after the consolidation was greater compared to the specimens having 5% and 10% rubber. In addition, it was more apparent when the rubber was increased to 30% and above. The changes of void ratio in per cent were 1.48, 2.06, 5, 10.03, 15.39, and 21.52 corresponding to the SA mixtures having rubber contents of 5, 10, 20, 30, 40, and 50%, as can be observed in Figure 5.3. Note that the change of void ratio before and after the consolidation for pure sand was just 1.11%.

For SB having rubber contents of 5, 10, 20, 30, and 40%, the initial void ratio slightly decreased with increasing rubber content; however, it increased when the rubber was increased to 50% (see Figure 5.1). When consolidated, the void ratio was observed to gradually decrease as the rubber content was increased; but, the rate of the decrease

was smaller when the rubber was increased to 50%. The change of void ratio before and after consolidation for SB was observed to be similar to that of SA, except that the percentage change was smaller (see Figure 5.3).

For SC having rubber contents from 5% to 40%, both initial and consolidated void ratios were observed to gradually decrease. When the rubber was increased to 50%, the initial void ratio then slightly increased, compared to 40% rubber; whereas, the consolidated void ratio continued to decrease. For SD, both initial and consolidated void ratios were observed to gradually decrease with increasing rubber content. In addition, it was observed that the change of void ratios before and after the consolidation for SC and SD had patterns similar to those of SA and SB.

When considering Figure 5.2 illustrating the consolidated void ratios against varied rubber content, it can be seen that the relationships may be approximated as linear. This was done by setting the interception of zero rubber content at 0.668 (e for pure sand), and the linear equations for the mixtures were drawn, and shown below:

$$e = 0.668 - 0.0009RC \quad \text{(for SA)} \quad \textbf{(Eq. 5. 1)}$$

$$e = 0.668 - 0.0023RC \quad \text{(for SB)} \quad \textbf{(Eq. 5. 2)}$$

$$e = 0.668 - 0.0046RC \quad \text{(for SC)} \quad \textbf{(Eq. 5. 3)}$$

$$e = 0.668 - 0.0055RC \quad \text{(for SD)} \quad \textbf{(Eq. 5. 4)}$$

where RC is rubber content in per cent; the linear relationships between e and rubber content were plotted and are shown in Figure 5.4. Moreover, it was observed that the greater the size of rubber the steeper the gradient of the void ratio curves, indicating that the size of rubber significantly affected the increase and decrease of void ratios of sand-rubber mixtures. Thus, it was interesting to further normalise Eq. 5.1 to Eq. 5.4. This was done by rewriting the equations, as shown below:

$$e = 0.668 - Fe(RC) \quad \textbf{(Eq. 5. 5)}$$

where Fe is a factor that needed to be determined. However, it can be seen that the factor Fe depended on the size of rubber, in other word, depended on the particle size ratio D_r/D_s. Thus, the relationship between Fe and D_r/D_s was plotted and is shown

in Figure 5.5; subsequently, the fitted curve was obtained, and *Fe* was formulated, as shown below:

$$Fe = 0.0026 \ln\left(\frac{D_r}{D_s}\right) - 0.0004 \qquad \textbf{(Eq. 5. 6)}$$

then, Eq. 5.5 was rewritten, and became:

$$e = 0.668 - \left\{0.0026 \ln\left(\frac{D_r}{D_s}\right) - 0.0004\right\} RC \qquad \textbf{(Eq. 5. 7)}$$

Table 5. 1 Summary of undrained monotonic triaxial compression tests

Group	Mixture	Test No.	Sand : Rubber Ratio	e_o	e	q_f (kPa)	p' at failure (kPa)	A_f
S	Pure Sand	TC100S	100 : 0	0.676	0.668	955	672	-0.27
SA	Sand + CT0515	TC95SA	95 : 5	0.673	0.662	773	589	-0.30
		TC90SA	90 : 10	0.688	0.674	405	329	-0.23
		TC80SA	80 : 20	0.699	0.661	143	113	0.24
		TC70SA	70 : 30	0.753	0.671	105	76	0.57
		TC60SA	60 : 40	0.763	0.637	95	71	0.63
		TC50SA	50 : 50	0.755	0.582	108	74	0.58
SB	Sand + CT1030	TC95SB	95 : 5	0.673	0.664	857	638	-0.30
		TC90SB	90 : 10	0.680	0.667	646	492	-0.27
		TC80SB	80 : 20	0.659	0.632	241	188	-0.03
		TC70SB	70 : 30	0.645	0.600	145	113	0.25
		TC60SB	60 : 40	0.644	0.562	124	91	0.40
		TC50SB	50 : 50	0.679	0.549	119	78	0.52
SC	Sand + CT2060	TC95SC	95 : 5	0.651	0.642	902	649	-0.28
		TC90SC	90 : 10	0.627	0.619	816	604	-0.28
		TC80SC	80 : 20	0.570	0.556	710	531	-0.27
		TC70SC	70 : 30	0.549	0.525	344	242	-0.08
		TC60SC	60 : 40	0.496	0.456	241	170	0.05
		TC50SC	50 : 50	0.517	0.452	185	128	0.19
SD	Sand + CT4010	TC95SD	95 : 5	0.642	0.634	916	654	-0.27
		TC90SD	90 : 10	0.615	0.606	851	618	-0.28
		TC80SD	80 : 20	0.559	0.546	780	589	-0.29
		TC70SD	70 : 30	0.523	0.506	582	434	-0.24
		TC60SD	60 : 40	0.472	0.436	381	268	-0.11
		TC50SD	50 : 50	0.411	0.379	282	196	0.00

Table 5. 2 Summary of undrained monotonic triaxial extension tests

Group	Mixture	Test No.	Sand : Rubber Ratio	e_o	e	q_f (kPa)	p' at failure (kPa)	A_f
S	Pure Sand	TE100S	100 : 0	0.675	0.668	-221	174	-1.00
SA	Sand + CT0515	TE95SA	95 : 5	0.678	0.669	-177	165	-1.03
		TE90SA	90 : 10	0.672	0.658	-153	127	-0.84
		TE80SA	80 : 20	0.700	0.668	-103	76	-0.44
		TE70SA	70 : 30	0.742	0.674	-73	53	-0.02
		TE60SA	60 : 40	0.758	0.650	-68	51	0.06
		TE50SA	50 : 50	0.741	0.592	-79	47	0.01
SB	Sand + CT1030	TE95SB	95 : 5	0.670	0.662	-212	170	-1.00
		TE90SB	90 : 10	0.666	0.653	-188	161	-0.99
		TE80SB	80 : 20	0.647	0.623	-132	103	-0.69
		TE70SB	70 : 30	0.650	0.606	-101	71	-0.38
		TE60SB	60 : 40	0.628	0.566	-96	65	-0.30
		TE50SB	50 : 50	0.663	0.564	-95	56	-0.20
SC	Sand + CT2060	TE95SC	95 : 5	0.664	0.656	-237	180	-1.01
		TE90SC	90 : 10	0.619	0.611	-228	176	-1.00
		TE80SC	80 : 20	0.585	0.571	-213	162	-0.96
		TE70SC	70 : 30	0.557	0.538	-152	125	-0.83
		TE60SC	60 : 40	0.517	0.487	-124	88	-0.57
		TE50SC	50 : 50	0.507	0.453	-102	70	-0.37
SD	Sand + CT4010	TE95SD	95 : 5	0.650	0.643	-217	182	-1.04
		TE90SD	90 : 10	0.622	0.614	-211	179	-1.04
		TE80SD	80 : 20	0.578	0.567	-216	163	-0.96
		TE70SD	70 : 30	0.524	0.511	-210	163	-0.97
		TE60SD	60 : 40	0.494	0.473	-139	106	-0.71
		TE50SD	50 : 50	0.433	0.401	-111	68	-0.38

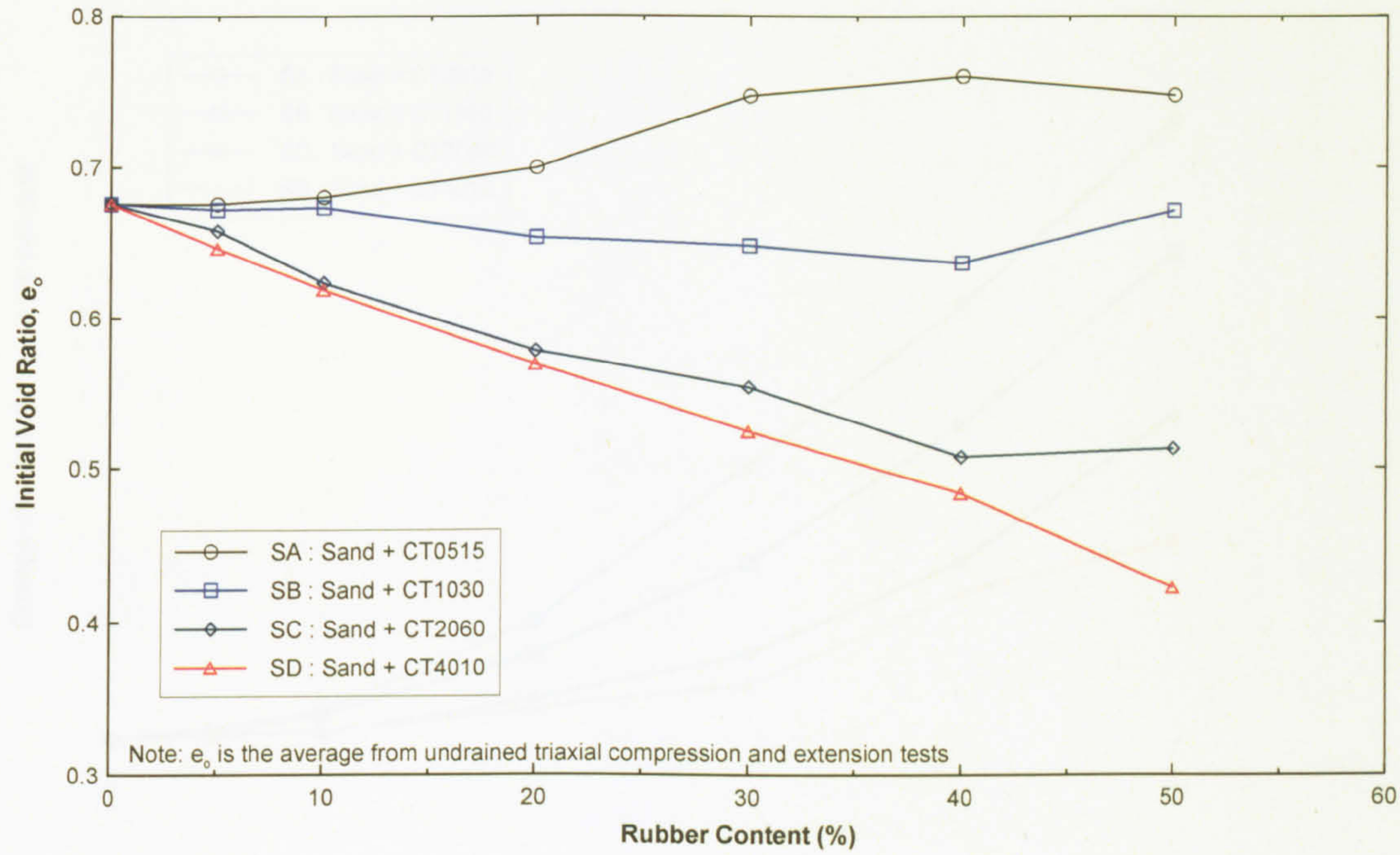

Figure 5. 1 Relationships between e_o and rubber content

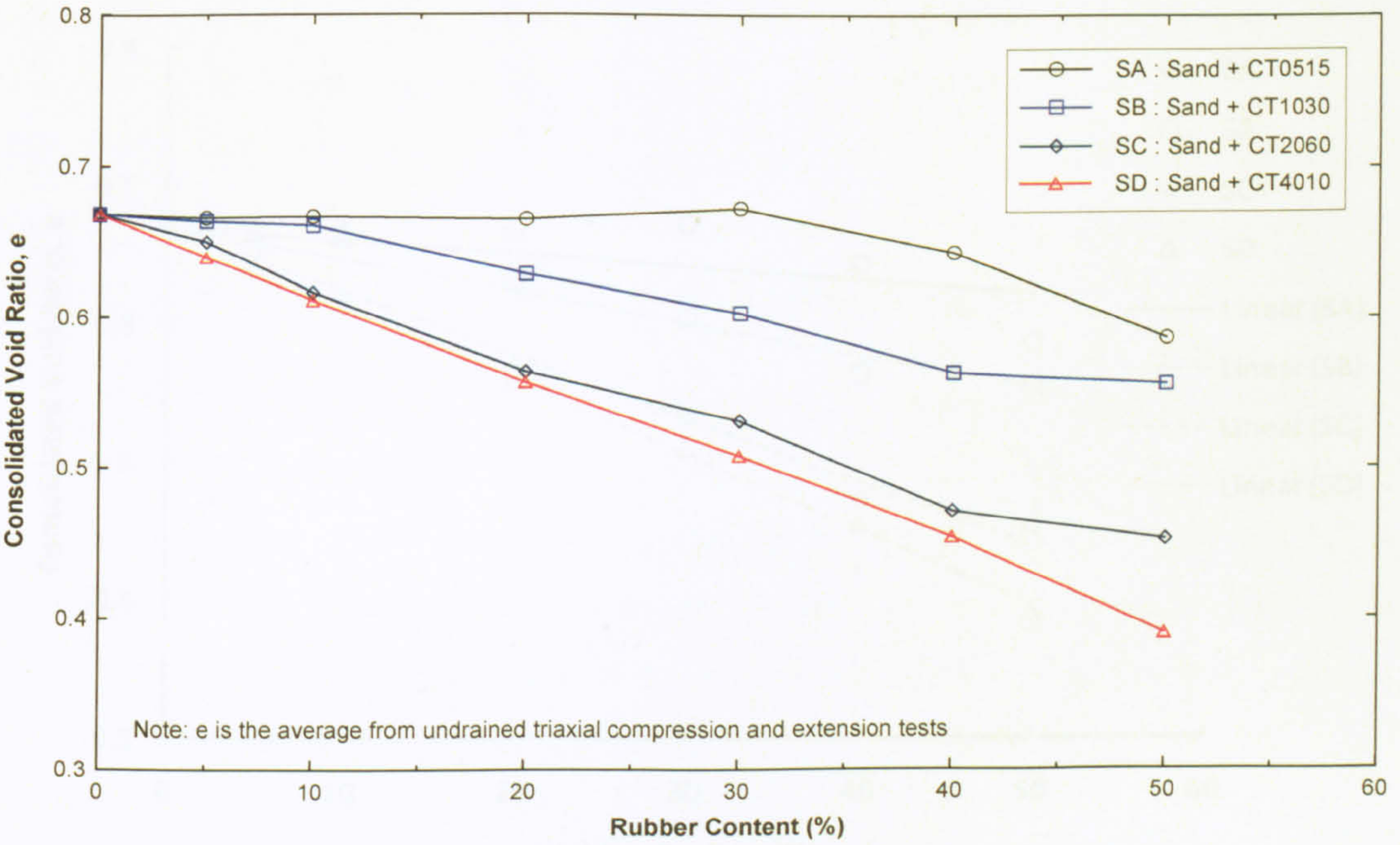

Figure 5. 2 Relationships between e and rubber content

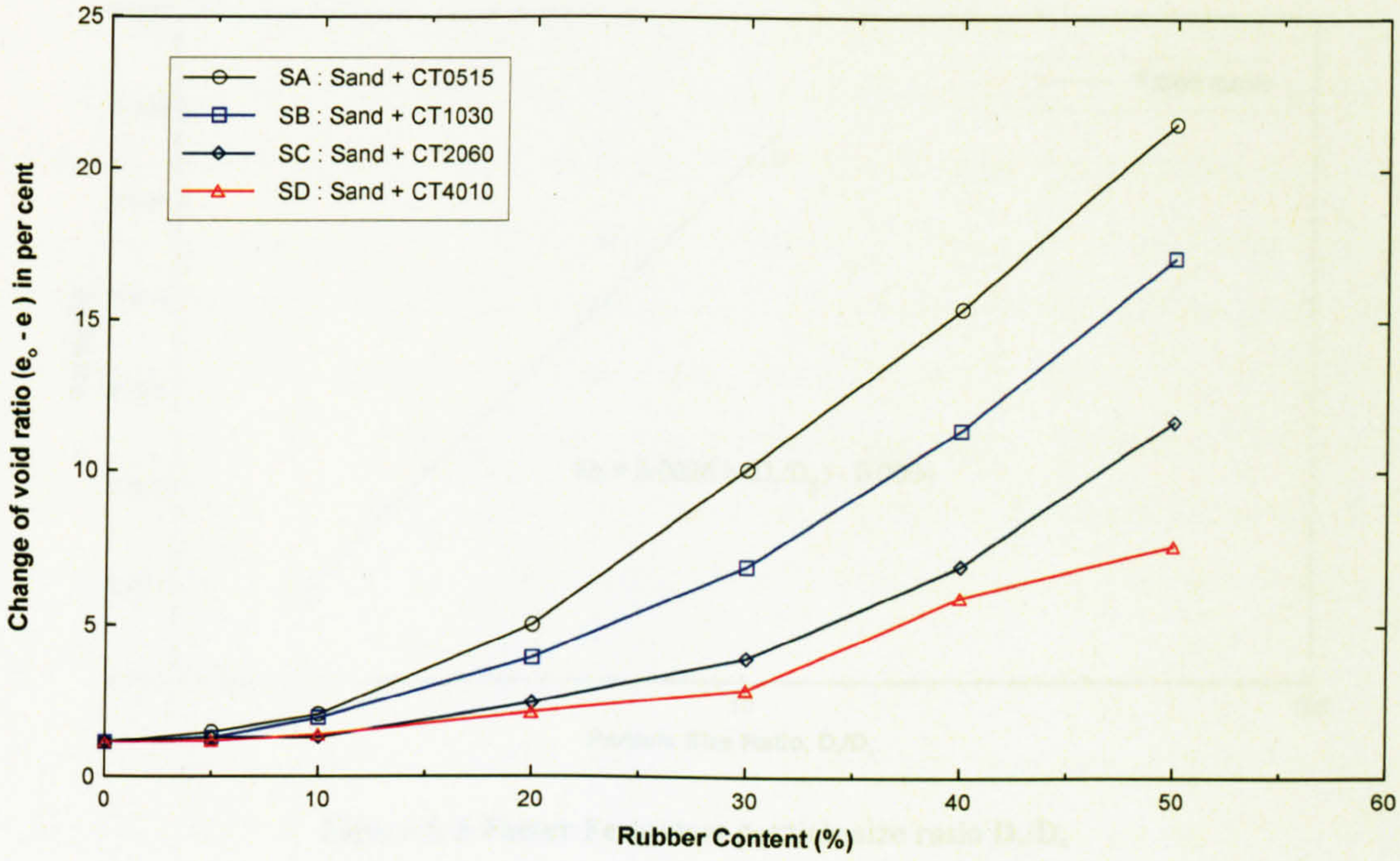

Figure 5. 3 Change of void ratio (e_o-e) versus rubber content

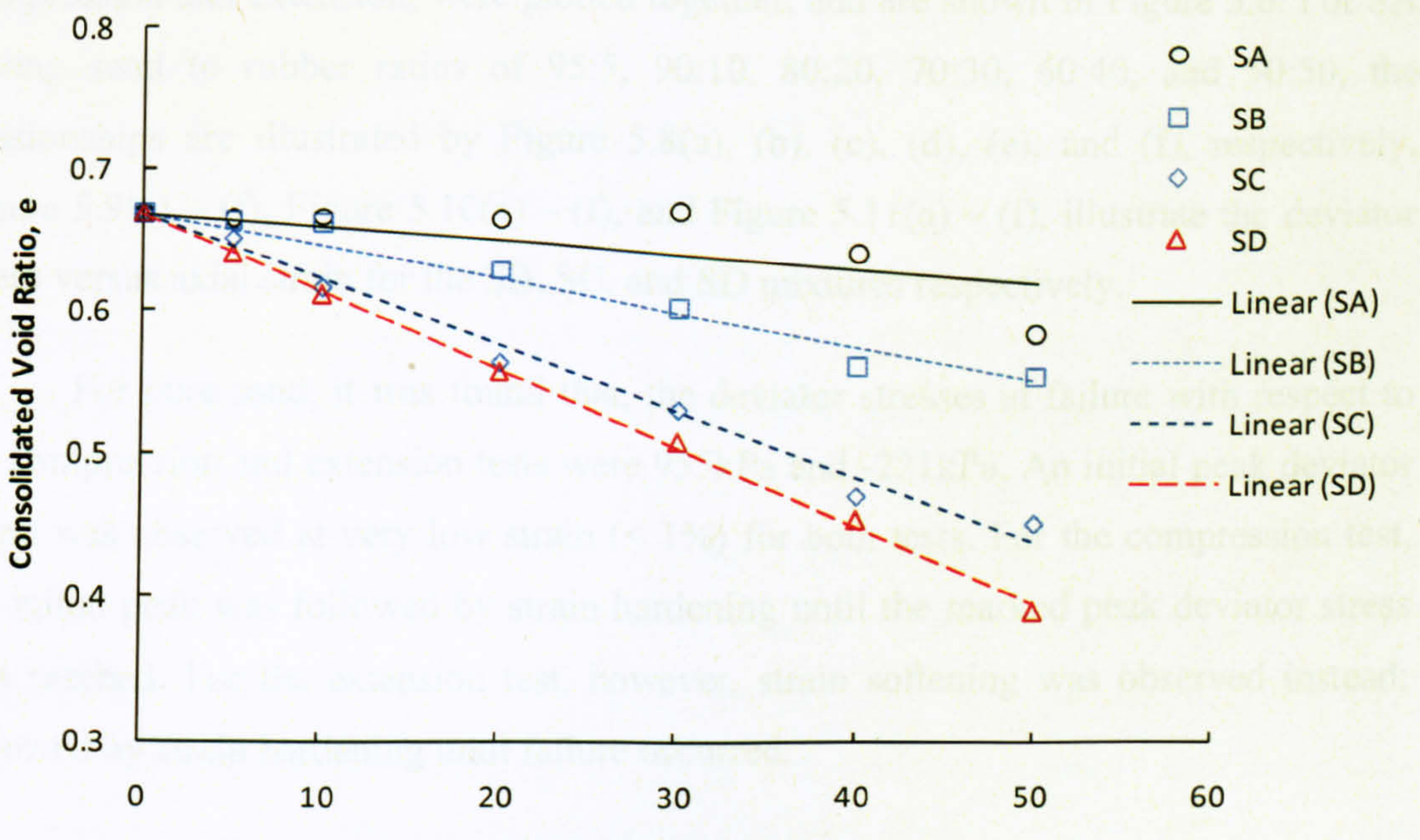

Figure 5. 4 Linear relationships between e and rubber content

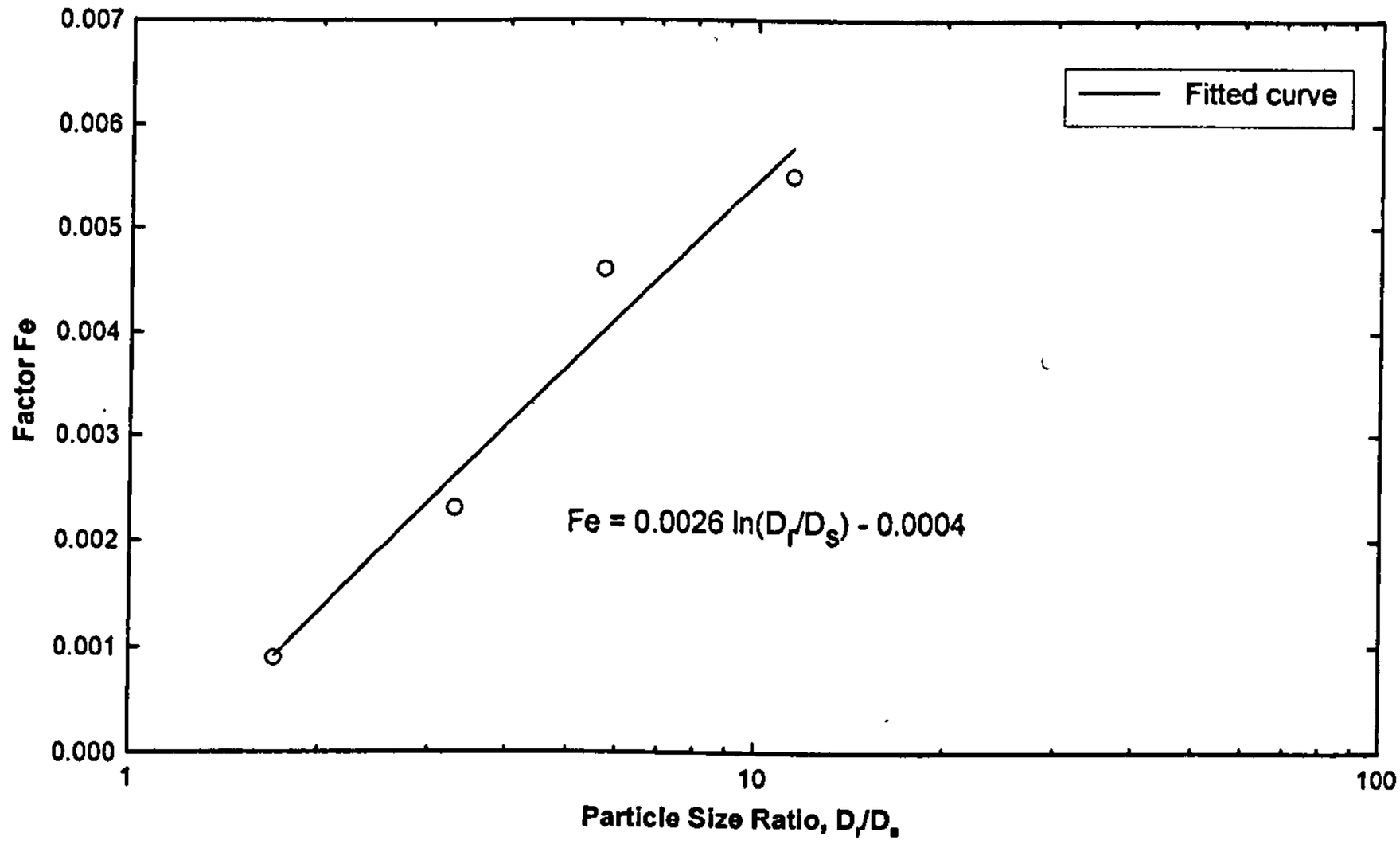

Figure 5. 5 Facter Fe against particle size ratio D_f/D_s

5.2.1 Stress - Strain Behaviour

The relationships between deviator stress and axial strain for pure sand, both in compression and extension, were plotted together, and are shown in Figure 5.6. For SA having sand to rubber ratios of 95:5, 90:10, 80:20, 70:30, 60:40, and 50:50, the relationships are illustrated by Figure 5.8(a), (b), (c), (d), (e), and (f), respectively. Figure 5.9(a) – (f), Figure 5.10(a) – (f), and Figure 5.11(a) – (f), illustrate the deviator stress versus axial strain for the SB, SC, and SD mixtures respectively.

For pure sand, it was found that, the deviator stresses at failure with respect to the compression and extension tests were 955kPa and -221kPa. An initial peak deviator stress was observed at very low strain (< 1%) for both tests. For the compression test, the initial peak was followed by strain hardening until the marked peak deviator stress was reached. For the extension test, however, strain softening was observed instead; followed by strain hardening until failure occurred.

As the peak deviator stress for pure sand in the compression test was reached (see stress-strain curve in Figure 5.6), a shear slip failure was also observed, which resembles the stress-strain behaviour of a dense specimen, as illustrated by Figure 5.7, showing a typical stress-strain curve of a shear test on a soil.

Furthermore, it was also observed that the failure for both compression and extension tests occurred when the axial strains reached approximately 8%. For the compression test, after failure, large strains were associated with a gradual decrease of the deviator stress. After 15% axial strain was reached, the deviator stress was slightly gradually decreased towards the constant, while the strain continued to decrease. This distinctive behaviour for saturated sand under undrained conditions has been recognised as a steady state (SS) (Castro, 1969; Zhang and Garga, 1997; Yamamuro and Lade, 1998). However, it was not quite reached at this point as the deviator stress was observed to continue gradually decreasing. The SS can also be seen for the extension test when the axial strain was approaching 15%.

A phase transformation (PT) at which the pore water pressure begins to decrease while the deviator stress increases (Ishihara *et al*, 1975; Hyodo *et al*, 1998) was observed when the axial strain was around 0.50%, for the compression test. In the case of extension test, the PT was observed when the axial strain reached -0.90%. Note that the PT for pure sand under the compression and extension tests is also illustrated in Figure 5.6.

For SA having a sand to rubber ratio of 95:5 (see Figure 5.8(a)), the stress-strain curves for the compression and extension tests exhibited the initial peak deviator stress at very low strain, similar to that of pure sand but at quite a lower strain. After that, strain hardening was observed until failure (peak) occurred at axial strains of 13.01% and -10.98% corresponding to the compression and extension tests, which were greater than that of 8% for pure sand. The q_f for the compression and extension tests were 773kPa and -177kPa, respectively. For the compression test, after 20% axial strain was reached, the deviator stress continued to noticeably decrease with increasing axial strain indicating that the SS was not quite reached. For the extension test, after the initial peak, the strain softening observed for pure sand was also observed. Subsequently, strain hardening was observed until the extension failure occurred at an axial strain of -10.98%. The PT points occurred when the axial strains reached 1% and -0.9% corresponding to the compression and extension tests.

When the rubber was increased to 10% for SA, the stress-strain behaviour was somewhat different to that of SA having 5% rubber. For example, for the compression test, after the initial peak, strain hardening was observed but at a rate that was lower

than that of the 95:5 mixture (see Figure 5.8(b)). Furthermore, even when the axial strain was as high as 20%, no peak deviator stress was observed. It should be noted that in this case q_f was taken as occurring at 15% axial strain. For the extension test, after the initial peak deviator stress occurred at very low strain, strain softening was observed for a short period, followed by the strain hardening towards the failure at about -13%. The q_f values for the compression and extension tests were 405kPa and -153kPa, respectively. The PT points for the compression and extension tests occurred when the axial strains reached 1.5% and -2%, respectively.

The stress-strain behaviour for SA containing 20% rubber (see Figure 5.8(c)) was observed to be quite different to those mixtures having 5% and 10% rubber. For the compression test, after the initial peak was reached at less then 1% axial strain, the deviator stress progressively increased with increasing axial strain. It can be seen that the curve after the initial peak was almost linear, and no peak deviator stress was observed. This distinctive behaviour suggests the influence of the rubber in sand-rubber mixtures was more pronounced when the rubber was increased to 20%. Another point that should be noted is that the rate of increase of the deviator stress is much smaller than that of the 95:5 and 90:10 mixtures, indicating the highly elastic properties of the rubber. For the extension test, strain softening was observed just after the initial peak deviator stress was reached. The deviator stress then gradually decreased almost linearly with a decrease in axial strain, similar to that observed for the compression test. The q_f values for the compression and extension tests were 143kPa and -103kPa, respectively. It is apparent that the difference between these two values of q_f is smaller than those mixtures having smaller quantities of rubber. The PT points for the compression and extension tests were observed when the axial strains reached about 3.55% and -2%, respectively.

For SA when the rubber was increased to 30% (see Figure 5.8(d)) the stress-strain behaviour was almost identical to that of SA having 20% rubber. This includes the characteristics of initial peak deviator stress, the linearity of the stress-strain curve, and the strain softening for the extension test. However, the deviator stress at failure was lower than that of SA having 20% rubber, i.e., 105kPa and -73kPa corresponding to compression and extension tests. The PT for the compression and extension tests occurred when the axial strains were 7.2% and -3.62%, respectively.

For SA having rubber content of 40% (see Figure 5.8(e)), it was observed that the stress-strain characteristics were quite similar to those of SA having 20% and 30% rubber, except that for the compression test the peak deviator stress now was observed when the axial strain reached 17.91%. It was also observed that q_f values for the compression and extension tests were very similar to that of SA having 30% rubber, i.e., 95kPa and -68kPa, respectively. The PT for the compression and extension tests occurred when the axial strains reached 11.59% and -6.33%, respectively.

For SA having 50% rubber (see Figure 5.8(f)), the stress-strain behaviour was observed to be similar to that of SA having rubber contents of 20%, 30%, and 40%, except that for the compression test no initial peak deviator stress was observed. However, the deviator stresses at failure for the compression and extension tests were 108kPa and -79kPa, which were slightly greater than those for SA having rubber contents of 30% and 40%, but still lower than that of SA having 20% rubber. The PT points for the compression and extension tests were observed when the axial strains reached 13.89% and -5.34%, respectively.

The stress-strain behaviour for SB having 5% rubber (see Figure 5.9(a)) was similar to that of SA having the same rubber content. However, it was observed that q_f values for the compression and extension tests were somewhat greater, i.e., 857kPa and -212kPa, respectively, compared to q_f for SA of 773kPa and -177kPa. This comparison indicates that when the test sand was mixed with bigger tyre chips, q_f was greater.

In addition, the PT for both compression and extension tests was also at axial strains similar to those for SA. For SB containing 10% rubber (see Figure 5.9(b)), the stress-strain behaviour was quite comparable to that of SA having the same rubber content. For the compression test, however, SB exhibited a peak deviator stress when the axial strain reached 19.02%, whereas for SA, this was not observed. Furthermore, q_f for both compression and extension tests was noticeably larger compared to that for SA. The PT for both compression and extension tests was met at a strain level similar to that of SA.

For SB having a rubber content of 20% (see Figure 5.9(c)), the stress-strain curves for both compression and extension tests were comparable to those of SA having the same rubber content. One distinction should however be noted that, both

compression and extension tests exhibited a peak deviator stress at very large strains, while SA did not. Also, the q_f values for both compression and extension tests were greater than those of SA, i.e., q_f for SB = 241kPa and -132kPa, respectively, compared to 143kPa and -103kPa for SA. The PT for the compression test was met at much smaller strain levels, compared to SA; nonetheless, for the extension test, it was met at a similar strain level. For SB having a rubber content of 30% (see Figure 5.9(d)), the similarities between SA and SB having 20% rubber content were also observed. This includes the peak deviator stress, the deviator stress at failure, and the PT characteristics.

For SB having 40% rubber (see Figure 5.9(e)), the stress-strain behaviour for the compression test was quite similar to that of SA having the same amount of rubber; but, the PT was at a smaller strain and q_f was greater. For the extension test, a peak deviator stress was observed at an axial strain around -12.25%, while it was not observed for SA. When the rubber added was the maximum of 50% (see Figure 5.9(f)), the stress-strain curves for SB were very similar to those for SA having the same rubber content. However, q_f obtained from the compression and extension tests were slightly greater, i.e., q_f for SB and SA = 119, -95kPa and 108, -79kPa, respectively.

For SC having 5% rubber (see Figure 5.10(a)), the stress-strain behaviour for both compression and extension tests was observed to be quite similar to that of SA and SB having the same rubber content. However, it was observed that the peak deviator stresses for both triaxial compression (TC) and triaxial extension (TE) were slightly greater than those of SB. Another point that should be noted is that the peak deviator stresses were met at a slightly smaller strain, compared to SA and SB. When the rubber was increased to 10%, the stress-strain curve for the compression test (see Figure 5.10(b)) was quite different to those of SA and SB. The peak deviator stress was met at around 10.95% axial strain, while it was met when the axial strain was 19.02% for SB, and none was observed for SA. For the extension test, however, the stress-strain curve was quite comparable to that of SA and SB. One distinction that should be noted is that q_f for both TC and TE were greater than SB and SA. However, PT for both TC and TE were observed at similar strain levels as occurred for SA and SB.

For SC having 20% rubber content (see Figure 5.10(c)), the stress-strain curve for the compression test exhibited a peak deviator stress at 18.13% axial strain, whereas

it was not observed for SA and SB. It can be seen that q_f is markedly greater than that of SA and SB having the same amount of rubber, i.e., q_f values for TC and TE were 344kPa and -152kPa, respectively, compared to 105kPa and -73kPa; 145kPa and -101kPa corresponding to SA and SB. However, the PT for both TC and TE were observed at similar strain levels as SA and SB.

Compared with SA and SB having the same rubber content of 30%, SC (see Figure 5.10(d)) exhibited quite different stress-strain behaviour. After the initial peak deviator stress was reached at an axial strain smaller than 1%, the deviator stress increased almost linearly with increasing axial strain. The rate of increase was observed to be much higher compared to both SA and SB. As a result, q_f values for TC and TE were markedly higher than those of SA and SB. However, a peak deviator stress was not observed even after the axial strain reached 20% and higher. Note that the peak deviator stress was observed for SB at around 15.3% axial strain, but was not observed for SA. Moreover, the PT for TC and TE were met at the axial strains smaller than those observed for SA and SB.

For SC having rubber contents of 40% (see Figure 5.10(e)) and 50% (see Figure 5.10(f)), the stress-strain characteristics were quite comparable to those of SA and SB having the same rubber amount. However, q_f values for TC and TE were greater, and the PT for TC was at smaller axial strains.

For SD having rubber contents of 5%, 10%, 20%, 30%, 40%, and 50% (see Figure 5.11(a), (b), (c), (d), (e), and (f), respectively), the stress-strain behaviour was observed to be very similar to that for SC having the same amount of rubber, except that q_f values were greater.

As just discussed, it can be seen that even when the sand to rubber ratios were the same; if the size of tyre chips added was different the stress-strain characteristics were somewhat dissimilar. This aspect can be graphically observed by plotting the stress-strain curves for a particular mixture having various sizes of rubber. Thus, the stress-strain characteristics for the SA mixtures, SB, SC, and SD, having 5% rubber were plotted altogether, and illustrated by Figure 5.12. For the SA mixtures, SB, SC, and SD, having 10%, 20%, 30%, 40%, and 50% rubber contents, the stress-strain curves are illustrated by Figures 5.13 – 5.17, respectively.

In addition, Figure 5.18 illustrates the stress-strain curves for SA with all sand-rubber ratios, including pure sand, in order that the stress-strain characteristics of all sand to rubber ratios as well as pure sand can be easily examined and compared. For SB, SC, and SD, the stress-strain curves for all sand to rubber ratios are illustrated by Figure 5.19, Figure 5.20, and Figure 5.21, respectively.

Overall, comparing the deviator stress at failure for SA, SB, SC, and SD having the same rubber content, it can be seen that the order from smaller to greater is SA, SB, SC, and SD, as illustrated by Figure 5.22. This suggests that the size of tyre chips mixed with the sand influences the shear strength of the mixture. This may owe to the nature of mixing two materials having different sizes, as already discussed. Regardless of the size of rubber mixed, the peak deviator stress was observed only when the rubber content was 20% and smaller. When the rubber portion was 30% and higher, almost every specimen did not exhibit a peak deviator stress. It may be concluded that for mixtures containing up to 20% rubber, the sand mainly influenced the stress-strain characteristics. However, when the rubber was increased to 30% and more, the stress-strain behaviour was then more dominated by the rubber. This is obvious when considering the deviator stresses at failure for SA and SB having rubber contents 30% and higher in that they were almost the same. In addition, for the mixtures containing rubber contents of 30% and higher, the failure conditions in the compression test were quite similar to those illustrated by Figure 5.7 (plastic contraction failure).

It was interesting to compare the shear strength characteristics of the mixtures to other studies. Unfortunately, so far most studies involving sand mixed with rubber have been investigated under drained conditions. This is because the size of recycled rubber is quite large thereby the pore water pressure can dissipate almost instantaneously when loaded. Thus, the comparison was not done.

However, there have been studies indicating that the addition of rubber increases the shear strength of sand. For example, the results from direct shear tests show that the addition of shredded tyres increase the shear strength of Portage sand, i.e., the initial friction angle of the mixtures is 67° compared to 34° for unreinforced sand (Foose *et al.*, 1996). The similar findings were also found by Ghazavi (2004). Furthermore, Ghazavi (2004) reported that an apparent cohesion was obtained when specimens containing rubber grains.

When considering the behaviour of the mixtures at a grain level, Ghazavi (2004) explained that during shearing sand grains tend to penetrate into the rubber grains resulting in an induced lateral pressure imposed from the sand to the rubber. Hence, there are two components, namely (1) the lateral pressures induced from sand grains to rubber, and (2) the friction mobilised between sand-rubber, rubber-rubber, and sand-sand, that cause the friction angle to increase.

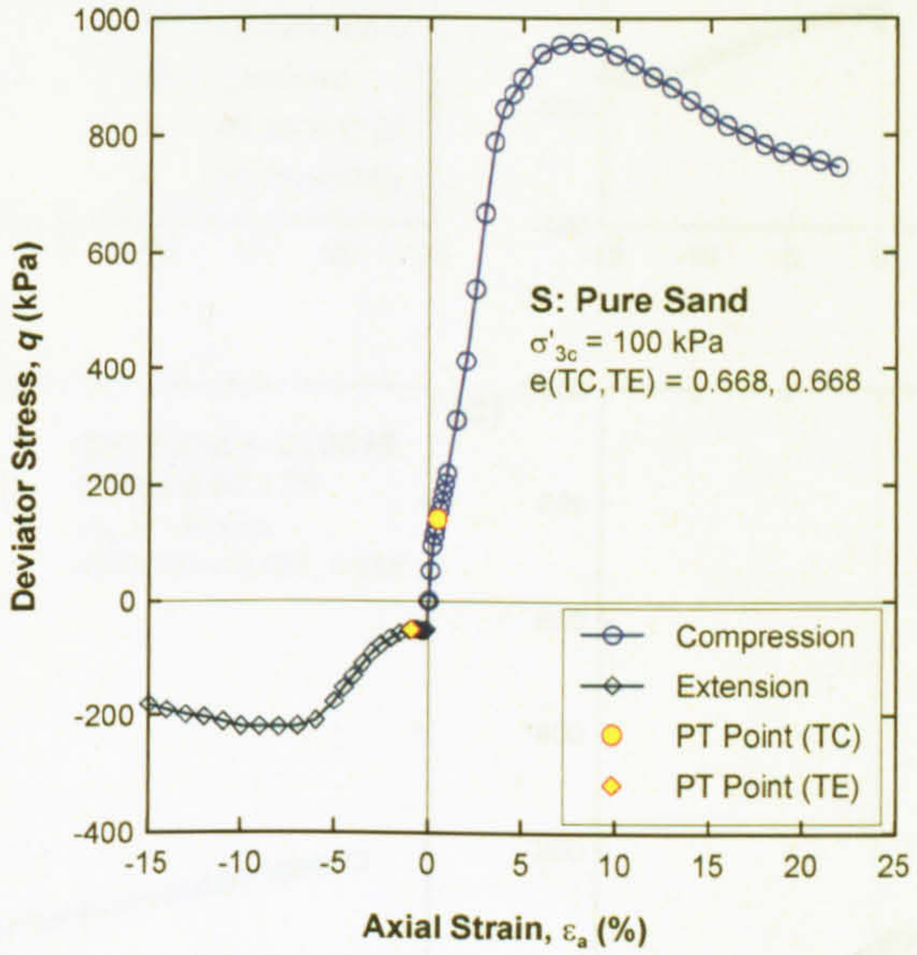

Figure 5. 6 Deviator stress versus axial strain for pure sand, S

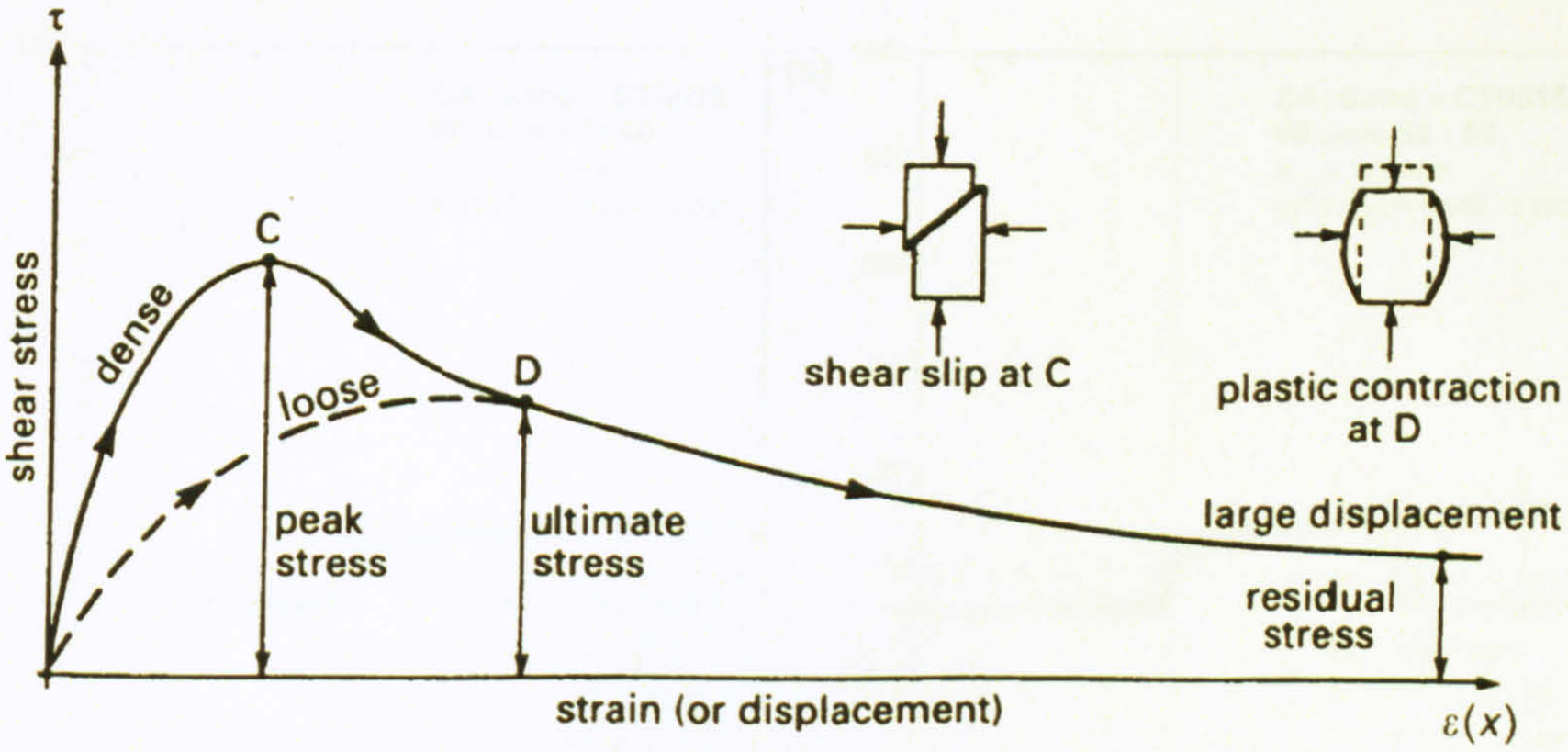

Figure 5. 7 Stress-strain curve of shear test on soil (after Whitlow, 1995)

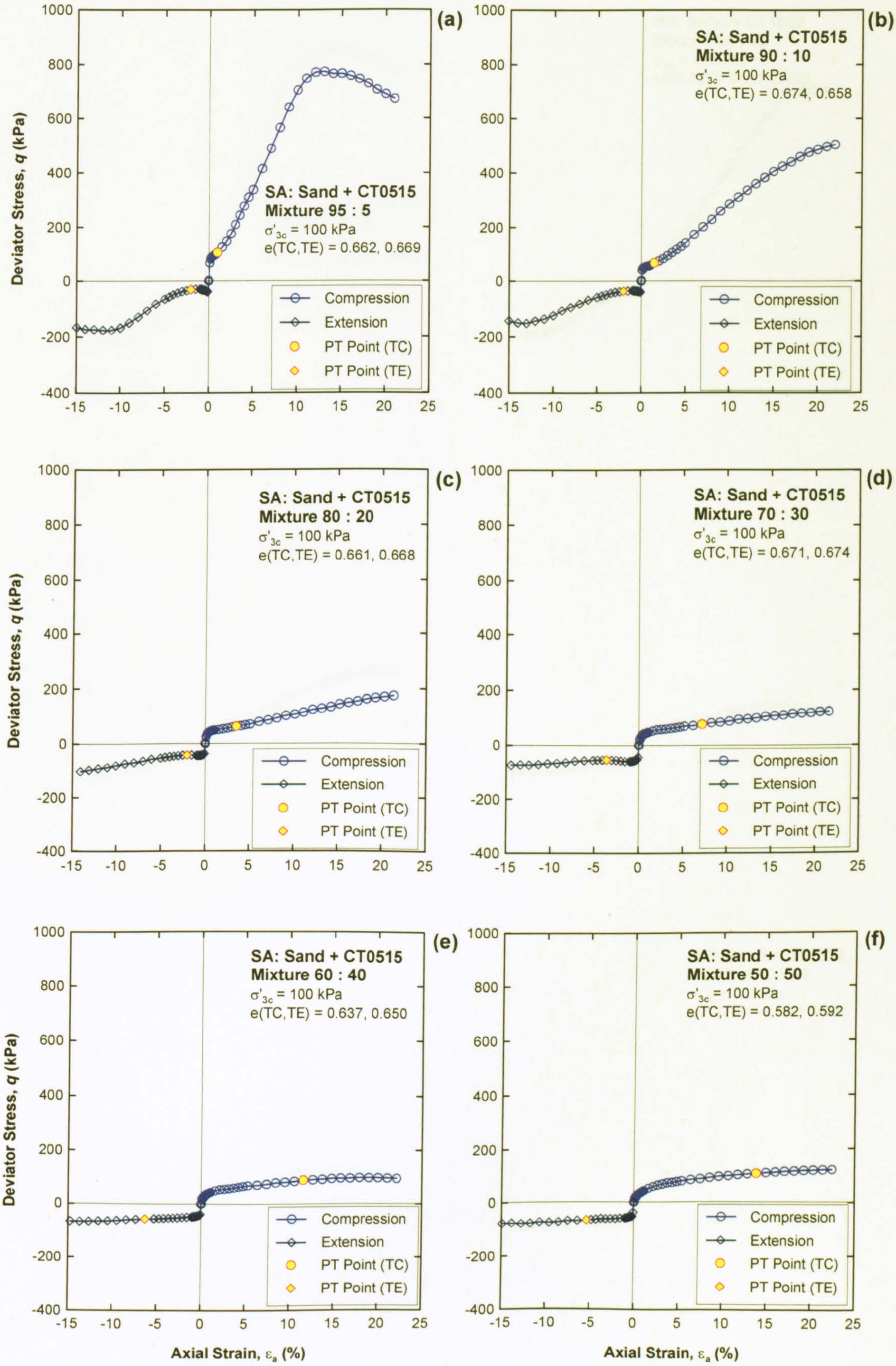

Figure 5. 8 Deviator stress versus axial strain for Sand + CT0515, SA

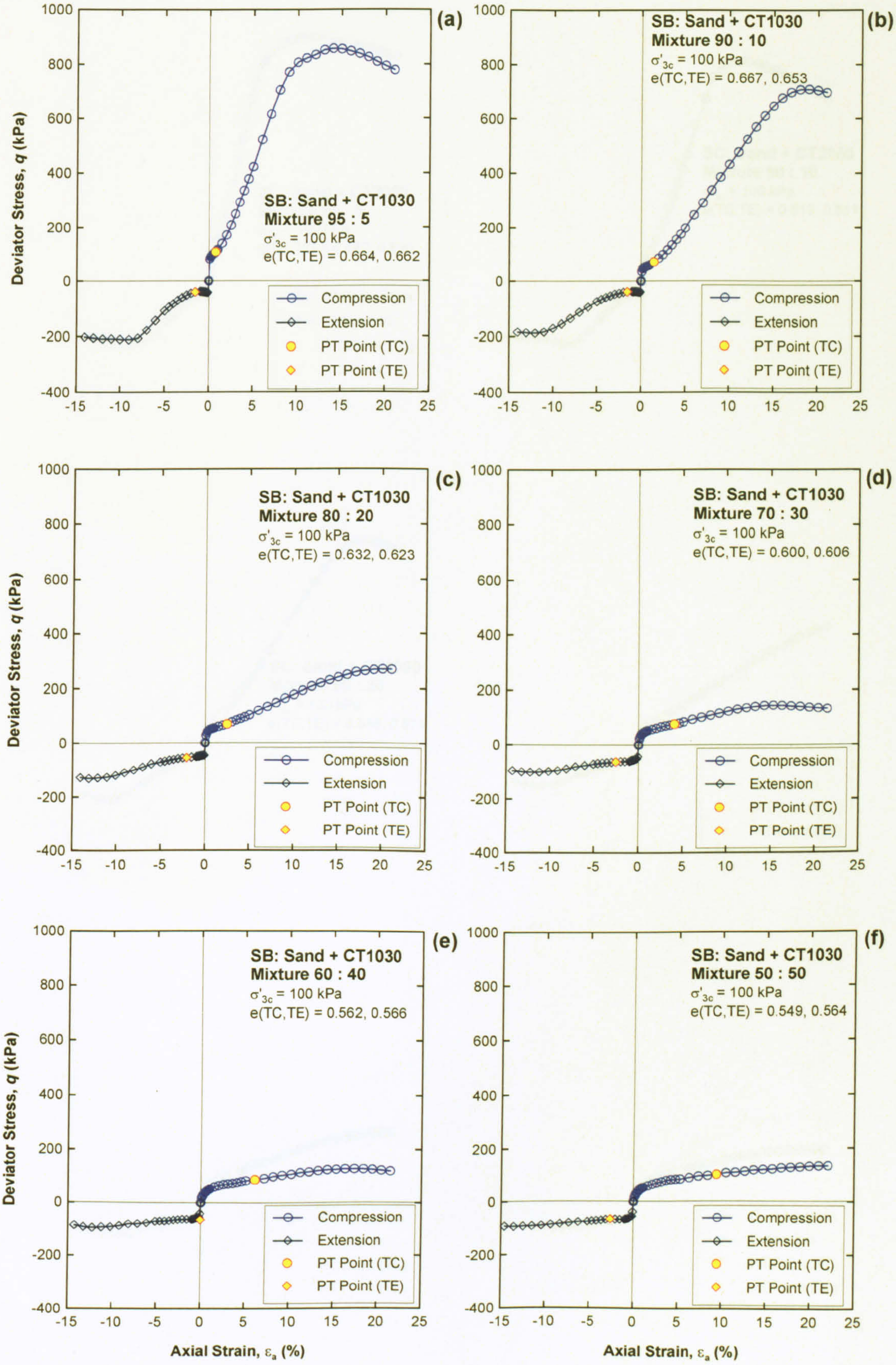

Figure 5. 9 Deviator stress versus axial strain for Sand + CT1030, SB

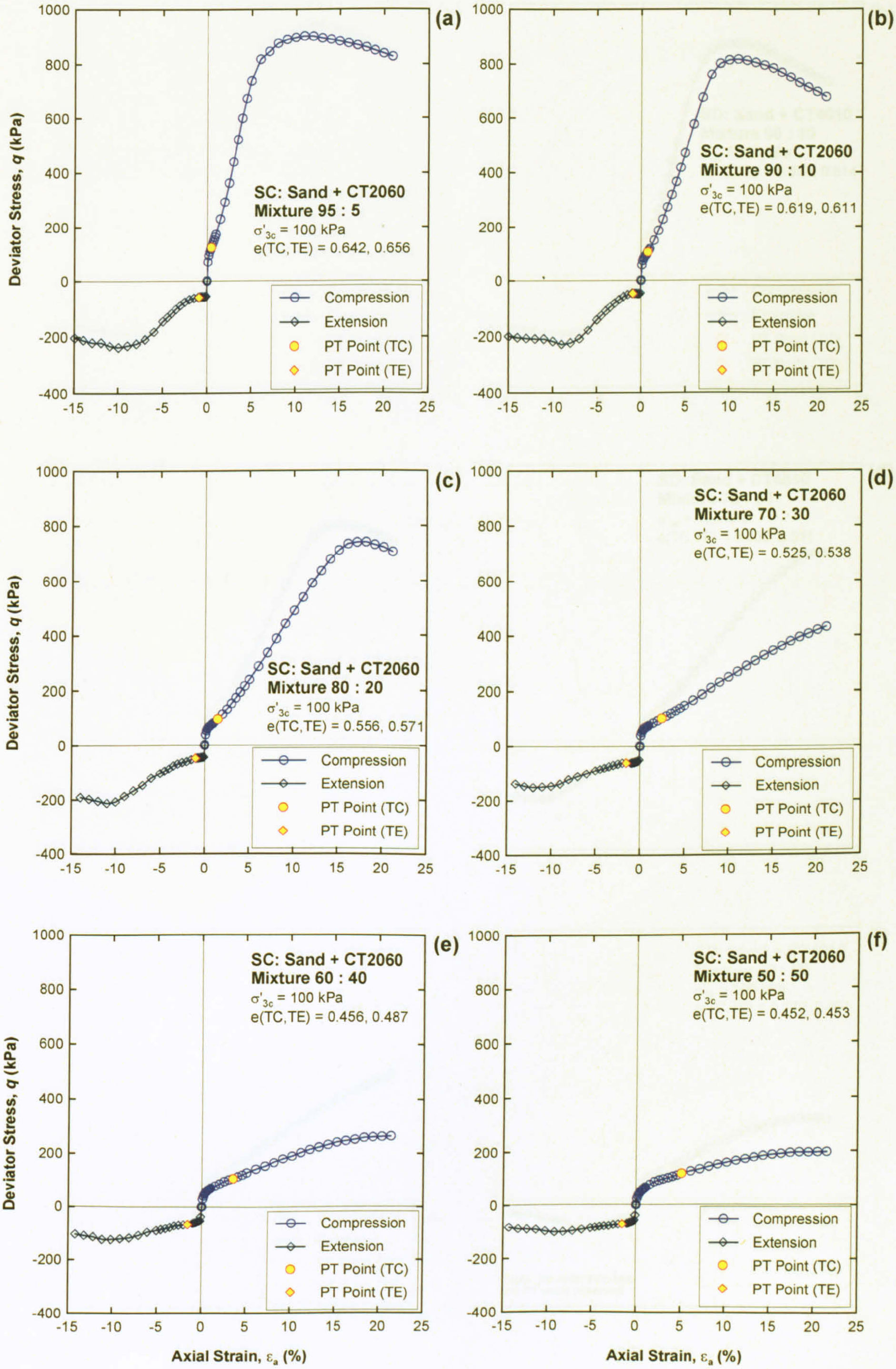

Figure 5. 10 Deviator stress versus axial strain for Sand + CT2060, SC

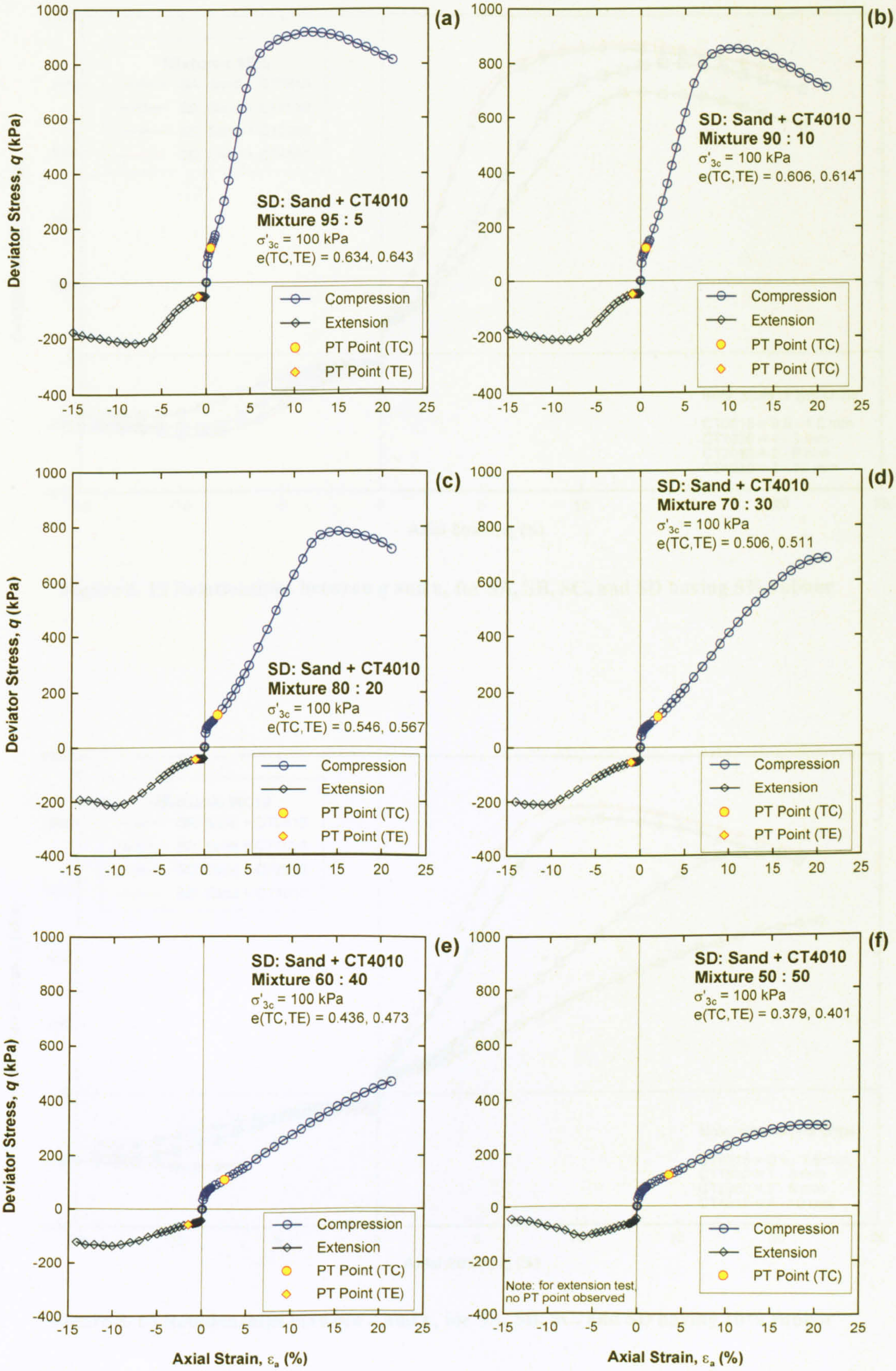

Figure 5. 11 Deviator stress versus axial strain for Sand + CT4010, SD

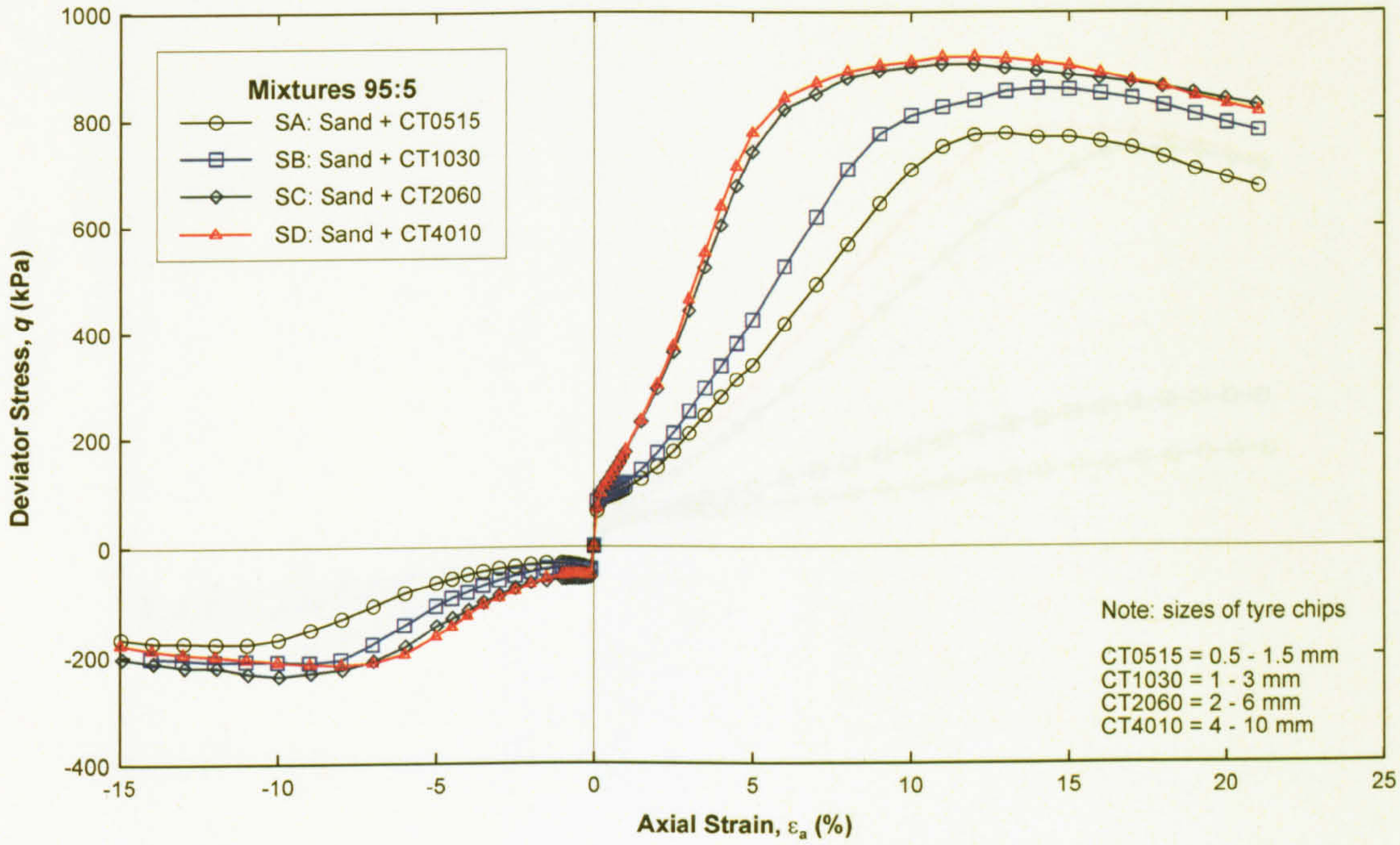

Figure 5. 12 Relationships between q and ε_a for SA, SB, SC, and SD having 5% rubber

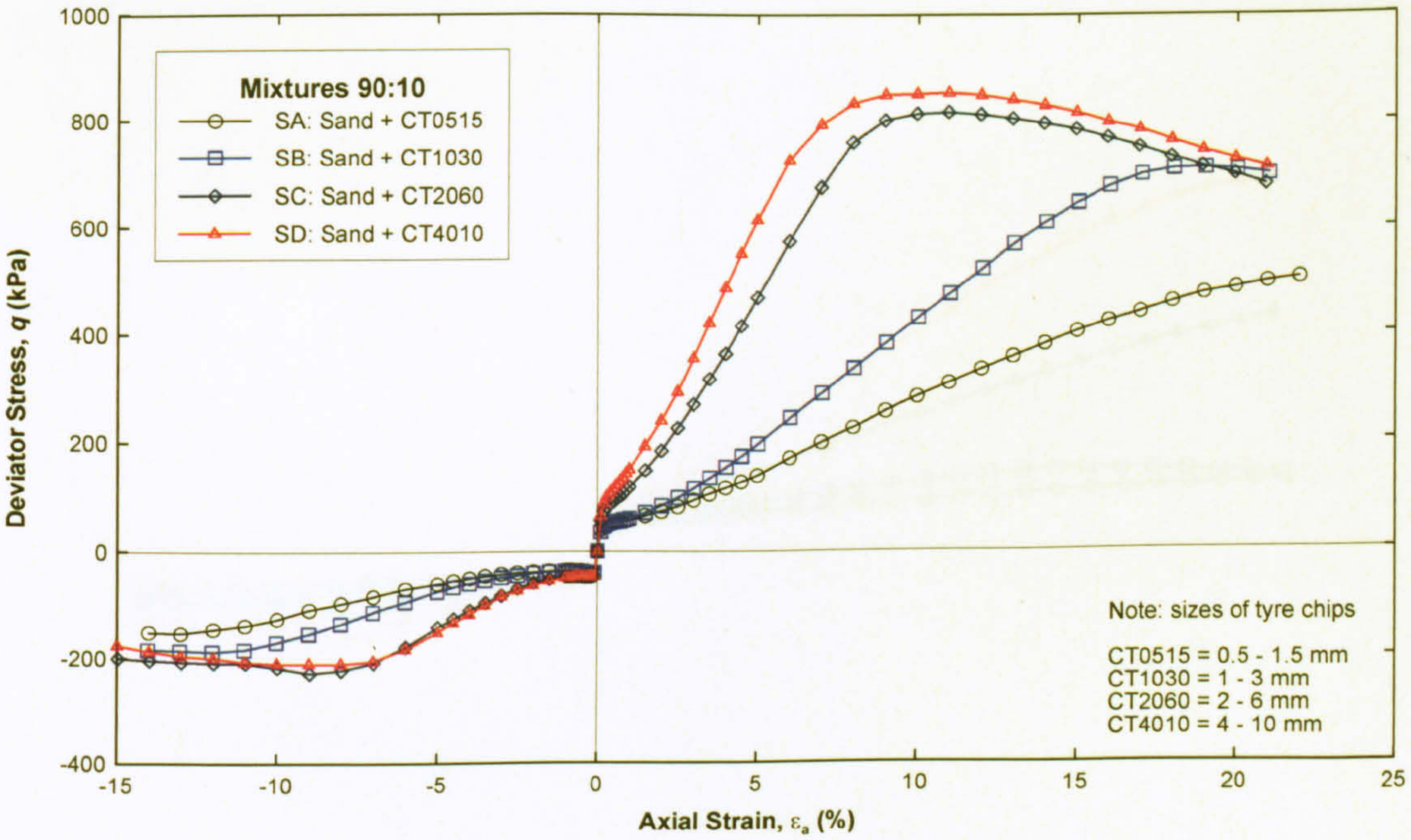

Figure 5. 13 Relationships between q and ε_a for SA, SB, SC, and SD having 10% rubber

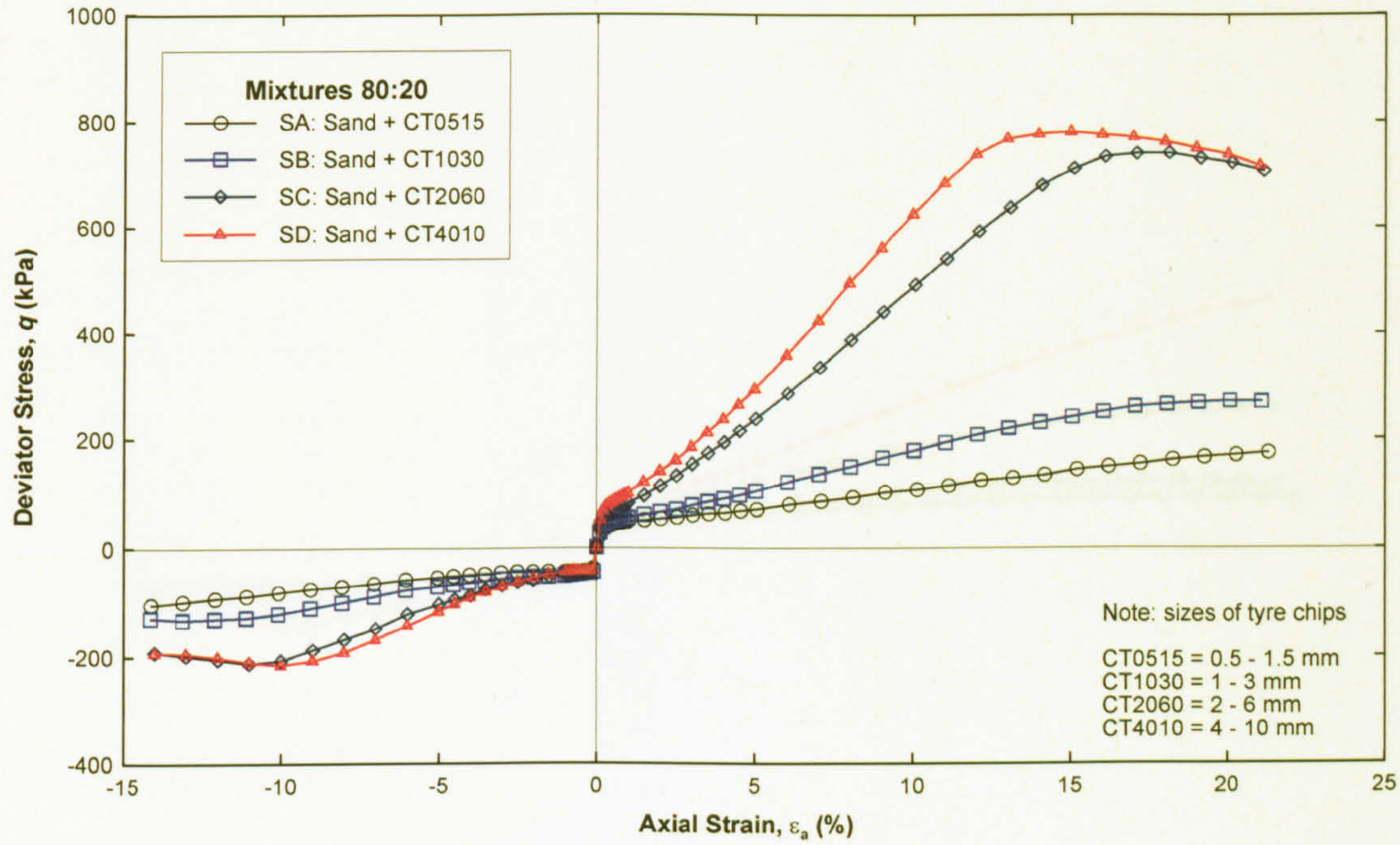

Figure 5. 14 Relationships between q and ε_a for SA, SB, SC, and SD having 20% rubber

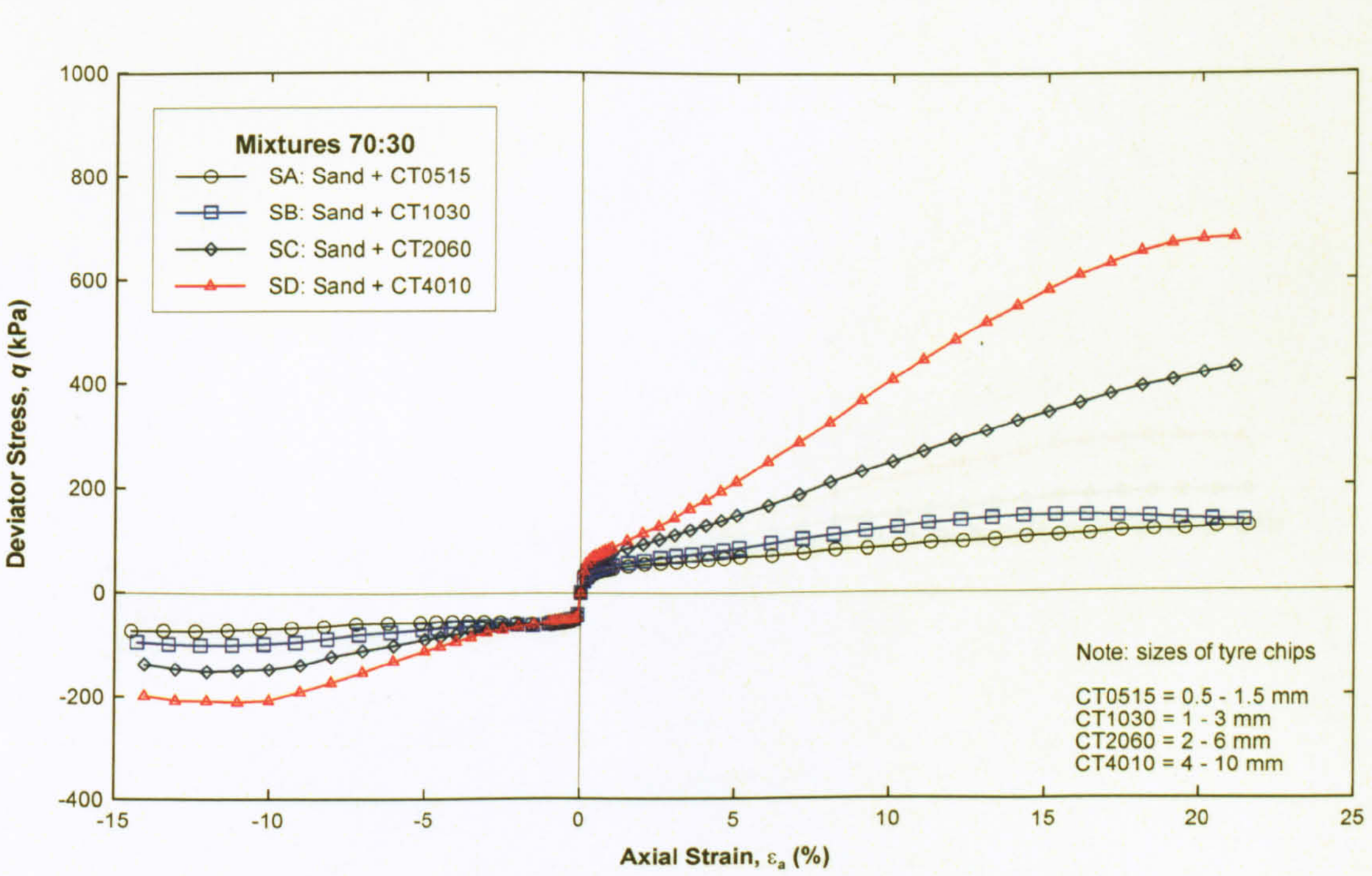

Figure 5. 15 Relationships between q and ε_a for SA, SB, SC, and SD having 30% rubber

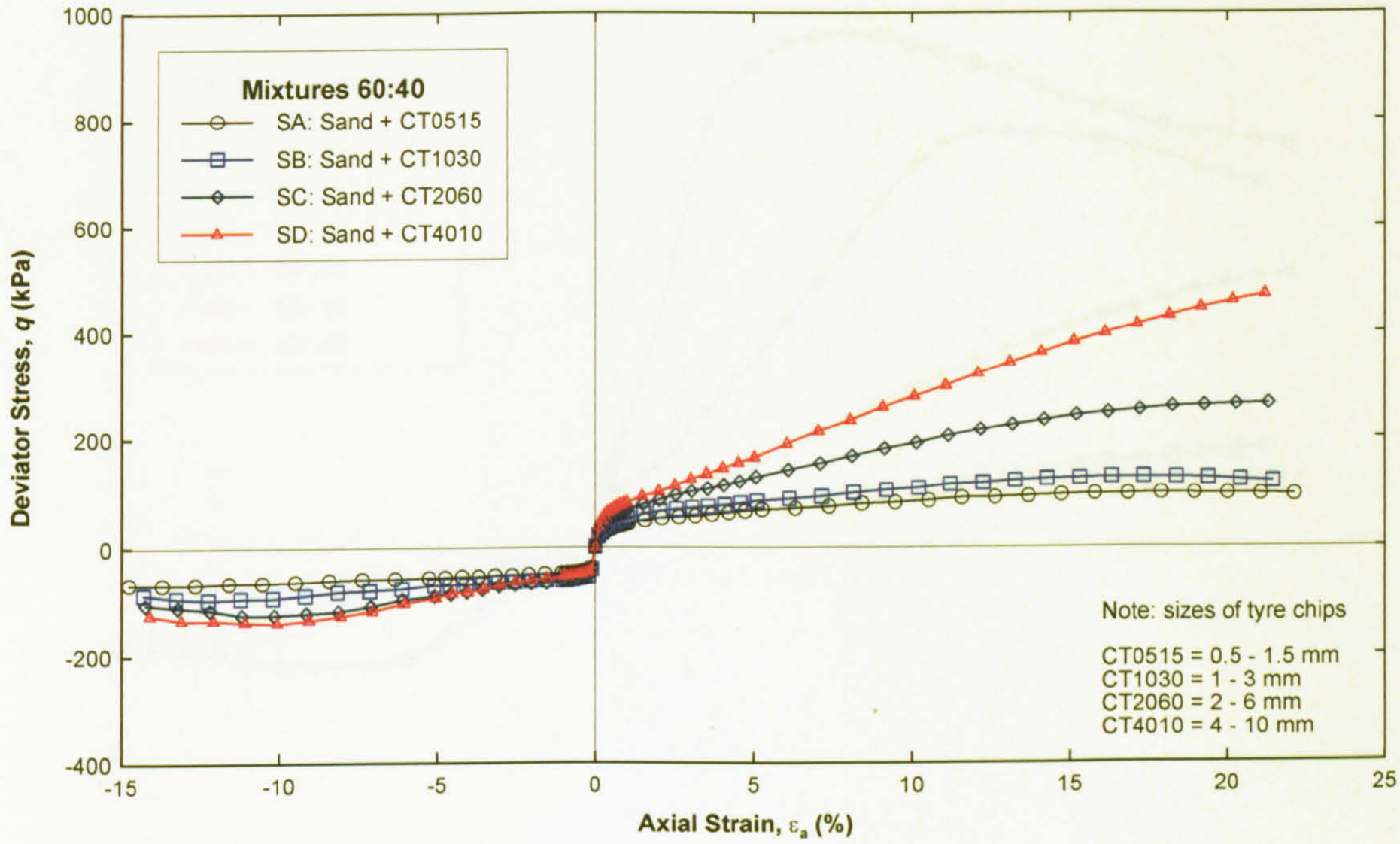

Figure 5. 16 Relationships between q and ε_a for SA, SB, SC, and SD having 40% rubber

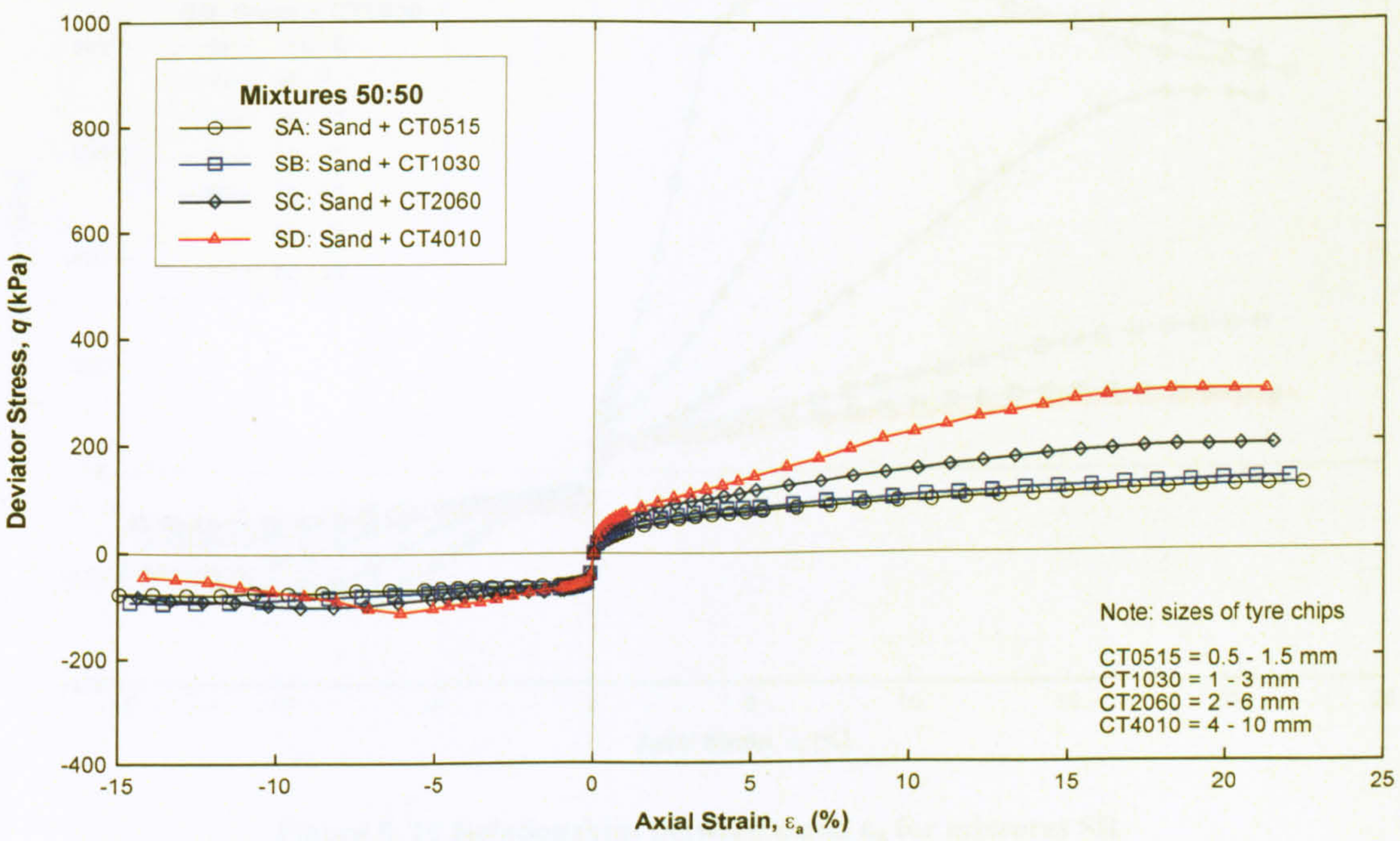

Figure 5. 17 Relationships between q and ε_a for SA, SB, SC, and SD having 50% rubber

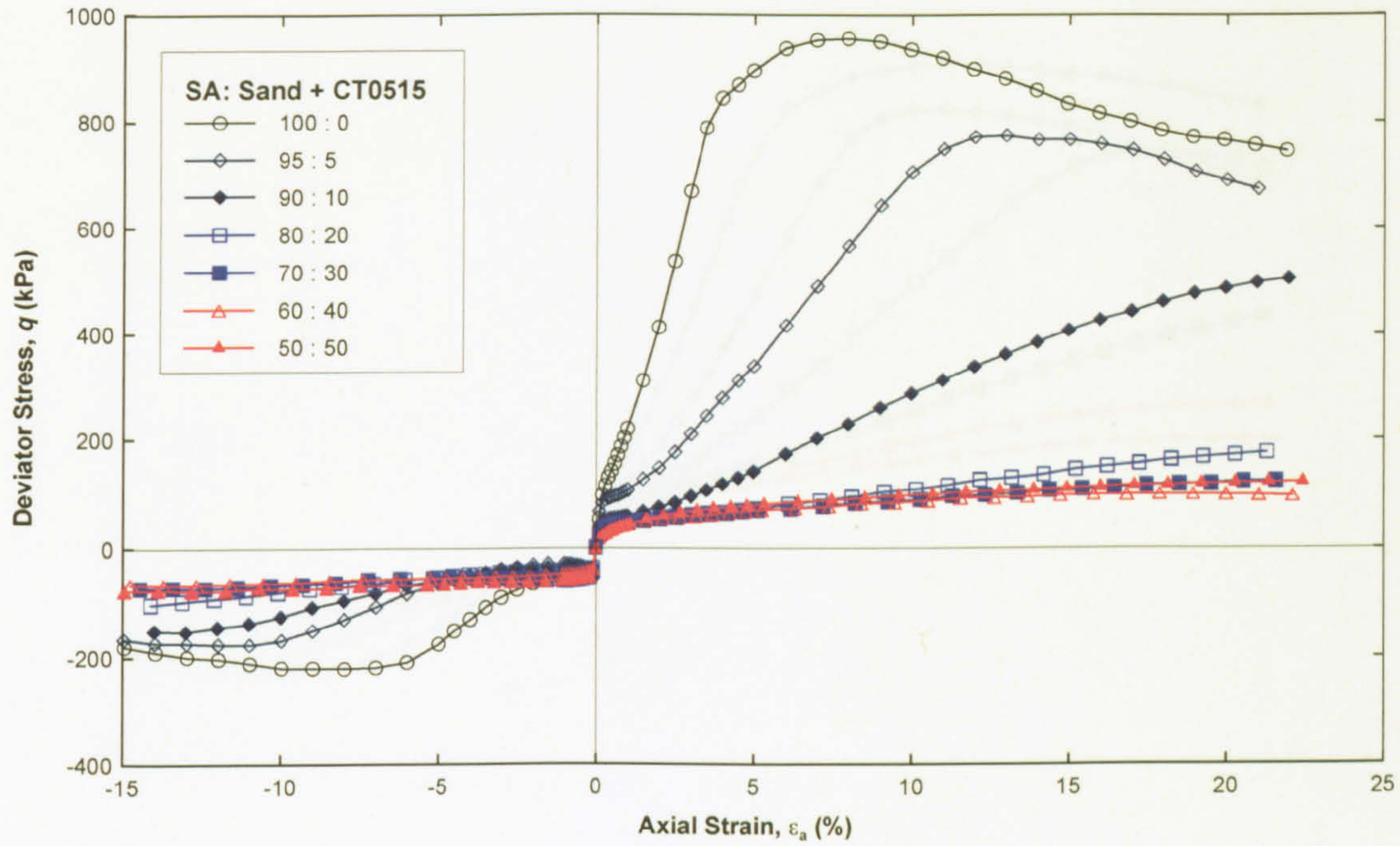

Figure 5. 18 Relationships between q and ε_a for mixtures SA

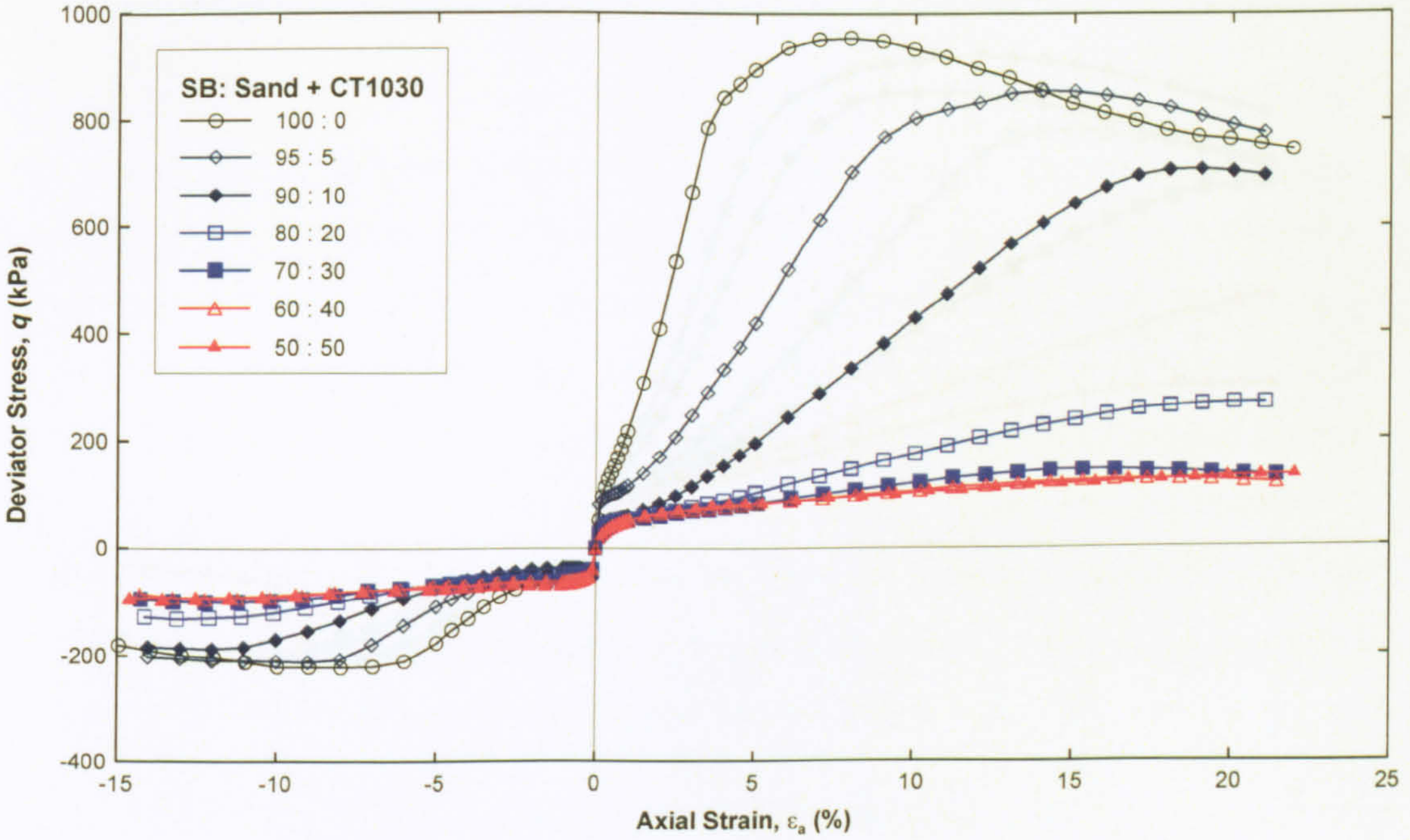

Figure 5. 19 Relationships between q and ε_a for mixtures SB

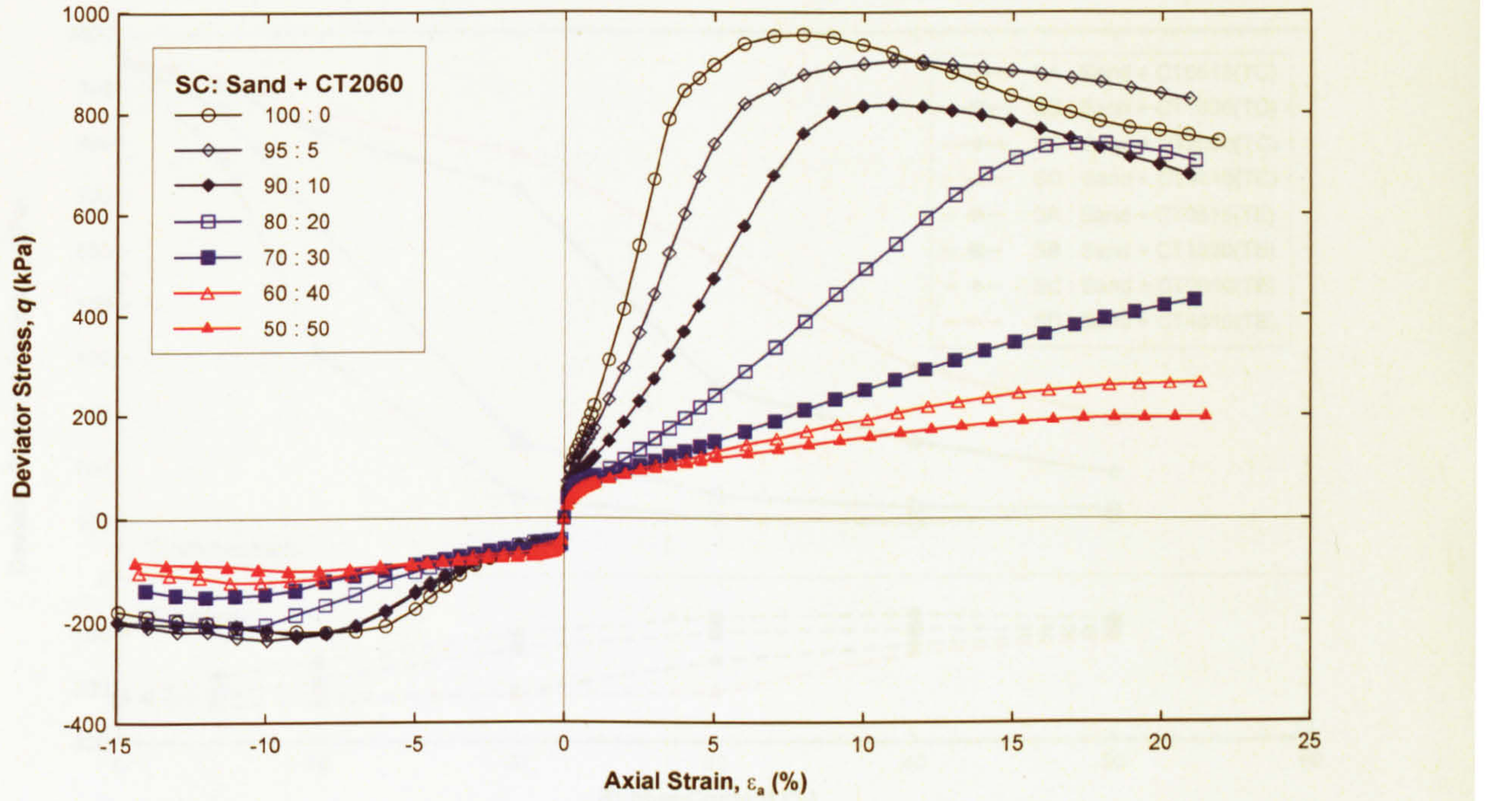

Figure 5. 20 Relationships between q and ε_a for mixtures SC

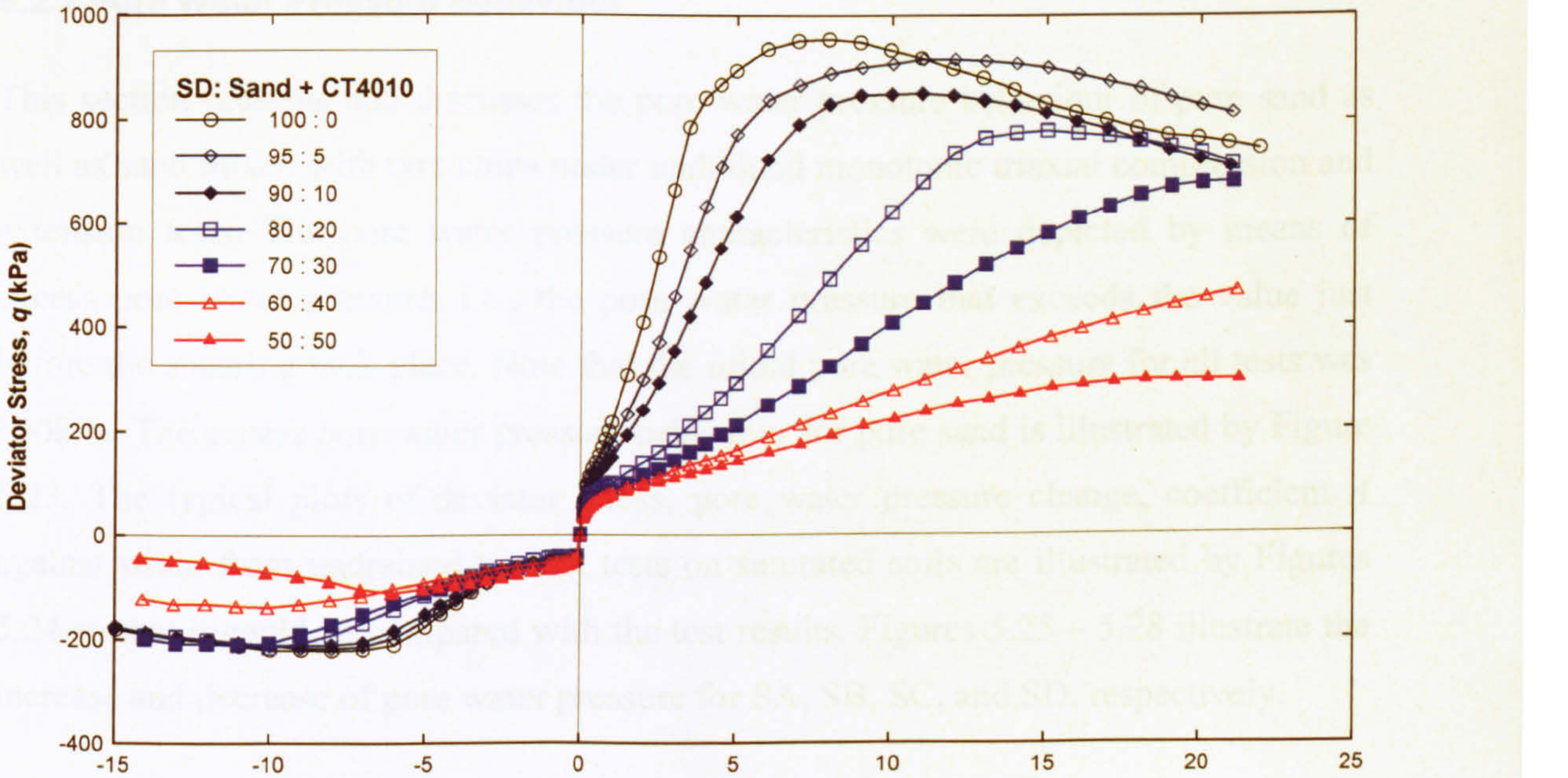

Figure 5. 21 Relationships between q and ε_a for mixtures SD

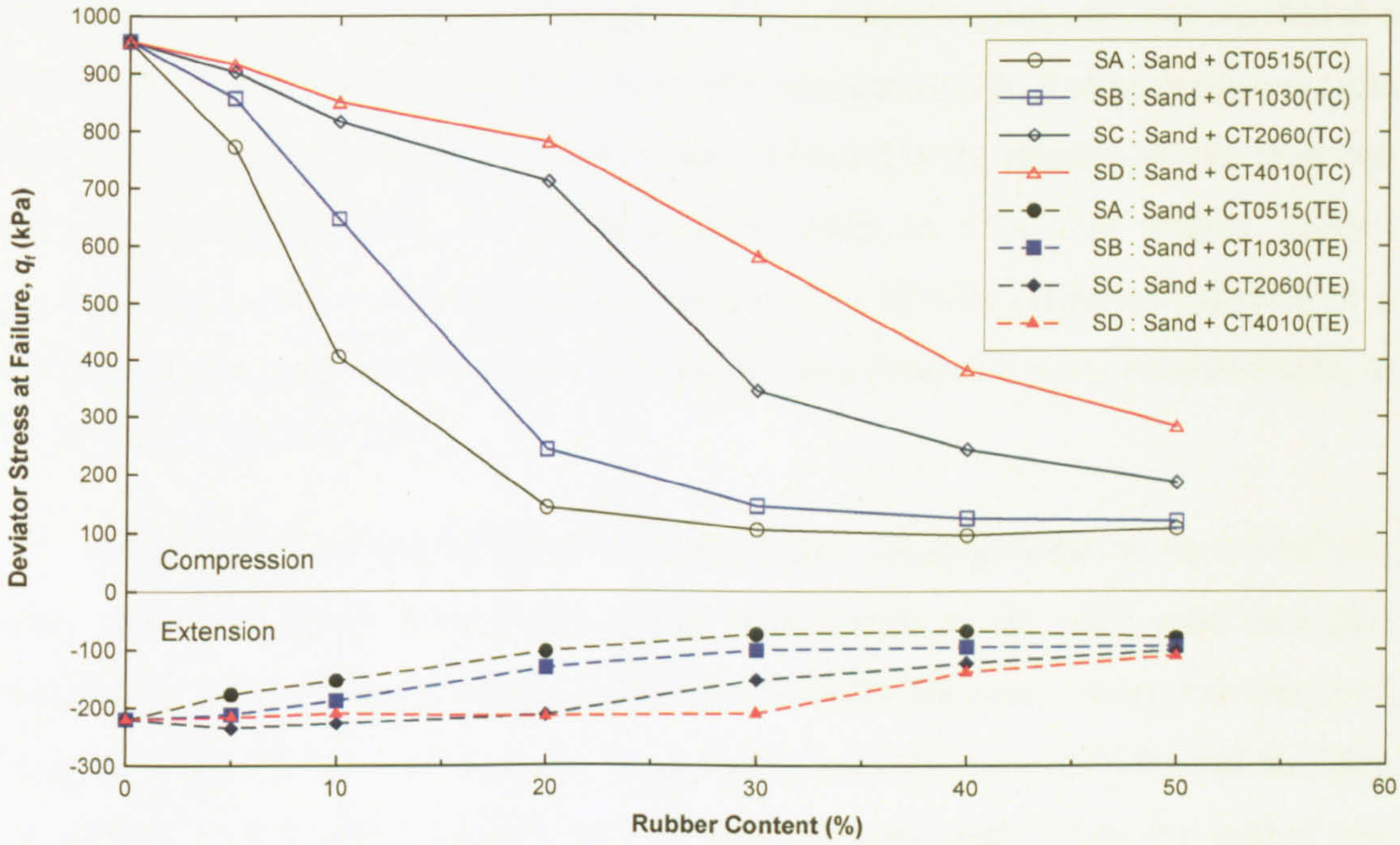

Figure 5. 22 q_f from undrained triaxial compression and extension tests versus rubber content

5.2.2 Pore Water Pressure Behaviour

This section presents and discusses the pore water pressure behaviour of pure sand as well as sand mixed with tyre chips under undrained monotonic triaxial compression and extension tests. The pore water pressure characteristics were depicted by means of excess pore water pressure, i.e., the pore water pressure that exceeds the value just before the shearing took place. Note that the initial pore water pressure for all tests was 190kPa. The excess pore water pressure behaviour for pure sand is illustrated by Figure 5.23. The typical plots of deviator stress, pore water pressure change, coefficient *A* against strain from undrained triaxial tests on saturated soils are illustrated by Figures 5.24 so that it could be compared with the test results. Figures 5.25 – 5.28 illustrate the increase and decrease of pore water pressure for SA, SB, SC, and SD, respectively.

The excess pore water pressure (Δu) for pure sand under TC (see Figure 5.23) at the beginning of shearing increased very rapidly to a maximum of 26.3kPa at around 0.4% axial strain. It then decreased very quickly at almost the same rate to the minimum excess pore water pressure Δu_{min} of around -254kPa after an axial strain of 7% was reached. After that, Δu was maintained until the end of testing at 22% axial strain. The behaviour observed for TC was also observed to be the case for TE. However, the

maximum excess pore water pressure Δu_{max} was somewhat higher, and was reached at a larger axial strain. When Δu_{max} of 34.2kPa was reached for TE, it then decreased quite rapidly; nonetheless, the rate of decrease was observed to be slightly slower than that for TC. In addition, Δu_{min} at the final axial strain of 15% was slightly greater, i.e., -230kPa. It can be seen that Δu generated by TC, initially increased followed by a marked decrease towards the end, resembling the behaviour of overconsolidated clay, as illustrated by Figure 5.24(f).

The sudden increase of Δu at the beginning of shearing followed by a relatively rapid dilative decrease towards the steady state observed for pure sand was also observed for SA having 5% rubber (see Figure 5.25(a)). However, Δu_{max} was observed to be as much as twice. For example, Δu_{max} for TC and TE were 46.5kPa and 56.7kPa, respectively, compared to 26.3kPa and 34.2kPa for pure sand. When the rubber was increased to 10% for SA (see Figure 5.25(b)), the pore water pressure behaviour was observed to be quite different to that of SA having 5% rubber. However, at the beginning the sudden increase of Δu was observed to be quite similar. When Δu_{max} of 41.4kPa was reached at around 1% axial strain, Δu was observed to gradually decrease until the end of the test; such that no period of constant Δu was observed as for SA having 5% rubber. The behaviour of Δu under TE was observed to be quite similar to that of TC. Nonetheless, Δu_{max} at low strain generated by TE was greater than that generated by TC, i.e., Δu_{max} for TE = 54.9kPa. After Δu_{max} was reached, the gradual decrease of Δu observed for TC was also observed for TE, but at a faster rate.

For SA having a rubber content of 20% (see Figure 5.25(c)), it can be seen that the behaviour of Δu was quite different to those of SA having 5% and 10% rubber. For TC the sudden increase of Δu at low strain observed for SA having 5% and 10% rubber was also observed, but Δu_{max} was relatively greater. After Δu, $_{max}$ of 61.1kPa was reached at about 3.04% axial strain, it gradually decreased towards the end of shearing at 21.3% axial strain at which Δu_{min} was just above zero. For TE, it was observed that Δu suddenly increased to a maximum value of 35.6kPa at -1.51% axial strain. It should be noted that when the rubber was increased to 20%, Δu_{max} for TE was significantly lower than for those having lower rubber contents. After Δu_{max} was reached, Δu was

observed to gradually decrease until the end of shearing; and, Δu_{min} was -56.6kPa at -16.14% axial strain.

The behaviour of Δu for SA having 30% rubber under TC (see Figure 5.25(d)) was observed to be similar to that of SA with 20% rubber; whereas, for TE, the slight difference of the decrease in Δu after Δu_{max} was reached was observed. For TC, Δu_{max} about the same as for SA with 20% rubber was reached at larger axial strain. It then gradually decreased towards the end of shearing. It was observed that the rate of decrease was relatively slower compared to that of SA with 20% rubber. In addition, Δu at the end of shearing was a little bit lower than Δu_{max}, i.e., Δu (end of shearing) = 50kPa and Δu_{max} = 67kPa. For TE, Δu_{max} of 28kPa was reached at -3.1% axial strain, followed by a gradual decrease until the end of shearing. The Δu_{min} of -2.7kPa was observed at the end of shearing, which was greater than that of SA with 20% rubber.

When the rubber was increased to 40%, it was observed that the behaviour of Δu (see Figure 5.25(e)) was comparable to that with 30% rubber, especially for TC. For TE, however, Δu_{max} was smaller; in fact, Δu was observed to increase only very slightly at the beginning, compared to SA with 5%, 10%, 20%, and 30% rubber. Then, it gradually decreased, and Δu at the end of shearing was approximately zero. For SA having a rubber content of 50%, the behaviour of Δu (see Figure 5.25(f)) generated by TC was observed to be similar to that of SA with 30% and 40% rubber contents, except that the rate of decrease of Δu after Δu_{max} reached was quite small. For TE, it was observed that Δu slightly increased until the axial strain was around -5%, it then gradually decreased towards the end of shearing; and, Δu at the end of shearing was nearly zero, which was similar to SA with 30% and 40% rubber.

As observed for SA with 5% rubber, the behaviour of Δu for SB having the same amount of rubber (see Figure 5.26(a)) was very similar. However, as the size of tyre chips was slightly greater, Δu_{max} for both TC and TE were observed to be slightly smaller. Furthermore, Δu_{min} for TC and TE obtained at the end of shearing was smaller than that of SA. For SB having 10% rubber (see Figure 5.26(b)), compared to SA with the same rubber content, it was observed that Δu_{max} for TC was reached at similar axial strain, but was slightly greater. However, from an axial strain of 19% onwards, Δu was observed to be nearly constant; whereas, for SA no such behaviour was observed. For

TE, Δu_{max} was observed to be quite comparable to that of SA. However, Δu_{min} was much smaller than that that for SA.

For SB having 20% rubber, the behaviour of Δu (see Figure 5.26(c)), was distinctive compared to those having smaller rubber contents of 5% and 10%. At the beginning of shearing, the increase and decrease of Δu was quite comparable to that of SA with the same rubber content. For TC, however, after Δu_{max} was achieved at around 1% axial strain, Δu progressively decreased to the end, and the final Δu was -39.1kPa; while, for SA, it was 19.1kPa. This large difference in Δu at the end of shearing observed for TC was also observed for TE, indicating the effects of the size of tyre chips on the pore water pressure behaviour.

For SB having 30% rubber, the behaviour of Δu (see Figure 5.26(d)) for TC was comparable to that of SA with the same rubber content. However, at the end of shearing Δu was observed to be constant; whereas, for SA, it was still decreasing. For TE, compared to that of SA, Δu was observed to increase initially; then it decreased at a much faster rate. In addition, Δu_{min} achieved at the end of shearing was around -42kPa compared to that of SA of just -2.4kPa.

The behaviour of Δu for SB having 40% rubber (see Figure 5.26(e)) under TC was observed to be quite comparable to that of SA having the same rubber content. However, the rate of decrease of Δu was slightly greater than that observed for SA. As such, Δu at the end of shearing was somewhat lower than that of SA. For TE, the difference in behaviour of Δu between SB and SA was similar to that for a rubber content of 30%.

For SB containing the maximum rubber content of 50% (see Figure 5.26(f)), it can be seen that the behaviour of Δu for TC was very similar to that for SA having 40% and 50% rubber. For TE, however, it was observed that up to -5% axial strain, Δu slightly increased just above zero. After that, it gradually decreased to the end of shearing.

For SC having rubber contents of 5% and 10% (see Figure 5.27(a) and (b)), the behaviour of Δu for both TC and TE was quite comparable to that of SB having 5% rubber. However, when the rubber was increased to 20% (see Figure 5.27(c)), the

behaviour of Δu for both TC and TE was observed to be quite similar to that of SB but with 10% rubber. For SC having rubber contents of 30% and 40% (see Figure 5.27(d) and (e)), it can be seen that the increase and decrease of pore water pressure for both TC and TE was comparable to that of SB having a rubber content of 20%. For SC containing the maximum rubber content of 50% (see Figure 5.27(f)), it was observed that Δu generated by TC was quite comparable to that of SA and SB having the same amount of rubber. However, it was observed that towards the end of shearing the rate of decrease of Δu was faster. As a result, Δu was lower than for SA and SB.

The behaviour of Δu for SD having rubber contents of 5% and 10% (see Figure 5.28(a) and (b)), even though having different mixtures, was observed to resemble the behaviour for SC with 10% rubber. For SD containing 20% rubber (see Figure 5.28(c)), the behaviour of Δu was observed to be comparable to that for SC containing the same rubber portion. When the rubber was increased to 30% (see Figure 5.28(d)), the behaviour of Δu was similar to that of SC with the same rubber content, except that Δu_{min} values achieved at the end of shearing for both TC and TE were much smaller, i.e., they were -199kPa and -217kPa, respectively, compared to -71kPa and -127kPa for SC.

When the rubber was increased to 40% for SD (see Figure 5.28(e)), the behaviour of Δu was observed to be similar to that of SC but with 30% rubber. For SD containing the maximum rubber content of 50% (see Figure 5.28(f)), the behaviour was quite different to that of SA, SB, and SC having the same rubber content. For example for TC, after Δu_{max} was observed at an axial strain of about 2.5% similar to SA, SB, and SC. Δu then was observed to progressively decrease at a faster rate until it was well below zero. This dilatant tendency was not seen for SA, SB or SC. For TE, it was observed that Δu briefly increased just above zero, followed by a gradual decrease to a minimum of -42.1kPa at -6.08% axial strain. After that, it progressively increased again almost linearly until the end of shearing.

Even though the mixtures had similar rubber contents, if the size of the rubber was not the same, the behaviour of Δu generated by the undrained monotonic triaxial compression and extension tests was observed to be somewhat different. These aspects for the mixtures 95:5 for SA, SB, SC, and SD are illustrated by Figure 5.29. Figures

5.30 – 5.34 illustrate the behaviour of Δu for the mixtures 90:10, 80:20, 70:30, 60:40, and 50:50, respectively. In addition, Figure 5.35 illustrates the behaviour of Δu for SA with all sand to rubber ratios, including pure sand, so that they can be compared. For SB, SC, and SD, having all sand to rubber ratios, the behaviour of Δu is illustrated by Figure 5.36, Figure 5.37, and Figure 5.38, respectively.

Considering Figure 5.29 presenting the behaviour of Δu for the mixtures 95:5, it can be seen that for TC, the behaviour is very similar. However, as the size of rubber was increased the generated pore water pressure was more negative, especially when comparing between SA and SB. For SC and SD, however, it can be seen that both increase and decrease of pore water pressure were similar. For TE, the changes of pore water pressure due to different size of rubber were similar to TC. These characteristics for the 95:5 mixtures were also found to be the case for the other mixtures, apart from the 50:50 mixtures under TE where SD exhibited the marked increase of pore water pressure as previously discussed (see Figure 5.34).

As evident in Figures 5.29 – 5.34, the tendency of more negative pore water pressure when the mixtures contained rubber with a bigger size such as SC and SD may suggest that they have the liquefaction resistance higher than the mixtures having smaller size of rubber such as SA and SB.

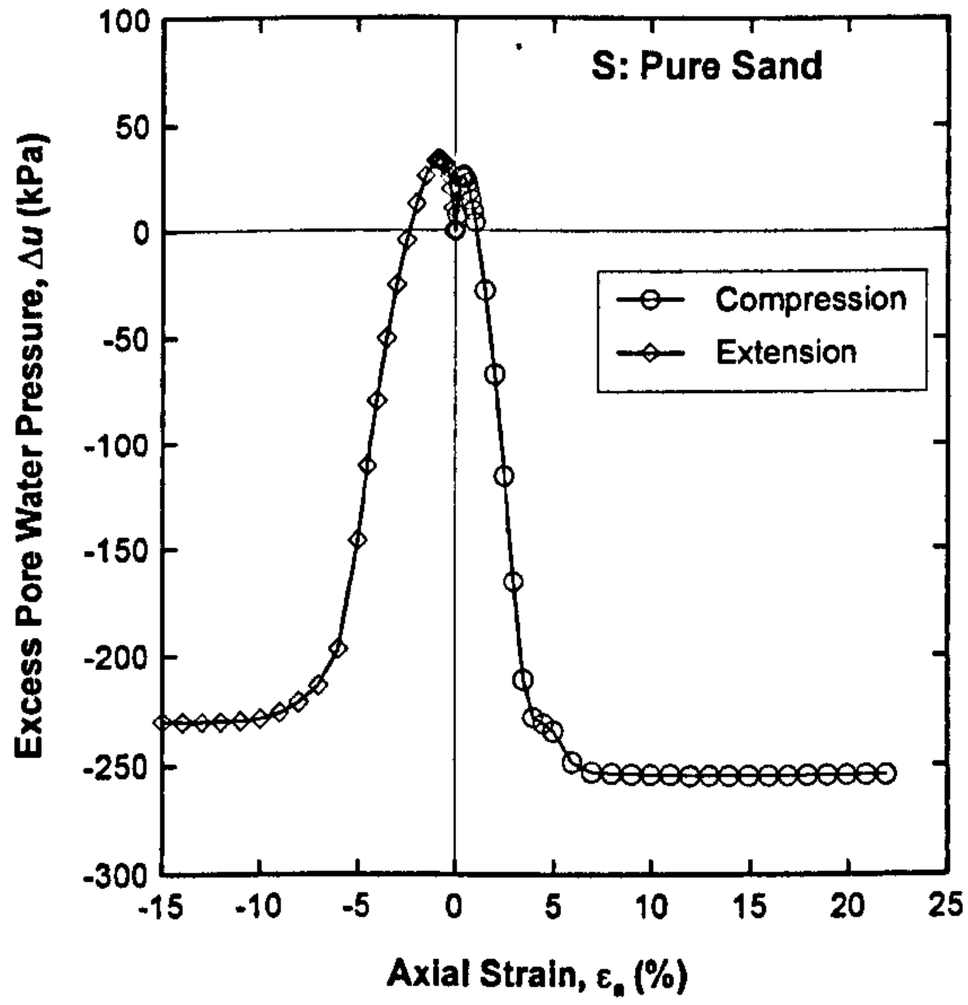

Figure 5. 23 Excess pore water pressure for pure sand, S

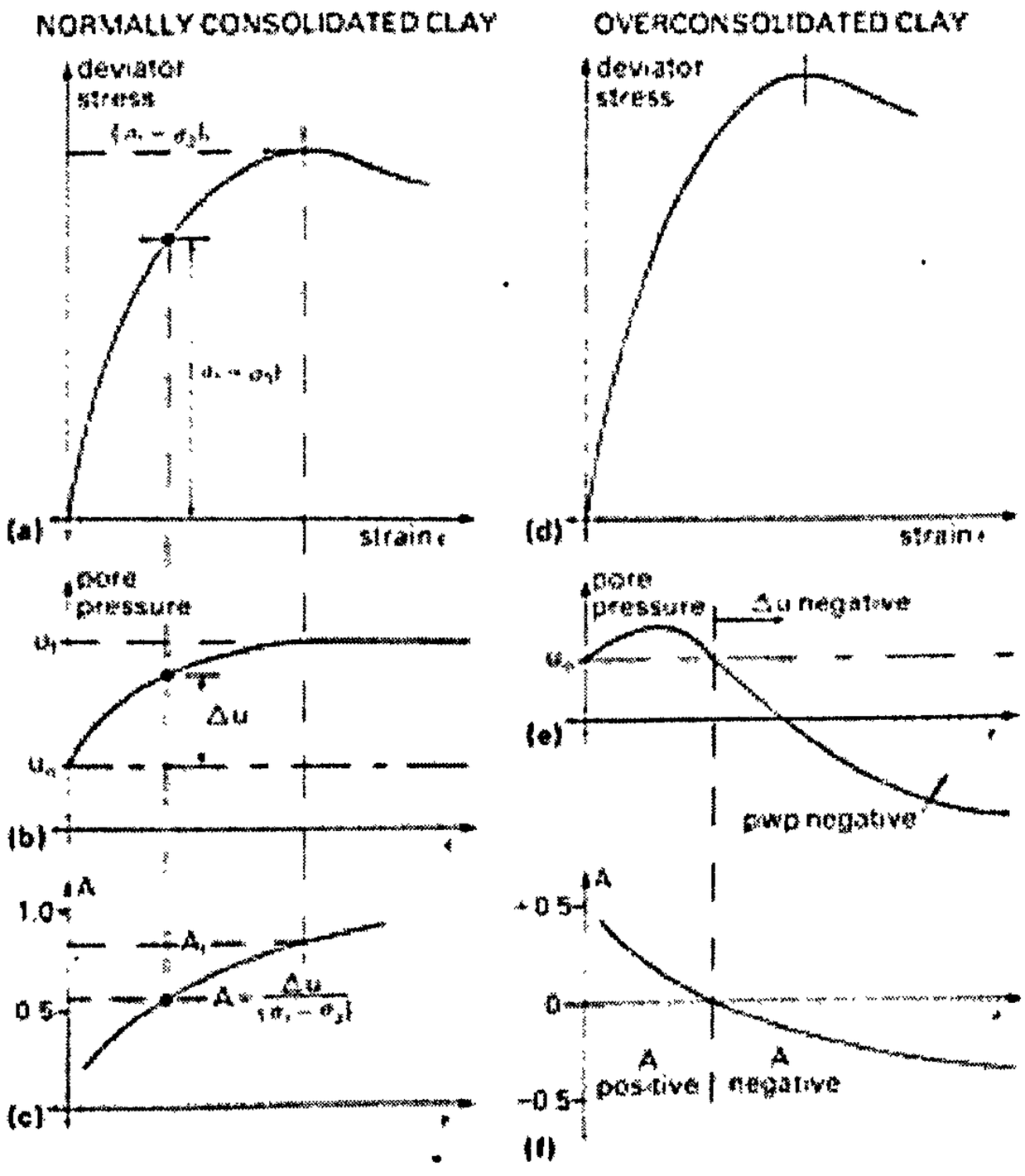

Figure 5. 24 Typical plots of deviator stress, pore pressure change and coefficient *A* against strain from undrained triaxial tests on saturated soils (after Head, 1986)

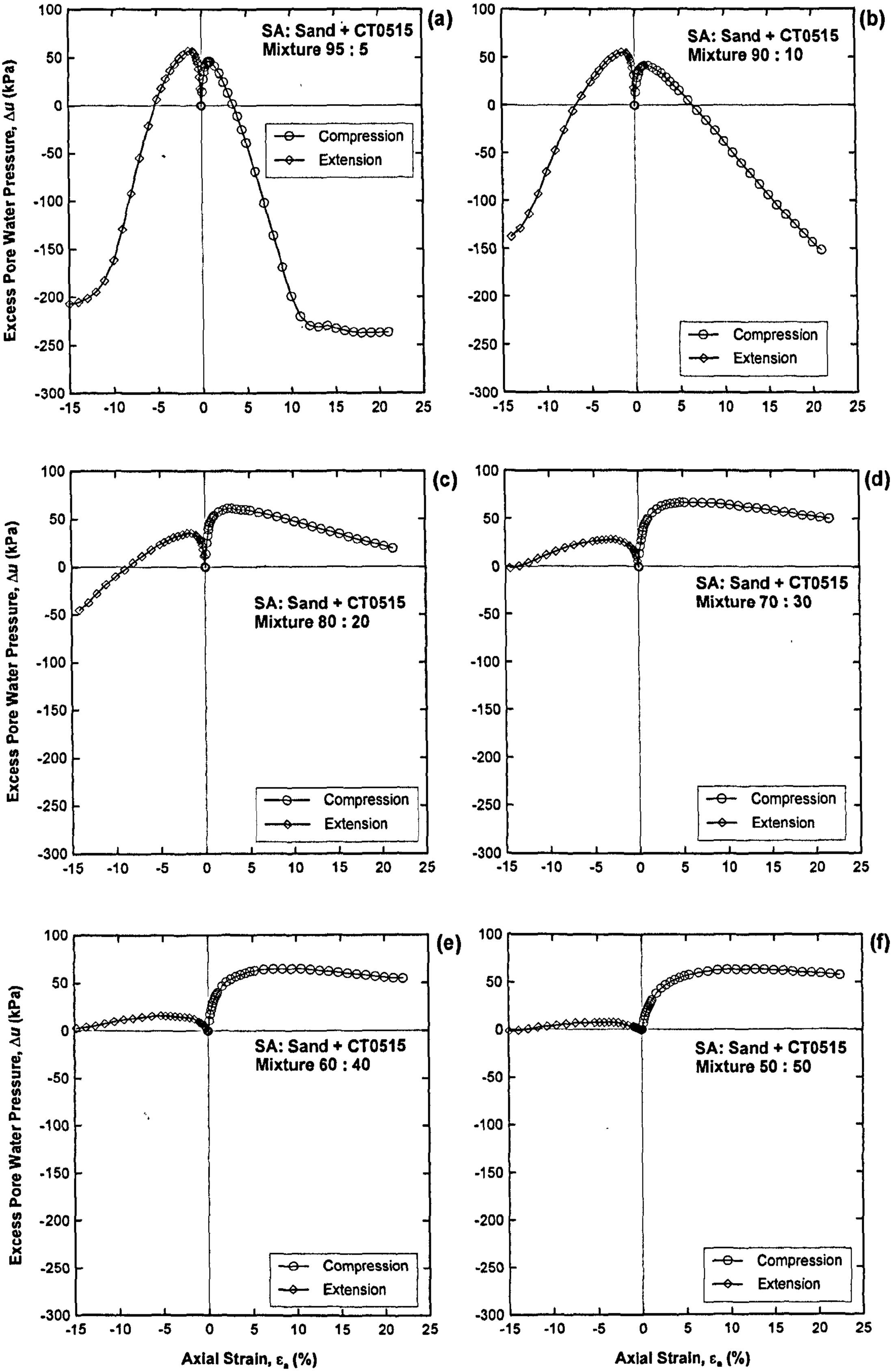

Figure 5. 25 Excess pore water pressure for Sand + CT0515, SA

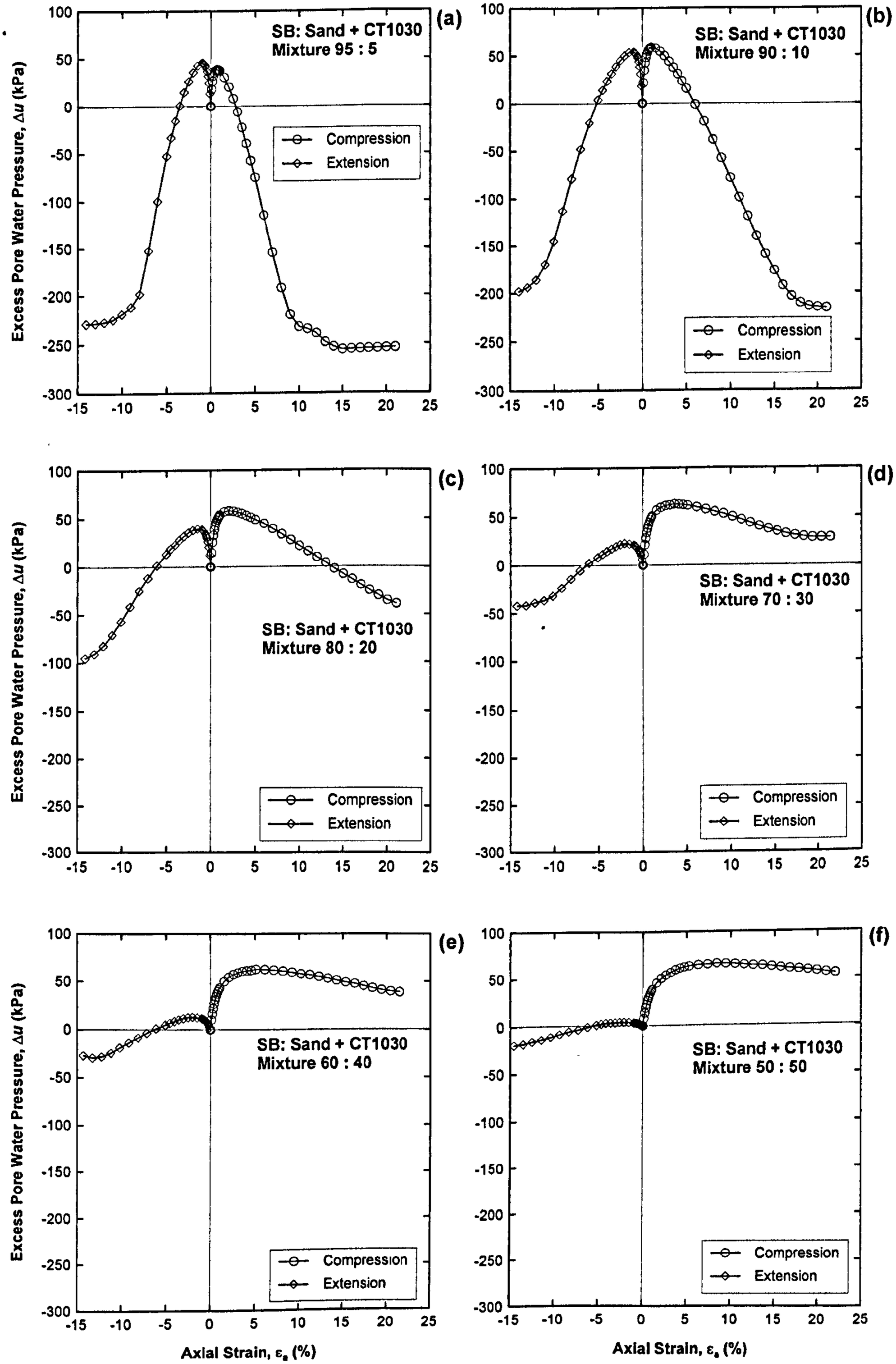

Figure 5. 26 Excess pore water pressure for Sand + CT1030, SB

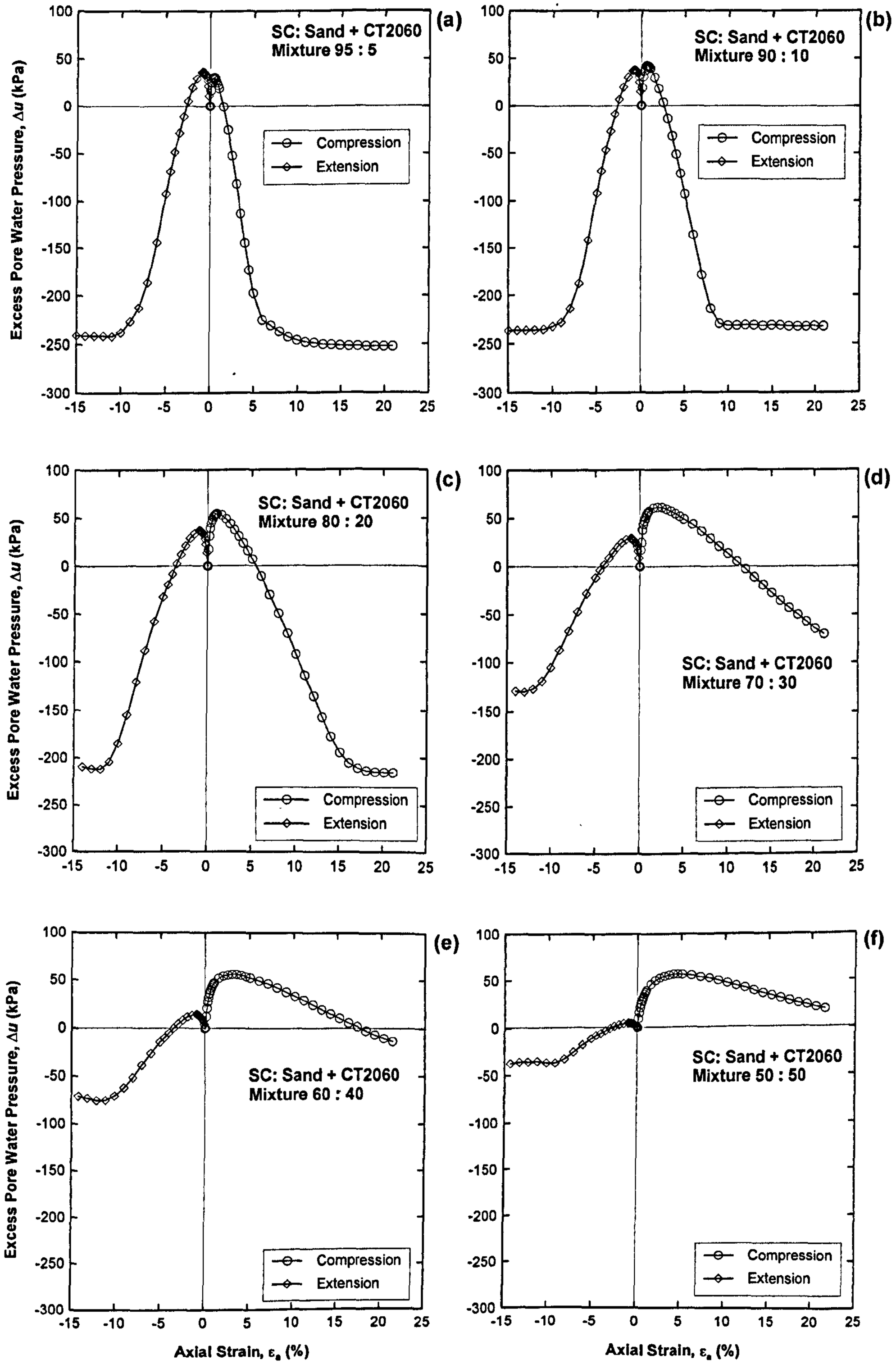

Figure 5. 27 Excess pore water pressure for Sand + CT2060, SC

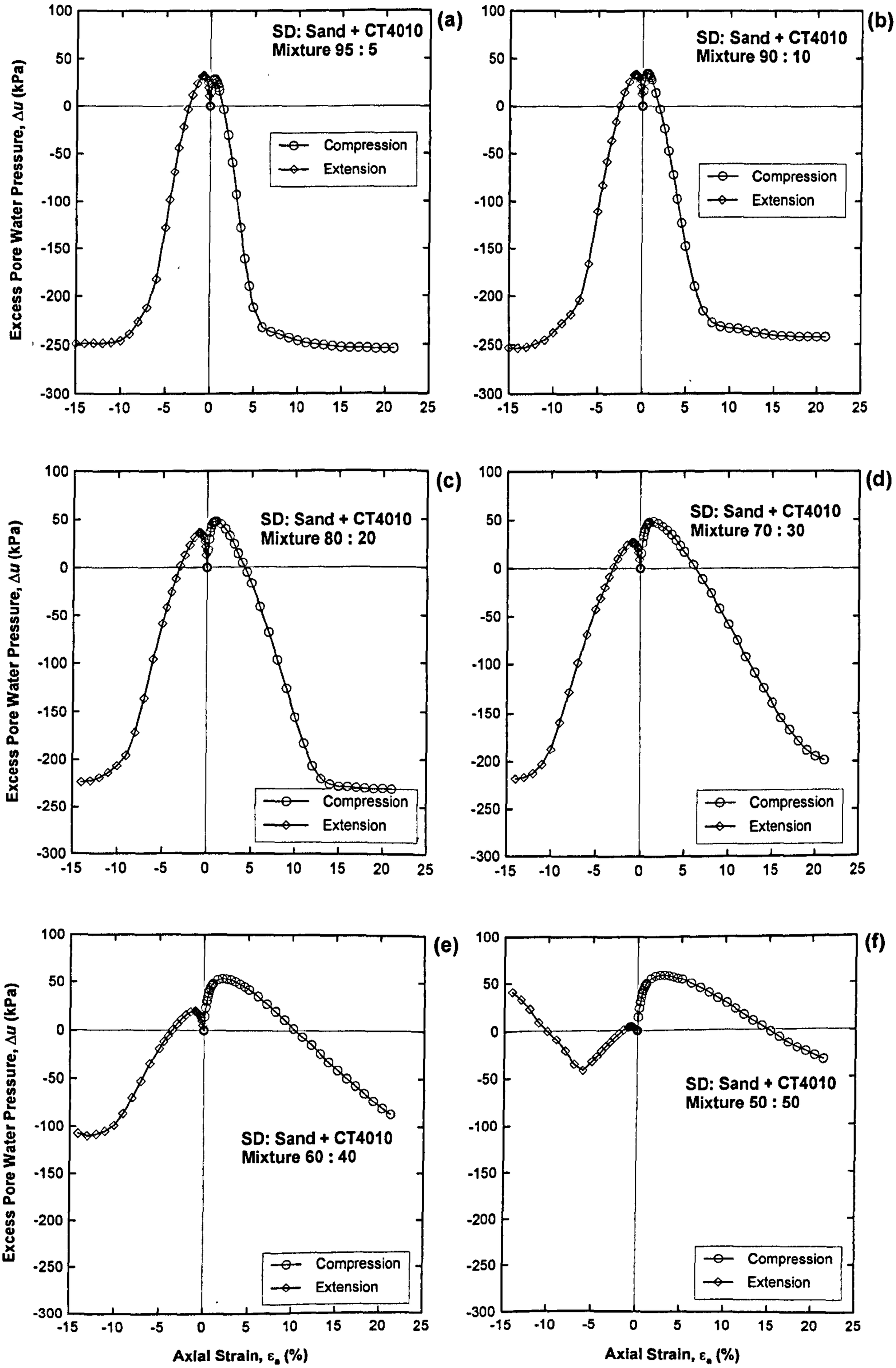

Figure 5. 28 Excess pore water pressure for Sand + CT4010, SD

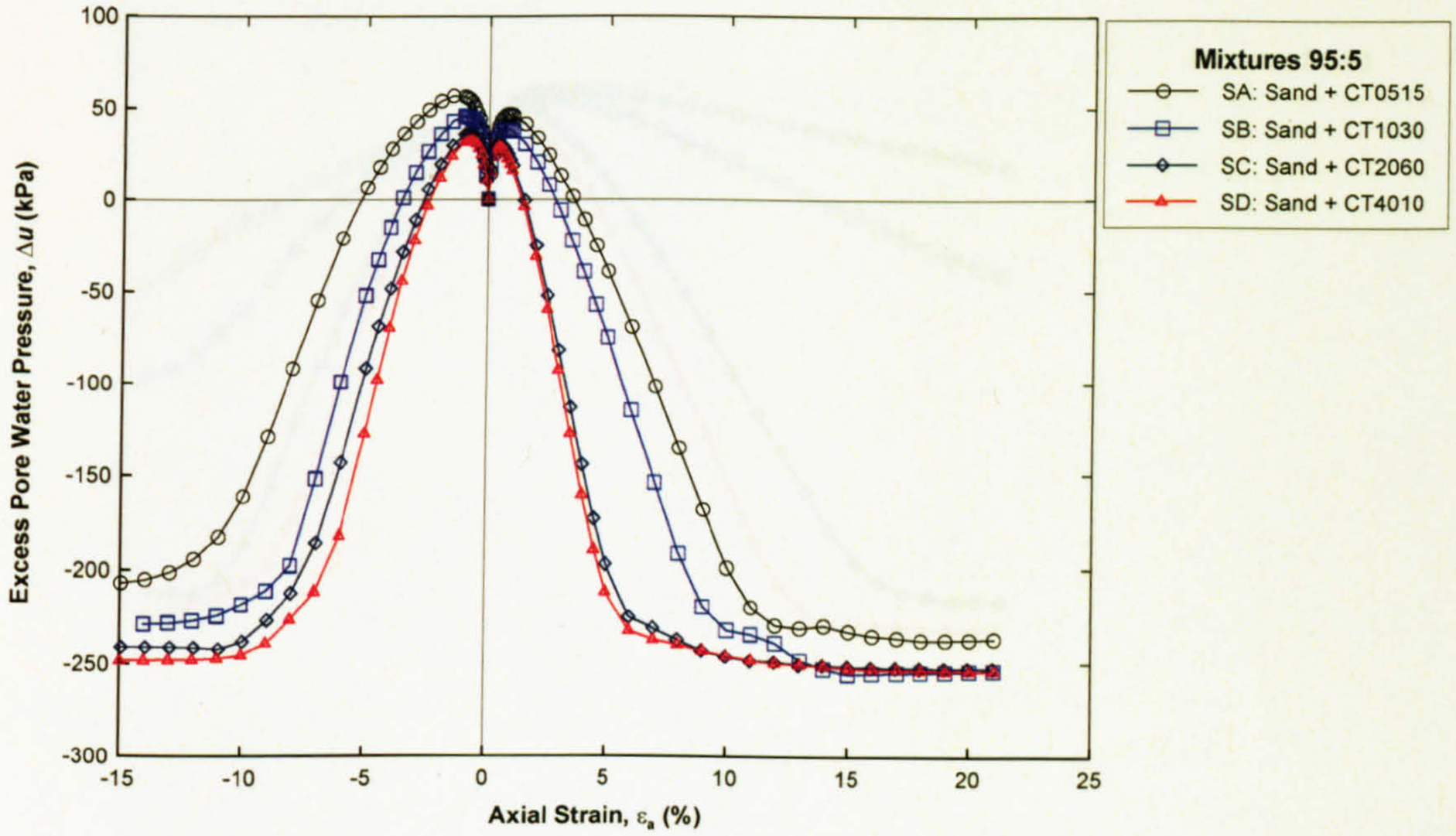

Figure 5. 29 Relationships between Δu and ε_a for SA, SB, SC, and SD having 5% rubber

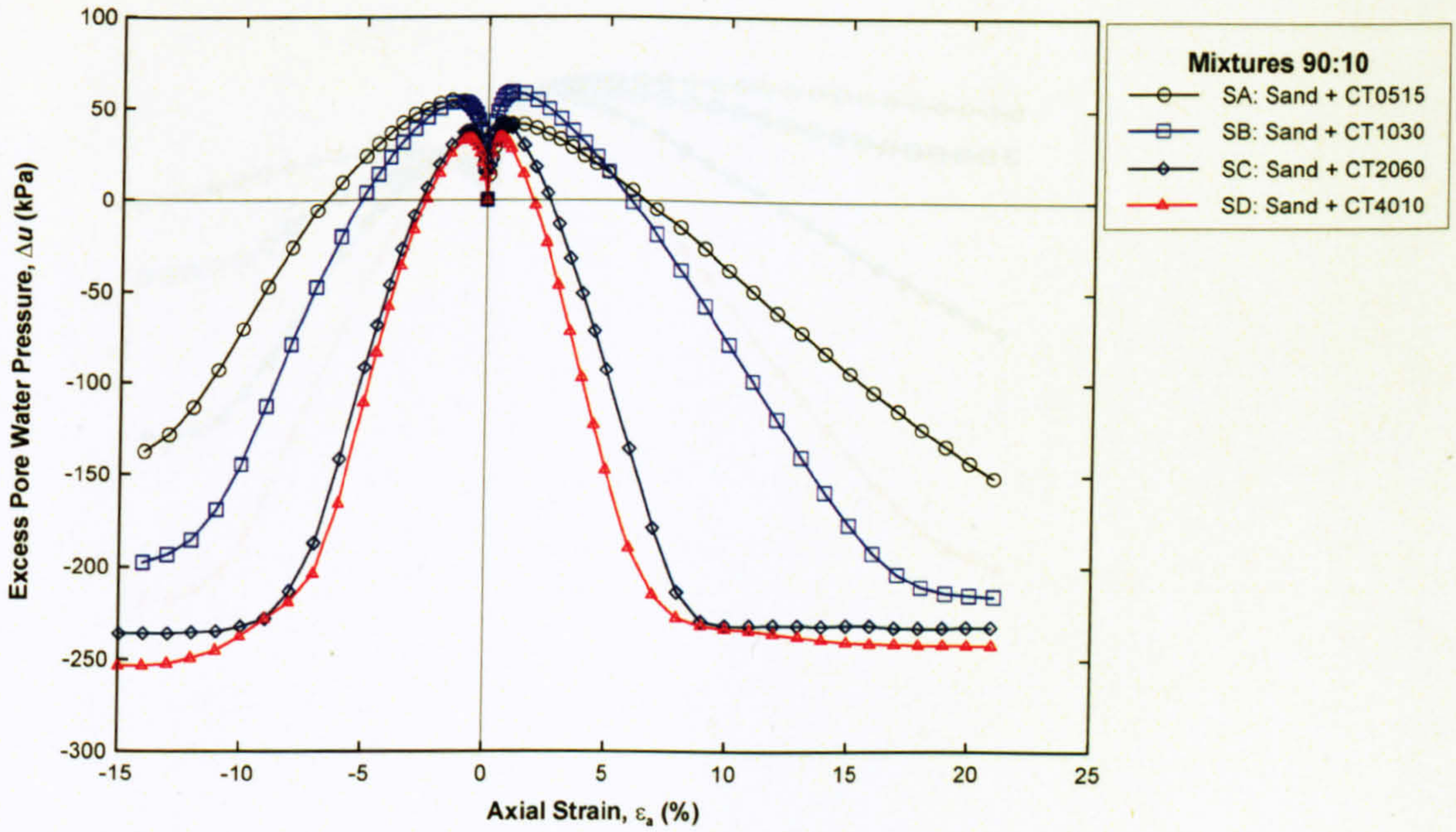

Figure 5. 30 Relationships between Δu and ε_a for SA, SB, SC, and SD having 10% rubber

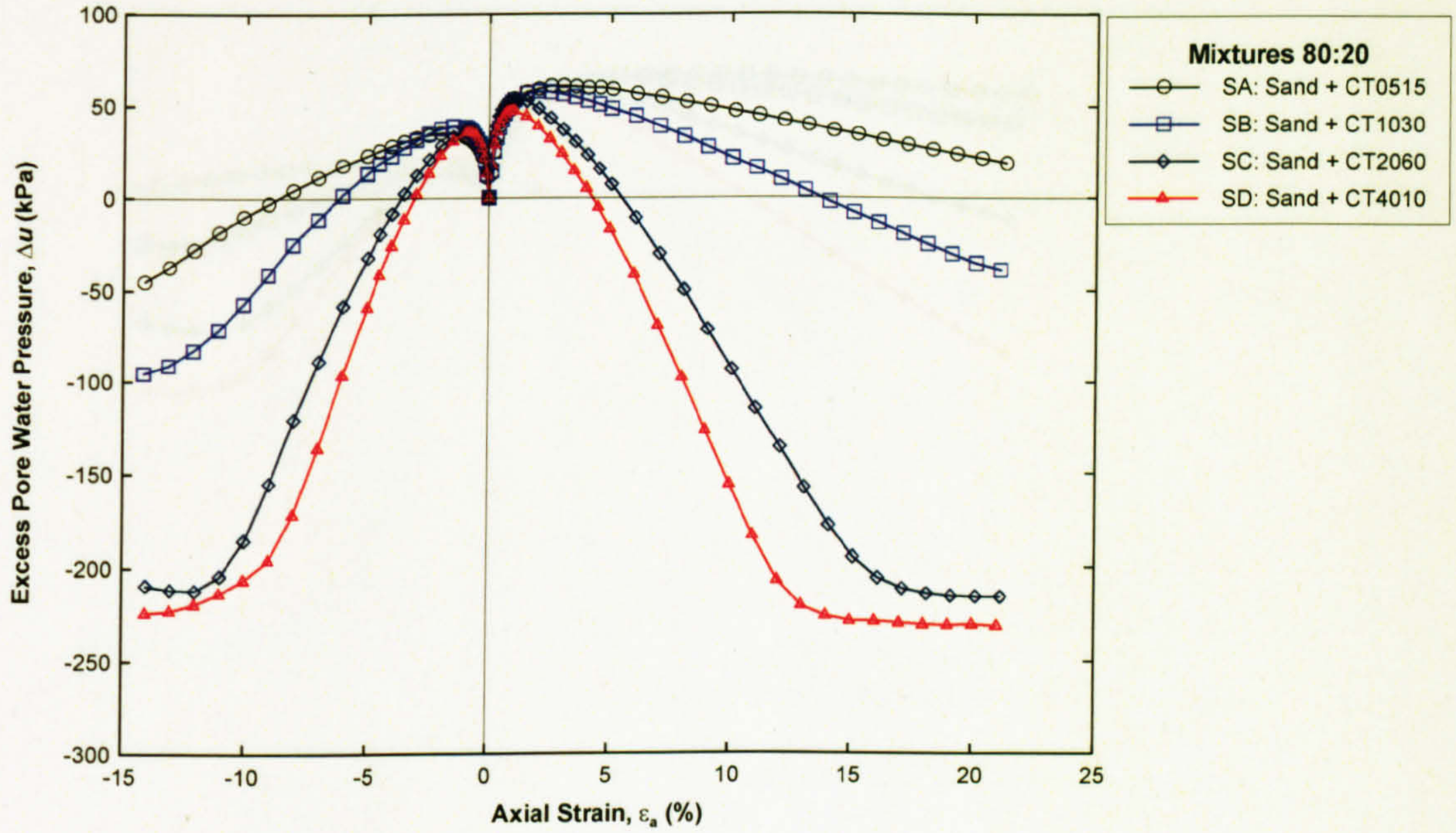

Figure 5. 31 Relationships between Δu and ε_a for SA, SB, SC, and SD having 20% rubber

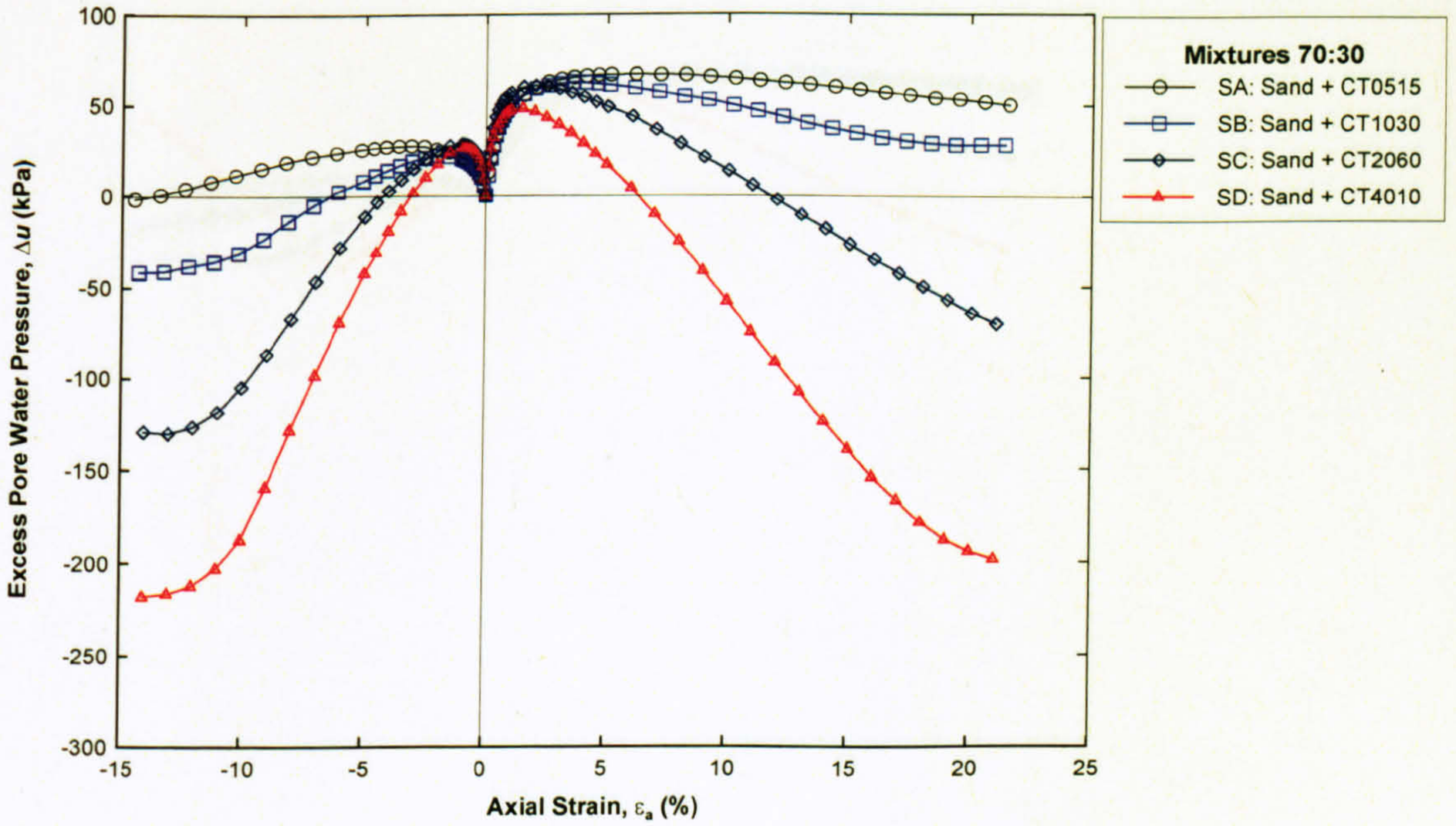

Figure 5. 32 Relationships between Δu and ε_a for SA, SB, SC, and SD having 30% rubber

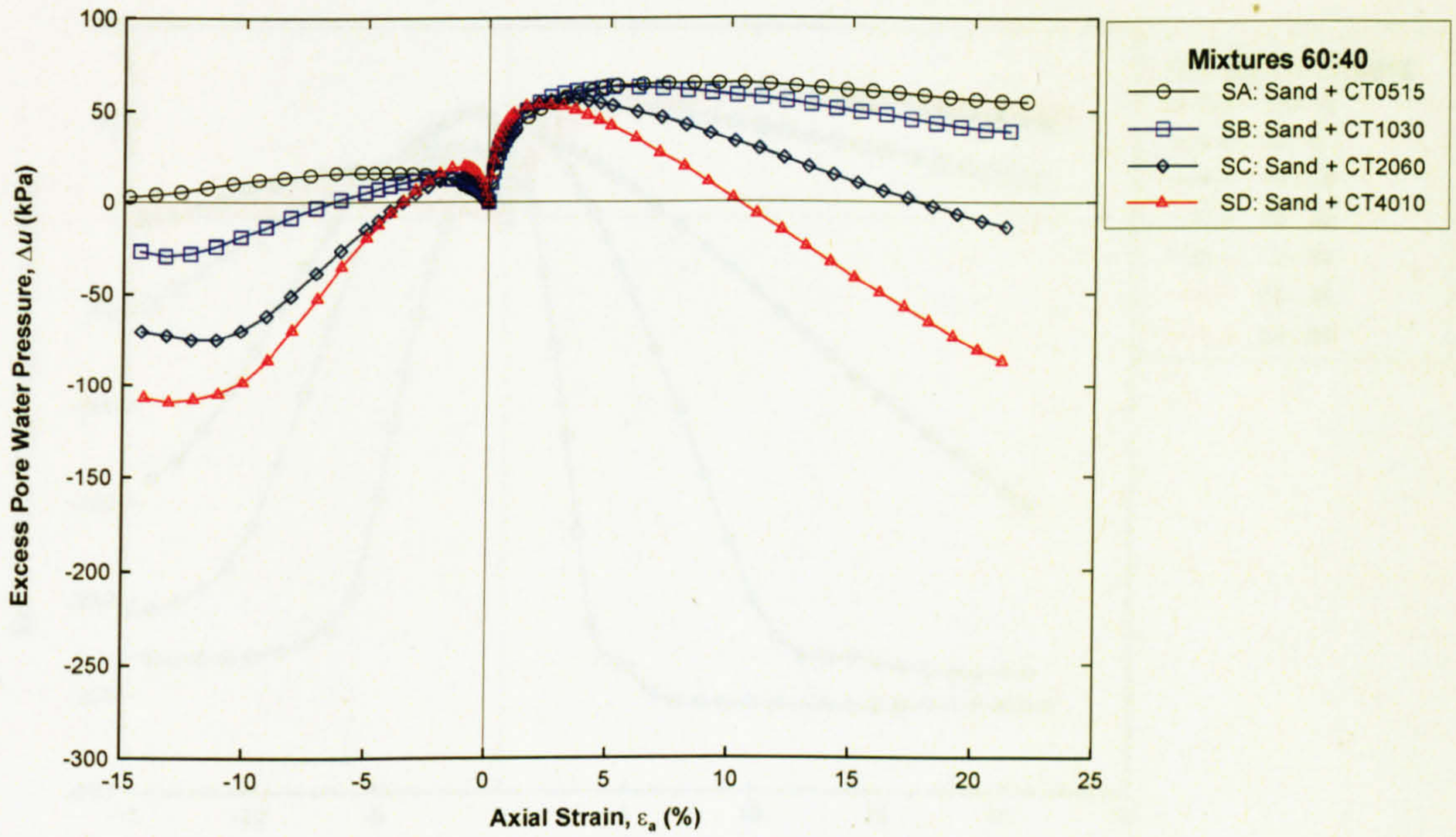

Figure 5. 33 Relationships between Δu and ε_a for SA, SB, SC, and SD having 40% rubber

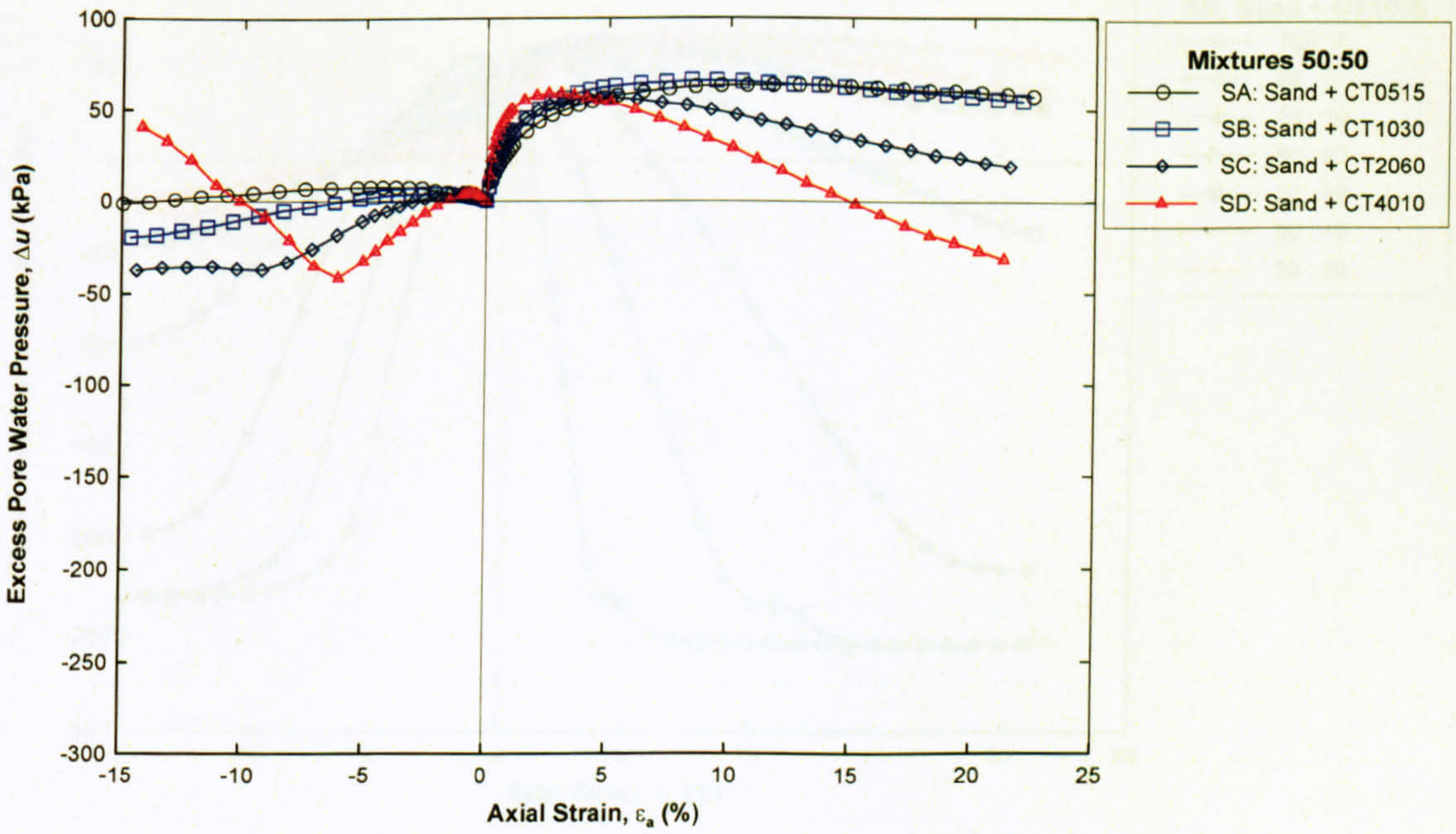

Figure 5. 34 Relationships between Δu and ε_a for SA, SB, SC, and SD having 50% rubber

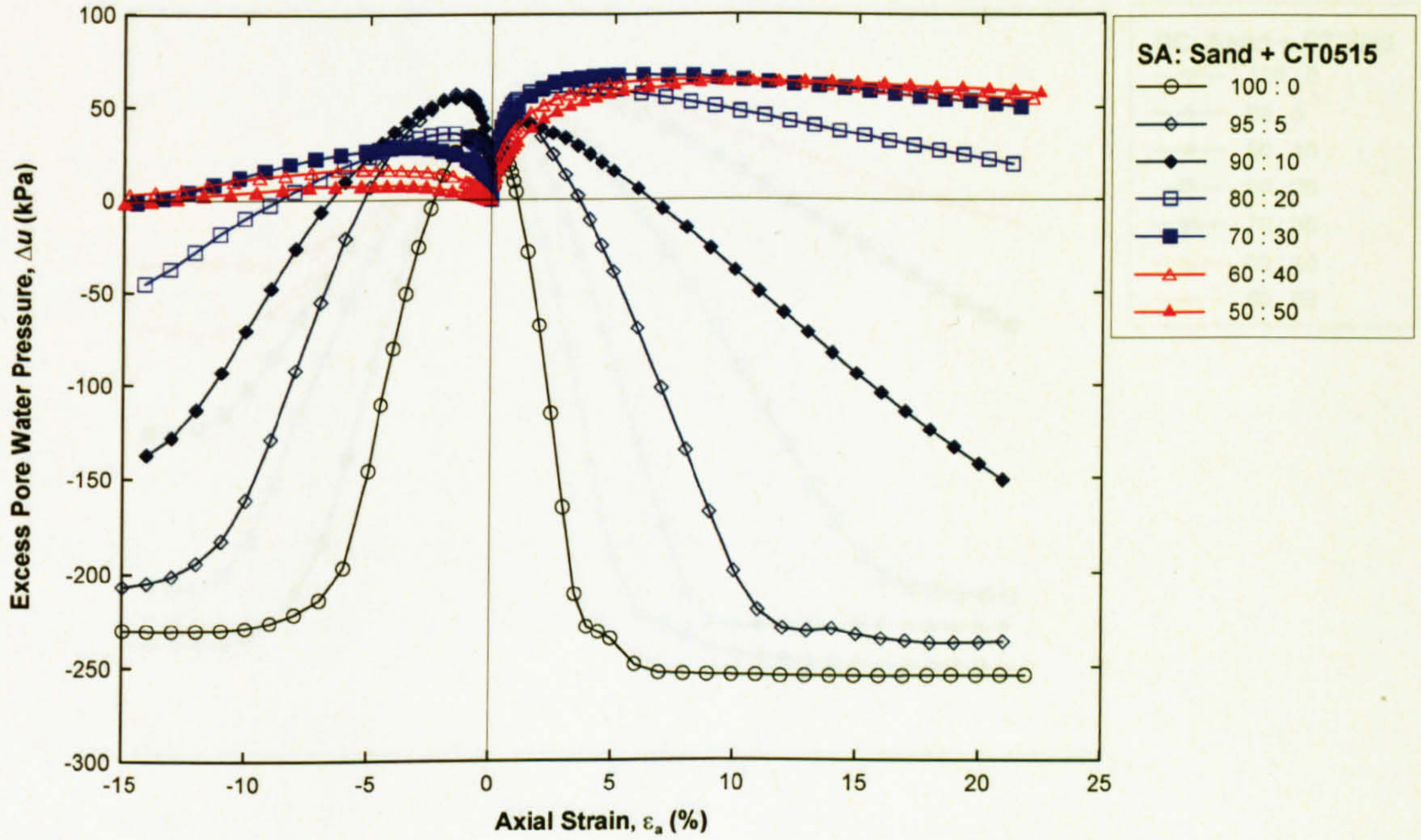

Figure 5. 35 Excess pore water pressure versus axial strain for mixtures SA

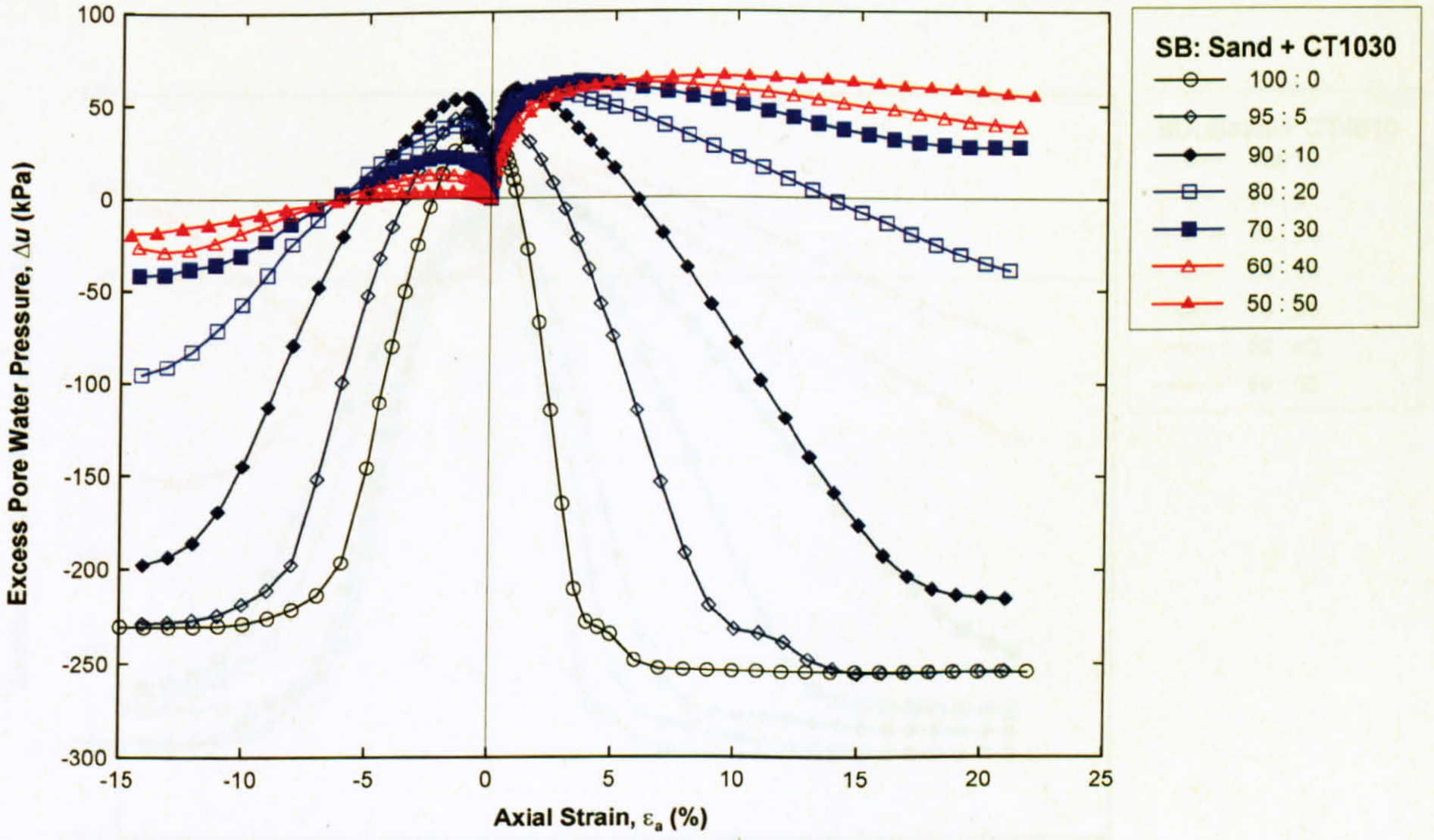

Figure 5. 36 Excess pore water pressure versus axial strain for mixtures SB

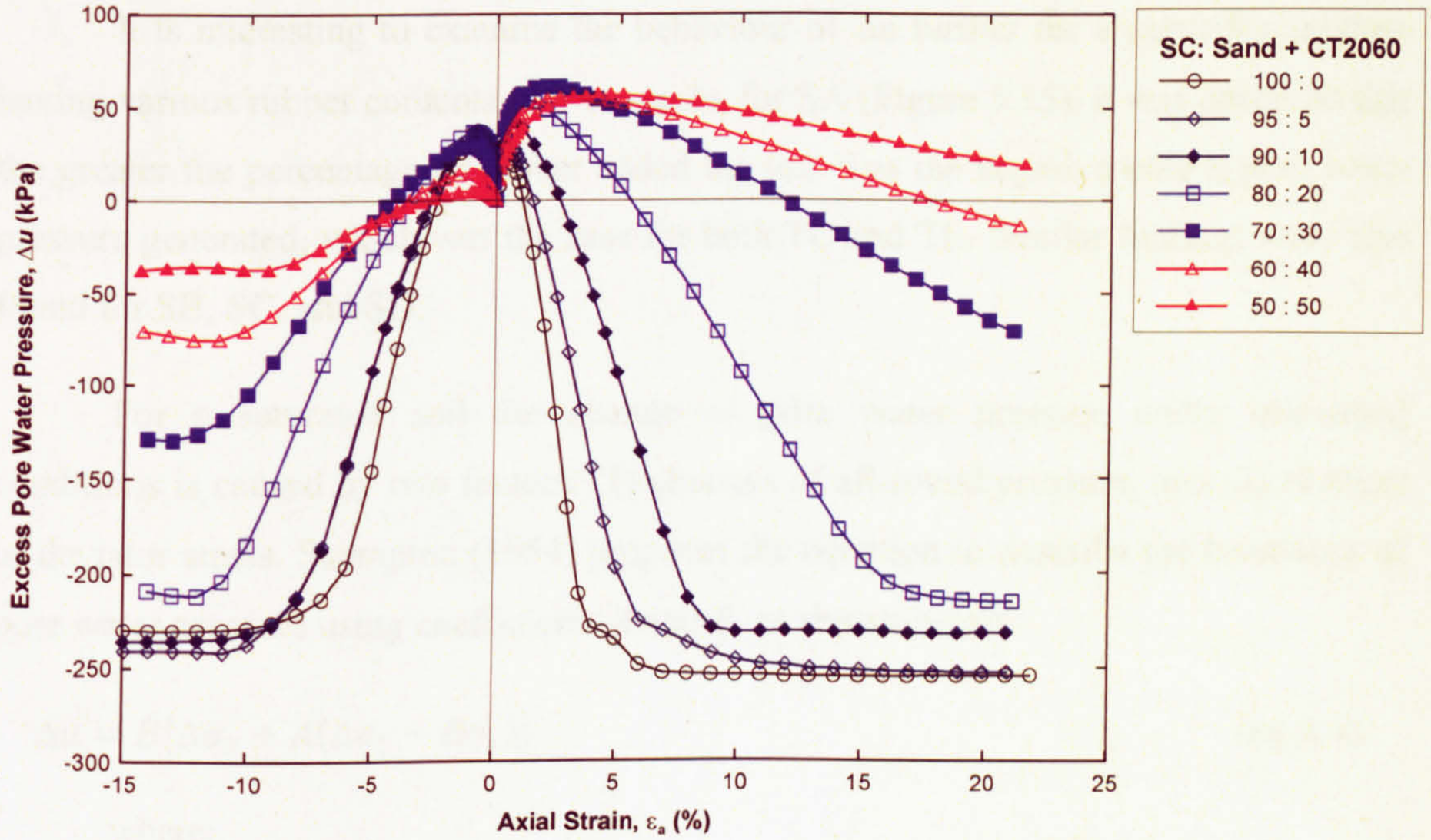

Figure 5. 37 Excess pore water pressure versus axial strain for mixtures SC

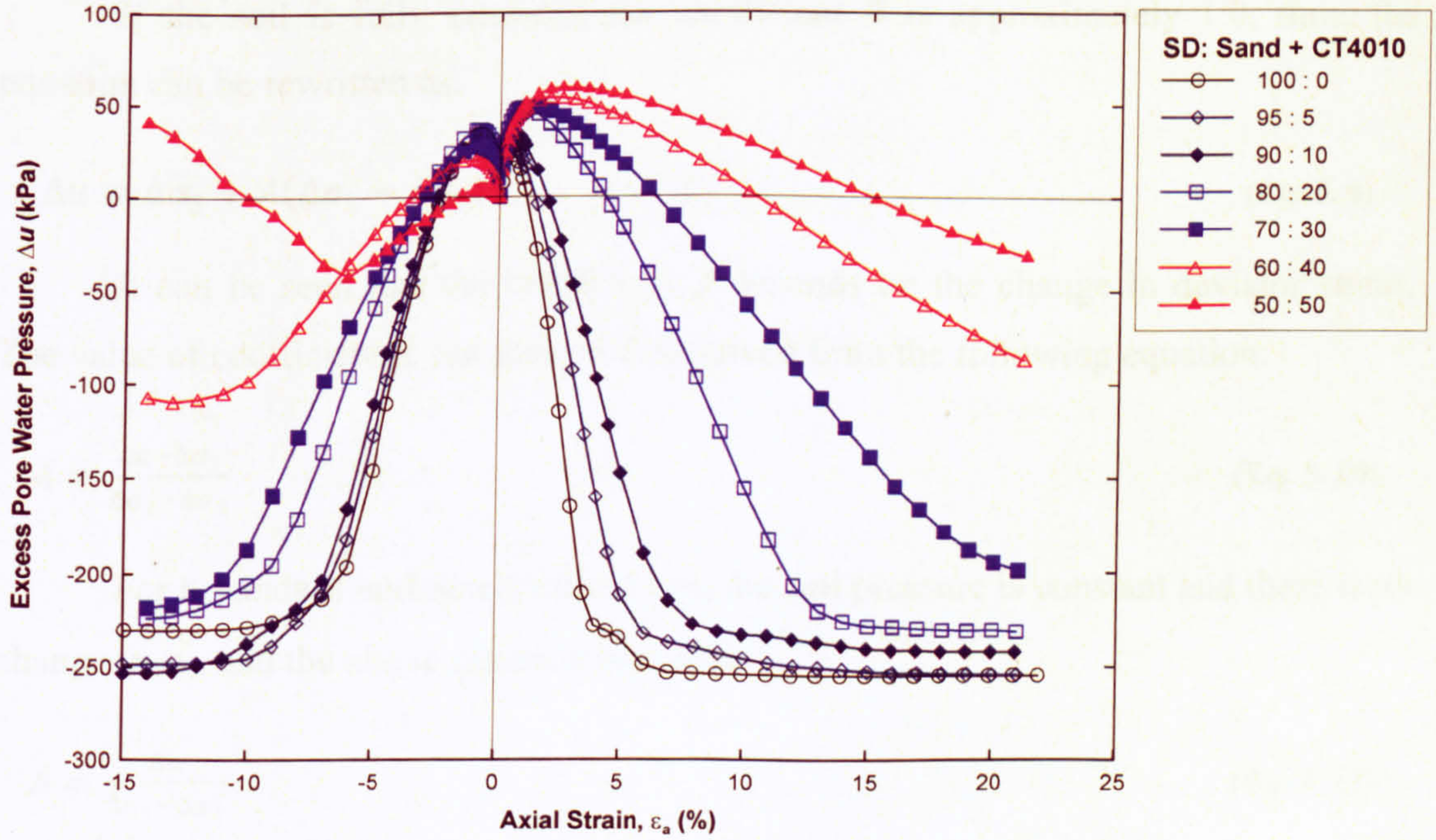

Figure 5. 38 Excess pore water pressure versus axial strain for mixtures SD

It is interesting to examine the behaviour of Δu further for a particular mixture having various rubber contents. For example, for SA (Figure 5.35), it was observed that the greater the percentage of rubber added the less was the negative excess pore water pressure generated, which was the case for both TC and TE. Similar findings were also found for SB, SC, and SD.

For a saturated soil the change of pore water pressure under undrained conditions is caused by two factors: (1) changes of all-round pressure, and (2) changes of deviator stress. Skempton (1954) proposes the equation to describe the behaviour of pore water pressure using coefficients *A* and *B*, as shown below:

$$\Delta u = B[\Delta\sigma_3 + A(\Delta\sigma_1 - \Delta\sigma_3)] \qquad \textbf{(Eq. 5. 8)}$$

where:

Δu = change in pore water pressure,

$\Delta\sigma_1$ = change in major principal stress, and

$\Delta\sigma_3$ = change in minor principal stress.

If the soil is fully saturated the coefficient *B* is approximately 1.0; thus, the equation can be rewritten as:

$$\Delta u = \Delta\sigma_3 + A(\Delta\sigma_1 - \Delta\sigma_3) \qquad \textbf{(Eq. 5. 9)}$$

It can be seen that the coefficient *A* depends on the change in deviator stress. The value of coefficient *A* can then be determined from the following equation:

$$A = \frac{\Delta u - \Delta\sigma_3}{\Delta\sigma_1 - \Delta\sigma_3} \qquad \textbf{(Eq. 5. 10)}$$

For a standard undrained triaxial test, the cell pressure is constant and there is no change in σ_3, and the above equation becomes:

$$A = \frac{\Delta u}{\Delta\sigma_1 - \Delta\sigma_3} \qquad \textbf{(Eq. 5. 11)}$$

It is apparent that the coefficient *A* can be determined at any point of loading. However, the value at failure is of more interest; and, the coefficient at failure is usually defined as A_f. Thus the equation for determining A_f can be established, as shown below:

$$A_f = \frac{u_f - u_o}{(\sigma_1 - \sigma_3)_f} \qquad \textbf{(Eq. 5. 12)}$$

where:

u_f = pore water pressure at failure,

u_o = initial pore water pressure, and

$(\sigma_1\text{-}\sigma_3)_f$ = change in principal stress at failure.

The values of A_f for the undrained triaxial compression and extension tests against the rubber content shown in Table 5.1 and Table 5.2 are graphically illustrated by Figure 5.39. For pure sand under TC, the value of A_f was -0.27, indicating that it was prepared in medium to dense state compared to the typical values provided by Bishop and Henkel, 1962, as shown in Table 5.3. On the other hand, under TE, A_f for pure sand was -1.0, showing much more negative value than that obtained from TC. This substantial difference of A_f is almost certainly an indication of a high degree of anisotropy for the tested sand of which may occur during sample preparation.

For SA, SB, SC, and SD, when 5% of tyre chips were added, the A_f values for TC were observed to be quite similar to that for pure sand. For example, they were -0.3, -0.3, -0.28, and -0.27 corresponding to SA, SB, SC, and SD. Even though their values were similar to that of pure sand, the deviator stresses at failure were somewhat smaller. This indicates that for SA, SB, SC, and SD having 5% rubber, the excess pore water pressure generated by undrained monotonic triaxial test were less negative than that generated for pure sand. This is evident when considering Figures 5.35 – 5.38 showing the excess pore water pressure against the axial strain corresponding to SA, SB, SC, and SD. It is possible that as the rubber has highly elastic properties, during shearing it may contract thereby increasing the positive pore water pressure. For SA, SB, SC, and SD having 5% rubber, A_f for TE, similarly to TC, were very similar to that of pure sand.

For SA, SB, SC, and SD, when the rubber was increased to 10%, A_f for TC was still similar to that of pure sand as well as mixtures having 5% rubber. Compared to mixtures with 5% rubber, however, they were slightly greater. For TE, A_f values for SB, SC, and SD were very similar to those having 5% rubber. However, for SA, it was less negative.

When the rubber was increased to 20%, A_f values for SC and SD obtained from TC were still similar to those mixtures with 5% and 10% rubber. For SA and SB of which the sizes of rubber are smaller than those of SC and SD, however, A_f values for TC were observed to be considerably greater. For TE, similarly to TC, A_f values for SC and SD were quite similar to the SC and SD mixtures with 5% and 10% rubber, However, for SA and SB, they increased markedly. When the rubber was increased to 30% and higher, it was observed that A_f values obtained from sand mixed with various sizes of tyre chips were more varied, i.e., for TC and TE the smaller the size of rubber mixed the greater the A_f observed.

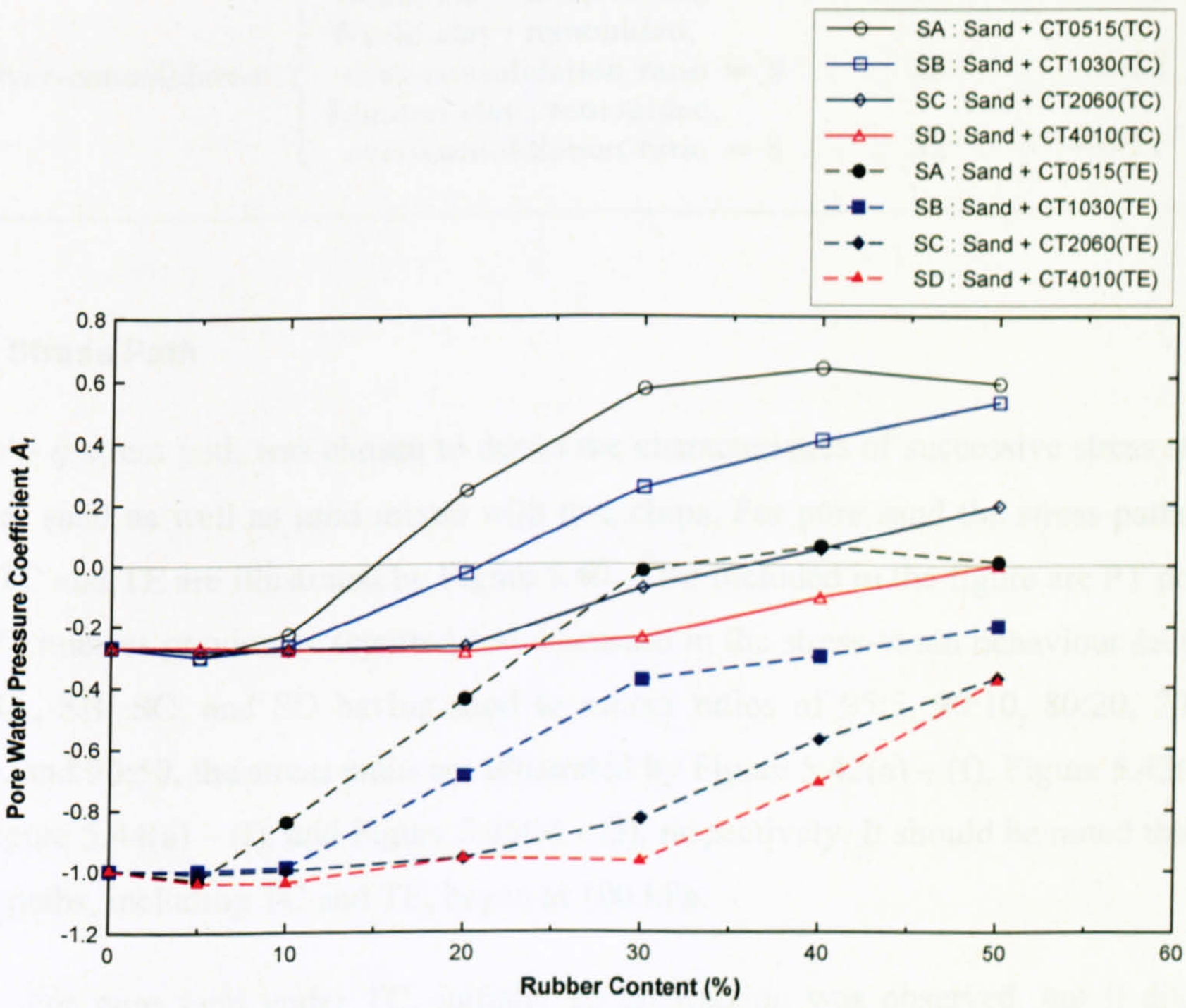

Figure 5. 39 A_f from undrained triaxial compression and extension tests versus rubber content

Table 5. 3 Typical value of A_f for various soil types: from consolidated-undrained tests (after Bishop and Henkel, 1962)

Type of Soil		*Plasticity Index*	*Value of A_f*
Normally consolidated	marine clay: undisturbed	60	+1·3
	London clay: remoulded	52	+0·97
	Weald clay: remoulded	25	+0·94
	alluvial sandy clay: undisturbed	18	+0·47
	loose sand	—	+0·08
	dense sand	—	−0·32
Over-consolidated	Weald clay: undisturbed	*c.* 25	−0·62
	Weald clay: remoulded, over-consolidation ratio = 8	25	−0·22
	London clay: remoulded, over-consolidation ratio = 8	52	−0·11

5.2.3 Stress Path

The p' - q stress path was chosen to depict the characteristics of successive stress states of pure sand as well as sand mixed with tyre chips. For pure sand the stress paths for both TC and TE are illustrated by Figure 5.40. Also included in the figure are PT points and PT lines as previously reported and discussed in the stress-strain behaviour section. For SA, SB, SC, and SD having sand to rubber ratios of 95:5, 90:10, 80:20, 70:30, 60:40, and 50:50, the stress paths are illustrated by Figure 5.42(a) – (f), Figure 5.43(a) – (f), Figure 5.44(a) – (f), and Figure 5.45(a) – (f), respectively. It should be noted that all stress paths, including TC and TE, began at 100 kPa.

For pure sand under TC, initially no contraction was observed, but it dilated slightly until the PT was met, indicating a dense sand behaviour. Note that the dilative and contractive characteristics for undrained shear tests are illustrated by Figure 5.41. The specimen then exhibited marked dilative behaviour as q and p' progressively increased until failure occurred at the maximum deviator stress and p'. After the shear failure occurred, the stress path moved backwards but with slightly steeper slope, as evident in the decrease of both q and p'. A steady state was not observed at the end of testing. For TE, contrary to TC, the stress path initially exhibited marked contractive

characteristics. Dilation was then observed when the stress path passed through the PT. In addition, after failure only q decreased, while p' continued to increase.

For SA having 5% rubber (see Figure 5.42(a)), the stress path for TC initially exhibited slight contractive behaviour until the PT. This was followed by marked dilative behaviour to failure where both q and p' began to decrease. This behaviour was observed to be quite similar to that of pure sand, apart from the slight contraction at the beginning of shearing. For TE, the stress path was quite comparable to that of pure sand, but it was observed that the initial positive pore pressures were slightly more pronounced.

When the rubber content was increased to 10% and higher, the stress paths for TC initially exhibited contractive behaviour, followed by marked dilation as observed for SA with 5% rubber and pure sand. However, no decrease of q and p' was observed for the mixtures having 10%, 20%, 30%, and 50% rubber (see Figure 5.42(b), (c), (d), (f)); whereas, for the mixtures containing 40% rubber (see Figure 5.42(e)) a slight decrease of q was observed, indicating that the peak deviator stress was achieved. For TE, the mixtures containing 10%, 20%, and 30% rubber exhibited stress paths similar to that of the mixture with 5% rubber. However, when the rubber was increased to 40% and higher, after the initial marked contractive tendency only a brief dilative period was observed; followed by renewed contractive behaviour, indicating that the necking of the specimen occurred (Hyodo *et al.*, 1998). In addition, for the mixtures with lower rubber contents of 5%, 10%, and 20%, it was observed that where PT points were met the stress path behaviour changed from contractive to dilative. However, for the mixtures containing higher rubber contents of 30%, 40%, and 50%, PT points were observed just after the stress path had changed from contractive to dilative.

For SB having 5%, 10%, 20%, 30%, 40%, and 50% rubber (see Figure 5.43(a) – (f)), the stress paths for both TC and TE were quite similar to those of SA with the same rubber contents.

When the size of rubber was slightly bigger, the stress paths for SC and SD were observed to be quite different, compared to those of SA and SB with the same amount of rubber. For example, for SC having 5% rubber (see Figure 5.44(a)), the stress path obtained from TC, instead of slight contractive behaviour at the beginning as observed

for SA and SB, the stress path was slightly dilative until the PT was met. This was followed by a marked dilative path until failure occurred, which was very similar to that of pure sand. In addition, the stress path for TE was also comparable to that of pure sand.

When the rubber was increased to 10% for SC (see Figure 5.44(b)), the stress paths for both TC and TE instead resembled to those of SA and SB but with 5% rubber. For SC with 20% and 30% rubber (see Figure 5.44(c), (d)), it was observed that the stress paths were comparable to those of SB but corresponding to 10% and 20% rubber. For SC containing 40% and 50% rubber (see Figure 5.44(e), (f)), the stress paths were quite equivalent to that of SB but with 30% rubber.

For SD of which the size of tyre chips was the biggest, the stress paths for the mixture containing 5% rubber (see Figure 5.45(a)), were comparable to those of pure sand and SC with the same rubber content. When the rubber was increased to 10% (see Figure 5.45(b)), the stress path for TC was distinct from those of SA, SB, and SC having the same rubber content: instead of having initially contractive behaviour, pore pressures were dilative until the PT was met, followed by more marked dilative behaviour until failure. This behaviour of SD with 10% rubber was very similar to that of SD but with 5% rubber. An initially contractive path was observed for SD when the rubber was increased to 20% (see Figure 5.45(c)), which was comparable to the stress paths SC with the same rubber content. For SD containing 40% and 50% rubber (see Figure 5.45(d), (e)), the stress paths obtained were quite similar to those of SC with the same rubber content. Although for SD containing the maximum rubber content of 50% (see Figure 5.45(f)), the stress path for TC was equivalent to that of SC with the same rubber content, that for TE was more distinct, i.e., after a brief dilative trend, a contractive stress path was observed.

It is worthwhile investigating the stress paths obtained from the mixtures having the same rubber content, but various size of tyre chips, so that the effects of size of tyre chips can be compared and examined. The stress paths, both TC and TE, for SA, SB, SC, and SD, all having the same rubber content of 5% are illustrated by Figure 5.46. Figures 5.47 - 5.51 illustrate the stress paths for SA, SB, SC, and SD, having rubber contents of 10, 20, 30, 40, and 50%, respectively.

It was observed that, as a whole, at the same sand to rubber ratio the stress paths for various sizes of rubber were somewhat similar. However, some distinctions should be noted: (1) at the beginning of shearing for TC the mixtures containing smaller size of tyre chips exhibited slightly contractive paths; whereas, for the mixtures containing larger size tyre chips no contractive tendency was observed, and (2) at the end of testing when the axial strain was just over 20% for TC and 15% for TE, the final q and p' were different, depending on the size of tyre chips added, i.e., the larger the size of tyre chips the greater q and p' were observed, indicating higher shear resistance. Note that the tendency for more dilative behaviour when the size of tyre chips was greater was also reported by Ghazavi and Sakhi (2005).

The stress paths for SA having sand to rubber ratios of 100:0, 95:5, 90:10, 80:20, 70:30, 60:40, and 50:50 are illustrated by Figures 5.52, so that the behaviour for a particular mixture with various rubber contents can be compared. Figure 5.53, Figure 5.54, and Figure 5.55 illustrate the stress paths for SB, SC, and SD, respectively.

Overall, the stress paths for the SA mixtures, SB, SC, and SD, after passing through PT, were very similar, regardless of the quantities of rubber added. For SA and SB under TC, it was observed that the reverse of the stress paths (changing of q and p' from increasing to decreasing) was only exhibited for 5% rubber. However, for SC and SD, the reverse was not observed for 30% rubber and higher. In addition, it was observed that, for both TC and TE, the greater the percentage of rubber added, the lower q and p' at the end of shearing.

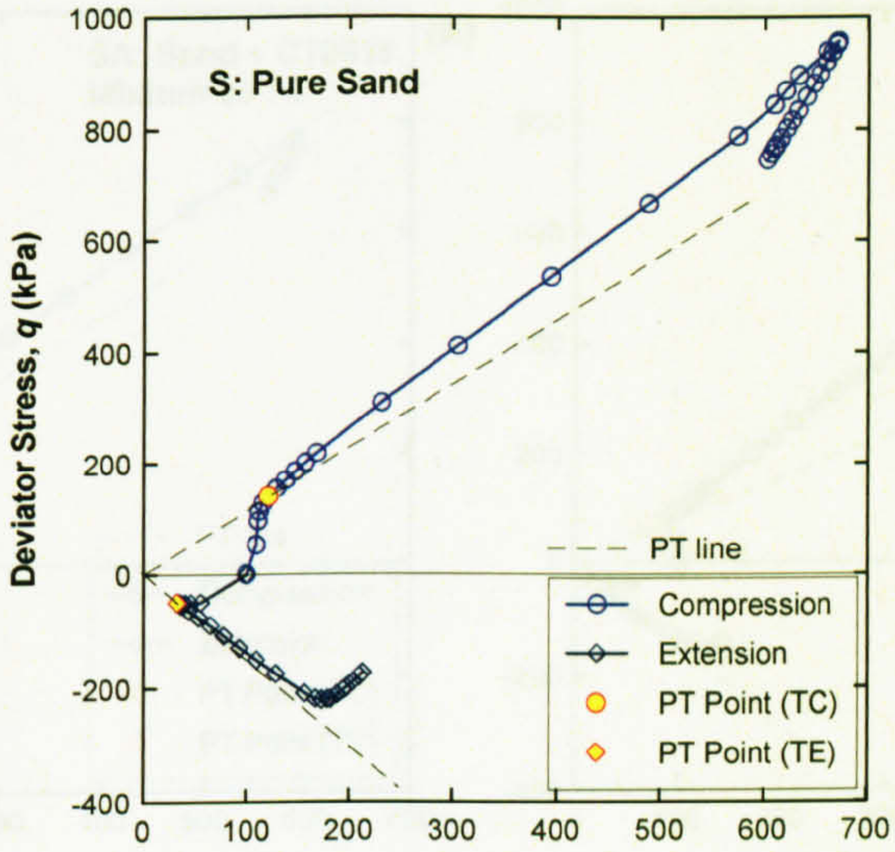

Figure 5. 40 Stress paths for pure sand, S

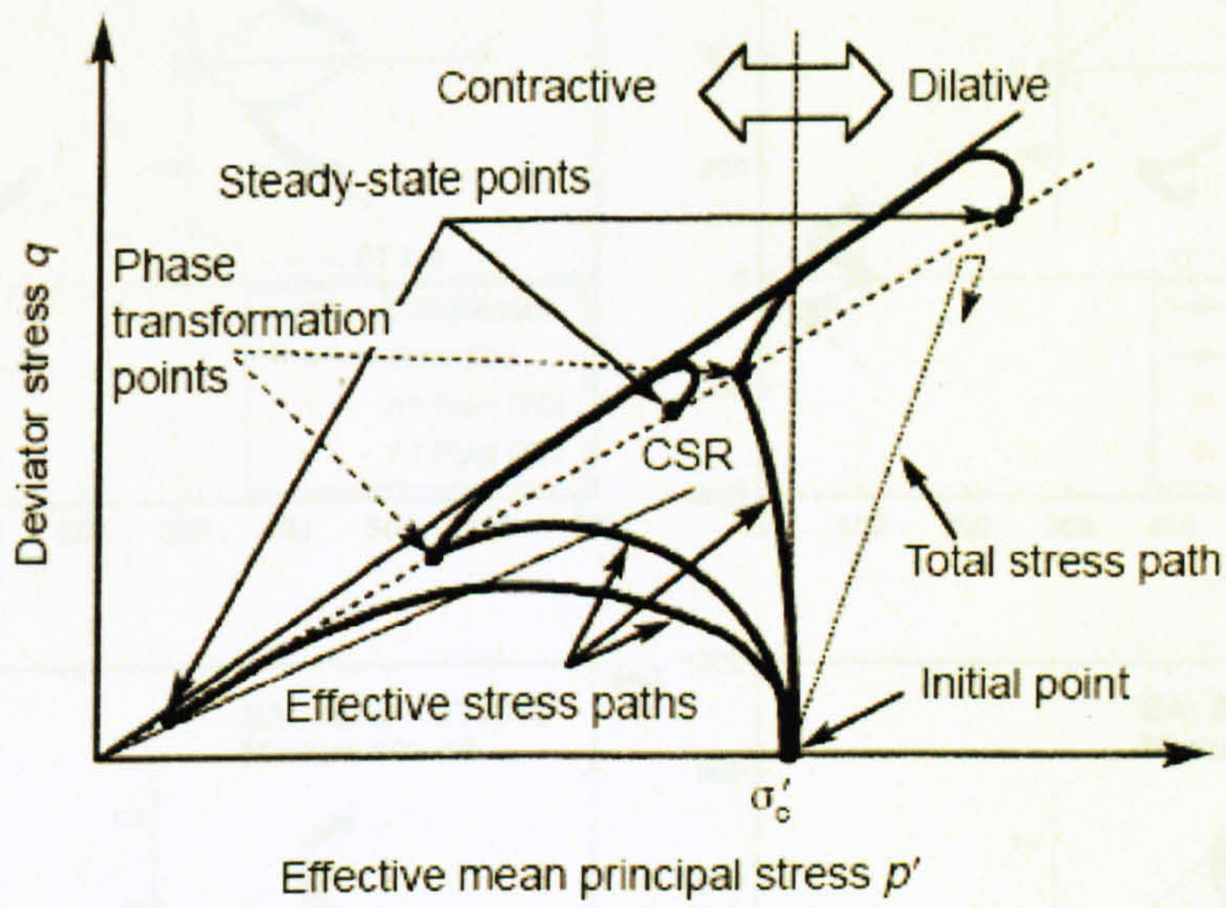

Figure 5. 41 Idealised stress paths for undrained shear tests (after Hyodo *et al.*, 1998)

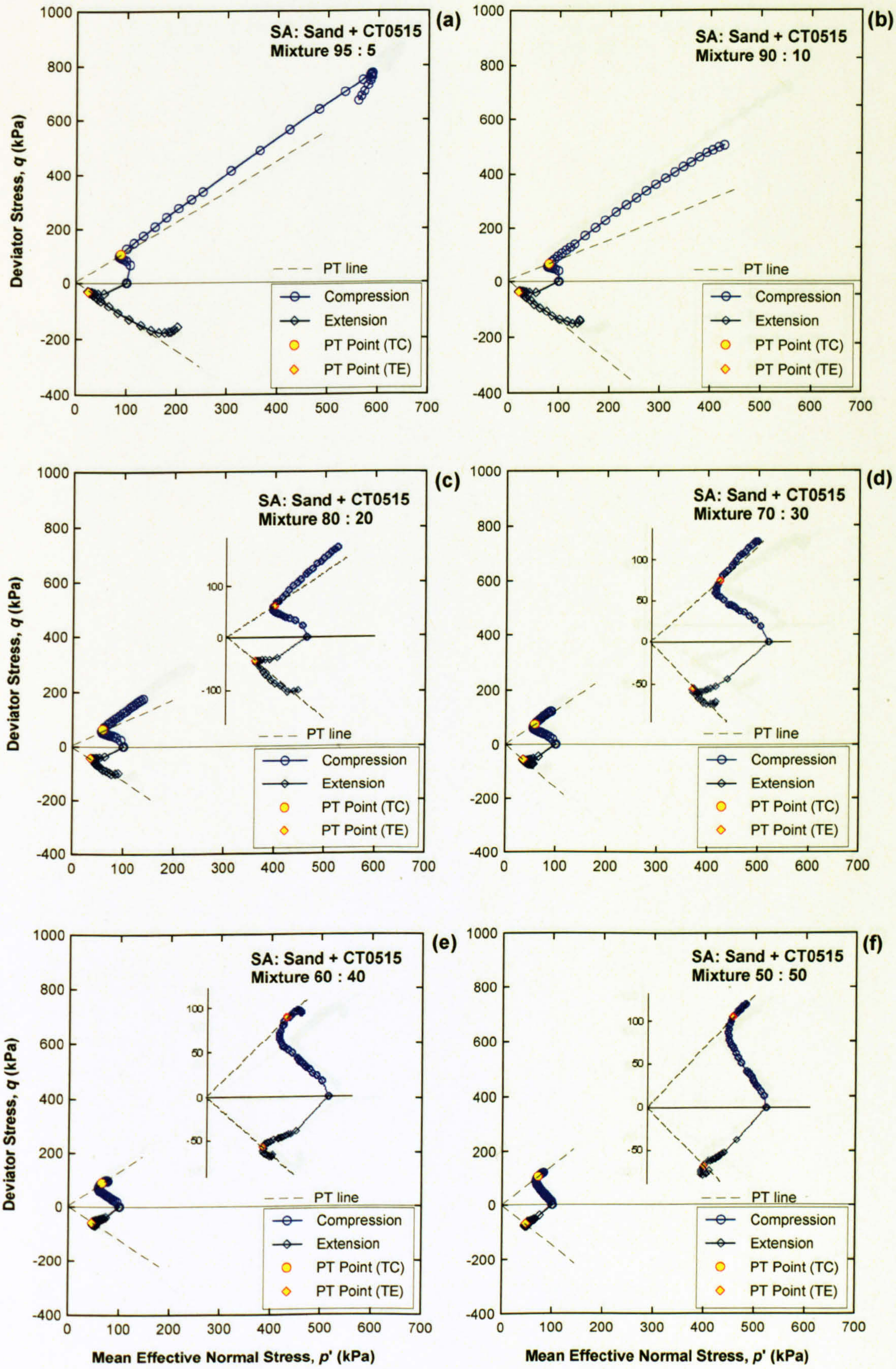

Figure 5. 42 Stress paths for Sand + CT0515, SA

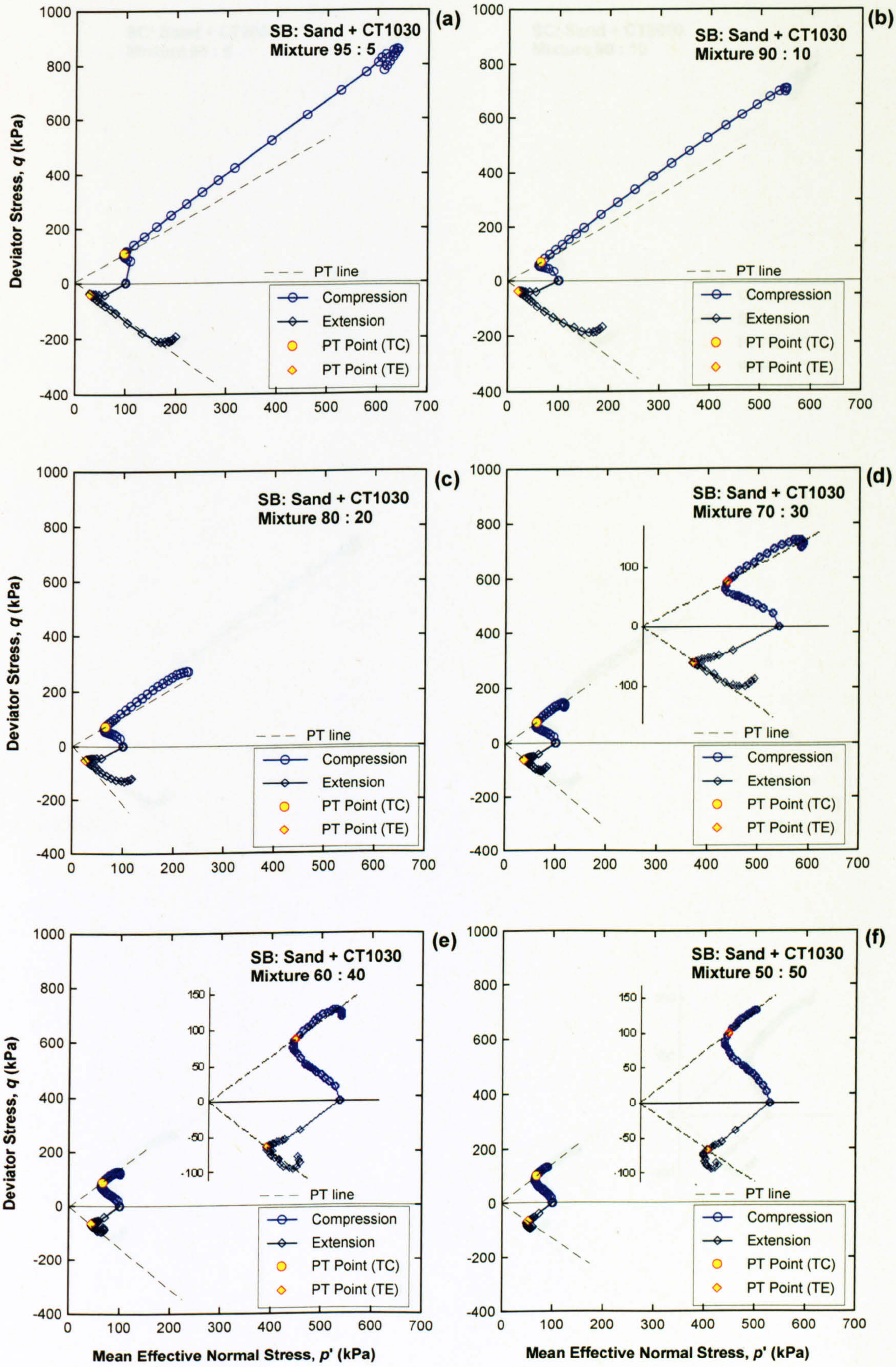

Figure 5. 43 Stress paths for Sand + CT1030, SB

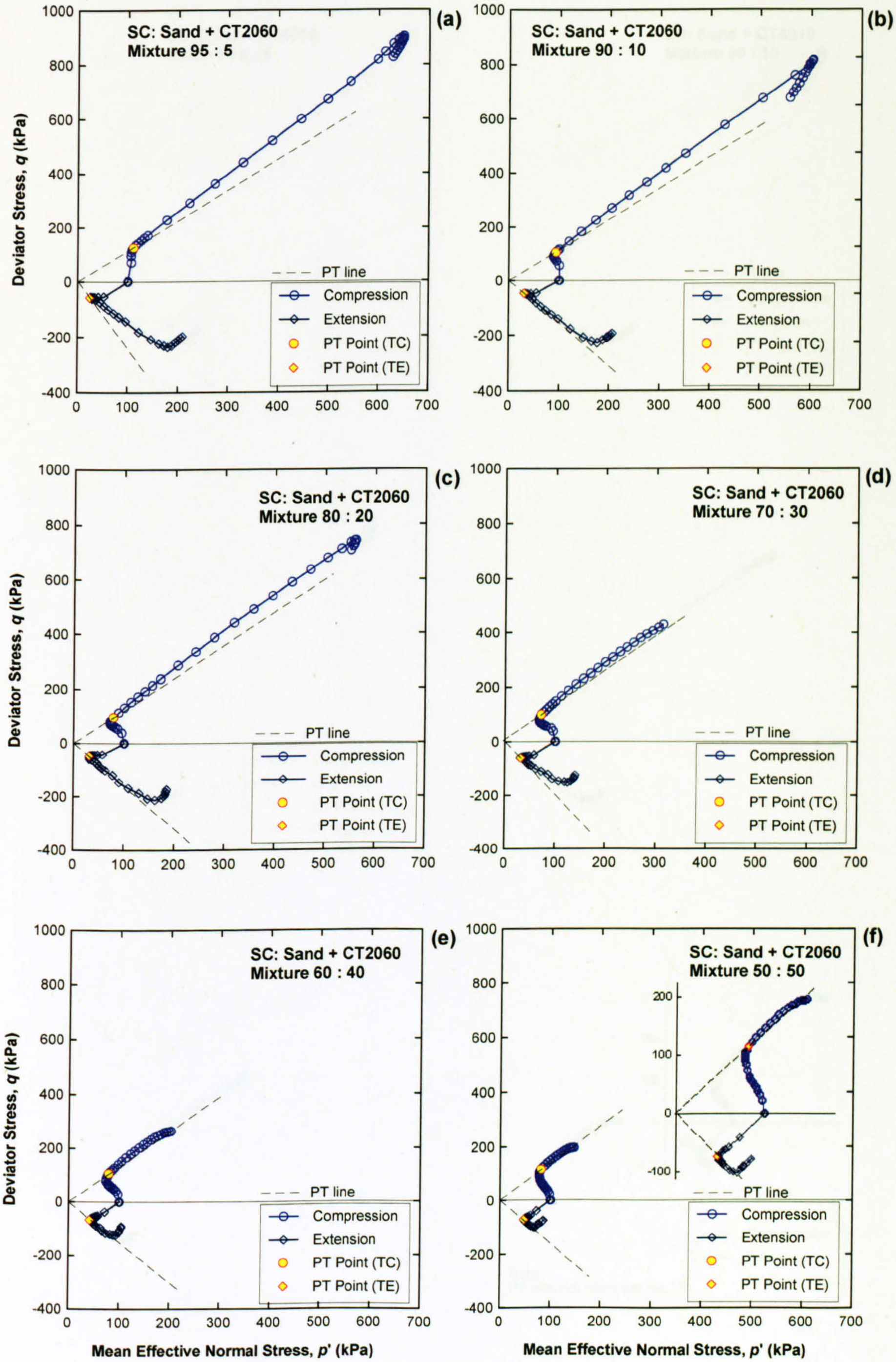

Figure 5. 44 Stress paths for Sand + CT2060, SC

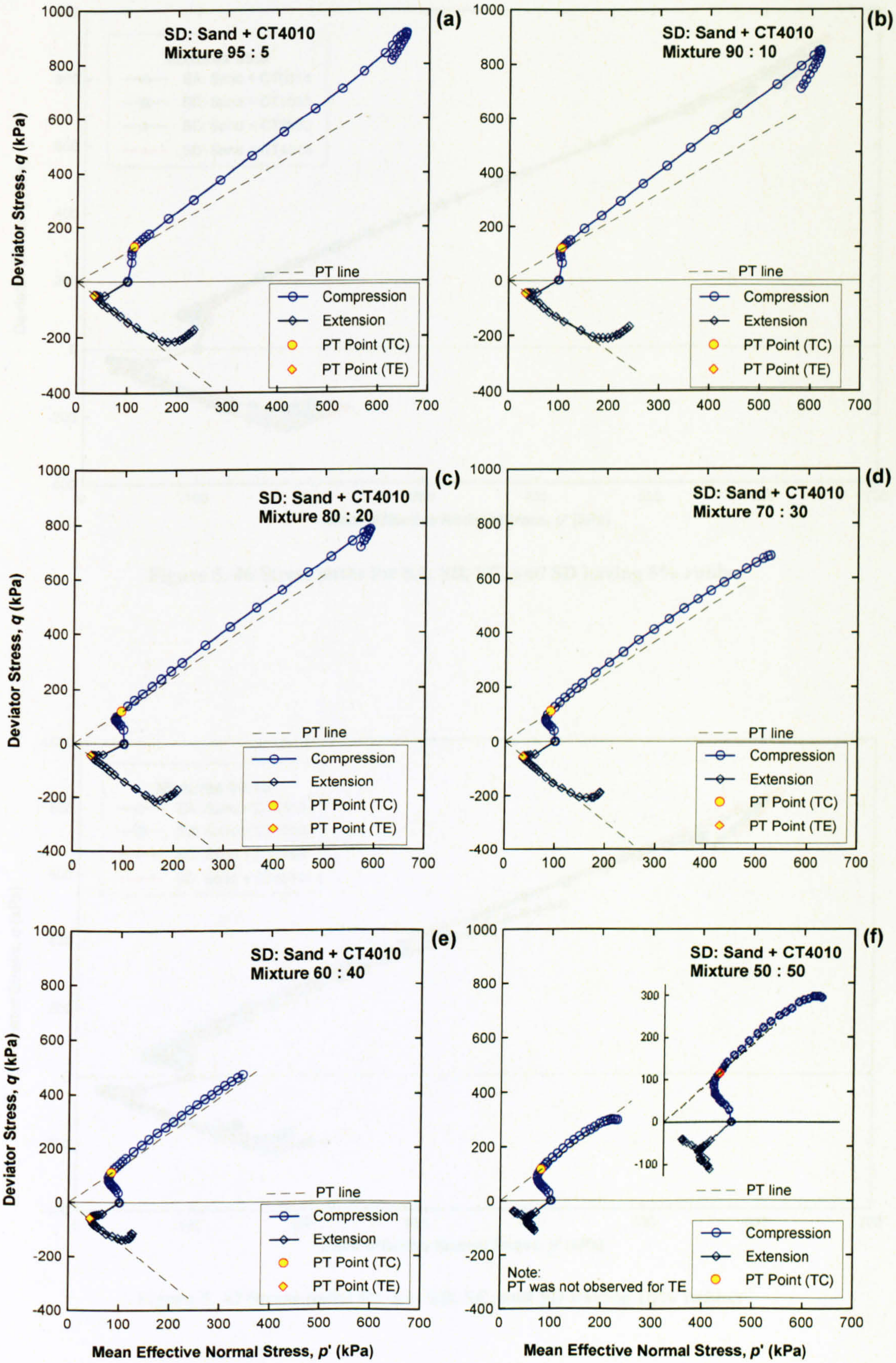

Figure 5. 45 Stress paths for Sand + CT4010, SD

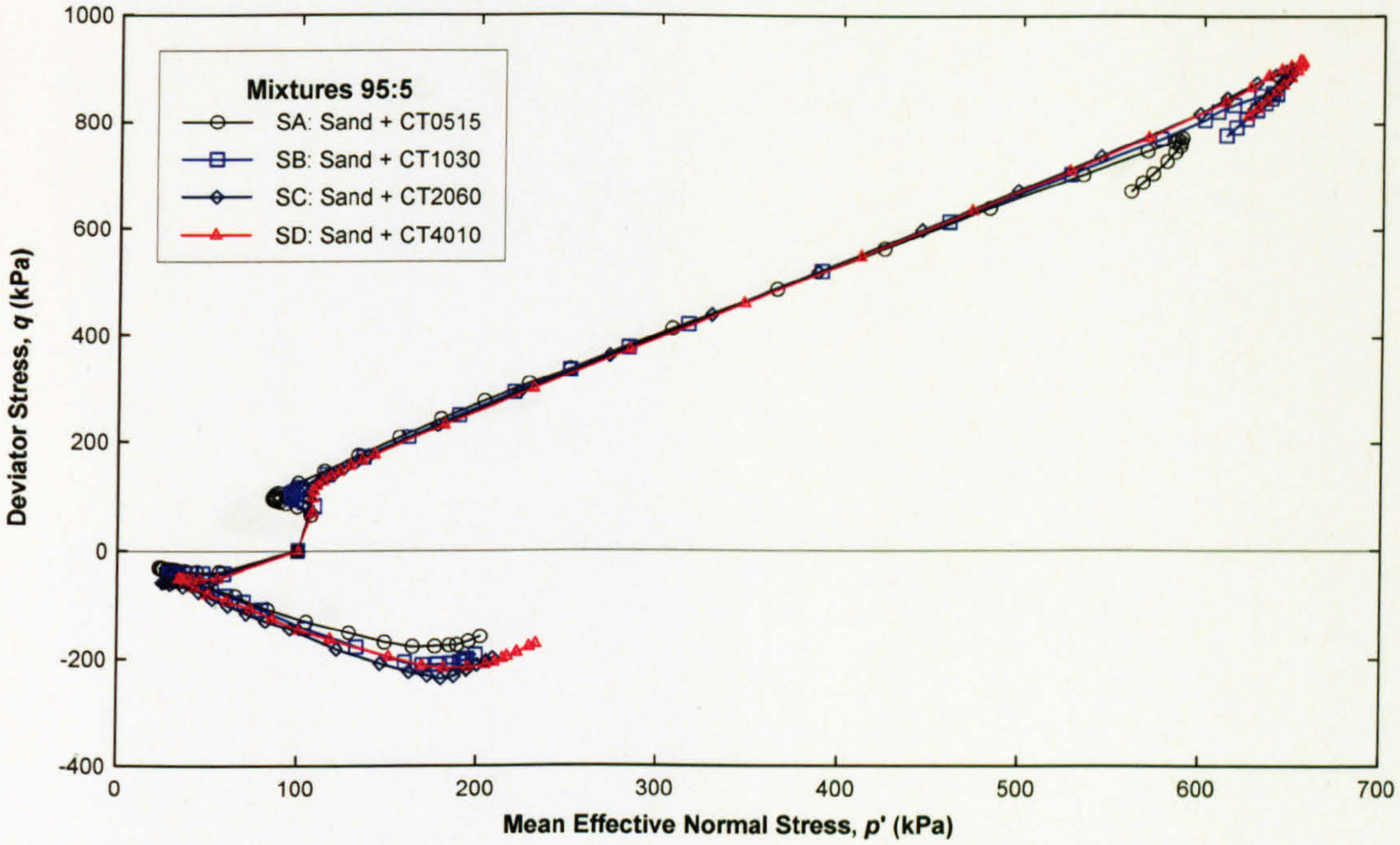

Figure 5. 46 Stress paths for SA, SB, SC, and SD having 5% rubber

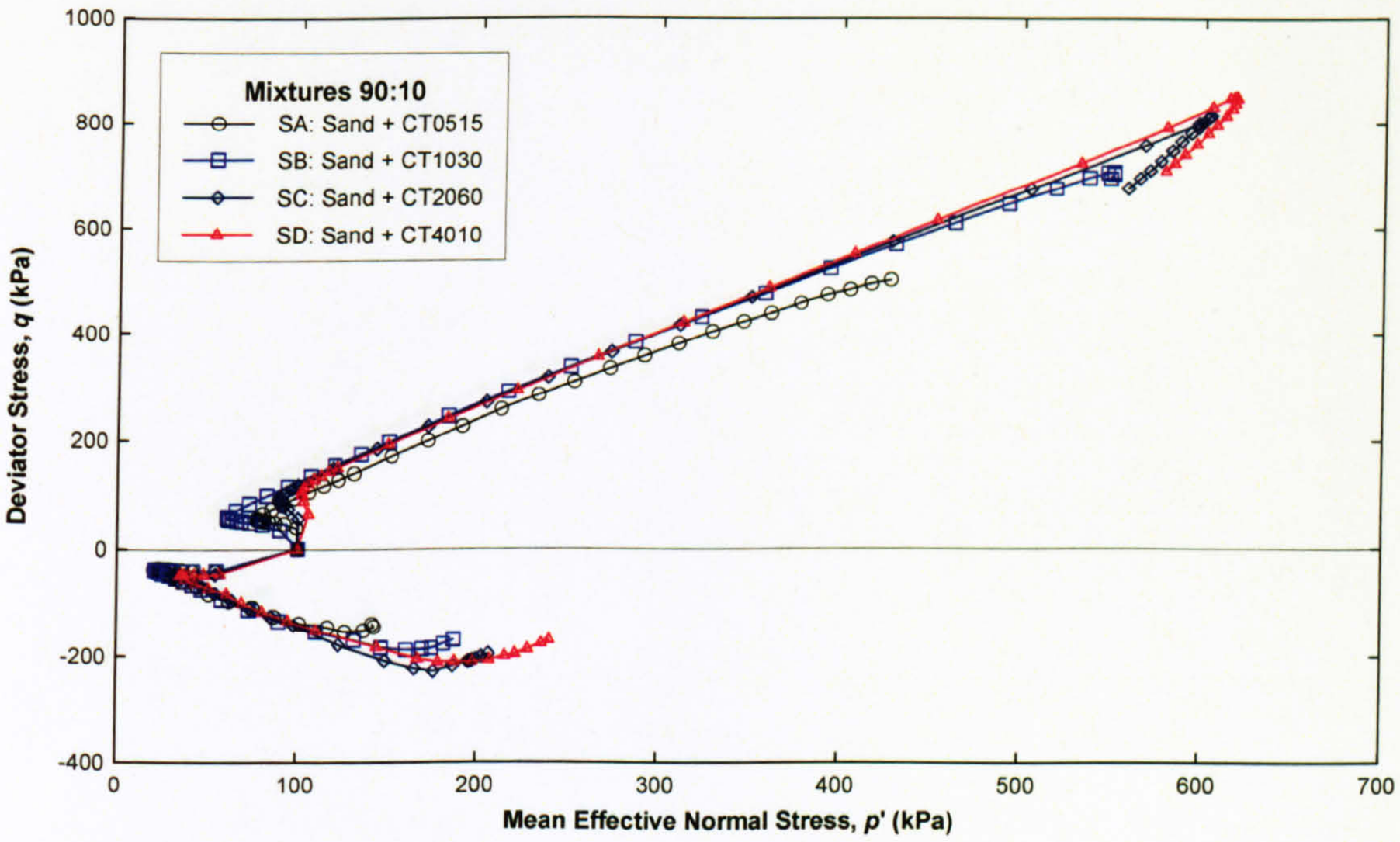

Figure 5. 47 Stress paths for SA, SB, SC, and SD having 10% rubber

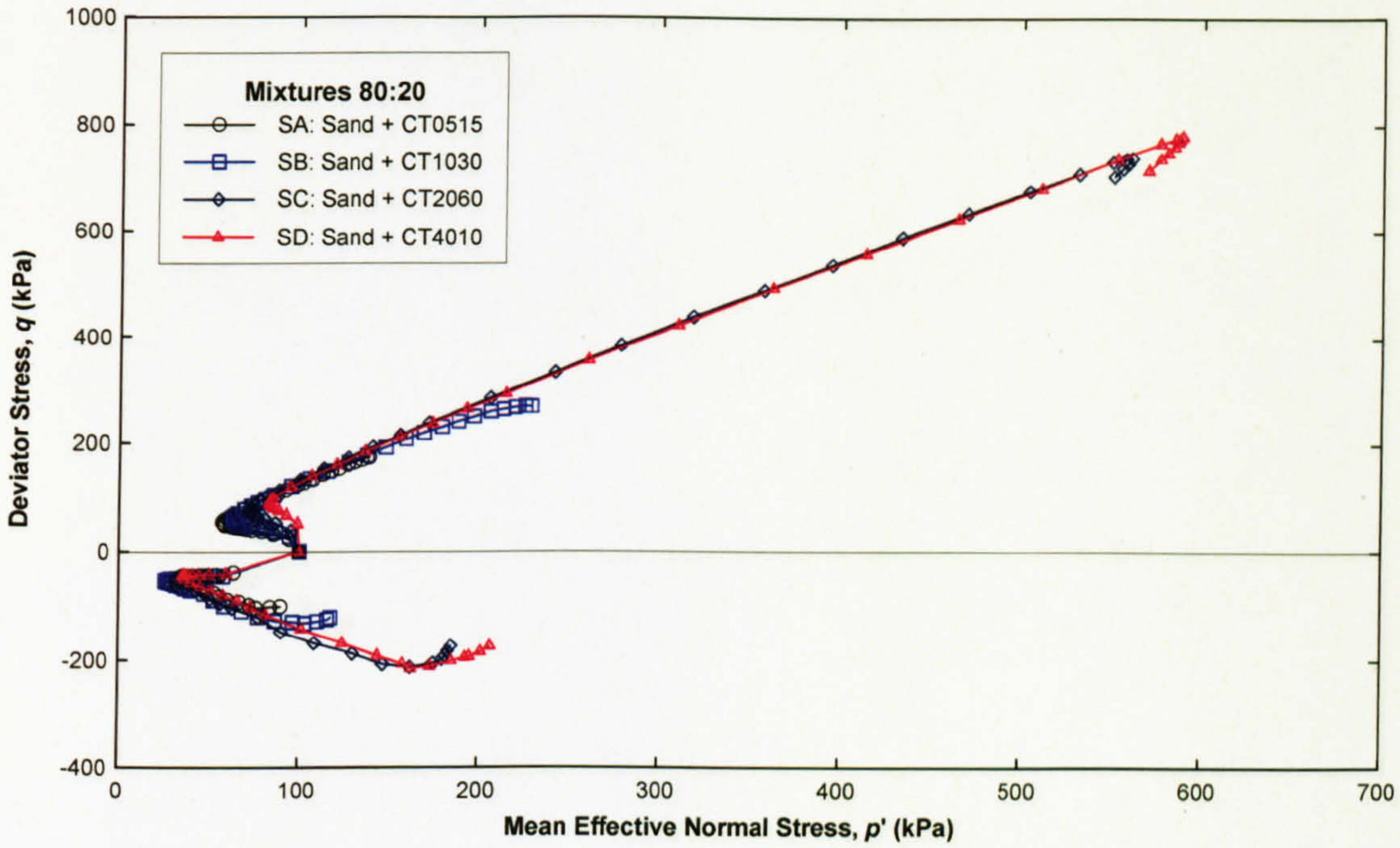

Figure 5. 48 Stress paths for SA, SB, SC, and SD having 20% rubber

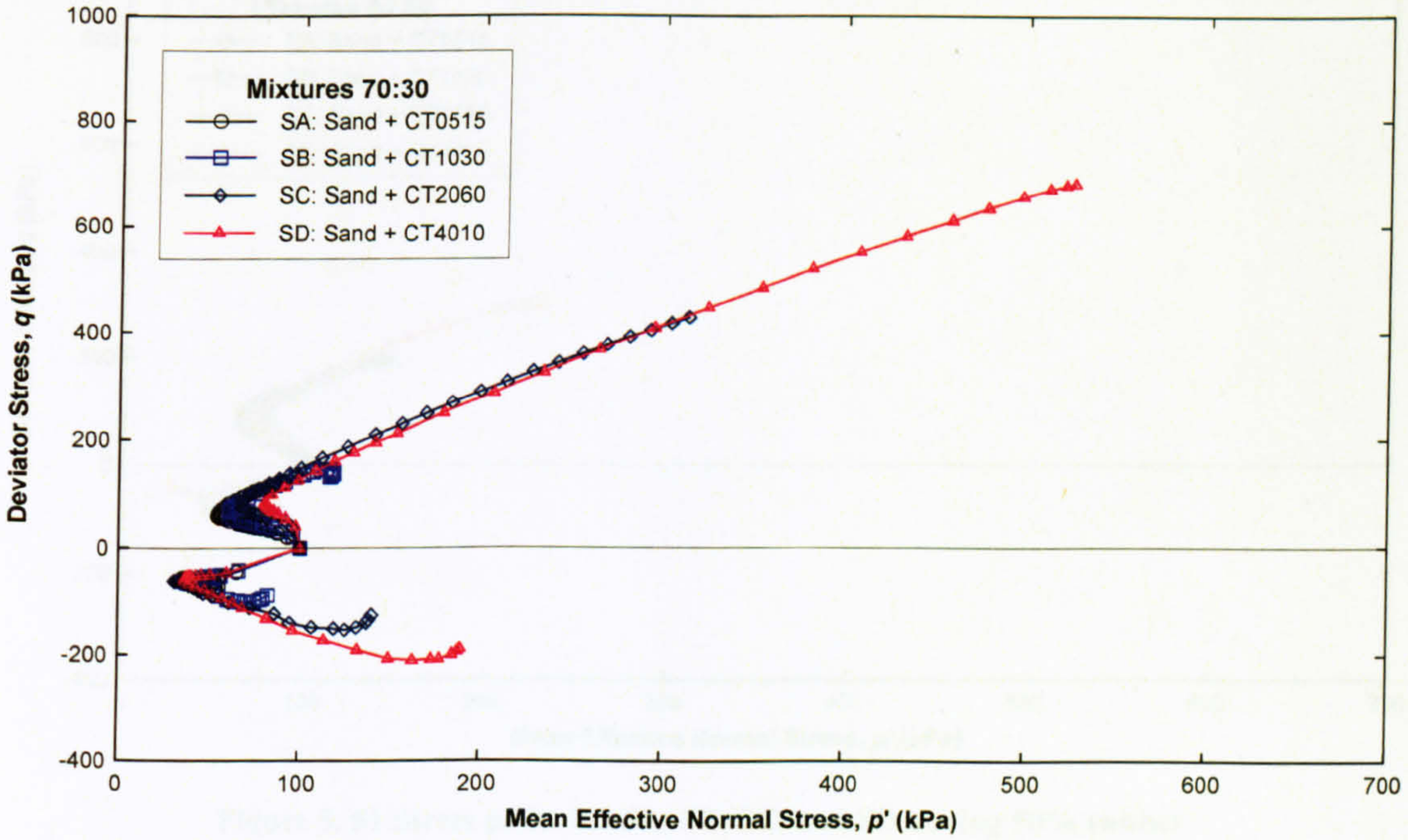

Figure 5. 49 Stress paths for SA, SB, SC, and SD having 30% rubber

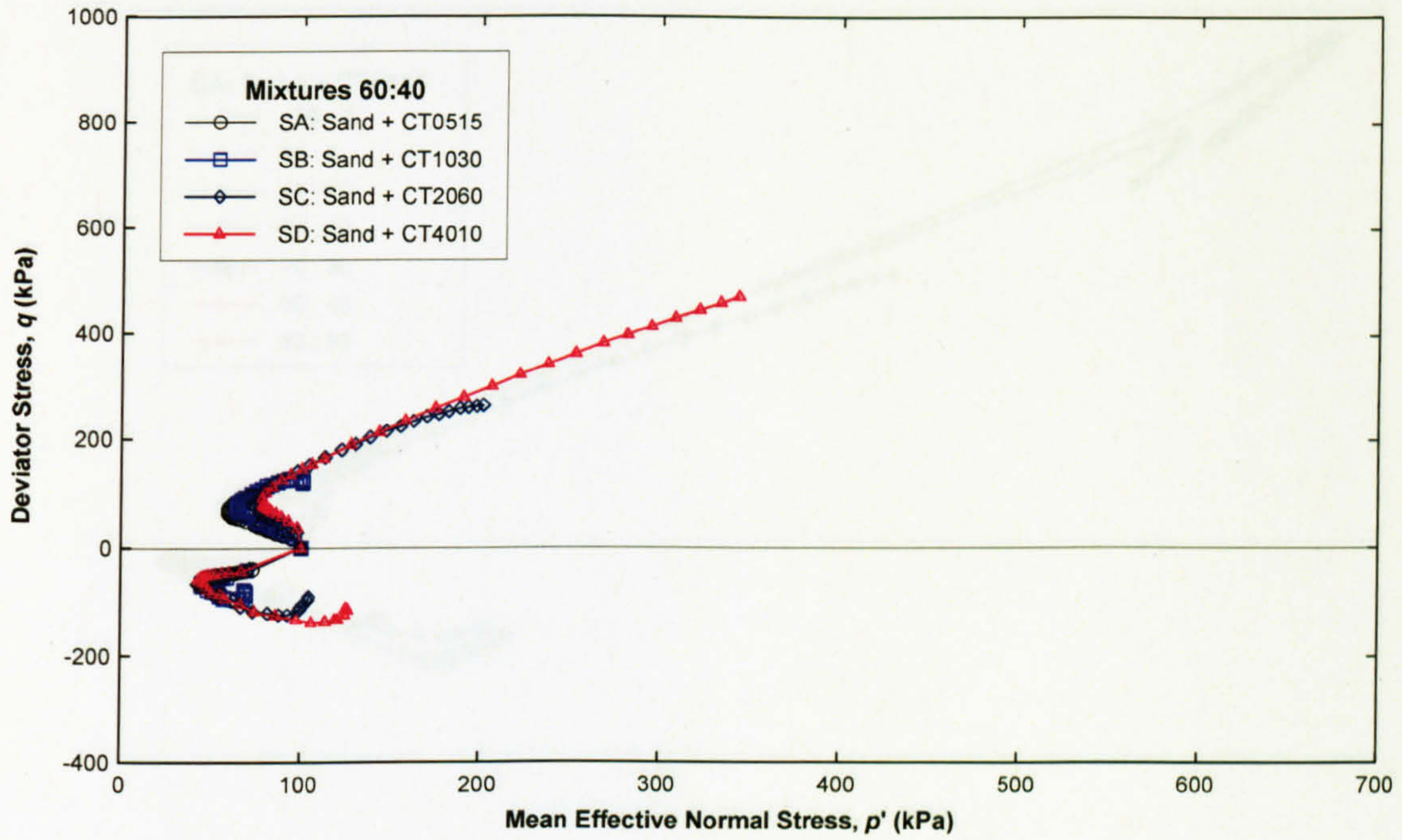

Figure 5. 50 Stress paths for SA, SB, SC, and SD having 40% rubber

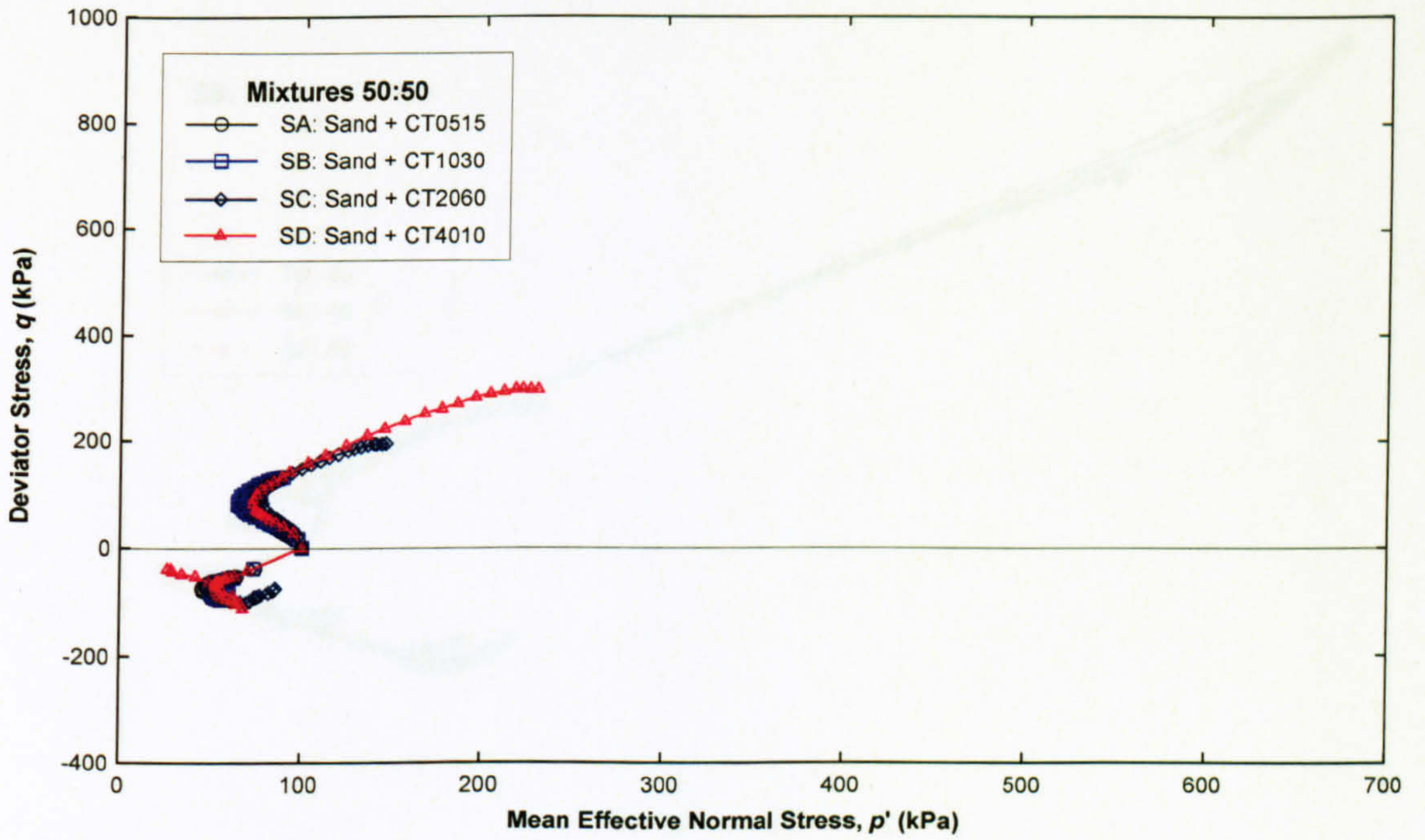

Figure 5. 51 Stress paths for SA, SB, SC, and SD having 50% rubber

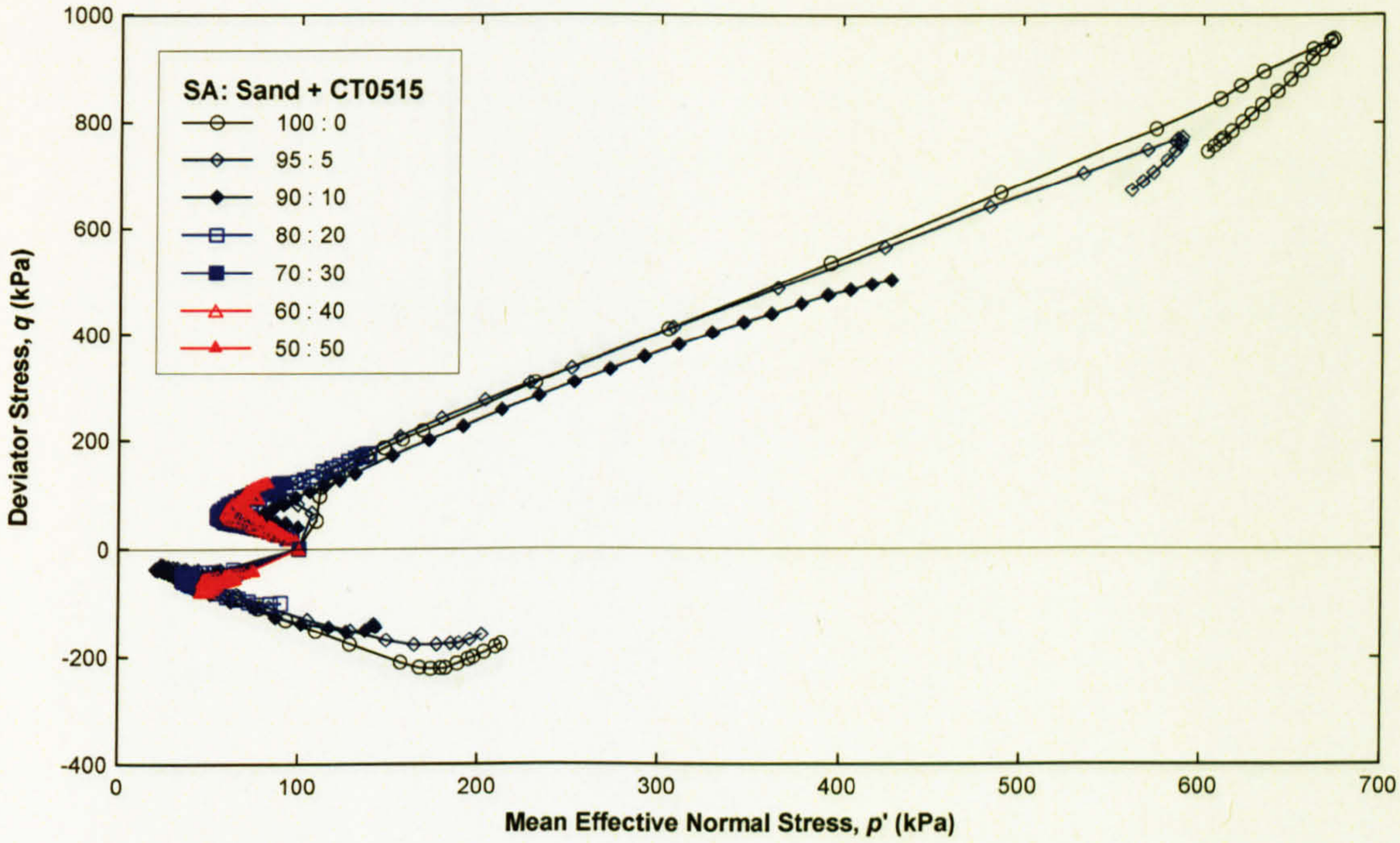

Figure 5. 52 Stress paths for mixtures SA

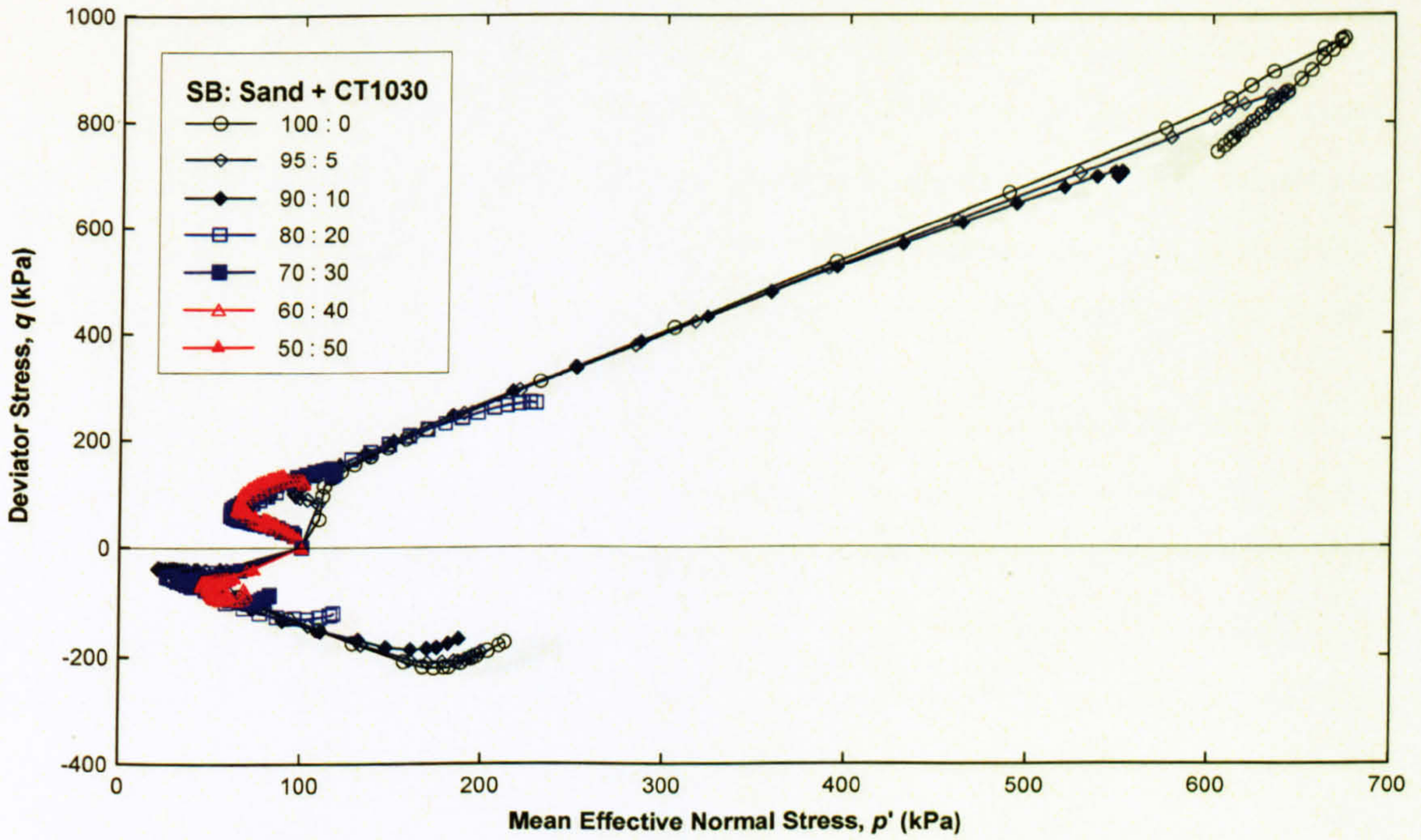

Figure 5. 53 Stress paths for mixtures SB

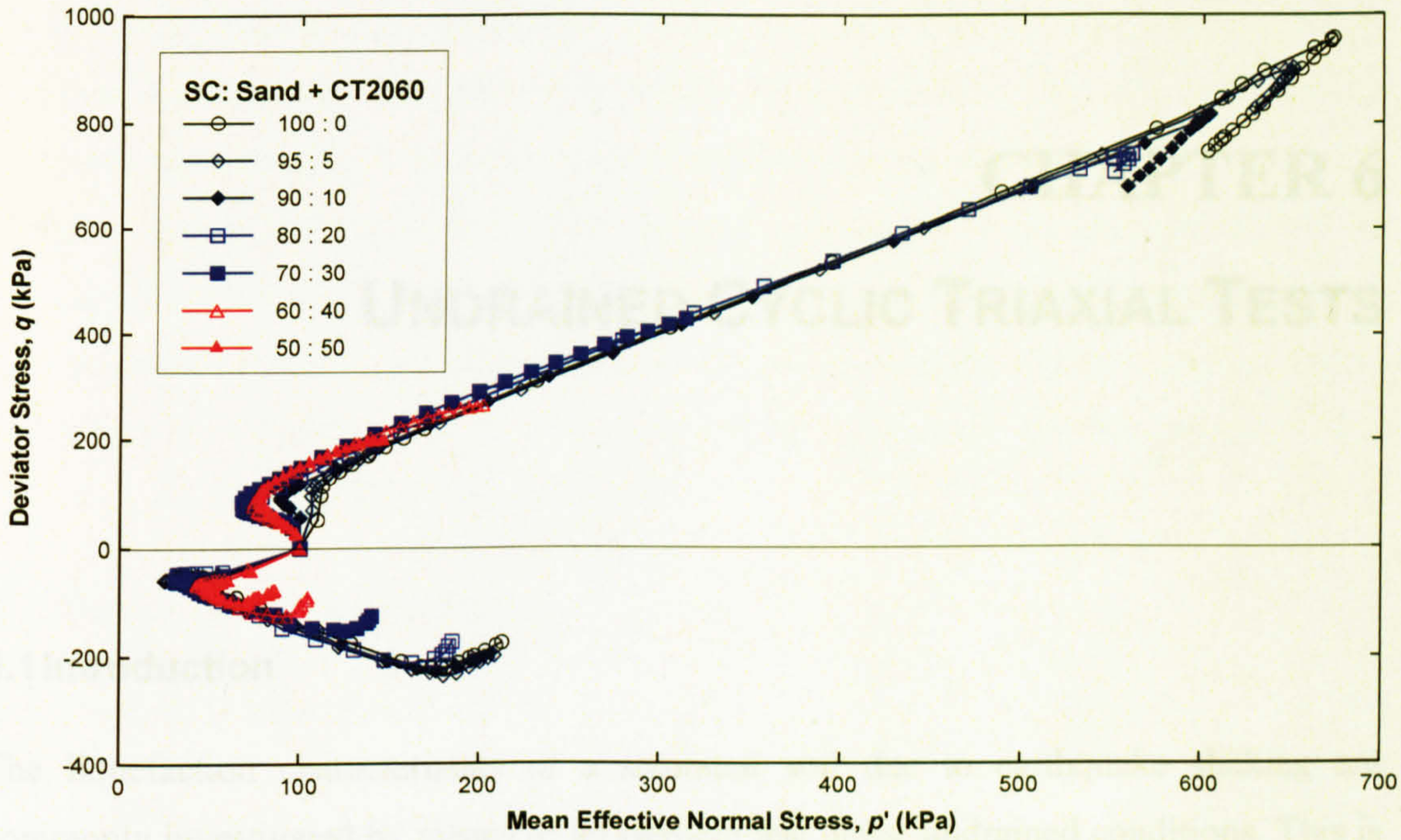

Figure 5. 54 Stress paths for mixtures SC

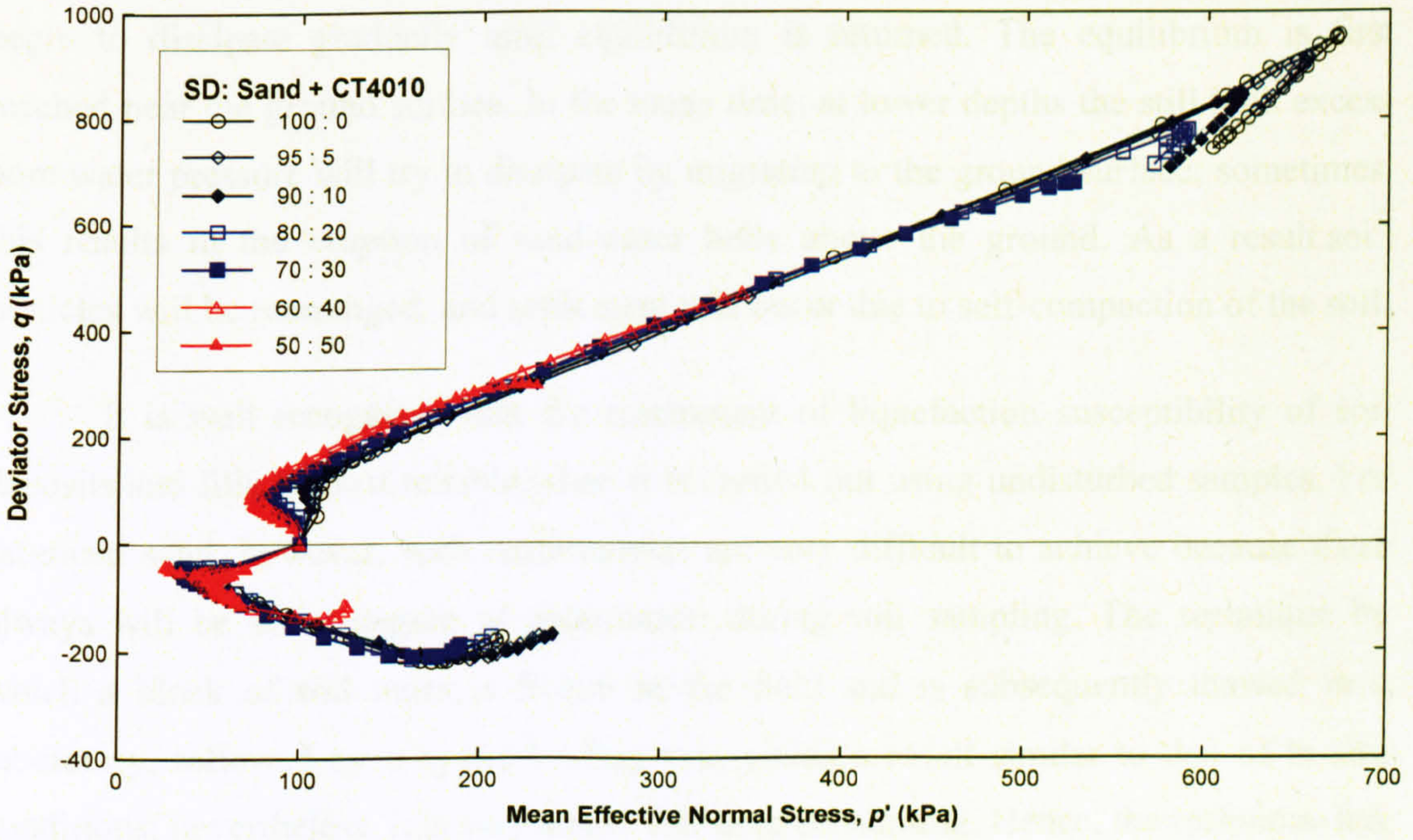

Figure 5. 55 Stress paths for mixtures SD

CHAPTER 6

UNDRAINED CYCLIC TRIAXIAL TESTS

6.1 Introduction

The liquefaction characteristics of a saturated soil due to earthquake shaking are commonly investigated by means of an element test under undrained conditions. This is based on the assumption that strong ground motion occurs over a very short period such that the excess pore water pressure is maintained for as long as the ground shaking continues. After the earthquake ceases, however, the excess pore water pressure will begin to dissipate gradually until equilibrium is returned. The equilibrium is first reached near the ground surface. In the mean time, at lower depths the still high excess pore water pressure will try to dissipate by migrating to the ground surface; sometimes, this results in the eruption of sand-water boils above the ground. As a result soil particles will be rearranged, and settlement will occur due to self-compaction of the soil.

It is well recognised that the assessment of liquefaction susceptibility of soil deposits and fills is most reliable when it is carried out using undisturbed samples. For saturated sand, however, such requirements are very difficult to achieve because there always will be some degree of disturbance during soil sampling. The technique by which a block of soil mass is frozen in the field and is subsequently thawed in a laboratory, followed by a cyclic loading test, yields a result similar to that of in situ conditions; nevertheless, it is very costly and time consuming. Hence, the technique has only been employed for critical projects such as nuclear power plants and radar stations.

For most developments, however, it is not practical to carry out such advanced techniques. As a result, the liquefaction characteristics have normally been studied by means of testing reconstituted samples that are brought to the same densities and stress states as in the field. The cyclic simple shear test is frequently used to reproduce the

shear stress generated by earthquake loading in a soil but this can equally well be achieved by a conventional triaxial apparatus. The test results from the cyclic triaxial test have been compared with case histories indicating that it provides a reliable result. For that reason, the cyclic triaxial test is used extensively in liquefaction studies. To simulate the earthquake loading conditions on the specimen a standard triaxial loading frame requires some modifications such as an ability to apply repeated cyclic loading (usually 0.1 – 1.0Hz) as well as an automated acquisition system connected to a computer for data recording and processing.

6.2 Results and Discussions

6.2.1 Cyclic Triaxial Test Results

The undrained cyclic triaxial test results (Figures 6.1 to 6.29) include the following graphs: (a) cyclic deviator stress q_{cyc} versus number of load cycles N, (b) axial strain ε_a versus N, (c) pore water pressure ratio $\Delta u/\sigma'_{3c}$ versus N, (d) q_{cyc} versus ε_a, and (e) q_{cyc} versus mean normal effective stress p'. Note that p' was obtained from $(\sigma'_1 + 2\sigma'_3)/3$ whereby σ'_1 and σ'_3 denote major and minor principal effective stresses.

Graph (a) is not only shows the cyclic deviator stress applied, but is also used to examine the sinusoidal wave form cycling loading throughout the test for uniformity of unsymmetrical compression-extension load peaks, non-uniformity of pulse duration, and load fall-off at large strains. Note that the cyclic deviator stress is sometimes plotted against time, instead of number of load cycles. However, if the liquefaction of a soil is of interest, it is more straightforward to plot the cyclic loading against the number of load cycles.

Graphs (b) and (c) are very useful in terms of identifying the cycle that the liquefaction failure occurs, by observing either 5% $\varepsilon_{a,DA}$ is reached for graph (b) or $\Delta u/\sigma'_{3c}$ is approximately 1.0 for graph (c). The stress-strain relationship can be examined in graph (d); which illustrates the degradation of soil stiffness during cyclic loading. The liquefaction can also be observed from graph (d) by examining the strain amplitude. Graph (e) illustrates the stress path that starts at the initial mean effective normal stress, and travels towards zero mean effective normal stress. In addition, the anisotropy of a soil can also be investigated from the stress path by examining its angles

during liquefaction. Normally the angle of the stress path in compression is higher than that in extension indicating the anisotropy of a soil.

The undrained cyclic triaxial test results for pure sand, S, are summarised in Table 6.1 which shows test number indicating the applied cyclic deviator stress; *B* value indicating the degree of saturation; initial void ratio *e*; void ratio after consolidation e_o,; applied cyclic deviator stress q_{cyc}; cyclic stress ratio *CSR*; number of cycles *N* at which $\Delta u/\sigma'_{3c}$ was approximately 1.0; and number of cycles *N* at which $\varepsilon_{a,DA}$ reached 5%, in other words, liquefaction.

For sand mixed with CT0515 tyre chips, SA mixtures, the test results are summarised and shown in Table 6.2. The summaries of the test results for sand mixed with CT1030 tyre chips (SB mixtures), CT2060 tyre chips (SC mixtures), and CT4010 tyre chips (SD mixtures), are in Tables 6.3, 6.4, and 6.5 respectively. Note that NA* in Tables 6.2, 6.3, 6.4, and 6.5 indicates that the tests were necessarily terminated before the pore water pressure ratio $\Delta u/\sigma'_{3c} \cong 1.0$ because either the maximum or minimum stroke of the actuator (± 15mm) was reached, i.e., the limitation of the test machine.

It can be seen that the range of q_{cyc} applied for pure sand shown in Table 6.1 in order to obtain the cyclic strength is between 25 and 43kPa. As expected, the greater the cyclic deviator stress applied the lower the number of cycles at which the specimen liquefied. During the consolidation it was observed that there was little change between the initial void ratio and the consolidated void ratio, that is, between 0.676 and 0.669, respectively. This may be because the consolidation pressure applied was just 100kPa.

For pure sand specimens tested with q_{cyc} of 43, 37, 32, 29, and 25kPa, the cycle numbers at which the liquefaction failure by means of 5% $\varepsilon_{a,DA}$ reached, occurred after 3, 5, 31, 98, and 204 cycles, respectively. Comparing the difference between the number of cycles at which the pore water pressure ratio was approximately 1.0 and the number of cycles at which the double amplitude axial strain reached 5%, it was surprisingly found to be almost the same, i.e., both criteria were met at similar cycles of loading. These findings are a confirmation of the double amplitude axial strain of 5% being used as a liquefaction failure criterion.

For SA (Table 6.2) with rubber contents of 5, 10, and 20%, the ranges of applied q_{cyc} were necessarily decreased corresponding to the increase of rubber in order to obtain the cyclic strength; that is, 20.5 - 36.5kPa, 16.5 - 28.5kPa, and 16 - 28kPa, respectively. However, when the mixtures contained much higher rubber contents, the ranges were reversed, i.e., they were 23 - 35kPa, 31 - 42kPa, and 37 - 51.5kPa for the mixtures with rubber contents of 30, 40, and 50%, respectively.

The similarity between N at $\Delta u/\sigma'_{3c} \cong 1.0$ and N at 5% $\varepsilon_{a,DA}$ for small rubber contents was found to be similar to that for pure sand. However when the specimens contained higher quantities of rubber, especially for the mixtures 70:30 and 50:50, only the 5% $\varepsilon_{a,DA}$ criterion was met; as the pore water pressure did not reach the initial effective stress owing to the limiting stroke of the actuator as previously discussed. For SA having 40% rubber, however, at lower q_{cyc} of 31 and 34kPa, both liquefaction failure criteria were met.

Another point that should be noted is that as the rubber content was increased, the difference between the initial void ratio and the consolidated void ratio was observed to be greater. This is apparent when considering the differences for the mixtures 60:40 and 50:50, which are 0.756 – 0.656 and 0.779 – 0.623, respectively. This, however, was expected to happen as the rubber is more elastic than the sand. Thus as more rubber was added, the greater the compressibility. Thus, when the rubber was added to the mixtures in higher quantities, the behaviour of the sand-rubber matrix may be governed by the rubber, not the sand. This is evident when comparing e_o and e of S and SA with 50% rubber. The e_o and e for S and SA with 50% rubber were 0.676 and 0.779; 0.669 and 0.623, respectively. It can be seen that the initial void ratio of S was lower than that of SA. However, after the consolidation the void ratio of SA was lower than that of S, verifying the initial assumption of highly elastic properties of the rubber.

For SB (Table 6.3) it was observed that the ranges of applied q_{cyc} for varied mixtures had a similar pattern to those of SA; that is, they gradually decreased for the mixtures having rubber contents of 5, 10, and 20%, and gradually increased for the mixtures having rubber contents of 30, 40, and 50%. Moreover, the comparison between N at $\Delta u/\sigma'_{3c} \cong 1.0$ and N at 5% $\varepsilon_{a,DA}$ as well as the difference between the initial void ratio and the consolidated void ratio were found to have the same trend as of SA.

For SC (Table 6.4) the decrease and increase of the ranges of applied q_{cyc} was observed to be similar to those of both mixtures SA and SB. In addition, the conditions at which the specimens liquefied and the difference of initial void ratio and consolidated void ratio were also found to be comparable with both SA and SB.

Those findings for SA and SB were also similar to the results for SD (Table 6.5), including the change of the ranges of applied q_{cyc}, the difference between e and e_o, and the comparison of liquefaction failure conditions. The distinction, however, was that it was only for the 50:50 mixtures that the condition at which $\Delta u/\sigma'_{3c} \cong 1.0$ was not met; for the rest both conditions of $\Delta u/\sigma'_{3c} \cong 1.0$ and $\varepsilon_{a,DA} = 5\%$ were met.

Table 6. 1 Summary of cyclic triaxial tests for pure sand, S

Sand : Rubber Ratio	Test No.	*B* value	e_o	e	q_{cyc} (kPa)	*CSR*	*N* at $\Delta u/\sigma'_{3c} \cong 1$	*N* at 5% $\varepsilon_{a,DA}$
100 : 0	100S430	0.98	0.672	0.665	43.0	0.215	2	3
	100S370	0.97	0.679	0.673	37.0	0.185	4	5
	100S320	0.97	0.680	0.674	32.0	0.160	31	31
	100S290	0.97	0.671	0.664	29.0	0.145	98	98
	100S250	0.97	0.676	0.670	25.0	0.125	204	204
	Average		0.676	0.669				

Table 6. 2 Summary of cyclic triaxial tests for sand mixed with CT0515 tyre chips, SA

Sand : Rubber Ratio	Test No.	*B* value	e_o	e	q_{cyc} (kPa)	*CSR*	*N* at $\Delta u/\sigma'_{3c} \cong 1$	*N* at 5% $\varepsilon_{a,DA}$
95 : 5	95S5A365	0.97	0.689	0.680	36.5	0.183	3	3
	95S5A296	0.99	0.688	0.681	29.6	0.148	20	22
	95S5A240	0.99	0.694	0.684	24.0	0.120	50	51
	95S5A225	0.98	0.686	0.676	22.5	0.113	61	61
	95S5A205	0.97	0.686	0.676	20.5	0.103	130	133
	Average		0.689	0.679				
90 : 10	90S10A285	1.00	0.689	0.676	28.5	0.143	8	8
	90S10A220	0.97	0.685	0.672	22.0	0.110	18	19
	90S10A185	0.98	0.693	0.680	18.5	0.093	58	57
	90S10A165	1.00	0.696	0.682	16.5	0.083	124	121
	Average		0.691	0.678				
80 : 20	80S20A280	1.00	0.705	0.677	28.0	0.140	10	7
	80S20A230	0.99	0.712	0.682	23.0	0.115	NA*	17
	80S20A195	0.99	0.718	0.687	19.5	0.098	44	39
	80S20A160	0.99	0.716	0.689	16.0	0.080	140	136
	Average		0.713	0.684				
70 : 30	70S30A350	1.00	0.747	0.682	35.0	0.175	NA*	8
	70S30A270	1.00	0.755	0.693	27.0	0.135	NA*	22
	70S30A245	0.99	0.758	0.688	24.5	0.123	NA*	57
	70S30A230	1.00	0.745	0.679	23.0	0.115	NA*	100
	Average		0.751	0.686				
60 : 40	60S40A420	1.00	0.758	0.654	42.0	0.210	NA*	4
	60S40A370	1.00	0.755	0.653	37.0	0.185	NA*	14
	60S40A340	1.00	0.750	0.669	34.0	0.170	53	34
	60S40A310	0.99	0.762	0.649	31.0	0.155	57	57
	Average		0.756	0.656				
50 : 50	50S50A515	0.99	0.786	0.630	51.5	0.258	NA*	4
	50S50A465	0.99	0.783	0.632	46.5	0.233	NA*	10
	50S50A420	1.00	0.780	0.626	42.0	0.210	NA*	29
	50S50A370	1.00	0.767	0.604	37.0	0.185	NA*	116
	Average		0.779	0.623				

Table 6. 3 Summary of cyclic triaxial tests for sand mixed with CT1030 tyre chips, SB

Sand : Rubber Ratio	Test No.	*B* value	e_o	e	q_{cyc} (kPa)	*CSR*	*N* at $\Delta u/\sigma'_{3c} \cong 1$	*N* at 5% $\varepsilon_{a,DA}$
95 : 5	95S5B270	0.98	0.678	0.670	27.0	0.135	8	8
	95S5B245	0.99	0.682	0.674	24.5	0.123	37	37
	95S5B225	0.98	0.684	0.675	22.5	0.113	50	51
	95S5B210	0.97	0.683	0.674	21.0	0.105	69	70
	Average		0.682	0.673				
90 : 10	90S10B260	0.98	0.669	0.656	26.0	0.130	10	10
	90S10B235	0.98	0.677	0.665	23.5	0.118	29	30
	90S10B213	0.98	0.676	0.664	21.3	0.107	52	54
	90S10B190	0.98	0.670	0.659	19.0	0.095	77	77
	Average		0.673	0.661				
80 : 20	80S20B256	0.99	0.666	0.647	25.6	0.128	14	13
	80S20B217	0.99	0.663	0.641	21.7	0.109	26	25
	80S20B195	0.98	0.672	0.651	19.5	0.098	57	57
	80S20B170	0.99	0.665	0.644	17.0	0.085	114	112
	Average		0.667	0.646				
70 : 30	70S30B340	0.99	0.644	0.605	34.0	0.170	NA*	8
	70S30B300	1.00	0.650	0.611	30.0	0.150	NA*	13
	70S30B260	0.99	0.642	0.602	26.0	0.130	39	33
	70S30B200	0.99	0.656	0.614	20.0	0.100	136	134
	Average		0.648	0.608				
60 : 40	60S40B550	0.99	0.642	0.580	55.0	0.275	NA*	4
	60S40B435	1.00	0.641	0.576	43.5	0.218	NA*	16
	60S40B350	0.99	0.600	0.536	35.0	0.175	104	71
	60S40B310	1.00	0.636	0.592	31.0	0.155	153	115
	Average		0.630	0.571				
50 : 50	50S50B540	0.99	0.660	0.557	54.0	0.270	NA*	6
	50S50B455	1.00	0.651	0.541	45.5	0.228	NA*	15
	50S50B445	1.00	0.627	0.511	44.5	0.223	NA*	37
	50S50B405	1.00	0.654	0.539	40.5	0.203	NA*	37
	50S50B350	0.99	0.644	0.545	35.0	0.175	NA*	88
	Average		0.647	0.539				

Table 6. 4 Summary of cyclic triaxial tests for sand mixed with CT2060 tyre chips, SC

Sand : Rubber Ratio	Test No.	*B* value	e_o	e	q_{cyc} (kPa)	*CSR*	*N* at $\Delta u/\sigma'_{3c} \cong 1$	*N* at 5% $\varepsilon_{a,DA}$
95 : 5	95S5C380	0.99	0.657	0.650	38.0	0.190	4	4
	95S5C360	1.00	0.653	0.646	36.0	0.180	11	11
	95S5C300	0.99	0.661	0.653	30.0	0.150	15	15
	95S5C250	1.00	0.654	0.646	25.0	0.125	85	87
	95S5C230	1.00	0.666	0.658	23.0	0.115	266	268
	Average		0.658	0.651				
90 : 10	90S10C365	0.99	0.625	0.616	36.5	0.183	2	3
	90S10C310	0.99	0.632	0.624	31.0	0.155	10	11
	90S10C260	0.99	0.623	0.615	26.0	0.130	36	36
	90S10C210	0.99	0.630	0.622	21.0	0.105	212	214
	Average		0.628	0.619				
80 : 20	80S20C320	0.99	0.591	0.579	32.0	0.160	5	5
	80S20C300	0.99	0.589	0.576	30.0	0.150	8	7
	80S20C250	1.00	0.595	0.583	25.0	0.125	16	16
	80S20C230	0.99	0.593	0.581	23.0	0.115	38	38
	80S20C212	1.00	0.587	0.573	21.2	0.106	71	72
	Average		0.591	0.578				
70 : 30	70S30C430	1.00	0.553	0.529	43.0	0.215	NA*	9
	70S30C350	1.00	0.553	0.525	35.0	0.175	27	21
	70S30C320	1.00	0.552	0.524	32.0	0.160	41	35
	70S30C280	0.99	0.549	0.522	28.0	0.140	98	95
	Average		0.552	0.525				
60 : 40	60S40C550	1.00	0.511	0.471	55.0	0.275	NA*	6
	60S40C440	1.00	0.515	0.474	44.0	0.220	28	15
	60S40C370	1.00	0.504	0.468	37.0	0.185	37	25
	60S40C300	1.00	0.511	0.473	30.0	0.150	166	143
	Average		0.510	0.472				
50 : 50	50S50C560	0.99	0.521	0.467	56.0	0.280	NA*	7
	50S50C495	1.00	0.524	0.464	49.5	0.248	NA*	13
	50S50C430	0.99	0.525	0.470	43.0	0.215	NA*	26
	50S50C345	0.99	0.530	0.471	34.5	0.173	NA*	82
	Average		0.525	0.468				

Table 6. 5 Summary of cyclic triaxial tests for sand mixed with CT4010 tyre chips, SD

Sand : Rubber Ratio	Test No.	*B* value	e_o	e	q_{cyc} (kPa)	*CSR*	*N* at $\Delta u/\sigma'_{3c} \cong 1$	*N* at 5% $\varepsilon_{a,DA}$
95 : 5	95S5D350	0.99	0.652	0.645	35.0	0.175	9	9
	95S5D325	1.00	0.657	0.650	32.5	0.163	14	15
	95S5D280	0.99	0.658	0.651	28.0	0.140	55	56
	95S5D240	1.00	0.661	0.654	24.0	0.120	193	194
	Average		0.657	0.650				
90 : 10	90S10D360	0.99	0.632	0.623	36.0	0.180	2	3
	90S10D305	1.00	0.616	0.608	30.5	0.153	22	23
	90S10D270	0.99	0.626	0.618	27.0	0.135	42	43
	90S10D225	1.00	0.629	0.622	22.5	0.113	147	148
	Average		0.626	0.618				
80 : 20	80S20D322	1.00	0.583	0.571	32.2	0.161	4	4
	80S20D240	1.00	0.580	0.569	24.0	0.120	27	27
	80S20D220	1.00	0.582	0.571	22.0	0.110	64	65
	80S20D205	0.99	0.585	0.574	20.5	0.103	270	271
	Average		0.583	0.571				
70 : 30	70S30D420	0.99	0.525	0.509	42.0	0.210	5	5
	70S30D330	0.98	0.522	0.509	33.0	0.165	19	17
	70S30D300	0.99	0.522	0.509	30.0	0.150	21	21
	70S30D250	0.99	0.515	0.501	25.0	0.125	36	34
	70S30D210	0.99	0.528	0.514	21.0	0.105	80	79
	Average		0.522	0.508				
60 : 40	60S40D555	0.98	0.492	0.461	55.5	0.278	4	3
	60S40D445	1.00	0.489	0.461	44.5	0.223	14	7
	60S40D340	1.00	0.489	0.459	34.0	0.170	38	33
	60S40D305	1.00	0.495	0.464	30.5	0.153	79	64
	Average		0.491	0.461				
50 : 50	50S50D550	0.99	0.429	0.396	55.0	0.275	NA*	11
	50S50D400	1.00	0.444	0.414	40.0	0.200	NA*	26
	50S50D365	1.00	0.452	0.419	36.5	0.183	NA*	30
	50S50D300	0.98	0.443	0.408	30.0	0.150	NA*	78
	Average		0.442	0.409				

The undrained cyclic triaxial test results for S, pure sand, are shown in Figures 6.1 - 6.5, for each q_{cyc} of 25, 29, 32, 37, and 43kPa , respectively. For sand mixed with tyre chips – SA, SB, SC, and SD – having sand to rubber ratios of 95:5, 90:10, 80:20, 70:30, 60:40, and 50:50, only the test results that had q_{cyc} similar to those tested with pure sand were selected and plotted in order that the liquefaction characteristics could be compared with those of pure sand. The rest of the cyclic triaxial test results, however, can be found in the CD-ROM attached. The selected results for SA mixtures having sand to rubber ratios of 95:5, 90:10, 80:20, 70:30, 60:40, and 50:50 are illustrated in Figures 6.6, 6.7, 6.8, 6.9, 6.10, and 6.11, respectively. Figures 6.12 - 6.17, Figures 6.18 - 6.23, and Figures 6.24 - 6.29 illustrate the selected results for the mixtures SB, SC, and SD, respectively.

For pure sand S, regardless of the level of applied cyclic deviator stresses, before the liquefaction occurred, the axial strain remained approximately zero (Figures 6.1(b) – 6.5(b)) suggesting that during this period of cyclic loading the sand particles were almost completely interlocked. When the pore water pressure ratio reached approximately 0.6 for q_{cyc} of 25, 29, and 32kPa; and 0.4 for q_{cyc} of 37 and 43kPa, however, the onset of liquefaction occurred after just a few more cycles of loading (Figures 6.1(c) – 6.5(c)). At this stage, the sand particles had lost contact with each other because the excess pore water pressure was approximately equal to the initial effective stress. When this happened, the soil behaved like a viscous fluid, as evident in the large strain generated (Figures 6.1(b) – 6 .5(b)). In addition, as the pore water pressure ratio approached 0.6, an abrupt increase of axial strain was also observed. The correspondence of the axial strain and the pore water pressure ratio can be observed when considering Figures 6.1(b) and (c) – Figures 6.5(b) and (c), all together.

Furthermore, it was observed that during cyclic loading the specimens strained largely in extension. At larger cycles when the pore water pressure ratio $\Delta u/\sigma'_{3c}$ approached 1.0, compressive strains were then observed, but much smaller than the extension strains. As a result, the specimens always failed in extension suggesting perhaps that some anisotropy was produced during sample preparation (Promputthangkoon and Hyde, 2008a). Moreover, the anisotropy is apparent when considering Figures 6.1(e) – 6.5(e), as the angle of the stress path in compression during the liquefaction is slightly higher than that in extension. The stress-strain relationships

(Figures 6.1(d) – 6.5(d)) of all q_{cyc} showed a sharp increase in deviator stress on the compression side at constant peak strain. This suggests that the tested sand has somewhat brittle behaviour.

For SA having sand to rubber ratios of 95:5, 90:10, 80:20, and 70:30; the specimens tested with q_{cyc} of 29.6kPa (Figure 6.6), 28.5kPa (Figure 6.7), 28kPa (Figure 6.8), and 27kPa (Figure 6.9), respectively, were chosen to compare their cyclic behaviour with pure sand tested with similar q_{cyc} of 29kPa (Figures 6.1). It was found that the onset of liquefaction for 95:5, 90:10, 80:20, and 70:30 mixtures occurred at 22, 8, 7, and 22 cycles (Table 6.2), respectively, compared to 98 cycles (Table 6.1) for pure sand tested with a similar q_{cyc}. It is apparent that the resistance to liquefaction of these particular mixtures is much lower than that of pure sand.

For SA having sand to rubber ratios of 60:40, and 50:50, both specimens tested with q_{cyc} of 37kPa (Figure 6.10 and Figure 6.11, respectively) were chosen to be compared with pure sand tested with the same q_{cyc}. The mixtures 60:40 and 50:50 liquefied at 14 and 116 cycles (Table 6.2), respectively, compared to pure sand that liquefied after only 5 cycles (Table 6.1). It can be seen that when the rubber content was increased to 40% and higher, the resistance to liquefaction was much improved. Another point that should be noted is the different stress-strain behaviour for S and SA. As mentioned before the stress-strain behaviour of pure sand was quite brittle; however, when the rubber was added a ductile response was observed (Figures 6.6(d) - 6.11(d)). These characteristics are even more obvious when considering the stress-strain curves for the mixtures 60:40 and 50:50 (Figure 6.10(d) and Figure 6.11(d), respectively.

As mentioned before, for pure sand, the strain in compression was much lower than that in extension. When considering SA, however, it was found that the difference between the two strains was smaller, compared to pure sand. This is obvious when comparing the axial strains of SA having 50% rubber (Figure 6.11(b)) for which the strains in compression and extension were almost the same at larger cycles indicating the effect of the rubber in the sand-rubber matrix.

For SB having sand to rubber ratios of 95:5, 90:10, 80:20, and 70:30; the specimens tested with q_{cyc} of 24.5kPa (Figure 6.12), 26kPa (Figure 6.13), 25.6kPa (Figure 6.14), and 26kPa (Figure 6.15), respectively, were chosen to compare the cyclic

behaviour with pure sand tested with similar q_{cyc} of 25kPa (Figure 6.1). The number of cycles at which these specimens liquefied were 37, 10, 13, and 33, respectively (Table 6.3), compared to 204 cycles (Table 6.1) for pure sand. This comparison shows that SB specimens having rubber contents of 5, 10, 20, and 30% are much worse than pure sand in terms of liquefaction resistance.

For SB containing tyre chips percentage of 40 and 50%, the specimens tested with q_{cyc} of 43.5kPa (Figures 6.16) and 44.5kPa (Figures 6.17) were chosen to be compared with pure sand tested with similar q_{cyc} of 43kPa (Figures 6.5). At 40 and 50%, the specimens liquefied after 16 and 37 cycles, compared to just 3 cycles for pure sand, showing a marked increase in the liquefaction resistance for both mixtures. The stress-strain curves (Figure 4.16(d) and Figure 4.17(d)) also exhibited ductile behaviour similar to that observed in SA.

The axial strain behaviour of SB, however, was not quite to the same as that of SA. When SB contained 40% rubber, it was observed that the axial strains in compression and extension were very similar, which was also observed in SA but with 50% rubber. However, when rubber of up to 50% was added, the strain in compression was instead much higher than in extension (Figure 6.17(b)).

For SC, the specimens having sand to rubber ratios of 95:5, 90:10, 80:20, and 70:30 (Figures 6.18 – 6.21), and tested with q_{cyc} of 30, 31, 32, and 32kPa, respectively, were chosen to be compared with pure sand tested with q_{cyc} of 32kPa (Figure 6.3). The number of cycles at which the aforementioned mixtures liquefied were 15, 11, 5, and 35 cycles, respectively (Table 6.4), compared to 31 cycles for pure sand (Table 6.1). In contrast to SA and SB, it can be seen that for SC with 30% rubber the liquefaction resistance is now slightly higher than that of pure sand.

For the mixtures SC containing 40 and 50% of rubber, the specimens tested with q_{cyc} of 44kPa (Figures 6.22) and 43kPa (Figures 6.23) were chosen to be compared with pure sand tested with similar q_{cyc} of 43kPa (Figures 6.5). The onset of liquefaction was observed after 15 and 36 cycles of loading corresponding to the mixtures 60:40 and 50:50, respectively. These results when compared to those of pure sand that liquefied after just 3 cycles indicate a great improvement in terms of the resistance to liquefaction.

For the last series, SD, the specimens having sand to rubber ratios of 95:5, 90:10, 80:20, and 70:30; and tested with q_{cyc} of 24kPa (Figure 6.24), 27kPa (Figure 6.25), 24kPa (Figure 6.26), and 25kPa (Figure 6.27), respectively, were chosen to be compared with pure sand tested with similar q_{cyc} of 25kPa (Figure 6.4). The onset of liquefaction for the above ratios occurred after 194, 43, 27, and 34 cycles, as shown by Table 6.5. All of these were lower than that of pure sand which the liquefaction occurred after 204 cycles (Table 6.1), indicating lower liquefaction resistance.

For SD having sand to rubber ratios of 60:40 and 50:50, the specimens tested with q_{cyc} of 44.5kPa (Figure 6.28) and 40kPa (Figure 6.29), respectively, were chosen to be compared with pure sand tested with similar q_{cyc} of 43kPa (Figure 6.5). This time, as seen in Table 6.5, the mixtures liquefied at 7 and 26 cycles, compared to 3 cycles for the case of pure sand specimen (Table 6.1), indicating an as well increase in liquefaction resistance.

From the test results reported and discussed, it can be concluded that for all mixtures of SA, SB, SC, and SD, the specimens having sand to rubber ratios of 95:5, 90:10, 80:20, had lower liquefaction resistance than that of pure sand tested with similar q_{cyc}. When the rubber content was increased to 30%, only SC had a liquefaction resistance higher than that of pure sand; the rest had lower liquefaction resistance. However, when the rubber content was increased to 40% and higher, the liquefaction resistance of all mixtures was greater than that of pure sand, compared at the same applied q_{cyc}.

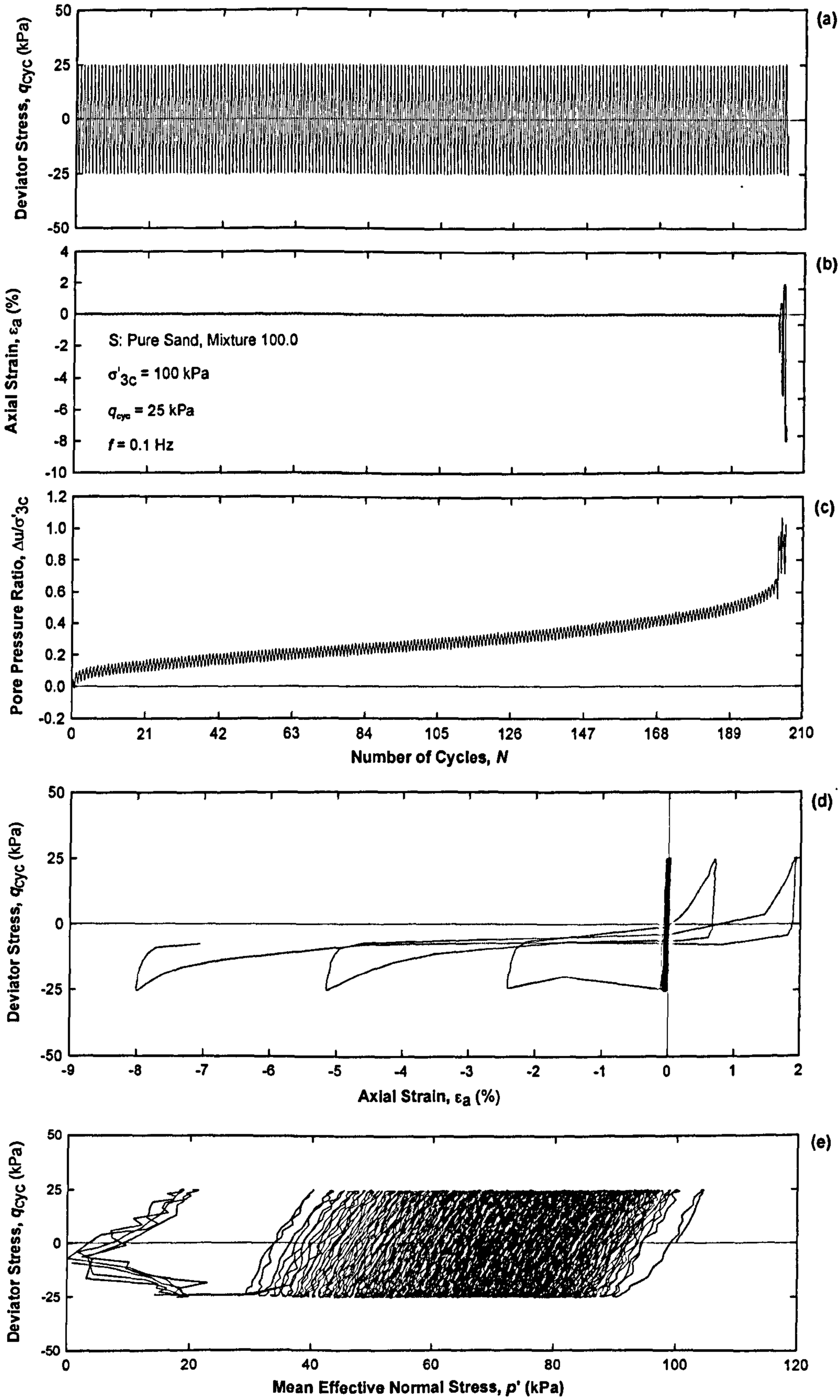

Figure 6. 1 Cyclic triaxial test results for S, q_{cyc} = 25 kPa

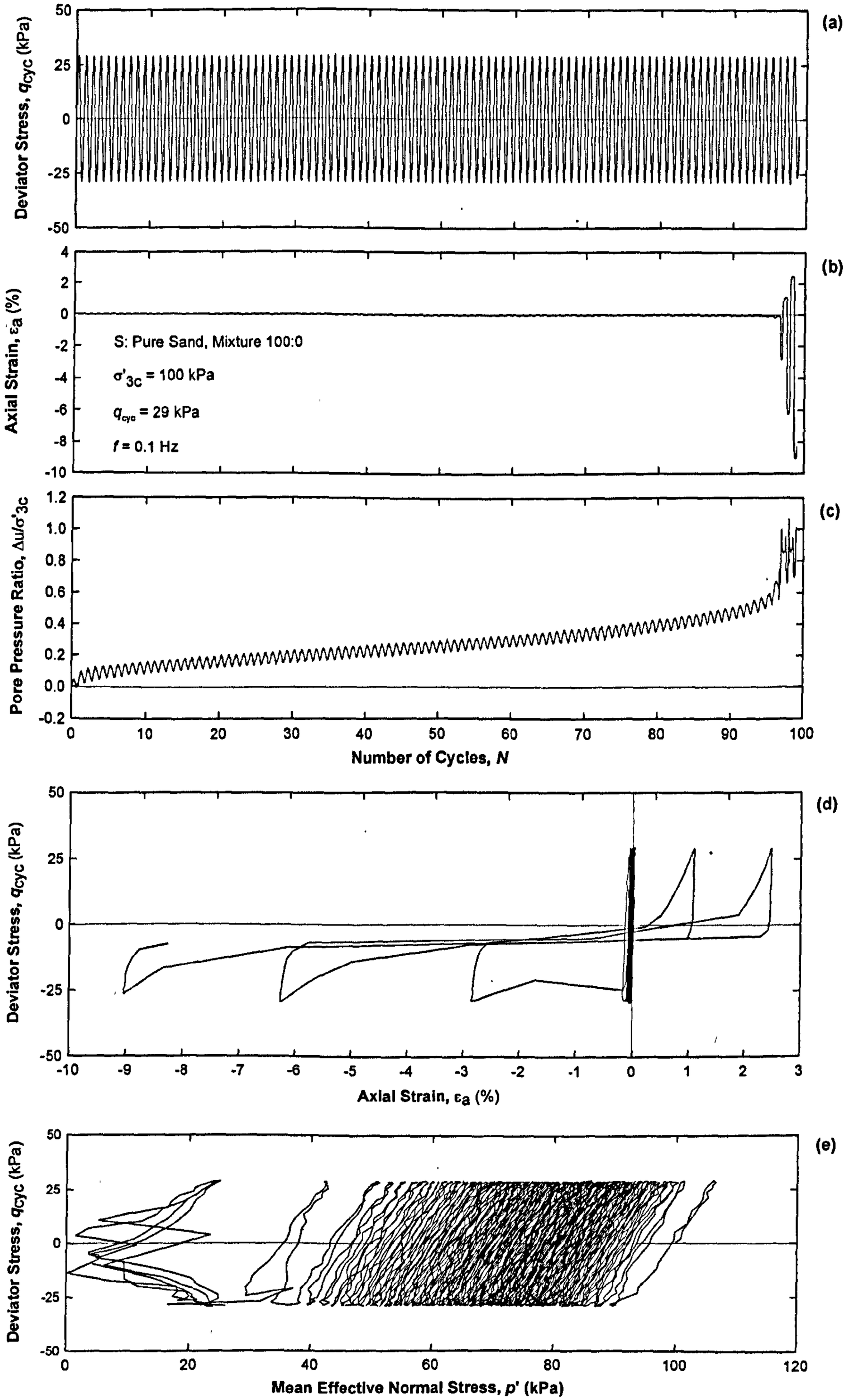

Figure 6. 2 Cyclic triaxial test results for S, q_{cyc} = 29 kPa

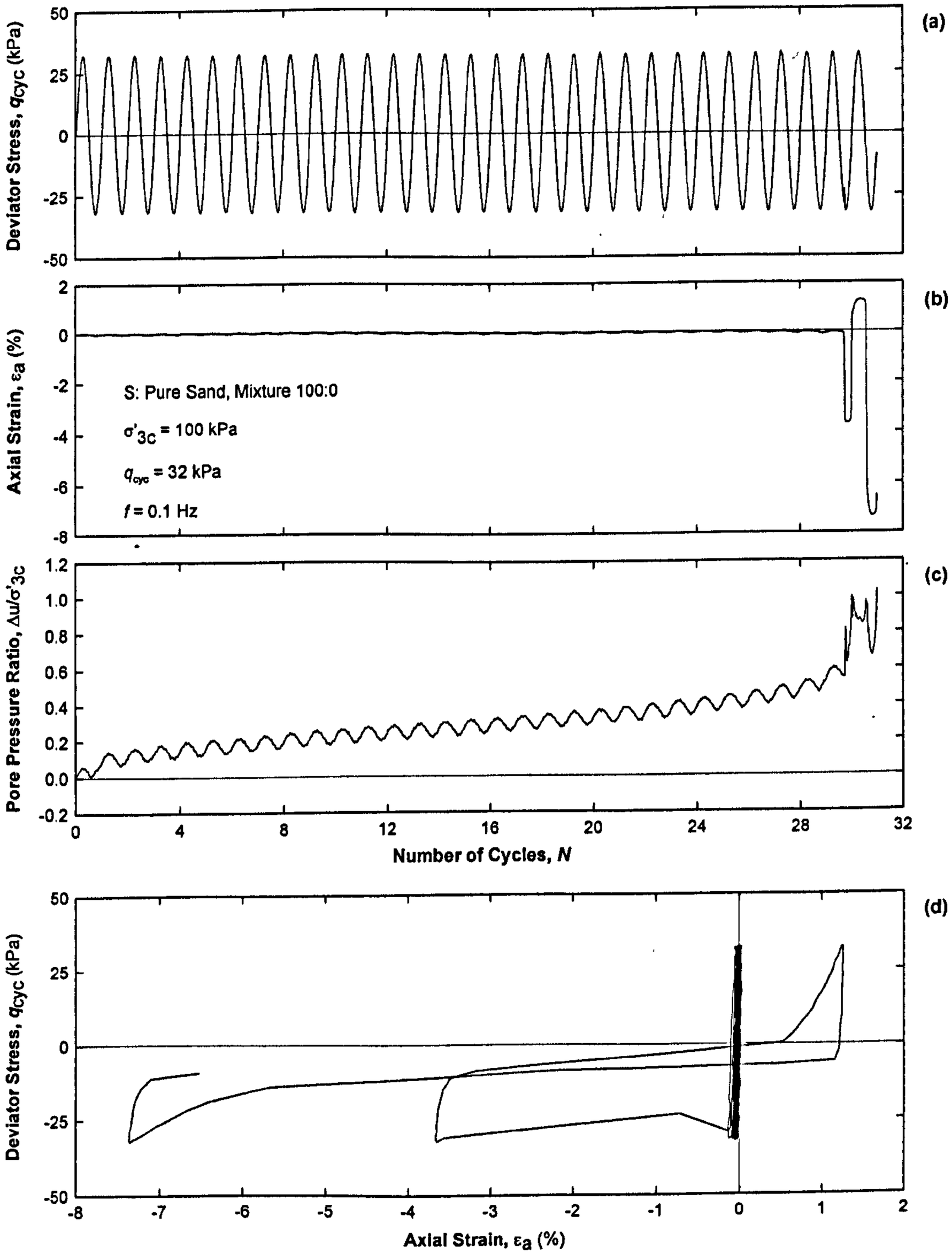

Figure 6. 3 Cyclic triaxial test results for S, q_{cyc} = 32 kPa

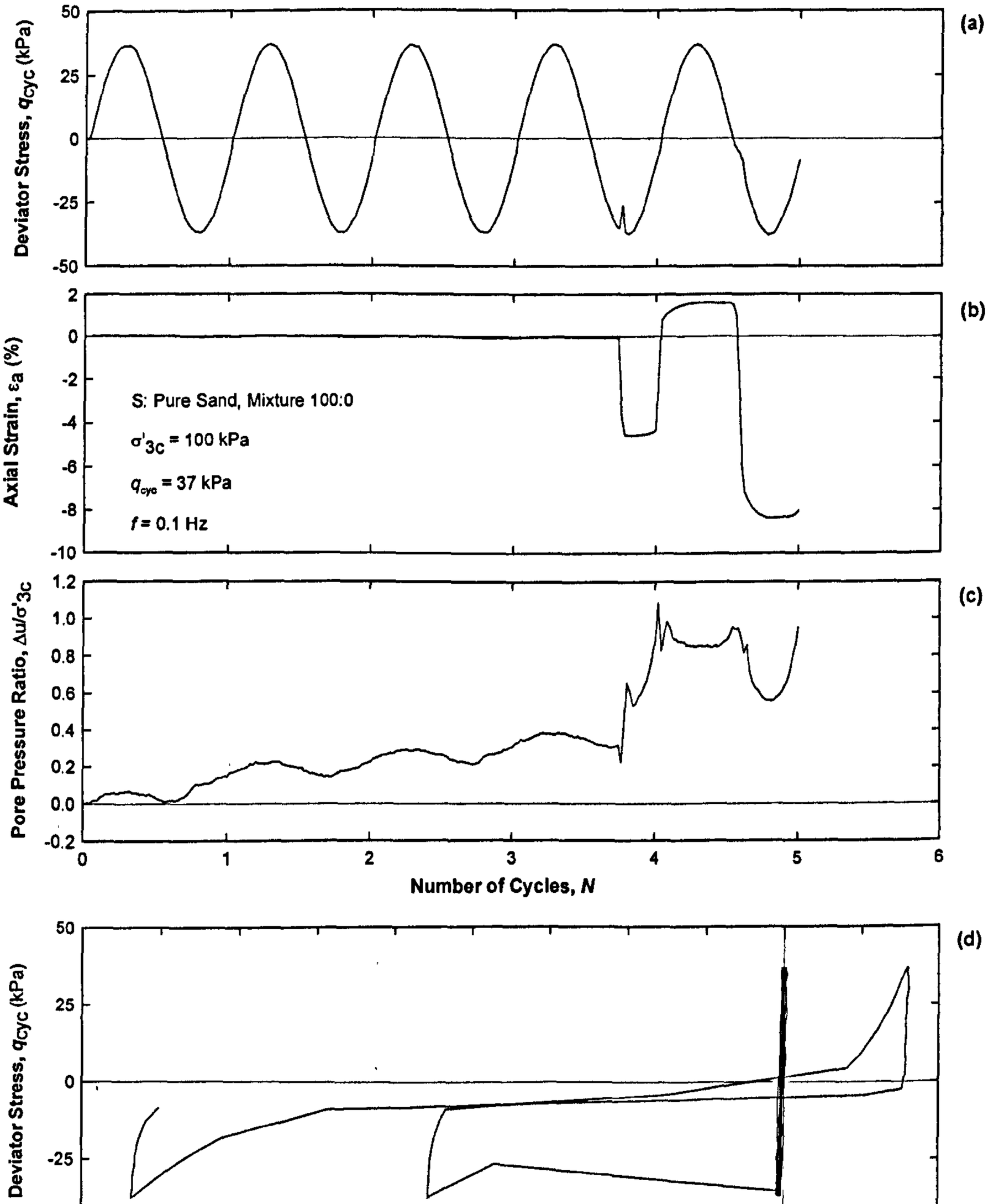

Figure 6. 4 Cyclic triaxial test results for S, q_{cyc} = 37 kPa

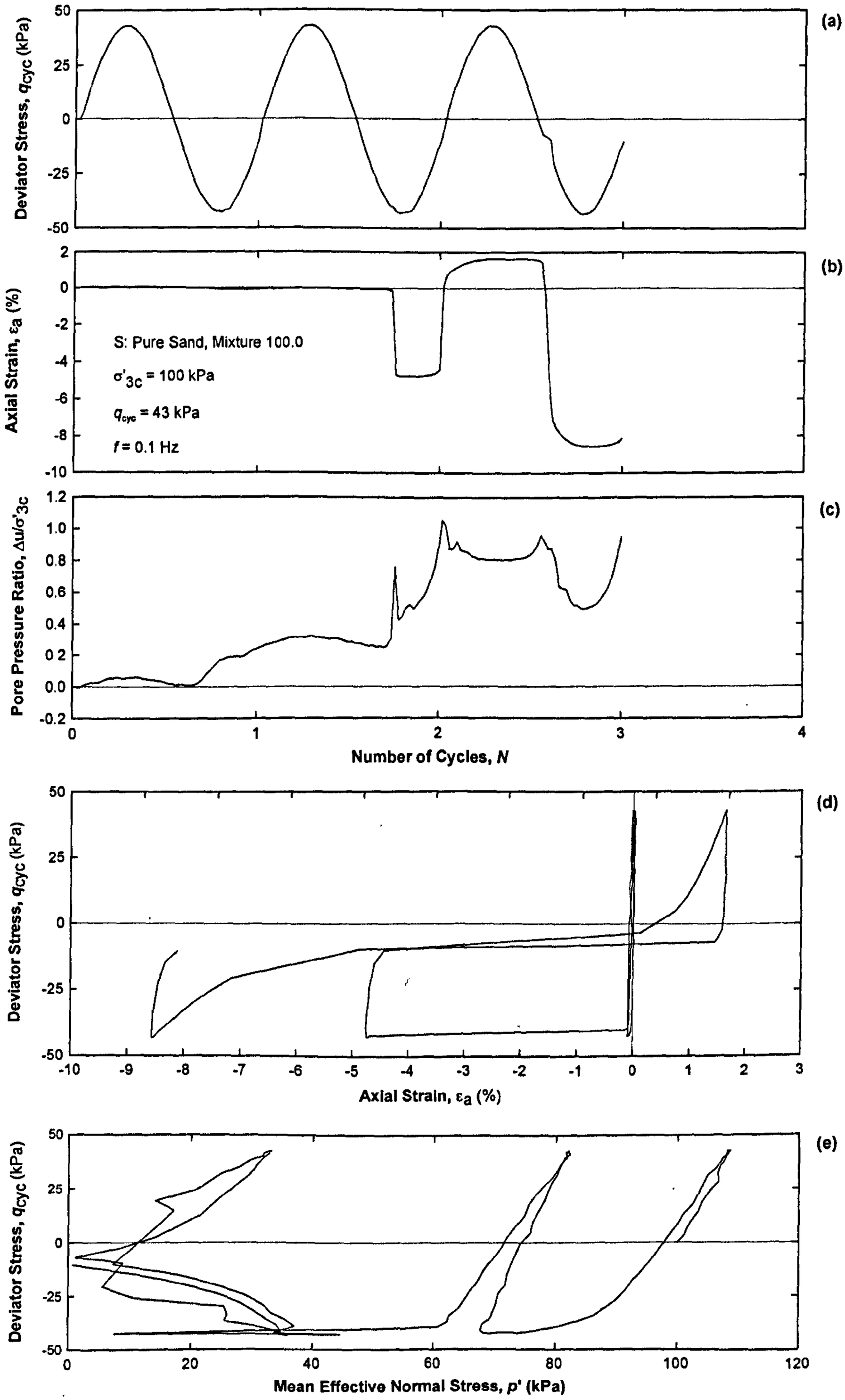

Figure 6. 5 Cyclic triaxial test results for S, q_{cyc} = 43 kPa

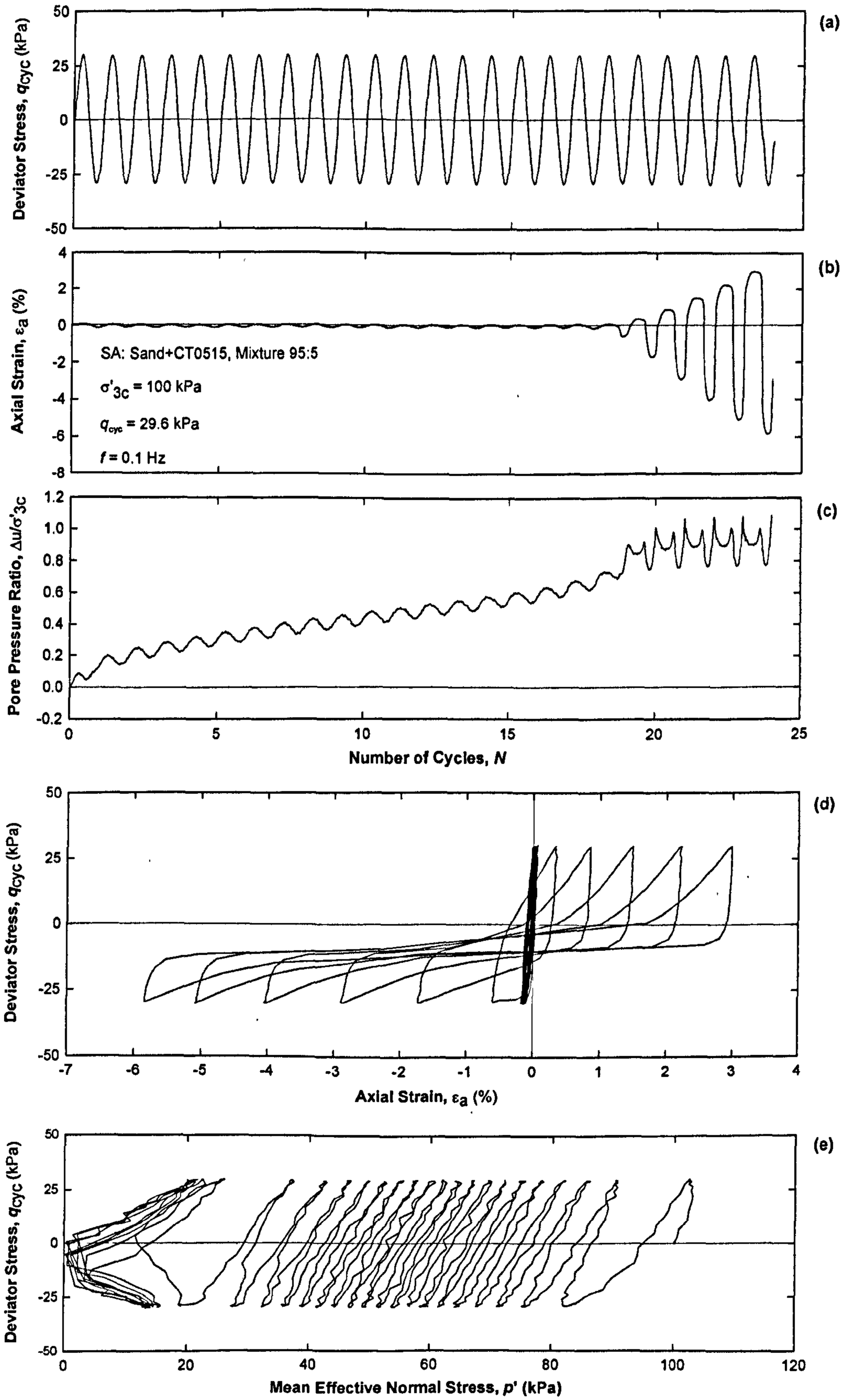

Figure 6. 6 Cyclic triaxial test results for SA with 5% rubber, q_{cyc} = 29.6 kPa

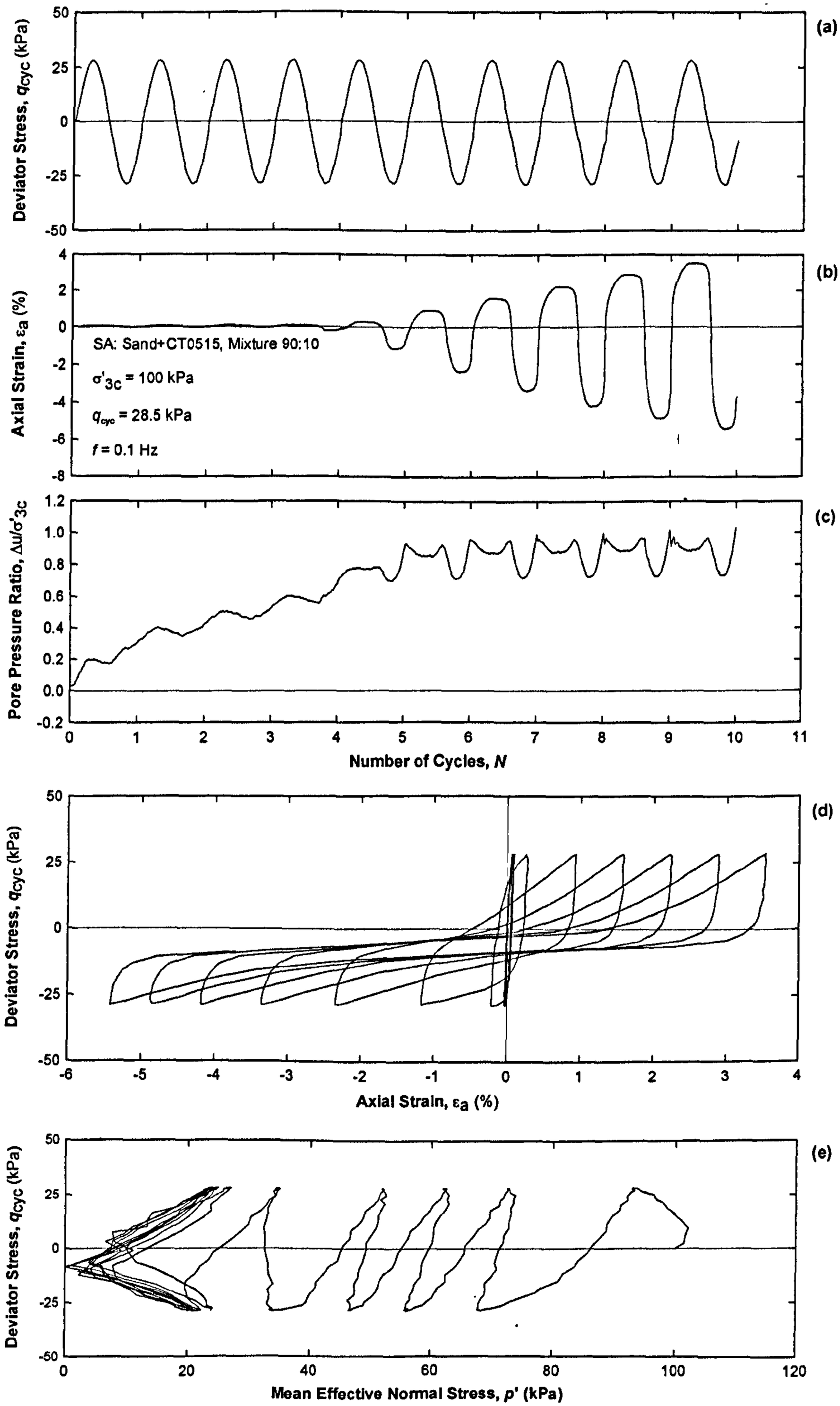

Figure 6. 7 Cyclic triaxial test results for SA with 10% rubber, q_{cyc} = 28.5 kPa

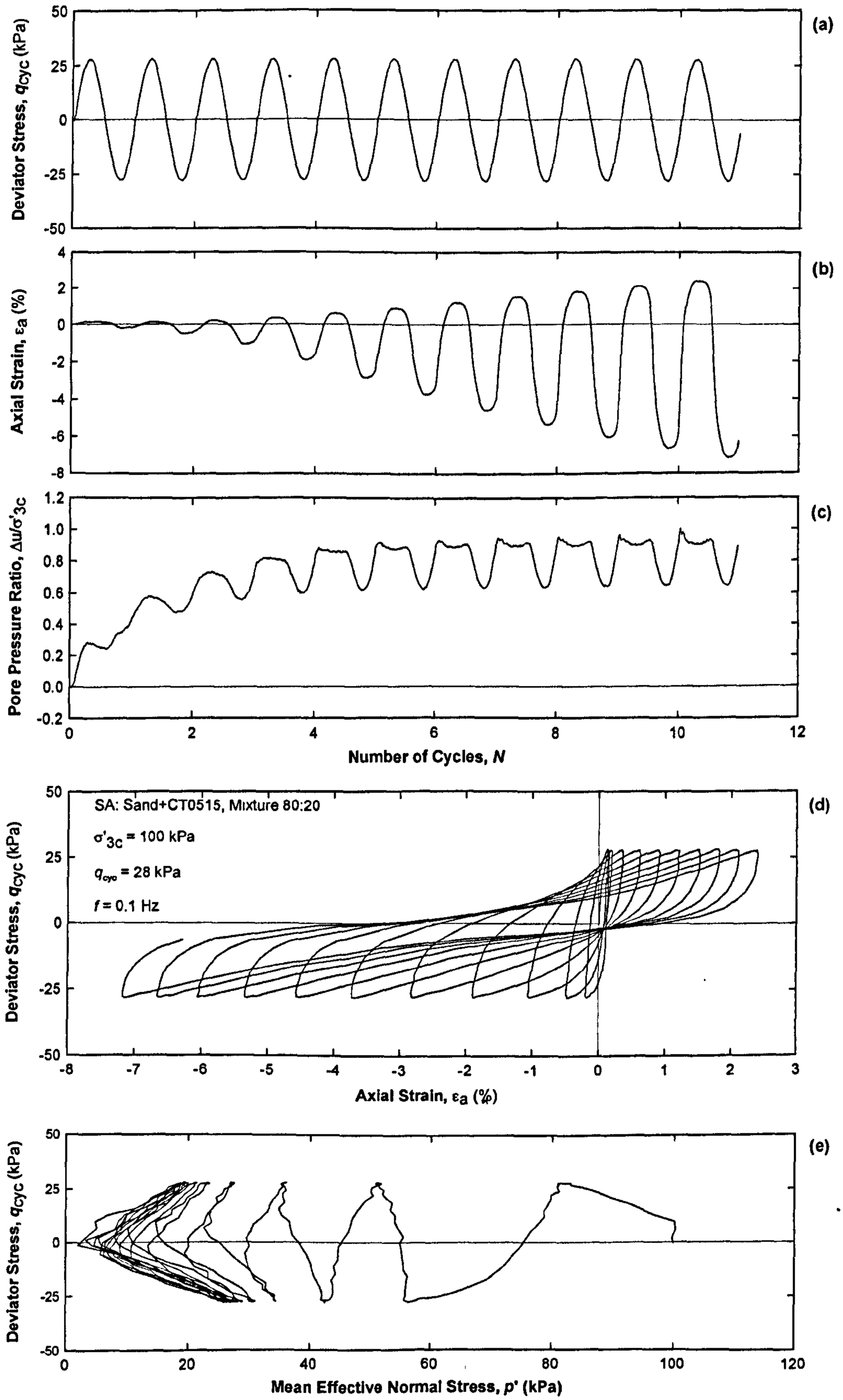

Figure 6. 8 Cyclic triaxial test results for SA with 20% rubber, q_{cyc} = 28 kPa

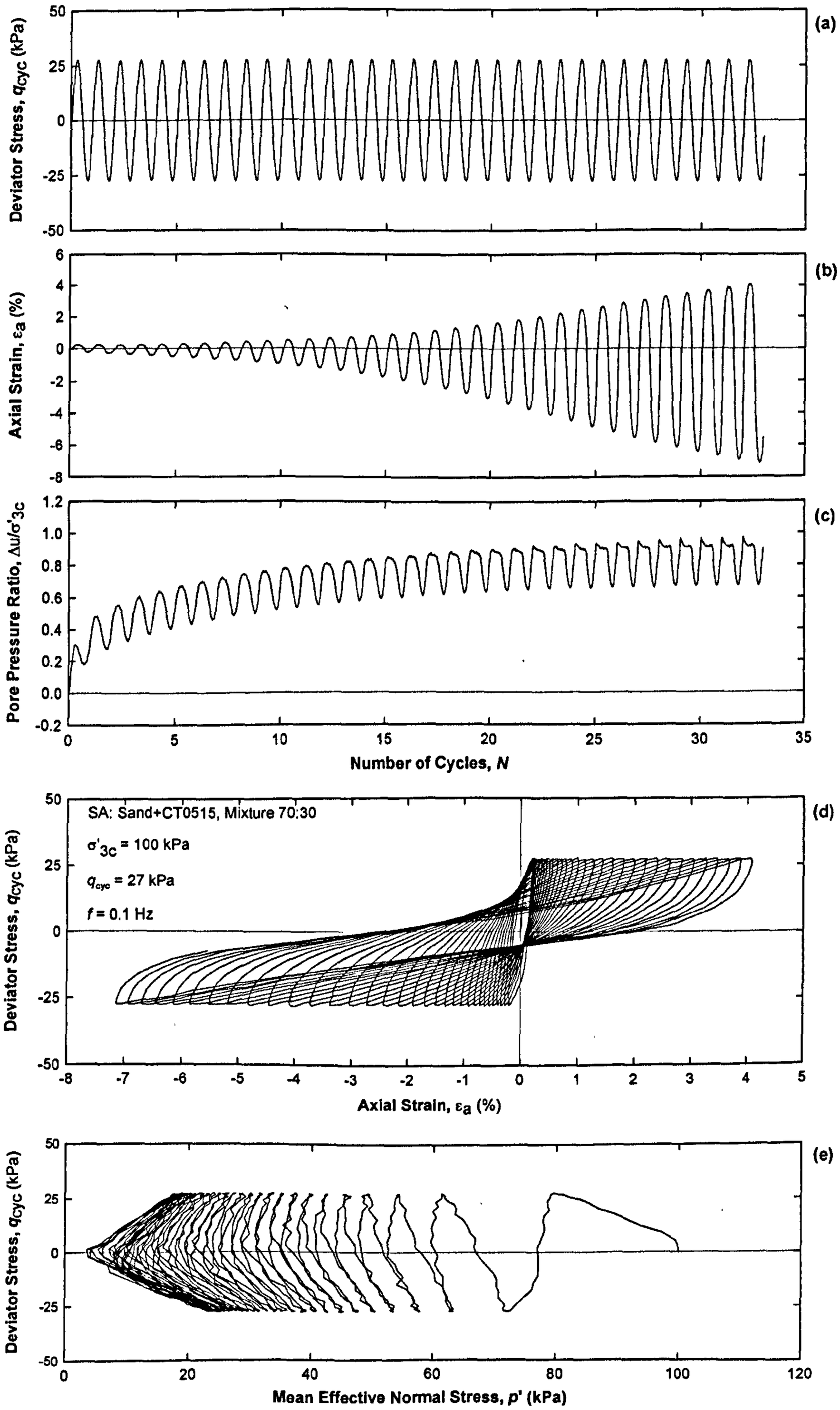

Figure 6. 9 Cyclic triaxial test results for SA with 30% rubber, q_{cyc} = 27 kPa

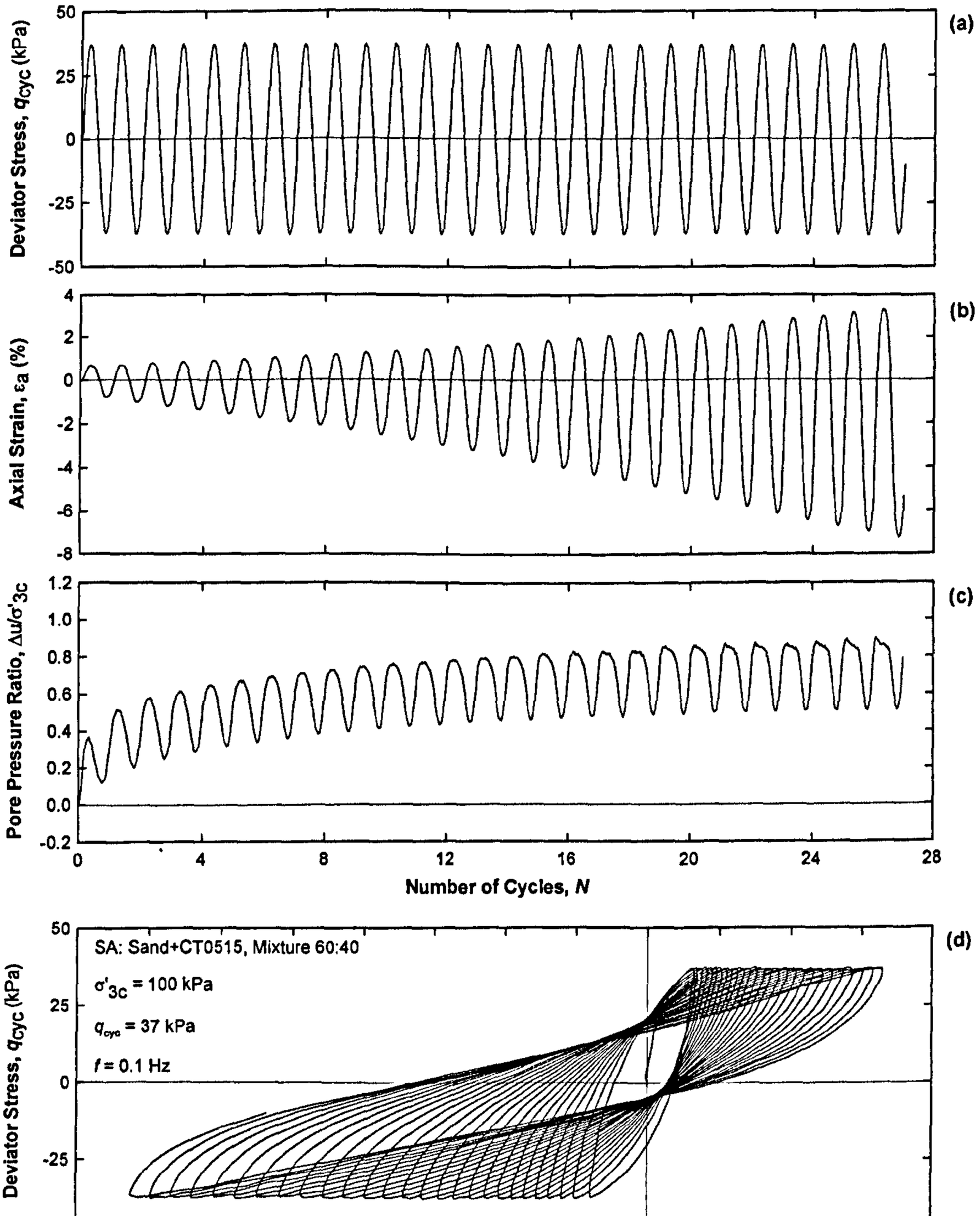

Figure 6. 10 Cyclic triaxial test results for SA with 40% rubber, q_{cyc} = 37 kPa

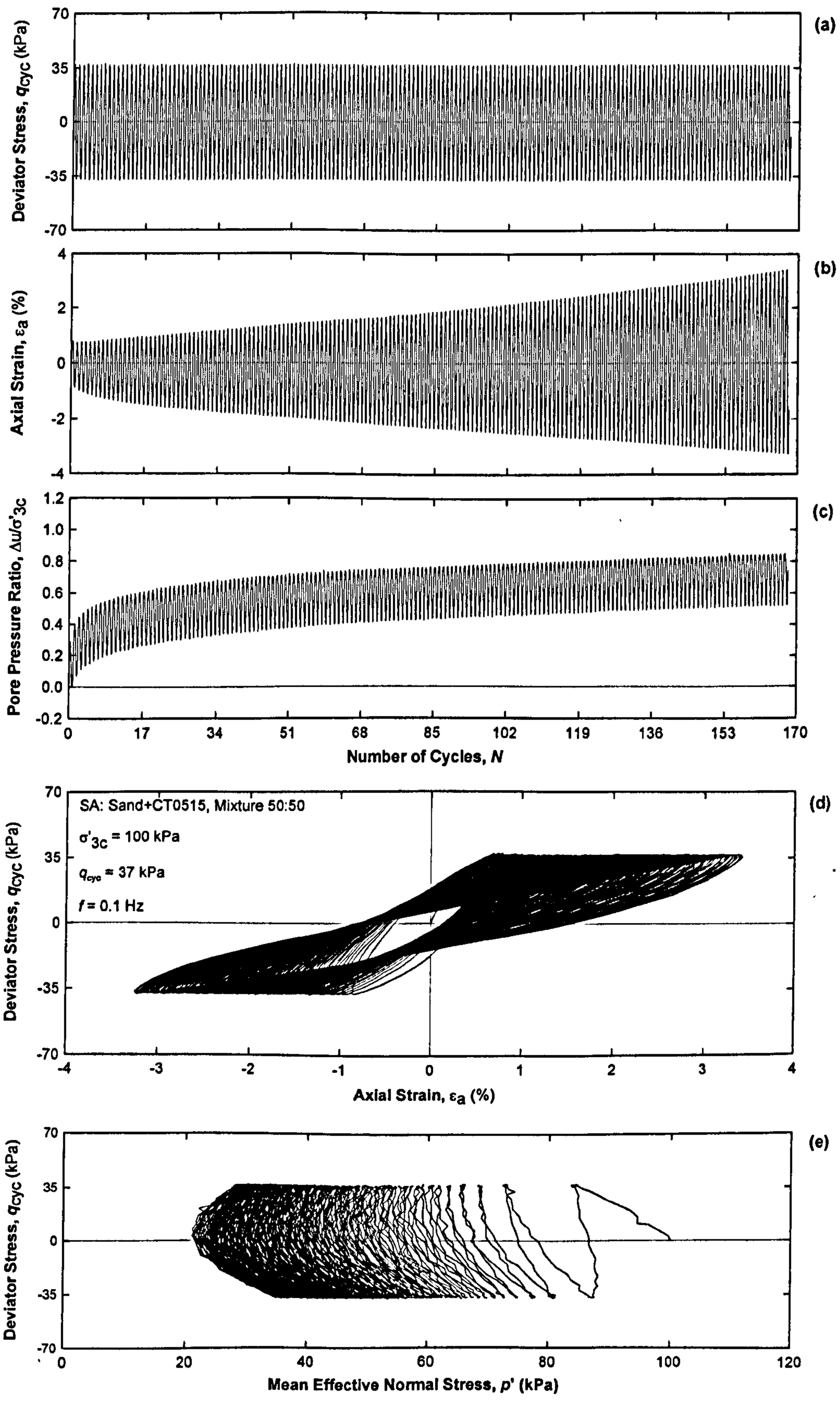

Figure 6. 11 Cyclic triaxial test results for SA with 50% rubber, q_{cyc} = 37 kPa

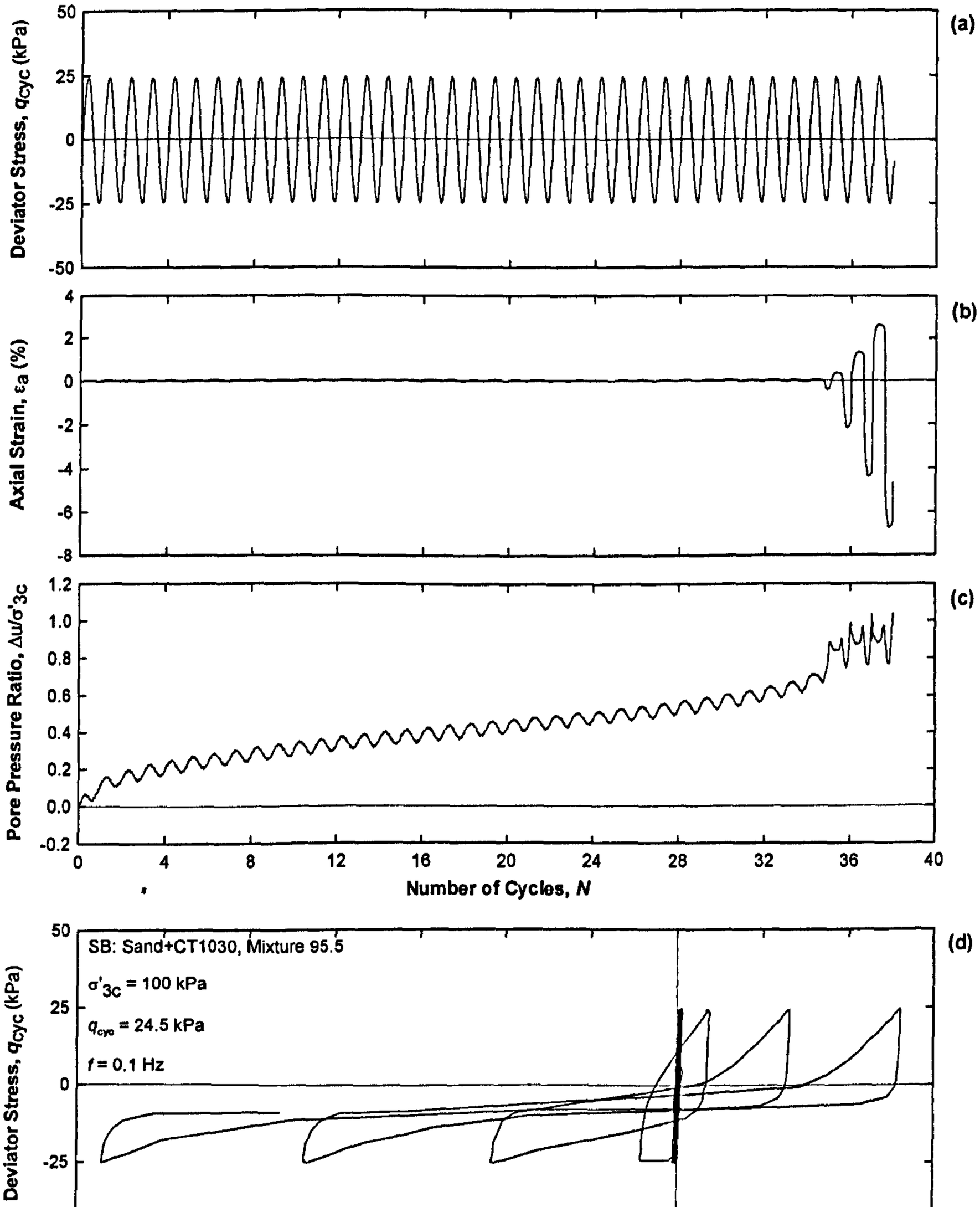

Figure 6. 12 Cyclic triaxial test results for SB with 5% rubber, q_{cyc} = 24.5 kPa

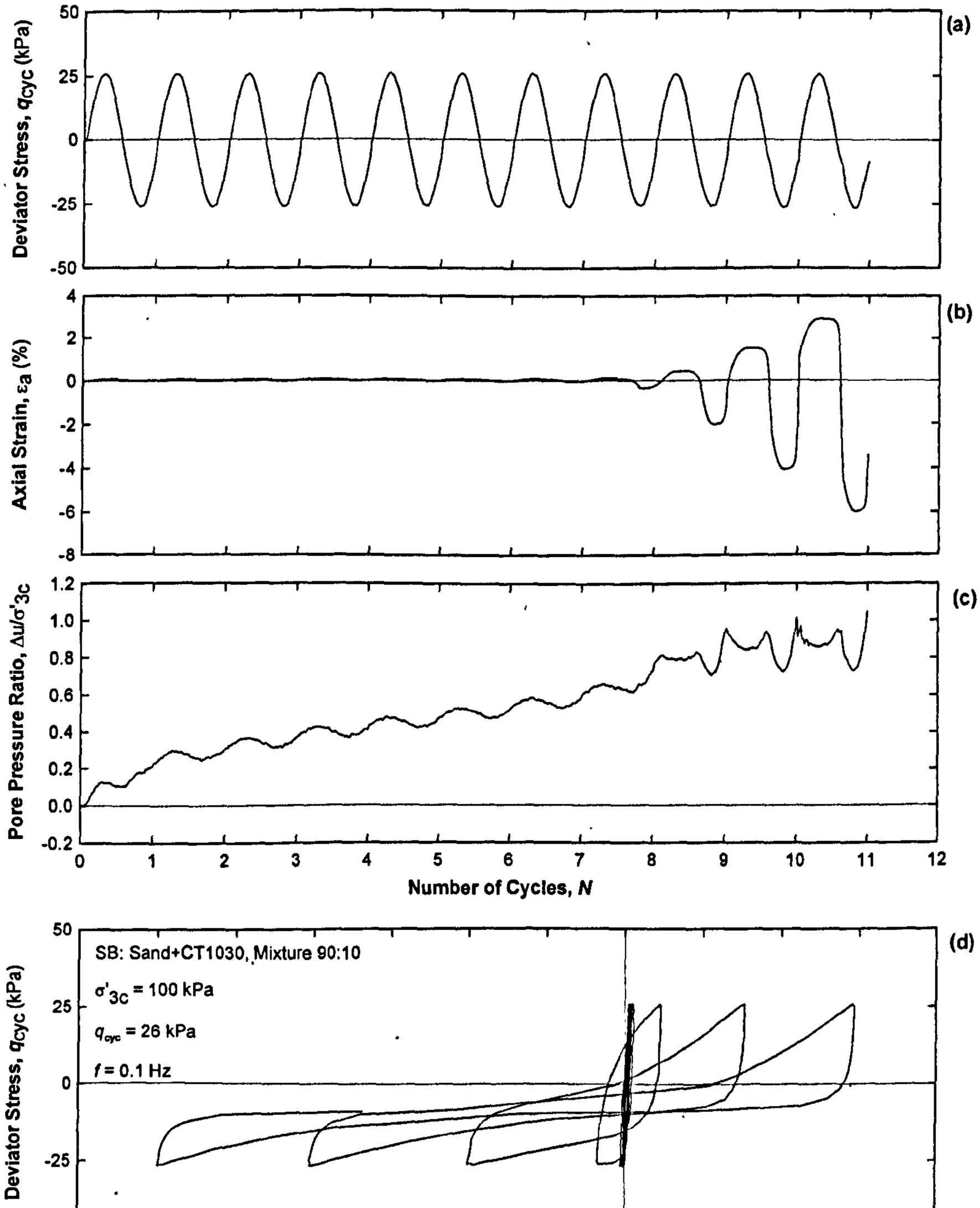

Figure 6. 13 Cyclic triaxial test results for SB with 10% rubber, q_{cyc} = 26 kPa

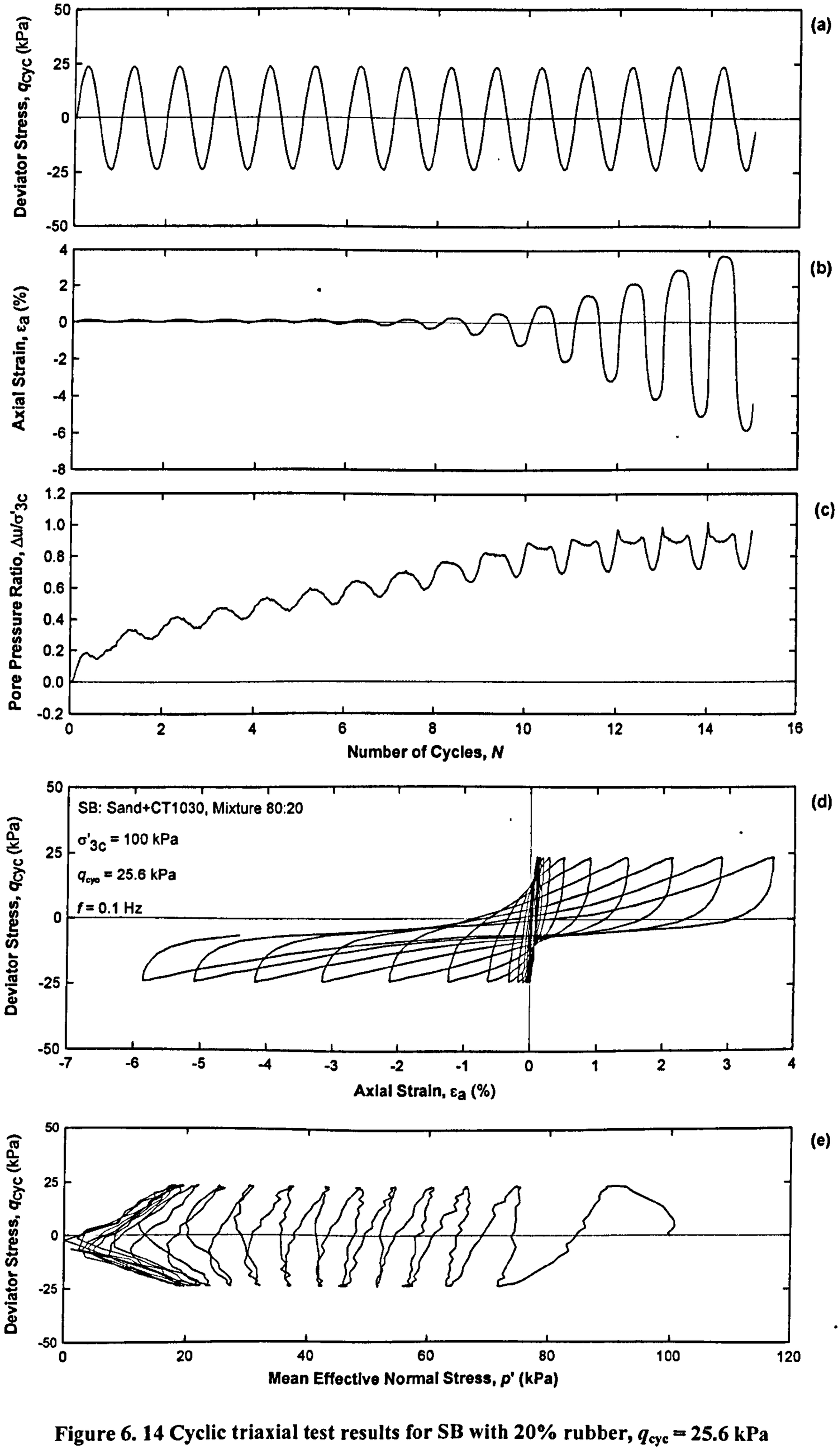

Figure 6. 14 Cyclic triaxial test results for SB with 20% rubber, q_{cyc} = 25.6 kPa

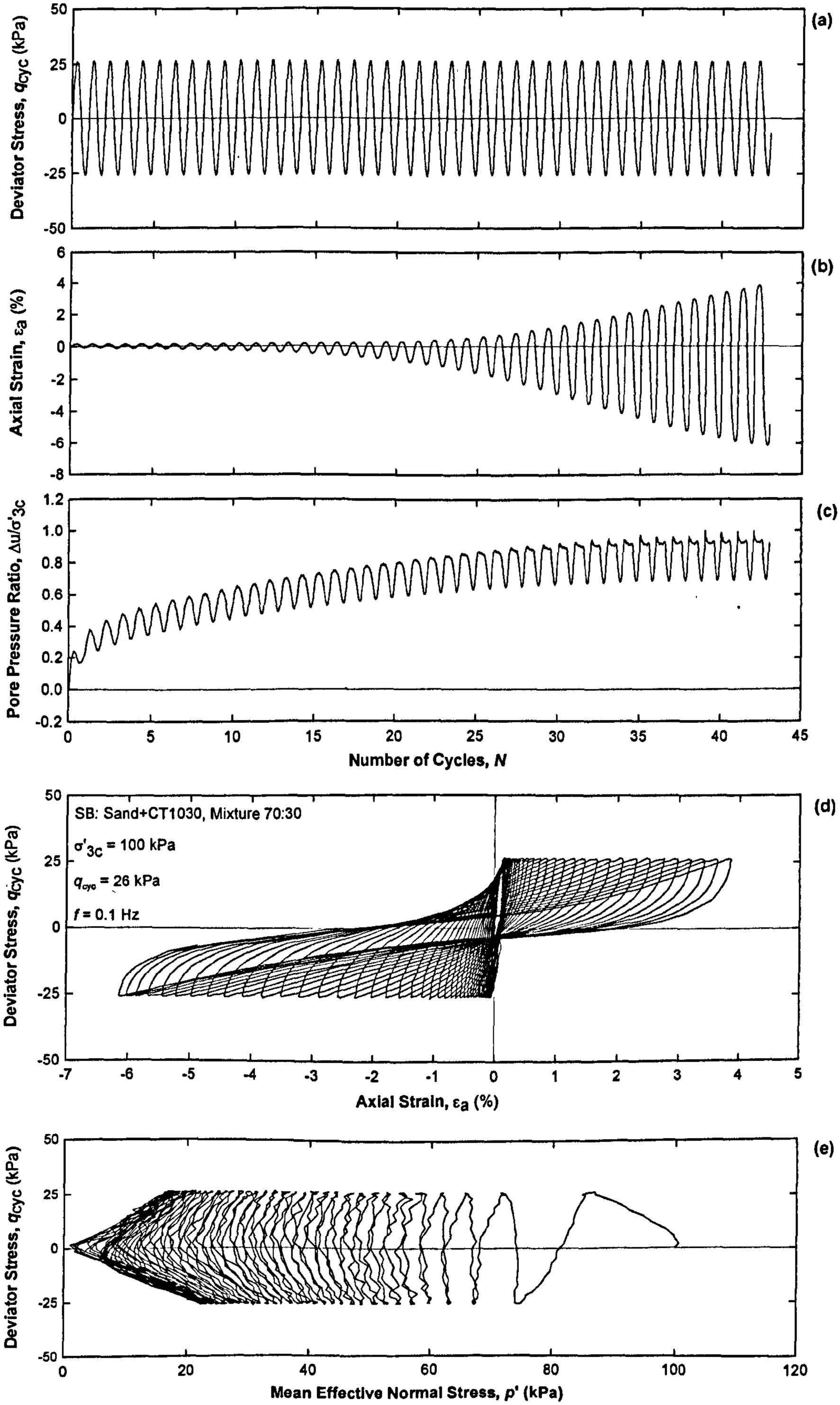

Figure 6. 15 Cyclic triaxial test results for SB with30% rubber, q_{cyc} = 26 kPa

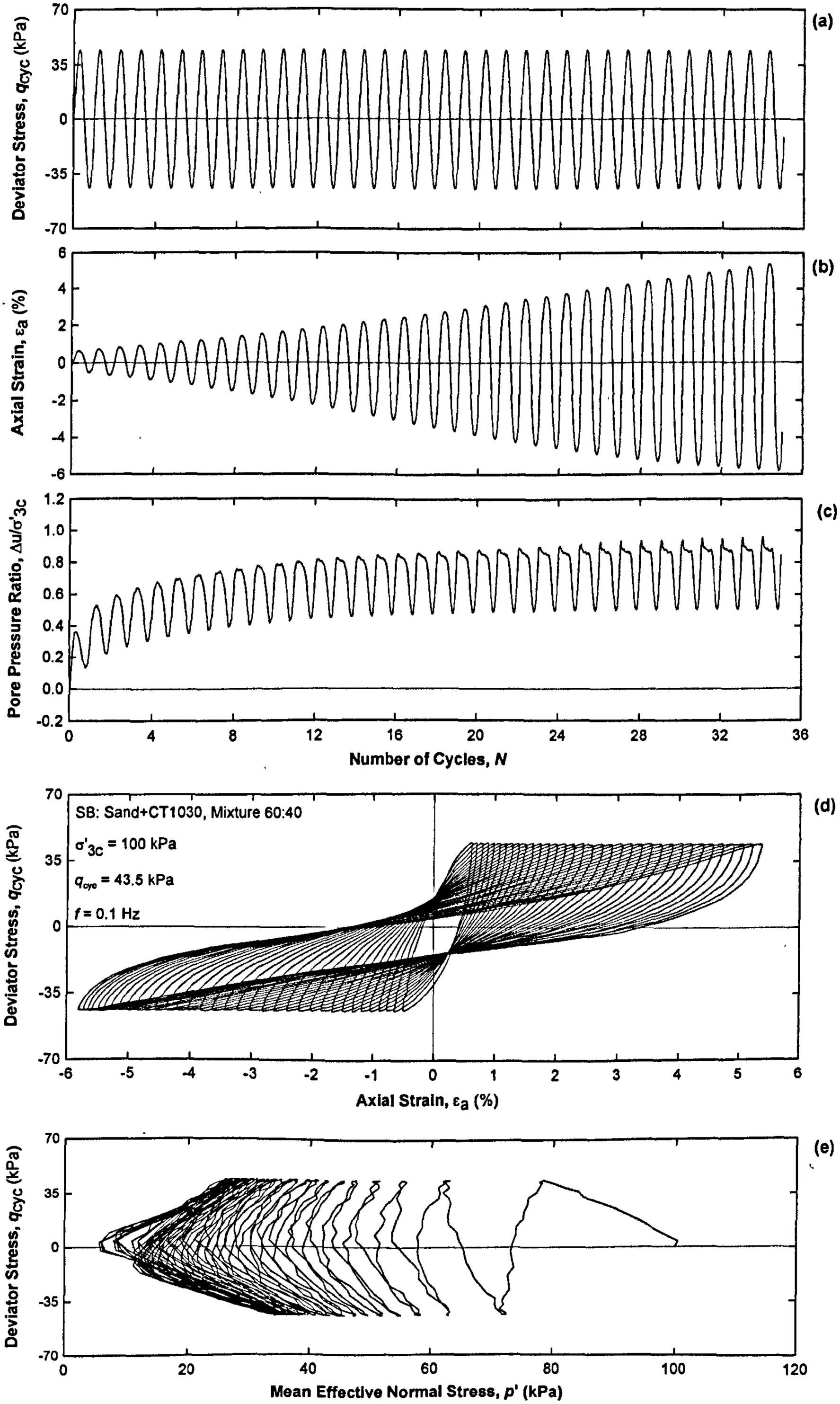

Figure 6. 16 Cyclic triaxial test results for SB with 40% rubber, q_{cyc} = 43.5 kPa

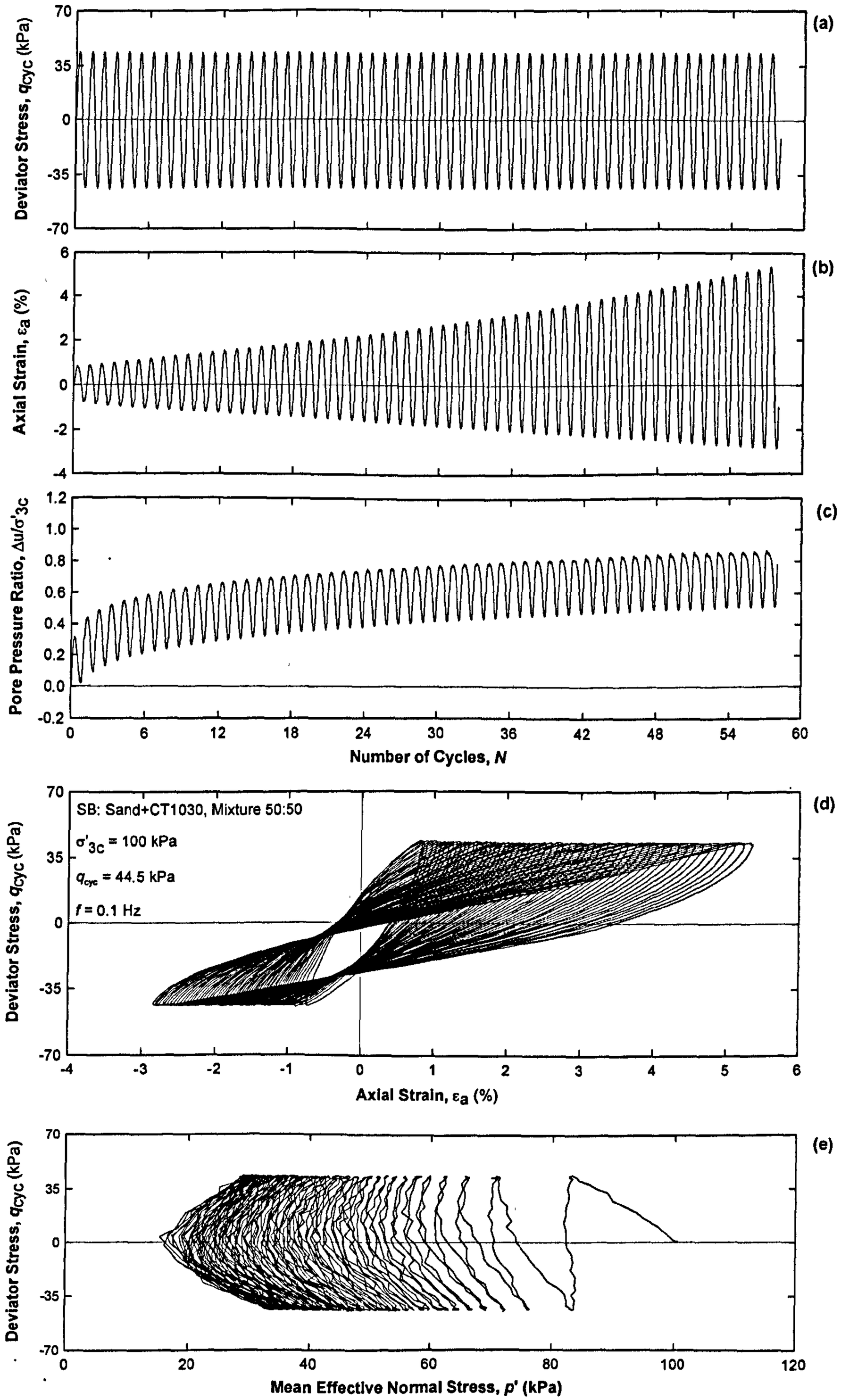

Figure 6. 17 Cyclic triaxial test results for SB with 50% rubber, q_{cyc} = 44.5 kPa

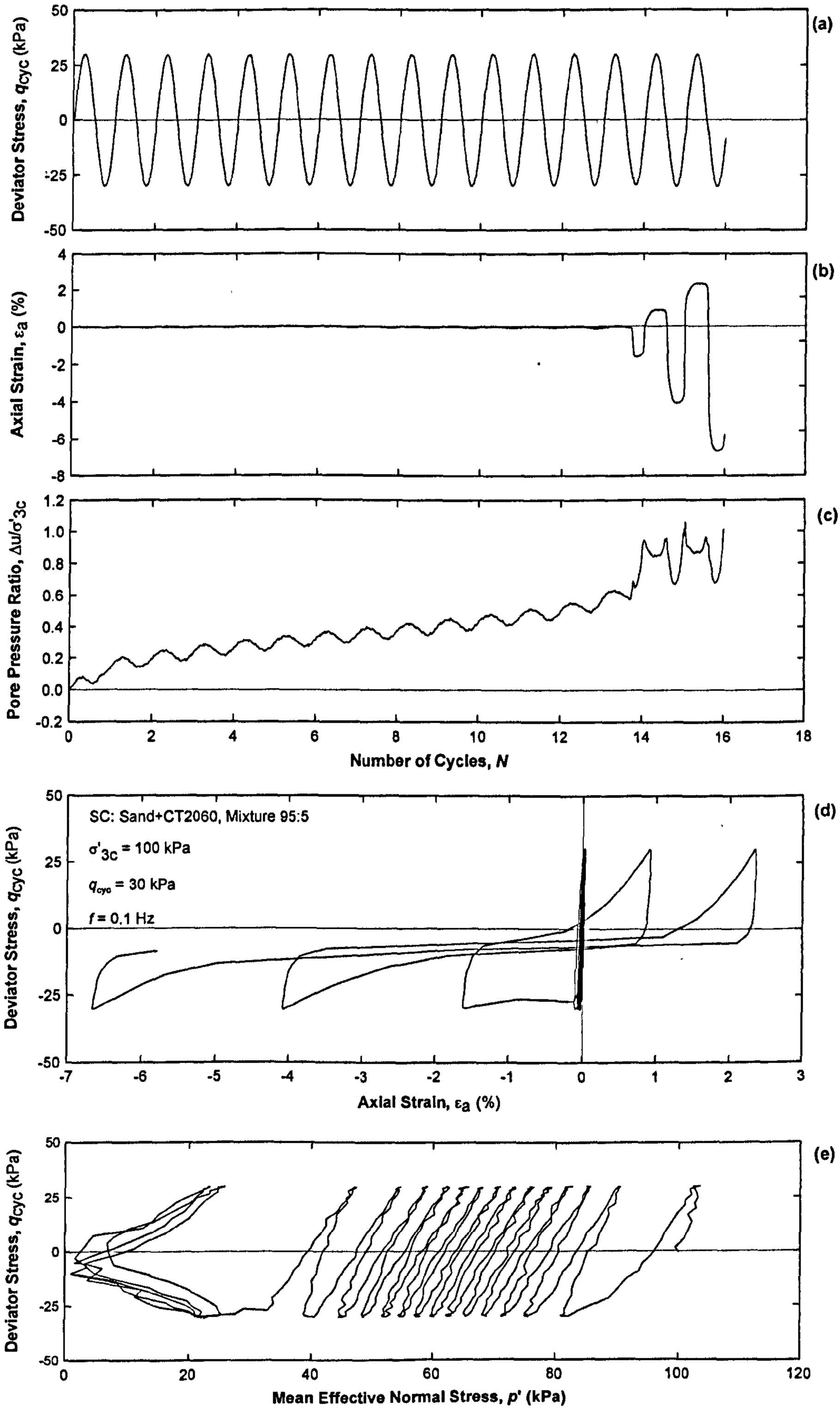

Figure 6. 18 Cyclic triaxial test results for SC with 5% rubber, q_{cyc} = 30 kPa

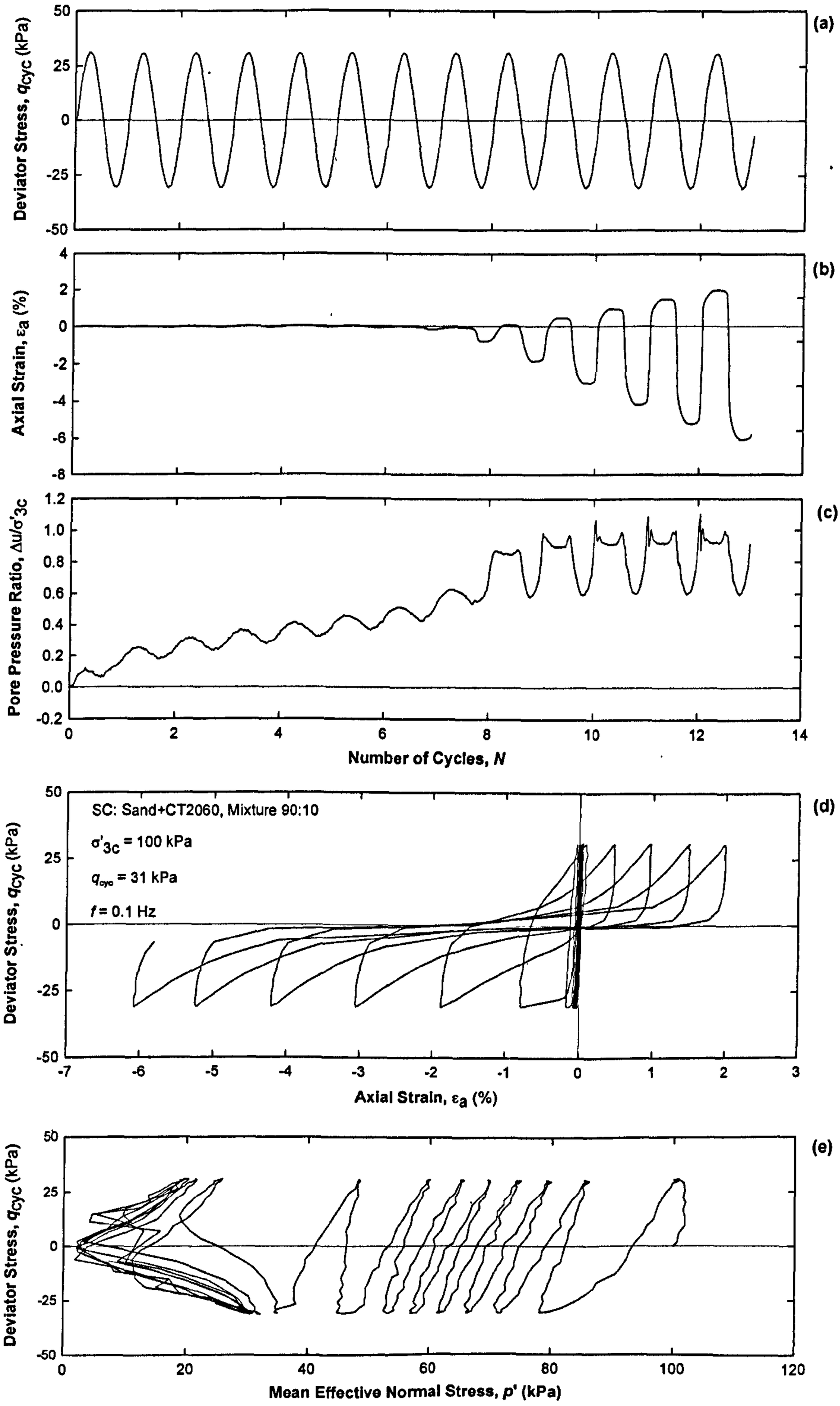

Figure 6. 19 Cyclic triaxial test results for SC with 10% rubber, q_{cyc} = 31 kPa

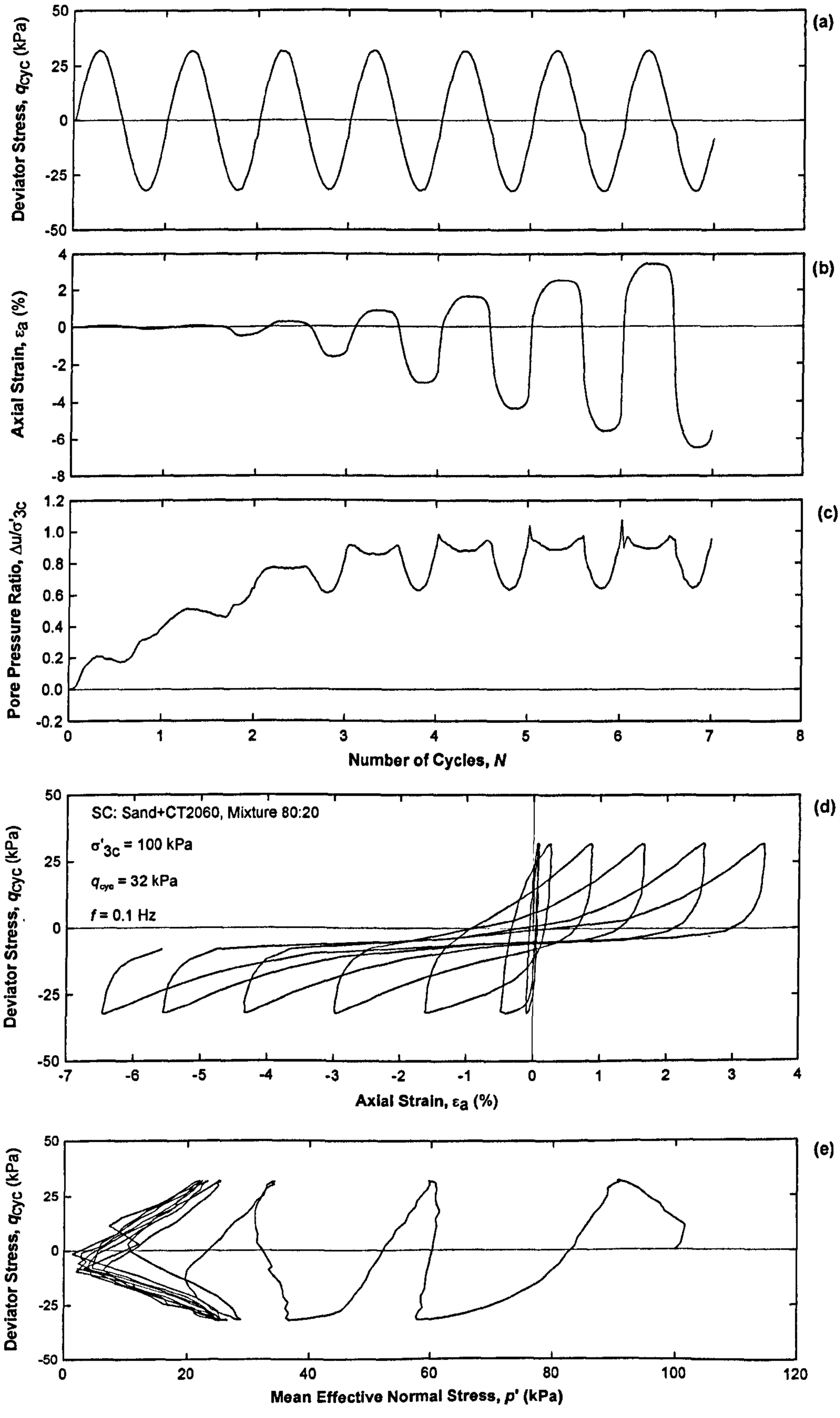

Figure 6. 20 Cyclic triaxial test results for SC with 20% rubber, q_{cyc} = 32 kPa

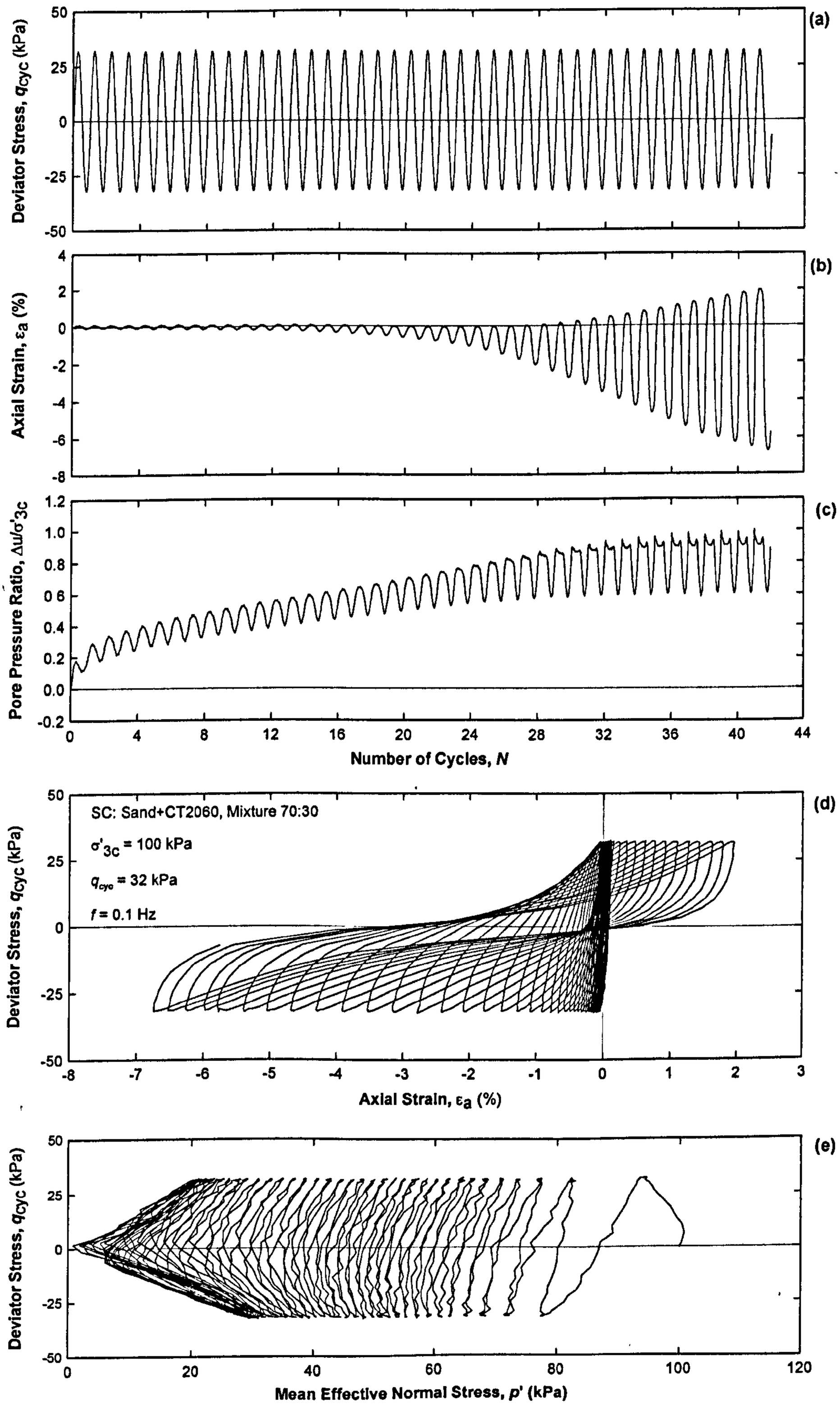

Figure 6. 21 Cyclic triaxial test results for SC with 30% rubber, q_{cyc} = 32 kPa

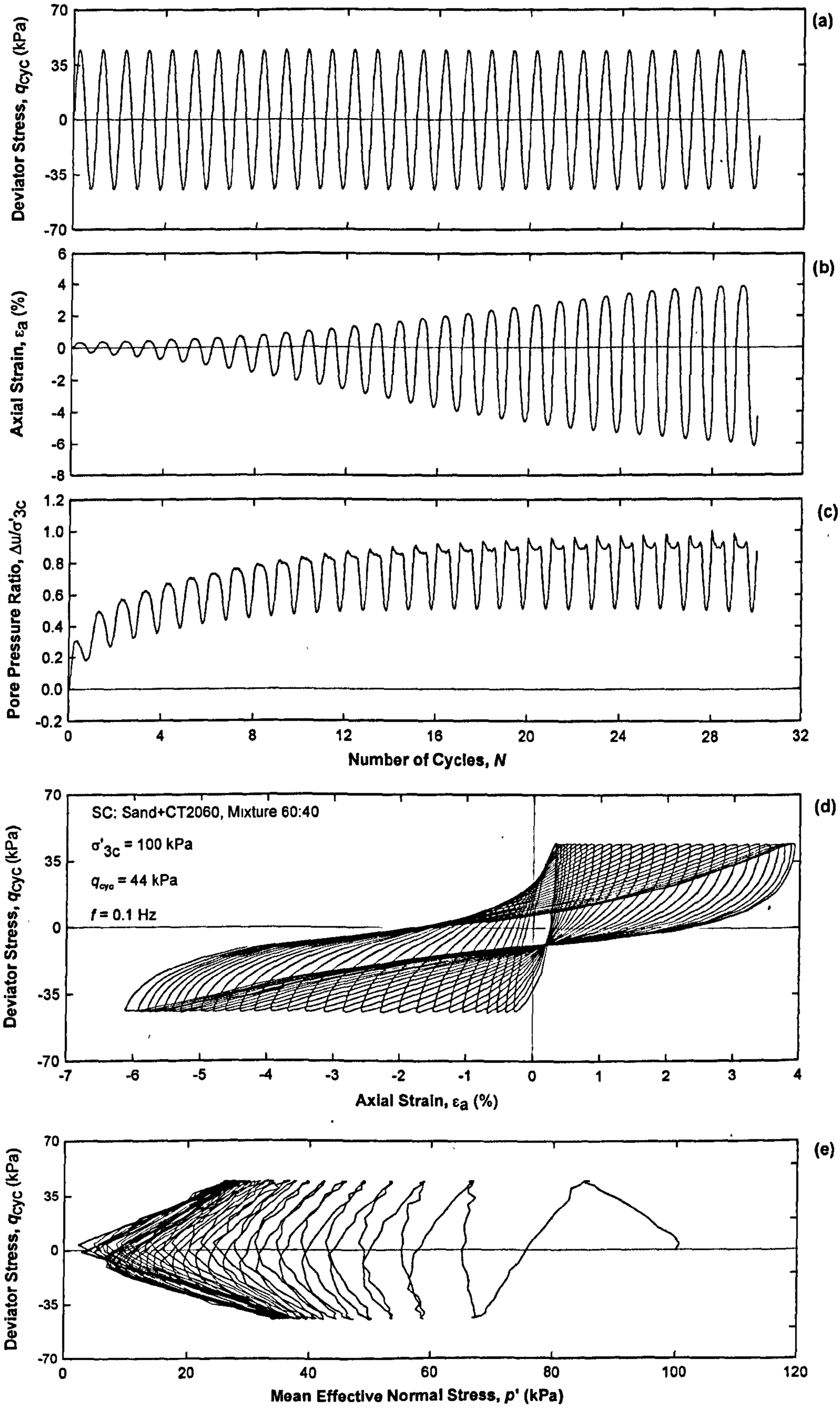

Figure 6. 22 Cyclic triaxial test results for SC with 40% rubber, q_{cyc} = 44 kPa

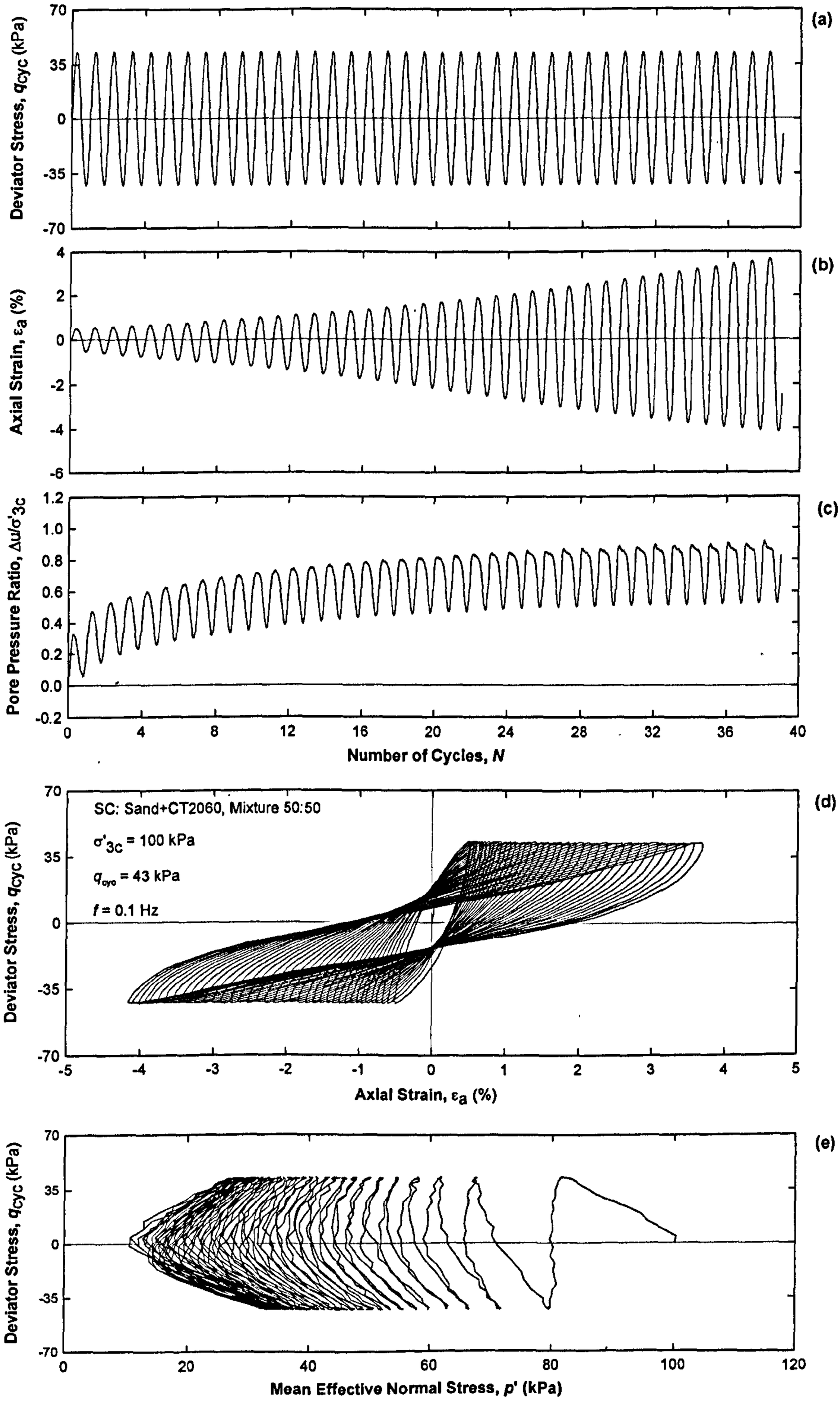

Figure 6. 23 Cyclic triaxial test results for SC with 50% rubber, q_{cyc} = 43 kPa

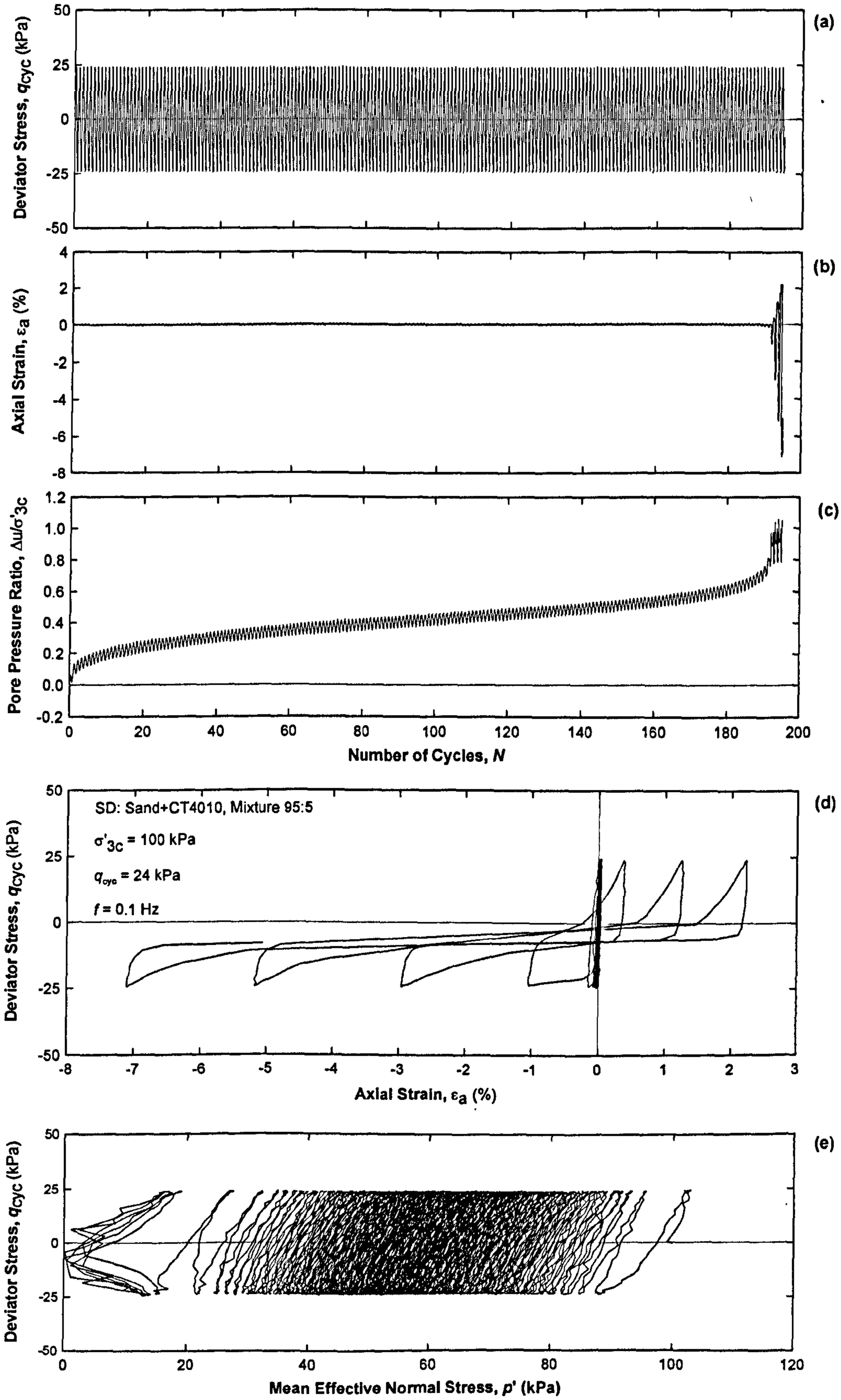

Figure 6. 24 Cyclic triaxial test results for SD with 5% rubber, q_{cyc} = 24 kPa

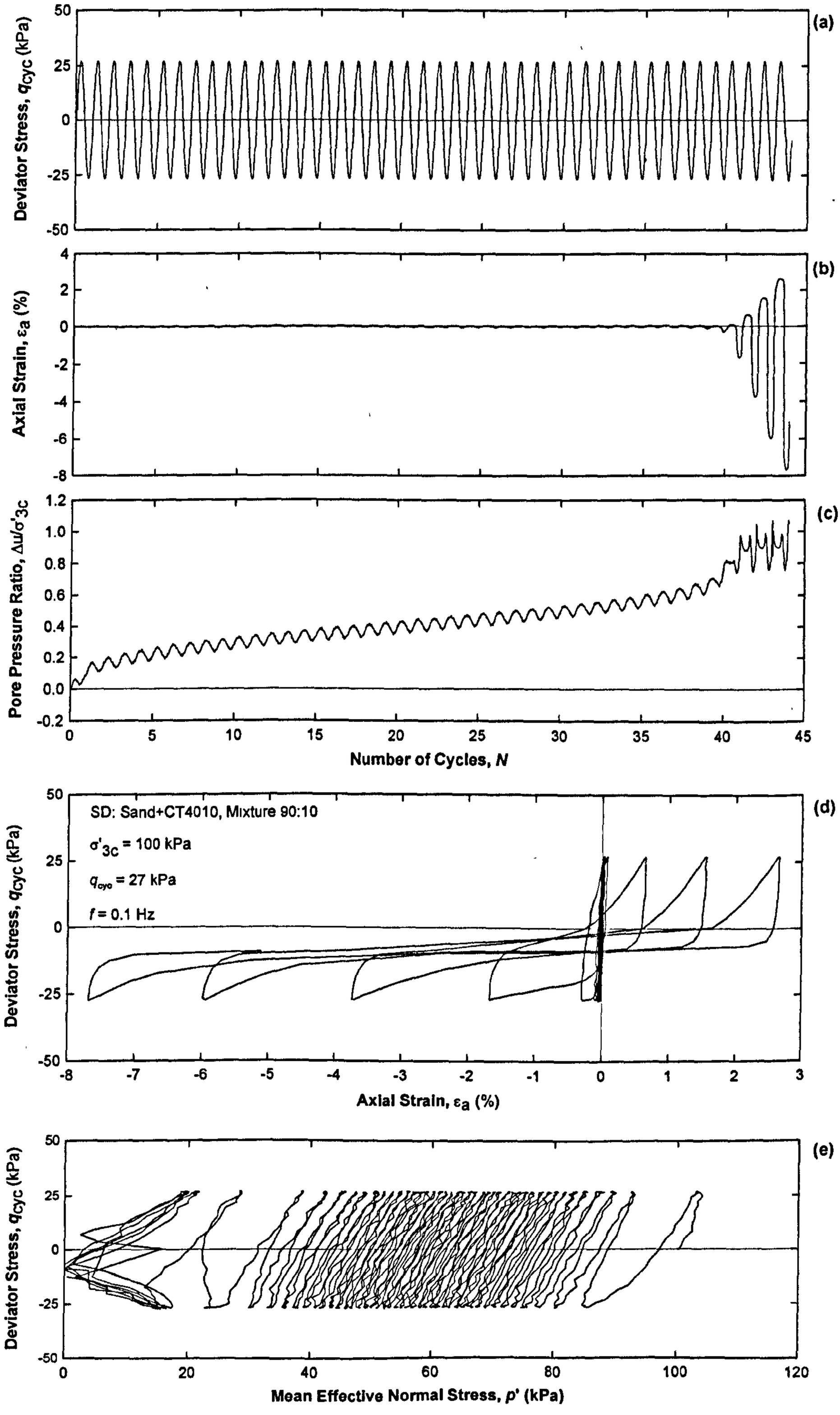

Figure 6. 25 Cyclic triaxial test results for SD with 10% rubber, q_{cyc} = 27 kPa

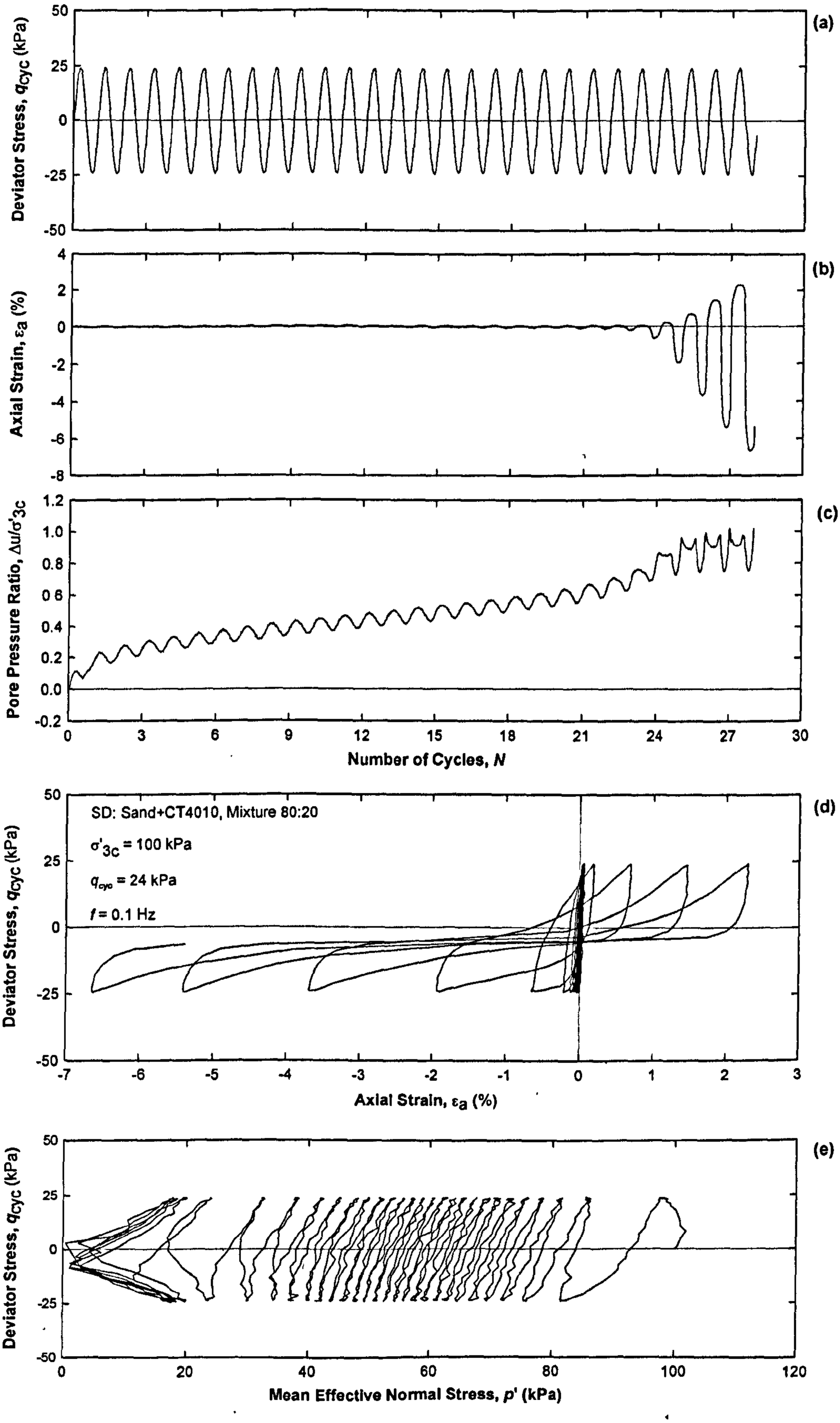

Figure 6. 26 Cyclic triaxial test results for SD with 20% rubber, q_{cyc} = 24 kPa

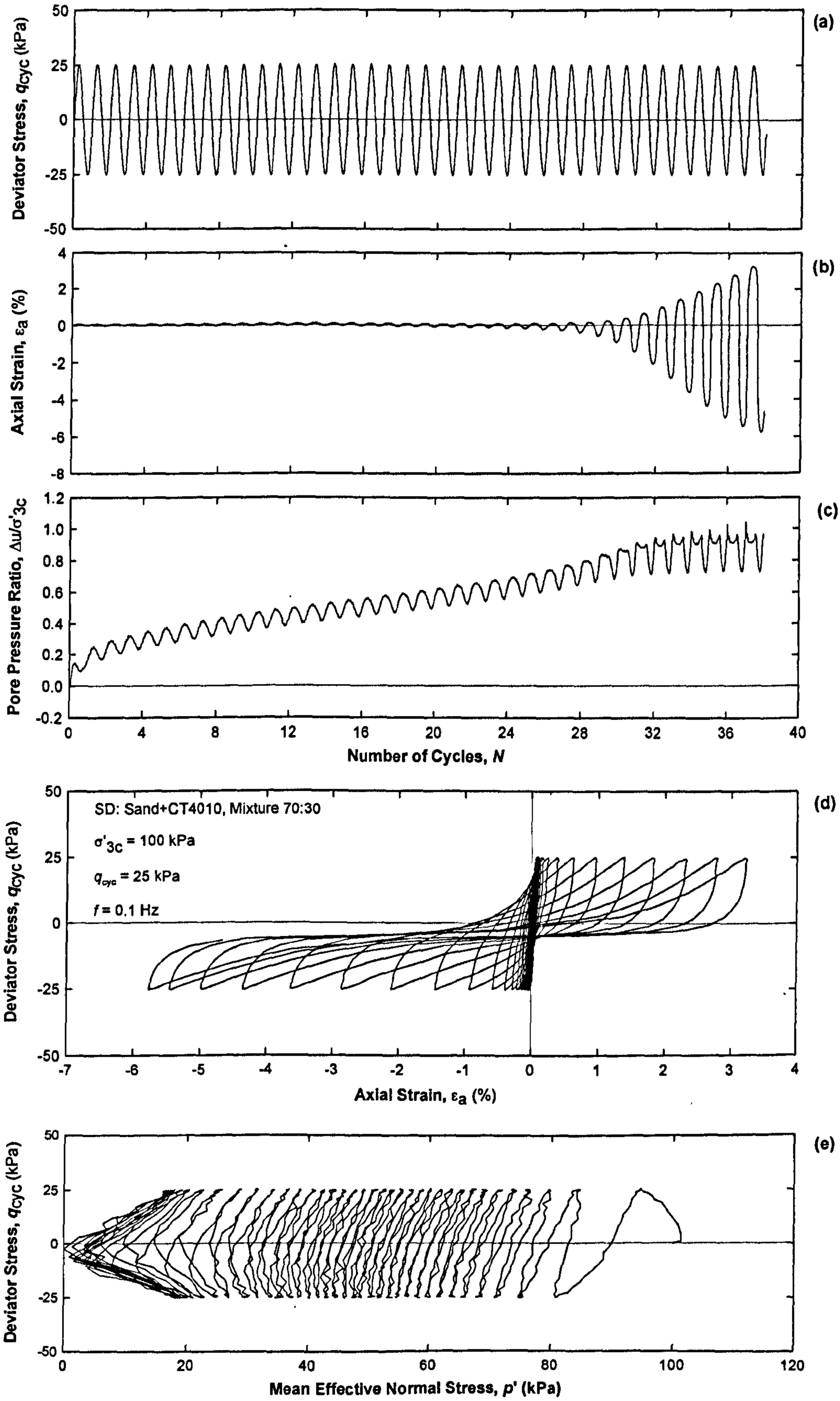

Figure 6. 27 Cyclic triaxial test results for SD with 30% rubber, q_{cyc} = 25 kPa

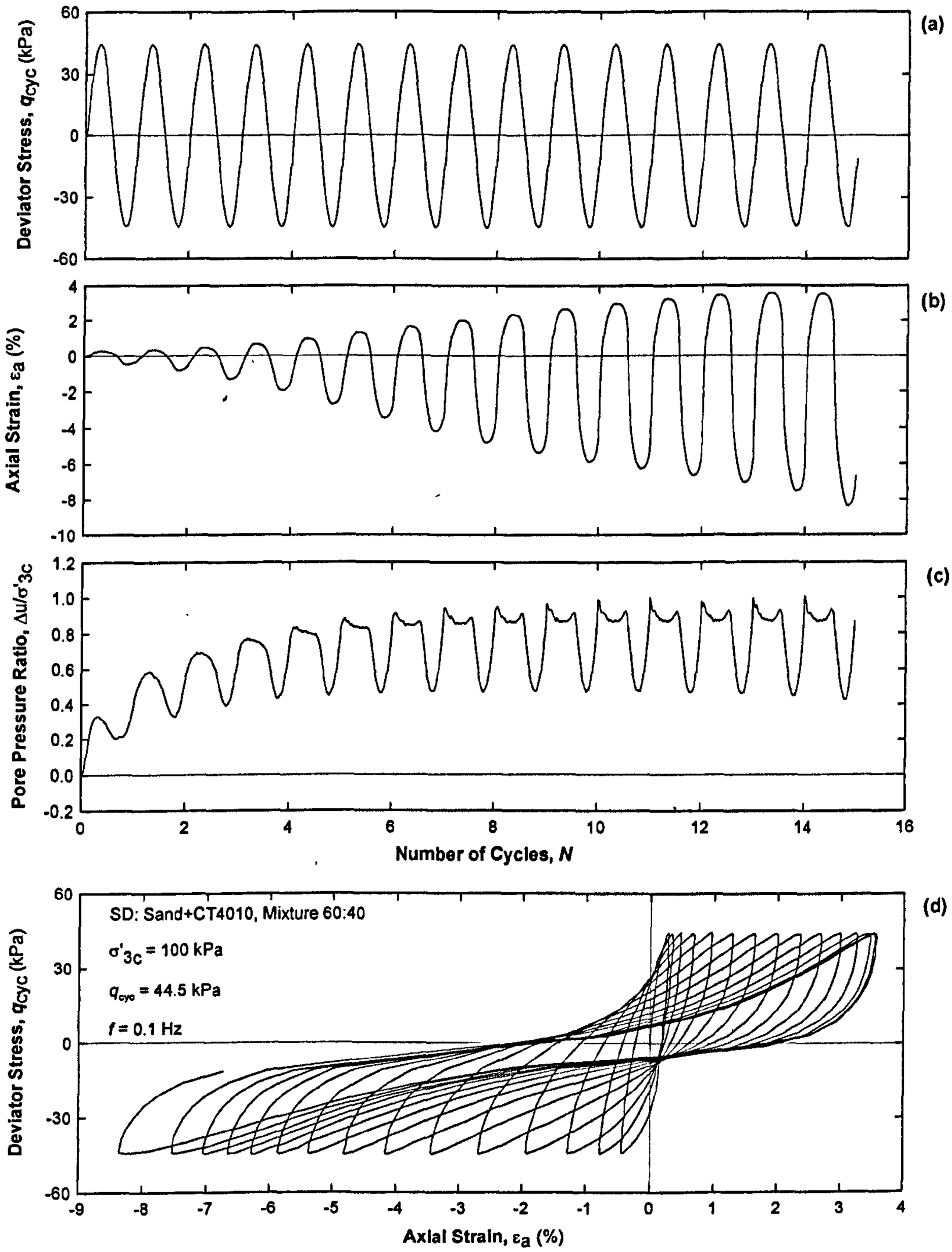

Figure 6. 28 Cyclic triaxial test results for SD with 40% rubber, q_{cyc} = 44.5 kPa

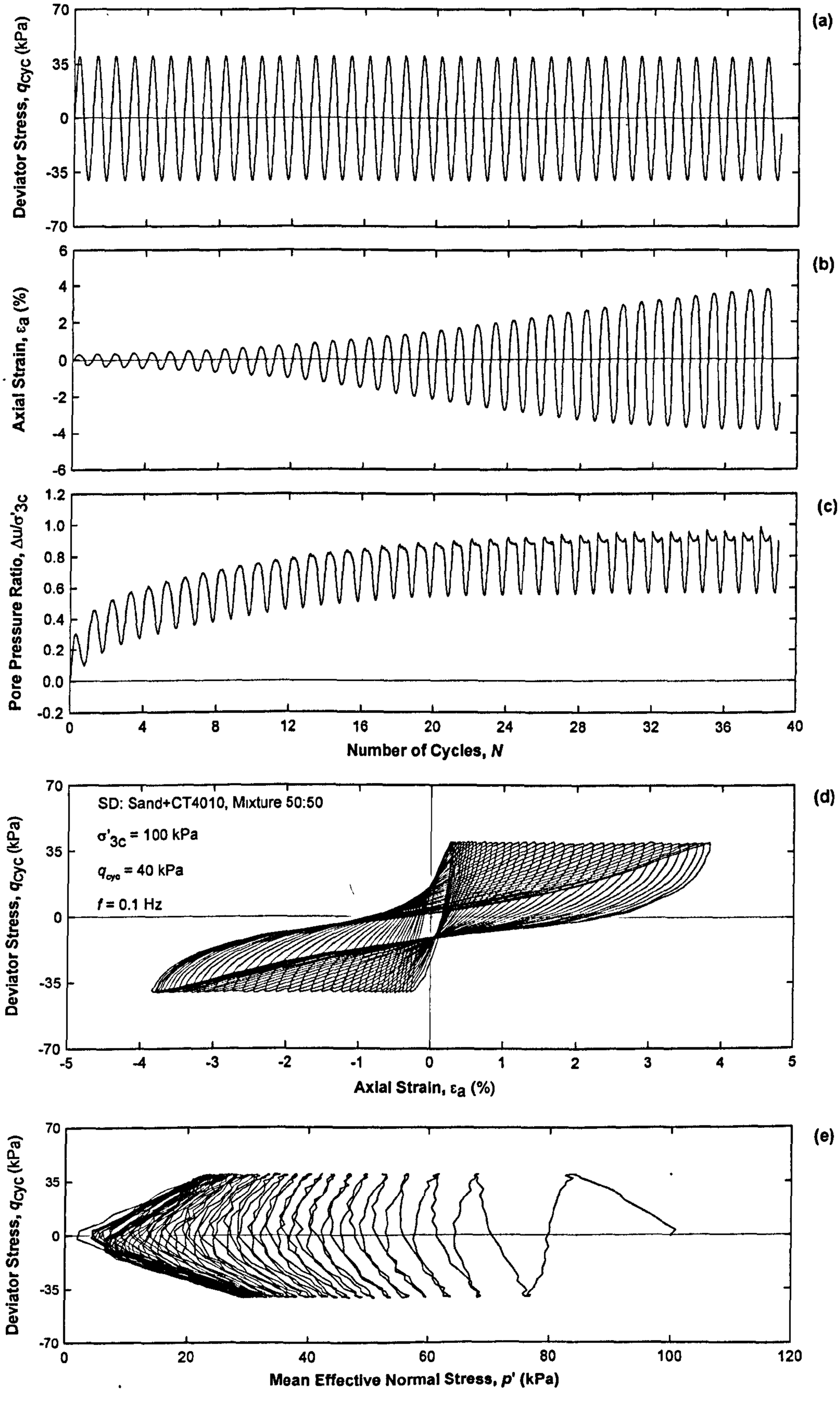

Figure 6. 29 Cyclic triaxial test results for SD with 50% rubber, q_{cyc} = 40 kPa

6.2.2 Cyclic Strength

The cyclic strength (Ishihara, 1993) is defined as the magnitude of the *CSR* required to produce 5% of either double amplitude axial strain $\varepsilon_{a,DA}$ in case of stress reversal or 5% of axial plastic strain $\varepsilon_{a,P}$ in case of no stress reversal after 20 cycles of uniform cyclic load application (Promputthangkoon and Hyde, 2008a). Note that in North America the cyclic strength is often derived from the *CSR* at $N = 15$ cycles. Also, it should be noted that the terms cyclic strength, liquefaction strength, and liquefaction resistance, are in fact the same, and can be used interchangeably.

In order to be able to plot the cyclic strength curve and obtain the cyclic strength, each specimen was tested with at least four different cyclic deviator stresses. The cyclic deviator stress levels were chosen such that the liquefaction occurred over a range of approximately 5 – 200 cycles, i.e., 3, 15, 55, and 181 cycles. The cyclic strength then was obtained by projecting the *CSR* at $N = 20$ cycles, as illustrated by Figure 6.30, which presents a typical cyclic strength curve as well as the cyclic strength.

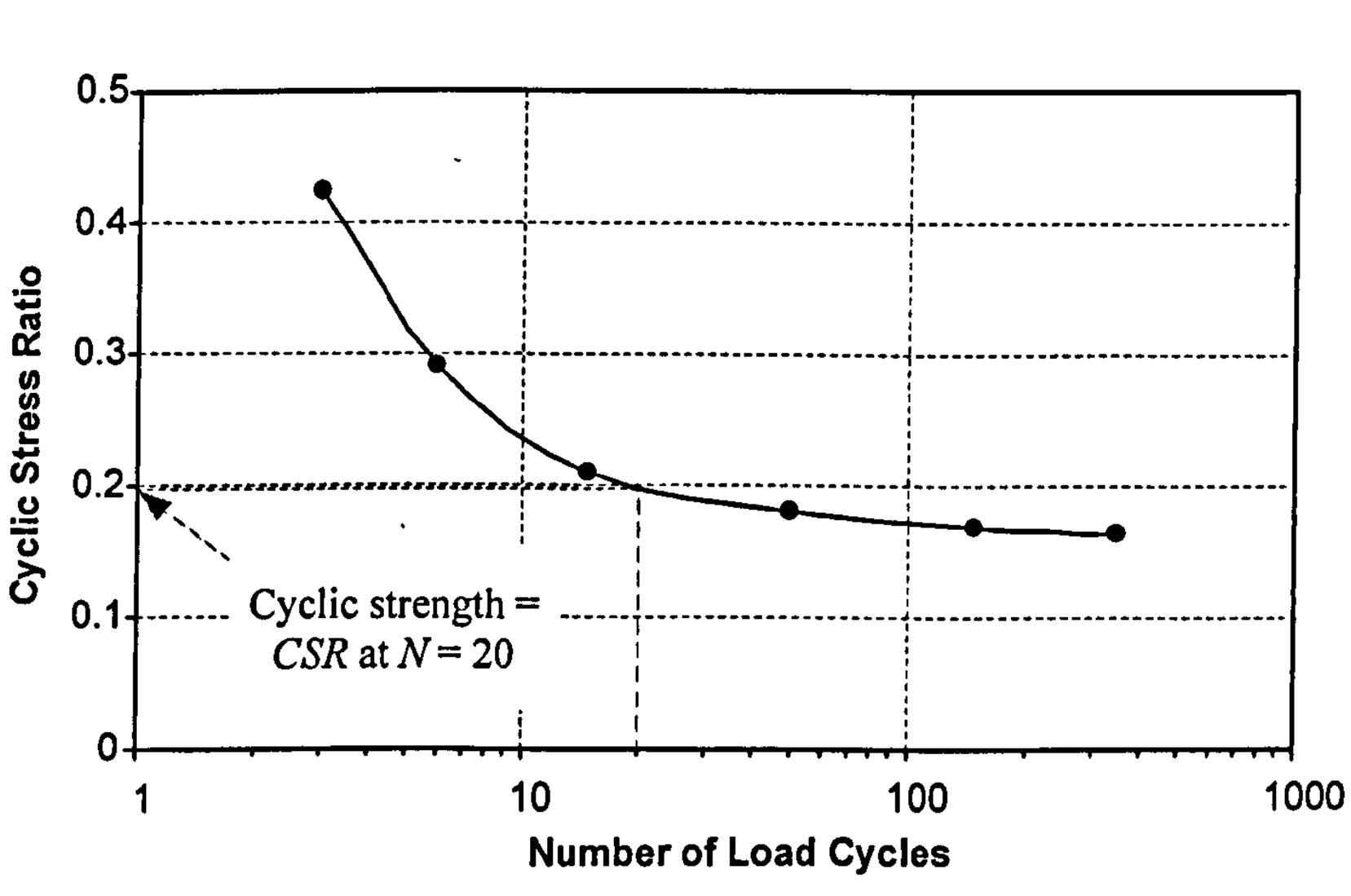

Figure 6. 30 Determination of cyclic strength

The cyclic strength curves were drawn using the test results previously shown in Tables 6.1 – 6.5. They illustrate the relationship between the cyclic stress ratio and the number of load cycles at which the specimens deformed axially to 5%. The cyclic strength curves for the mixtures SA, SB, SC, and SD, are plotted and illustrated by Figure 6.31, Figure 6.32, Figure 6.33, and Figure 6.34, respectively. The cyclic

strengths obtained from Figures 6.31 - 6.34 are shown in Table 6.6 which presents the summaries of the cyclic strength for SA, SB, SC, and SD. The variation of the cyclic strength in relation to the rubber contents of all mixtures was plotted and is shown in Figure 6.35.

The cyclic strength of Leighton Buzzard 16/30 sand used in this research was 0.167 (see Table 6.6). This is comparable to 0.140 for Soma sand having a void ratio of 0.863 (Hyodo *et al.*, 2008), and 0.150 for standard Toyoura sand with 70% relative density (Hyodo *et al.*, 1998), which is the same as for Masado sand having 60% relative density investigated by Hyodo *et al.* (1998).

When considering Figure 6.31 illustrating the cyclic strength curves for SA, it was striking to find out that all had almost the same gradient, regardless of the amount of rubber added. The curve for 95:5 mixtures was observed to be noticeably lower than that of pure sand, indicating lower liquefaction resistance. When the rubber was increased to 10 and 20%, the curves were observed to be even lower than the curve for 95:5 mixtures. At 20% rubber, however, the curve was the lowest, indicating the worst liquefaction resistance. Note that the curves for 10 and 20% rubber were surprisingly almost identical, implying that they had the same liquefaction resistance despite having different amount of rubber content.

When the rubber was increased up to 30%, the cyclic strength curve then began to change direction by moving upwards, but was still below the curve for pure sand. The cyclic strength curve was higher than that of pure sand only after the rubber content was increased to 40%, but still not significant. When the rubber was increased to 50%, however, the cyclic strength was markedly higher than that of pure sand.

For SB containing 5, 10, and 20% rubber, it was observed that the curves were almost the same; nonetheless, they were much lower than that for pure sand. Comparing these three mixtures, the order of the liquefaction resistance from low to high is: 20,.10, and 5% (see Figure 6.32), which is the same as found for SA. It was also observed that all three curves had a similar gradient to that of pure sand.

For SB having 30, 40, and 50% rubber contents, the gradients of the cyclic strength curves were observed to be slightly steeper than that of pure sand. The liquefaction resistance for SB having 30% rubber was almost the same as for SA having

the same rubber content. However, when the rubber was increased to 40 and 50%, the cyclic strength curves were very similar, and much higher than that of pure sand. This is different from SA where with 40% rubber the curve was just slightly higher than the pure sand curve; it was much higher only when the rubber was increased to 50%.

For SC (Figure 6.33) it was observed that the pattern of cyclic strength curves was quite similar to that of SB. However, there was one difference as the cyclic strength curve was higher than that of pure sand when the rubber was increased to just 30%; whereas for SA and SB having the same rubber content, the curves were still lower than that of pure sand. These findings for SC were found to be similar for the cyclic strength curves for SD as well (Figure 6.34). However, for SD, only the mixtures 60:40 and 50:50 curves were higher than that of pure sand.

Considering Figure 6.35, it can be seen that all mixtures – SA, SB, SC, and SD – had a similar trend. The cyclic strengths for SA, SB, SC, and SD having 5% rubber content are lower than that of pure sand. It continues to drop until the rubber content reaches 20%, which is the lowest point. However, when the rubber content is increased to 30%, the cyclic strength begins to increase. Then, the increasing trend for the cyclic strength continues almost linearly towards the end (50% rubber).

Surprisingly, it was found for all groups of mixtures having a rubber content of 20% the cyclic strength was the lowest despite the fact that the densities were not the same. Another point that should be stressed is that groups SA, SB, and SD exhibit greater cyclic strength than that of pure sand only after the rubber was increased to 40% and higher. For SC, however, the cyclic strength was observed to be higher than that of pure sand when the rubber was increased to 30% and higher. Furthermore, it was observed that at 50% rubber content the cyclic strength of all groups is very similar. This suggests that for the mixtures having 50% rubber, the liquefaction characteristics were dominated by the rubber, the sand acted only as a fill in the inter-granular voids of the rubber.

From the cyclic strength curves illustrated by Figures 6.31 – 6.34, we could predict the *CSR* at any cycle as well as the cyclic strength by the power equation, as shown below:

$$CSR = \frac{q_{cyc}}{2\sigma'_{3c}} = \frac{a}{N^b} \qquad \textbf{(Eq. 6. 1)}$$

Where factors a and b are the factors that control the position and slope, respectively, of the *CSR* curve, and are summarised in Table 6.7.

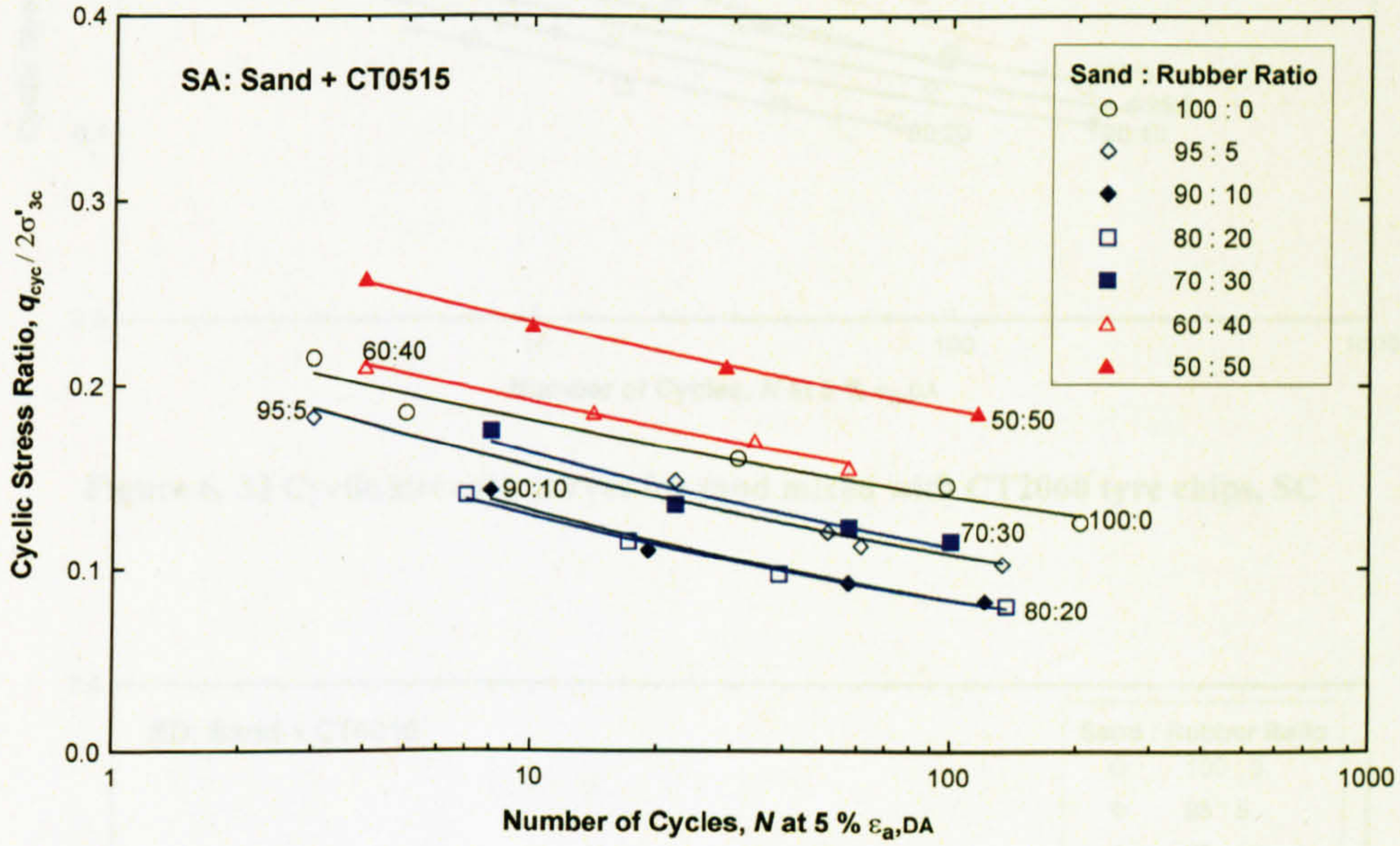

Figure 6. 31 Cyclic strength curves for sand mixed with CT0515 tyre chips, SA

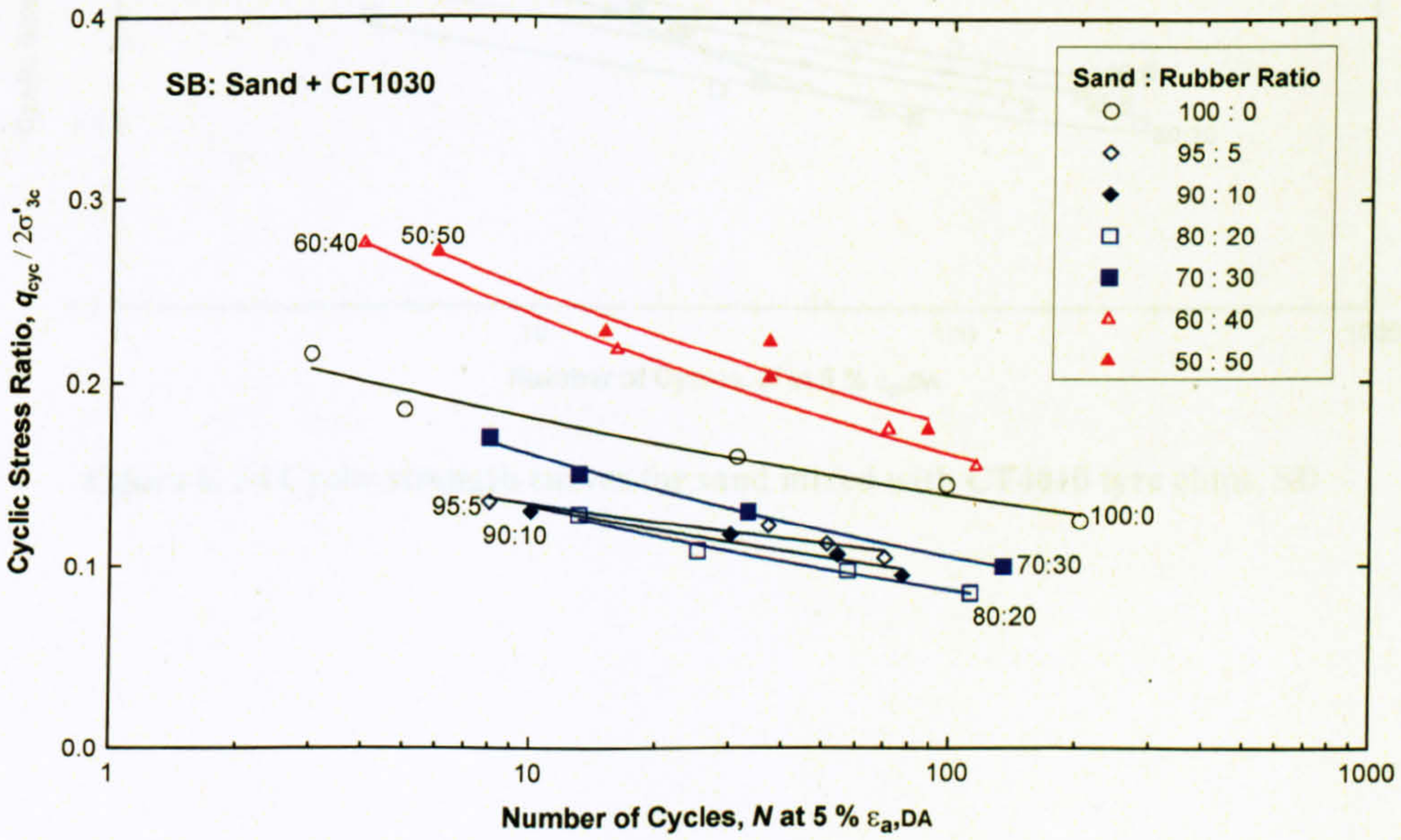

Figure 6. 32 Cyclic strength curves for sand mixed with CT1030 tyre chips, SB

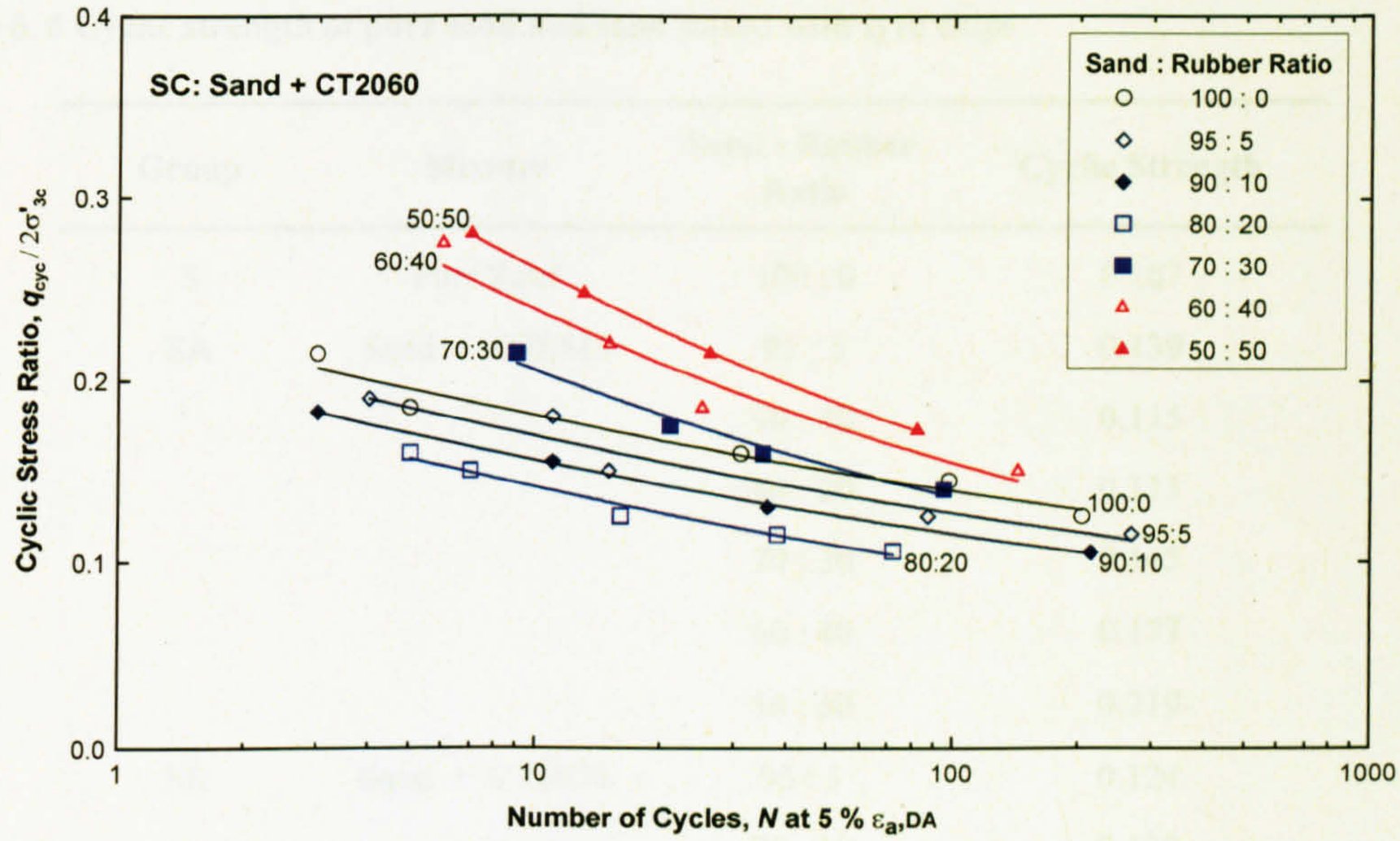

Figure 6. 33 Cyclic strength curves for sand mixed with CT2060 tyre chips, SC

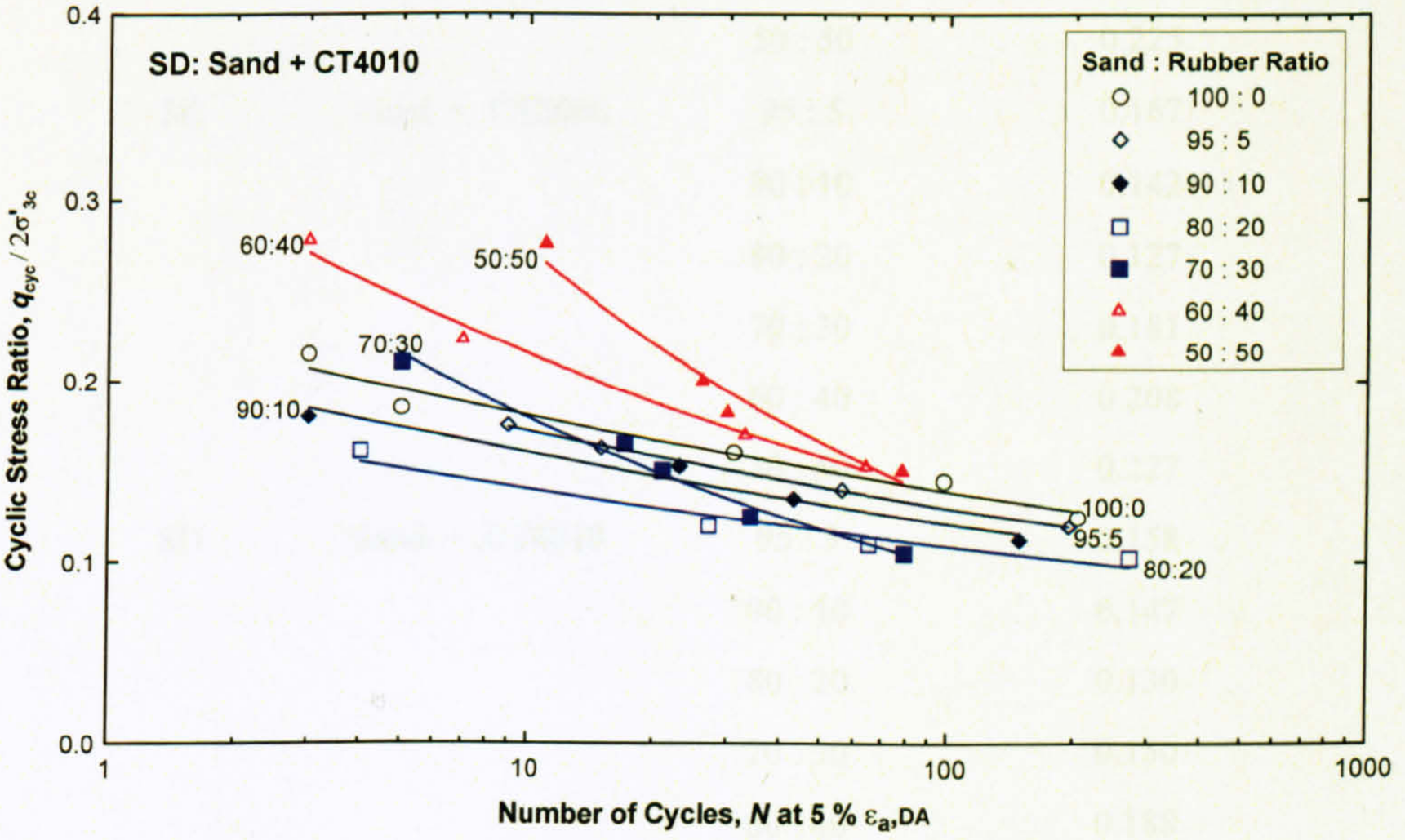

Figure 6. 34 Cyclic strength curves for sand mixed with CT4010 tyre chips, SD

Table 6. 6 Cyclic strength of pure sand and sand mixed with tyre chips

Group	Mixture	Sand : Rubber Ratio	Cyclic Strength
S	Pure Sand	100 : 0	0.167
SA	Sand + CT0515	95 : 5	0.139
		90 : 10	0.115
		80 : 20	0.113
		70 : 30	0.145
		60 : 40	0.177
		50 : 50	0.219
SB	Sand + CT1030	95 : 5	0.124
		90 : 10	0.120
		80 : 20	0.116
		70 : 30	0.142
		60 : 40	0.211
		50 : 50	0.225
SC	Sand + CT2060	95 : 5	0.167
		90 : 10	0.142
		80 : 20	0.127
		70 : 30	0.181
		60 : 40	0.208
		50 : 50	0.227
SD	Sand + CT4010	95 : 5	0.158
		90 : 10	0.147
		80 : 20	0.130
		70 : 30	0.150
		60 : 40	0.188
		50 : 50	0.220

Table 6. 7 Factors *a* and *b* for predicting the *CSR*

Group	Mixture	Sand : Rubber Ratio	factor *a*	factor *b*
S	Pure Sand	100 : 0	0.23	0.11
SA	Sand + CT0515	95 : 5	0.16	0.22
		90 : 10	0.21	0.20
		80 : 20	0.20	0.19
		70 : 30	0.24	0.16
		60 : 40	0.25	0.11
		50 : 50	0.29	0.10
SB	Sand + CT1030	95 : 5	0.17	0.11
		90 : 10	0.19	0.14
		80 : 20	0.20	0.18
		70 : 30	0.25	0.18
		60 : 40	0.35	0.17
		50 : 50	0.35	0.15
SC	Sand + CT2060	95 : 5	0.23	0.13
		90 : 10	0.21	0.13
		80 : 20	0.20	0.15
		70 : 30	0.31	0.18
		60 : 40	0.37	0.19
		50 : 50	0.23	0.11
SD	Sand + CT4010	95 : 5	0.23	0.12
		90 : 10	0.21	0.12
		80 : 20	0.18	0.11
		70 : 30	0.33	0.26
		60 : 40	0.33	0.19
		50 : 50	0.56	0.31

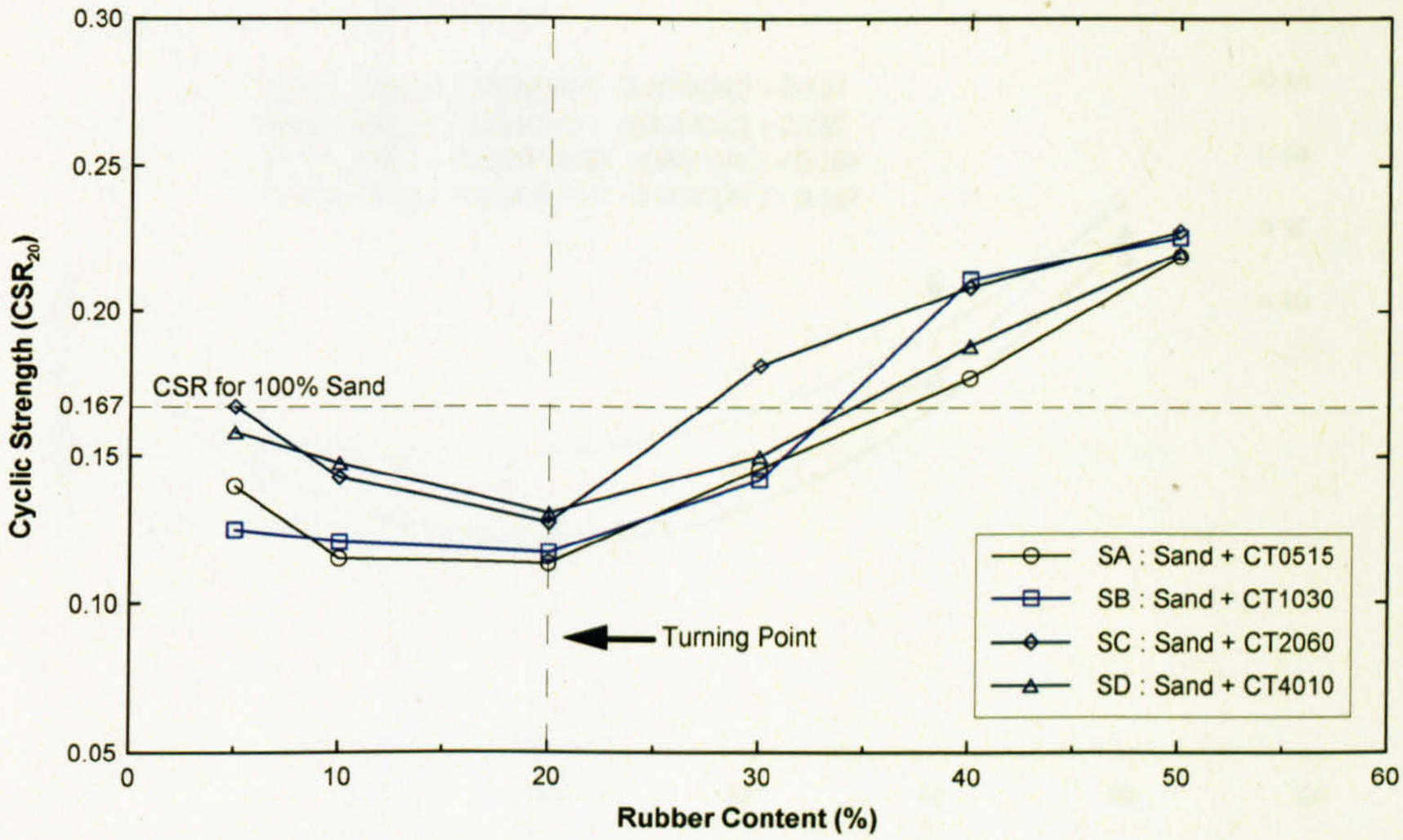

Figure 6. 35 **Cyclic strength versus rubber content**

It can be seen that the cyclic strengths with various rubber contents for SA, SB, SC, and SD shown in Figure 6.35 have a similar parabolic form. Hence, the cyclic strength data was fitted to second order polynomial equations to determine the cyclic strength at any rubber content. This was done by defining cyclic strength for pure sand, i.e., the intercept on the cyclic strength axis, as 0.167. Then, a second order polynomial equation was employed to draw the cyclic strength curves using the data points from Figure 6.35. The smooth cyclic strength curves are illustrated by Figure 6.36, and the equations are shown below:

$$CSR_{20} = 0.0001(RC)^2 - 0.0048(RC) + 0.167 \quad \text{(for SA)} \quad \textbf{(Eq. 6. 2)}$$

$$CSR_{20} = 0.0001(RC)^2 - 0.0047(RC) + 0.167 \quad \text{(for SB)} \quad \textbf{(Eq. 6. 3)}$$

$$CSR_{20} = 0.00007(RC)^2 - 0.0023(RC) + 0.167 \quad \text{(for SC)} \quad \textbf{(Eq. 6. 4)}$$

$$CSR_{20} = 0.00009(RC)^2 - 0.0031(RC) + 0.167 \quad \text{(for SD)} \quad \textbf{(Eq. 6. 5)}$$

where:

CSR_{20} = cyclic strength (derived from *CSR* at 20 cycles), and

RC = rubber content in per cent.

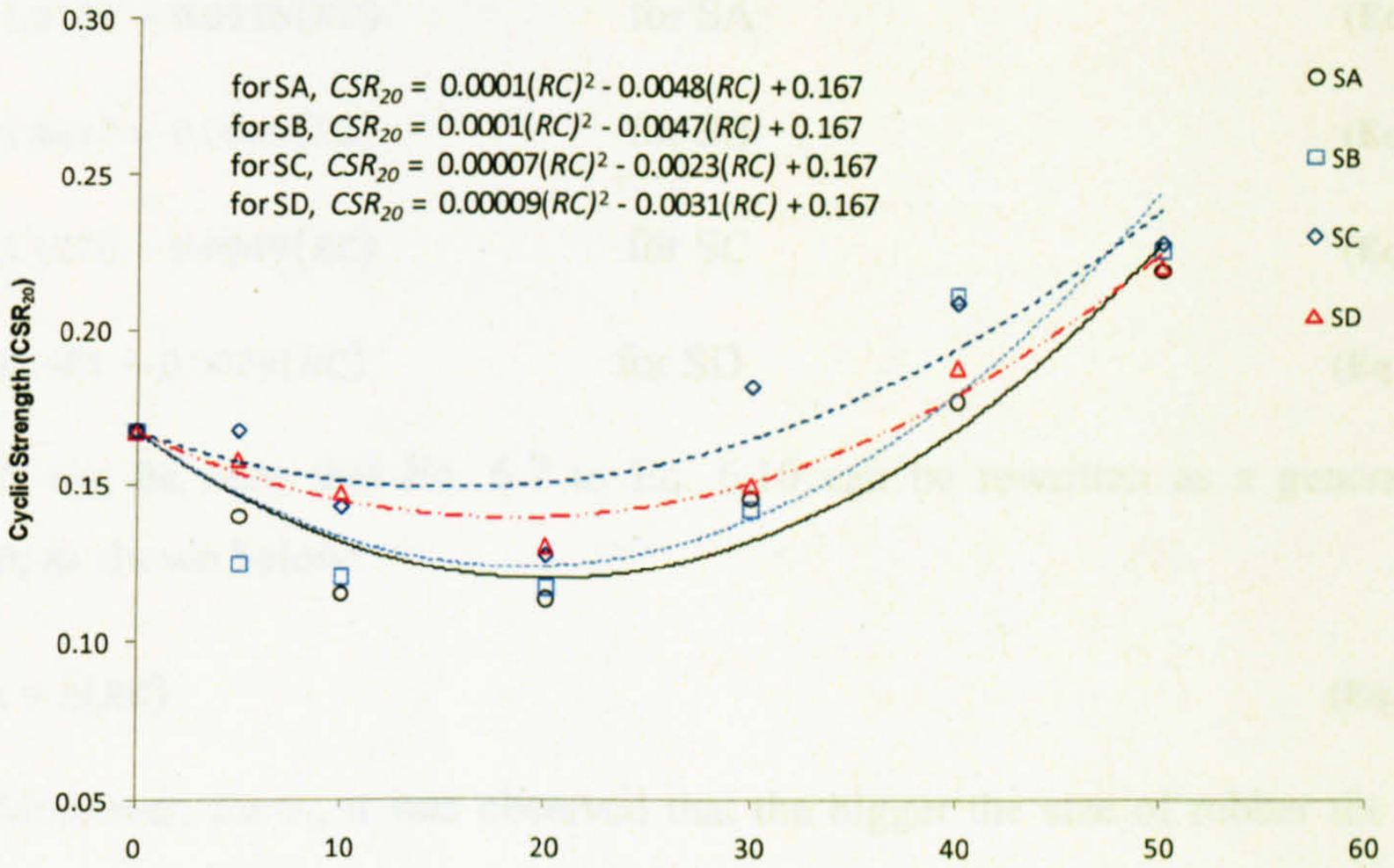

Figure 6. 36 Calculated cyclic strength versus rubber content

It is apparent that, from cyclic strength curves shown in Figure 6.36, the cyclic strength gradually decreases as the rubber content increases from 0 to approximately 20%; after which it gradually increases. This indicates that when the mixtures contained around 20% of rubber the cyclic characteristics were transitional. This may be explained by considering the void ratio of the sand and rubber fractions separately.

The void ratios for the mixtures were further analysed, and are shown in Table 6.8. The inter-rubber void ratio e_r was defined as the ratio of the voids V_v (including the sand) to the solid volume of rubber. Likewise, the inter-sand void ratio e_s is the ratio of the voids V_v (including the rubber) to the solid volume of sand. Each void ratio was plotted, and they are illustrated in Figure 6.37.

For e_s, it can be seen that the change in void ratio is approximately linear indicating that they may be further normalised in terms of the equation y = a + bX. On the other hand, the e_r curves are highly non-linear. However, no matter what size of tyre chip, at the same sand to rubber ratios the inter-rubber void ratios were surprisingly found to be very similar. As such, they could be represented by just one curve. The linearised curves for e_s and the power curve representing e_r for all sizes of tyre chips are illustrated by Figure 6.38. The equations representing the changes of inter-rubber void ratios and inter-sand void ratios are shown below:

$$e_r = 4.416 - 1.1145 \ln(RC) \qquad \textbf{(Eq. 6. 6)}$$

$$e_s = 1.8124 - 0.0118(RC) \quad \text{for SA} \quad \textbf{(Eq. 6. 7)}$$

$$e_s = 1.4447 - 0.0079(RC) \quad \text{for SB} \quad \textbf{(Eq. 6. 8)}$$

$$e_s = 1.1270 - 0.0049(RC) \quad \text{for SC} \quad \textbf{(Eq. 6. 9)}$$

$$e_s = 0.9481 - 0.0029(RC) \quad \text{for SD} \quad \textbf{(Eq. 6. 10)}$$

It can be seen that Eq. 6.7 to Eq. 6.10 can be rewritten as a general linear equation, as shown below:

$$e_s = a + b(RC) \quad \textbf{(Eq. 6. 11)}$$

Moreover, for e_s, it was observed that the bigger the size of rubber the smaller the slope indicating that the size of rubber highly influenced the inter-sand void ratio of sand-rubber mixtures. This is evident when considering the gradual changes of the factors forming Eq. 6.7 to Eq. 6.10. Thus, the factors a and b were plotted against the particle size ratio to determine the relationship, and are illustrated by Figure 6.39. Next, the equations for the factors a and b were obtained, as shown below:

$$a = 2.018 - 0.4637 \ln\left(\frac{D_r}{D_s}\right) \quad \textbf{(Eq. 6. 12)}$$

$$b = 0.0047 \ln\left(\frac{D_r}{D_s}\right) - 0.0139 \quad \textbf{(Eq. 6. 13)}$$

Then, substituting the factors a and b, and Eq. 6.11 became:

$$e_s = \left[2.018 - 0.4637 \ln\left(\frac{D_r}{D_s}\right)\right] + \left[0.0047 \ln\left(\frac{D_r}{D_s}\right) - 0.0139\right] RC \quad \textbf{(Eq. 6. 14)}$$

From these results and analyses, it may be concluded that the cyclic strength of the sand mixed with rubber having a bigger size is higher than the mixtures containing a smaller size of rubber. Furthermore, the cyclic characteristics were transitional for mixtures containing rubber of around 20%. This can be seen when considering the changes of e_r between 10 and 30%. For instance, when the mixtures contained rubber contents from 5 to 10% (see e_r curve in Figure 6.38), e_r decreased sharply. Then, when the rubber was increased from 10 to 30%, the rate of the decrease decreased. Subsequently, when the mixtures contained rubber higher than 30%, the rate of the decrease was approximately constant.

Table 6. 8 Inter-rubber void ratios and inter-sand void ratios

Group	Sand : Rubber Ratio	Solid Vol. of Sand (cu.cm)	Solid Vol. of Rubber (cu.cm)	V_s (cu.cm)	V_v (cu.cm)	e	e_s	e_r
SA	95 : 5	867	46	913	620	0.679	0.715	13.588
	90 : 10	818	91	909	616	0.678	0.753	6.775
	80 : 20	703	176	879	601	0.684	0.855	3.419
	70 : 30	589	252	842	577	0.686	0.979	2.285
	60 : 40	488	325	813	534	0.656	1.094	1.641
	50 : 50	399	399	798	497	0.623	1.246	1.246
SB	95 : 5	867	46	913	615	0.673	0.709	13.465
	90 : 10	822	91	913	603	0.661	0.734	6.610
	80 : 20	730	183	913	590	0.646	0.807	3.229
	70 : 30	635	272	908	552	0.608	0.869	2.027
	60 : 40	541	361	902	515	0.571	0.952	1.428
	50 : 50	429	429	857	462	0.539	1.077	1.077
SC	95 : 5	880	46	926	602	0.651	0.685	13.012
	90 : 10	850	94	944	585	0.619	0.688	6.193
	80 : 20	769	192	961	556	0.578	0.723	2.892
	70 : 30	683	293	976	512	0.525	0.750	1.750
	60 : 40	595	396	991	467	0.472	0.786	1.179
	50 : 50	494	494	989	463	0.468	0.936	0.936
SD	95 : 5	882	46	929	604	0.650	0.684	13.000
	90 : 10	851	95	946	584	0.618	0.686	6.178
	80 : 20	774	193	967	553	0.571	0.714	2.856
	70 : 30	700	300	1000	508	0.508	0.726	1.695
	60 : 40	609	406	1016	468	0.461	0.769	1.153
	50 : 50	528	528	1056	432	0.409	0.819	0.819

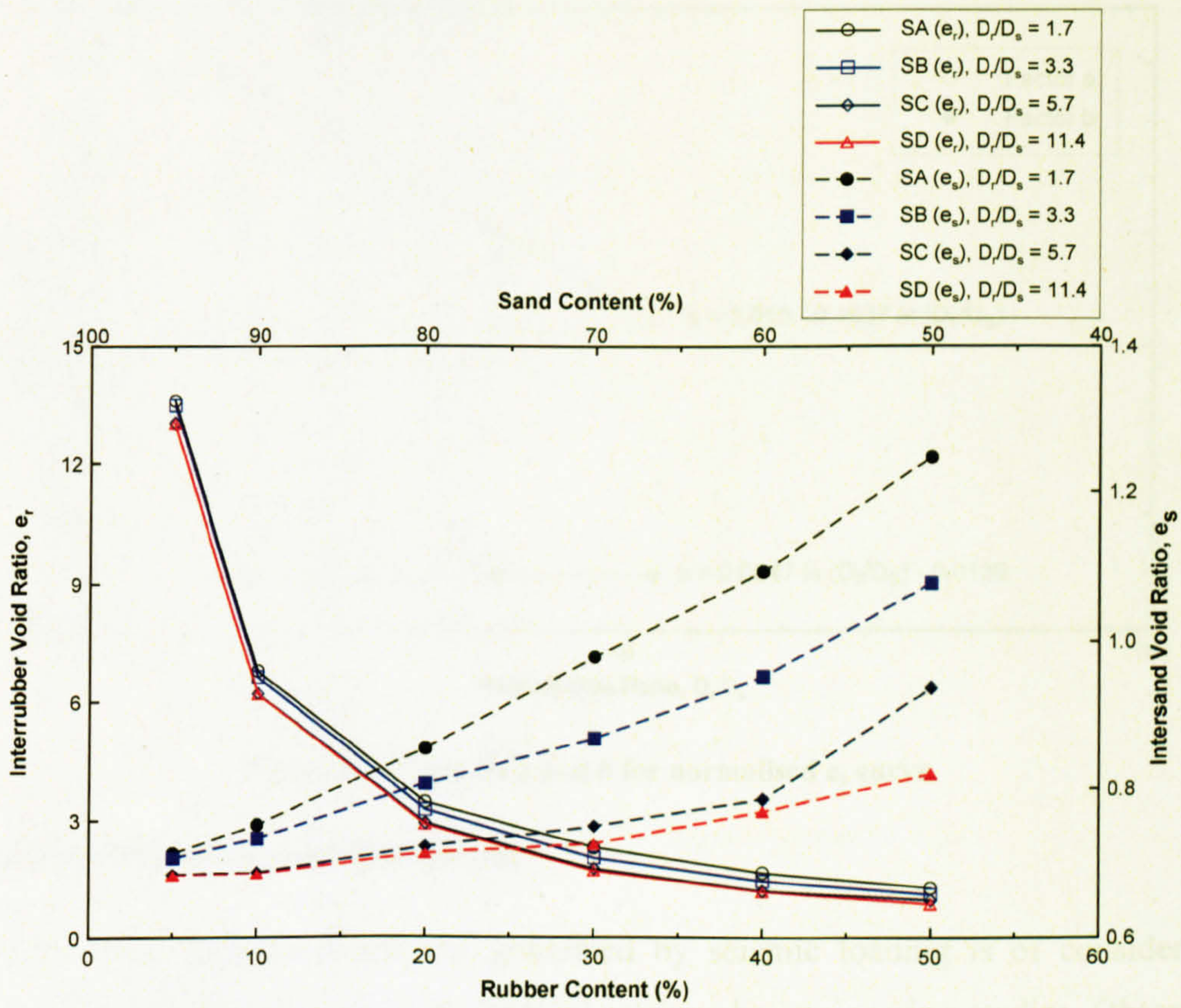

Figure 6. 37 e_r and e_s vs. varied rubber and sand contents

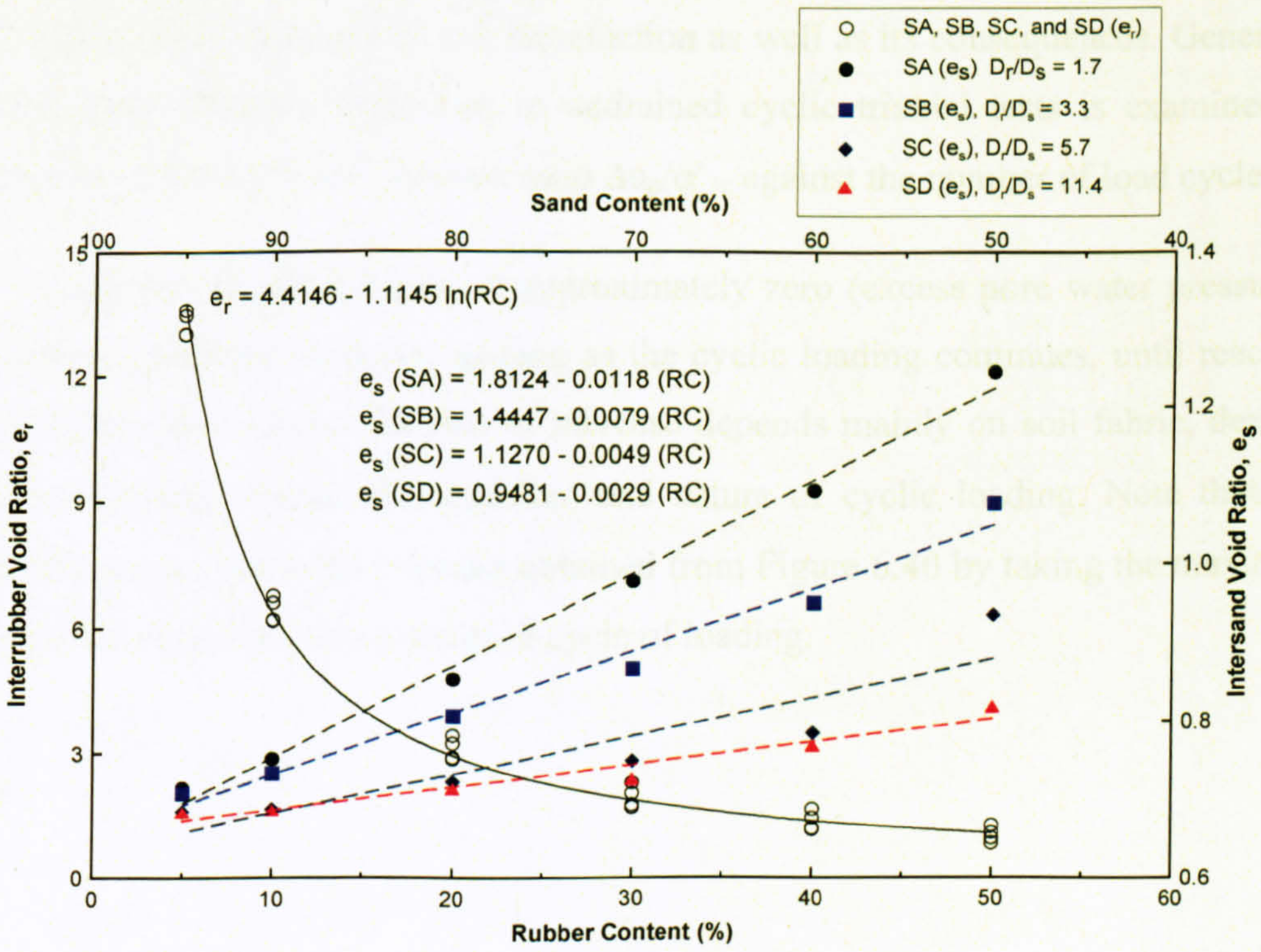

Figure 6. 38 Normalised curves for e_r and e_s

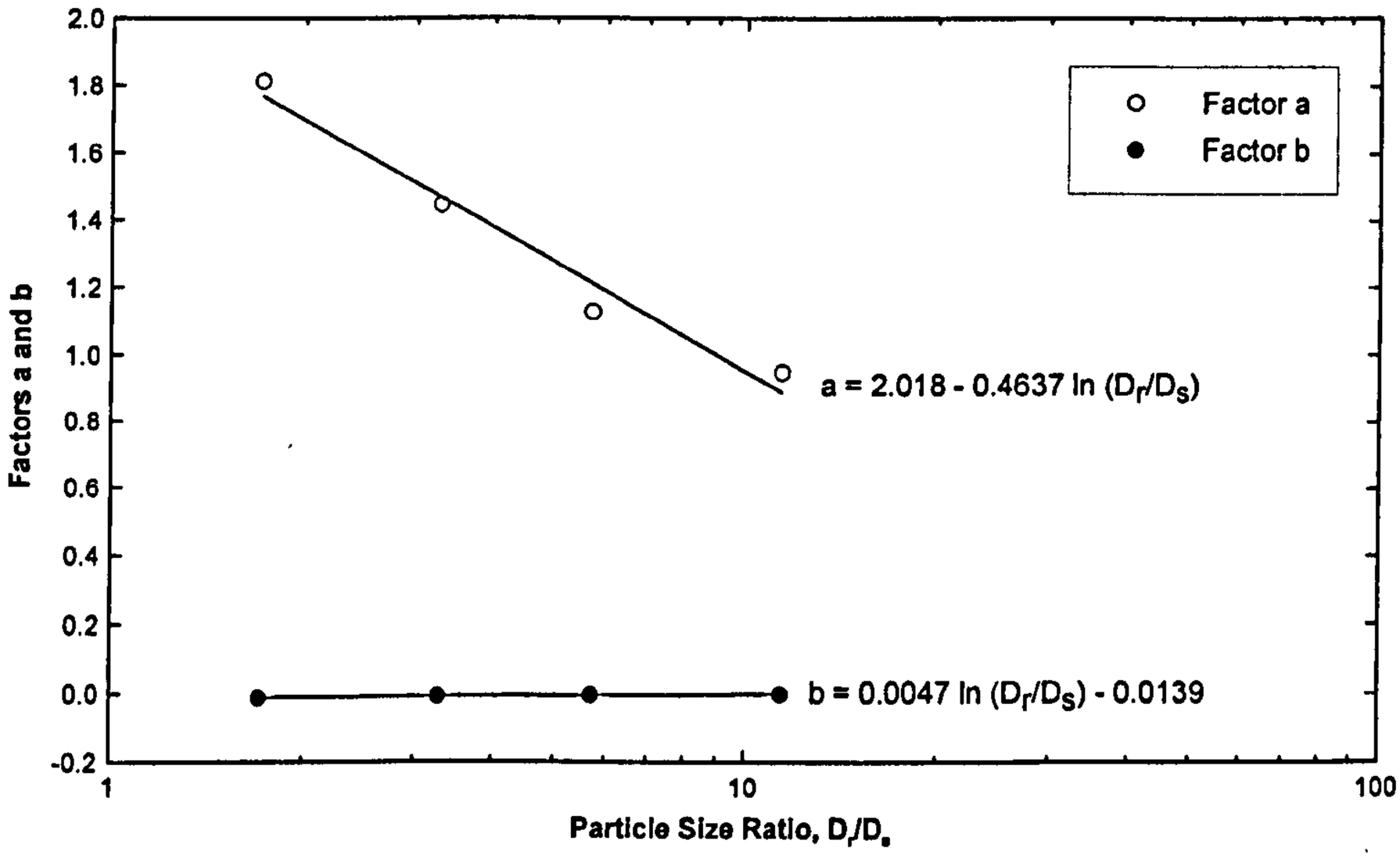

Figure 6. 39 Factors *a* and *b* for normalised e_s curve

6.2.3 Pore Water Pressure Behaviour

The pore water pressure behaviour generated by seismic loading is of considerable interest in soil liquefaction and geotechnical earthquake engineering studies. Observing the rate of increase of pore water pressure against the number of load cycles or time could predict the occurrence of soil liquefaction as well as its consequences. Generally, the pore water pressure behaviour in undrained cyclic triaxial tests is examined by plotting the peak pore water pressure ratio $\Delta u_p/\sigma'_{3c}$ against the number of load cycles *N*.

Basically, the ratio begins at approximately zero (excess pore water pressure = 0), and then gradually increases as long as the cyclic loading continues, until reaching the initial effective stress. The rate of increase depends mainly on soil fabric, density, initial stress state, degree of saturation, and nature of cyclic loading. Note that Δu_p denotes the peak pore water pressure obtained from Figure 6.40 by taking the maximum positive pore water pressure from each cycle of loading.

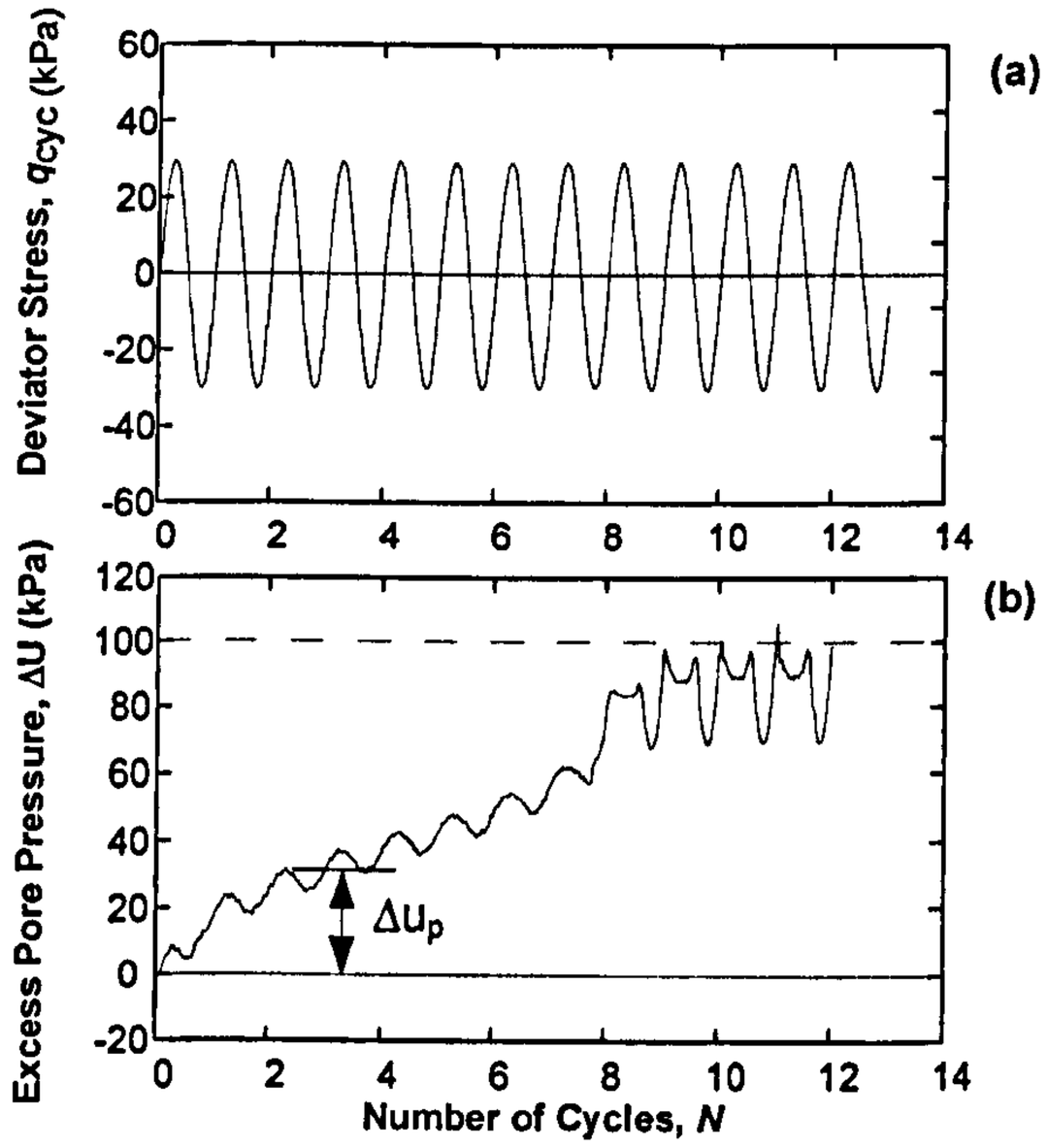

Figure 6. 40 Definition of peak pore water pressure, Δu_p

The behaviour of peak pore water pressure ratio for pure sand S, subjected to applied cyclic deviator stresses ranging from 25 to 43kPa is plotted and shown in Figure 6.41. For sand mixed with CT0515 tyre chips, SA, having sand to rubber ratios of 95:5, 90:10, 80:20, 70:30, 60:40, and 50:50, the pore water pressure behaviour is illustrated by Figure 6.42. Figures 6.43, 6.44, and 6.45 illustrate the pore water pressure behaviour for the mixtures SB, SC, and SD, respectively.

For pure sand (Figure 6.41) tested with the smallest q_{cyc} of 25kPa, the pore water pressure increased slowly and steadily until it reached a ratio of about 0.67 after 203 cycles; then, when subjected to two more cycles of loading, it abruptly liquefied. When q_{cyc} was raised to 29kPa, the rate of increase of pore water pressure was noticeably higher, compared to q_{cyc} of 25kPa. This time, however, the liquefaction occurred when the ratio reached only 0.57 after 95 cycles.

For the specimen tested with q_{cyc} of 32kPa, the behaviour was quite similar to those tested with q_{cyc} of 29kPa, except that the specimen liquefied abruptly when the ratio reached 0.50 after just 28 cycles of loading. Comparing all those three specimens (tested with 25, 29, and 32kPa) it was found that the rate of increase of pore water pressure gradually increased with an increase of applied q_{cyc}, as evident in the steeper of the plotted curves corresponding to the increase of q_{cyc}. For q_{cyc} of 37 and 43kPa the

specimens liquefied after only few cycles of loading; in other words, no gradual increase of pore water pressure was observed.

For the mixtures SA, the pore water pressure behaviour can be divided into two groups: group (1) mixtures 95:5, 90:10, and 80:20, and group (2) mixtures 70:30, 60:40, and 50:50, based on the shape of the pore water pressure ratio along the course of cyclic loading. For group (1) the specimens tested at low to moderate cyclic deviator stresses, the ratio first increased to approximately 0.2 - 0.3 at about 10 cycles. Then, it increased steadily and gradually until the specimen liquefied. However, when the specimens were tested with higher cyclic deviator stress the ratio increased very rapidly and liquefied only after 3-8 cycles, as illustrated by Figure 6.42((a), (b), and (c)). These results are in contrast to the behaviour of group (2). The pore pressure ratio of group (2) first increased to approximately 0.4 - 0.5, then it built up slowly and gradually until the specimens liquefied (Figure 6.42((d), (e), and (f))).

Another point that should be noted for group (2) is that during the early cycles of loading, the ratio was observed to increase very rapidly, but the rate of increase slowed down at larger numbers of cycles. This distinctive behaviour, compared to group (1), is apparent when considering Figure 6.42(f), which illustrates the build up of pore water pressure for the mixture 50:50 (Promputthangkoon and Hyde, 2008b). When considering the pore water pressure behaviour of SA as a whole, regardless of the level of q_{cyc} applied, it was found that the more rubber added the higher the pore water pressure ratio at early cycles of loading observed, especially when comparing between the mixtures 95:5 (Figure 6.42(a)) and 50:50 (Figure 6.42(f)).

The SB mixtures having sand to rubber ratios of 95:5 and 90:10 (Figure 6.43((a) and (b))) both exhibited similar pore water pressure behaviour when tested at low to moderate cyclic deviator stresses. At the beginning the ratios increased rapidly to roughly 0.2 - 0.3, followed by a steady increase until reaching around 0.62. The liquefaction failure then occurred after 4 - 5 cycles for the mixture 95:5 and after 8 - 10 cycles for the mixture 90:10. It was also observed that the rate of increase was much higher than that of pure sand suggesting that these mixtures could accelerate the liquefaction. However, when both 95:5 and 90:10 mixtures were tested at the highest cyclic deviator stresses, they liquefied after only a few cycles, as pure sand and SA did.

When the rubber content was increased to 20%, the specimen with the lowest q_{cyc} exhibited behaviour similar to that of the 95:5 and 90:10 mixtures tested with similar $q_{cyc,}$ except that when the ratio reached 0.68 it did not liquefy abruptly. Instead, the ratio increased gradually for other 46 cycles, and subsequently liquefied (Figure 6.43(c)). For the specimen tested with q_{cyc} of 19.5kPa, the behaviour was quite similar to that of SB having sand to rubber ratios of 95:5 and 90:10 tested at the lowest q_{cyc}. At higher q_{cyc}, however, the pore water pressure increased very rapidly till liquefaction occurred.

For SB containing 30% rubber with the lowest q_{cyc} of 20kPa (Figure 6.43(d)) the pore water pressure behaviour was similar to that of SB with 20% rubber tested with q_{cyc} of 17kPa, while the others exhibited a rapid increase of pore water pressure. When the rubber was increased up to 40% (Figure 6.43(e)) and 50% (Figure 6.43(f)), the behaviour was similar to that of SA having 50% rubber. Moreover, the sudden increase of pore water pressure at the beginning of cyclic loading for SB exhibited a similar pattern to SA.

For SC containing 5 and 10% rubber, the pore water pressure response is illustrated by Figures 6.44(a) and (b), respectively. Both mixtures tested with low to moderate q_{cyc} exhibited a rapid increase of pore water pressure ratio at early cycles, to approximately 0.2. Then, it increased steadily until reaching about 0.6. The period of the steady increase of pore water pressure was carried on for around 200 and 150 cycles for the specimens having rubber contents of 5 and 10%, respectively. Both mixtures then liquefied abruptly after a further 15 cycles of loading.

For the mixtures with 20% rubber (Figure 6.44(c)) and 30% rubber (Figure 6.44(d)), the behaviour was somewhat similar to that of SA with sand to rubber ratios of 95:5 and 90:10, respectively. For the specimens having higher percentage of rubber, 40 and 50% (Figure 6.44(e) and (f)), the behaviour was observed to be the same as of SB having 30% rubber and SB having 50% rubber, respectively.

For SD having rubber content of 5% and 10% (Figure 6.45(a) and (b)), the pore water pressure behaviour was similar to that of SC having the same rubber content. For SD with 20% rubber, however, the behaviour was quite similar to that of SC with 5% rubber. For SD having 30% rubber (Figure 6.45(c)), it was observed that the pore water

pressure was equivalent to that of SC having the same rubber content. When the rubber was increased higher to 40 and 50% (Figure 6.45(e) and (f)), the pore water pressure behaviour appeared to be comparable to that of SC having 50% rubber.

The pore water pressure behaviour of saturated sand is well understood. Sand particles are relatively incompressible and non-crushable under normal pressures encountered in civil engineering projects (< 700kPa); thus, when they are subjected to cyclic loading under undrained conditions, the stress is transmitted from particle to particle directly as well as to the surrounding pore water. This process will progressively generate the excess pore water pressure; eventually, it may be equal to the initial effective stress. The consequence is that the shear strength is reduced, in the worst case, to zero.

When a small amount of tyre chips was added, the behaviour of the sand mixed with tyre chips was still dominated by the sand because its particles still contacted to each other, and the rubber acted as fill in the sand-rubber matrix. This resembles the cyclic characteristics of compound sand with gravel studied by Evans and Zhou, 1995. They suggested that when the amount of gravel in sand-gravel mixture was small, the gravel may be considered to float in the sand-gravel matrix. However, when more tyre chips were added, the sand particles now no longer form a continuous matrix but are contained in the voids between the rubber instead. As the rubber is highly elastic, during cyclic loading the sand particles in the mixtures may be embedded into the surrounding rubber. As a result, instead of transmitting the stress directly to other sand particles as well as the surrounding pore water, some stress may be absorbed by the deformed rubber owing to its highly elastic properties, thereby delaying the increase of pore water pressure. As strong ground motion occurs over a very short period, if the rubber in sand-rubber mixtures could delay the increase of pore water pressure until the earthquake stops, liquefaction could also be prevented.

This phenomenon may also be explained by considering an aspect of mixing two materials having different particle size. For example the consolidated void ratio for pure sand was 0.669 (see Table 6.1). For SA, SB, SC, and SD having 50% rubber at which the cyclic strengths were the greatest, the consolidated void ratios were 0.623 (Table 6.2), 0.539 (Table 6.3), 0.468 (Table 6.4), and 0.409 (Table 6.5), respectively. It can be seen that the void ratios for SA, SB, SC, and SD are much lower than that for pure sand,

especially for SC and SD. This is because SC and SD were mixed with much larger size rubber particles, compared to the size of sand; that is, mean particle size D_{50} for sand = 0.7mm, while D_{50} for SC and SD = 4 and 8mm, respectively. This suggests that the sand, in the sand-rubber matrix with 50:50 mixes, acted as a fill in the inter-particle voids of rubber. As a result, the liquefaction characteristics were predominantly governed by the rubber.

The effects of the rubber on the pore water pressure behaviour of sand-tyre chips mixtures were also reported by Hyodo *et al.*, 2008. They concluded that the tyre chips could control the build up of excess pore water pressure, particularly when the sand fraction was low.

As soil liquefaction may also be triggered by other means of loading such as pile driving, constant ocean waves, and even static loads due to sloping ground. Based on the test results, we shall know that a soil will liquefy when the excess pore water pressure is increased to a certain level. In practice, we therefore can prevent the soil to liquefy by installing an instrument to monitor the pore water pressure during construction activities. As long as the pore water pressure is still quite below the level that might trigger the onset of the liquefaction, we may continue the activity. Otherwise, other measures are needed.

When closely considering the pore water pressure behaviour shown in Figures 6.41 - 6.45, it was found that the behaviour for the same mixture, even though subjected to different cyclic deviator stress, had a similar trend. Therefore, it was interesting to normalise the pore water pressure behaviour for further analysis. This was done, for each mixture, by normalising the number of load cycles (N) by the number of cycles at which the double amplitude axial strain was reached 5% (N_f).

The normalised pore water pressure curve for pure sand S is illustrated by Figure 6.46. For SA, SB, SC, and SD, the normalised curves are illustrated by Figure 6.47, Figure 6.48, Figure 6.49, and Figure 6.50, respectively. Accordingly, the formula for predicting the pore water pressure generated by the cyclic triaxial test was obtained as:

$$\frac{\Delta u_p}{\sigma'_{3c}} = c\left(\frac{N}{N_f}\right)^d \qquad \textbf{(Eq. 6. 15)}$$

The equation is in a power form comprising two factors, *c* and *d*, which control the position and slope of the pore water pressure curve. The factors *c* and *d* for S, SA, SB, SC, and SD are summarised and shown in Table 6.9.

For pure sand, it was observed that there was little scatter except for higher cyclic deviator stresses of 37 and 43kPa where some scatter was observed at very early cycles. However, when the normalised number of cycles was approaching 1.0; there was little scatter observed.

For SA having sand to rubber ratios of 95:5, 90:10, 80:20, and 70:30, the points lie close to the normalised curves. However, similar scattering of data found for pure sand when tested with higher cyclic deviator stresses was also observed. When the mixtures contained higher rubber contents of 40 and 50%, the scattering of data was notable. In this case, the normalisation was done by averaging the data, as can be seen in Figure 6.47(e) and (f). For SB (see Figure 6.48), it was found that the normalised pore water pressure had similar behaviour to that of SA.

For SC, however, the aggregation of points was observed only for the 80:20 and 70:30 mixtures. For the rest, the scattering was clearly observed, especially for the mixtures 95:5 (Figure 6.49(a)) and 50:50 (Figure 6.49(f)).

For SD, the curves for 70:30, 60:40, and 50:50 mixtures (Figures 6.50(d), (e), and (f)) exhibited low scatter, in contrast to SA, SB, and SC. For the mixtures 95:5, 90:10, and 80:20, however, the scattering was observed, especially for 95:5 mixtures.

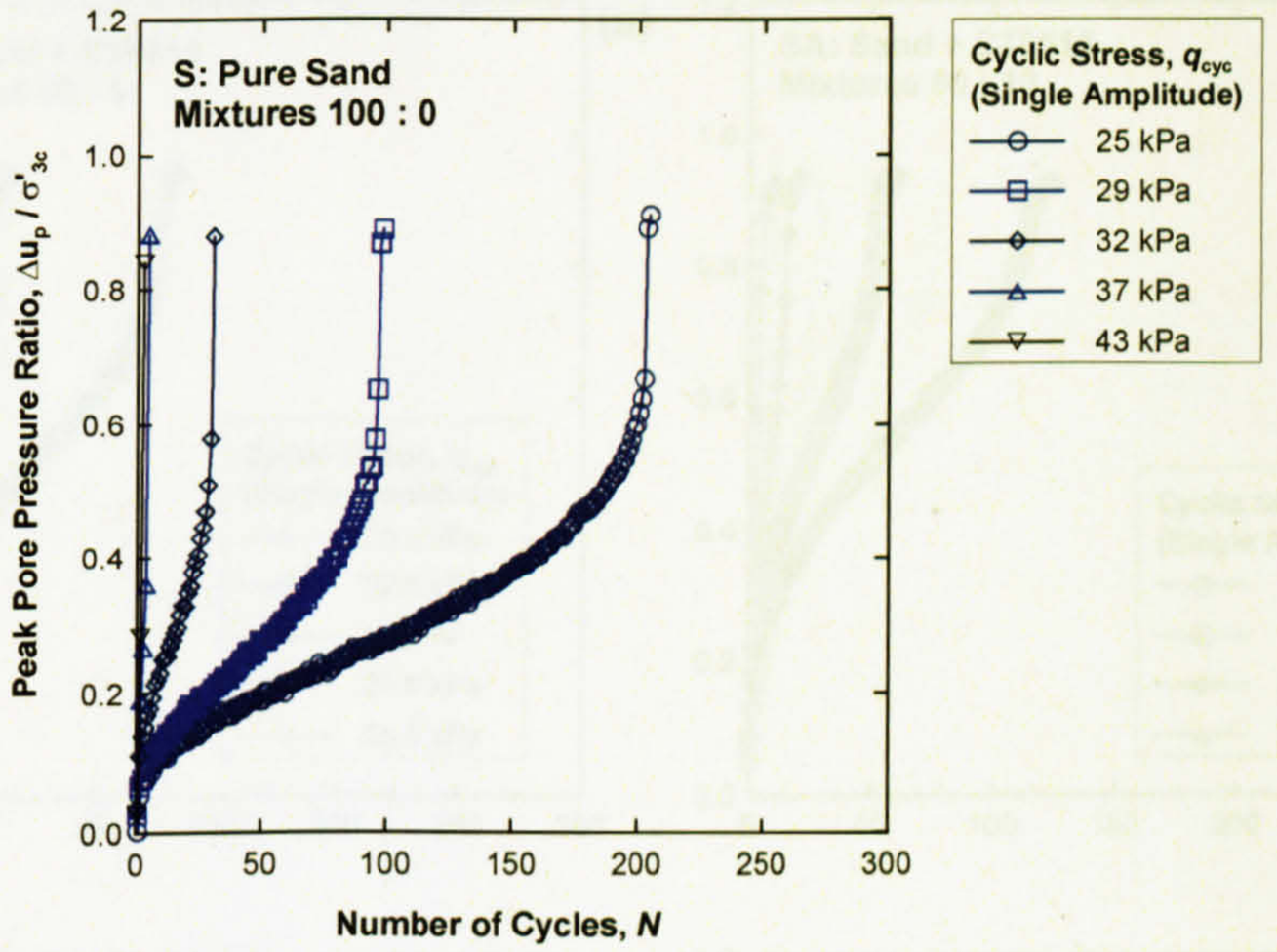

Figure 6. 41 Pore water pressure behaviour for S, Pure Sand

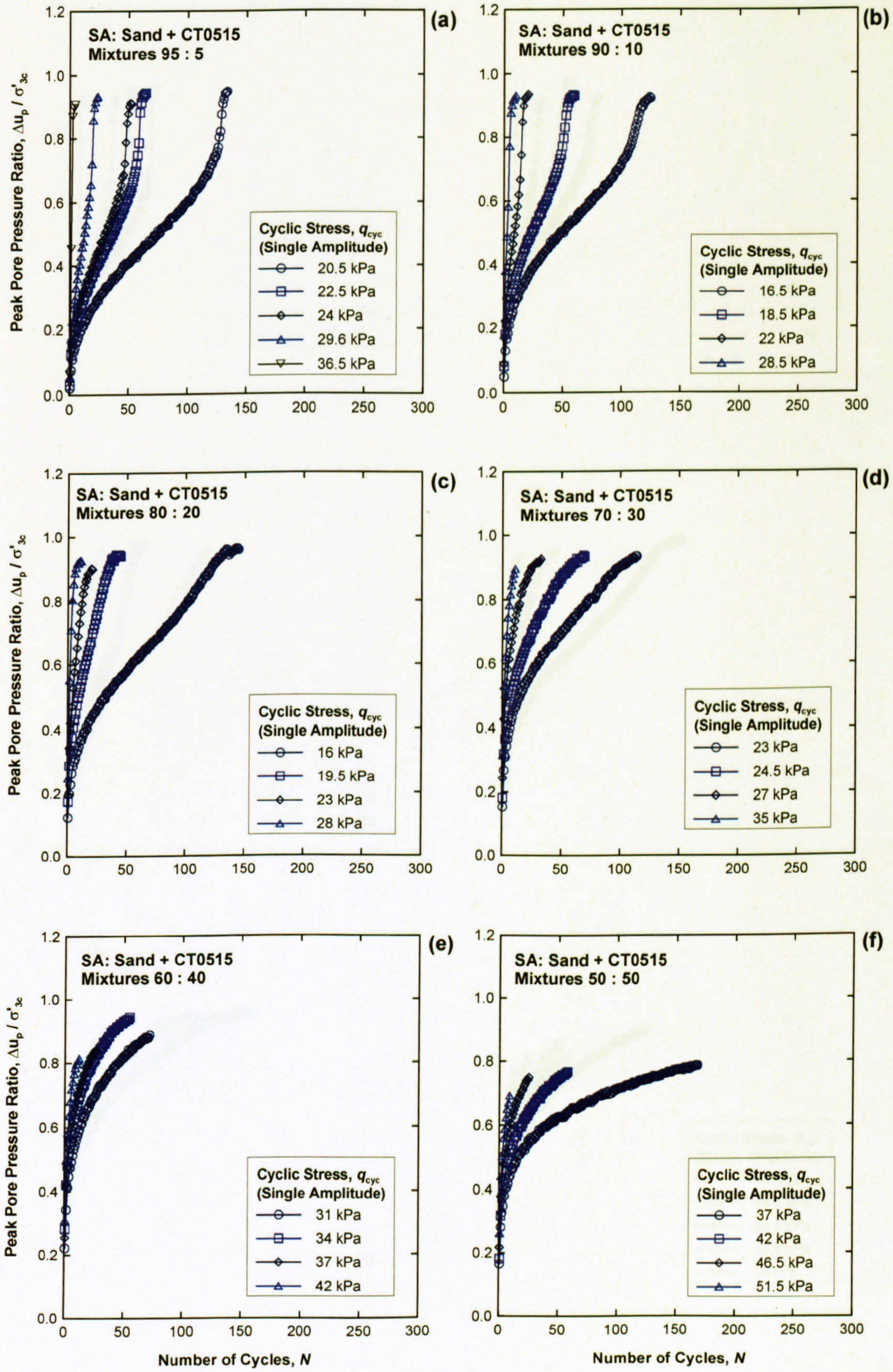

Figure 6. 42 Pore water pressure behaviour for SA, Sand + CT0515

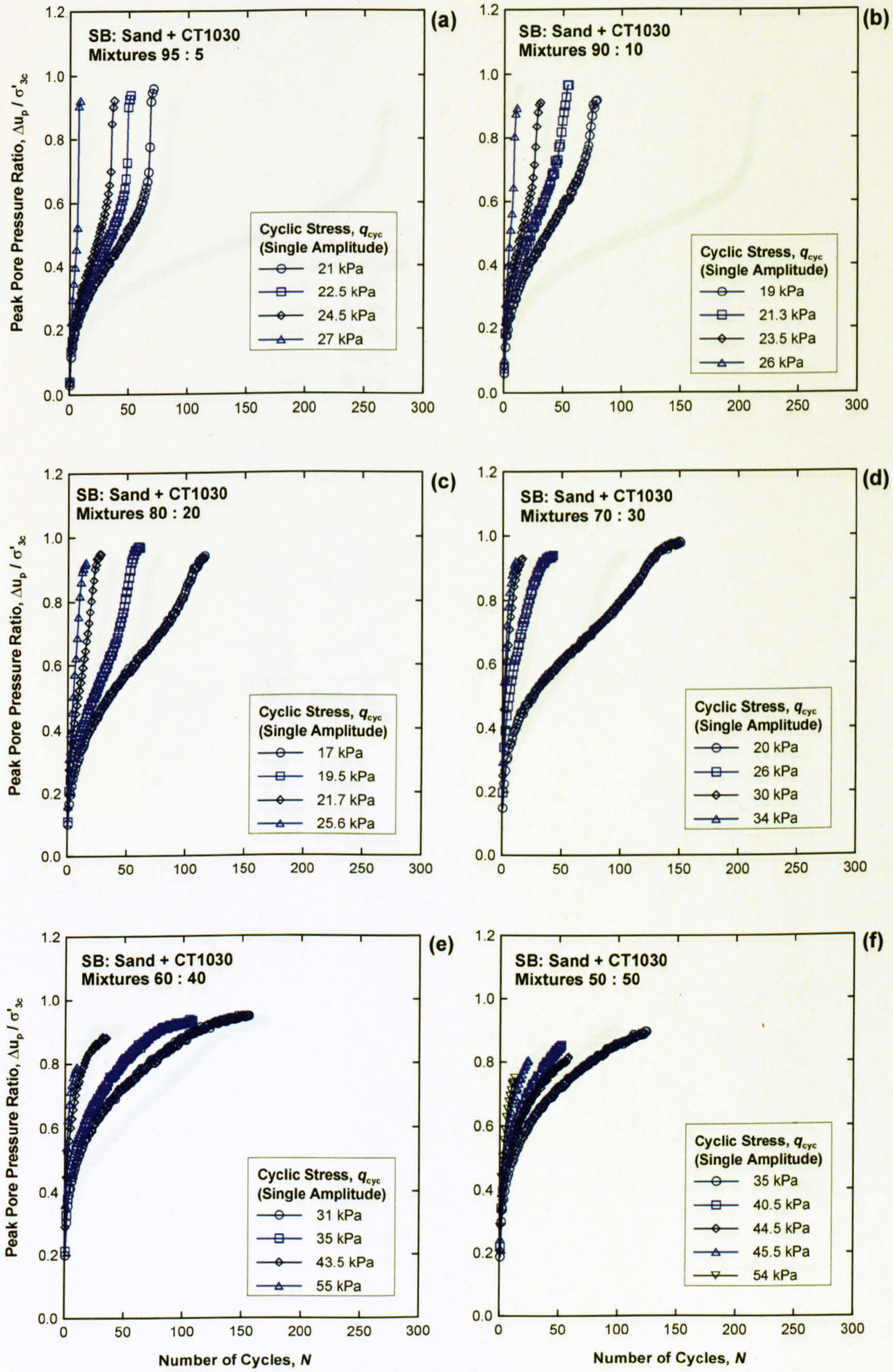

Figure 6. 43 Pore water pressure behaviour for SB, Sand + CT1030

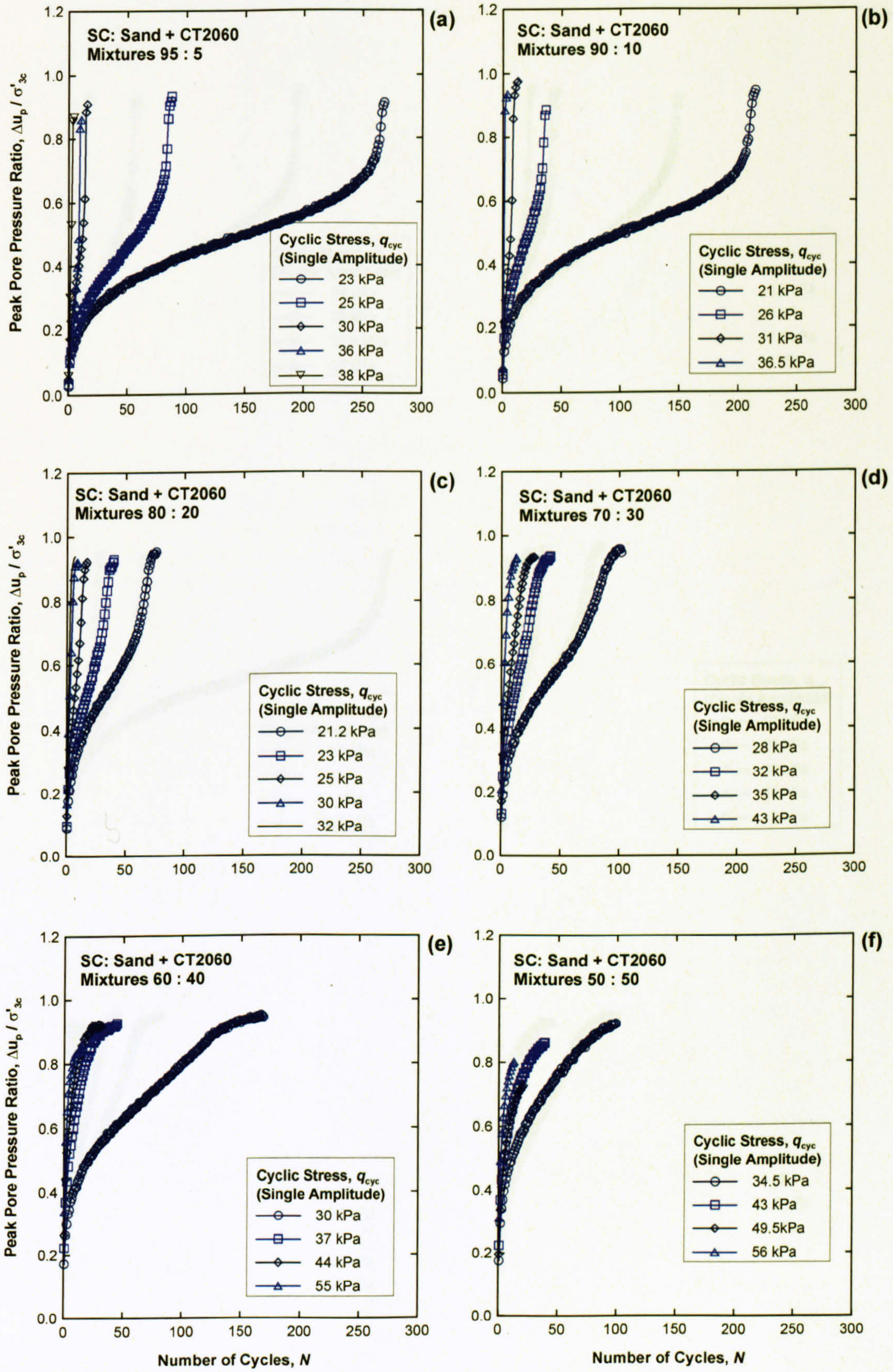

Figure 6. 44 Pore water pressure behaviour for SC, Sand + CT2060

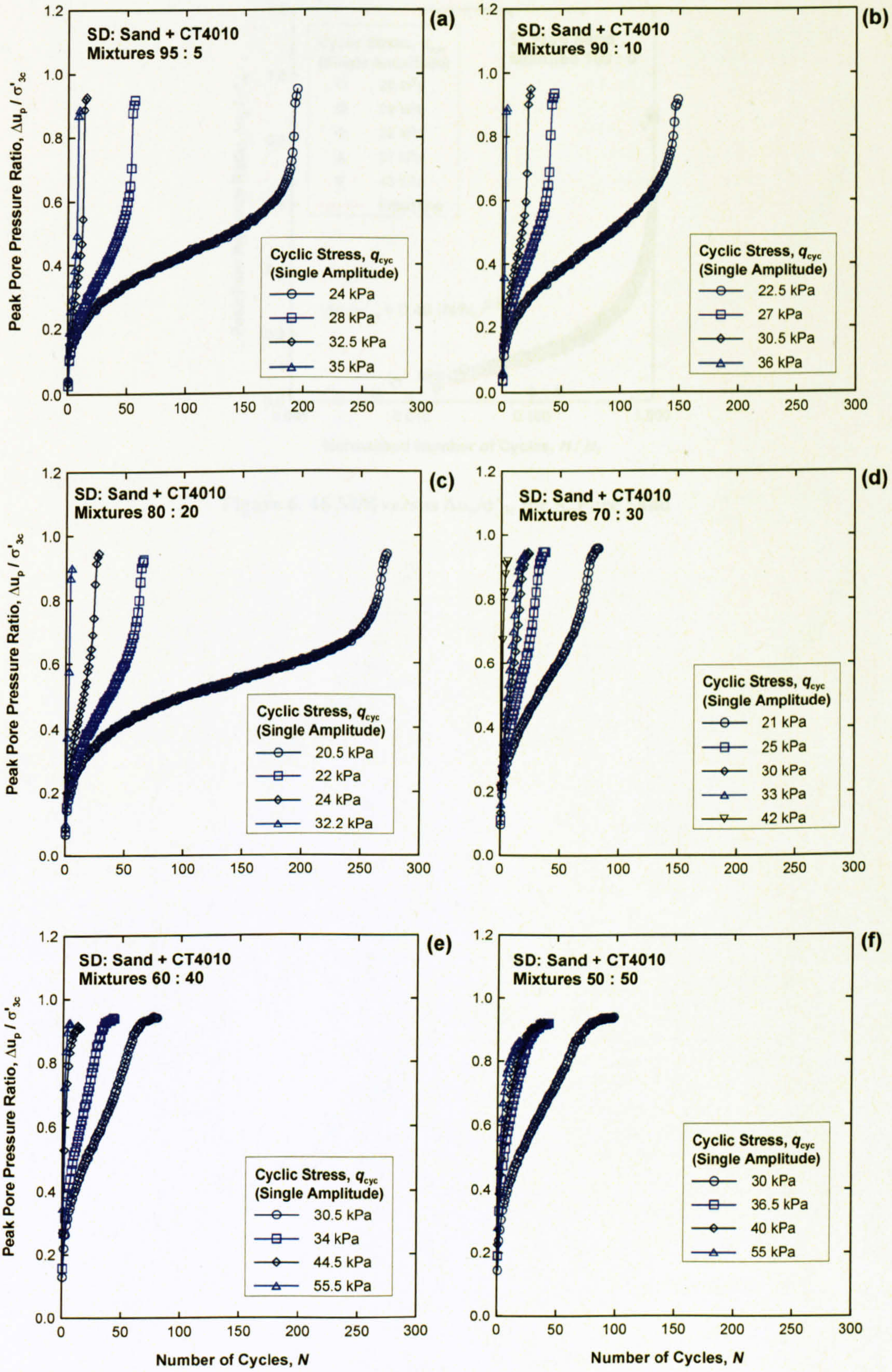

Figure 6. 45 Pore water pressure behaviour for SD, Sand + CT4010

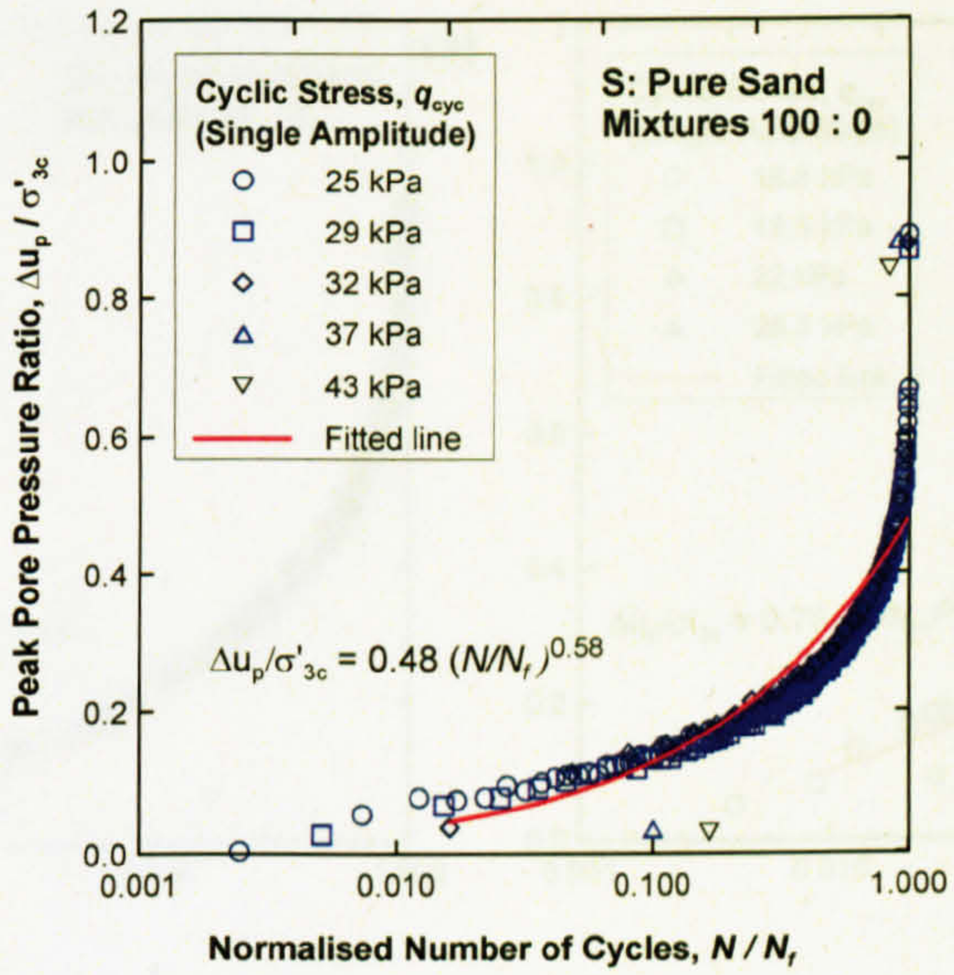

Figure 6. 46 N/N_f versus $\Delta u_p/\sigma'_{3c}$ for S, Pure Sand

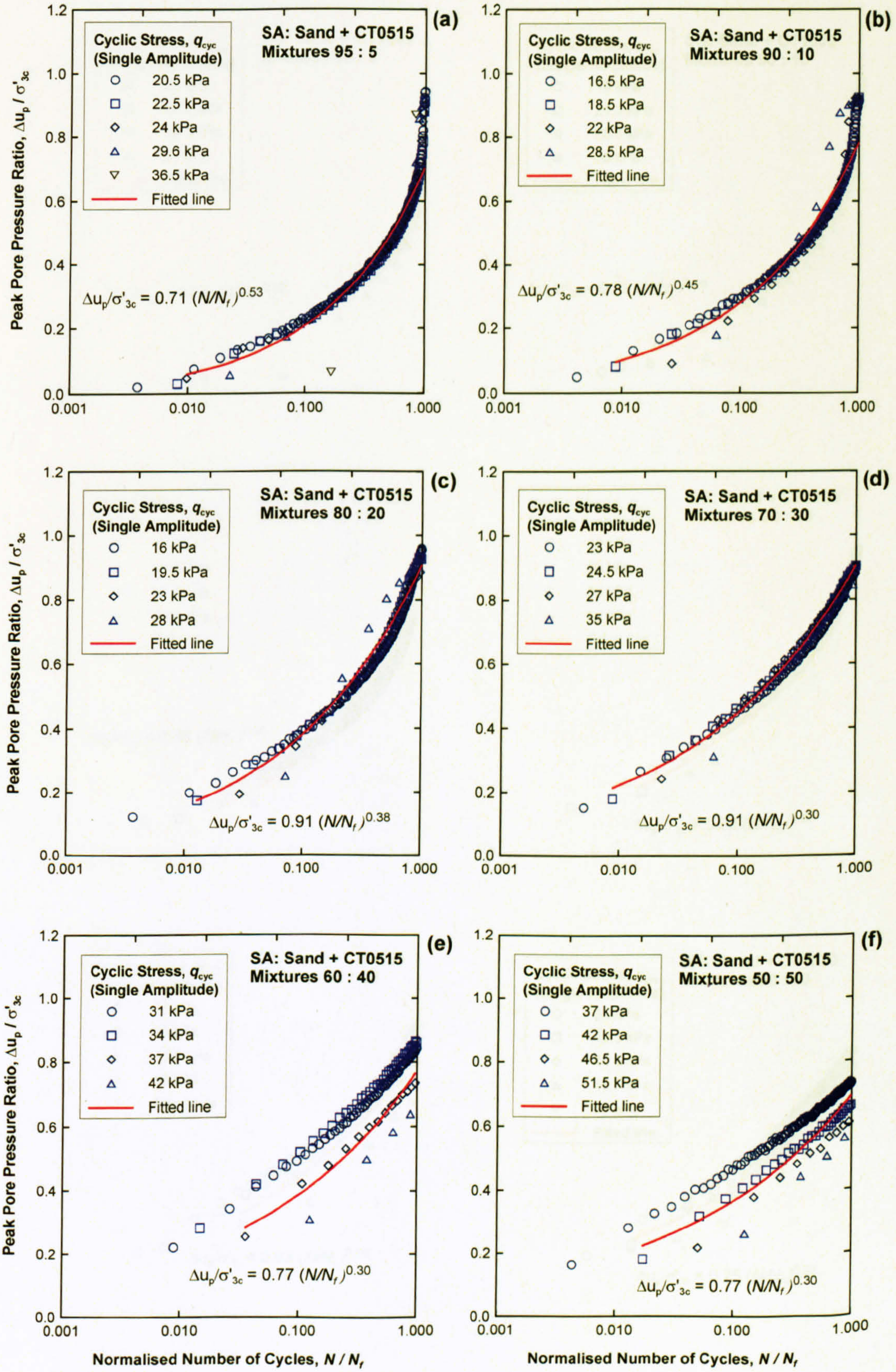

Figure 6. 47 N/N_f versus $\Delta u_p/\sigma'_{3c}$ for SA, Sand + CT0515

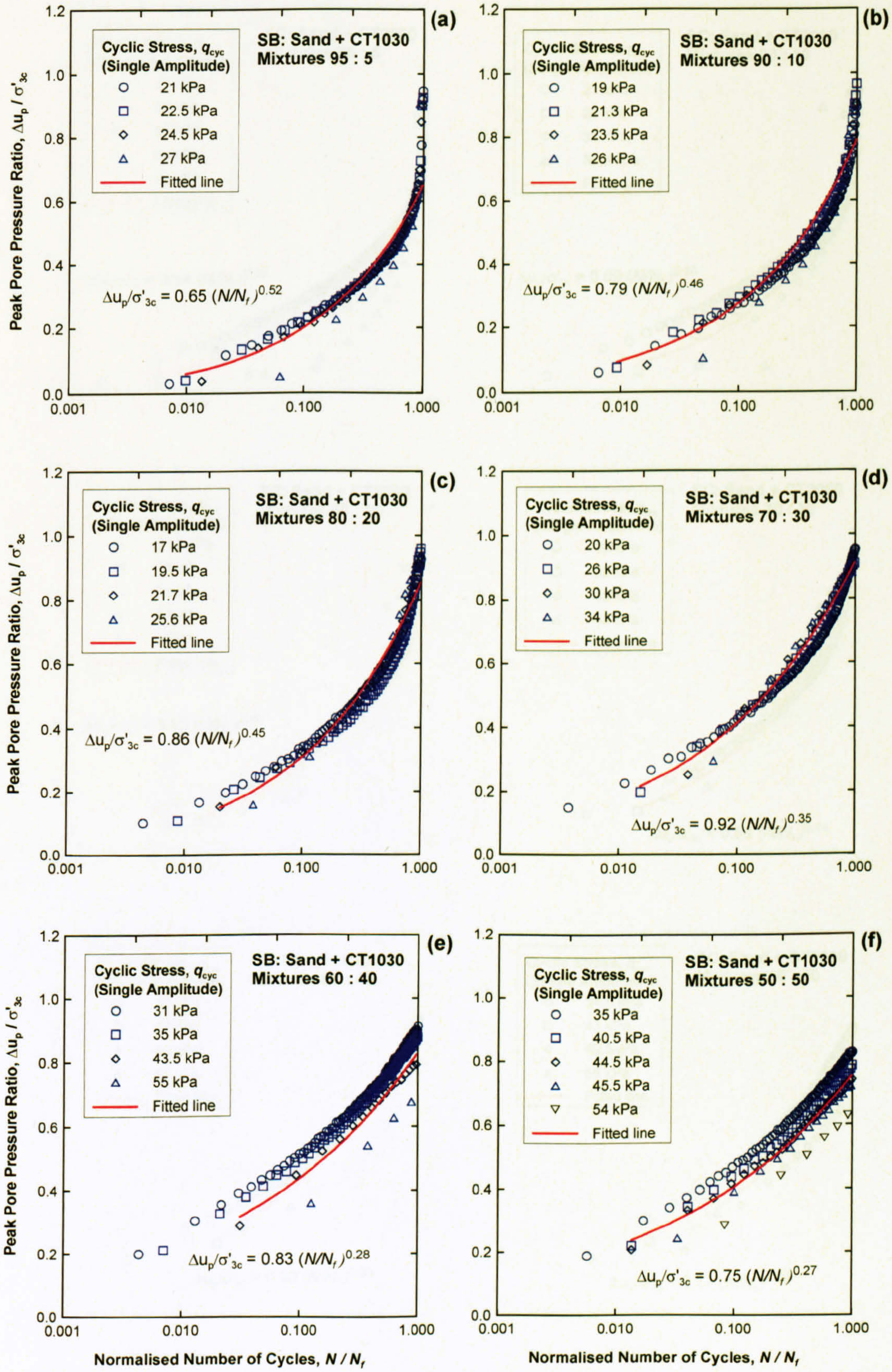

Figure 6. 48 N/N_f versus $\Delta u_p/\sigma'_{3c}$ for SB, Sand + CT1030

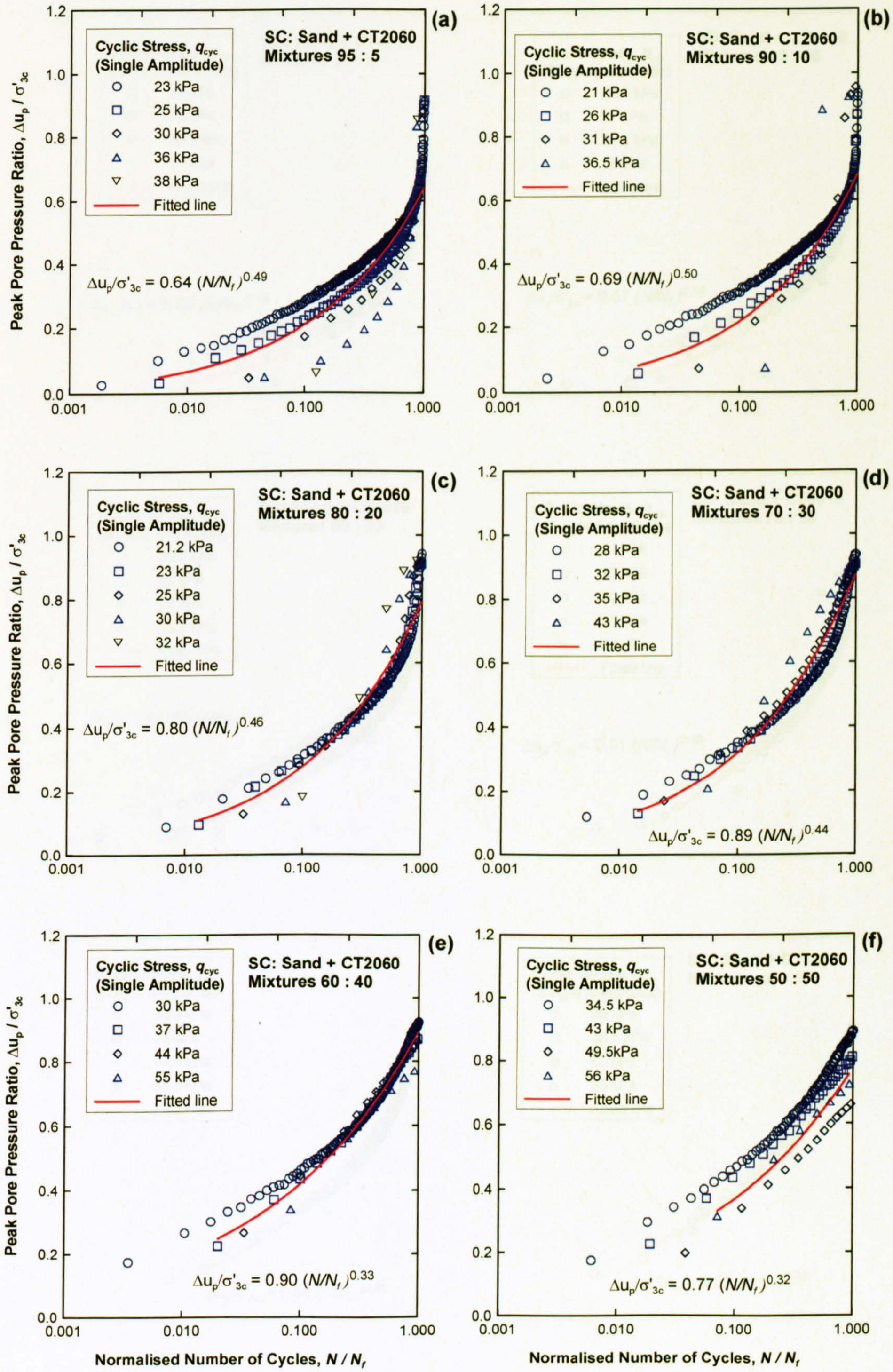

Figure 6. 49 N/N_f versus $\Delta u_p/\sigma'_{3c}$ for SC, Sand + CT2060

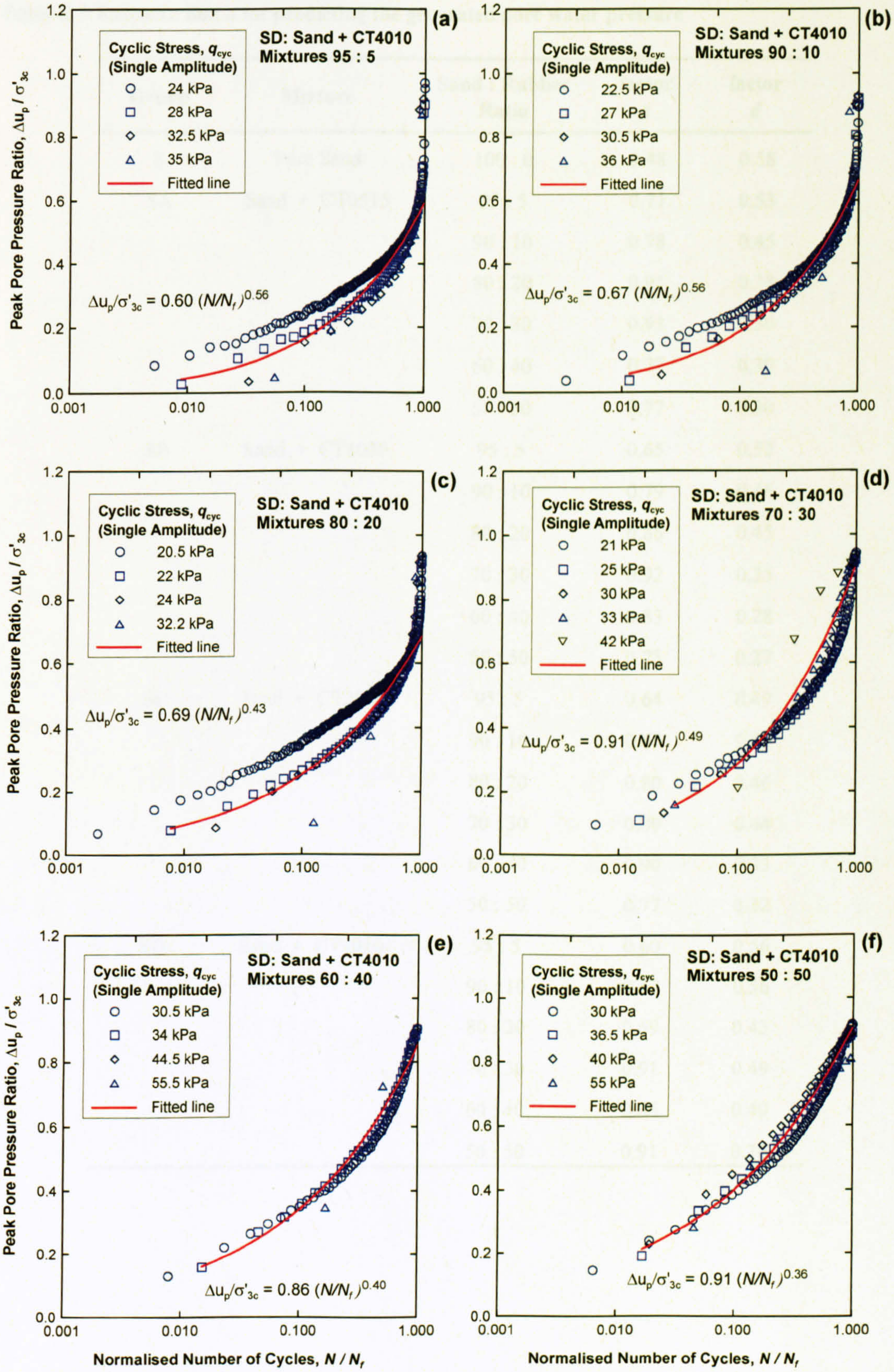

Figure 6. 50 N/N_f versus $\Delta u_p/\sigma'_{3c}$ for SD, Sand + CT4010

Table 6. 9 Factors *c* and *d* for predicting the generated pore water pressure

Group	Mixture	Sand : Rubber Ratio	factor *c*	factor *d*
S	Pure Sand	100 : 0	0.48	0.58
SA	Sand + CT0515	95 : 5	0.71	0.53
		90 : 10	0.78	0.45
		80 : 20	0.91	0.38
		70 : 30	0.91	0.30
		60 : 40	0.77	0.30
		50 : 50	0.77	0.30
SB	Sand + CT1030	95 : 5	0.65	0.52
		90 : 10	0.79	0.46
		80 : 20	0.86	0.45
		70 : 30	0.92	0.35
		60 : 40	0.83	0.28
		50 : 50	0.75	0.27
SC	Sand + CT2060	95 : 5	0.64	0.49
		90 : 10	0.69	0.50
		80 : 20	0.80	0.46
		70 : 30	0.89	0.44
		60 : 40	0.90	0.33
		50 : 50	0.77	0.32
SD	Sand + CT4010	95 : 5	0.60	0.56
		90 : 10	0.67	0.56
		80 : 20	0.69	0.43
		70 : 30	0.91	0.49
		60 : 40	0.86	0.40
		50 : 50	0.91	0.36

6.2.4 Strain Behaviour

The previous section which described the pore water pressure behaviour generated by cyclic loading is important in terms of the occurrence of liquefaction. Soils deposited both naturally and artificially, however, are not necessarily fully saturated all of the time. This implies that the soil will not liquefy as the pore water pressure will never reach the initial effective stress due to the lesser degree of saturation. From geotechnical design and construction points of view, apart from the shear strength, the settlement and deformation are the most important factors. Even though the soil, by definition is not liquefied; but, if the settlement and deformation caused by soil softening is greater than the allowance, damage is therefore foreseeable. As a result, a limiting strain level is customarily used for the liquefaction failure conditions.

To investigate the strain behaviour of a soil subjected to uniform cyclic loading, the axial strain is plotted showing both compression and extension. Bearing in mind that if the soil is anisotropically consolidated and the static shear stress is greater than the desired cyclic deviator stress, the axial strain will occur only in compression. The so called double amplitude axial strain $\varepsilon_{a,DA}$ can be obtained by measuring the strain in both compression and extension from one complete cycle of loading, as described schematically by Figure 6.51. Then $\varepsilon_{a,DA}$ is plotted against the number of cycles for further analysis. As the double amplitude axial strain is used to define the liquefaction failure conditions, it is common practice to observe the strain behaviour as a combination of compression and extension strain.

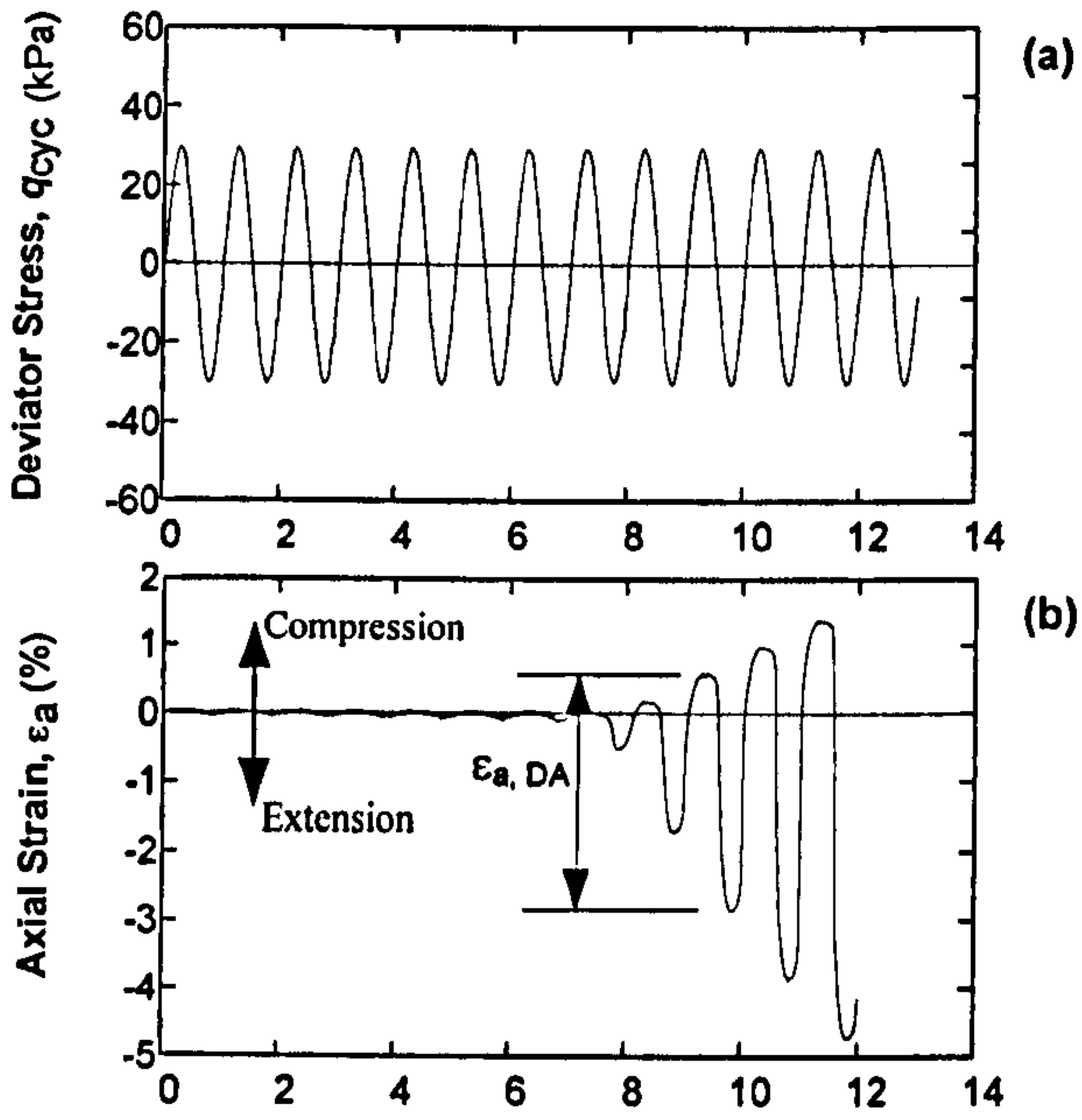

Figure 6. 51 Definition of double amplitude axial strain, $\varepsilon_{a,\,DA}$

The strain behaviour during cyclic loading for pure sand, S, with applied cyclic deviator stresses ranging from 25 to 43kPa was plotted, and is shown in Figure 6.52. For sand mixed with CT0515 tyre chips, SA, having sand to rubber ratios of 95:5, 90:10, 80:20, 70:30, 60:40, and 50:50, the strain behaviour is illustrated by Figure 6.53. Figures 6.54, 6.55, and 6.56 illustrate the strain behaviour for the mixtures SB, SC, and SD, respectively.

The behaviour of double amplitude axial strain generated by cyclic loading for pure sand was distinctive when compared to the strain behaviour of SA, SB, SC, and SD. For pure sand, regardless of the level of q_{cyc} applied, it was observed that all specimens exhibited similar behaviour. The strains initially remained virtually zero until the last few cycles when they increased almost vertically, without any gradual change observed, to a level greater than 8% (Figure 6.52).

During the period of virtually zero strain, it may be that the sand particles were interlocked thereby no axial strain was produced. However, as the test was undrained, the pore water pressure built up progressively. As the cyclic loading continued the effective stress was also gradually decreased because of the increased pore water pressure, thereby lowering the degree of interlocking. Eventually, the interlocking was completely destroyed due to the excess pore water pressure, and the particles flowed, as evident in the sudden increase of axial strain.

For SA having sand to rubber ratios of 95:5 and 90:10 the strain behaviour was quite the same to those of pure sand, but before the abrupt increase of axial strain occurred the very small gradual change from virtually zero strain to larger strain was observed (Figures 6.53(a) and (b)). The mixture 80:20 also exhibited similar behaviour to those of mixtures 95:5 and 90:10, except that the more gradual change of strain from zero to higher was observed (Figure 6.53(c)) for the specimens tested with q_{cyc} of 16 and 19.5kPa. This gradual change of strain indicates that the rubber in the sand-rubber matrix had some influence on the strain behaviour.

When the rubber content was increased to 30% the initial strain of the specimens tested with 23 and 24.5 kPa q_{cyc}, unlike mixtures 95:5, 90:10, and 80:20, did not begin at zero, but started at approximately 0.2%. Also, no period of constant strain was observed; instead, it progressively increased until reaching approximately 1%; subsequently, it increased abruptly to greater than 8% (Figure 6.53(d)). For SA having 40% of rubber, the initial strain generated by cyclic loading started at around 0.8%, followed by the sudden increase until the liquefaction failure occurred (Figure 6.53(e)). For the mixture 50:50 , the strain initiated at around 1.6% and then increased almost linearly until greater than 6%. The linearity of the increase, however, depended on the level of q_{cyc} applied; the greater the q_{cyc} the higher rate of increase observed, as evident in the slope of the strain versus number of cycles curves shown in Figure 6.53(f).

The strain behaviour of SB having sand to rubber ratios of 95:5 (Figure 6.54(a)), 90:10 (Figure 6.54(b)), and 80:20 (Figure 6.54(c)) was comparable to those of SA having the same mixtures. However, it was found that the mixtures 70:30 (Figure 6.54(d)) exhibited strain behaviour similar to those of SA but with 20% rubber. Meanwhile, the SB specimens with 40% (Figure 6.54(e)) and 50% (Figure 6.54(f)) rubber contents had the strain behaviour similar to those of SA with 30 and 40% rubber, respectively.

For SC having rubber contents of 5% (Figure 6.55(a)) and 10% (Figure 6.55(b)) the strain was observed to be equivalent to those of SA with the same mixture. However, for SC with 20% rubber (Figure 6.55(c)) the behaviour seemed to be similar to SB but with 10% rubber. For higher percentages of rubber of 30% (Figure 6.55(d)), 40% (Figure 6.55(e)), and 50% (Figure 6.55(f)), the behaviour was similar to those of SA with 20, 30, and 40% rubber, respectively.

For SD having rubber contents of 5% (Figure 6.56(a)), 10% (Figure 6.56(b)), and 20% (Figure 6.56(c)) it was observed that the strain behaviour was similar to those of SA having 10% of rubber. However, for the mixtures with 30% rubber (Figure 6.56(d)) the strain behaviour was equivalent to those of SA with 20%. When the rubber was increased to 40% (Figure 6.56(e)) and 50% (Figure 6.56(f)) the specimens exhibited similar strain behaviour to SA but with 30% rubber.

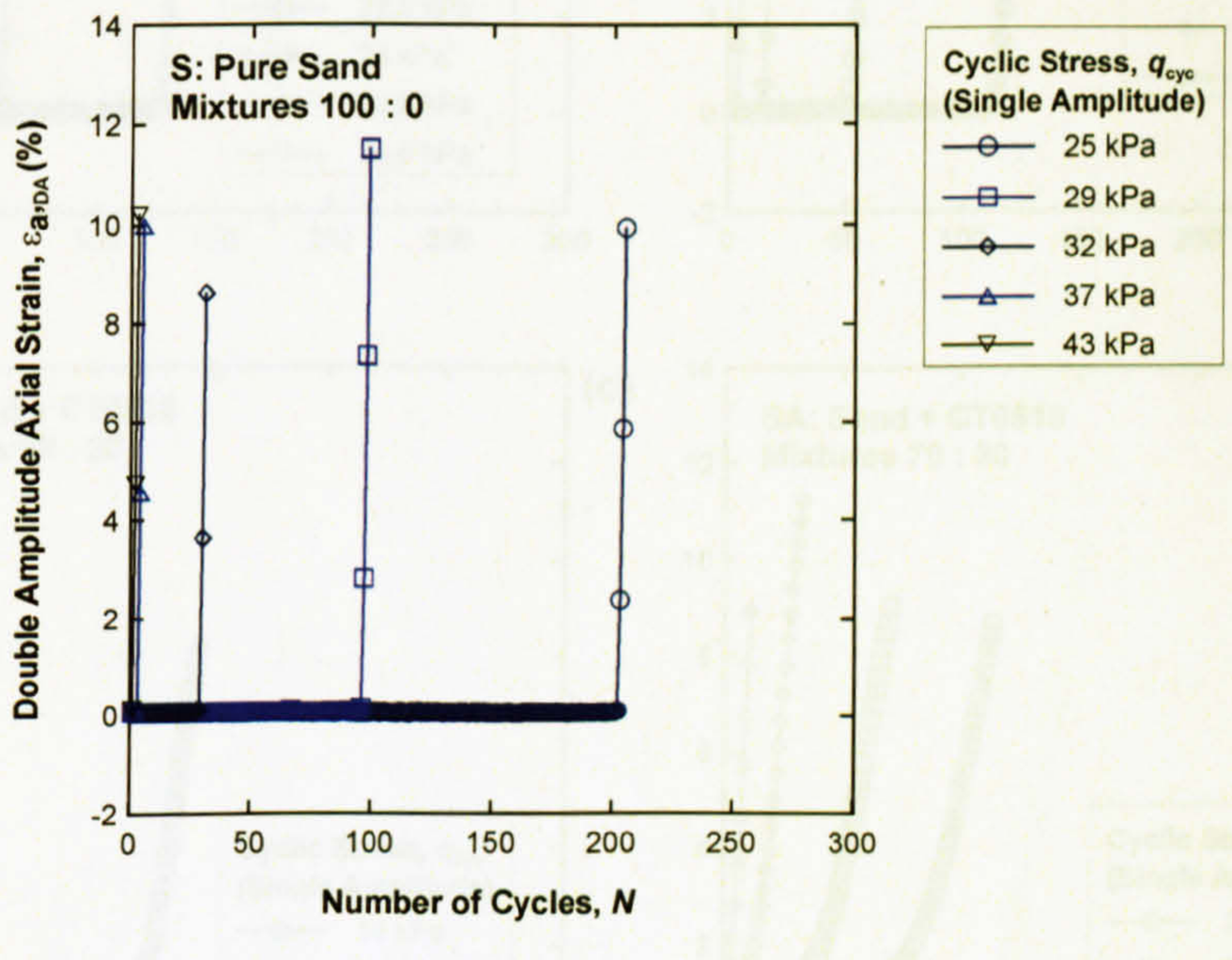

Figure 6. 52 Strain behaviour for S, Pure Sand

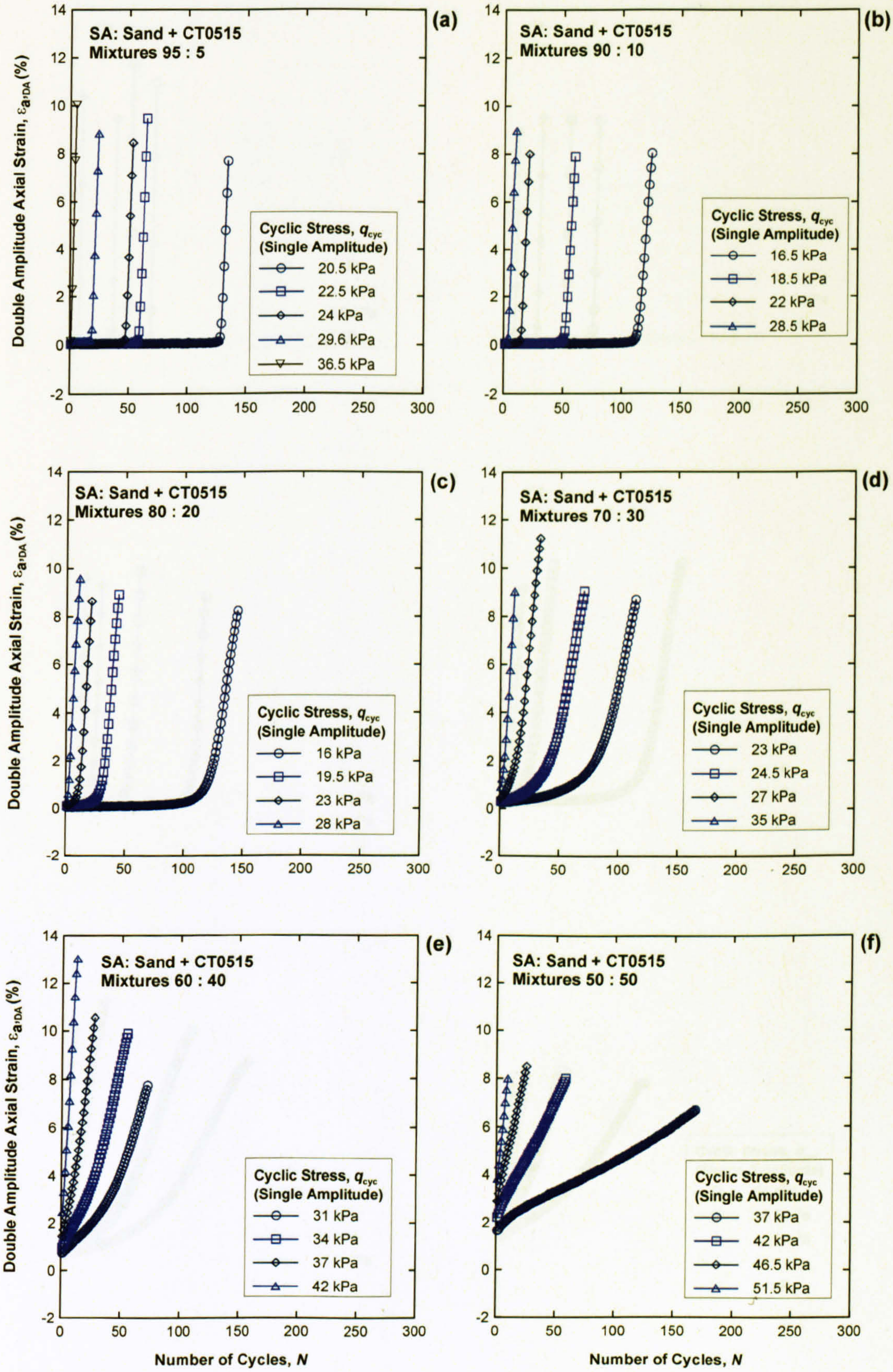

Figure 6. 53 Strain behaviour for SA, Sand + CT0515

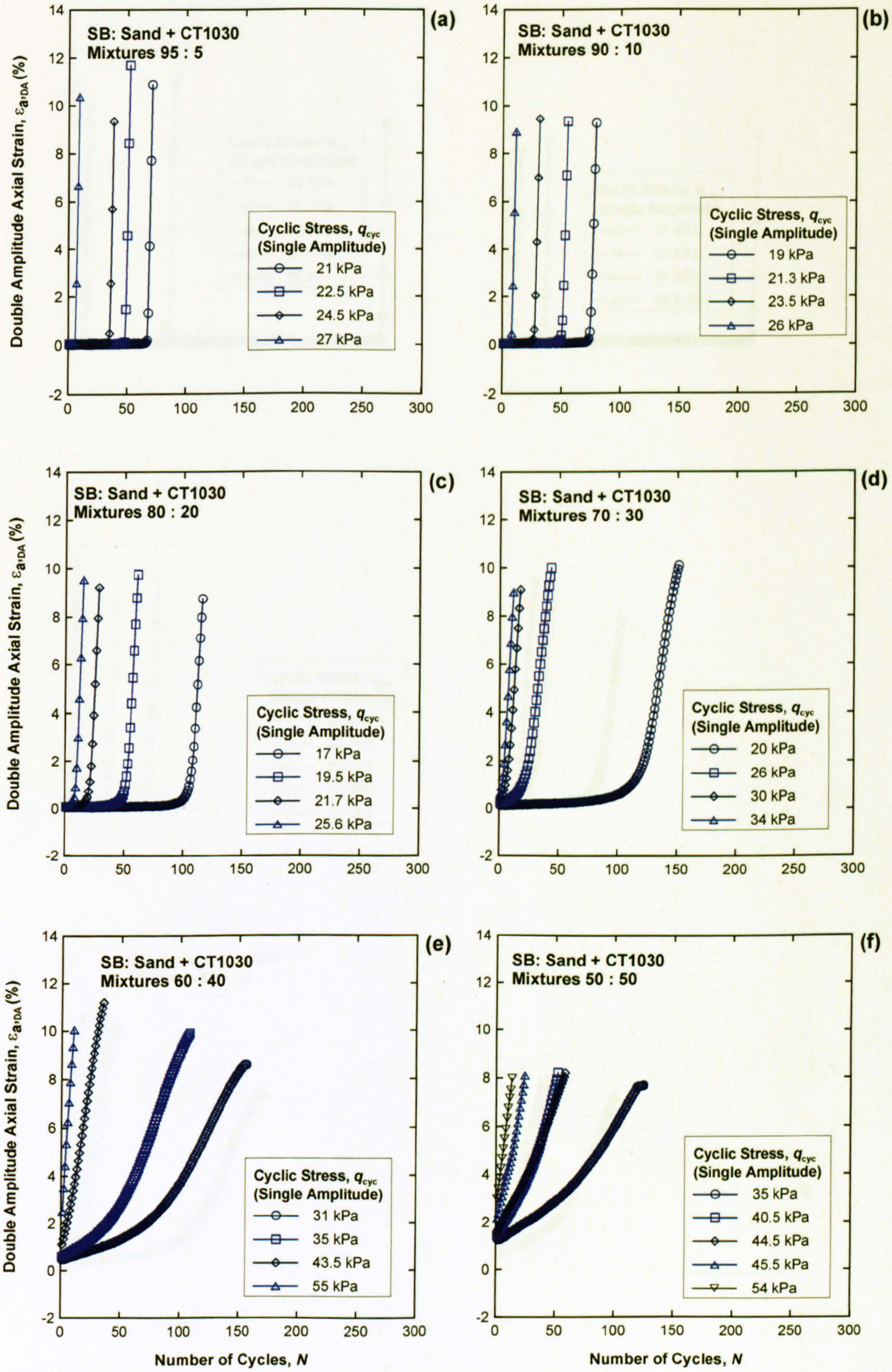

Figure 6. 54 Strain behaviour for SB, Sand + CT1030

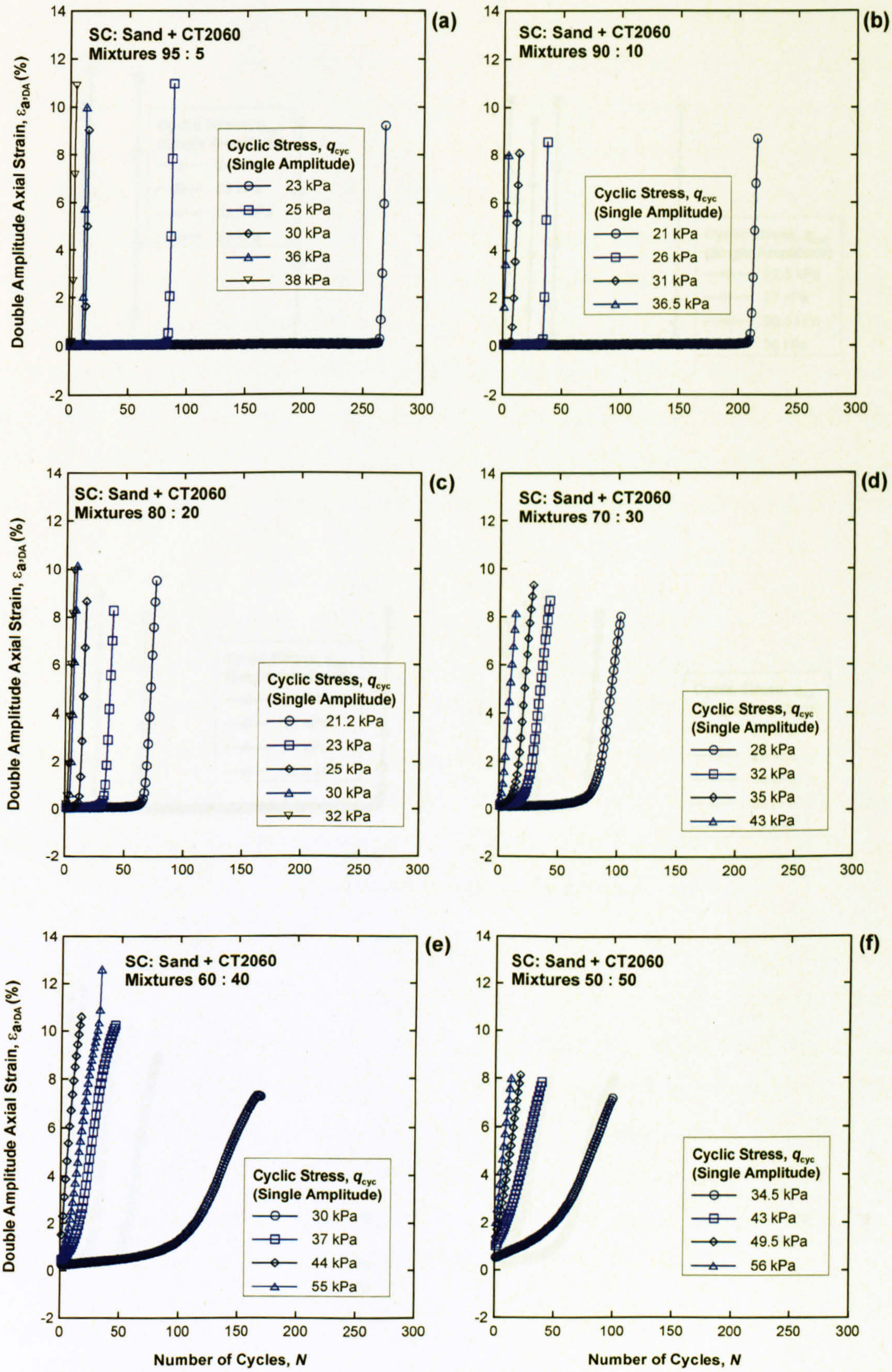

Figure 6. 55 Strain behaviour for SC, Sand + CT2060

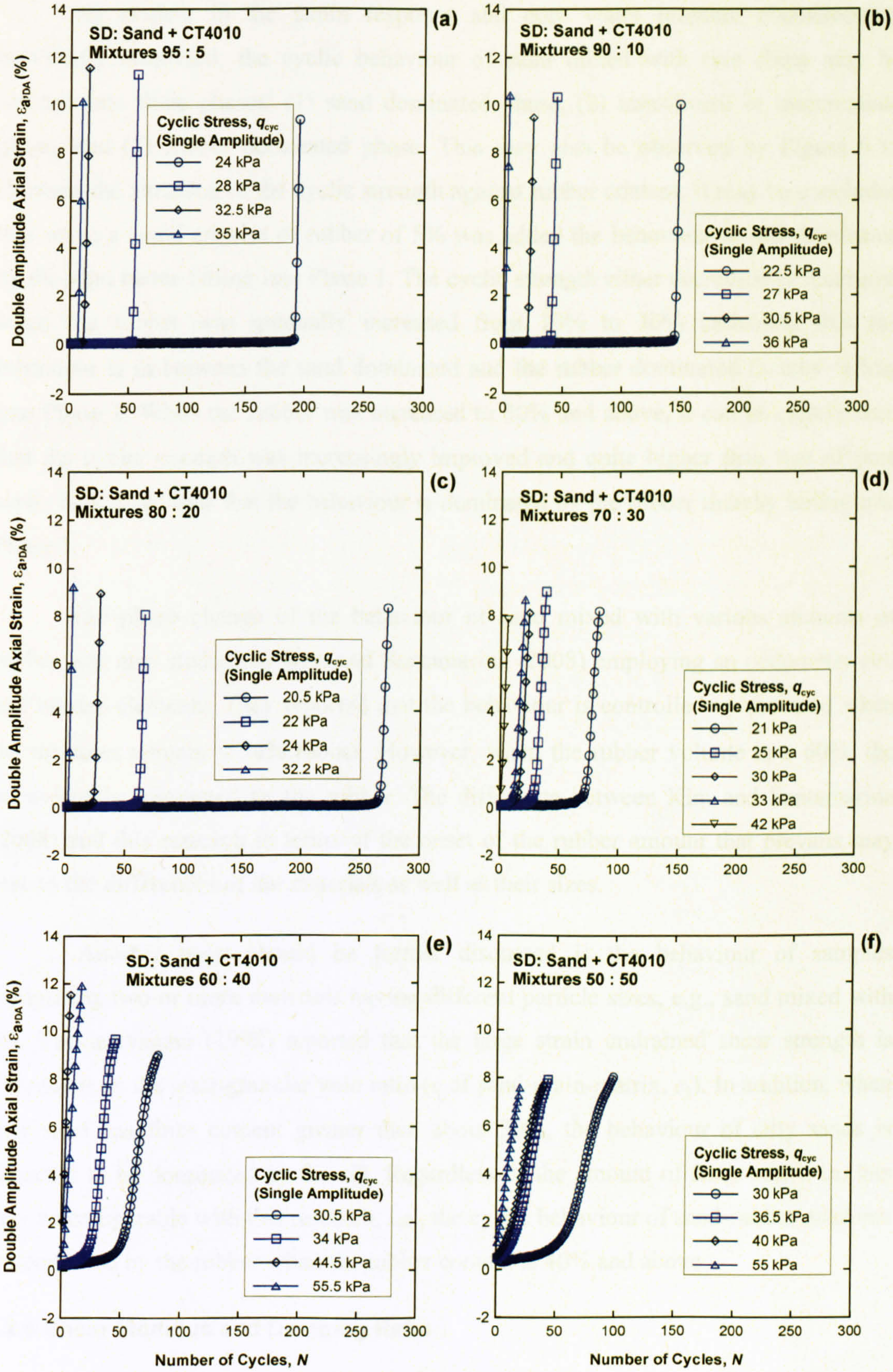

Figure 6. 56 Strain behaviour for SD, Sand + CT4010

As evident in the strain response and pore water pressure characteristics previously discussed, the cyclic behaviour of sand mixed with tyre chips may be divided into three phases: (1) sand dominated phase, (2) transitional or intermediate phase, and (3) rubber dominated phase. This may also be observed by Figure 6.35 showing the variation of the cyclic strength against rubber content. It may be concluded that when a small amount of rubber of 5% was added the behaviour is still dominated by the sand hence falling into Phase 1. The cyclic strength either decreased or increased when the rubber was gradually increased from 10% to 30% indicating that the behaviour is in-between the sand dominated and the rubber dominated thereby falling into Phase 2. When the rubber was increased to 40% and above, it can be clearly seen that the cyclic strength was increasingly improved and quite higher than that of pure sand. This is obvious that the behaviour is dominated by the rubber thereby falling into Phase 3.

The phase change of the behaviour of sand mixed with various amounts of rubber was also studied by Kim and Santamarina (2008) employing an oedometer cell and bender elements. They reported that the behaviour is controlled by the sand when the mixtures contain ≤ 30% rubber. However, when the rubber volume is ≥ 60%, the behaviour is dominated by the rubber. The difference between Kim and Santamarina (2008) and this research in terms of the onset of the rubber amount that prevails may owe to the differences of the materials as well as their sizes.

Another point should be further discussed is the behaviour of samples comprising two or more materials having different particle sizes, e.g., sand mixed with silt. Thevanayagam (1998) reported that the large strain undrained shear strength is dependent on the inter-granular void ratio (e of sand-grain-matrix, e_s). In addition, when silty sand has fines content greater than about 30%, the behaviour of silty sands is expected to be dominated by the silt. Regardless of the amount of fines mixed in, this may be comparable with this research, i.e., the cyclic behaviour of sand-rubber mixtures is dominated by the rubber when the rubber content is 40% and above.

6.2.5 Shear Modulus and Damping Ratio

Shear modulus and damping ratio will be included and discussed altogether in Chapter 7 Bender Element Tests.

CHAPTER 7

BENDER ELEMENT TESTS

7.1 Introduction

The bender element test (BE), is increasingly acquiring attention from researchers because it measures small-strain shear modulus G_{max}, a vital parameter employed in dynamic analysis and design. At very low shear strain the behaviour of a soil is regarded as linear. As such, the BE test is also known as a low strain, non-destructive test. One important benefit that should be mentioned is that as the BE test is conducted at low strain a specimen is still unchanged from its original state. As a result, after the BE test has been finished other soil tests can follow, e.g., unconfined compression tests, standard and cyclic triaxial tests, and one-dimensional compression tests.

Other cyclic loading tests such as the cyclic triaxial test and the cyclic simple shear test also provide the shear modulus G of a soil, but at much larger strain; they are therefore called high strain tests. Combining G_{max} obtained from the BE test and G from the cyclic loading test then would enable us to draw a complete picture of the degradation of soil stiffness against shear strain. Using this curve, together with other properties, both static and dynamic problems involving engineering soils therefore can be analysed. For that reasons, the bender elements developed and fabricated by Chan (2006) were modified to be able to fit into the triaxial cell thereby allowing both BE and cyclic triaxial tests to be done using the same specimen..

7.2 Interpretation of BE signals

The main purpose of the BE test is to determine the travel time of shear waves that travel through a soil specimen thereby obtaining the shear wave velocity, and hence the small strain shear modulus. Unfortunately, choosing the arrival time of shear waves is not straightforward due to several factors such as near-field effects, electronic coupling-crosstalk, and boundary conditions. As a result, several techniques have been developed to provide the accurate means for interpreting the BE signals.

Normally, interpretation techniques are categorised into two groups: visual picking and numerical techniques. The visual picking method is dependent on an individual deciding which point is the arrival time for the shear waves, whereas the numerical method employs such mathematical techniques as Fast Fourier Transform (FFT) to avoid any bias.

7.2.1 First Arrival

This method is simply done by deciding on what point is the arrival time of shear waves. Note that the First Arrival (FA) is also known as visual picking (e.g., Chan, 2006). Although the technique seems to be straightforward, it is quite controversial as to which point is in fact the arrival time, i.e., A, B, C, or D, as illustrated by Figure 7.1. Points A, B, C, and D, are called first deflection, first bump maximum, zero voltage after first bump, and major first peak, respectively (Lee and Santamarina, 2005).

Unfortunately, there has not been consistency in picking the arrival time even within the same report. Point A has been employed as first arrival time, but studies by Salinero *et al.* (1986) pointed out that it might instead be the arrival of compression waves, P-waves. Moreover, Brignoli *et al.* (1996) suggested that the period between point A and point B may be because of near field effects. Point B is the point when the output signal begins to change direction, i.e., from negative slope to positive slope; whereas, point C is where the signal becomes zero voltage. Point D is the first major arrival peak of the receiving (output) signal. In this research, point B was used as the beginning of shear wave arrival, the same as Brignoli *et al.* (1996).

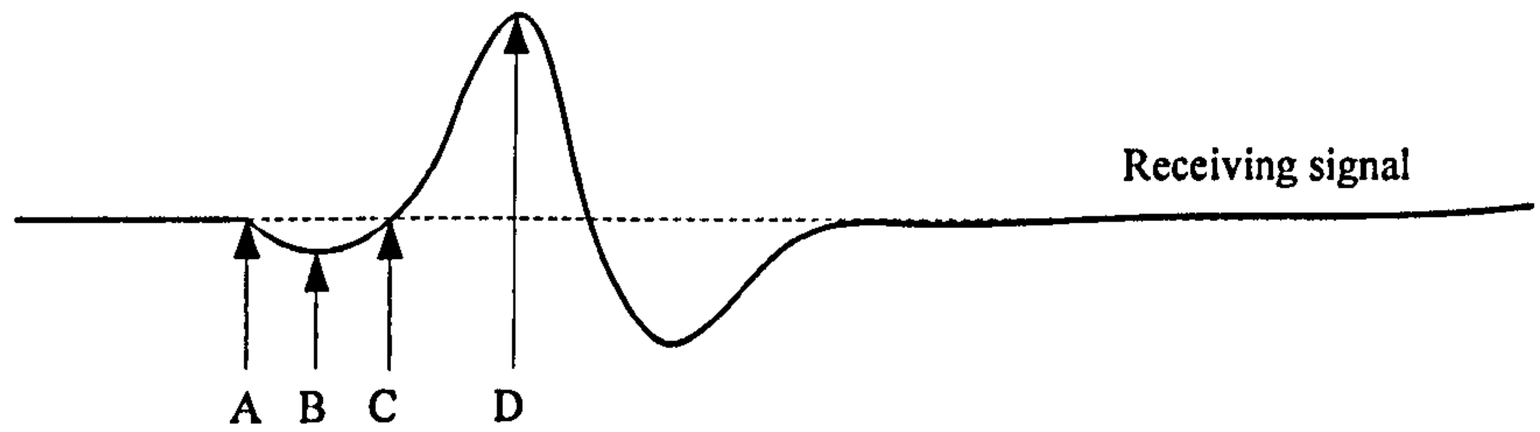

Figure 7. 1 Typical BE output signal

7.2.2 First Major Peak to Peak

The principle of first major Peak to Peak method (PP) (Viggiani and Atkinson, 1995; Brignoli *et al.*, 1996; Chan, 2006) is simply to determine the travel time of shear waves by measuring the time between the first major peak of the input and output signals, as illustrated by Figure 7.2. These are also called characteristic peaks of the input and output signals by Arulnathan *et al.* (1998). Note that apart from the first major signal peak shown in Figure 7.2, first troughs and zero crossings of the input and output signals can also be used to determine the travel time (Arulnathan *et al*, 1998).

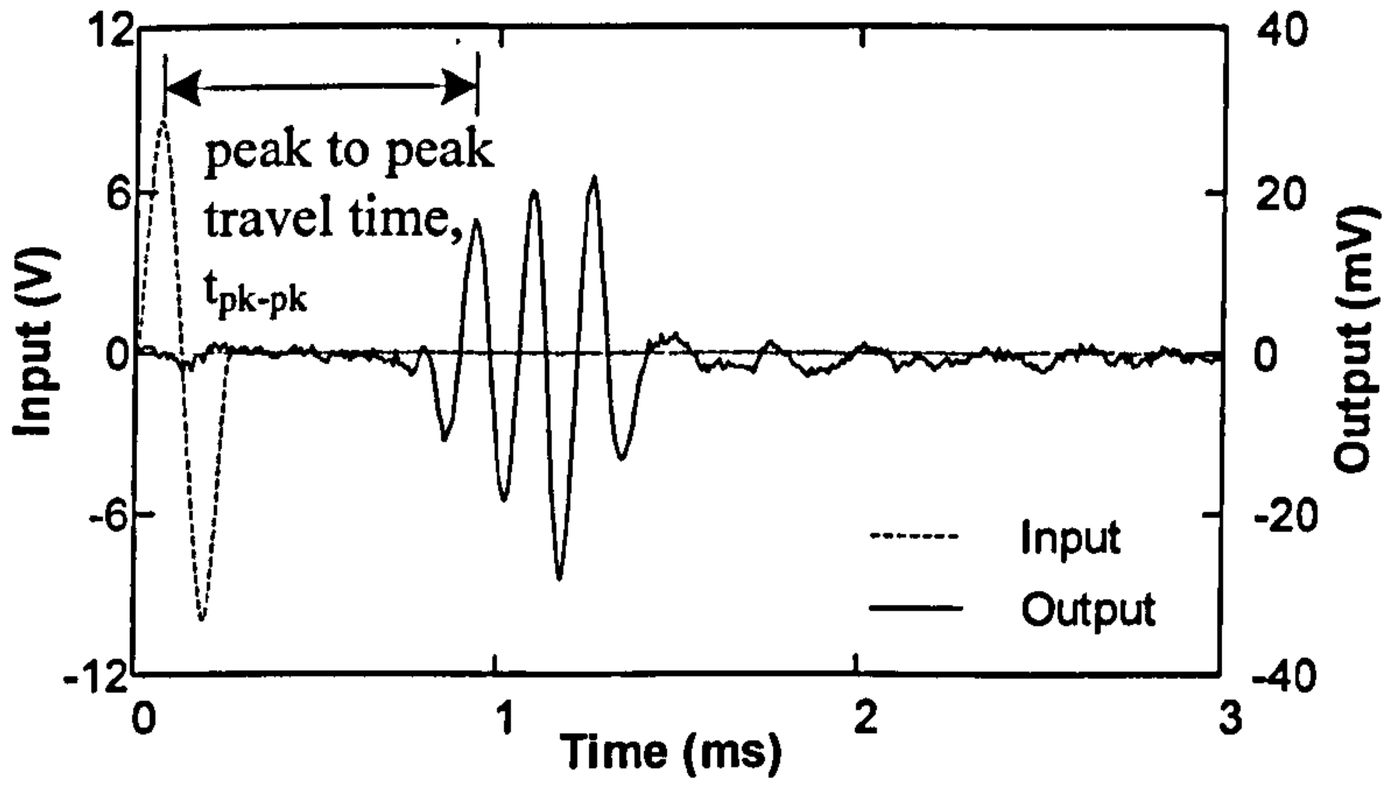

Figure 7. 2 Determination of travel time by first major peak to peak method

7.2.3 Cross Correlation

The Cross Correlation method (CC) (Viggiani and Atkinson, 1995; Arulnathan *et al.*, 1998) employs a mathematical technique called Fast Fourier Transform (FFT) to analyse the arrival time of shear waves. Mathematically, the technique is to determine the correlation between two functions. In the bender element test, the cross correlation function $CC_{xy}(t)$ examines the degree of correlation of two signals, input (X(T)) and output (Y(T)), and is defined as:

$$CC_{xy}(t) = \lim_{T_r \to \infty} \frac{1}{T_r} \int_{T_r} X(T)Y(T+t)dT \qquad \textbf{(Eq. 7. 1)}$$

where:

T_r = time record, and

t = time shift between two signals.

It can be seen that an algorithm that can acquire time-domain test data from an oscilloscope, and then perform FFT is needed to carry out the cross correlation analysis. Fortunately, all functions needed for analysing the BE signals by CC are provided by Matlab® from the MatWorks Inc. Hence, a small computer program was developed for this purpose. Basically, the program first imported the time-domain test data from the oscilloscope into Matlab®. Then, the cross-correlation function of the two signals was calculated.

In more detail, the linear spectra of both input X(T) and output Y(T) signals were first determined using FFT ("fft" function in Matlab®), as shown below:

$$L_y(f) = FFT[Y(T)] \qquad \textbf{(Eq. 7. 2)}$$

$$L_x(f) = FFT[X(T)] \qquad \textbf{(Eq. 7. 3)}$$

where:

$L_y(f)$ = linear spectrum of output signal Y(T), and

$L_x(f)$ = linear spectrum of input signal X(T).

Basically, these processes transformed the time-domain data into the frequency-domain data in order that FFT can be applied. Next, the cross-power spectrum $G_{xy}(f)$ of the linear spectra of both input X(T) and output Y(T) signals was determined by the following equation:

$$G_{xy}(f) = L_x(f).L_y^*(f) \qquad \textbf{(Eq. 7. 4)}$$

Where $L_y^*(f)$ is the complex conjugate of linear spectrum of output signal ("conj" function in Matlab®). Subsequently, the time-domain cross correlation $CC_{xy}(t)$ was calculated by performing the inverse of FFT ("ifft" function in Matlab®) of the frequency-domain cross-power spectrum $G_{xy}(f)$, as shown below:

$$CC_{xy}(t) = IFFT[G_{xy}(f)] \qquad \textbf{(Eq. 7. 5)}$$

In practice, $CC_{xy}(t)$ is normalised by its maximum value $CC_{xy,max}$, i.e., $CC_{xy}(t)/CC_{xy,max}$. Then, the normalised cross-correlation is plotted against the time. The time at which the value of $CC_{xy}(t)/CC_{xy,max} \cong 1.0$ (maximum value) was then taken as the time shift t_{cc} between input and output signals. In other words, t_{cc} represents the travel time of shear waves for the wave forms (Viggiani and Atkinson, 1995).

The example of the determination of travel time by using a cross correlation function is illustrated by Figures 7.3 – 7.5. First, the input and output signals are taken from an oscilloscope, as shown in Figure 7.3. Next, the linear spectra of the input and output are determined using FFT provided by Matlab® (Figure 7.4). The frequency-domain linear spectra are then converted to time-domain employing the inverse of FFT, resulting in the plot of $C_{xy}(t)/CC_{xy,max}$ (Figures 7.5).

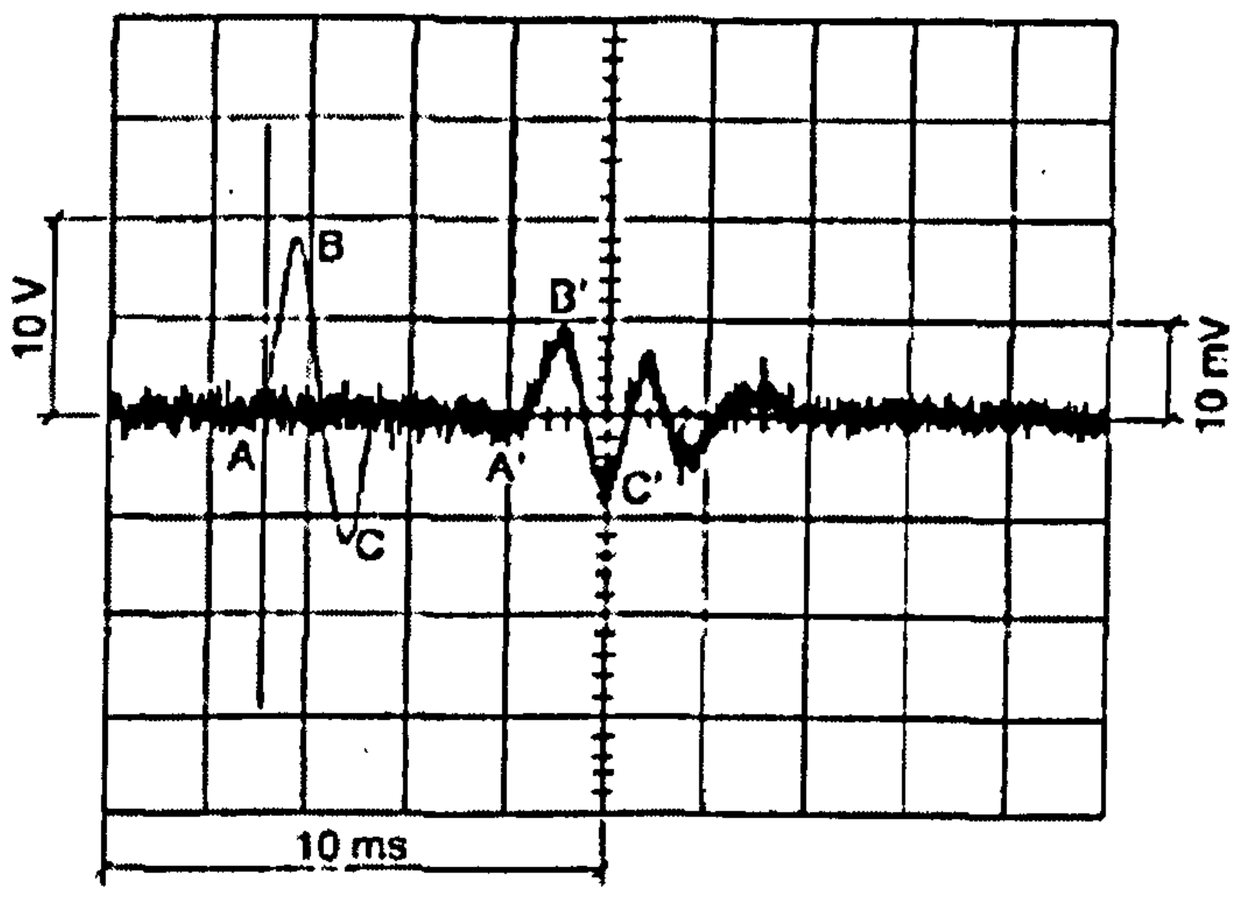

Figure 7. 3 Typical oscilloscope signals from a bender element test with a sine pulse excitation (after Viggiani and Atkinson, 1995)

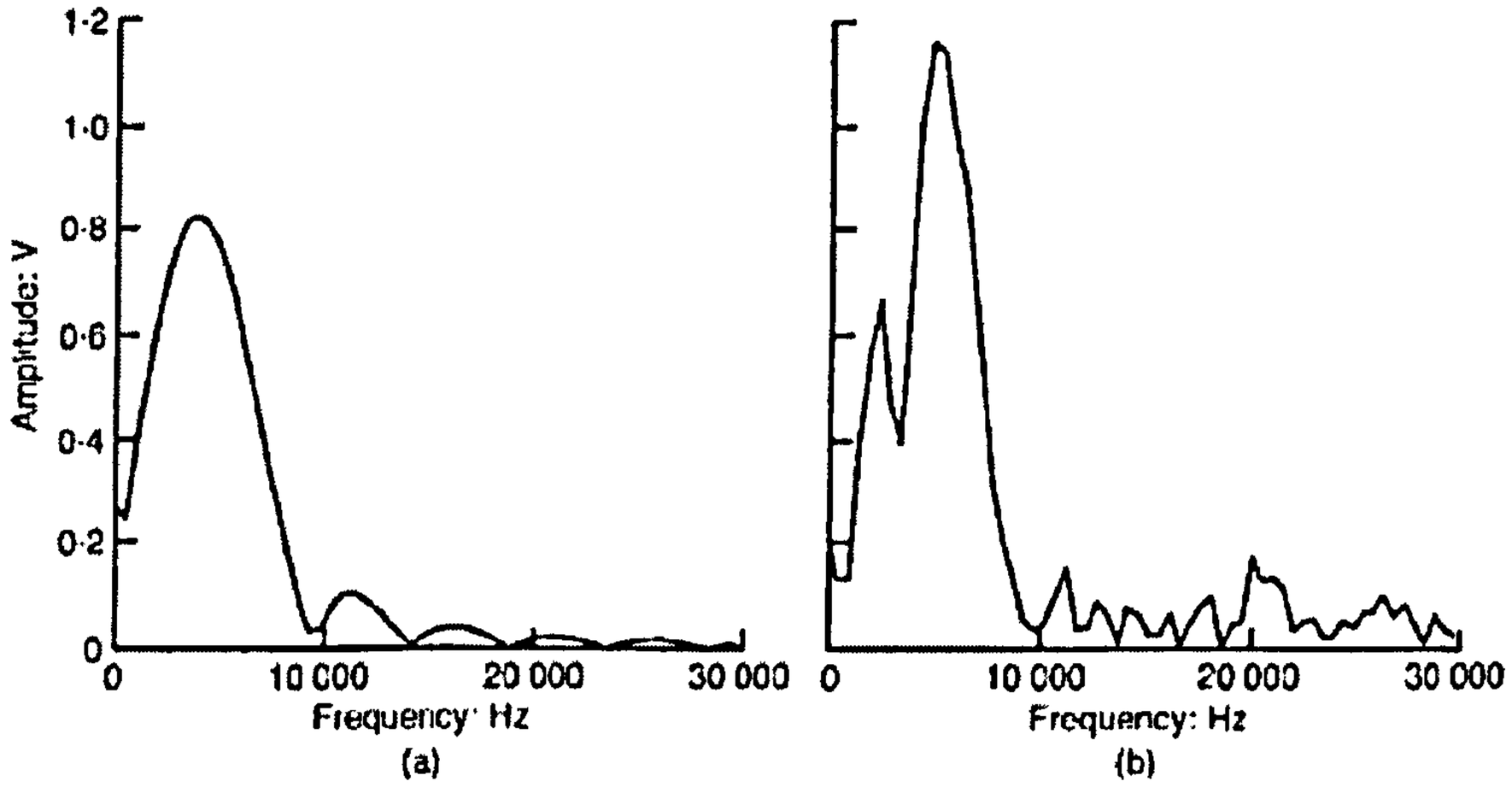

Figure 7. 4 Linear spectra for the signals shown in Figure 7.3: (a) transmitter; (b) receiver (after Viggiani and Atkinson, 1995)

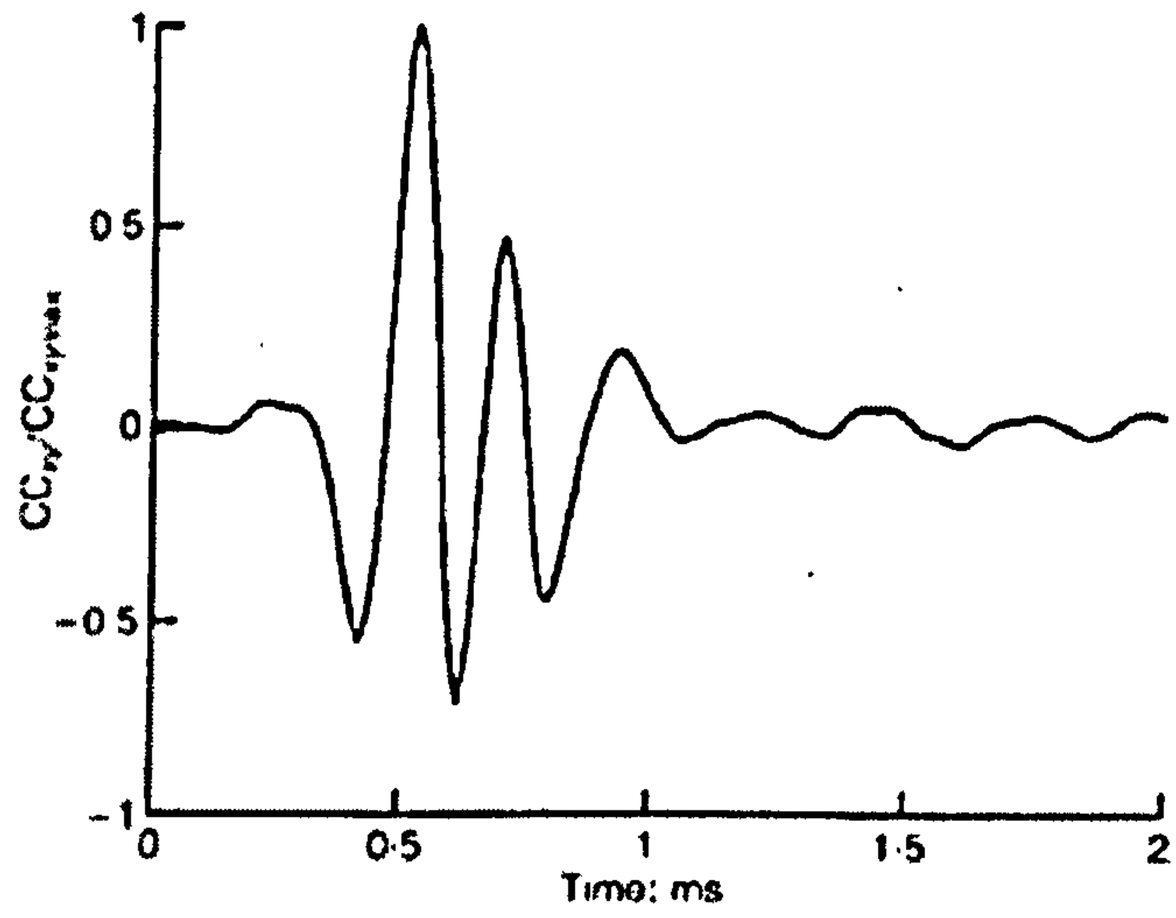

Figure 7. 5 Cross correlation of the signals shown in Figure 7.3 (after Viggiani and Atkinson, 1995)

7.3 Results and Discussion

7.3.1 Shear Wave Velocities and Small Strain Shear Moduli

The undrained cyclic behaviour of a total of 106 specimens, including five pure sand and 101 sand-tyre chip mixtures, has been investigated. Each specimen, after consolidation and before the cyclic load was applied, was subjected to bender element testing in order that the dynamic properties at very low strain could be studied.

The BE test results for pure sand subjected to input frequencies ranging from 2-16kHz are shown in Table A.1 (Appendix), presenting test number, input frequency f_{in}

of driving voltage, shear wave velocity and small-strain shear modulus obtained by FA, PP, and CC. Note that the range of the input frequencies f_{in} employed is similar to that of Leong *et al.* (2005). For the SA mixtures having sand to rubber ratios of 95:5, 90:10, 80:20, 70:30, 60:40, and 50:50, the BE signals are shown in Table A.2, Table A.3, Table A.4, Table A.5, Table A.6, and Table A.7, respectively. Tables A.8 – A.13, Tables A.14 – A.19, Tables A.20 – A.25, show the BE results for the SB, SC, and SD mixtures respectively. It should be noted that for some mixtures containing rubber contents of 30% and higher, when higher input frequencies were applied (e.g., 7, 11, and 16kHz), the V_s and G_{max} were not reported because the receiving signals were not clear enough to interpret, so much so that they were abandoned. This may be because of the highly elastic properties of the rubber distorting the signals.

To obtain the cyclic strength for each mixture, 4 – 5 different cyclic deviator stresses were tested, thereby 4 -5 specimens were prepared. For example, for pure sand shown in Table A.1, five specimens were tested: BE100S430, BE100S370, BE100S320, BE100S290, and BE100S250. Notice that the last three numbers indicate the cyclic deviator stress applied (in kPa) multiplied by 10. For each sand to rubber ratio, even though the specimens were subjected to different cyclic deviator stresses, they were prepared the same way and therefore had similar densities. Furthermore, the BE test had been done before the cyclic triaxial test began. Thus, all specimens having the same sand to rubber ratio should have had similar shear wave velocities and small-strain shear moduli. The BE results for the specimens having the same sand to rubber ratio therefore were averaged for the purpose of analysis and discussion of the results.

The BE test results for pure sand S averaged from Table A.1 are summarised in Table 7.1. Table 7.2, Table 7.3, Table 7.4, Table 7.5, show the summaries of the BE results for SA (averaged from Tables A.2 – A.7), SB (averaged from Tables A.8 – A.13), SC (averaged from Tables A.14 – A.19), and SD (averaged from Tables A.20 – A.25), respectively.

The BE input and output signals for pure sand tested with the input frequencies of 2, 4, 7, 11, and 16kHz are illustrated by Figure 7.6. They depict the pulse-sine-wave form input signals and the output voltage, shown on the left column; and normalised cross correlation function $CC_{xy}/CC_{xy,max}$ plotted against time in ms (1/1000 second), shown on the right column. For SA having sand to rubber ratios of 95:5, 90:10, 80:20,

70:30, 60:40, and 50:50, the selected BE results are illustrated by Figures 7.7 – 7.12, respectively. For SB, SC, and SD, having sand to rubber ratios of 95:5, 90:10, 80:20, 70:30, 60:40, and 50:50, the selected BE results are illustrated by Figures 7.13 – 7.18, Figures 7.19 – 7.24, and Figures 7.25 – 7.30, respectively. Note that only one result that represents each sand-rubber mixture is plotted and shown, the rest can be found in the CD-ROM attached.

The effects of varied input frequencies of 2, 4, 7, 11, and 16kHz on the V_s obtained by FA for the SA, SB, SC, and SD mixtures are illustrated by Figure 7.31, Figure 7.32, Figure 7.33, and Figure 7.34, respectively. Figures 7.35 – 7.38 and Figures 7.39 – 7.42 illustrate the effects of various input frequencies on the V_s obtained by PP and CC, respectively. The changes of the shear wave velocity and small strain shear modulus obtained by PP corresponding to the varied rubber contents from 5 to 50% for SA, SB, SC, and SD were plotted, and are illustrated by Figure 7.43 and Figure 7.44, respectively.

In Table 7.1 presenting the BE results for pure sand S, it was observed that both V_s and G_{max} determined by means of FA gradually increased with increasing input frequency, i.e., V_s = 219 – 240m/s and G_{max} = 96 – 115MPa, corresponding to the f_{in} from 2 – 16kHz. This may suggest that the V_s obtained by FA depend on the frequency of the input voltage (see Figures 7.31 – 7.34 for 100:0 curves). However, these findings did not apply to the results obtained by the other two interpretation methods, PP and CC. For example, for PP, the V_s for the f_{in} of 2, 4, 7, 11, and 16kHz were 229, 222, 223, 227, and 230m/s, respectively. On the other hand, for CC, the V_s for the f_{in} of 2, 4, 7, 11, and 16kHz were 207, 222, 221, 221, and 221m/s, respectively.

The interpretation of the BE signals for pure sand using PP (see Figures 7.35 – 7.38) and CC (see Figures 7.39 – 7.42) methods suggests that the signals are not dependent on the input frequency, which is contrary to the test results interpreted by FA. The values of V_s and G_{max} for pure sand averaged for all f_{in} by FA, PP, and CC, were 229m/s and 104MPa, 226m/s and 102MPa, and 218m/s and 95MPa, respectively. This implies that FA yields the maximum V_s and G_{max}, followed by PP and CC. Comparing the results obtained by all three techniques, it can be seen that the results by PP are in-between the other two, implying that they could be used as a mean value (see

Table 7.1). For pure sand, it may be concluded that the V_s obtained by PP and CC were more consistent than those obtained by FA, regarding to the various f_{in}.

The V_s averaged from all f_{in} for pure sand by FA, PP, and CC, were 229, 226, and 218m/s, respectively; and, it was interesting to compare the V_s from this research to other studies. For example, Andrus and Stokoe (2000) estimated the shear wave velocity for sandy soil (fines <= 5%) of 200 - 215m/s, which is quite similar to this research. This comparison for the sand provides some degree of confidence for the BE results for sand mixed with tyre chips. In addition, as G_{max} is such an important parameter in dynamic analysis, there have been several studies reporting its values for various soil types. For sandy soil, Hardin and Black (1968) reported that G_{max} may be estimated from the following equations:

$$G_{max} = \frac{6908(2.17-e)^2}{1+e}\sqrt{\sigma'_{3c}} \quad \text{(kPa, for round-grained)} \qquad \textbf{(Eq. 7. 6)}$$

$$G_{max} = \frac{3230(2.97-e)^2}{1+e}\sqrt{\sigma'_{3c}} \quad \text{(kPa, for angular-grained)} \qquad \textbf{(Eq. 7. 7)}$$

Where σ'_{3c} is effective confining pressure in kPa (or consolidation pressure in triaxial test). Substituting e of 0.669 and σ'_{3c} of 100kPa for pure sand, into the above equations, it was found that G_{max} for round-grained sand and angular-grained sand were 93MPa and 102MPa, respectively. Comparing these two values with G_{max} obtained by the BE test of 102MPa (by PP), it was striking to find out that they were very similar. This confirms that, as can be seen in the equations, the shear modulus is correlated solely to void ratio and effective stress, regardless of the size of a soil (Lambe and Whitman, 1979).

In Table 7.2 summarising the BE results for SA, it was observed that both V_s and G_{max} significantly decreased with increasing rubber content. For example, the V_s and G_{max} obtained by PP for the mixtures 95:5, 90:10, 80:20, 70:30, 60:40, and 50:50; were 232m/s and 104MPa, 211m/s and 85MPa, 177m/s and 55MPa, 149m/s and 38MPa, 113m/s and 21MPa, and 93m/s and 13MPa, respectively. This indicates that the more rubber was added the lower the observed shear wave velocity and shear modulus. Furthermore, the decrease of V_s and G_{max} with increasing rubber content was also found to be the case for the results obtained by the other two methods, PP and CC. In addition,

it was observed that, apart from the mixtures 95:5, all mixtures had lower V_s and G_{max} compared to pure sand, indicating lower stiffness.

Note that for SA, when the rubber was increased to 30 and 40%, the output signals produced by the f_{in} of 11 and 16kHz were so noisy that they were not reported. For SA having 50% rubber, however, only the output signals produced by the f_{in} of 2 and 4kHz that were analysed and reported. This suggests that the rubber in sand-rubber matrices may distort the shear waves so much so that the receiver could not detect the signals properly.

Apart from 95:5 mixtures, both V_s and G_{max} for SA obtained by FA slightly increased with increasing f_{in}, suggesting that they may be dependent on the frequency of driving voltage, which was quite similar to the findings for pure sand. However, as this research employed only one type of wave form, pulse-sine-wave, this may not be the case if other types of wave form were tested. For the mixtures 95:5, however, the V_s and G_{max} either increased or decreased with increasing of f_{in}, i.e., the V_s determined by FA tested with the f_{in} of 2, 4, 7, 11, and 16kHz were 243, 255, 245, 238, and 250m/s, respectively.

Similar findings to those for pure sand in which the results interpreted by PP were between those obtained by FA and CC, were also found for SA. In addition, the sequence of V_s and G_{max} obtained by the three interpretation methods for all mixtures from high to low is also the same as that for pure sand, i.e., FA > PP > CC. Comparing all three methods, it was observed that the V_s and G_{max} obtained by means of PP were the most consistent, for varied input frequencies.

In Table 7.3 showing the summary of BE results for SB, the output signals produced by all input frequencies for the mixtures 95:5, 90:10, and 80:20 were all interpreted and reported. However, when the rubber content was increased to 30%, the output signals produced by 16kHz input frequency were un-interpretable. For the 60:40 and 50:50 mixtures, only the output signals from the input frequencies of 2 and 4kHz that were recorded and interpreted. Notice that the difficulty in the interpretation of the output signals for SB when the rubber content was increased to 30% and higher was observed to be similar to that of SA. It may be concluded that the distortion of the shear

waves was because of higher proportions of rubber in the sand-rubber mixtures, especially when higher input frequencies were employed.

Apart from the BE results of the mixtures 95:5 interpreted by PP, it was observed that the V_s by FA, PP, and CC tested with the lowest f_{in} of 2kHz was notably lower that that tested with a higher f_{in}. For example, V_s for the 95:5, 90:10, 80:20, 70:30, and 60:40 mixtures determined by FA tested with the f_{in} of 2 and 4kHz were 196 and 206m/s, 185 and 195m/s, 192 and 202m/s, 165 and 179m/s, and 133 and 147m/s, respectively. It was found that, however, when the f_{in} were higher, i.e., 7, 11, and 16kHz, the results were quite consistent. This indicates that V_s and G_{max} for SB obtained by FA may be dependent on the f_{in}; thus, choosing the values for dynamic analysis should be considered with caution.

The V_s and G_{max} for SB were the greatest when the mixtures contained 5% rubber, and progressively decreased with increasing of rubber content. For example, the V_s and G_{max} for the mixtures having rubber content of 5, 10, 20, 30, 40, and 50% were 201m/s and 79MPa; 188m/s and 68MPa; 189m/s and 65MPa; 158m/s and 44MPa; 120m/s and 24MPa; 104m/s and 17MPa, respectively. It was also found that the results obtained by PP were in-between the results determined by FA and CC, i.e., FA>PP>CC. Note that these findings are also the same as found for SA and pure sand.

In Table 7.4 showing the summary of BE tests for SC, for the mixtures having 5, 10, and 20% rubber, the output signals from all f_{in} were recorded and interpreted. For the mixtures containing 30 and 40% rubber, however, only the output signals produced by the f_{in} of 2 and 4kHz were analysed; whereas, for the 50:50 mixtures only the signals produced by f_{in} of 2kHz were recorded and analysed.

For SC, it was observed that the V_s obtained by FA increased with increasing f_{in}; however, this was not the case for the results analysed by PP and CC. This suggests that the V_s for SC obtained by FA are quite dependent on f_{in}. The V_s obtained by PP for the 95:5, 90:10, 80:20, 70:30, 60:40, and 50:50 mixtures were 211, 207, 184, 189, 155, and 127m/s, respectively. Unlike SA and SB, the V_s for SC progressively decreased when the rubber content was increased from 5 to 20%, it then slightly increased when the rubber was increased to 30%. After that, it continued to decrease almost linearly as the rubber content was increased to 40 and 50%, as can be seen in Figure 7.43. It was also

found that, for SC, the V_s and G_{max} obtained by PP were in-between the results by obtained FA (maximum) and CC (minimum), similar to those of SA, SB, and pure sand.

For SD (see Table 7.5), the output signals produced by all f_{in} were recorded and analysed only for the 95:5 and 90:10 mixtures. For the 80:20, 70:30, and 50:50 mixtures only the output signals produced by the f_{in} of 2, 4, and 7kHz were analysed and reported. For the 60:40 mixtures, only the signals produced by the f_{in} of 2 and 4kHz were analysed.

For all sand to rubber ratios of SD, it was observed that the V_s and G_{max} obtained by FA gradually decreased with increasing of f_{in}. Apart from the results for the 95:5 mixtures obtained by PP, these findings were also found to be the case when the signals were analysed by the other two methods, PP and CC. This suggests that, for SD, the V_s and G_{max} obtained by FA depend on the input frequency. At this point, it may be concluded that the V_s and G_{max} for sand-rubber mixtures when analysed by employing the FA technique, are very dependent on the frequency of the input voltage. Thus, if they are to be employed in dynamic analysis, a conservative value should be used.

The V_s for SD analysed by PP for the 95:5, 90:10, 80:20, 70:30, 60:40, and 50:50 mixtures were 213, 208, 188, 200, 170, and 155m/s, respectively, showing a similar trend to that previously found for SC: the V_s gradually decreased when the rubber content was 5, 10, and 20%; however, when the rubber was increased to 30% the V_s instead slightly increased. When the rubber was increased to 40%, the V_s continued to decrease, and carried on when the mixtures contained 50% of rubber (see Figure 7.43). It was also found for SD that V_s and G_{max} determined by PP were in-between that obtained by FA and CC, as shown previously for pure sand, SA, SB, and SC.

The typical BE signals for pure sand are illustrated by Figure 7.6, including the input voltage and output voltage shown on the left, and $CC_{xy}/CC_{xy,max}$ shown on the right, with the input frequencies of 2, 4, 7, 11, and 16kHz. Overall, the output signals for pure sand were very clear to interpret, except for the f_{in} of 2kHz where there was some noise, suggesting that a frequency as low as 2kHz may not be suitable for the tested sand. Above all, for the sand it was found that the f_{in} of 4kHz produced the output signal that was the easiest to analyse.

For the f_{in} of 2 and 4kHz, the first bump of the output (point A illustrated by Figure 7.1) was detected at about 710μs, and the first arrival of shear waves (by means of point B illustrated by Figure 7.1) was detected at the time of 850 and 840μs, respectively. Note that the first bump of the output signal is normally taken as the reflection of the primary P-wave, not the arrival of shear waves (Lee and Santamarina, 2005). When the applied f_{in} was higher, the first arrival times of shear waves were slightly shifted to the left, i.e., they were 820, 790, and 760μs for the f_{in} of 7, 11, and 16kHz, respectively.

It is apparent that the arrival of the shear wave obtained by FA depends on the input frequency. However, when the travel time was determined by measuring the difference between the first positive peak of input signals and the first positive peak of output signal, it was found that the frequency dependency previously found was not the case. When analysing by employing the cross-correlation function proposed by Viggiani and Atkinson (1995), however, it was found that, the travel time was quite consistent, regardless of the f_{in}. For example, the time at which the $CC_{xy}/CC_{xy,max}$ values were maximum (approximately 1.0) for the f_{in} of 2, 4, 7, 11, and 16kHz were 875, 850, 850, 850, and 850μs, respectively. It is apparent that, except for the f_{in} of 2 kHz, they are exactly the same, indicating frequency independency.

For SA with 5% rubber (Figure 7.7), at the f_{in} of 2, 4, 7kHz, the output signals were clearer than the signals produced by the f_{in} of 11 and 16kHz. This suggests that for SA having 5% rubber, a higher input frequency could produce the noise that causes the analysis of the signals difficult. These findings were also found to be similar to those of SA having rubber contents of 10% (Figure 7.8) and 20% (Figure 7.9).

For SA having rubber contents of 30, 40, and 50%, at higher f_{in} of 7, 11, and 16kHz, there was so much noise that the output signals were abandoned because they were un-interpretable (Figures 7.10-5.12, respectively). Notice that regardless of the percentage of rubber added into the mixtures for SA, it was found that the f_{in} of 2kHz produced the clearest signals. This should be noted as for pure sand the f_{in} of 2kHz produced the poorest signals.

It was also found that for SA containing rubber contents of 30% and higher, and tested with the f_{in} of 2kHz, the time between the first bump (P-wave arrival, point A

illustrated by Figure 7.1) and the lowest output voltage (point B illustrated by Figure 7.1) was much wider, compared to the signals produced by higher f_{in}. This caused the determination of the travel time of shear waves by FA problematic. This is obvious when considering the BE signals for SA having rubber contents of 40 and 50% illustrated by Figure 7.11 and Figure 7.12, respectively. However, there was no such problem when PP and CC techniques were employed to determine the travel time.

For SB with 5% rubber (Figure 7.13), at the f_{in} of 2kHz, there was little noise found at the beginning of the output signal, as found for pure sand, but still interpretable. When the rubber was increased to 10, 20, and 30%, the output signals were quite clear and it was easy to determine the travel time (see Figure 7.14, Figure 7.15, and Figure 7.16, respectively). For SB having rubber contents of 40% (Figure 7.17) and 50% (Figure 7.18), however, a similar difficulty in the determination of travel time by means of FA as found for SA was also observed.

Those findings for SA and SB, e.g., the characteristics of output signals with varied input frequency, the noise of the output signals when higher input frequencies were employed, and the difficulty in the determination of travel time of shear waves by FA when the rubber was increased to 40 and 50%, were also found for SC and SD (see Figures 7.19-7.24 and Figures 7.25-7.30, respectively).

Considering Figure 7.43 (V_s versus rubber content) and Figure 7.44 (G_{max} versus rubber content) together, it can be seen that the characteristics of shear wave velocity and small-strain shear modulus of sand mixed with tyre chips versus various rubber content may be divided into two groups: (1) SA and SB, and (2) SC and SD. For the purpose of the discussion of the BE results, it should be emphasised herein again that the sizes of tyre chips from smaller to bigger are as followed: A (0.5 - 1.5mm), B (1.0 - 3.0mm), C (2.0 - 6.0mm), and D (4.0 - 10.0mm).

From Figure 7.43 and Figure 7.44, it is apparent that for the mixtures containing 20% rubber, both V_s and G_{max} for SA, SB, SC, and SD, are very similar, regardless of the size of tyre chips added. This suggests that when Leighton Buzzard 16/30 Sand is mixed with tyre chips CT0515 (A), CT1030 (B), CT2060 (C), and CT4010 (D), with a sand to rubber ratio of 80:20, the dynamic properties are not influenced by the size of

tyre chips. Interestingly, the cyclic strengths for SA, SB, SC, and SD were also the lowest when the mixtures contained 20% of rubber (Figure 6.35, Chapter 6).

It can be seen that the relationship between V_s and G_{max} versus rubber content for group (1) may be considered approximately linear. On the other hand, group (2) exhibited a highly non-linear relationship. However, for the purpose of analysis and design, group (2) may also be approximated as linear. It should be noted that as the curves for group (2) are highly non-linear, making use of them must be considered cautiously, in particular when the mixtures contain 5 to 30% rubber.

For the relationship between the V_s and rubber content, the linearization was done by setting the V_s of 226m/s (V_s for pure sand, see Table 7.1) as the intercept for zero rubber content, as illustrated by Figure 7.45. For G_{max}, a similar technique was employed, but the intercept for G_{max} at zero rubber content was 102MPa (G_{max} for pure sand by PP, see Table 7.1), and the linear relationship between G_{max} and rubber content is illustrated by Figure 7.46. The linear equation representing the relationship between the G_{max} and the rubber content is shown by Eq. 7.8; and Eq. 7.9 shows the linear relationship between V_s and the rubber content.

$$G_{max} = 102 - F_G \cdot RC \qquad \text{(MPa)} \qquad \textbf{(Eq. 7. 8)}$$

$$V_s = 226 - F_V \cdot RC \qquad \text{(m/s)} \qquad \textbf{(Eq. 7. 9)}$$

where:

F_G = 1.935, 1.867, 1.523, and 1.276 for SA, SB, SC, and SD,

F_V = 2.643, 2.468, 1.816, and 1.366 for SA, SB, SC, and SD, and

RC = rubber content in per cent.

It was observed that the factors F_G and F_V varied in relation to the size of rubber, in other word, the particle size ratio D_r/D_s. Therefore they were plotted against D_r/D_s for further analysis, and are illustrated by Figure 7.47. As a result, the relationships between the two were obtained, hence Eq. 7.8 and Eq. 7.9 became:

$$G_{max} = 102 - \left[2.1964 - 0.3698 \ln\left(\frac{D_r}{D_s}\right)\right] \cdot RC \qquad \text{(MPa)} \qquad \textbf{(Eq. 7. 10)}$$

$$V_s = 226 - \left[3.1279 - 0.7141 \ln\left(\frac{D_r}{D_s}\right)\right] \cdot RC \qquad \text{(m/s)} \qquad \textbf{(Eq. 7. 11)}$$

Table 7. 1 Summary of BE tests (averaged) for pure sand, S

Test No.	Sand : Rubber Ratio	f_{in} (kHz)	First Arrival (FA)		Peak to Peak (PP)		Cross Correlation (CC)	
			V_s (m/s)	G_{max} (MPa)	V_s (m/s)	G_{max} (MPa)	V_s (m/s)	G_{max} (MPa)
BE100S	100 : 0	2	219	96	229	105	207	86
		4	223	99	222	99	222	98
		7	227	103	223	99	221	98
		11	235	110	227	103	221	97
		16	240	115	230	105	221	97
		Average	**229**	**104**	**226**	**102**	**218**	**95**

Table 7. 2 Summary of BE tests (averaged) for SA

Test No.	Sand : Rubber Ratio	f_{in} (kHz)	First Arrival (FA)		Peak to Peak (PP)		Cross Correlation (CC)	
			V_s (m/s)	G_{max} (MPa)	V_s (m/s)	G_{max} (MPa)	V_s (m/s)	G_{max} (MPa)
BE95SA	95 : 5	2	243	114	232	104	227	100
		4	255	127	230	102	226	99
		7	245	117	234	106	223	96
		11	238	110	230	103	222	96
		16	250	122	233	106	219	93
		Average	**246**	**118**	**232**	**104**	**223**	**97**
BE90SA	90 : 10	2	213	86	208	83	207	82
		4	220	92	208	82	203	78
		7	225	96	209	83	200	76
		11	231	102	213	86	200	76
		16	230	101	217	90	196	73
		Average	**224**	**95**	**211**	**85**	**201**	**77**
BE80SA	80 : 20	2	176	56	171	53	170	52
		4	186	63	175	54	167	51
		7	193	67	177	55	166	50
		11	195	69	180	56	165	49
		16	199	72	181	56	162	48
		Average	**190**	**65**	**177**	**55**	**166**	**50**
BE70SA	70 : 30	2	161	44	145	36	136	32
		4	169	49	155	41	133	30
		7	167	48	147	37	133	30
		11	-	-	-	-	-	-
		16	-	-	-	-	-	-
		Average	**165**	**47**	**149**	**38**	**134**	**31**
BE60SA	60 : 40	2	123	25	111	20	105	18
		4	125	26	113	21	105	18
		7	126	26	114	21	101	17
		11	-	-	-	-	-	-
		16	-	-	-	-	-	-
		Average	**125**	**26**	**113**	**21**	**104**	**18**
BE50SA	50 : 50	2	109	19	91	13	83	11
		4	105	17	95	14	86	12
		7	-	-	-	-	-	-
		11	-	-	-	-	-	-
		16	-	-	-	-	-	-
		Average	**107**	**18**	**93**	**13**	**85**	**11**

Table 7. 3 Summary of BE tests (averaged) for SB

Test No.	Sand : Rubber Ratio	f_{in} (kHz)	First Arrival (FA)		Peak to Peak (PP)		Cross Correlation (CC)	
			V_s (m/s)	G_{max} (MPa)	V_s (m/s)	G_{max} (MPa)	V_s (m/s)	G_{max} (MPa)
BE95SB	95 : 5	2	196	74	200	78	190	70
		4	206	83	198	76	199	77
		7	208	84	201	79	195	74
		11	214	89	204	81	194	73
		16	219	93	204	81	194	73
		Average	**209**	**85**	**201**	**79**	**194**	**74**
BE90SB	90 : 10	2	185	65	177	60	173	57
		4	195	72	186	66	183	64
		7	201	77	190	69	181	63
		11	206	81	194	72	182	63
		16	209	84	194	72	180	62
		Average	**199**	**76**	**188**	**68**	**180**	**62**
BE80SB	80 : 20	2	192	68	180	59	177	58
		4	202	74	184	62	180	59
		7	211	82	190	66	177	57
		11	212	82	194	69	179	58
		16	206	78	197	71	175	56
		Average	**205**	**77**	**189**	**65**	**178**	**58**
BE70SB	70 : 30	2	165	48	150	40	143	36
		4	179	56	159	44	143	36
		7	185	60	160	45	155	42
		11	189	63	162	46	147	38
		16	-	-	-	-	-	-
		Average	**180**	**57**	**158**	**44**	**147**	**38**
BE60SB	60 : 40	2	133	29	117	23	110	20
		4	147	36	122	25	111	20
		7	-	-	-	-	-	-
		11	-	-	-	-	-	-
		16	-	-	-	-	-	-
		Average	**140**	**33**	**120**	**24**	**110**	**20**
BE50SB	50 : 50	2	119	22	101	16	92	13
		4	118	22	107	18	90	13
		7	-	-	-	-	-	-
		11	-	-	-	-	-	-
		16	-	-	-	-	-	-
		Average	**118**	**22**	**104**	**17**	**91**	**13**

Table 7. 4 Summary of BE tests (averaged) for SC

Test No.	Sand : Rubber Ratio	f_{in} (kHz)	First Arrival (FA)		Peak to Peak (PP)		Cross Correlation (CC)	
			V_s (m/s)	G_{max} (MPa)	V_s (m/s)	G_{max} (MPa)	V_s (m/s)	G_{max} (MPa)
BE95SC	95 : 5	2	207	84	211	87	198	77
		4	209	86	207	84	206	83
		7	215	90	210	86	204	82
		11	221	95	212	88	204	81
		16	225	99	213	89	202	80
		Average	**215**	**91**	**211**	**87**	**203**	**81**
BE90SC	90 : 10	2	202	79	199	76	186	67
		4	212	87	204	80	203	80
		7	220	94	209	84	201	78
		11	221	95	211	86	203	79
		16	224	97	212	86	202	79
		Average	**216**	**90**	**207**	**83**	**199**	**77**
BE80SC	80 : 20	2	180	60	174	56	169	53
		4	193	69	182	62	178	59
		7	200	75	186	64	179	59
		11	205	78	190	67	181	61
		16	204	77	190	67	179	59
		Average	**196**	**72**	**184**	**63**	**177**	**58**
BE70SC	70 : 30	2	203	74	181	59	170	52
		4	207	77	196	69	167	50
		7	-	-	-	-	-	-
		11	-	-	-	-	-	-
		16	-	-	-	-	-	-
		Average	**205**	**76**	**189**	**64**	**168**	**51**
BE60SC	60 : 40	2	172	51	148	38	137	32
		4	179	55	162	45	141	34
		7	-	-	-	-	-	-
		11	-	-	-	-	-	-
		16	-	-	-	-	-	-
		Average	**175**	**53**	**155**	**41**	**139**	**33**
BE50SC	50 : 50	2	148	35	127	26	109	19
		4	-	-	-	-	-	-
		7	-	-	-	-	-	-
		11	-	-	-	-	-	-
		16	-	-	-	-	-	-
		Average	148	35	127	26	109	19

Table 7. 5 Summary of BE tests for (averaged) SD

Test No.	Sand : Rubber Ratio	f_{in} (kHz)	First Arrival (FA)		Peak to Peak (PP)		Cross Correlation (CC)	
			V_s (m/s)	G_{max} (MPa)	V_s (m/s)	G_{max} (MPa)	V_s (m/s)	G_{max} (MPa)
BE95SD	95 : 5	2	213	89	213	89	196	75
		4	214	90	210	86	209	86
		7	219	94	213	89	208	85
		11	225	100	214	90	208	85
		16	230	103	216	91	206	83
		Average	**220**	**95**	**213**	**89**	**205**	**83**
BE90SD	90 : 10	2	202	79	197	75	188	68
		4	211	86	206	82	203	80
		7	218	92	210	86	204	80
		11	222	95	213	87	205	81
		16	228	101	214	89	199	77
		Average	**216**	**91**	**208**	**84**	**200**	**77**
BE80SD	80 : 20	2	184	63	172	55	167	52
		4	198	73	192	69	187	65
		7	208	81	200	75	189	66
		11	-	-	-	-	-	-
		16	-	-	-	-	-	-
		Average	**197**	**73**	**188**	**66**	**181**	**61**
BE70SD	70 : 30	2	209	79	193	67	186	62
		4	214	83	202	74	190	65
		7	215	83	206	76	193	67
		11	-	-	-	-	-	-
		16	-	-	-	-	-	-
		Average	**213**	**81**	**200**	**72**	**189**	**65**
BE60SD	60 : 40	2	179	55	161	45	137	32
		4	195	66	178	55	136	32
		7	-	-	-	-	-	-
		11	-	-	-	-	-	-
		16	-	-	-	-	-	-
		Average	**187**	**60**	**170**	**50**	**137**	**32**
BE50SD	50 : 50	2	161	43	147	36	140	32
		4	173	49	157	41	148	36
		7	173	49	162	43	148	36
		11	-	-	-	-	-	-
		16	-	-	-	-	-	-
		Average	**169**	**47**	**155**	**40**	**146**	**35**

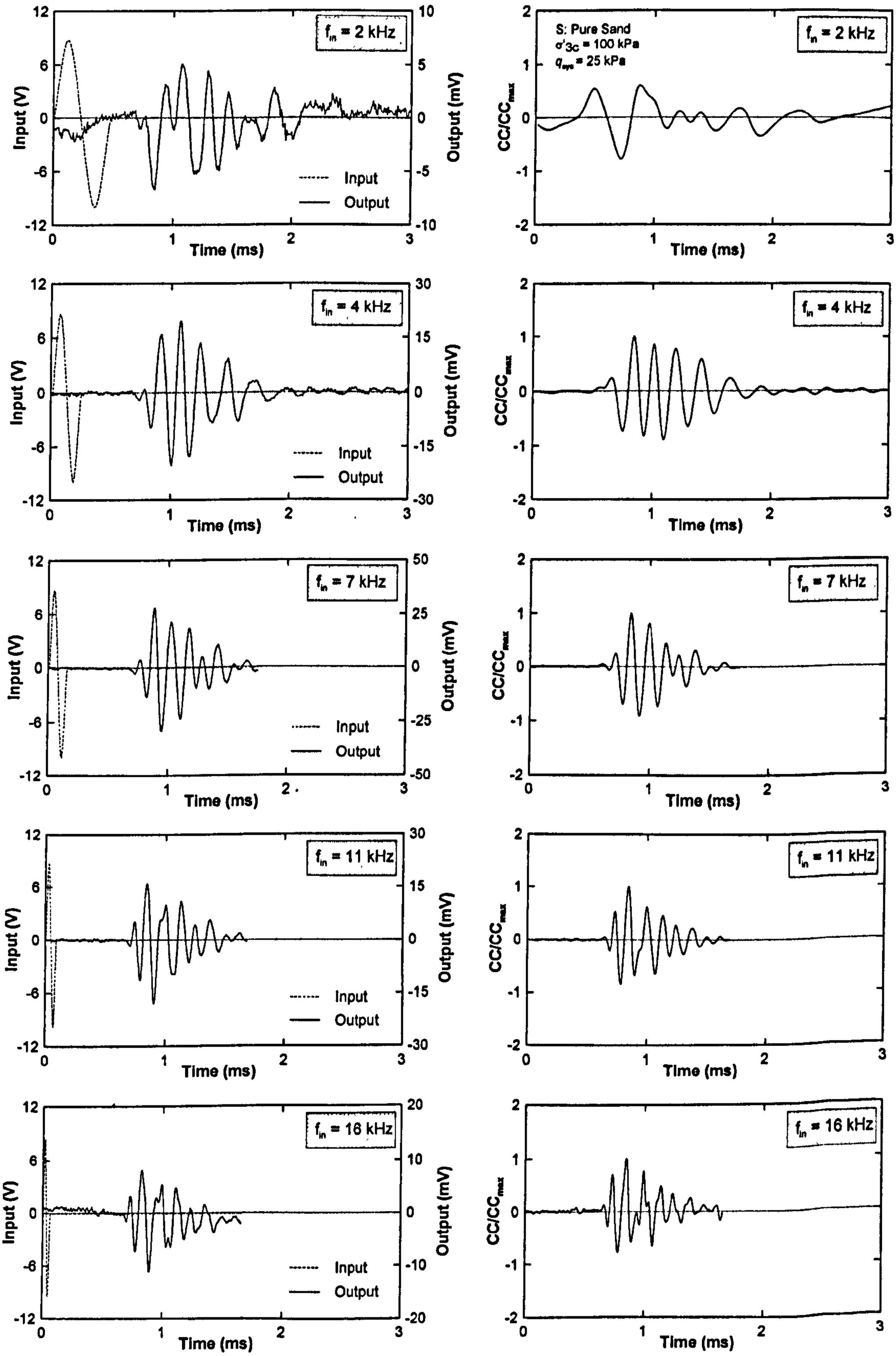

Figure 7. 6 Typical BE signals for pure sand, S

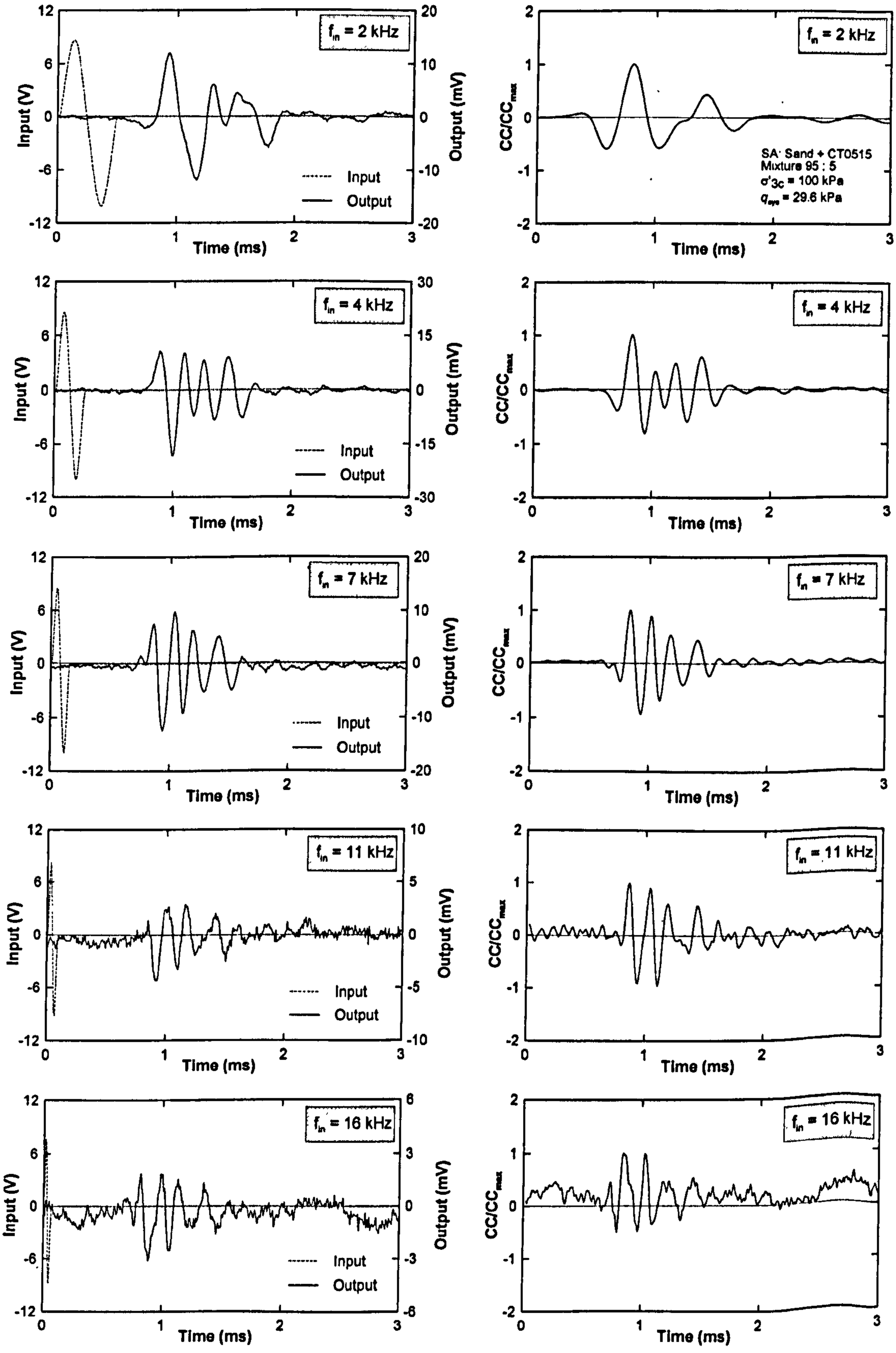

Figure 7. 7 Typical BE signals for SA with 5% rubber

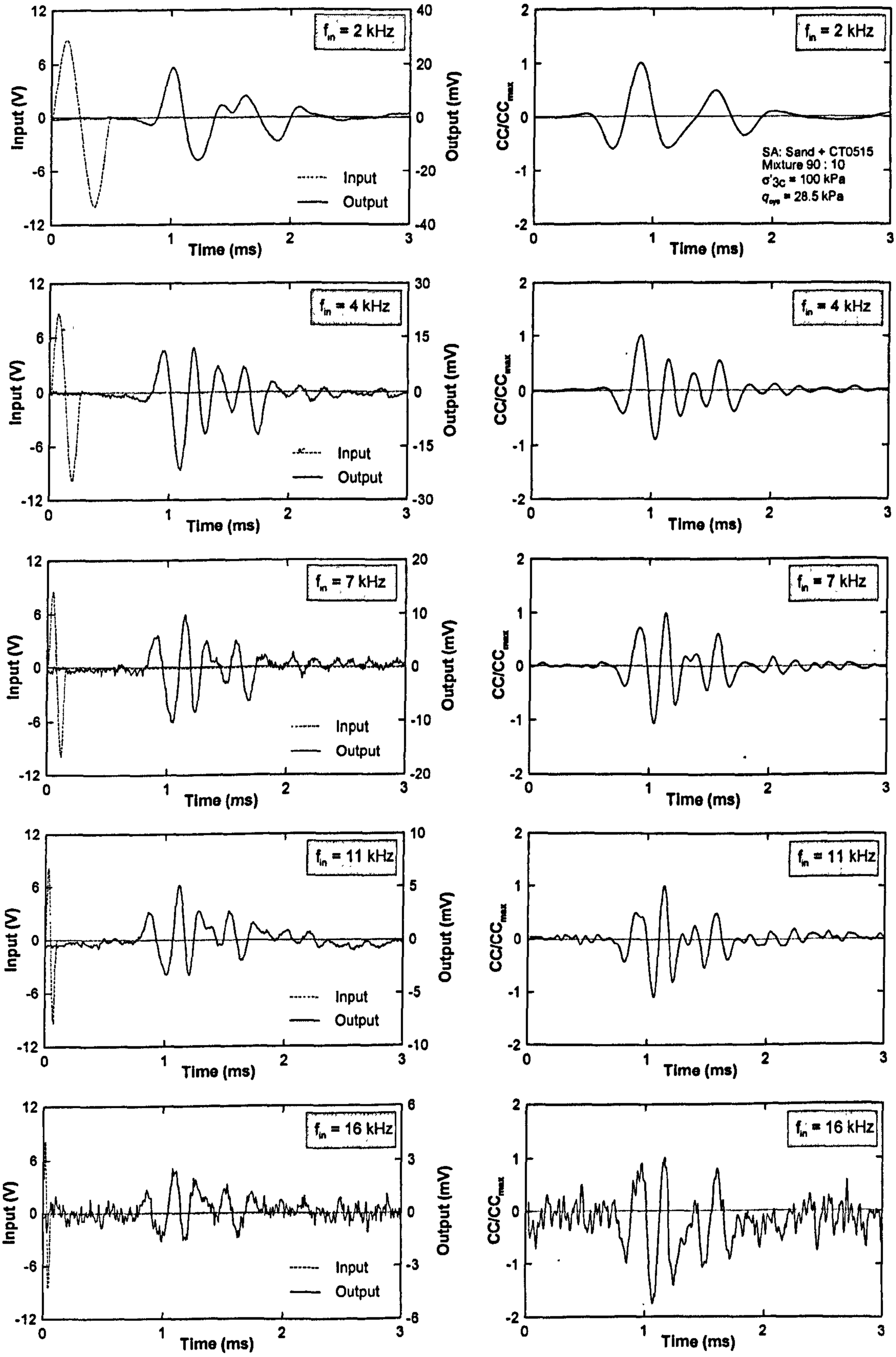

Figure 7. 8 Typical BE signals for SA with 10% rubber

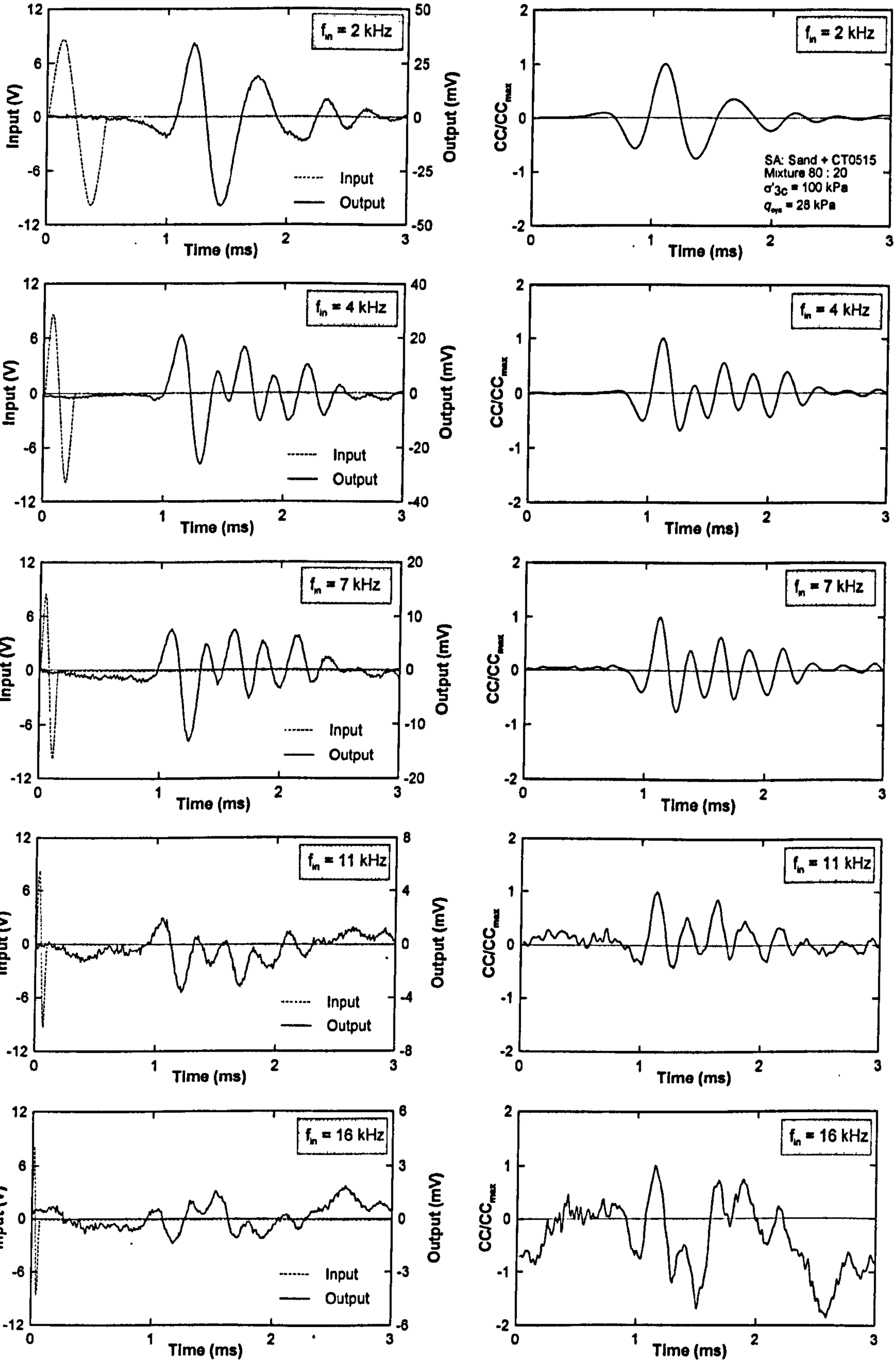

Figure 7. 9 Typical BE signals for SA with 20% rubber

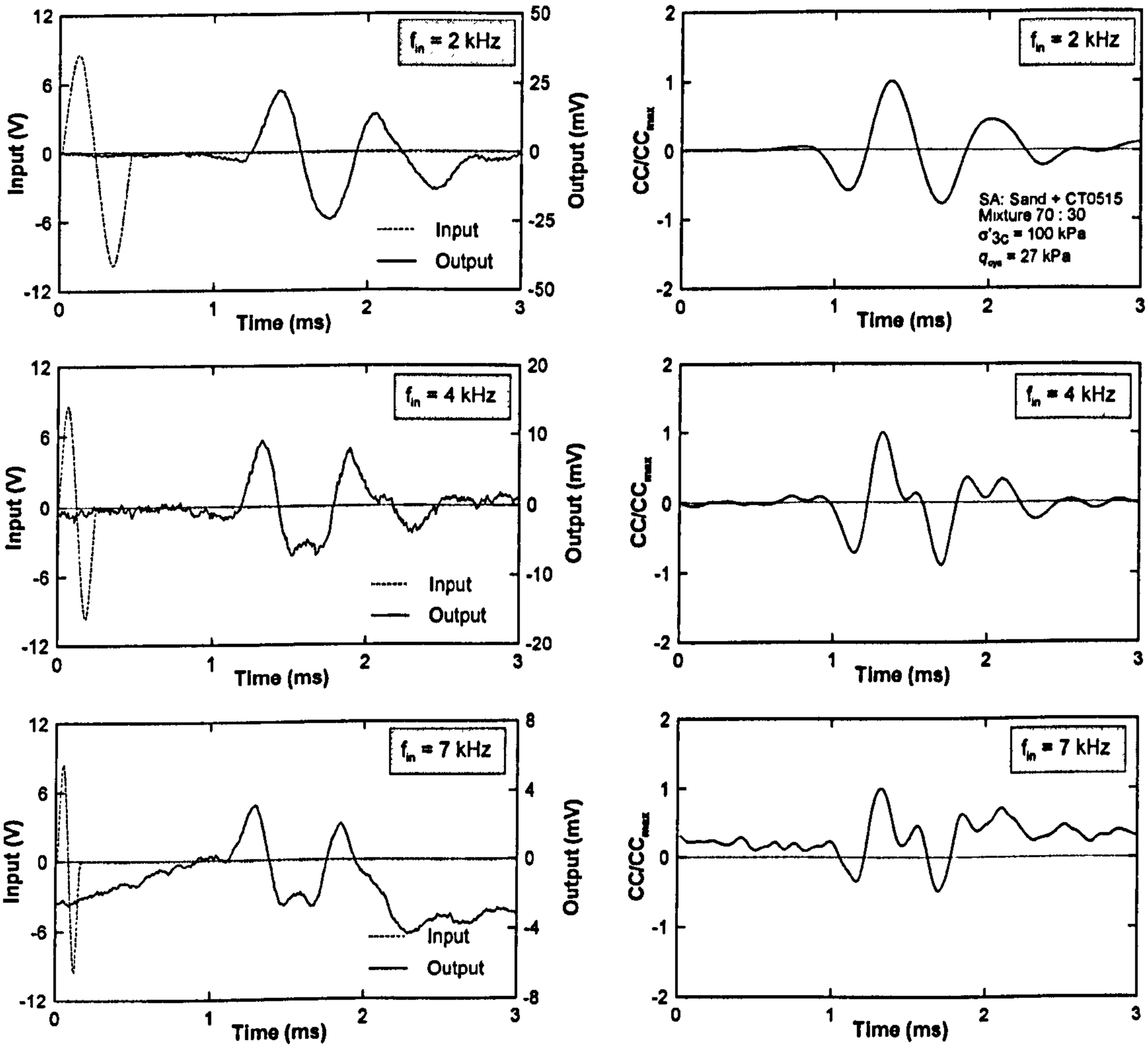

Figure 7. 10 Typical BE signals for SA with 30% rubber

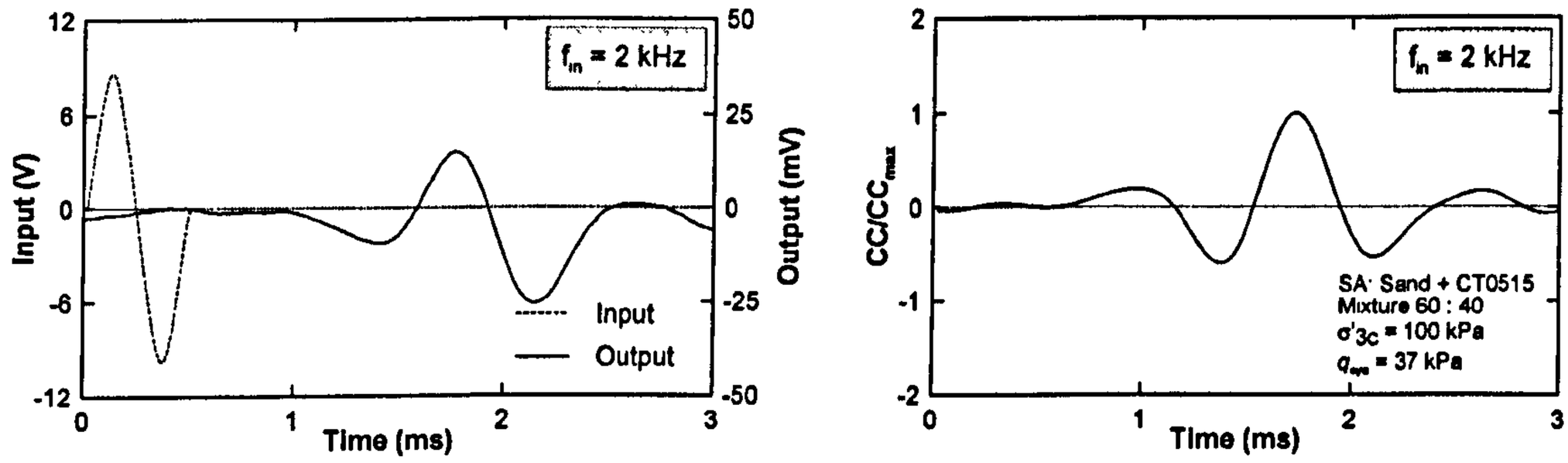

Figure 7. 11 Typical BE signals for SA with 40% rubber

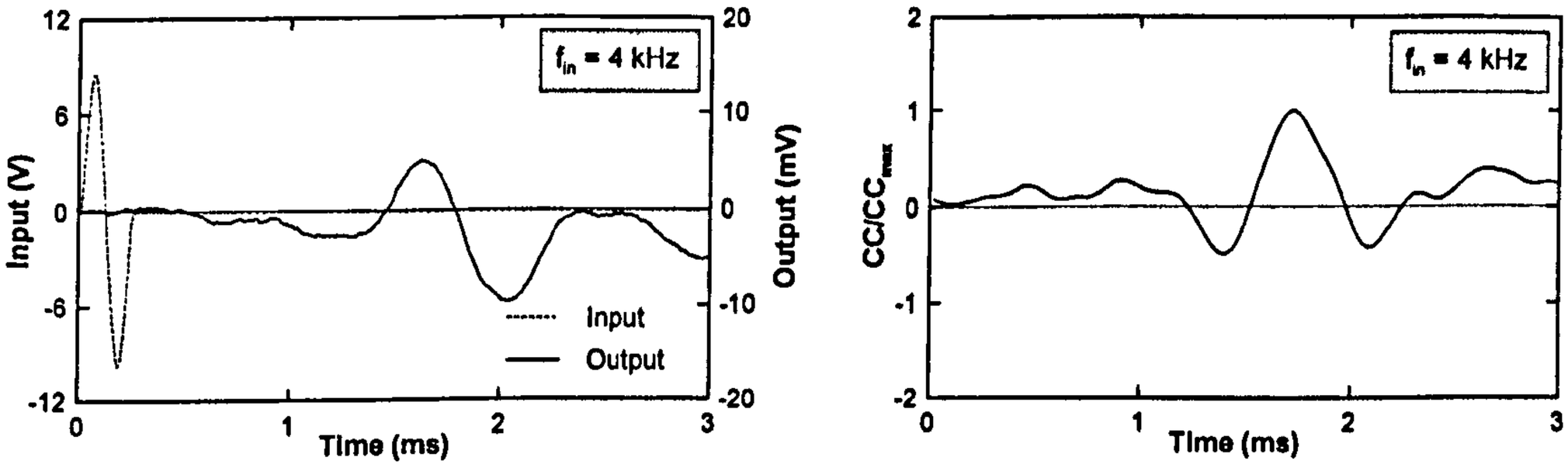

Figure 7. 12 Typical BE signals for SA with 50% rubber

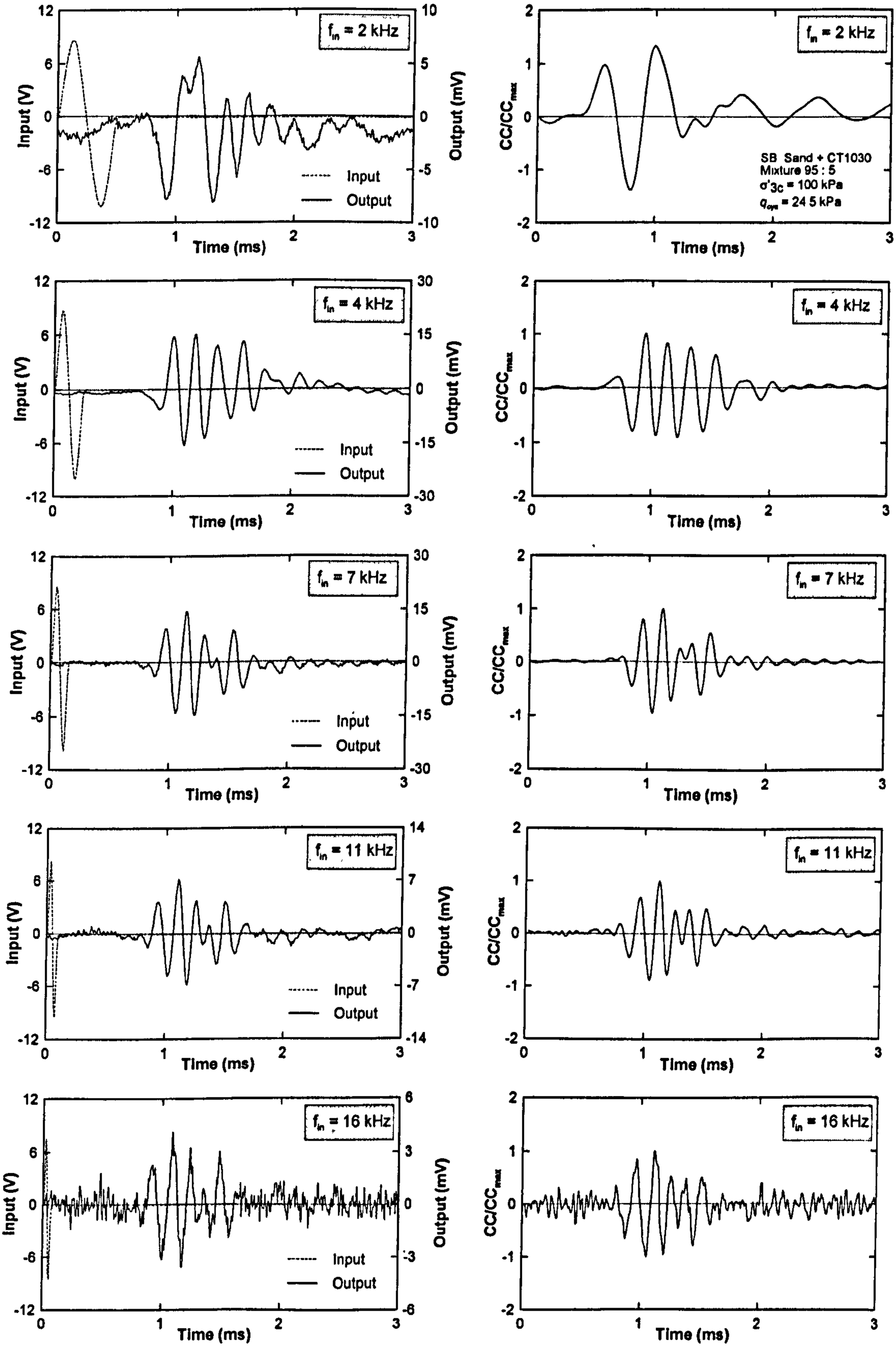

Figure 7. 13 Typical BE signals for SB with 5% rubber

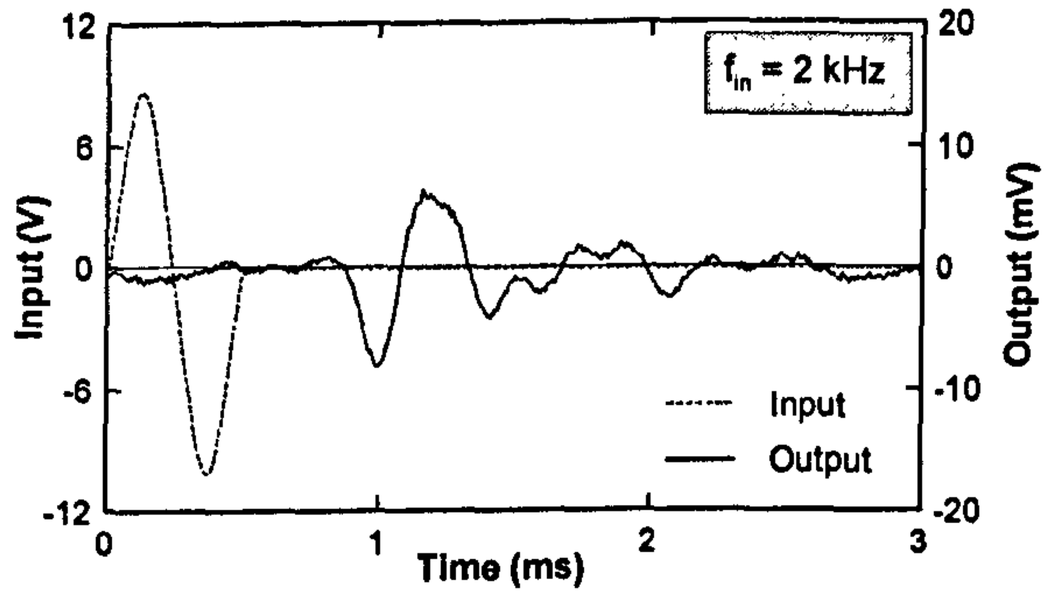

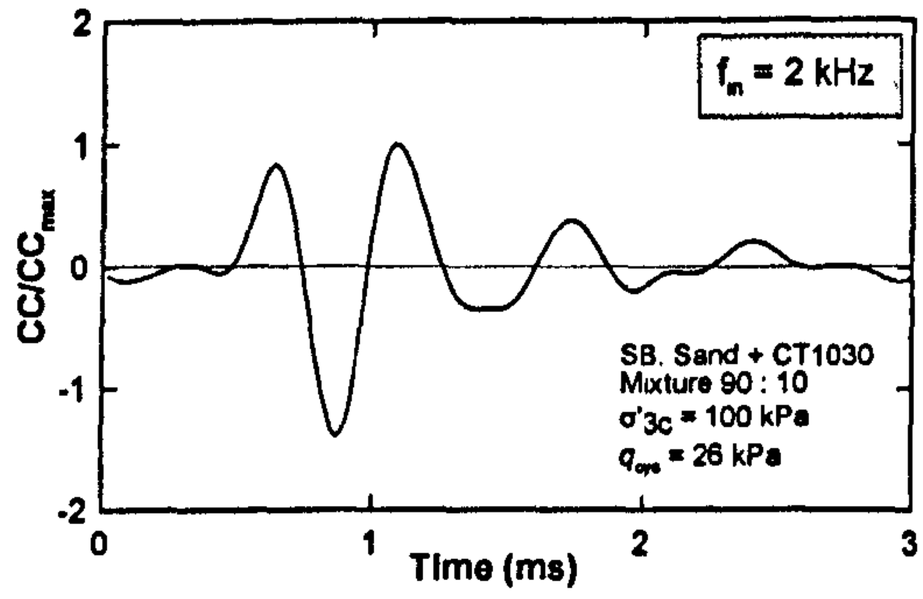

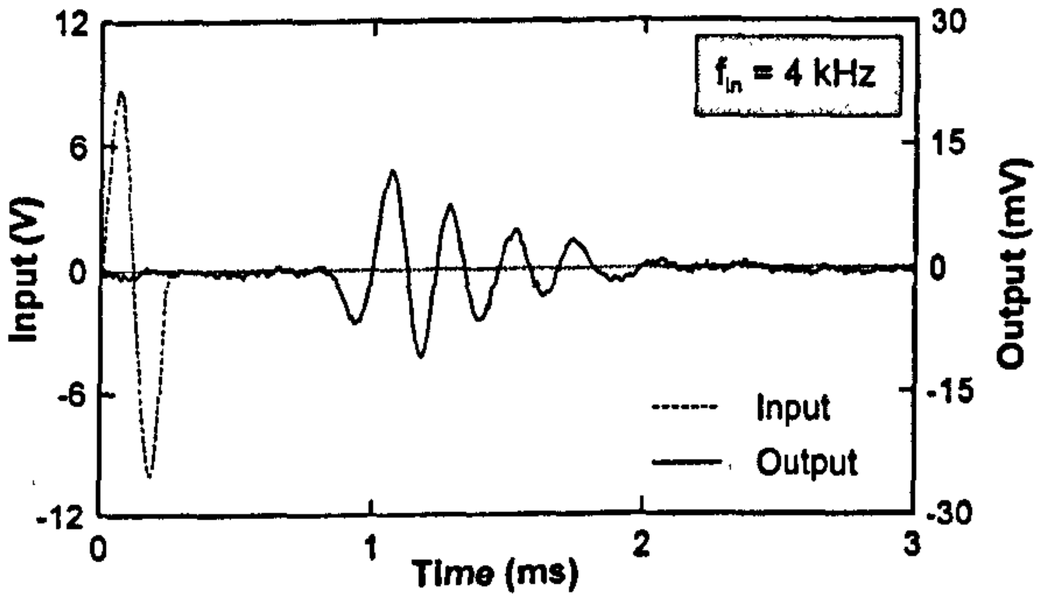

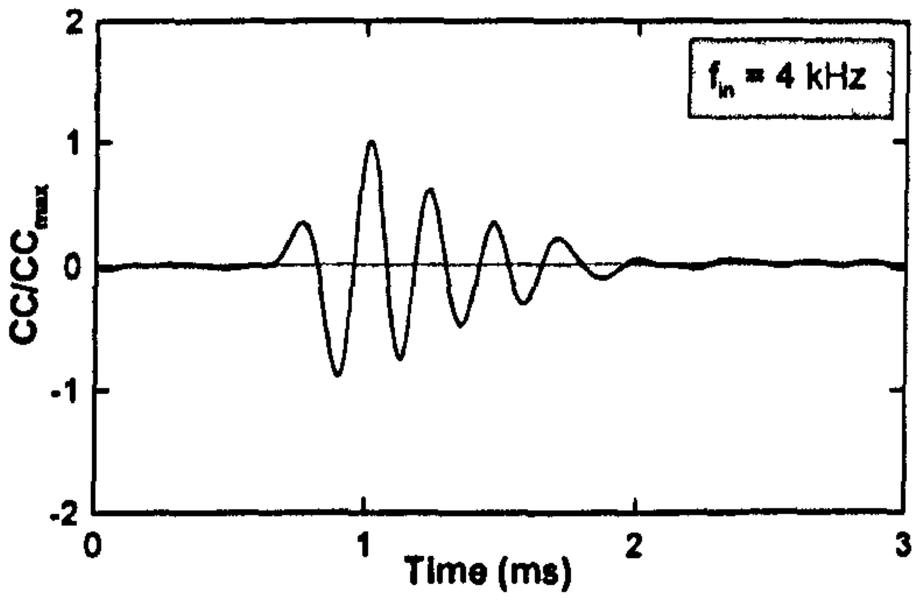

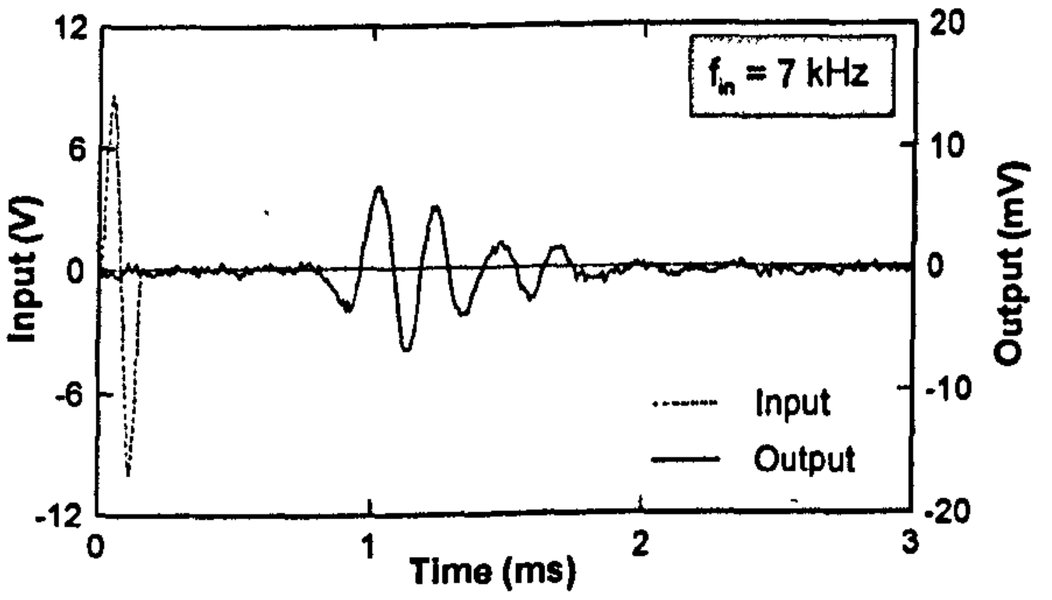

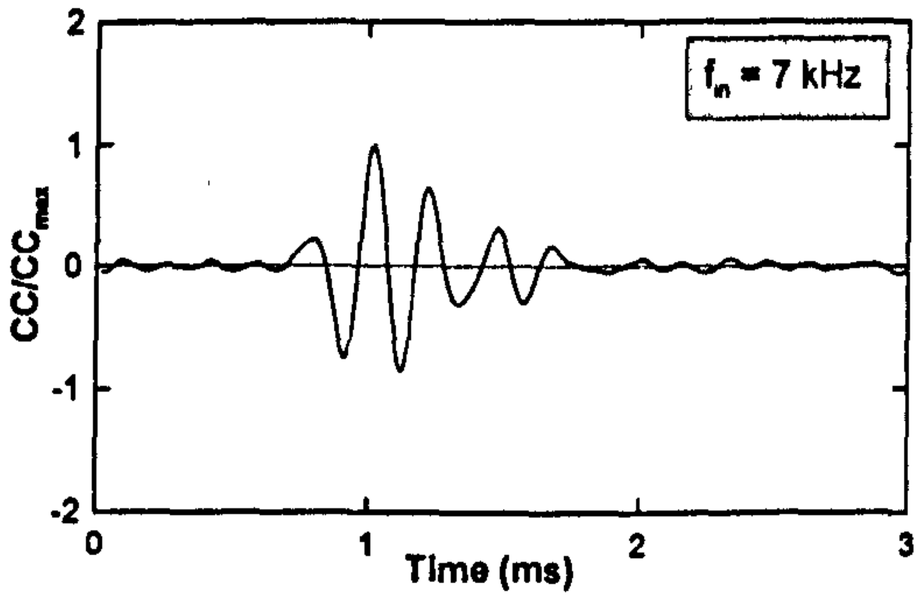

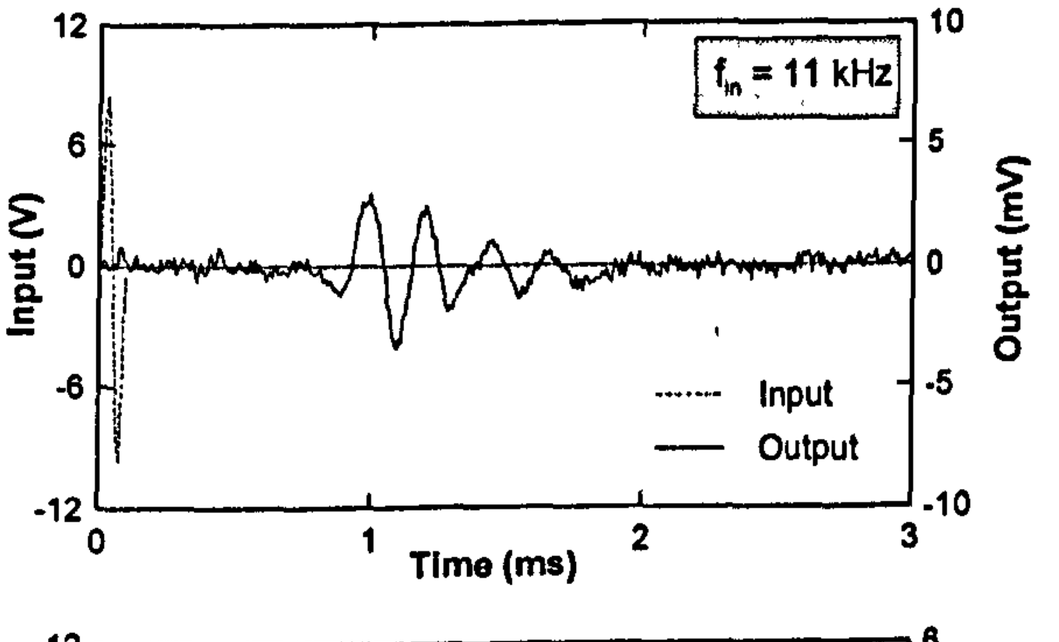

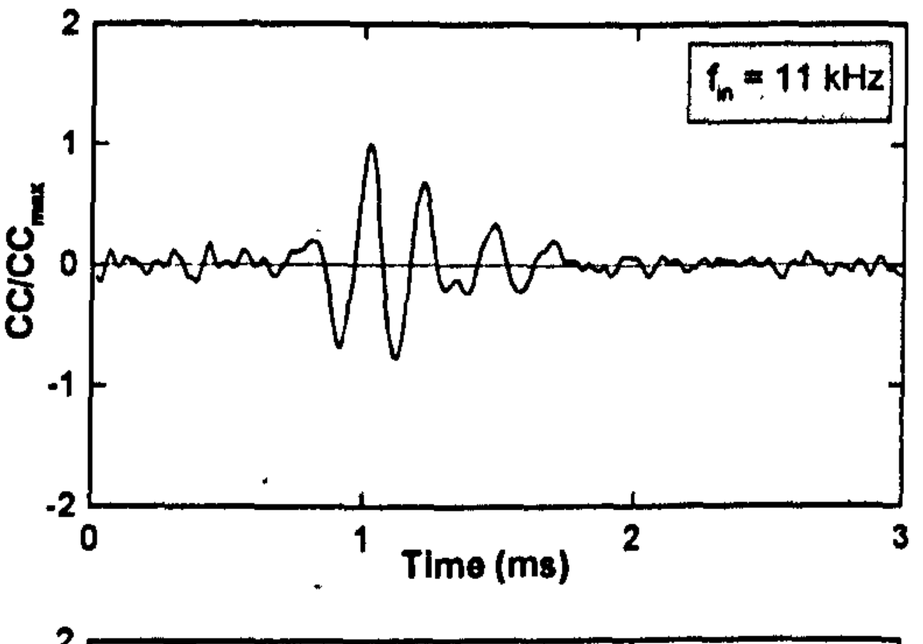

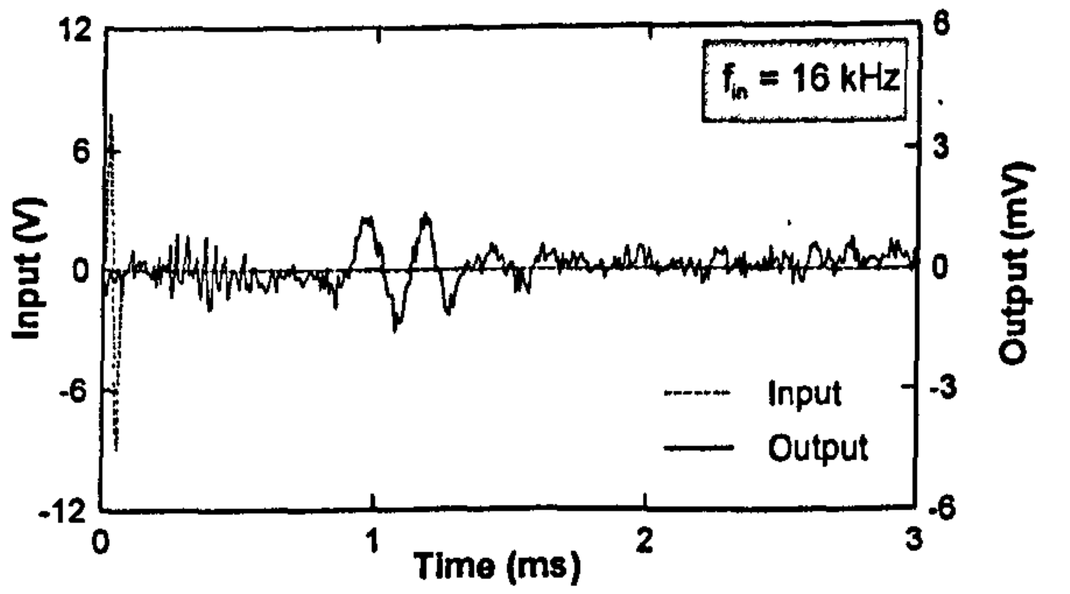

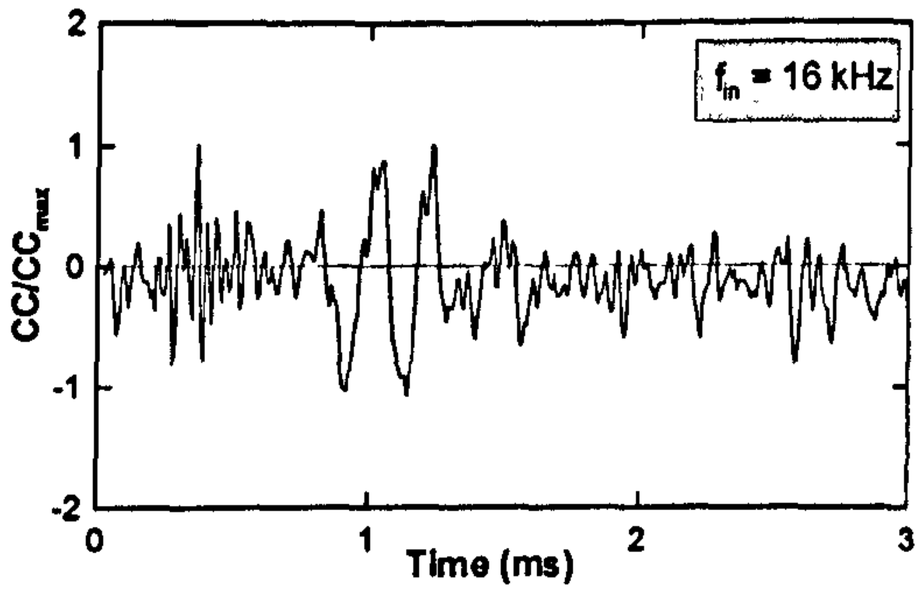

Figure 7. 14 Typical BE signals for SB with 10% rubber

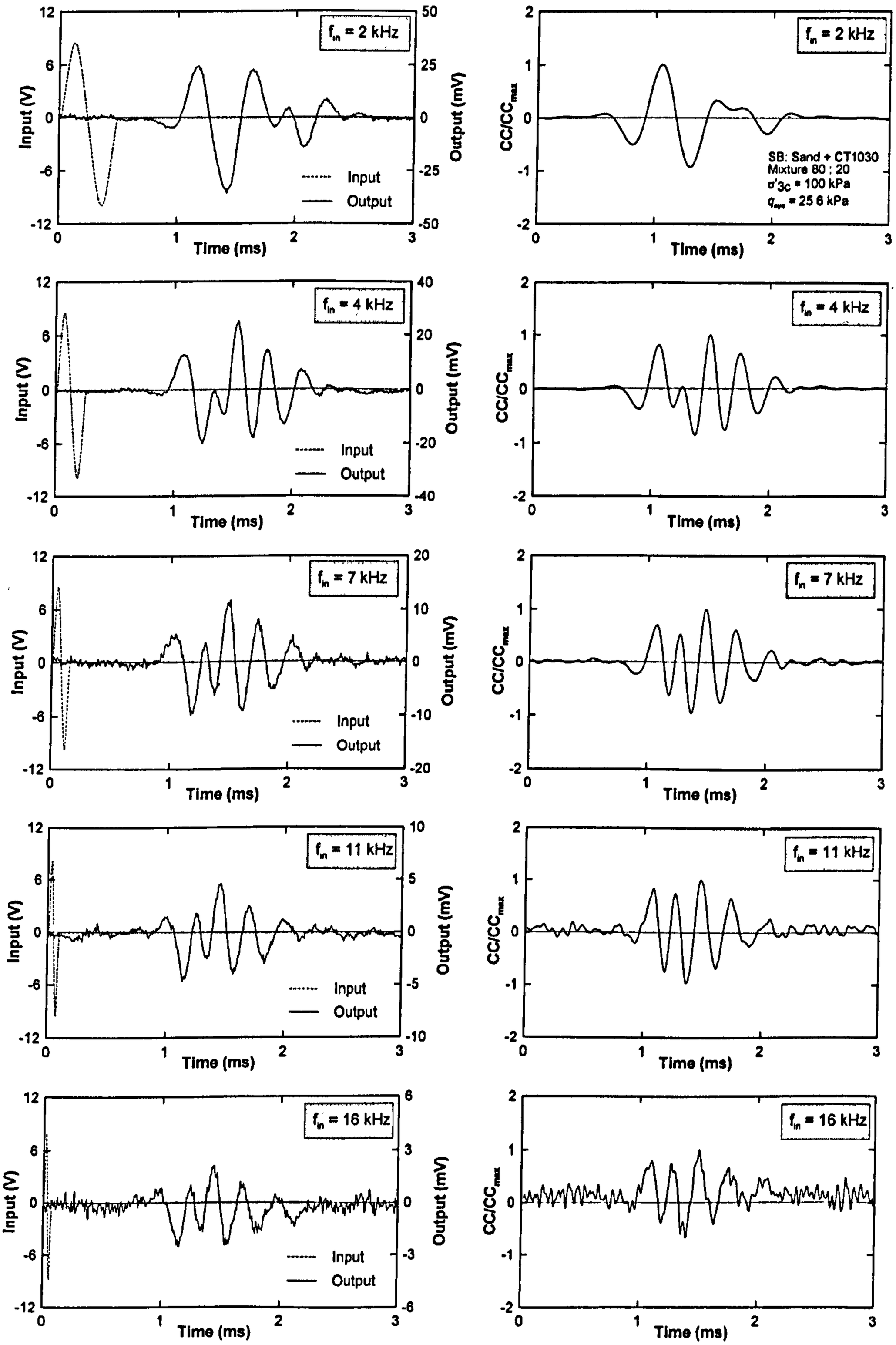

Figure 7. 15 Typical BE signals for SB with 20% rubber

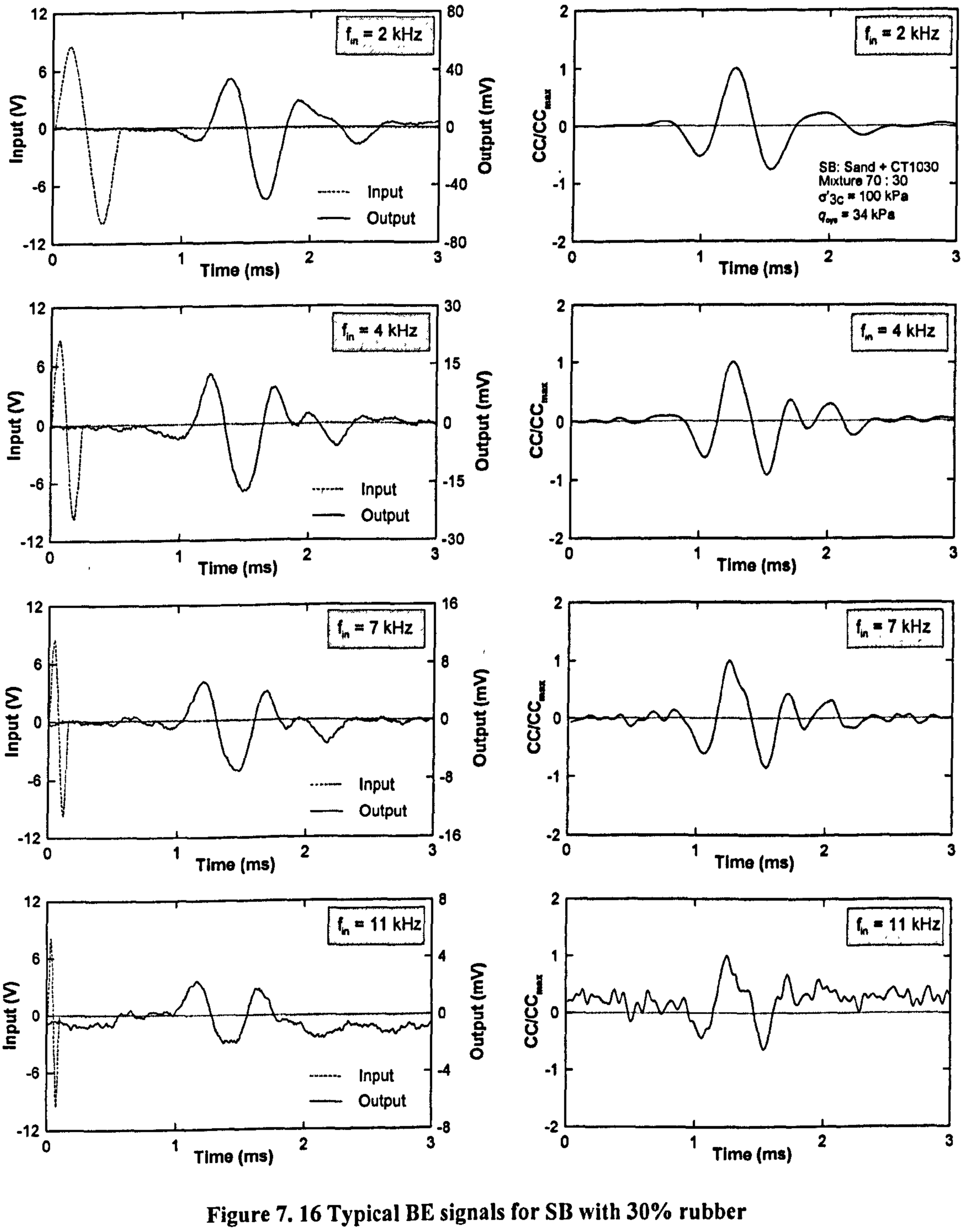

Figure 7. 16 Typical BE signals for SB with 30% rubber

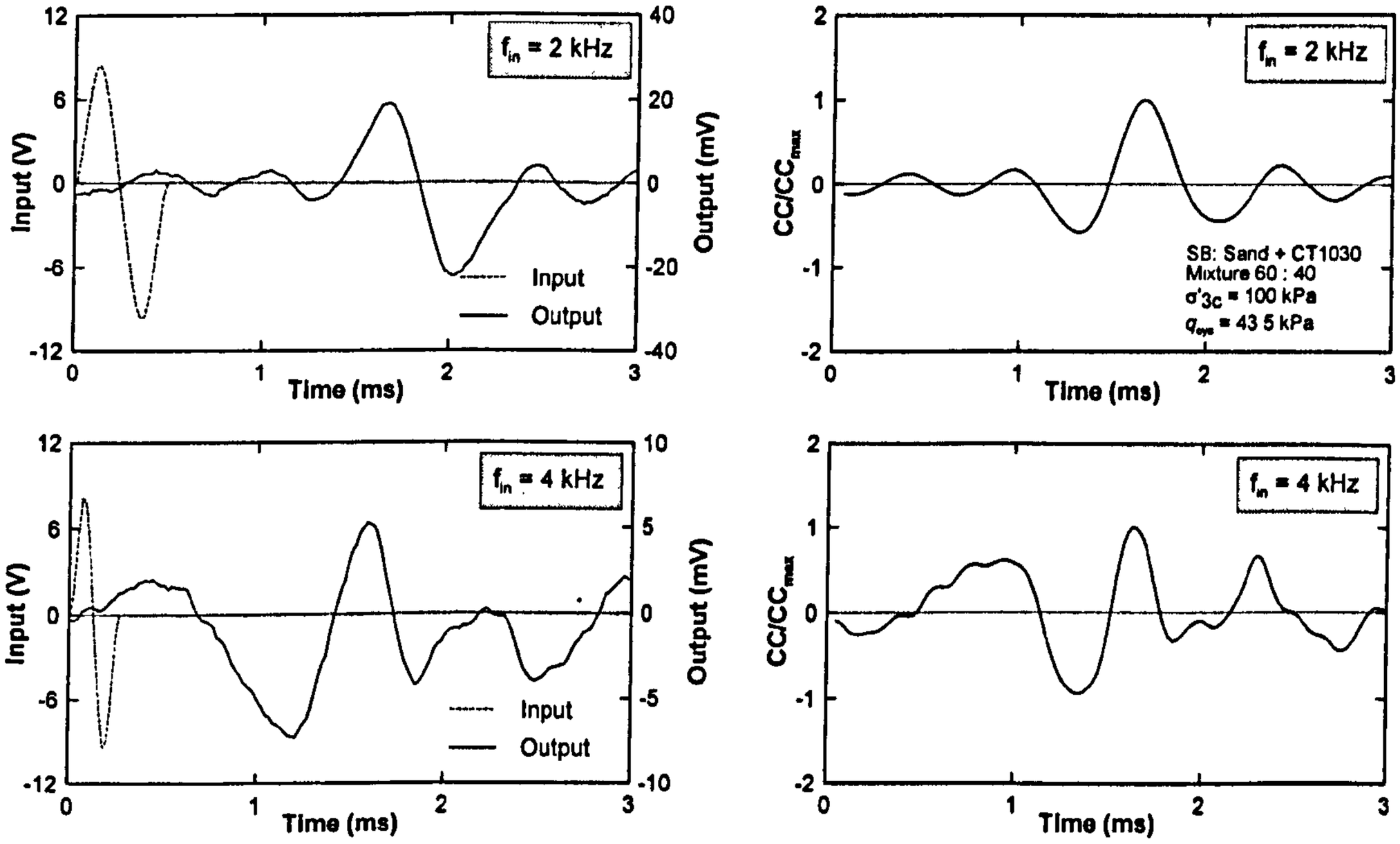

Figure 7. 17 Typical BE signals for SB with 40% rubber

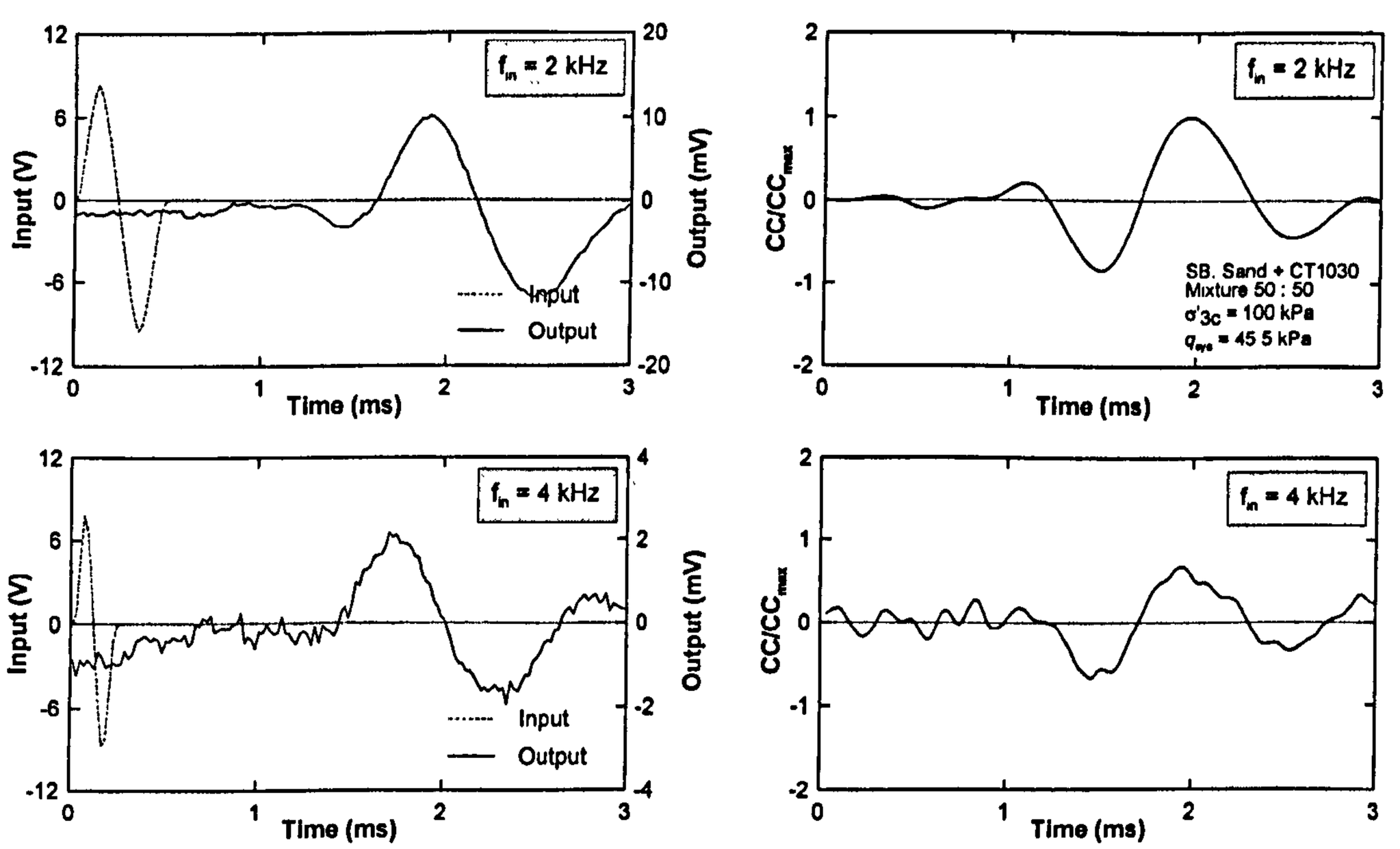

Figure 7. 18 Typical BE signals for SB with 50% rubber

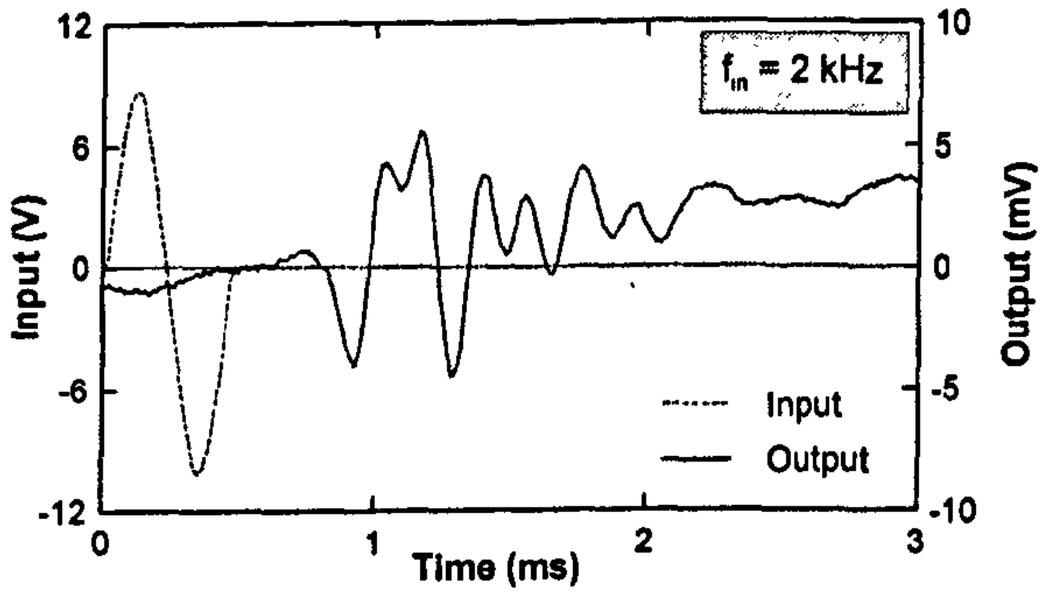

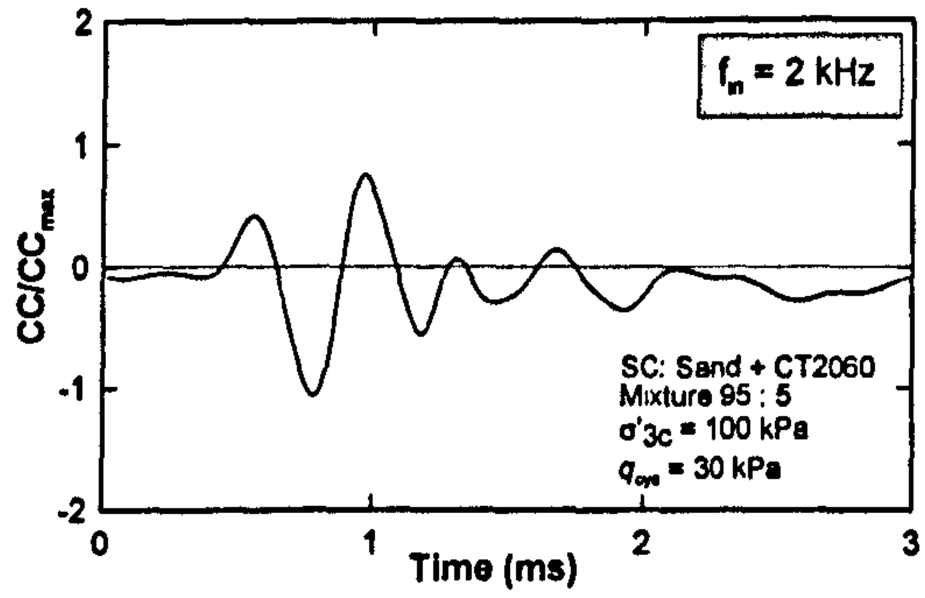

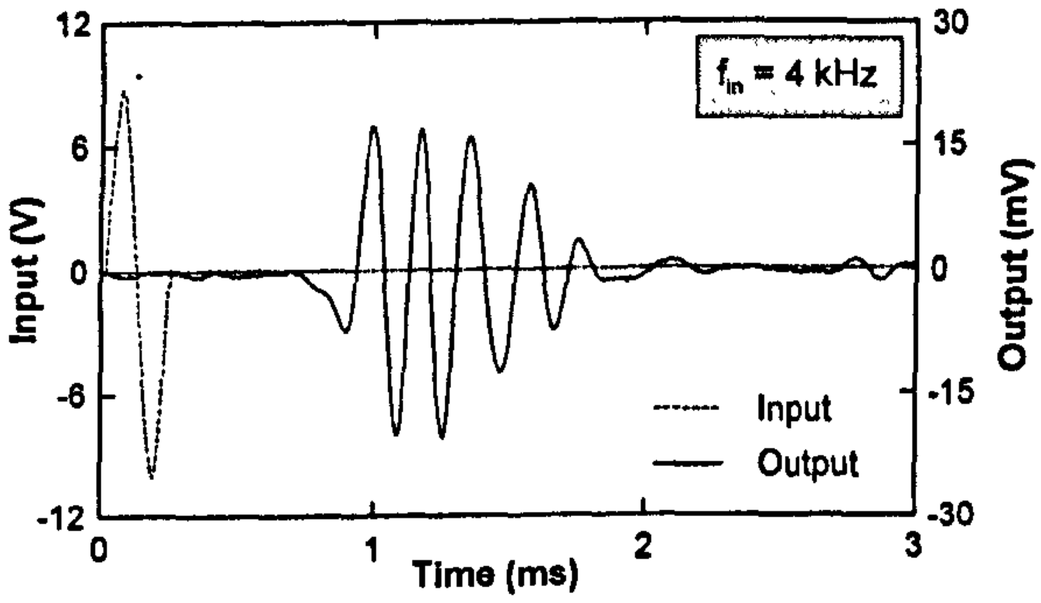

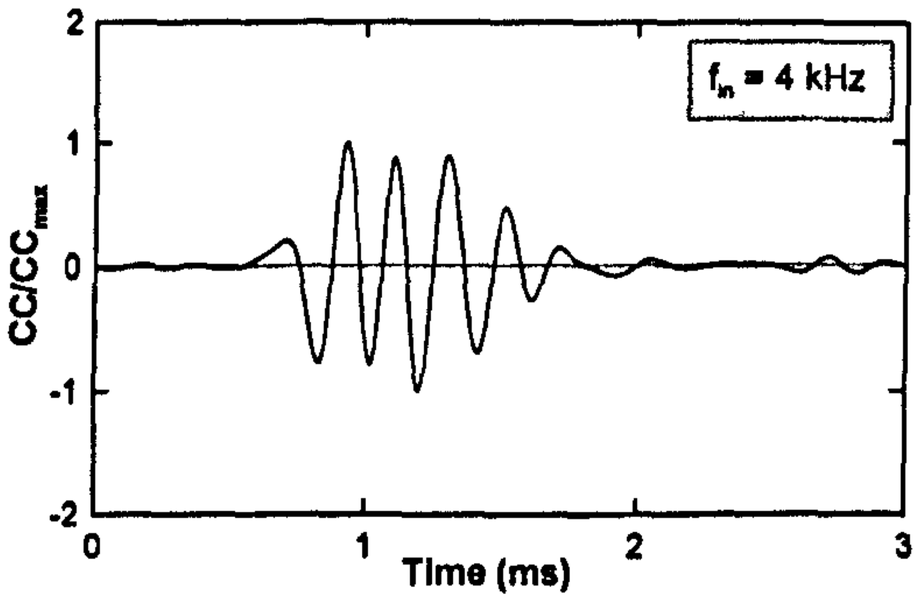

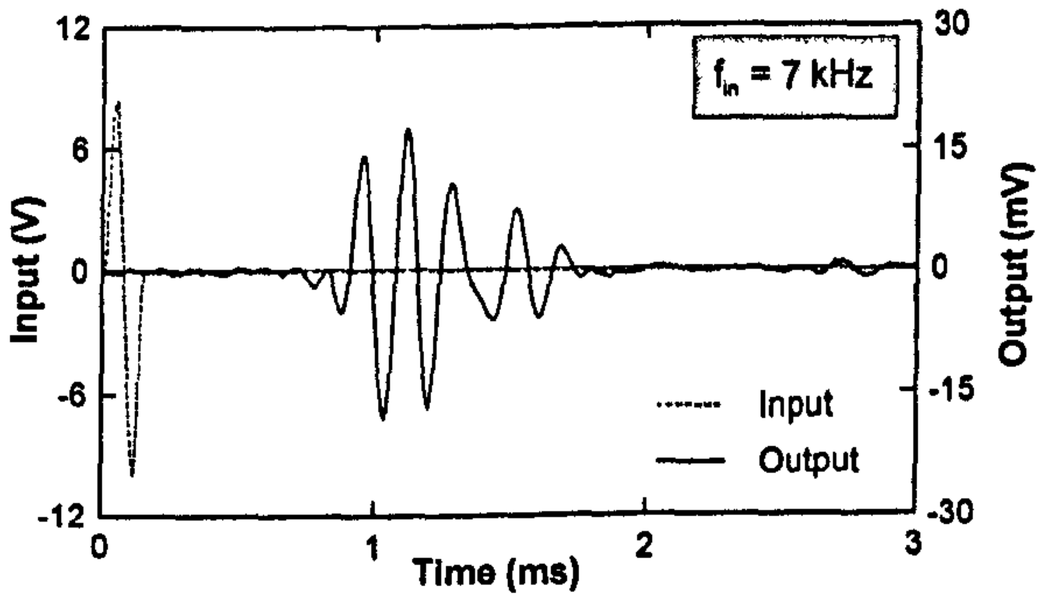

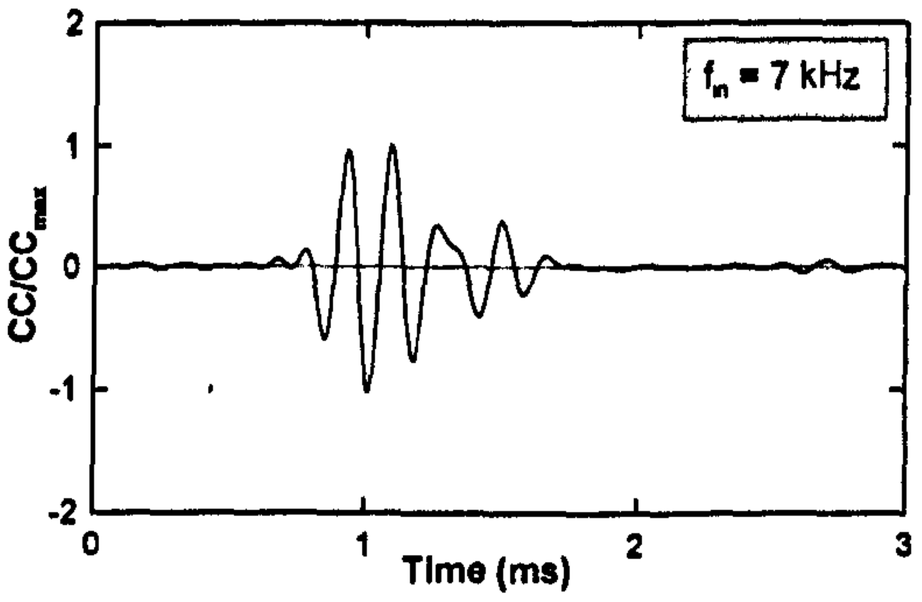

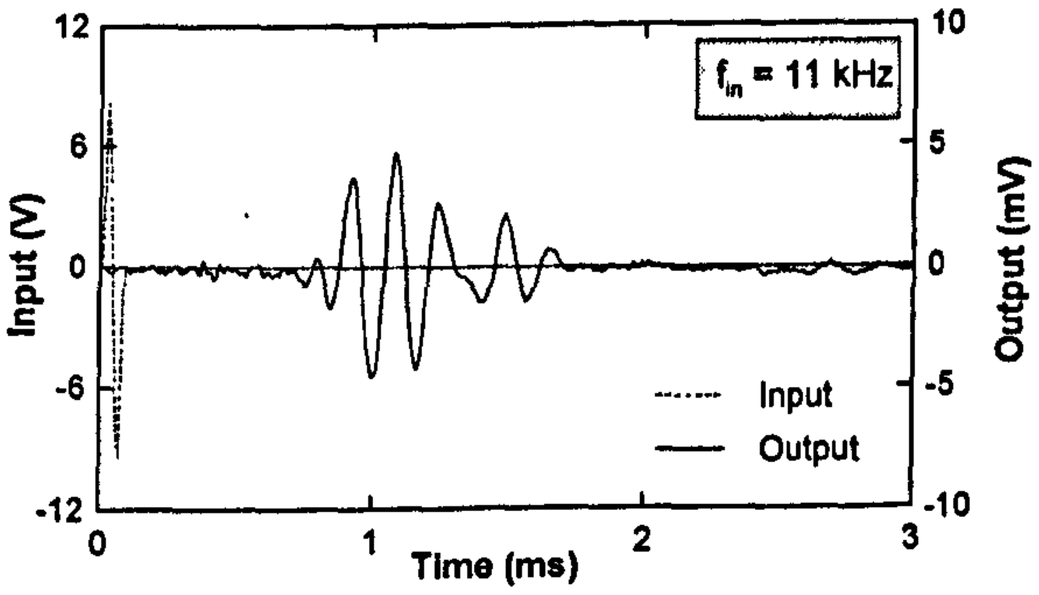

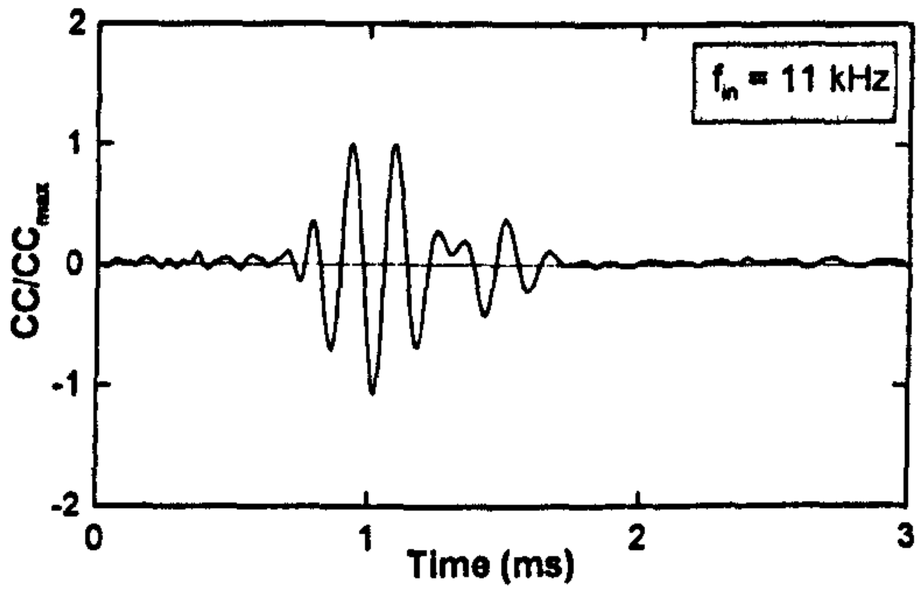

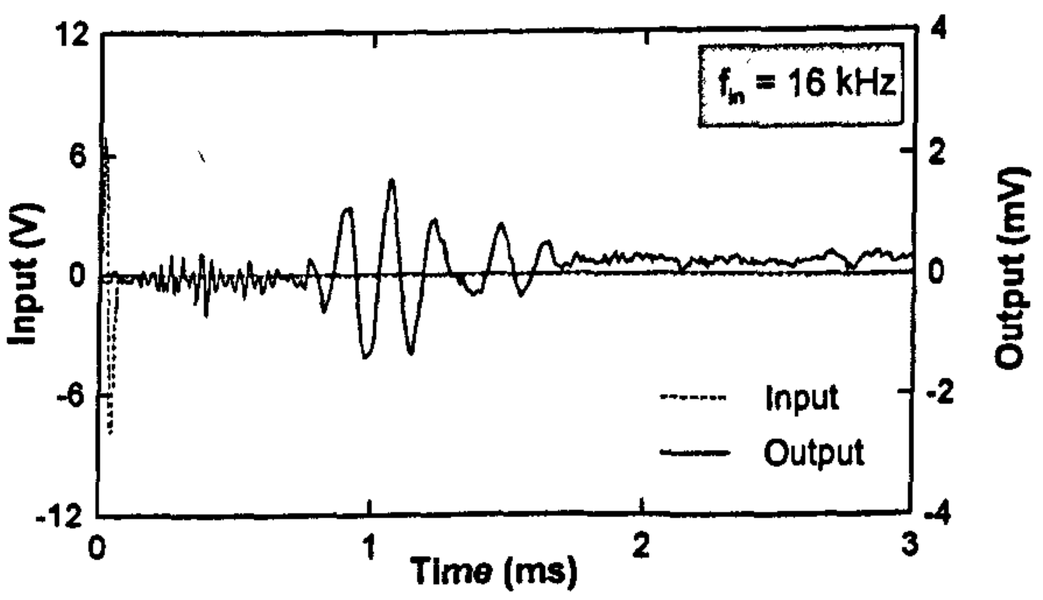

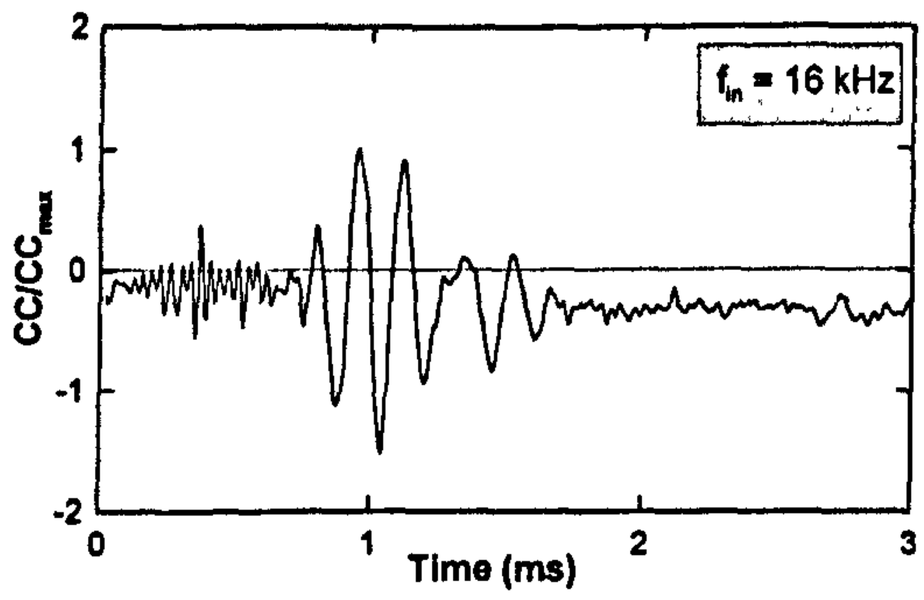

Figure 7. 19 Typical BE signals for SC with 5% rubber

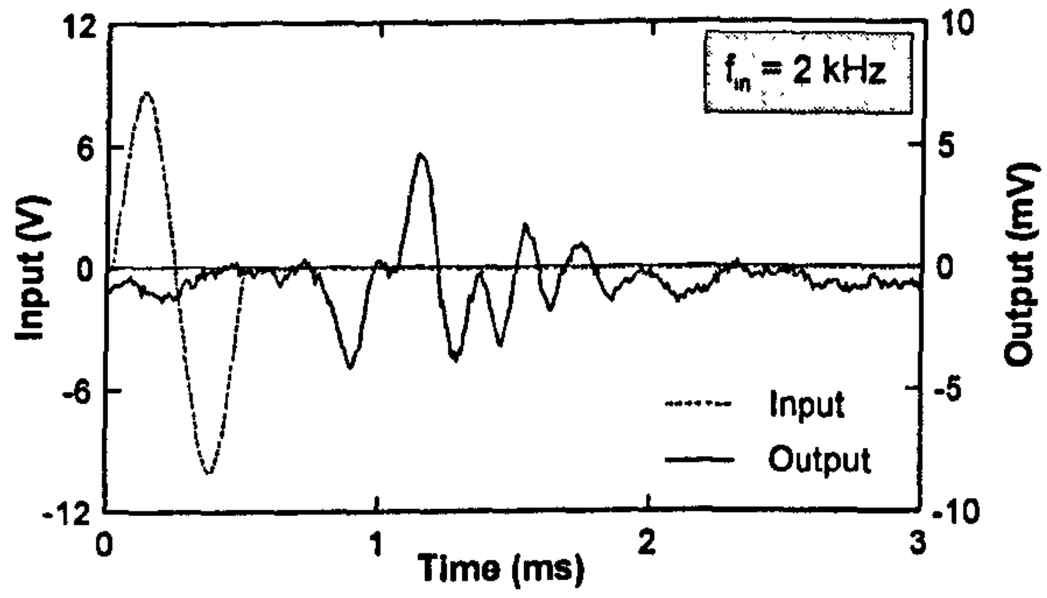

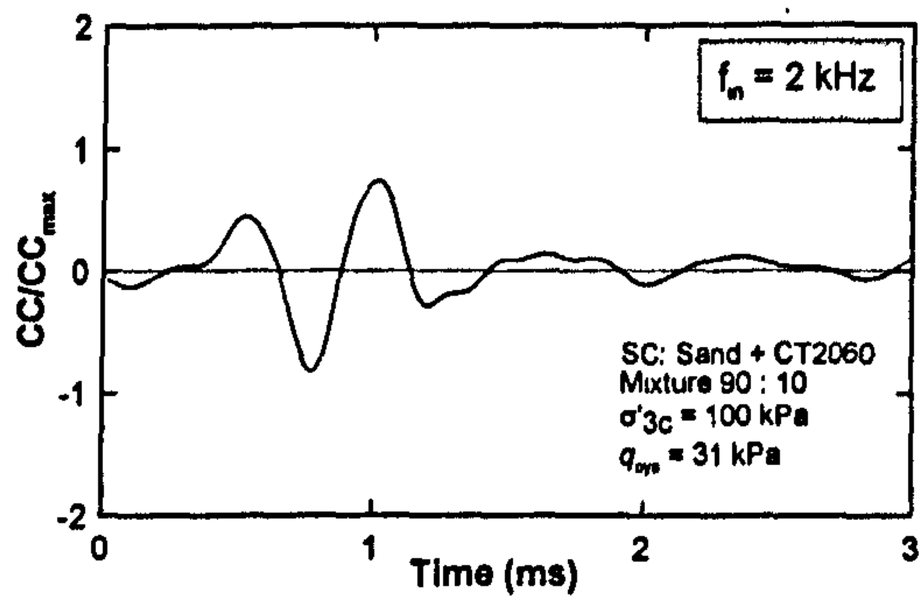

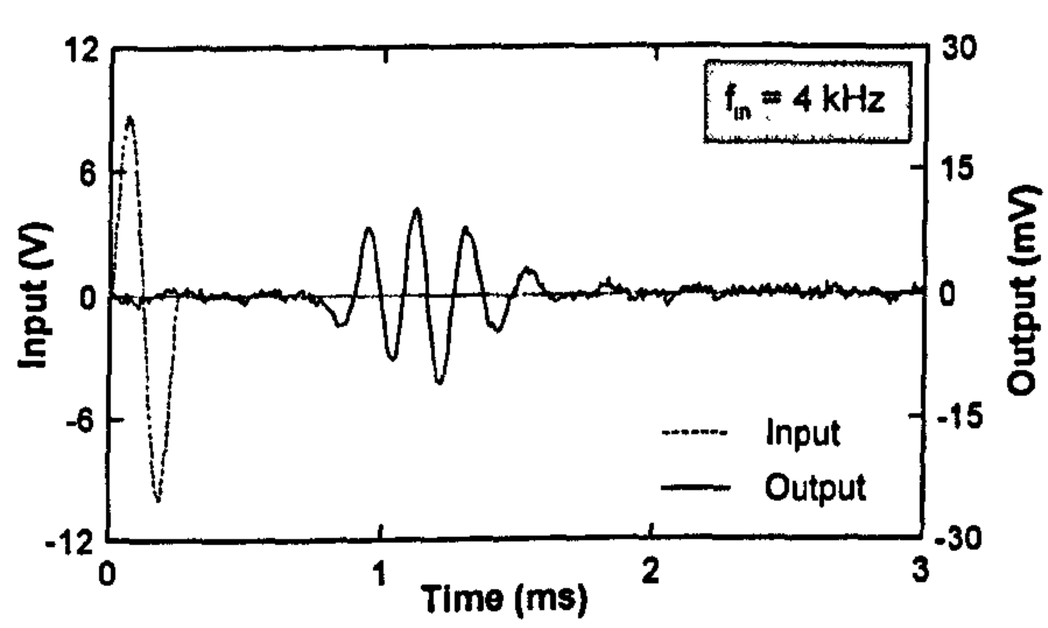

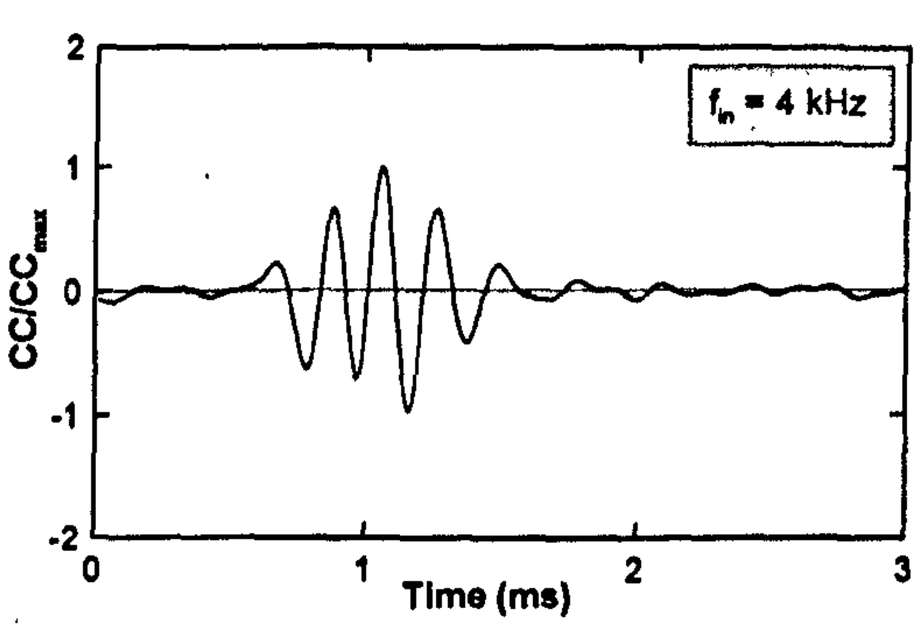

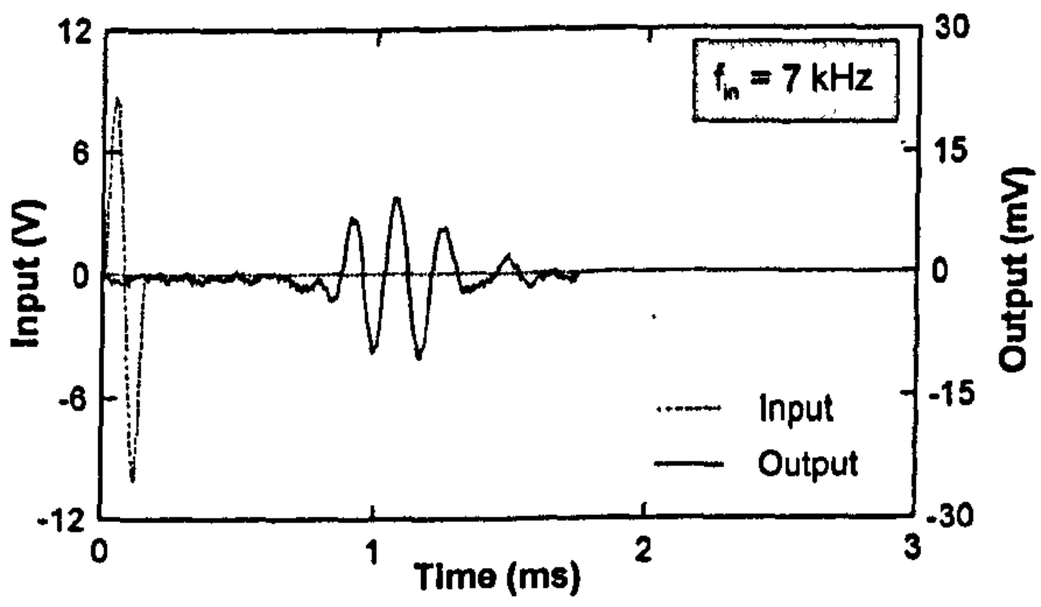

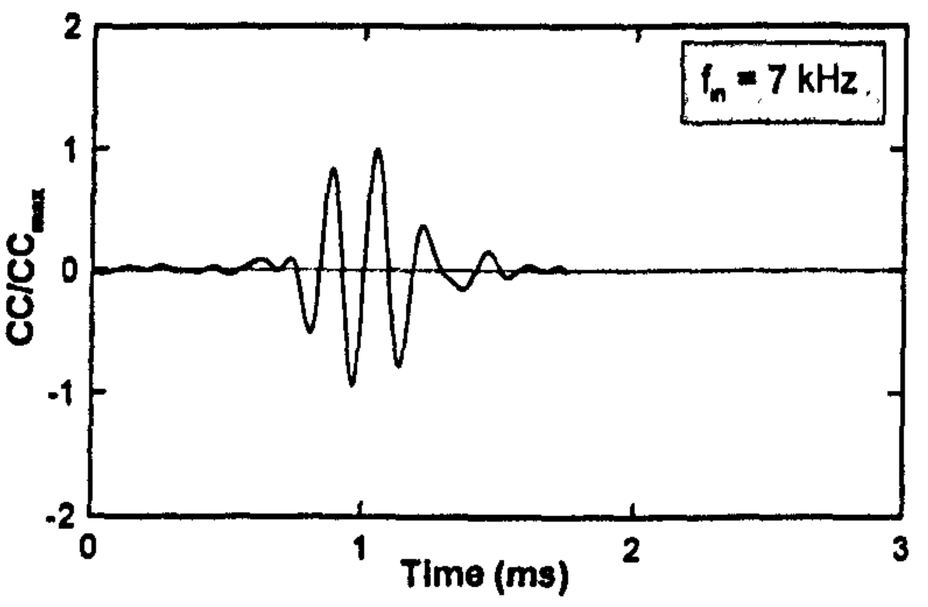

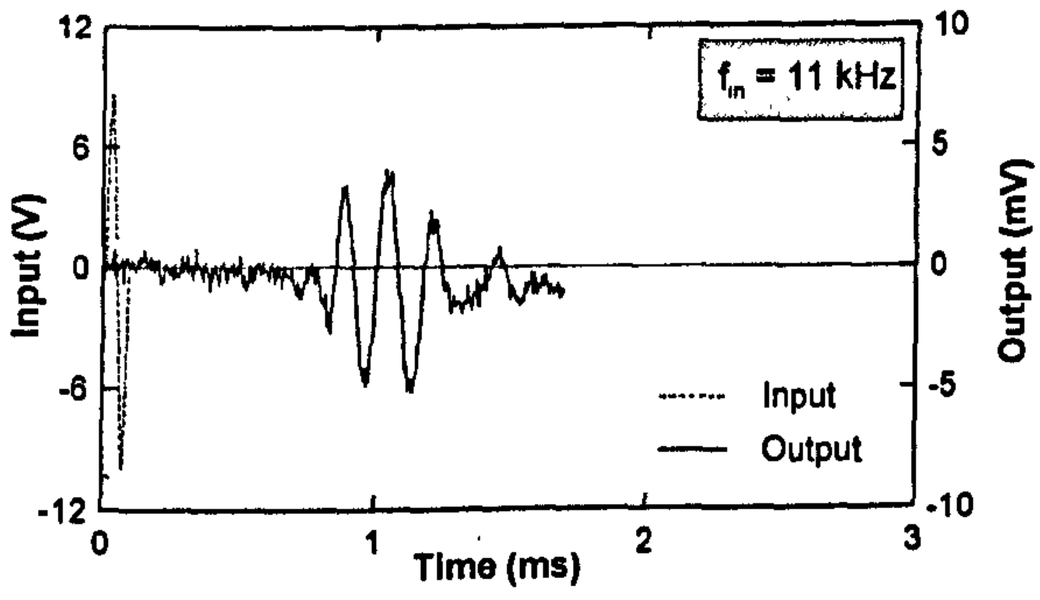

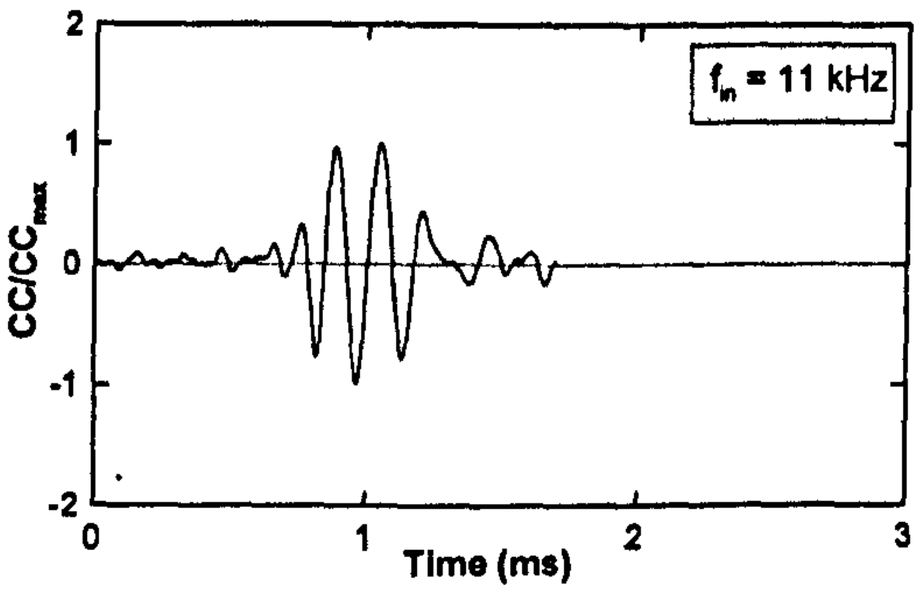

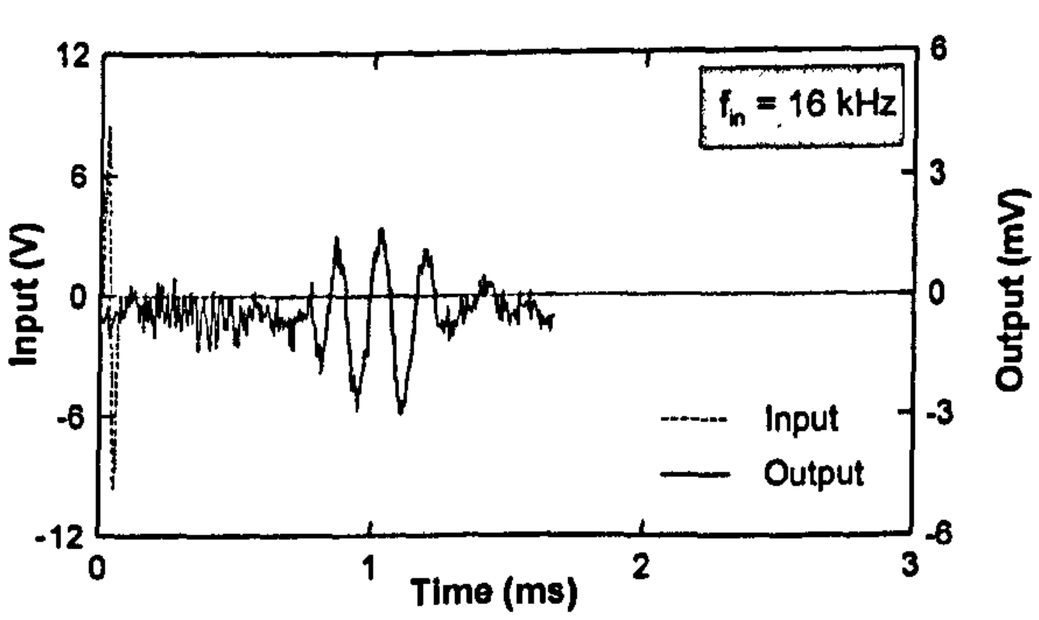

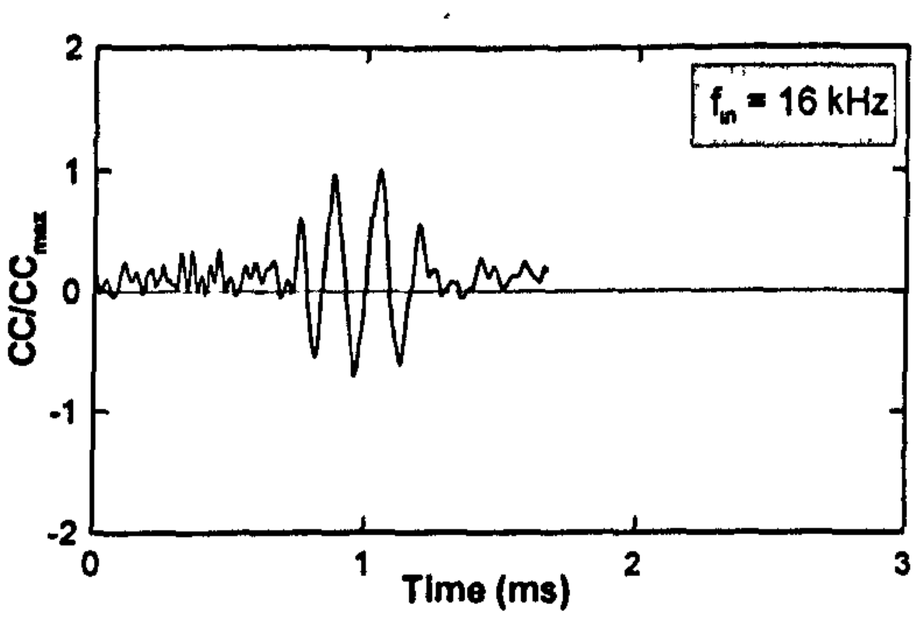

Figure 7. 20 Typical BE signals for SC with 10% rubber

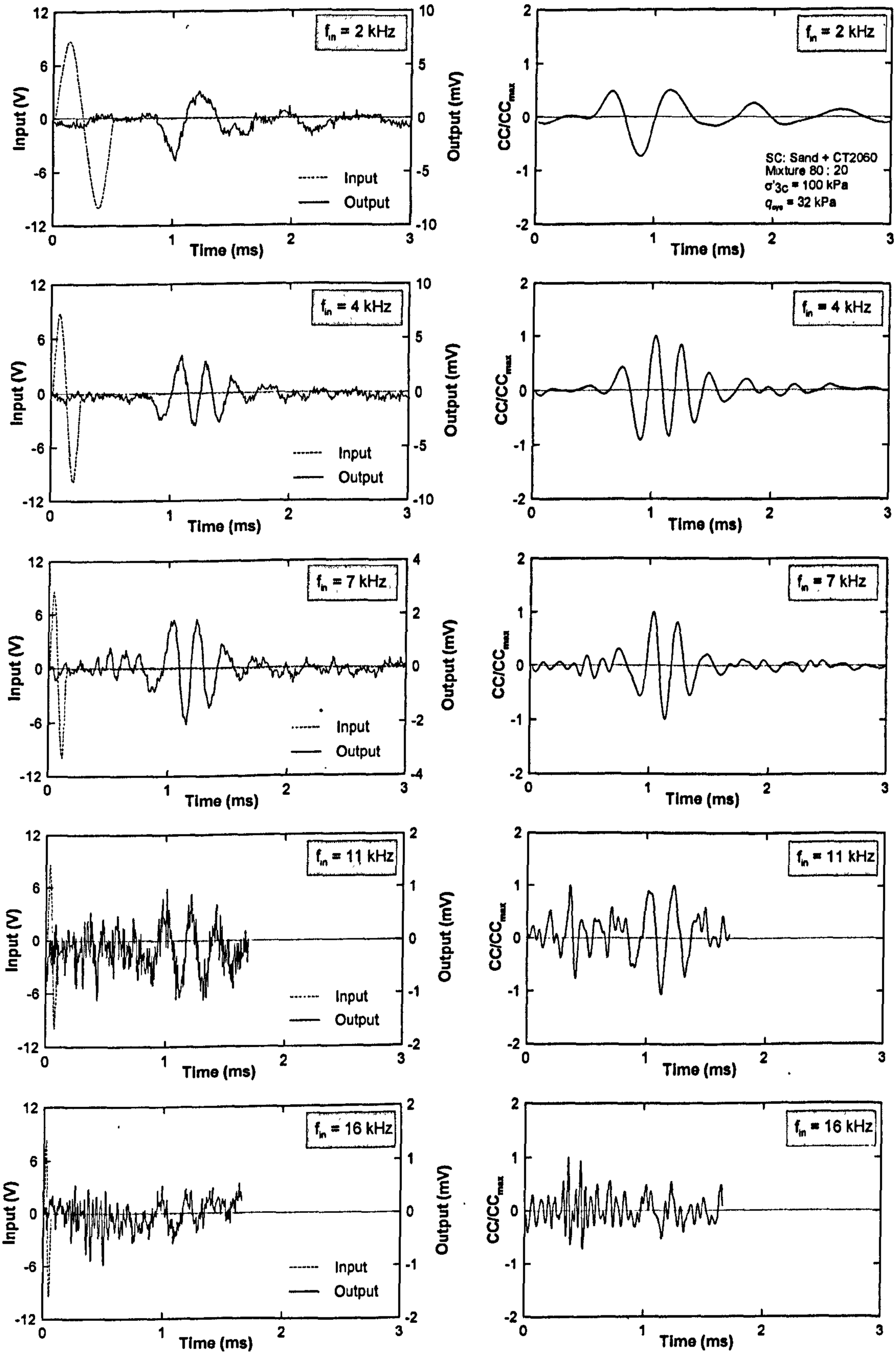

Figure 7. 21 Typical BE signals for SC with 20% rubber

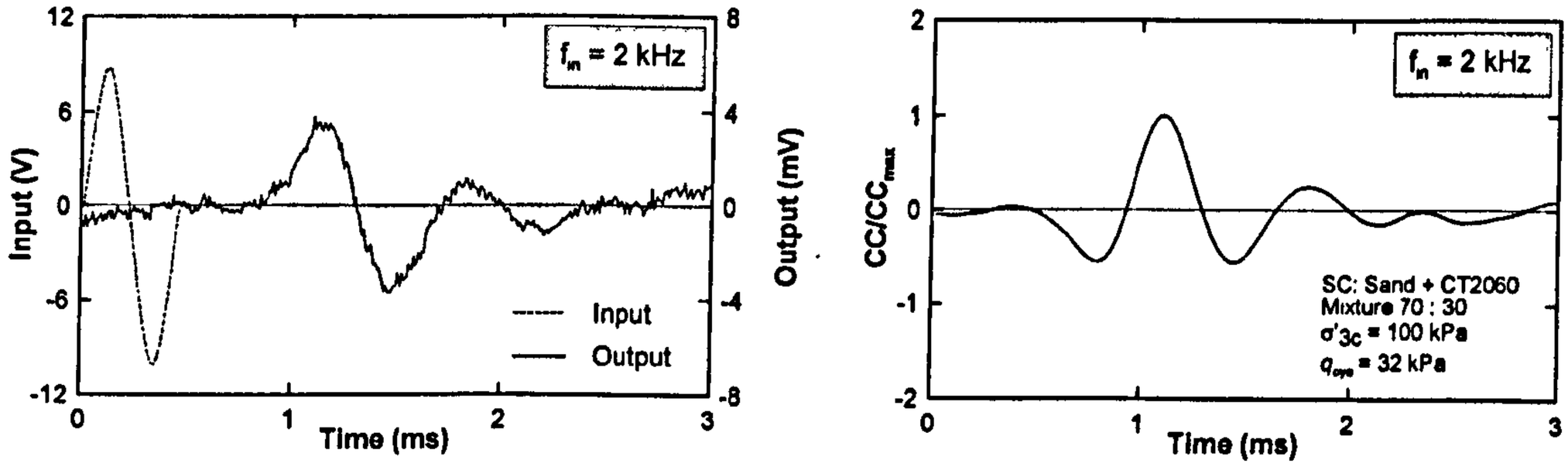

Figure 7. 22 Typical BE signals for SC with 30% rubber

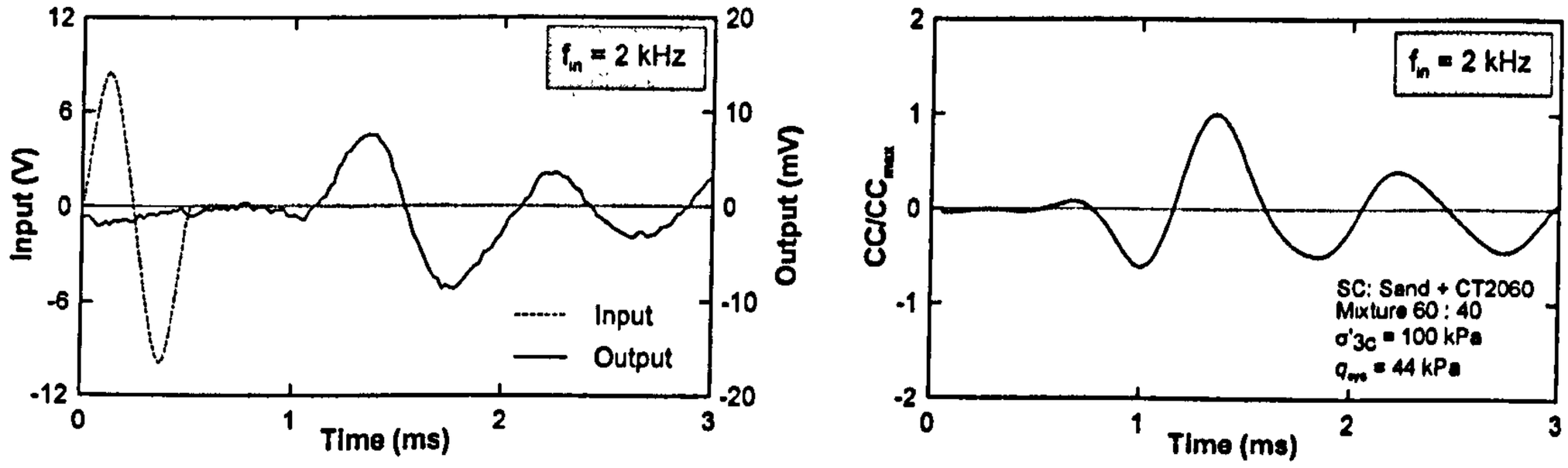

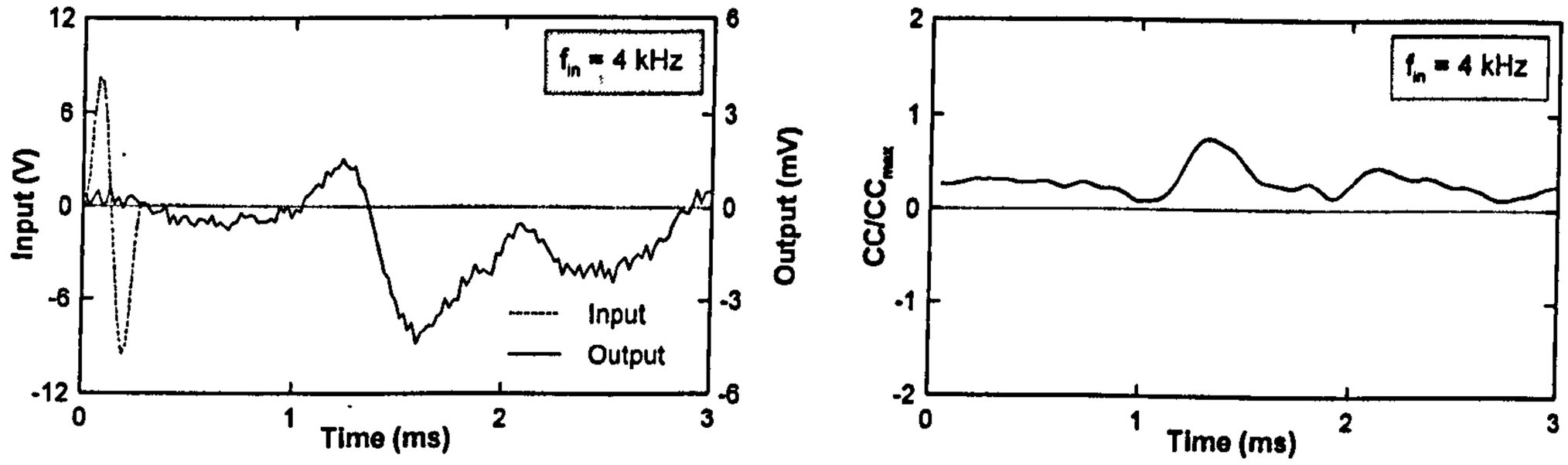

Figure 7. 23 Typical BE signals for SC with 40% rubber

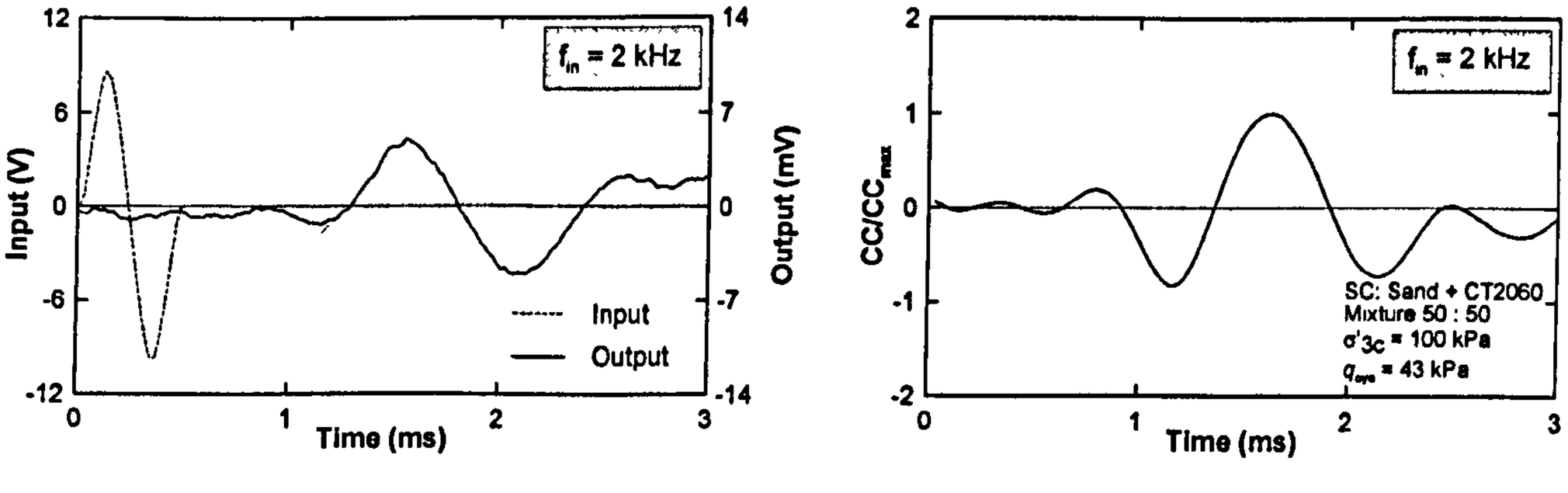

Figure 7. 24 Typical BE signals for SC with 50% rubber

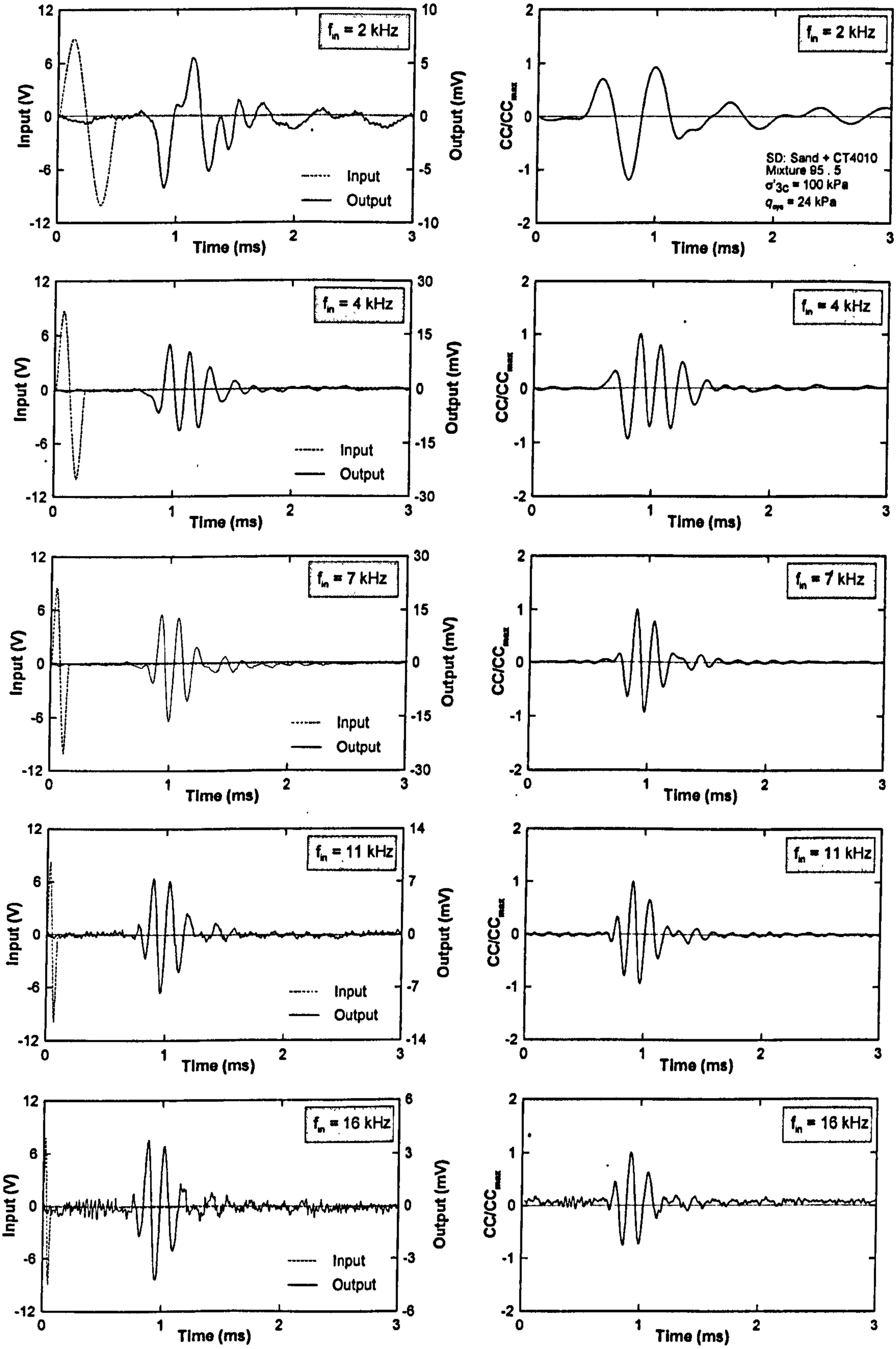

Figure 7. 25 Typical BE signals for SD with 5% rubber

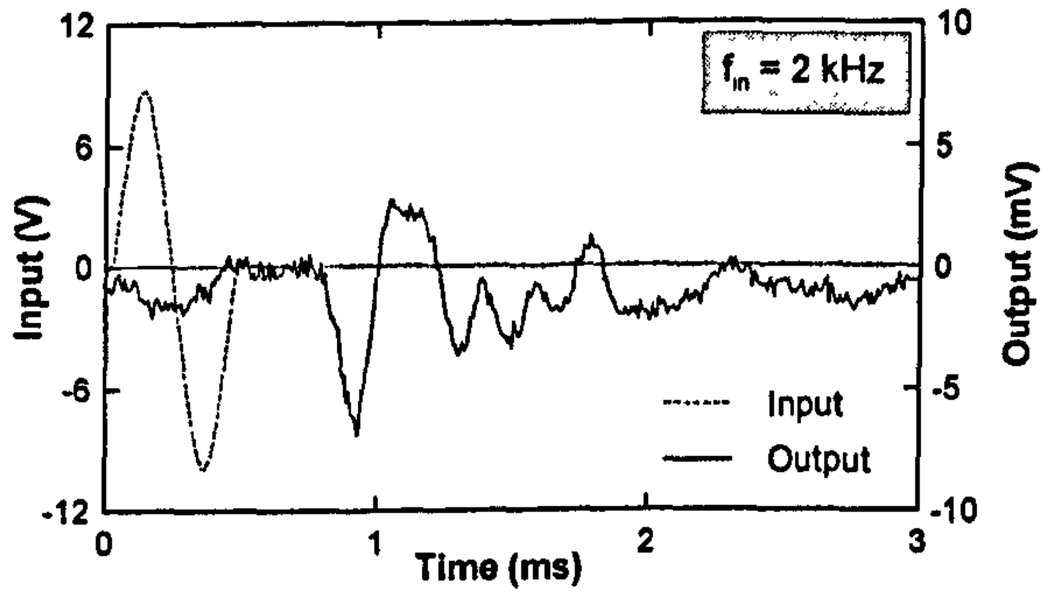

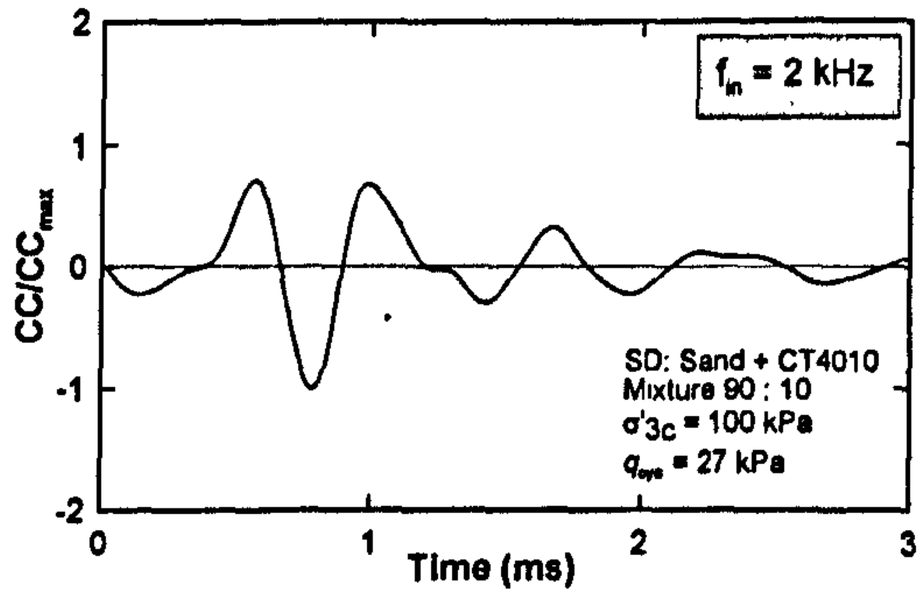

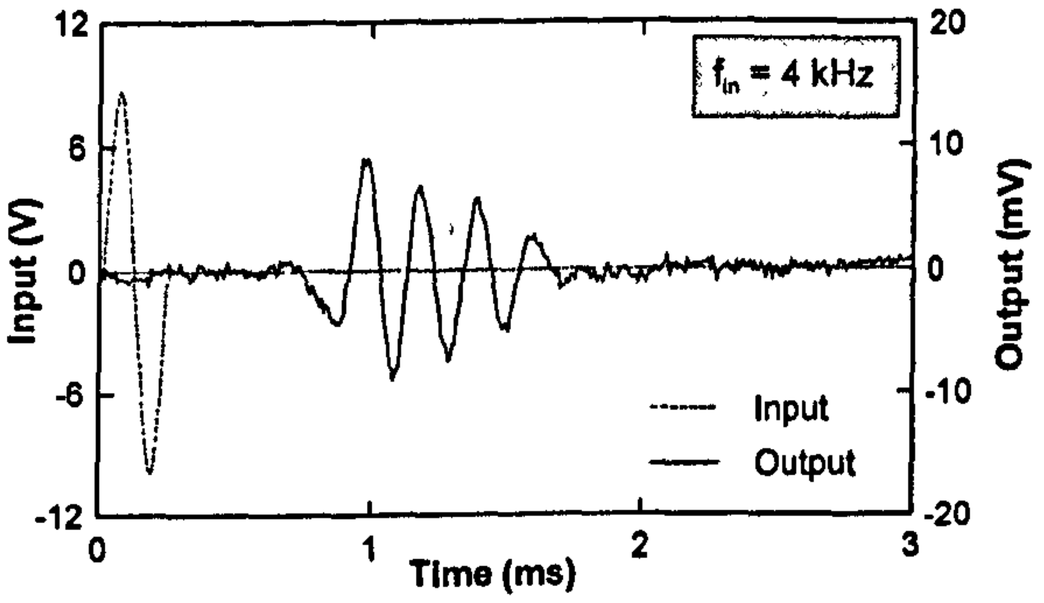

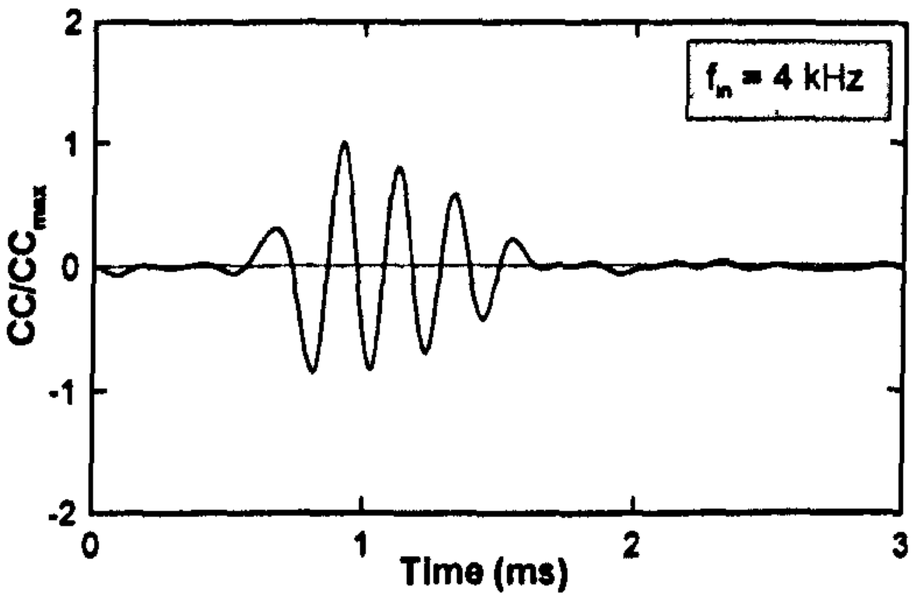

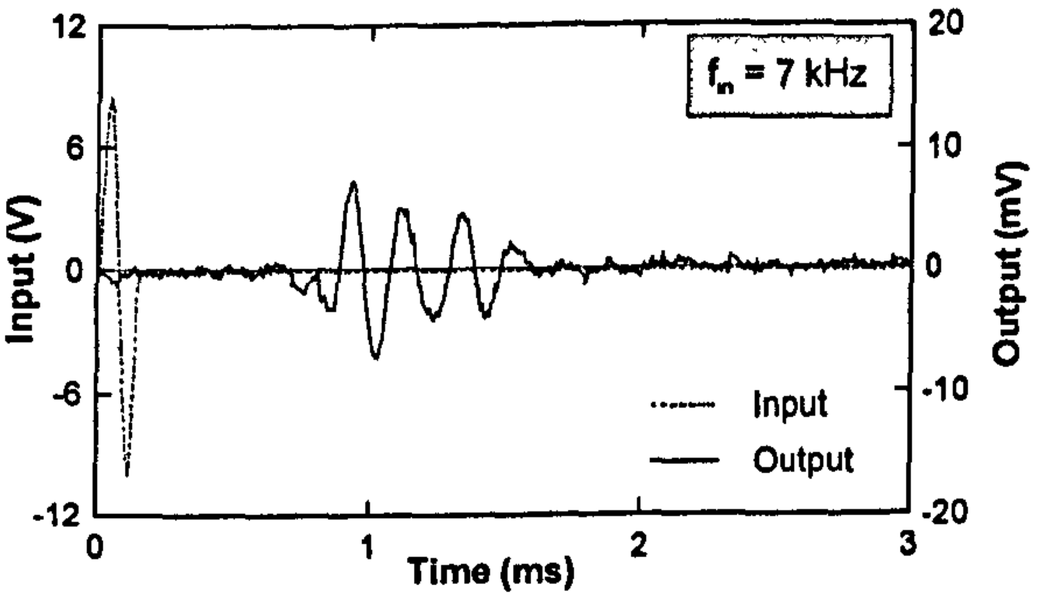

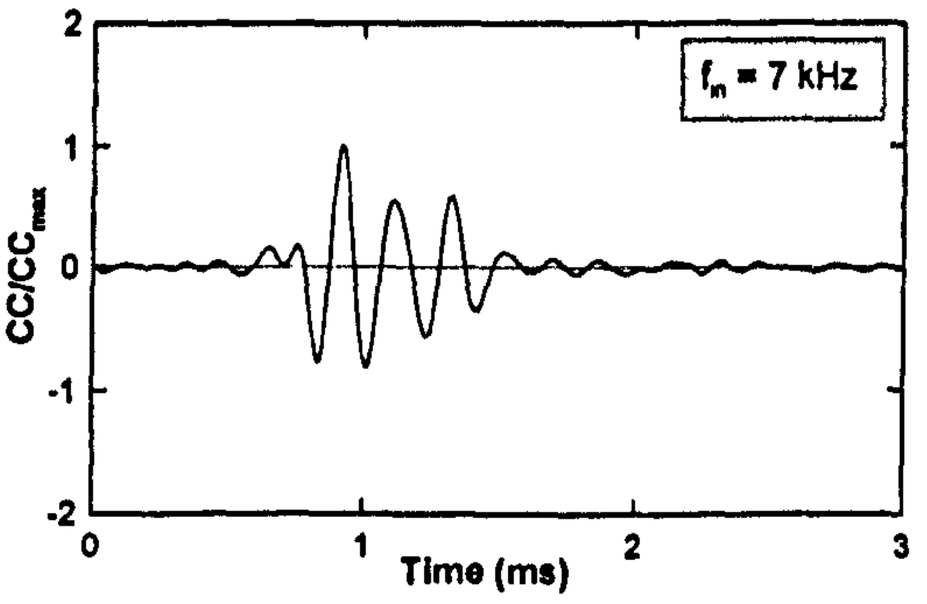

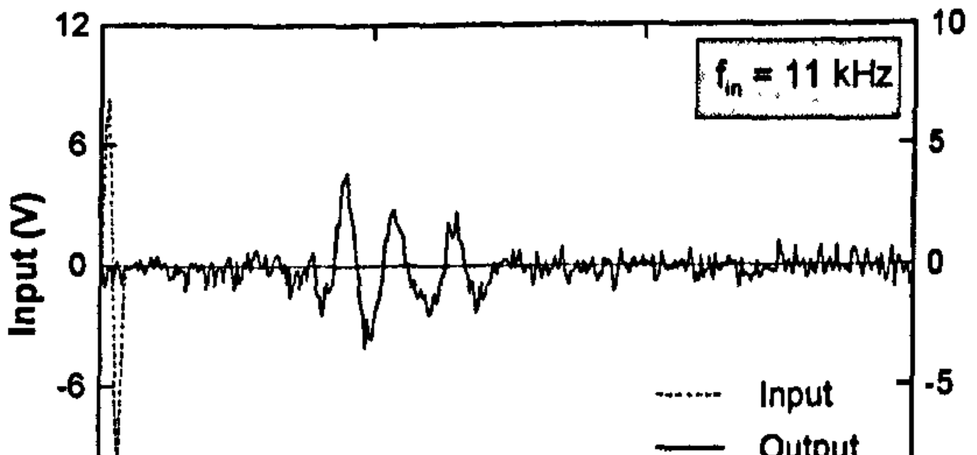

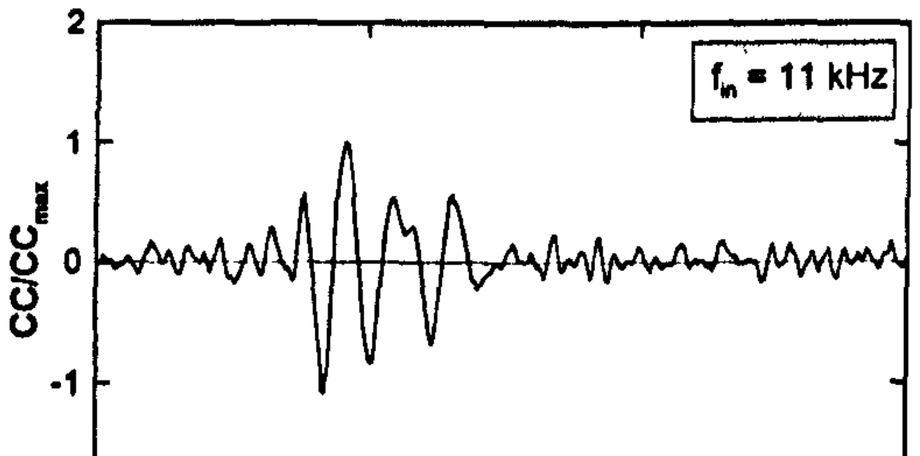

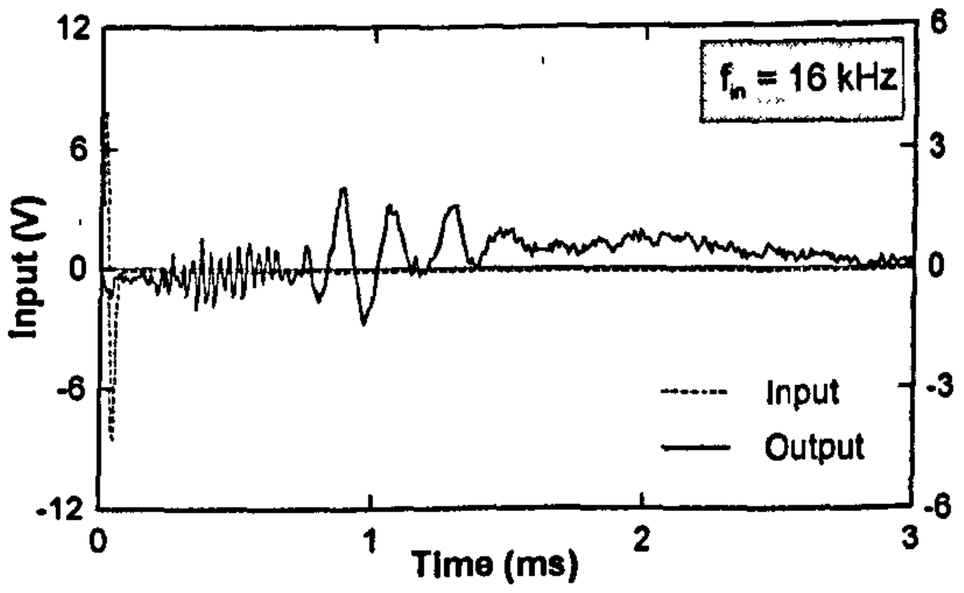

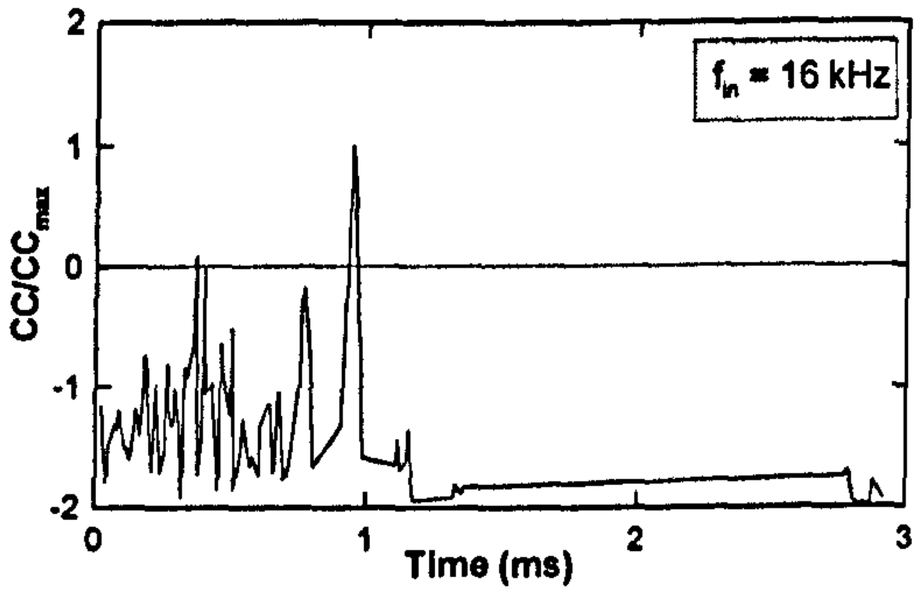

Figure 7. 26 Typical BE signals for SD with 10% rubber

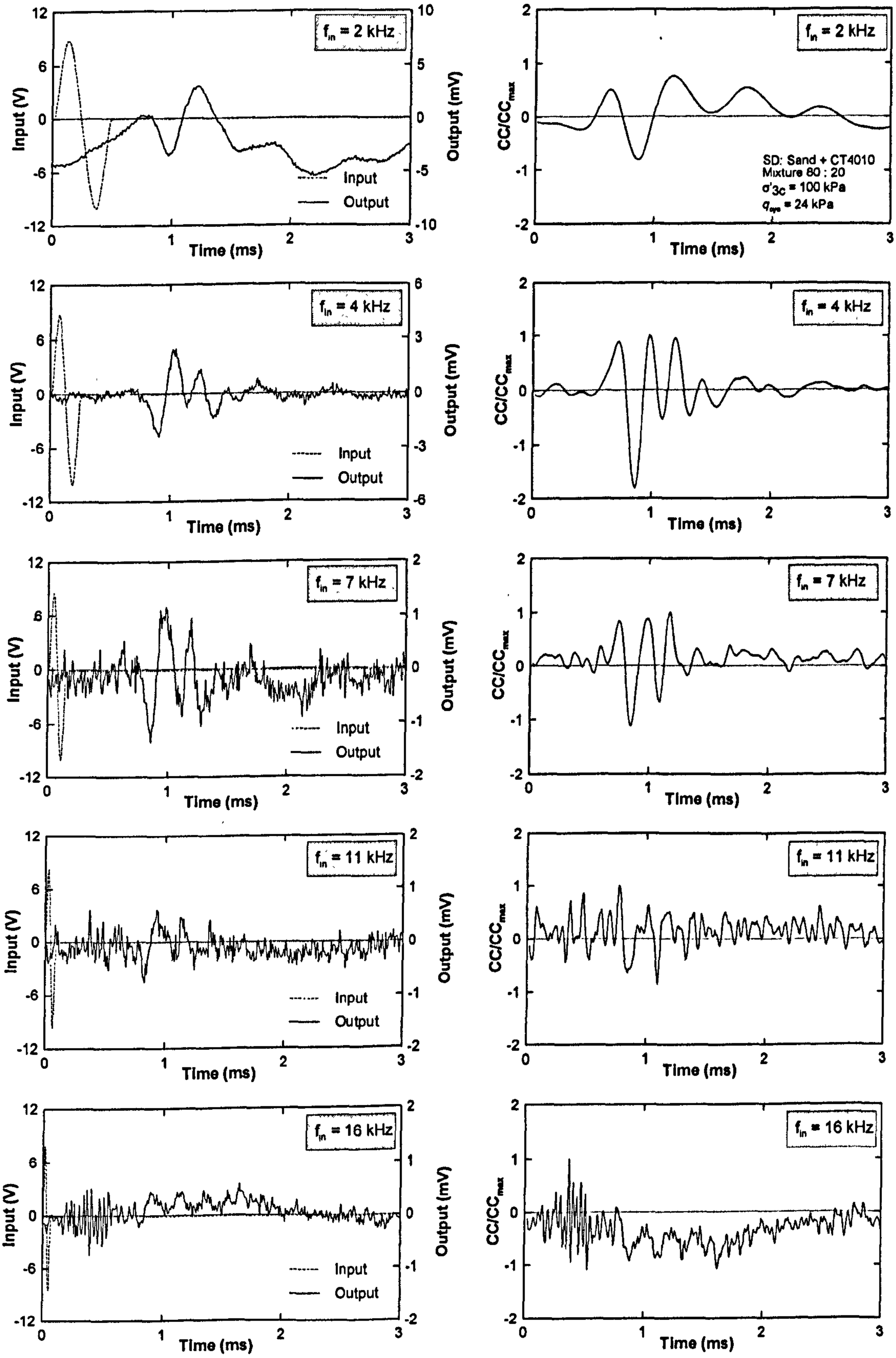

Figure 7. 27 Typical BE signals for SD with 20% rubber

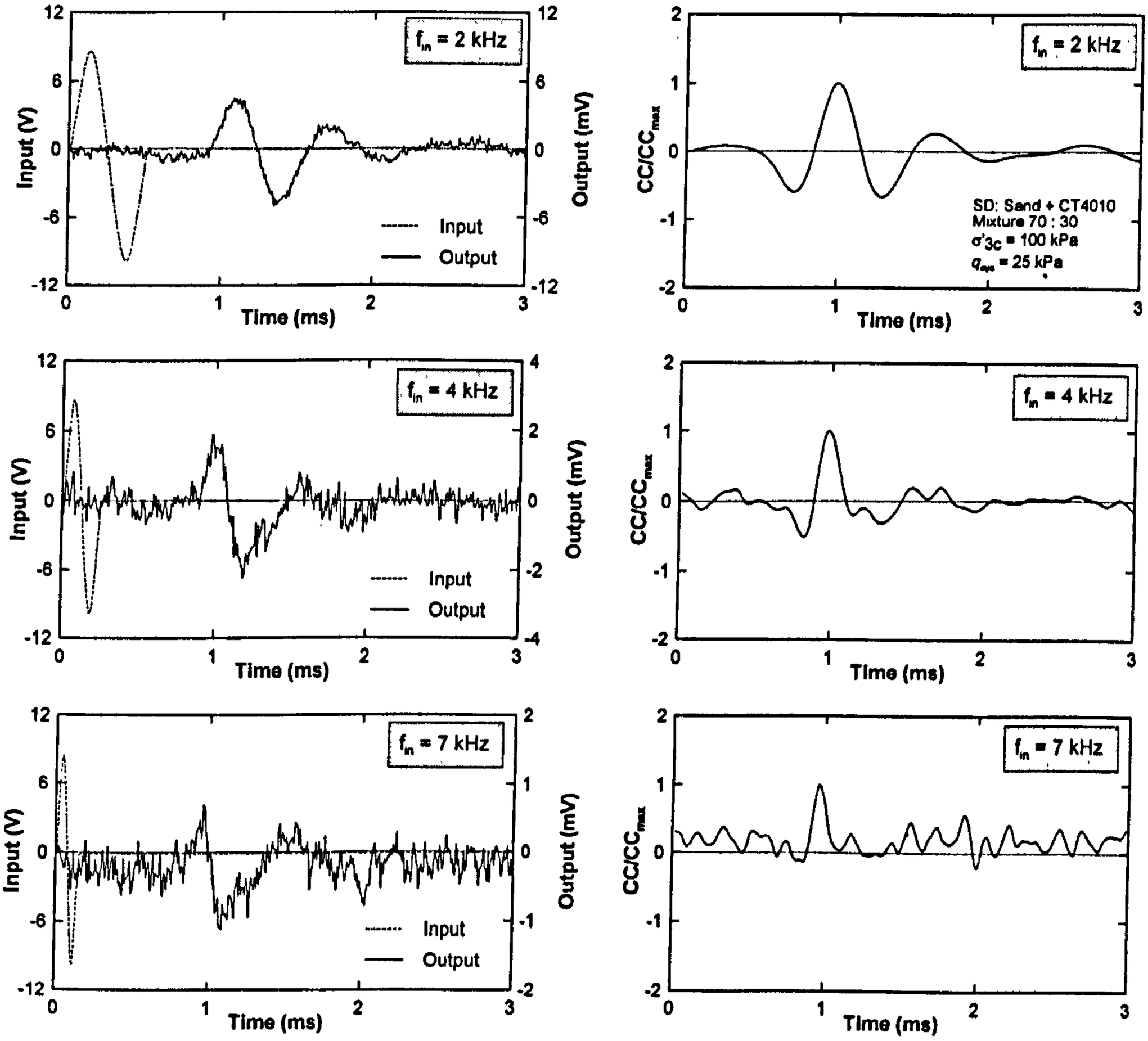

Figure 7. 28 Typical BE signals for SD with 30% rubber

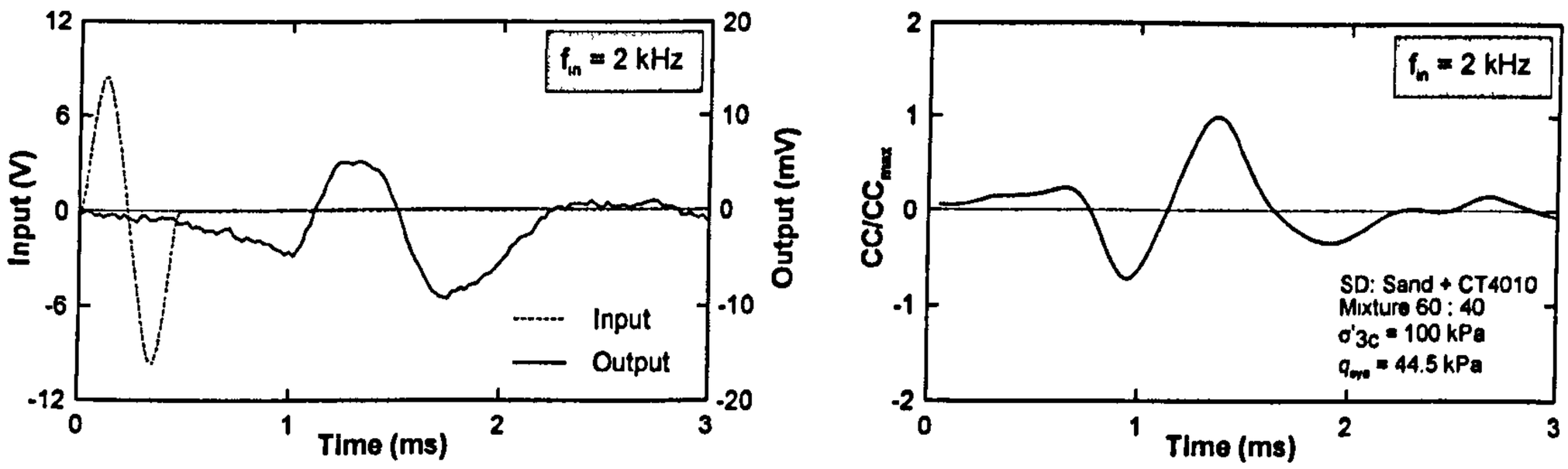

Figure 7. 29 Typical BE signals for SD with 40% rubber

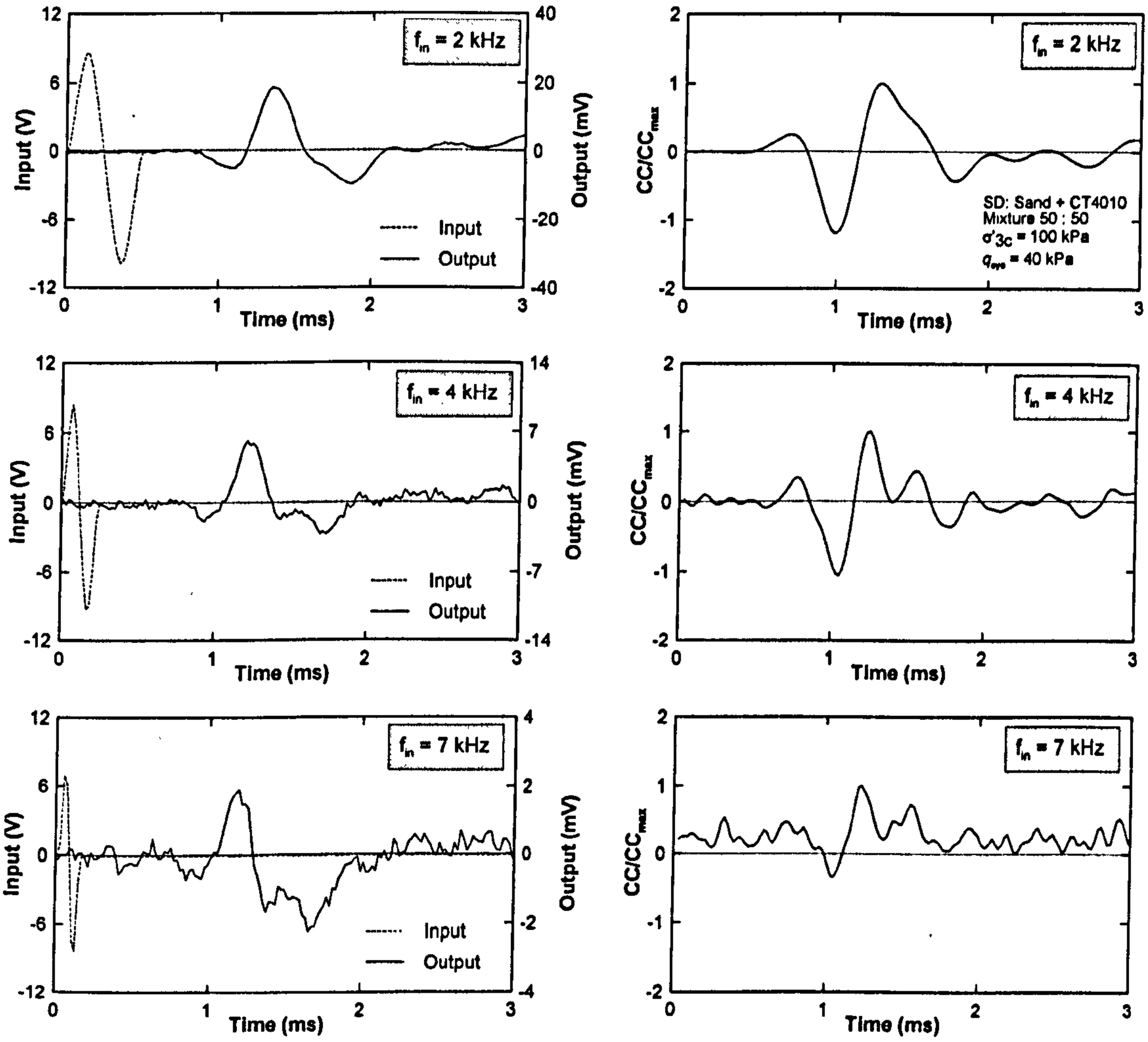

Figure 7. 30 Typical BE signals for SD with 50% rubber

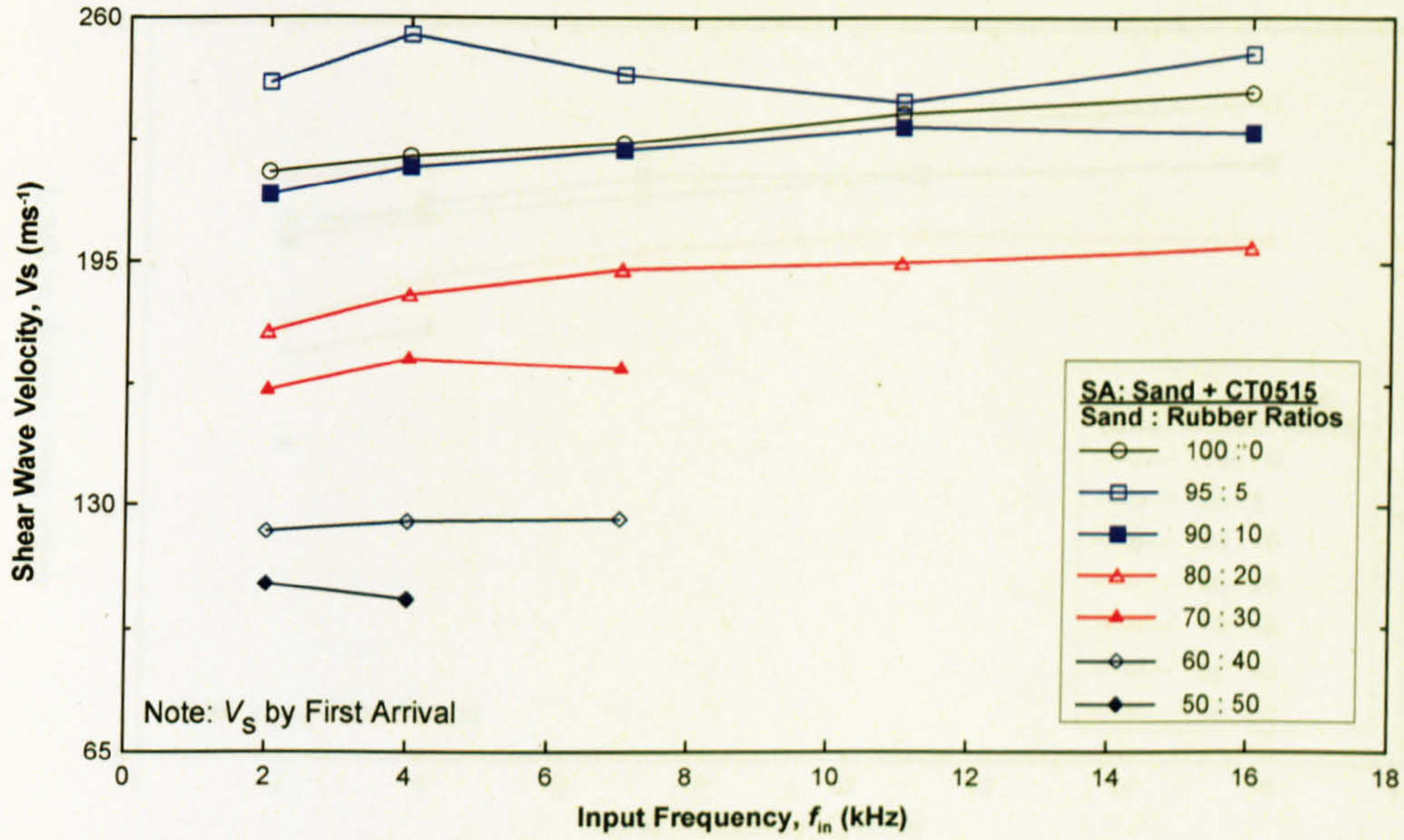

Figure 7. 31 Shear wave velocity (by FA) versus input frequency for SA

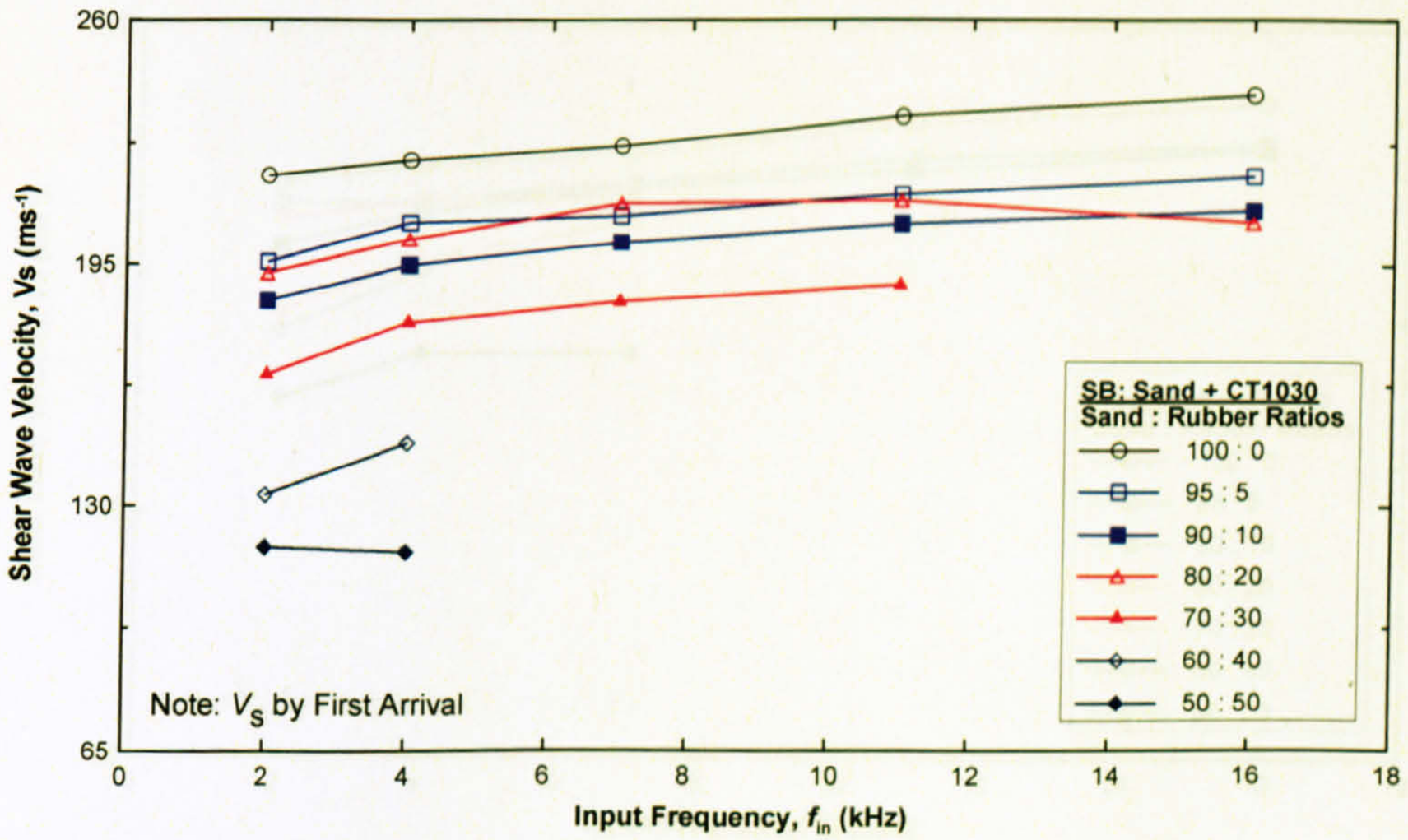

Figure 7. 32 Shear wave velocity (by FA) versus input frequency for SB

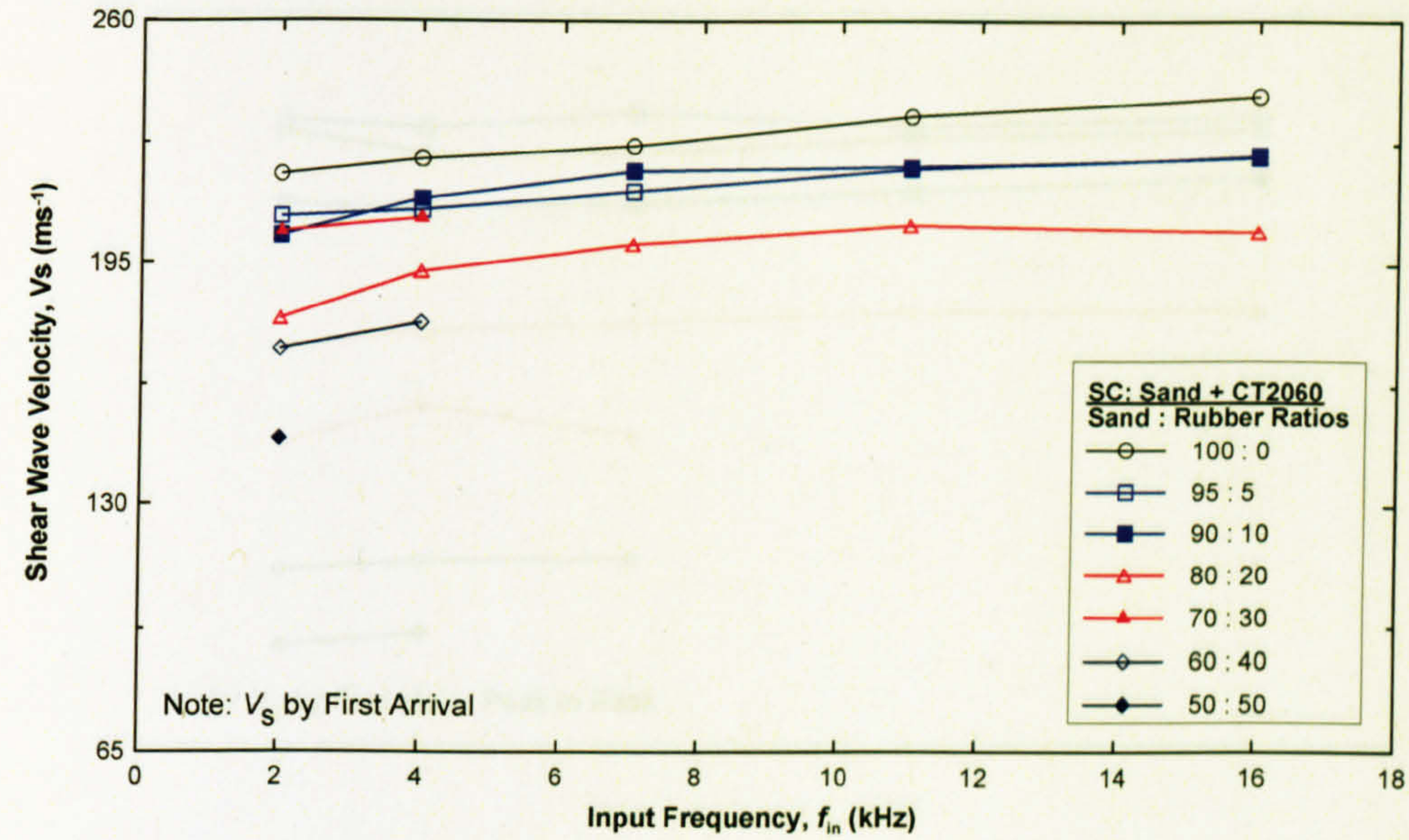

Figure 7. 33 Shear wave velocity (by FA) versus input frequency for SC

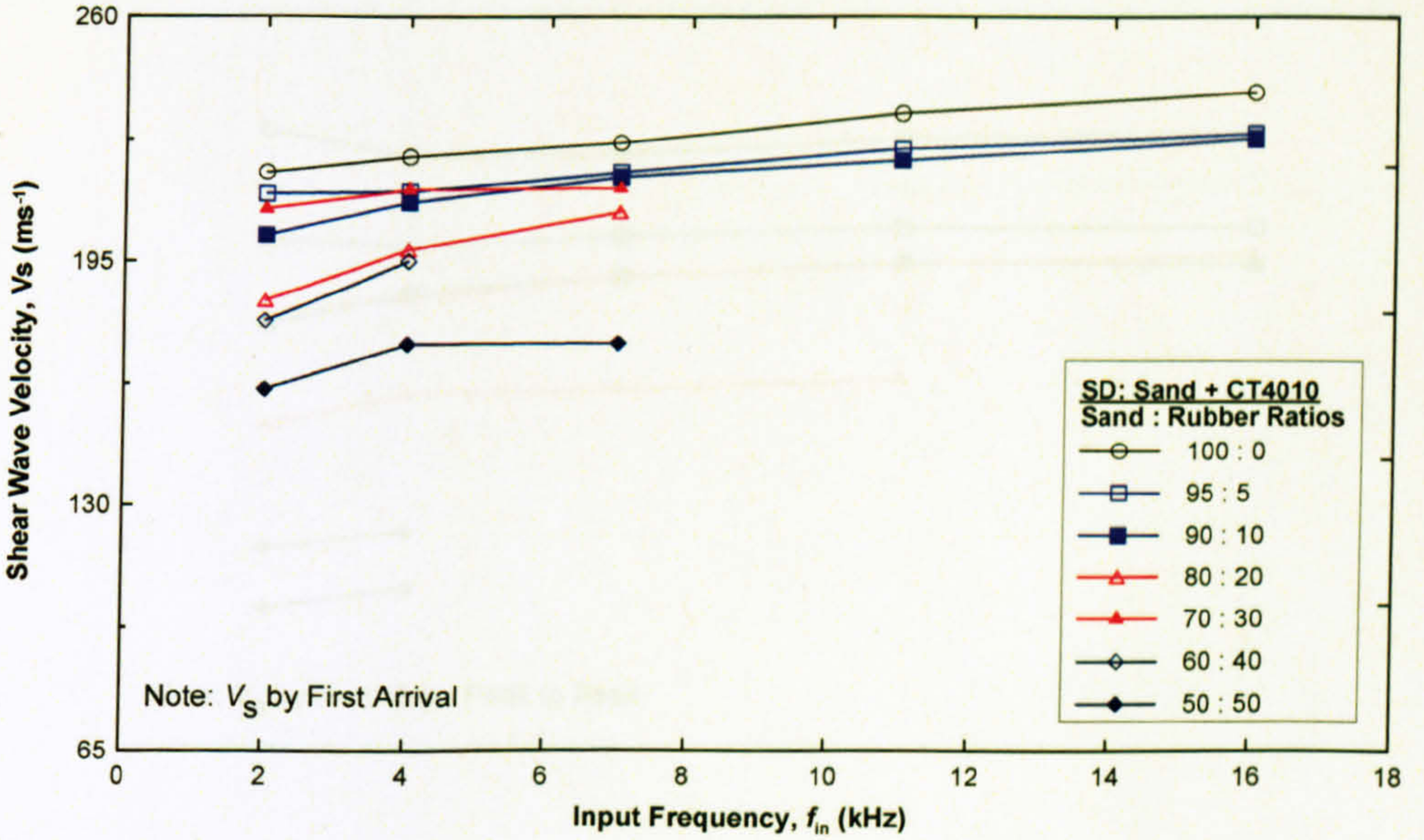

Figure 7. 34 Shear wave velocity (by FA) versus input frequency for SD

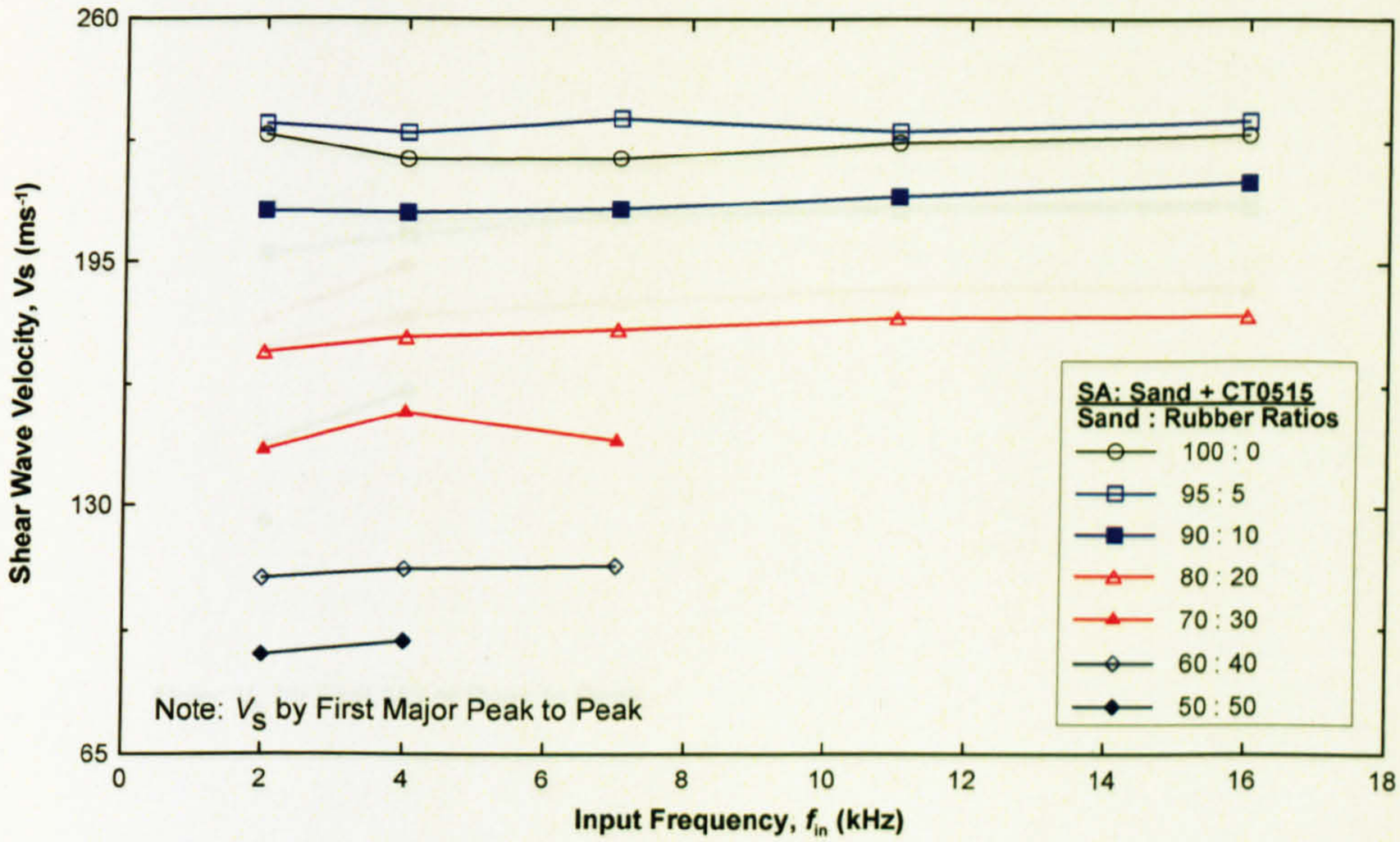

Figure 7. 35 Shear wave velocity (by PP) versus input frequency for SA

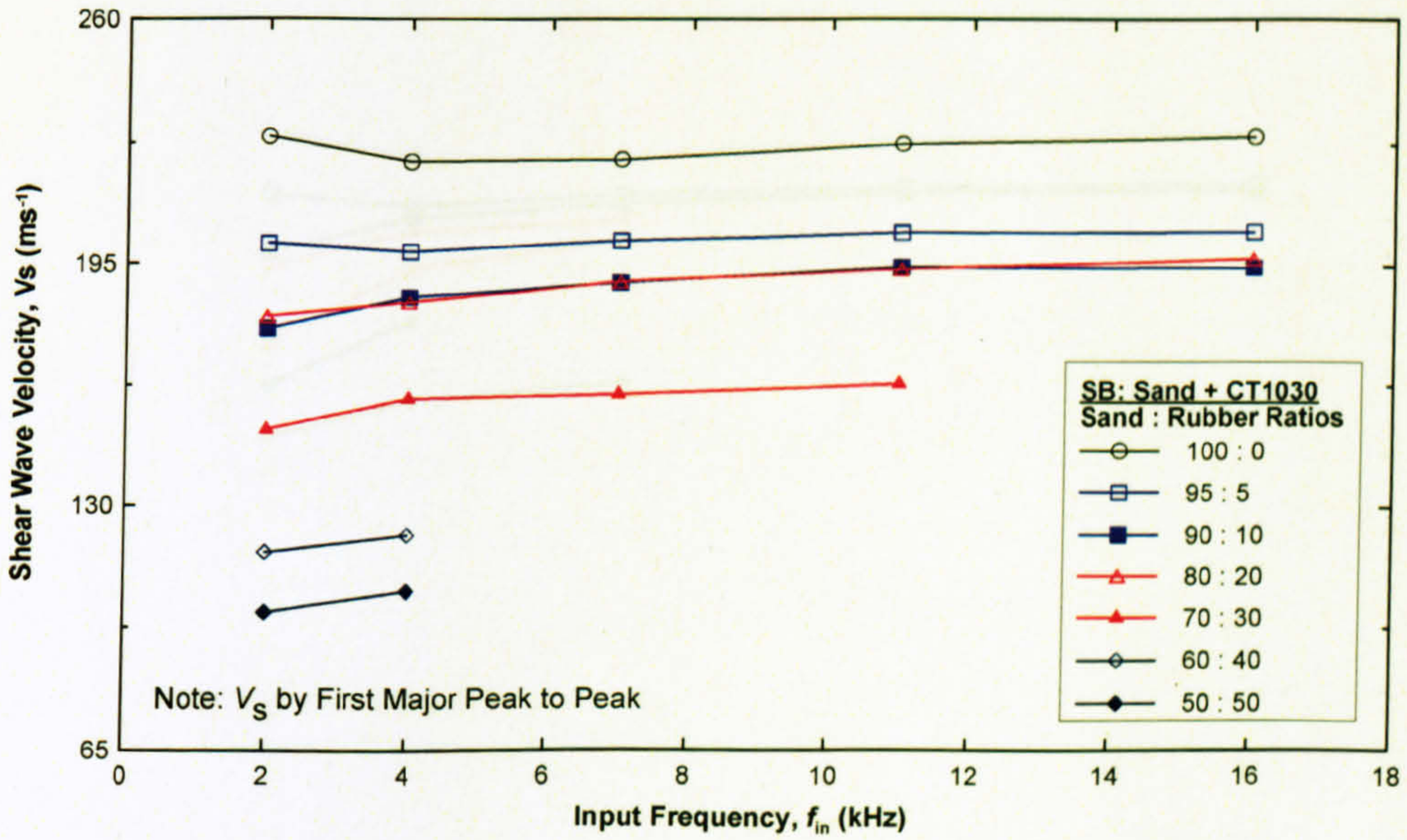

Figure 7. 36 Shear wave velocity (by PP) versus input frequency for SB

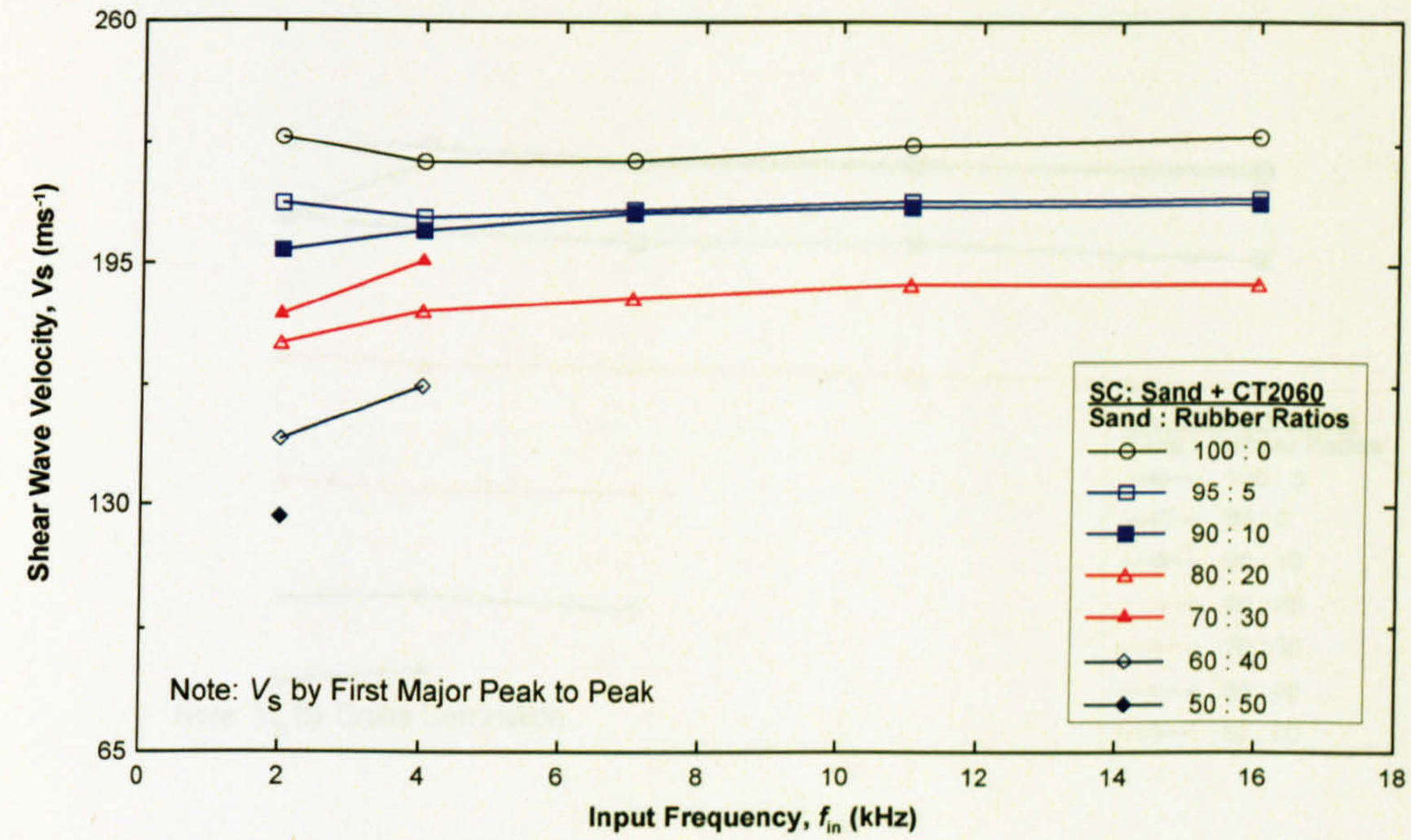

Figure 7. 37 Shear wave velocity (by PP) versus input frequency for SC

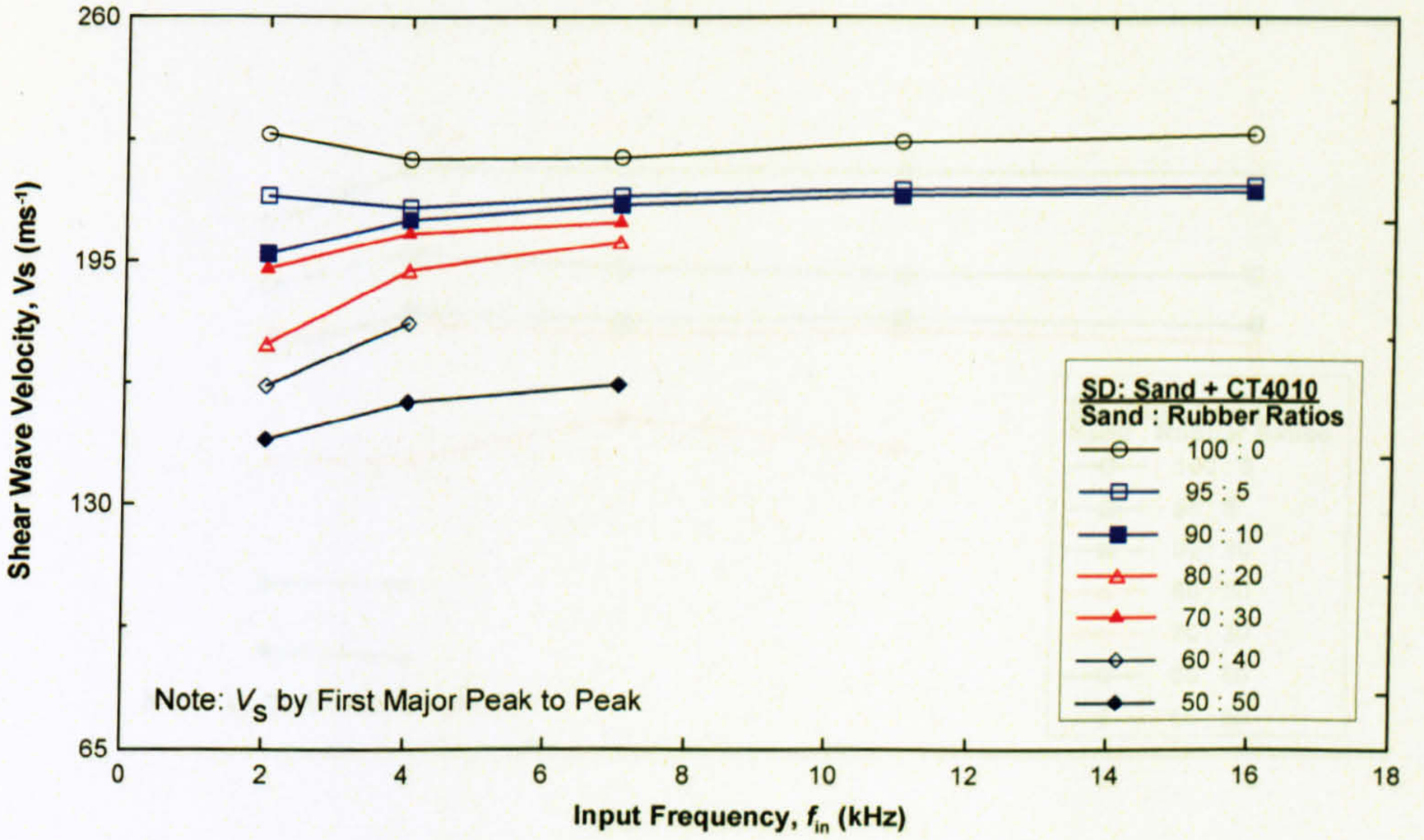

Figure 7. 38 Shear wave velocity (by PP) versus input frequency for SD

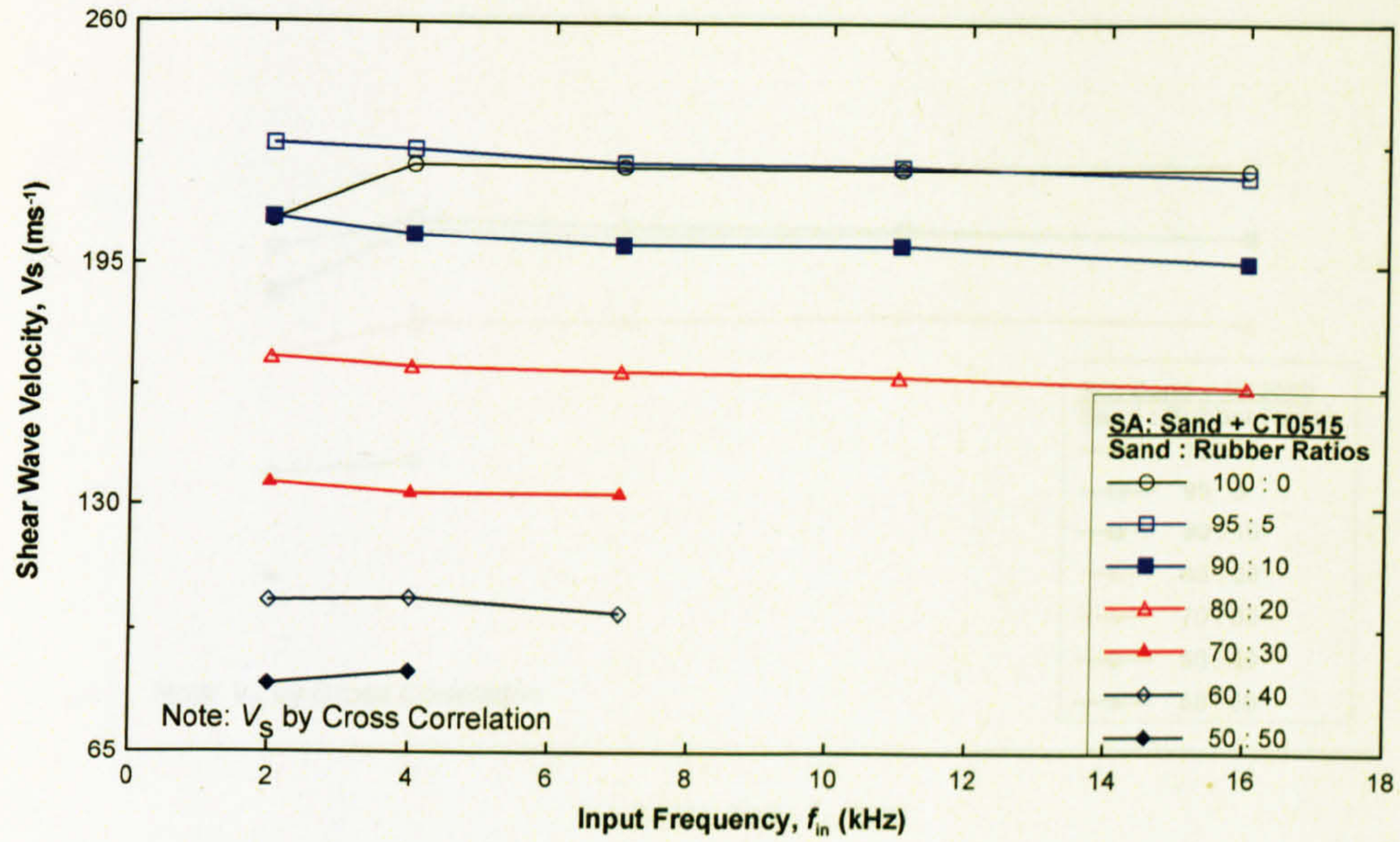

Figure 7. 39 Shear wave velocity (by CC) versus input frequency for SA

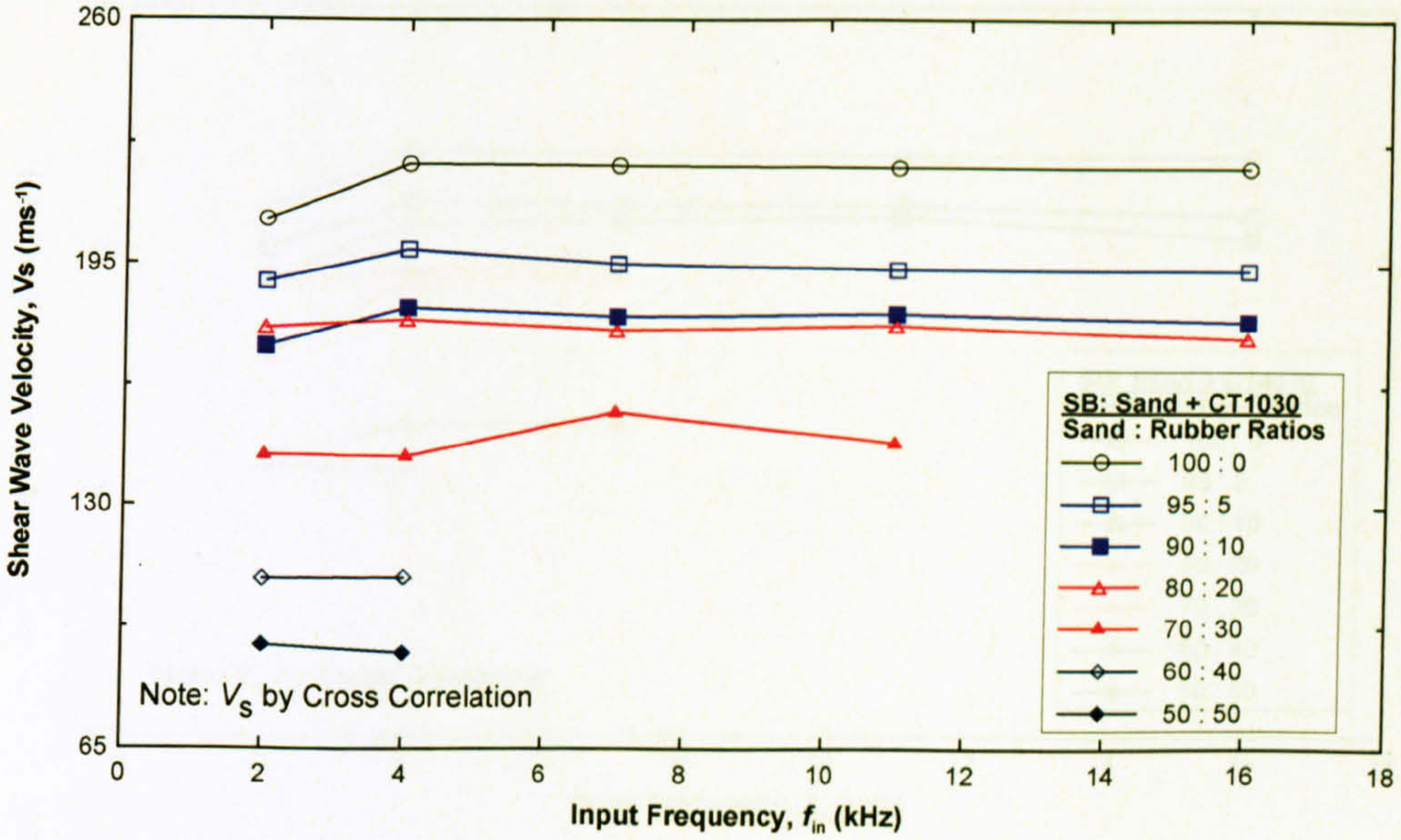

Figure 7. 40 Shear wave velocity (by CC) versus input frequency for SB

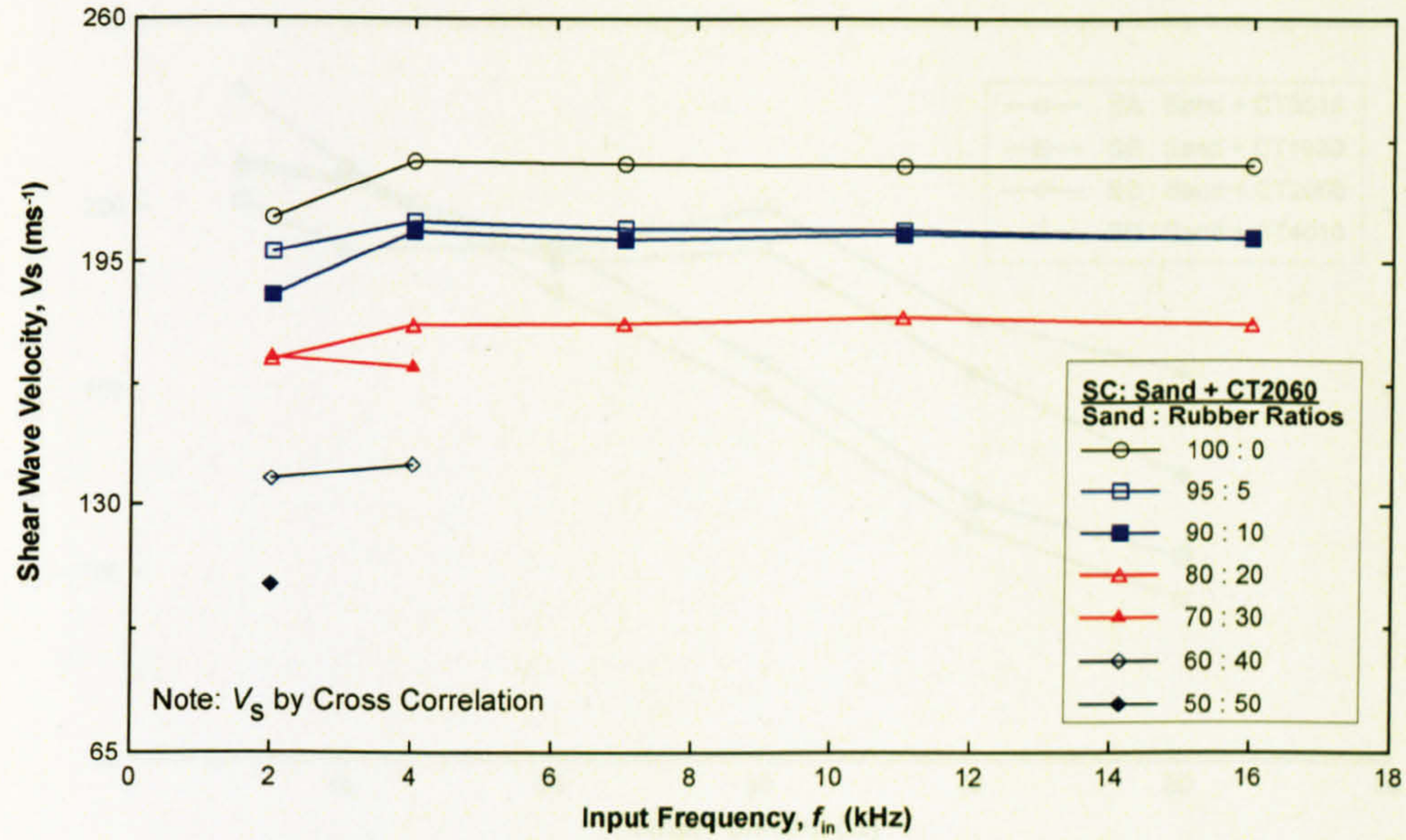

Figure 7. 41 Shear wave velocity (by CC) versus input frequency for SC

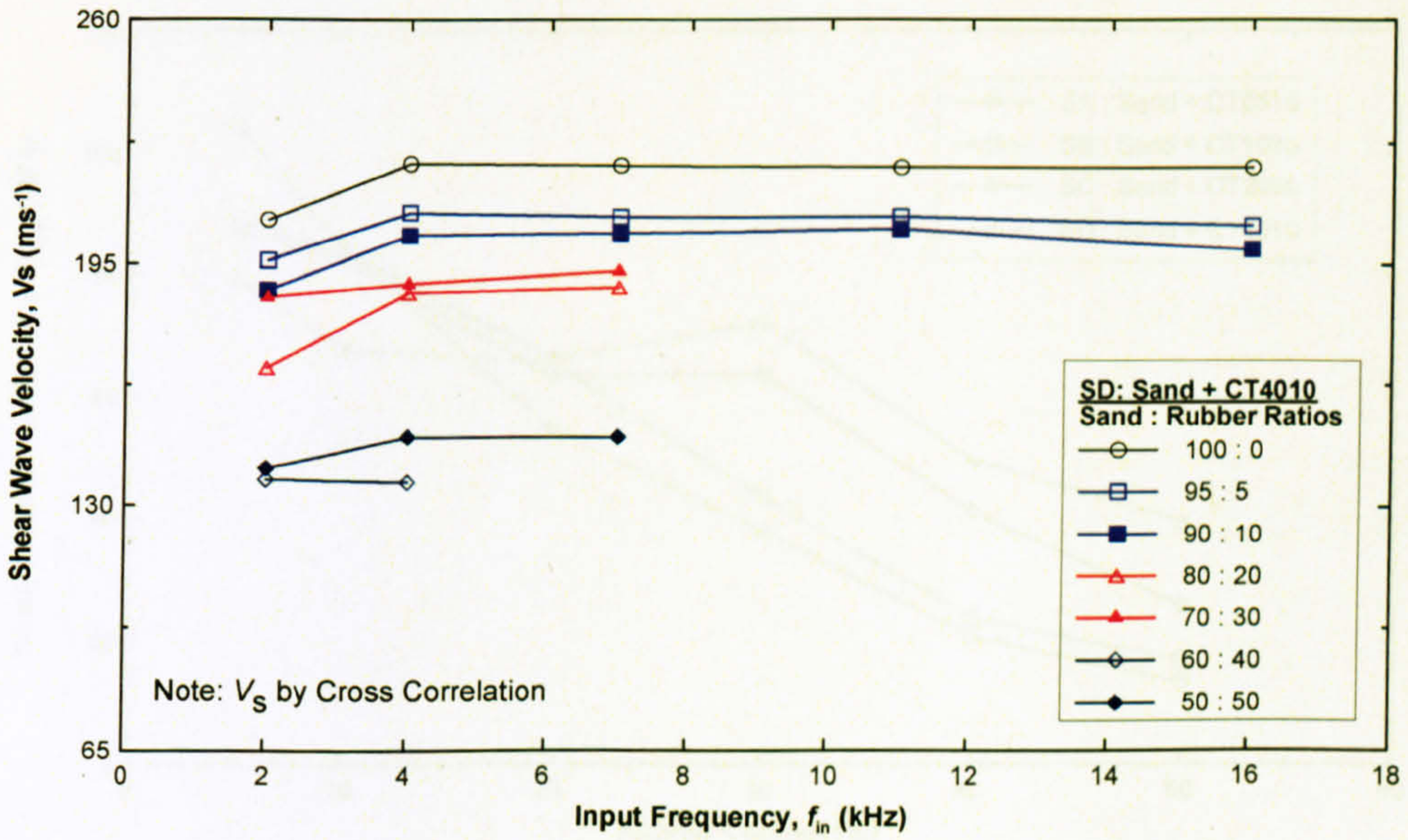

Figure 7. 42 Shear wave velocity (by CC) versus input frequency for SD

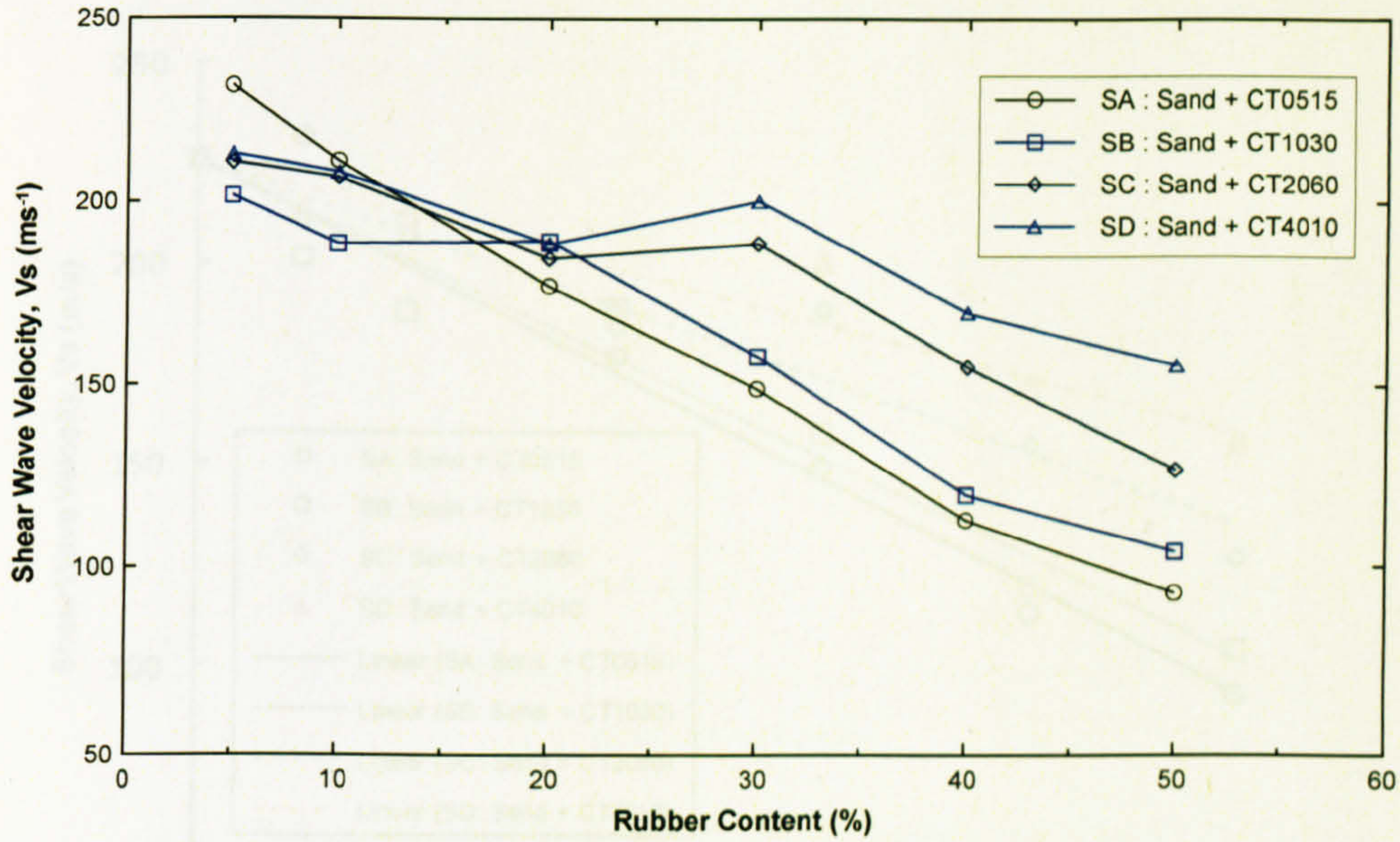

Figure 7. 43 Shear wave velocity (by PP) versus rubber content

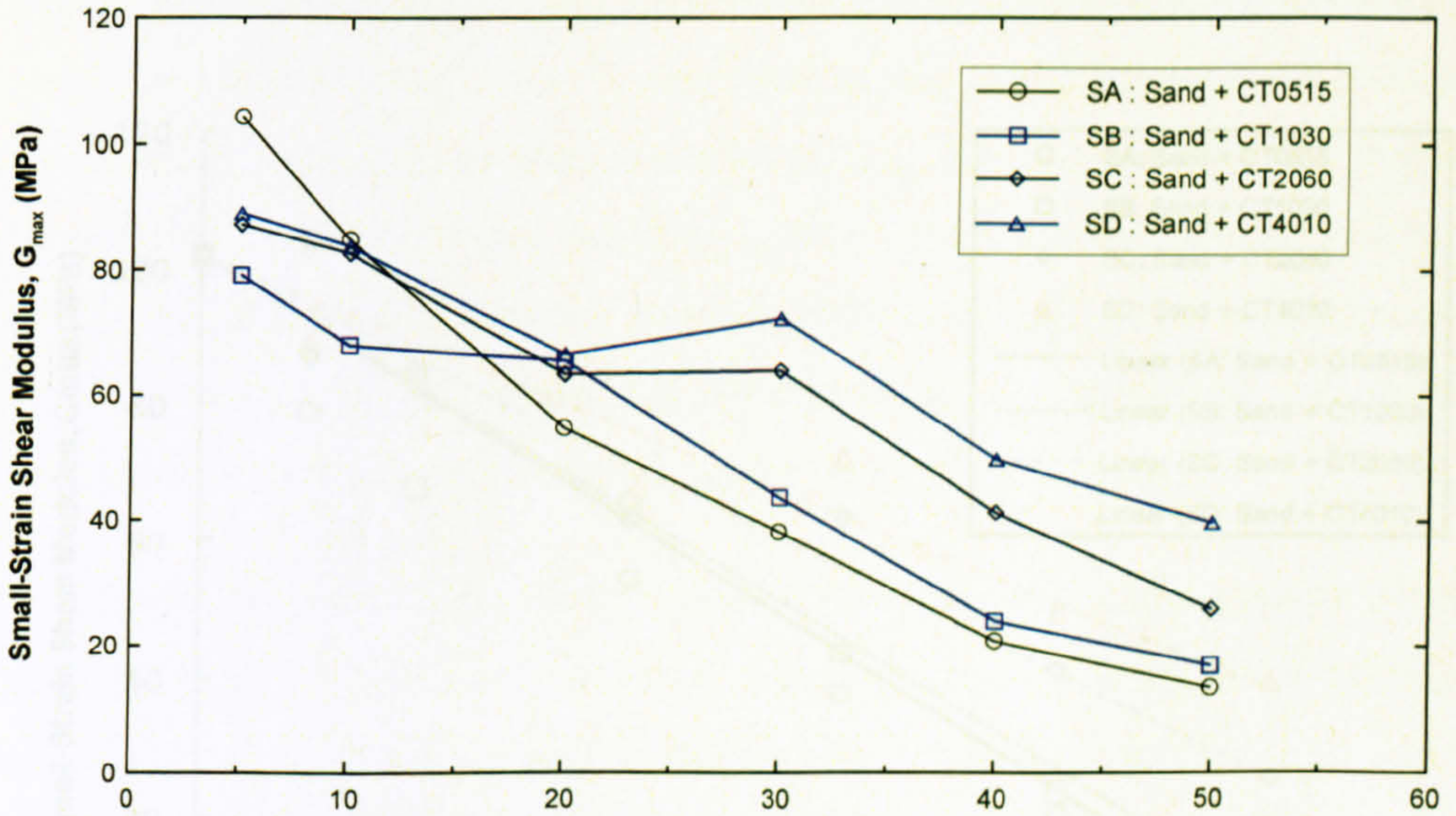

Figure 7. 44 Small-strain shear modulus (by PP) versus rubber content

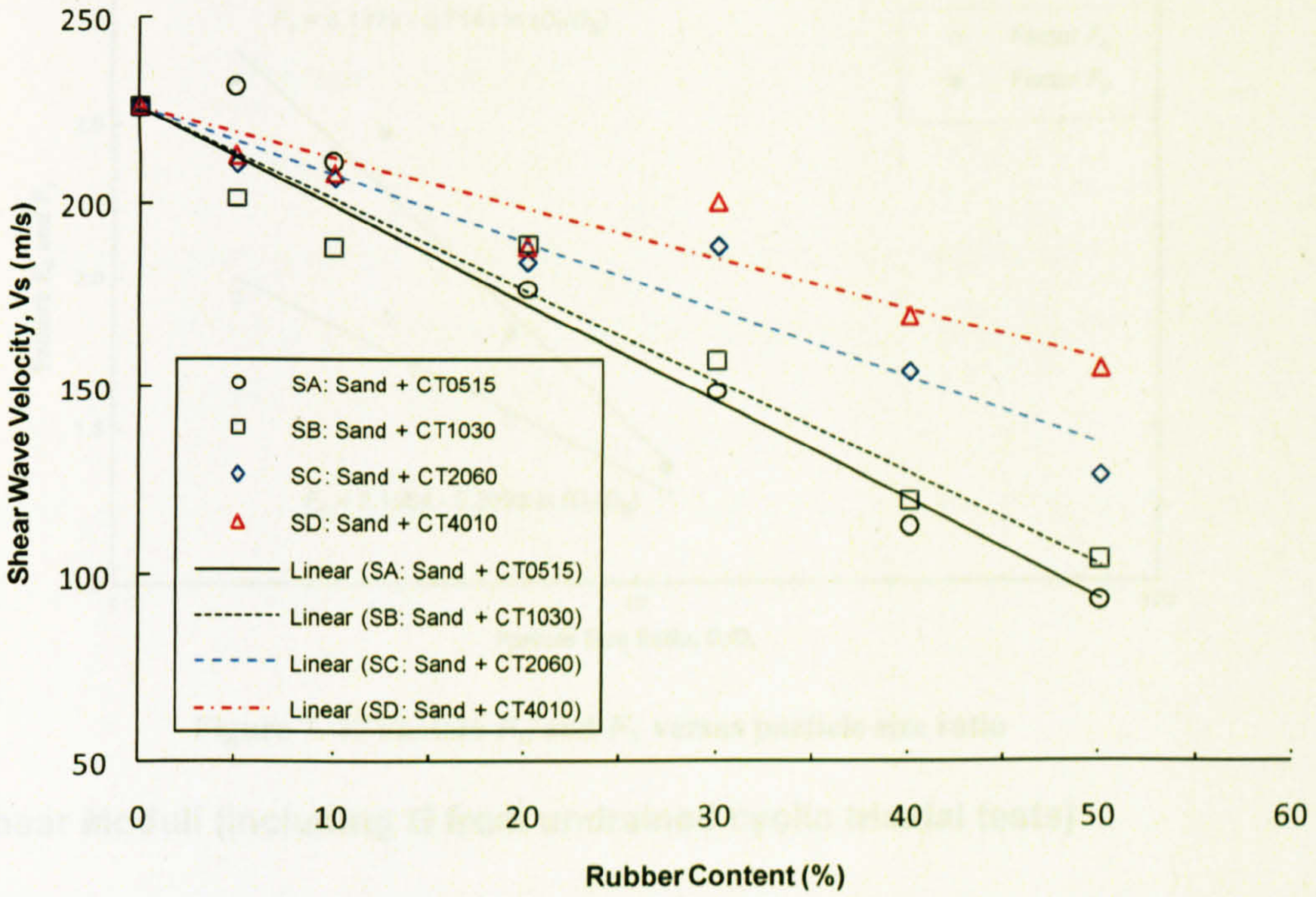

Figure 7. 45 Linear relationship between G_{max} and rubber content

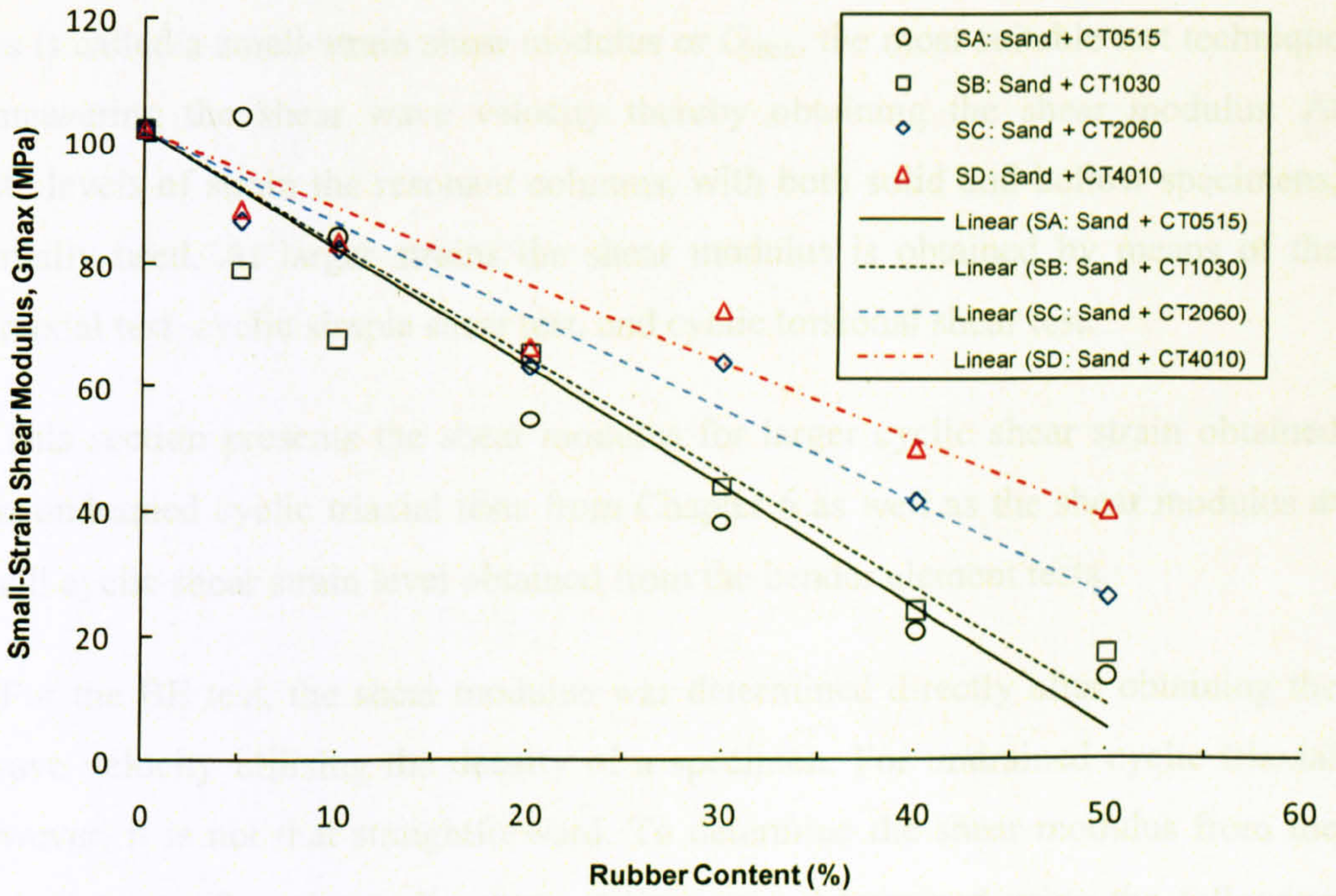

Figure 7. 46 Linear relationship between V_s and rubber content

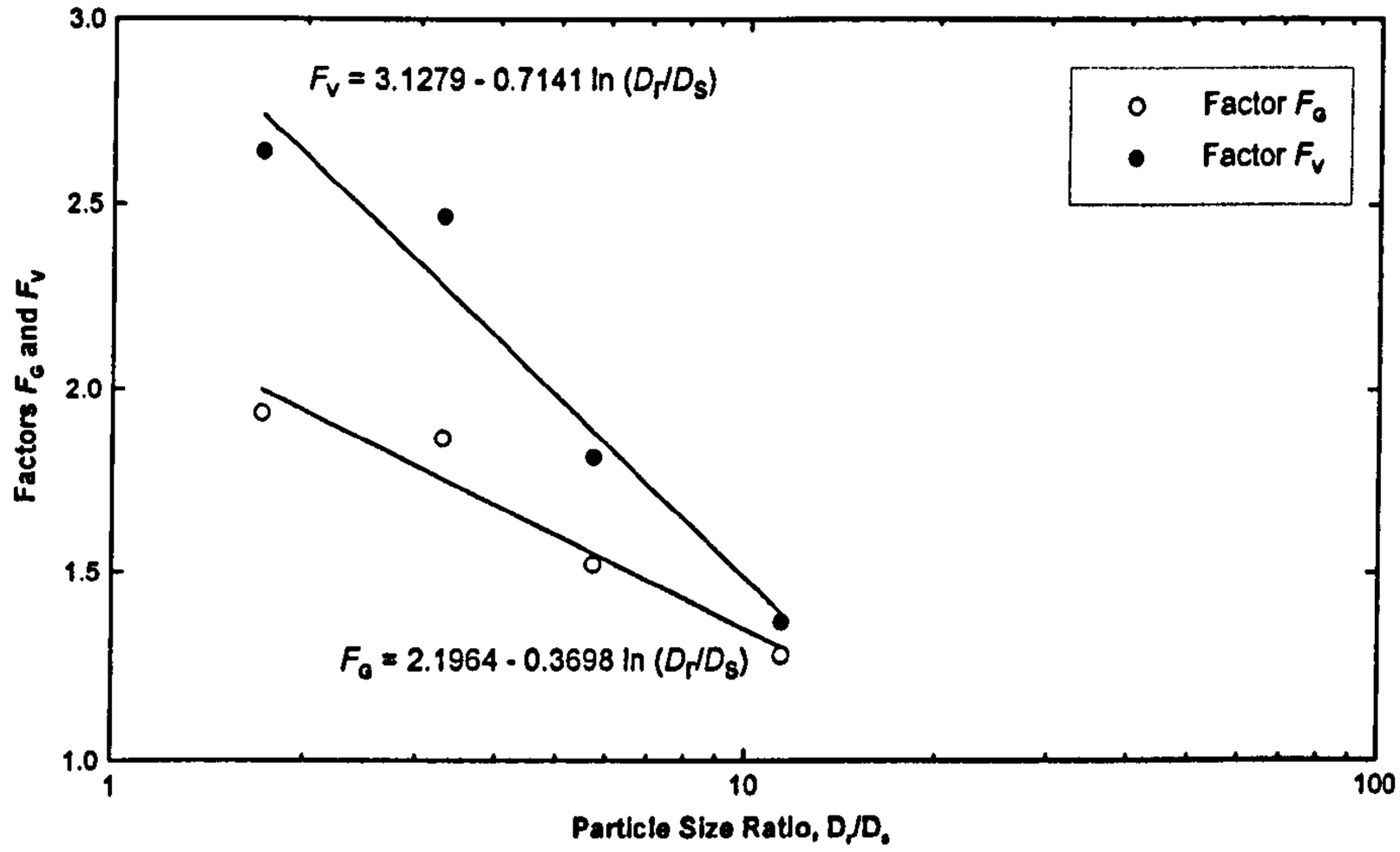

Figure 7. 47 Factors F_G and F_V versus particle size ratio

7.3.2 Shear Moduli (Including *G* from undrained cyclic triaxial tests)

Apart from the damping factor, the shear modulus is one of the most important parameters used in analysis and design involving seismic loading. As the shear modulus is dependent on the shear strain level, many devices have been developed to provide the soil stiffness at various strain levels. For example, at very small strain at which the shear modulus is called a small-strain shear modulus or G_{max}, the most suitable test technique is by measuring the shear wave velocity thereby obtaining the shear modulus. At modulate levels of strain the resonant columns, with both solid and hollow specimens, are normally used. At larger strains the shear modulus is obtained by means of the cyclic triaxial test, cyclic simple shear test, and cyclic torsional shear test.

This section presents the shear modulus for larger cyclic shear strain obtained from the undrained cyclic triaxial tests from Chapter 6 as well as the shear modulus at very small cyclic shear strain level obtained from the bender element tests.

For the BE test, the shear modulus was determined directly after obtaining the shear wave velocity utilising the density of a specimen. For undrained cyclic triaxial test, however, it is not that straightforward. To determine the shear modulus from the cyclic triaxial test, first the cyclic shear strain γ was determined using the following equation:

$$\gamma = (1 + \mu) \cdot \varepsilon_a \qquad \textbf{(Eq. 7. 12)}$$

where:

μ = Poisson's ratio, and

ε_a = axial strain.

In this research because all specimens were fully saturated before subjecting to undrained cyclic loading, the Poisson's ratio therefore was assumed to be 0.5 (Bishop and Hight, 1977; Rollins *et al.*, 1998).

Next, the elastic modulus (E) was determined by taking the relationship between the cyclic deviator stress (q_{cyc}) and the axial strain (ε), as follows:

$$E = \frac{q_{cyc}}{\varepsilon_a} \qquad \textbf{(Eq. 7. 13)}$$

Note that the elastic modulus determination by means of the cyclic triaxial test is illustrated by Figure 7.48. The shear modulus G then was obtained by the following equation:

$$G = \frac{E}{2\cdot(1+\mu)} \qquad \textbf{(Eq. 7. 14)}$$

It should be stressed that both E and G are dependent on the strain level. If the cyclic loading applied is constant throughout, the strain will gradually increase, hence decreasing E and G. This can be clearly seen when considering Figure 7.49 illustrating the gradation of shear modulus against the shear strain.

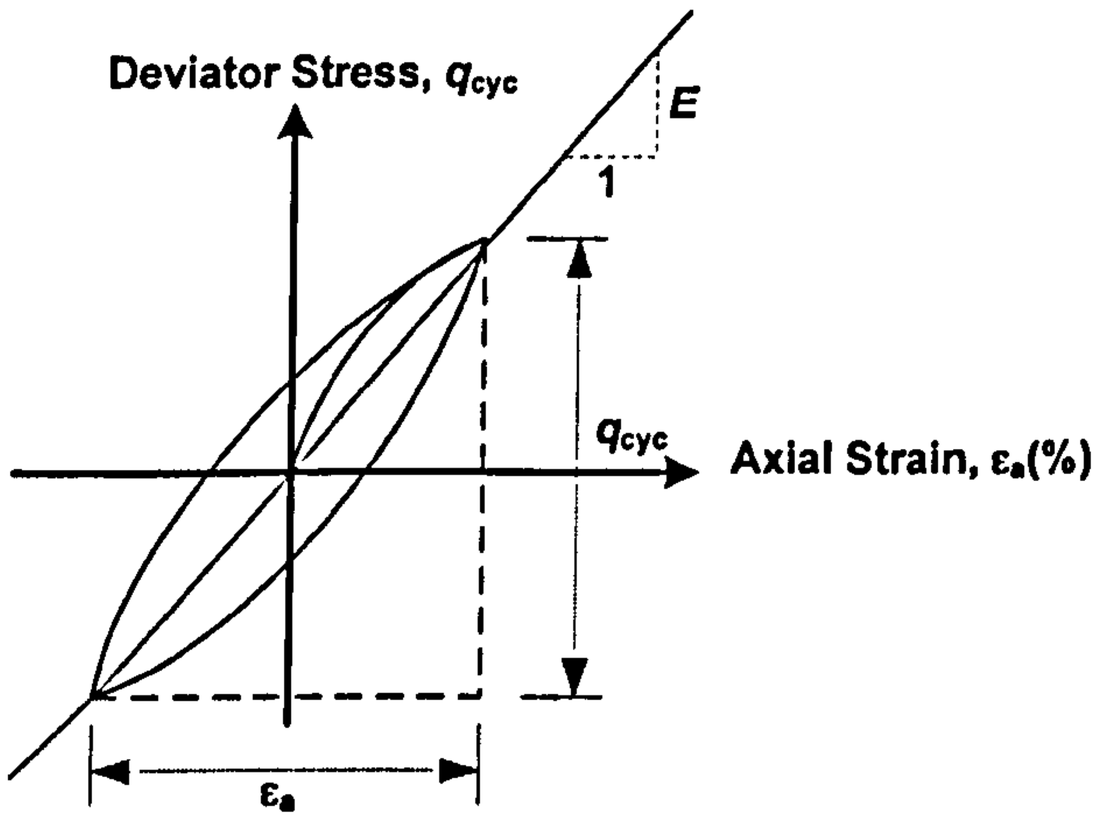

Figure 7. 48 Elastic modulus determination by cyclic triaxial test

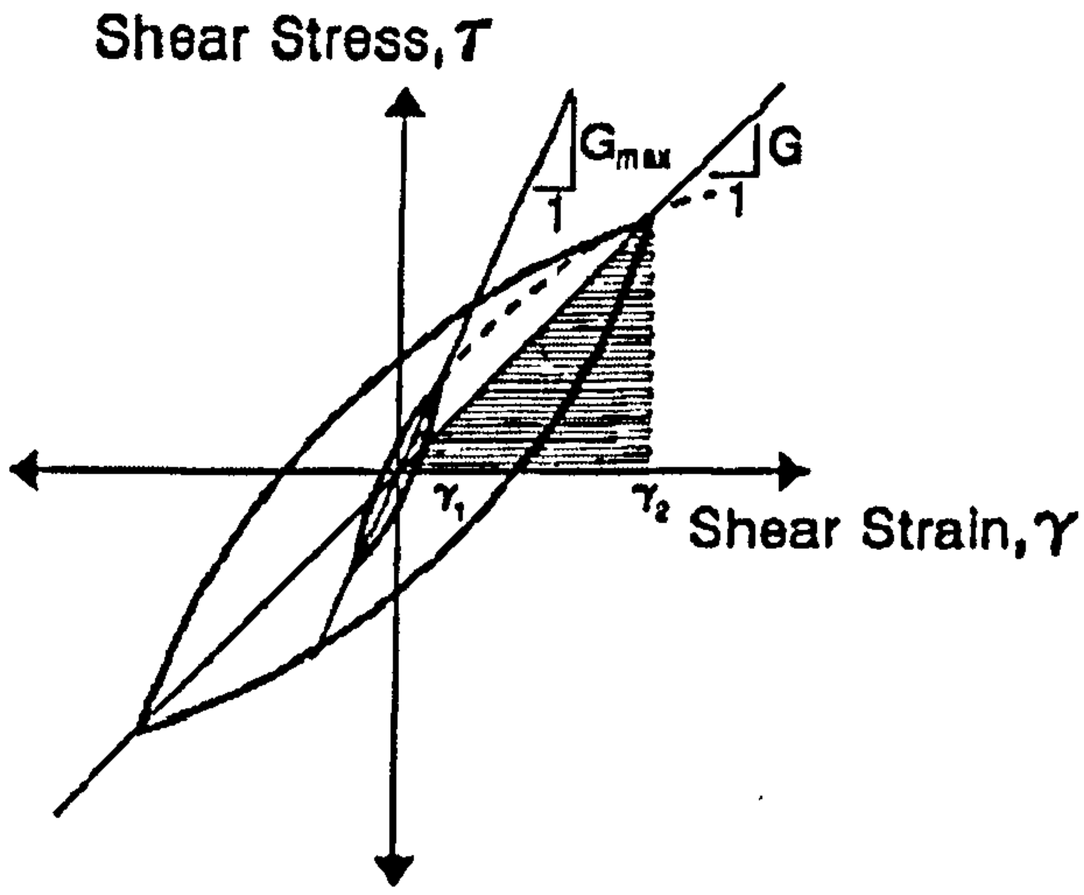

Figure 7. 49 Hysteretic stress-strain relationships at different strain amplitude (after Rollins *et al.*, 1998)

In practice, the shear modulus is normalised by its maximum value, i.e., G/G_{max}, for the sake of employing the curve in the analysis and design. The relationships between G/G_{max} and cyclic shear strain for sand-tyre chip mixtures SA, SB, SC, and SD are illustrated by Figure 7.50, Figure 7.51, Figure 7.52, and Figure 7.53, respectively. It was observed that the cyclic shear strain levels generated by the undrained cyclic triaxial test were approximately between 0.03 – 10%. However, the cyclic shear strain generated by the BE test was assumed to be as low as 0.0001%. In addition, as mentioned before, this research did not cover the shear modulus for the cyclic shear strain ranging between 0.0001 - 0.03%. Thus, to complete the whole picture of the stiffness gradation the interpolation between those two sets of data was required. This was done by acquiring the missing data (G/G_{max} values between 0.0001 - 0.03% cyclic shear strain) provided by Rollins *et al.* (1998).

To be able to observe and compare the characteristics of stiffness degradation between pure sand and sand-rubber mixtures, three interpolated curves were plotted for each mixture SA, SB, SC, and SD; (1) pure sand, (2) sand mixed with 5% rubber, and (3) sand mixed with 50% rubber.

It was observed that the gradation of shear modulus for pure sand was very similar to those of SA, SB, SC, and SD, having 5% rubber. This suggests that, in terms of stiffness, there was only a very marginal effect when 5% of rubber was added, regardless of the size of tyre chips mixed. When the rubber was increased to 50%,

however, the curve was shifted to the right significantly, especially for SA (Figure 7.50). However, when considering all mixtures SA, SB, SC, and SD, it was found that the bigger the size of tyre chips mixed the narrower the gap between the curves for 5% and 50% rubber. This is obvious when all curves shown in Figures 7.50 – 7.53 were plotted together in Figure 7.54. The gradations of shear modulus versus cyclic shear strain obtained from the interpolated curves are summarised and shown in Table 7.6.

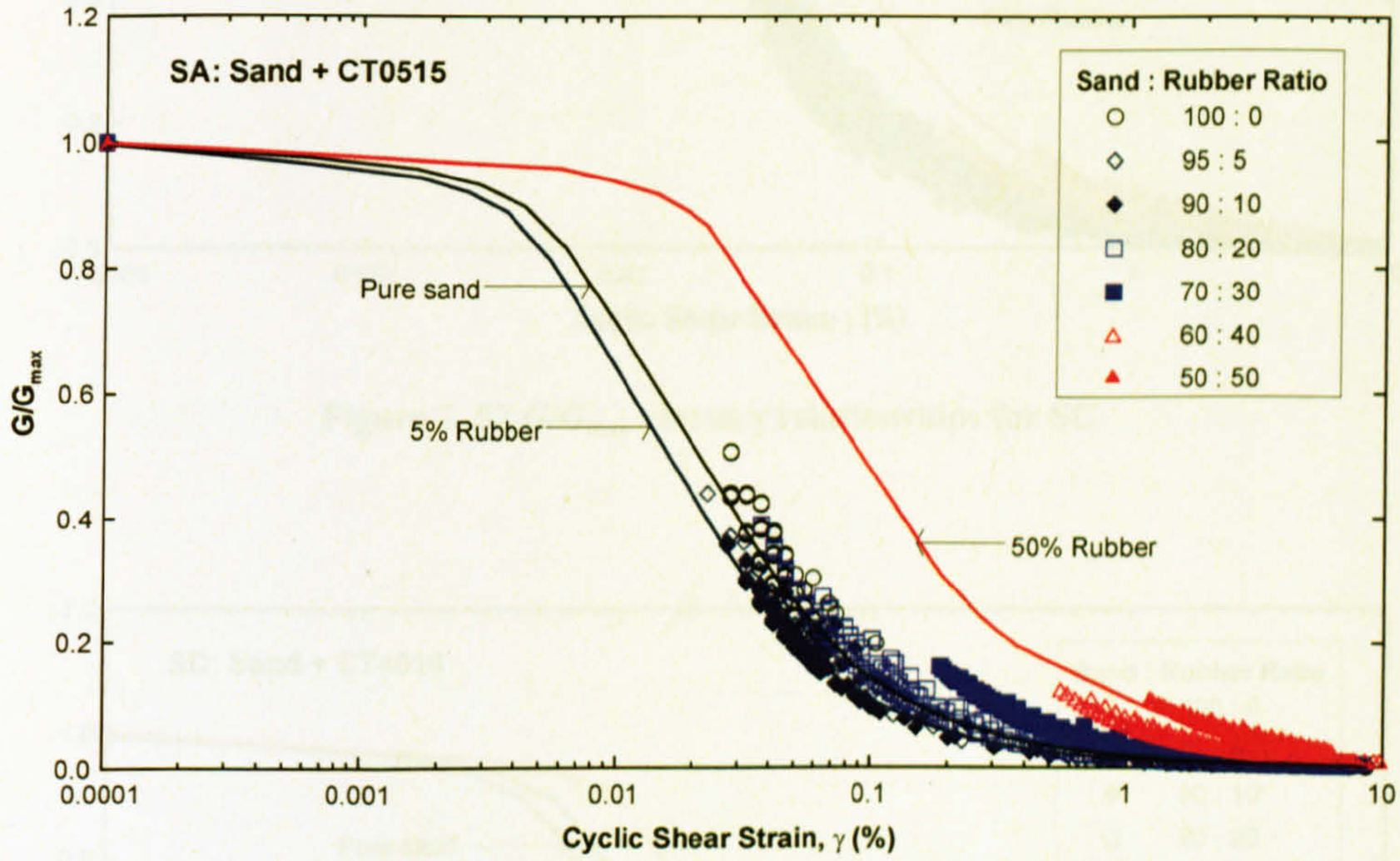

Figure 7. 50 G/G_{max} versus γ relationships for SA

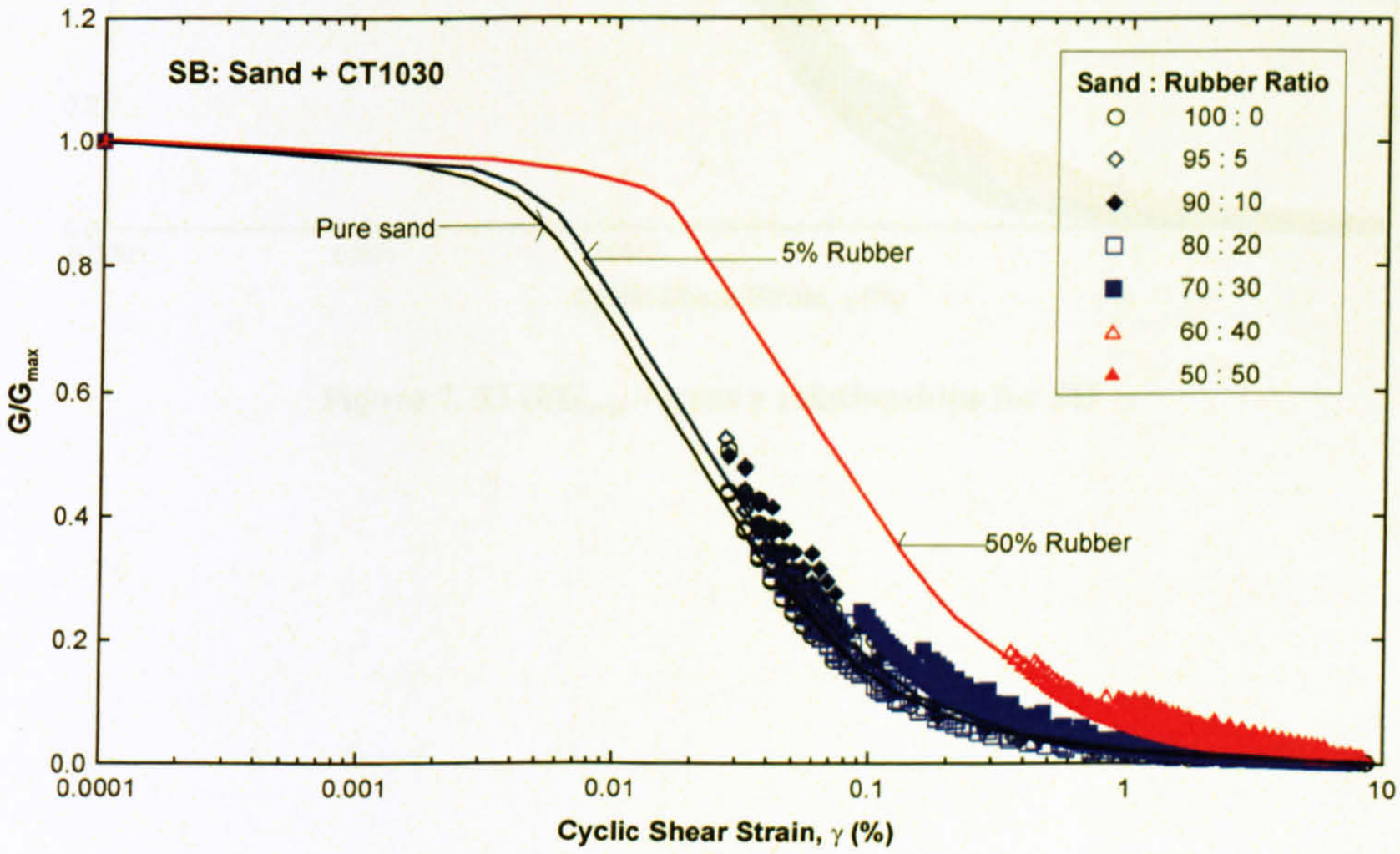

Figure 7. 51 G/G_{max} versus γ relationships for SB

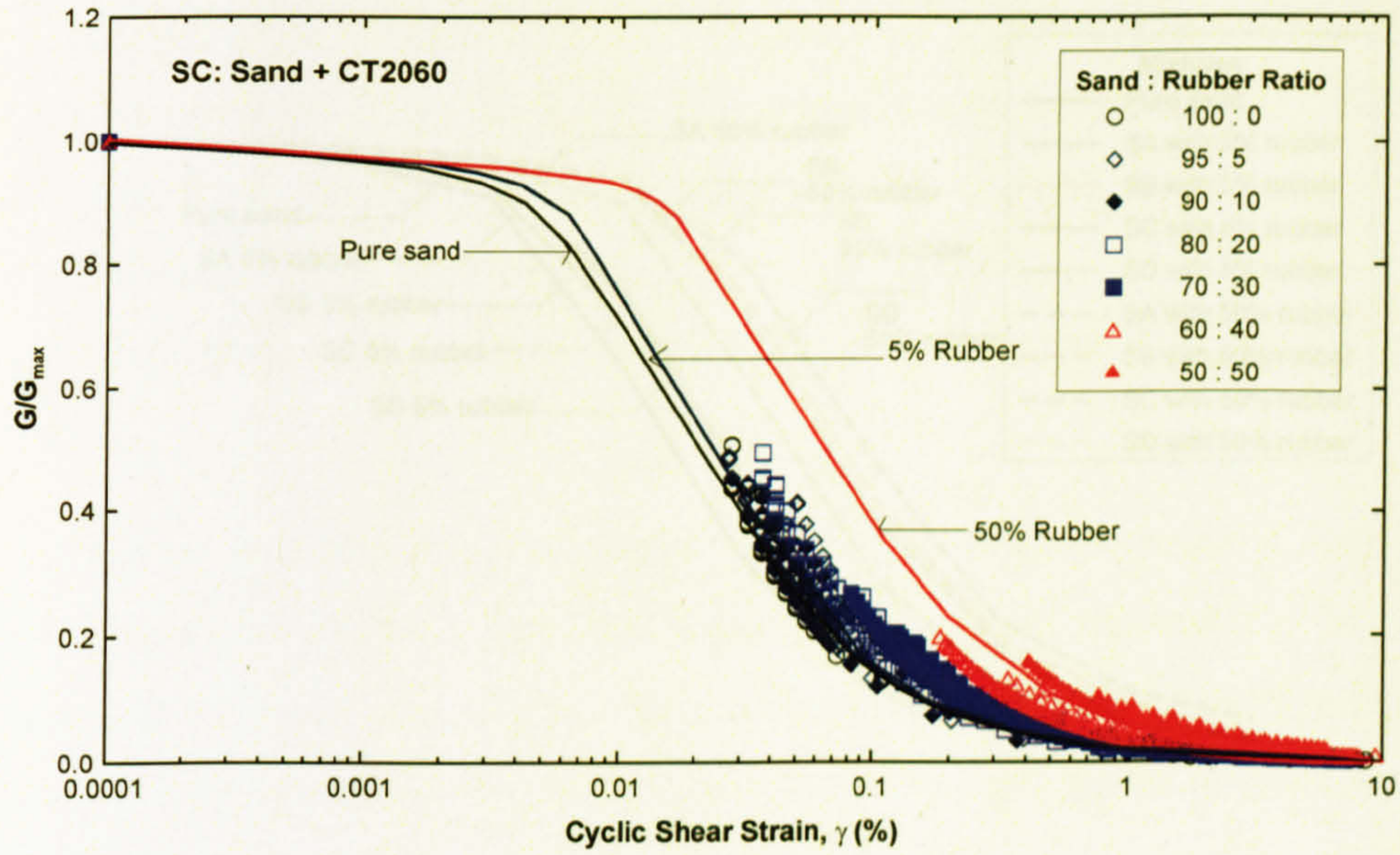

Figure 7. 52 G/G_{max} versus γ relationships for SC

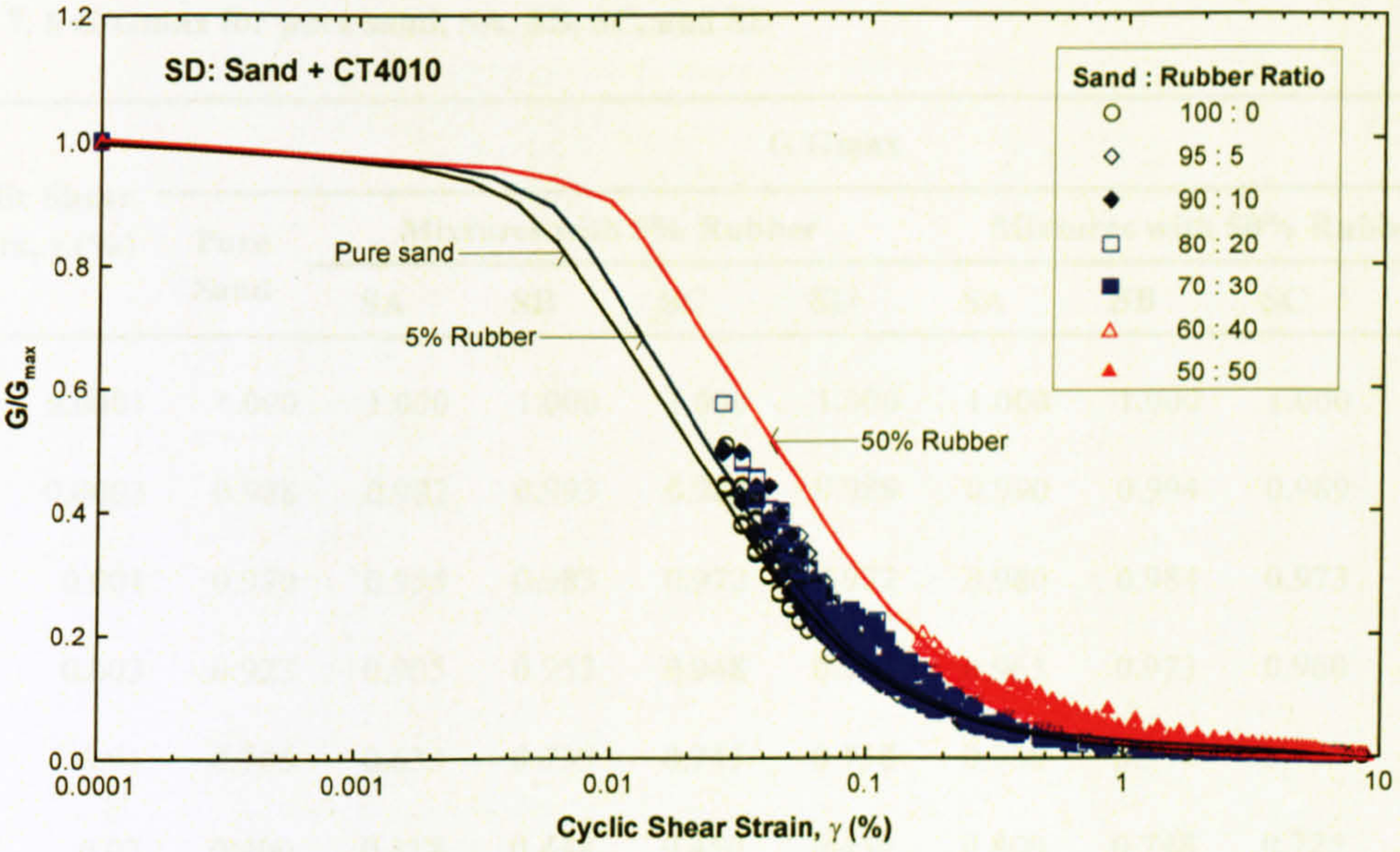

Figure 7. 53 G/G_{max} versus γ relationships for SD

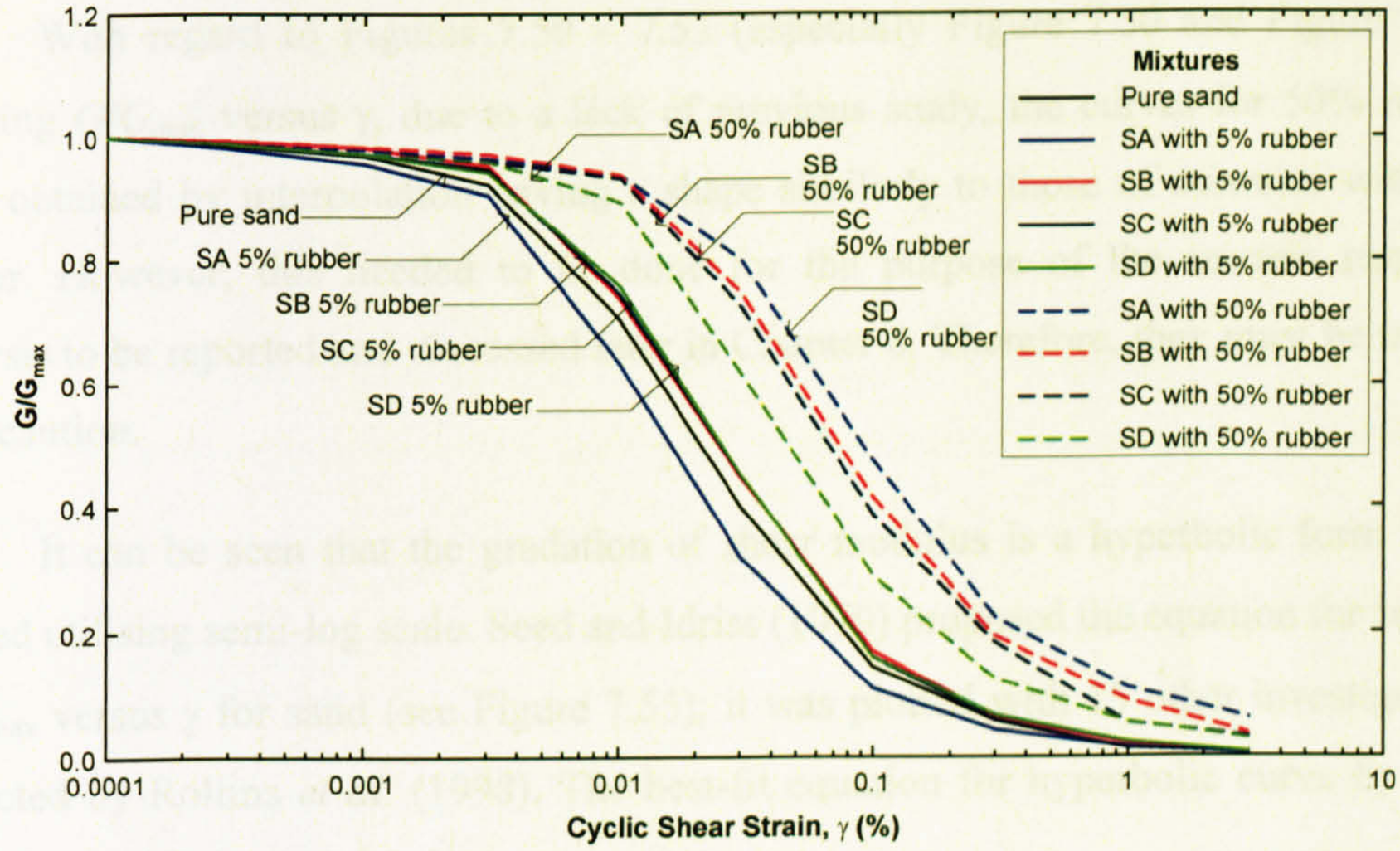

Figure 7. 54 G/G_{max} versus γ relationships for pure sand, SA, SB, SC, and SD

Table 7. 6 G/Gmax for pure sand, SA, SB, SC, and SD

Cyclic Shear Strain, γ (%)	G/Gmax								
	Pure Sand	Mixtures with 5% Rubber				Mixtures with 50% Rubber			
		SA	SB	SC	SD	SA	SB	SC	SD
0.0001	1.000	1.000	1.000	1.000	1.000	1.000	1.000	1.000	1.000
0.0003	0.988	0.982	0.993	0.989	0.989	0.990	0.994	0.989	0.989
0.001	0.970	0.955	0.983	0.972	0.972	0.980	0.984	0.973	0.973
0.003	0.923	0.905	0.953	0.948	0.943	0.965	0.973	0.960	0.960
0.01	0.705	0.633	0.739	0.745	0.758	0.938	0.938	0.933	0.894
0.03	0.400	0.318	0.448	0.450	0.450	0.800	0.748	0.725	0.618
0.1	0.145	0.110	0.170	0.160	0.160	0.473	0.413	0.385	0.288
0.3	0.060	0.045	0.064	0.061	0.068	0.223	0.193	0.183	0.125
1	0.014	0.017	0.023	0.015	0.025	0.110	0.090	0.055	0.056
3	0.006	0.005	0.007	0.007	0.007	0.063	0.038	0.033	0.030

With regard to Figures 7.50 – 7.53 (especially Figure 7.50 and Figure 7.51) showing G/G_{max} versus γ, due to a lack of previous study, the curves for 50% rubber were obtained by interpolation having a shape similarly to those of mixtures with 5% rubber. However, this needed to be done for the purpose of the seismic response analysis to be reported and discussed later in Chapter 8. Therefore, they must be treated with caution.

It can be seen that the gradation of shear modulus is a hyperbolic form when plotted utilising semi-log scale. Seed and Idriss (1970) proposed the equation for best-fit G/G_{max} versus γ for sand (see Figure 7.55); it was plotted with 15 other investigations collected by Rollins *et al.* (1998). The best-fit equation for hyperbolic curve by Seed and Idriss (1970 is shown below:

$$\frac{G}{G_{max}} = \frac{1}{[1.2+16\gamma(1+10^{(-20\gamma)})]} \qquad \textbf{(Eq. 7. 15)}$$

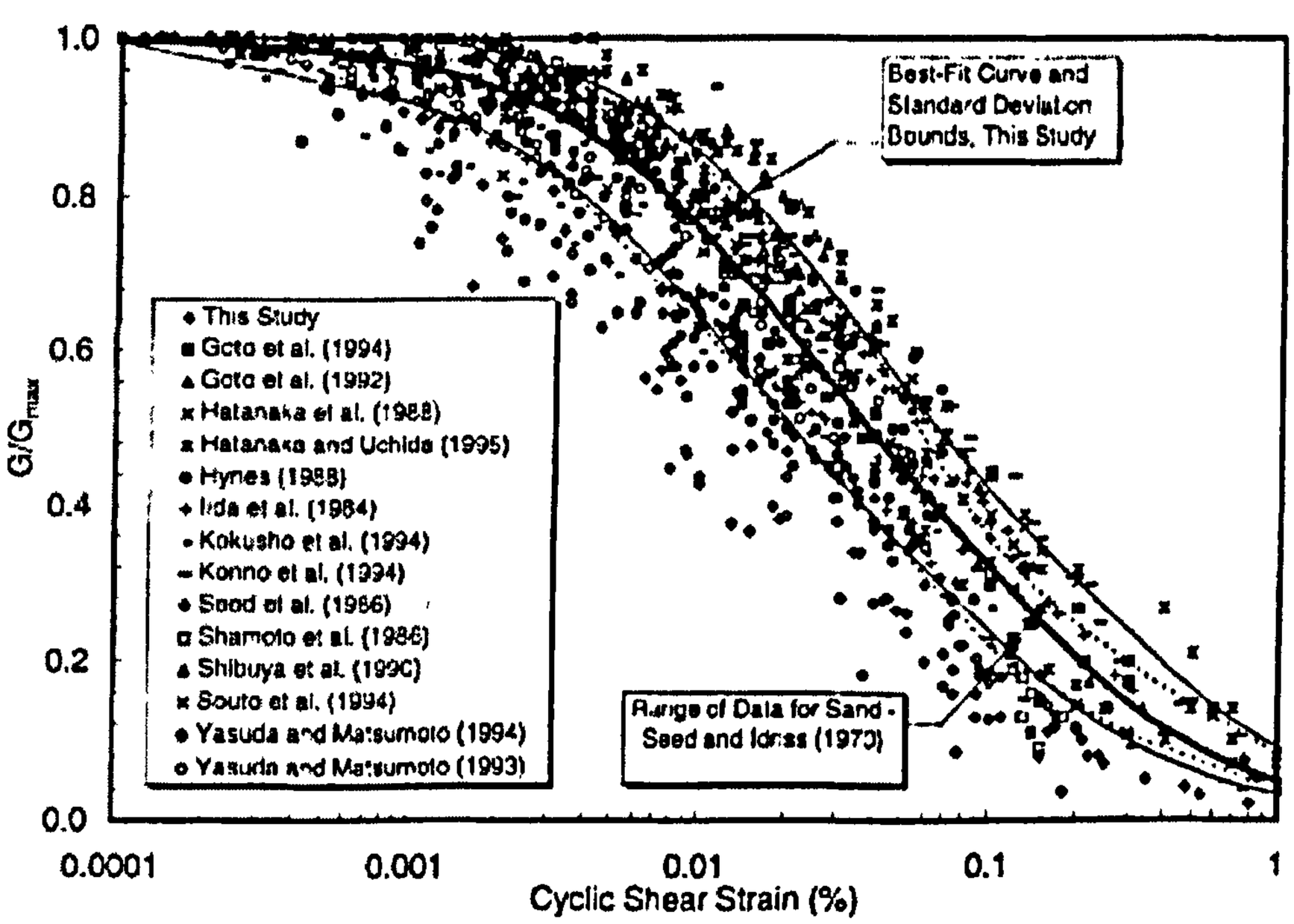

Figure 7. 55 G/G_{max} versus γ relationships for gravelly soils along with best-fit curve and ± one standard deviation bounds for entire data set (after Rollins *et al.*, 1998)

This research adopted the equation proposed by Seed and Idriss (1970) to fit the data points for the test sand shown in Figure 7.54 by rewriting Eq. 7.15 to be:

$$\frac{G}{G_{max}} = \frac{1}{[A+B\gamma(C+D^{(-E\gamma)})]} \qquad \textbf{(Eq. 7. 16)}$$

There are five variables; A, B, C, D, and E, in Eq. 7.16. By varying all variables the outcome was the equation that reasonably fitted the data points for the sand tested, as shown below:

$$\frac{G}{G_{max}} = \frac{1}{[1+15.7\gamma(1.3+0.85^{(-20\gamma)})]} \qquad \textbf{(Eq. 7. 17)}$$

For sand mixed with tyre chips SA, SB, SC, and SD, however, it was found that Eq. 7.16 needed to be modified by keeping three variables but varying the other two; the rewritten equation for best-fit for sand mixed tyre chips is:

$$\frac{G}{G_{max}} = \frac{1}{[1+B\gamma(C+0.76^{(-20\gamma)})]} \qquad \textbf{(Eq. 7. 18)}$$

where:

B = 9.6, 6.1, 5.2, 4.6 for SA, SB, SC, SD, with 5% rubber,

= 9.8, 6.5, 5.9, 5.4 for SA, SB, SC, SD, with 50% rubber,

C = 4.5, 4.9, 6.2, 6.4 for SA, SB, SC, SD, with 5% rubber, and

= 0.2, 0.85, 1.1, 2.7 for SA, SB, SC, SD, with 50% rubber.

7.3.3 Damping Ratios (from undrained cyclic triaxial tests)

Damping ratio is the ratio that describes the loss of energy of a material or system. The damping ratio is dependent on the level of shear strain, similar to the shear modulus but in the opposite way, i.e., the larger the shear strain the greater the damping ratio. For a cyclic triaxial test, given a stress strain loop illustrated by Figure 7.56, the damping ratio can be determined by Eq. 7.19.

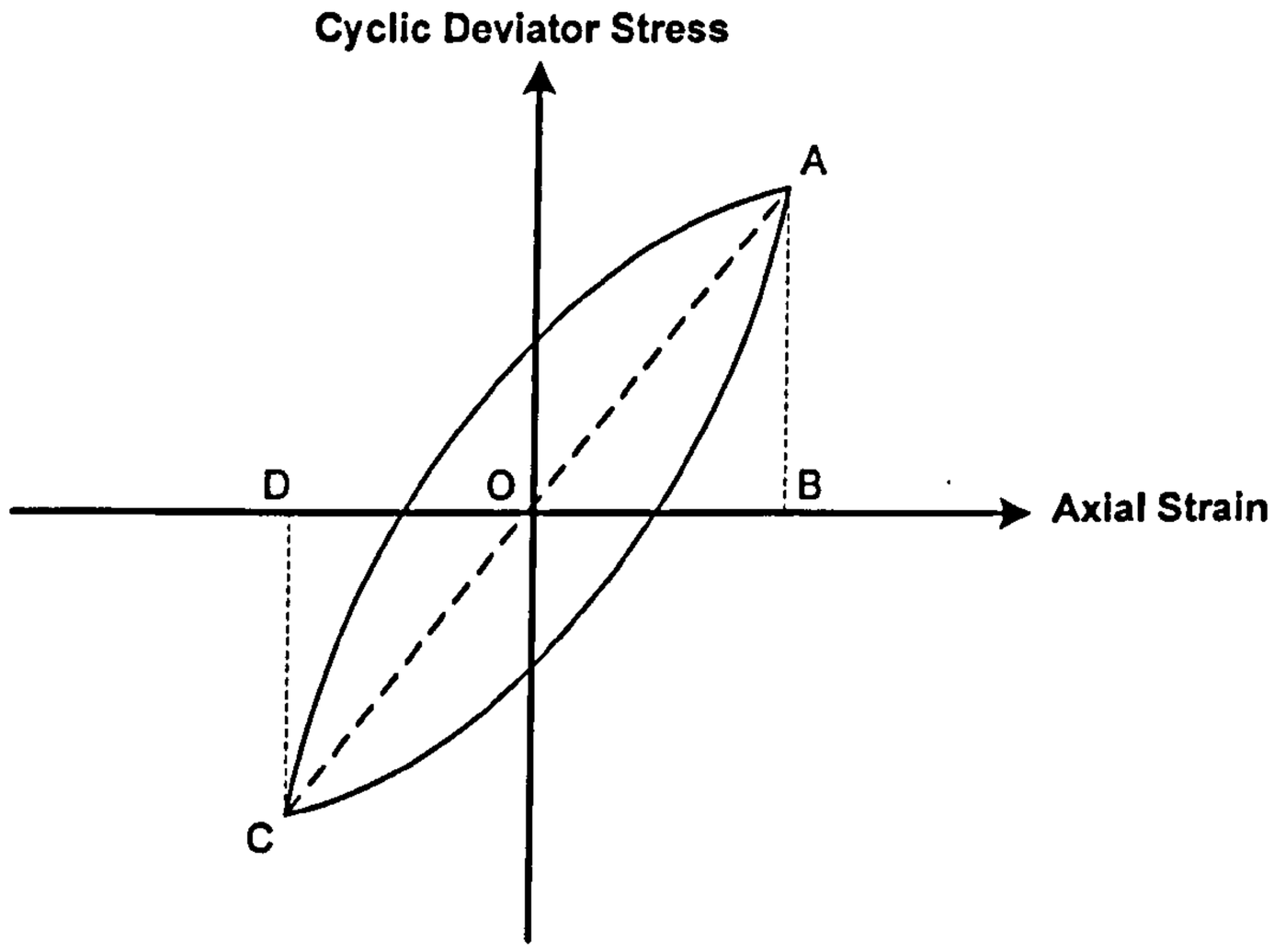

Figure 7. 56 Damping ratio determination from cyclic triaxial test

$$D = \frac{1}{2\pi} \frac{area\ of\ hysteris\ loop}{(area\ of\ triangle\ AOB)+(area\ of\ triangle\ COD)} \qquad \textbf{(Eq. 7. 19)}$$

The damping ratios in per cent for SA having rubber contents of 5, 10, 20, 30, 40, and 50% are illustrated by Figure 7.57(a) – (f), respectively. They also include the values for pure sand in order that the effect of rubber content could be investigated. For the mixtures SB, SC, and SD, the damping ratios are illustrated by Figures 7.58 – 7.60, respectively. In addition, for all SA sand to rubber ratios, the damping ratios were plotted together for further analysis, and are shown in Figure 7.61. Figures 7.62 – 7.64 show the results for all sand to rubber ratios of SB, SC, and SD, respectively.

Considering the damping ratio at 0.1% cyclic shear strain, it was observed that the value for SA with 5% rubber was just slightly greater than that of pure sand, suggesting that this small amount of rubber has very little effect on the damping value. When the rubber was increased to 10% for SA, however, its damping ratio was visibly greater than that of S, but still not significant. A substantial difference was observed only when the rubber was increased to 20%, which was almost three times greater. As the rubber was increased to 30% and higher, even though no data exists at the same cyclic shear strains as for pure sand, it may be assumed that their values are higher.

The behaviour of the damping ratio for SB and SC was observed to be very similar; hence, they may be reported and discussed as a group. For the mixtures having 5 and 10% rubber, it can be seen that the damping ratios were considerably higher than

those of pure sand and SA with the same rubber content. The damping ratio was observed to be even greater when the rubber was increased to 20 and 30%. However, when the rubber was increased to 40 and 50%, the generated damping ratios occurred at the cyclic shear strain much greater than 0.1%. Thus, they could not be compared with pure sand. Nonetheless, they may also be assumed to be much higher than that of pure sand.

For SD the behaviour of the damping ratio was observed to be slightly different to SB and SC. At 5% rubber, the damping ratio was higher than that of pure sand, but slightly less than those of SB and SC. This was also the case for the mixtures containing rubber contents of 10, 20, and 30%. Similar to SA, SB, and SC, the damping ratios for SD having rubber contents of 40 and 50% were observed at a cyclic shear strain considerably greater than 0.1%. It should be noted that for SA, SB, SC, and SD having rubber contents of 40% and higher, the reason the damping ratios were observed at much higher cyclic shear strain is that they required greater cyclic deviator stresses to trigger the liquefaction. As such, the range of cyclic shear strain generated was larger compared to the mixtures having lower amounts of rubber.

It is interesting to compare the damping ratio of the test sand with other studies. For example, at 0.1% cyclic shear strain, it can be seen that the damping ratio for pure sand was approximately 5%. Rollins *et al.* (1998) studied the shear modulus and damping relationships for gravelly sands having mean particle size of 0.5mm by employing cyclic triaxial tests with 100kPa confining pressure similar to this research. Their results showed that the damping ratios at 0.1% cyclic shear strain with respect to upper and lower bounds were 2% and 6% (see Figure 7.65), which is quite similar to this research.

Moreover, the damping ratio of Fraction E silica sand saturated with silicone oil at 50cS viscosity was investigated by using dynamic centrifuge test (Brennan *et al.*, 2005). The results, as illustrated by Figure 7.66, shows that at 0.1% shear strain the damping ratio is about 6%, also comparable to this research.

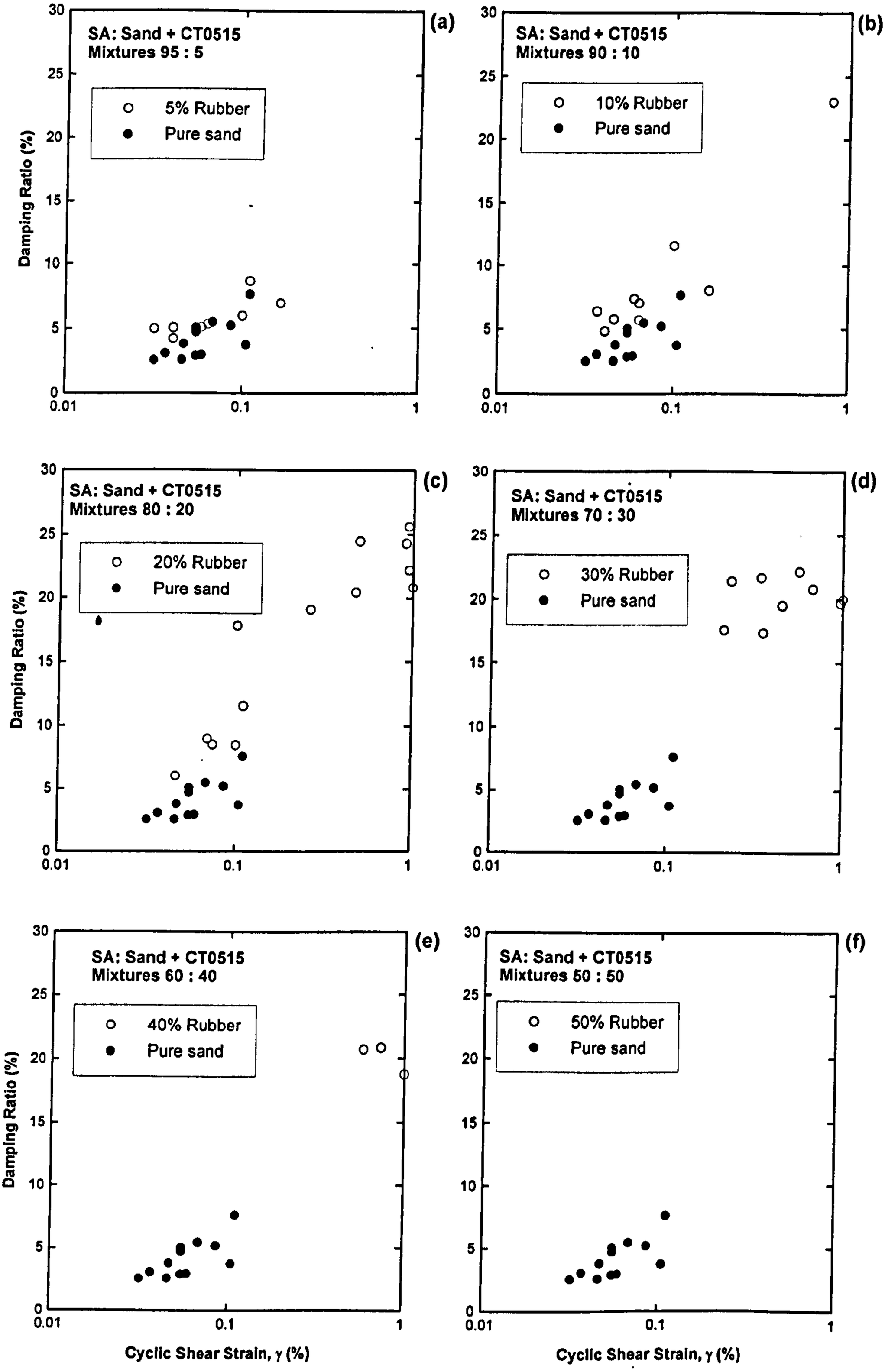

Figure 7. 57 Damping ratios for pure sand and SA

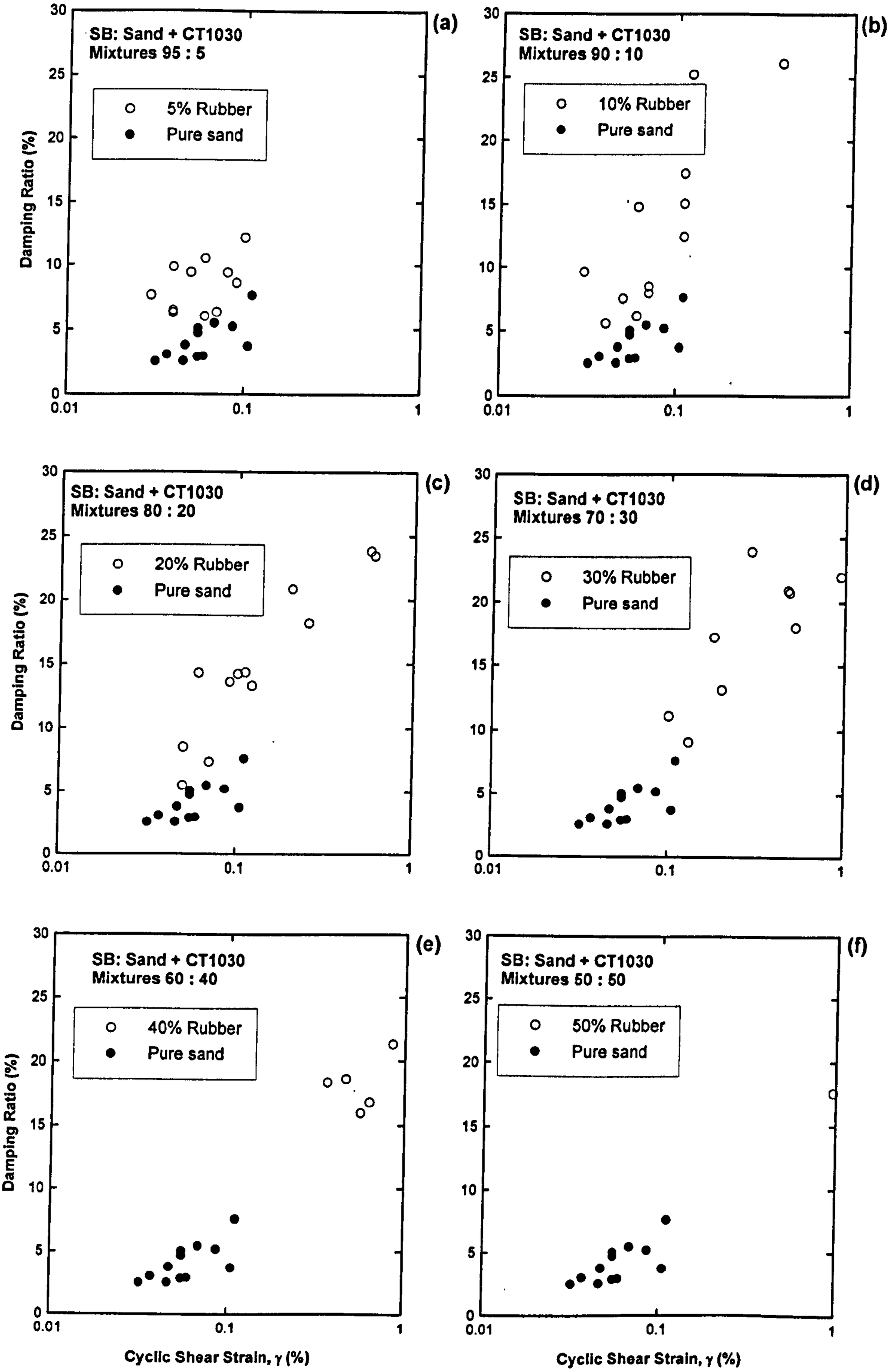

Figure 7. 58 Damping ratios for pure sand and SB

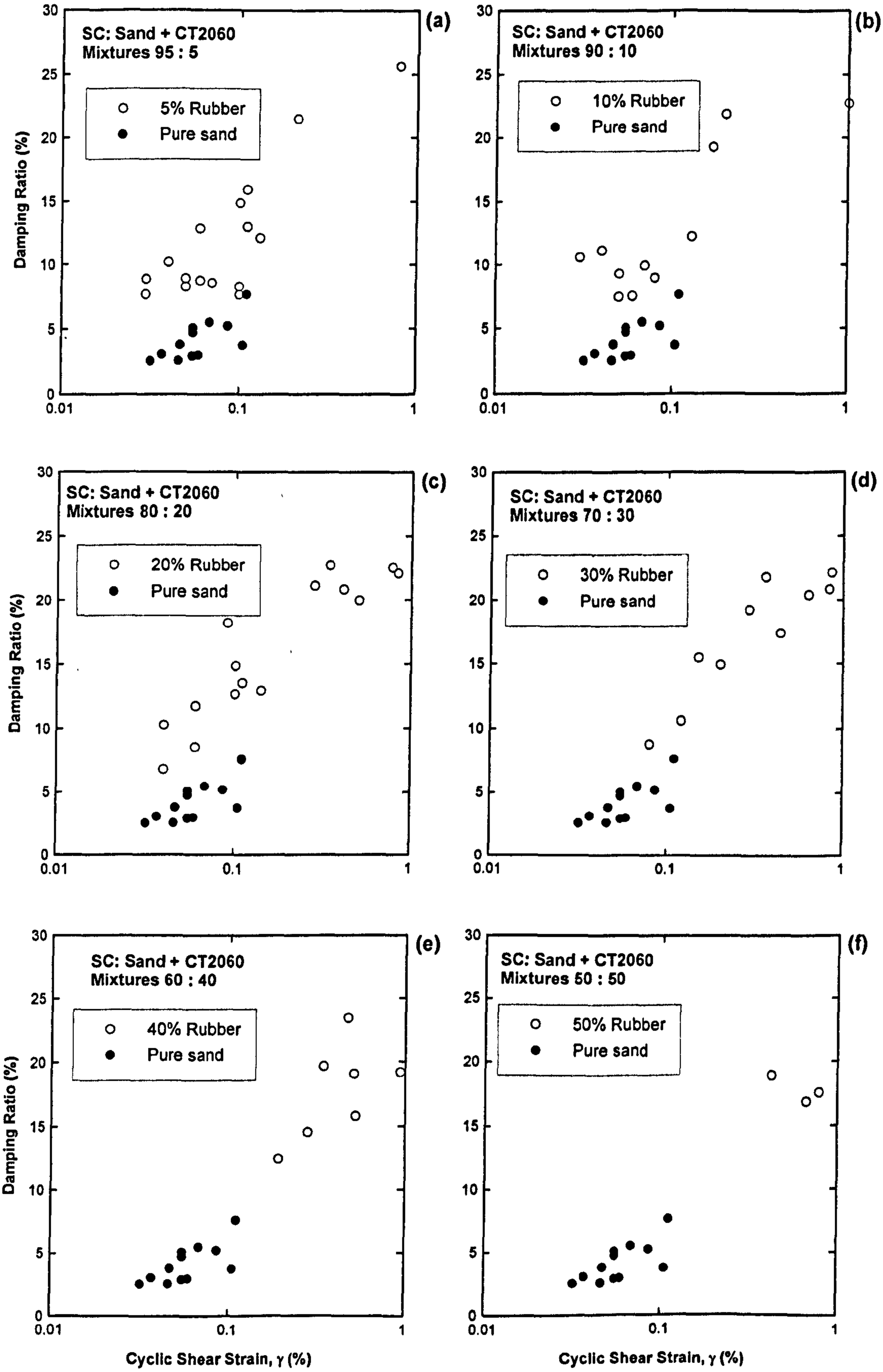

Figure 7. 59 Damping ratios for pure sand and SC

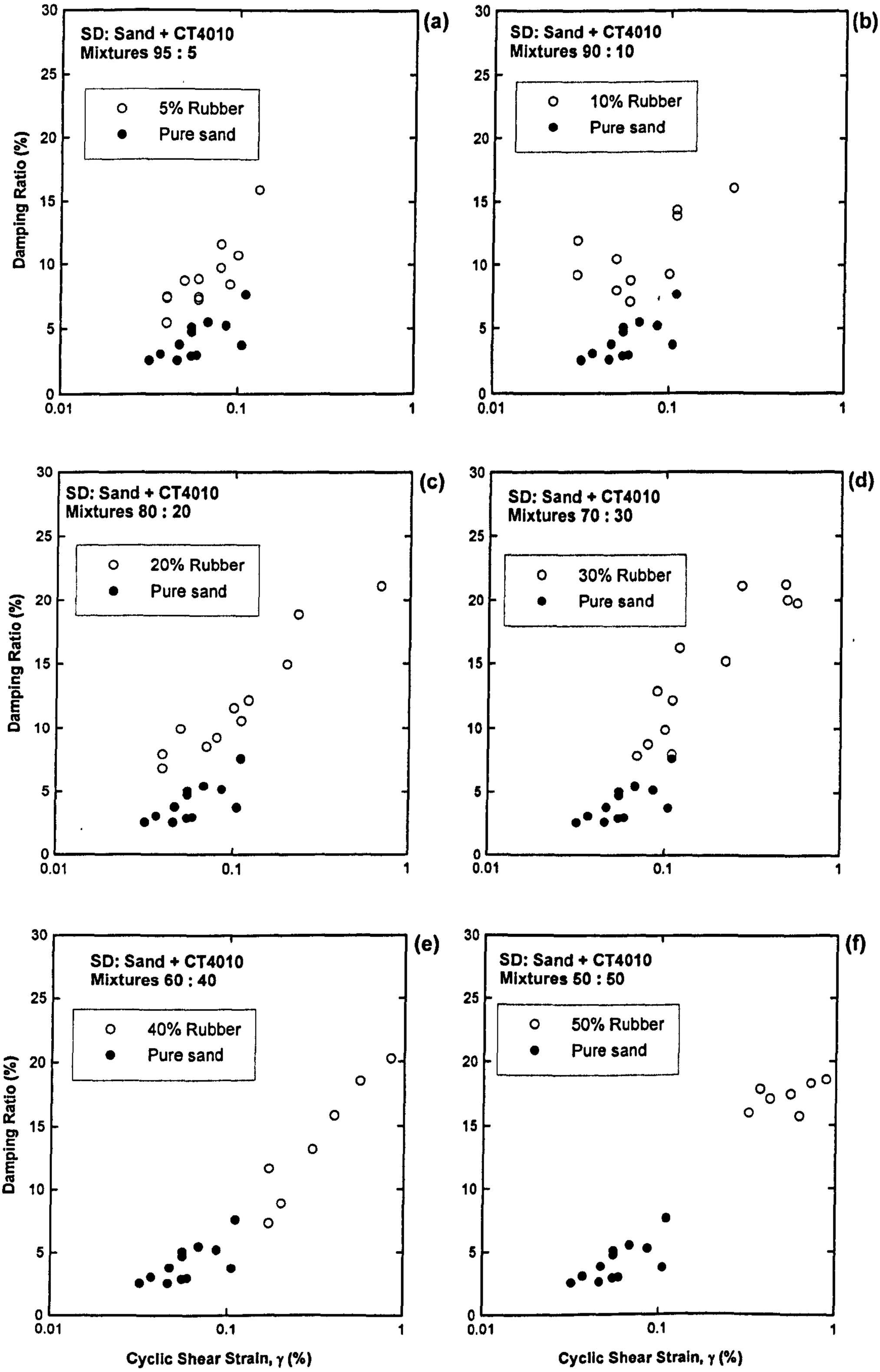

Figure 7. 60 Damping ratios for pure sand and SD

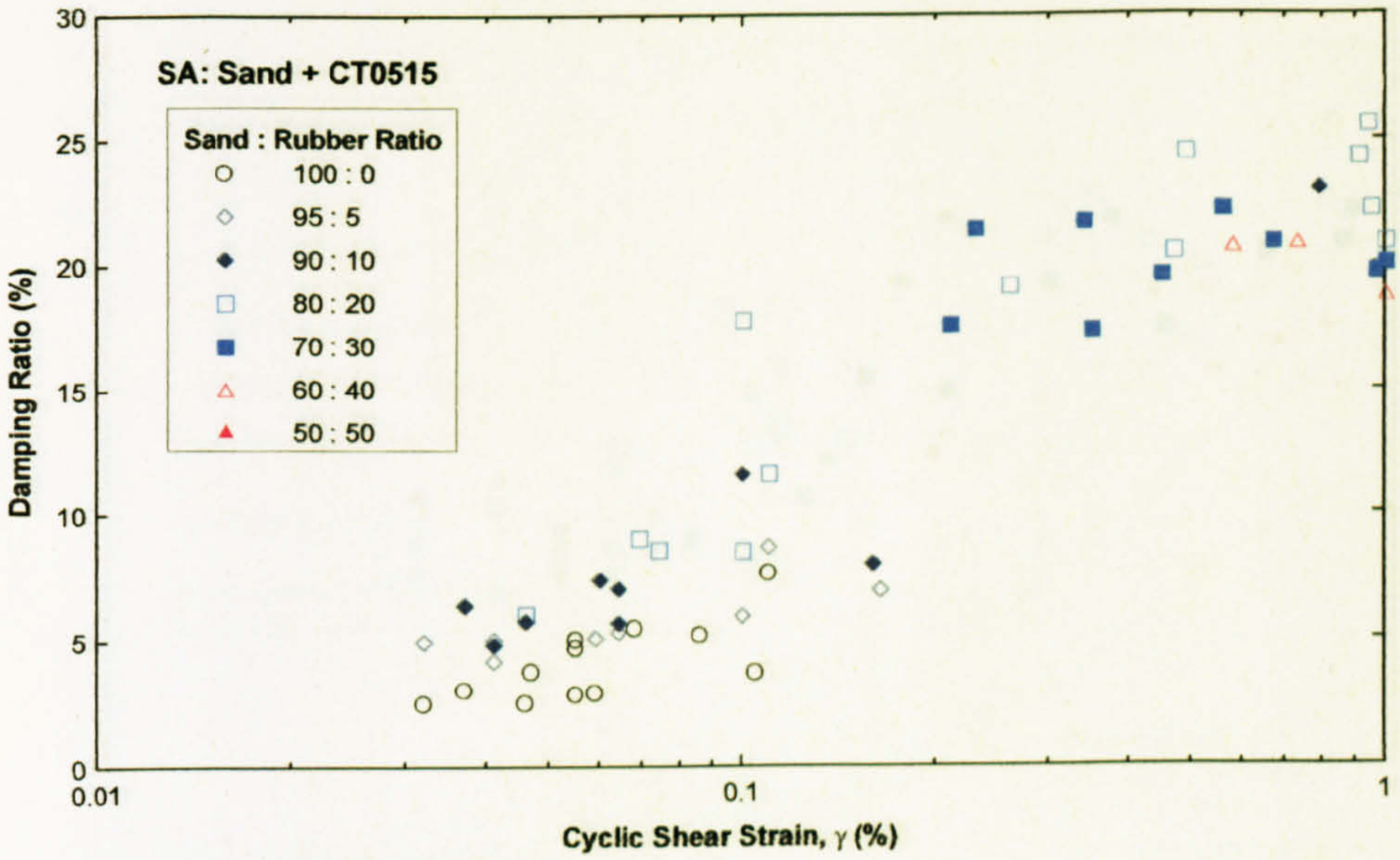

Figure 7. 61 Damping ratios mixtures SA

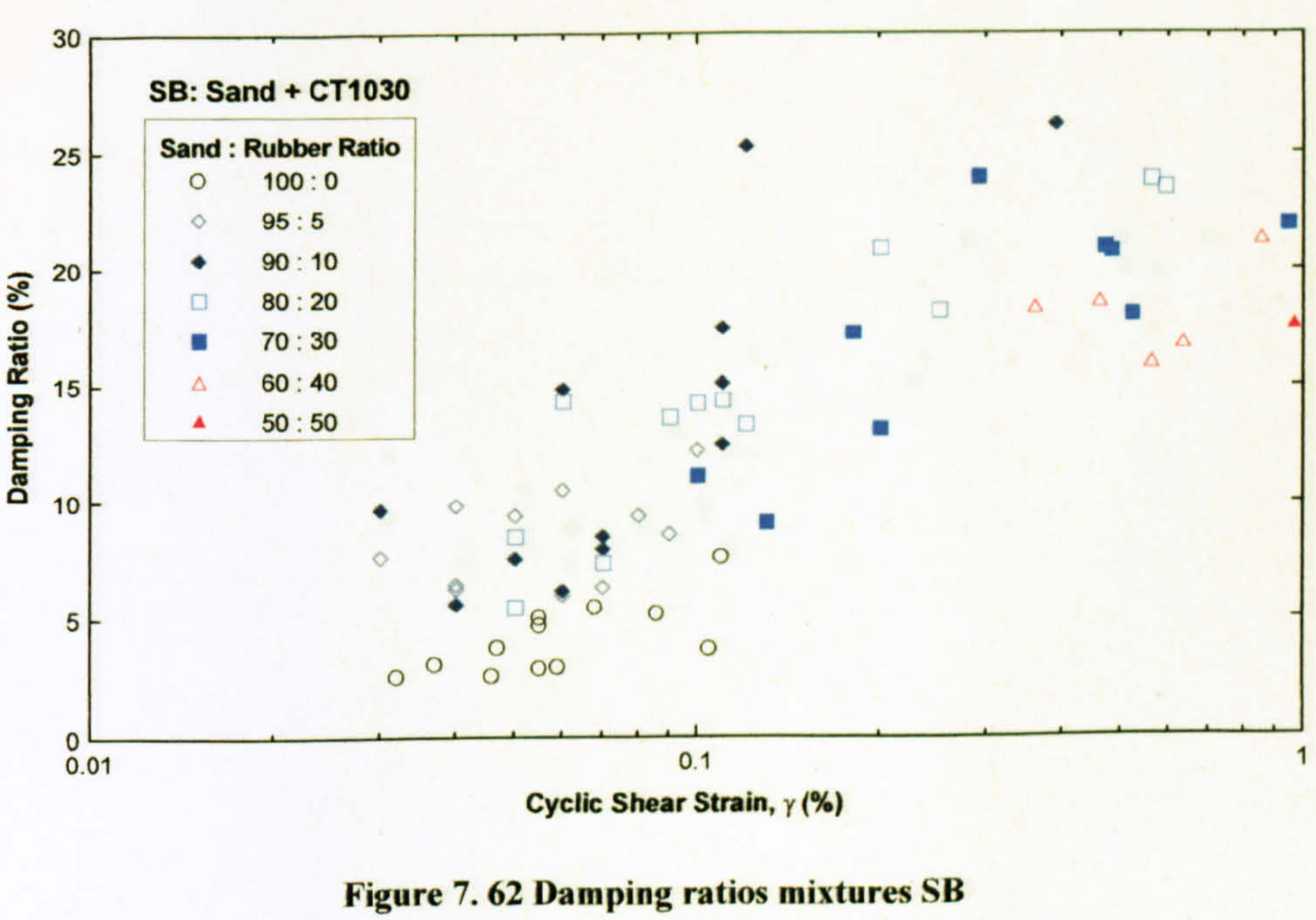

Figure 7. 62 Damping ratios mixtures SB

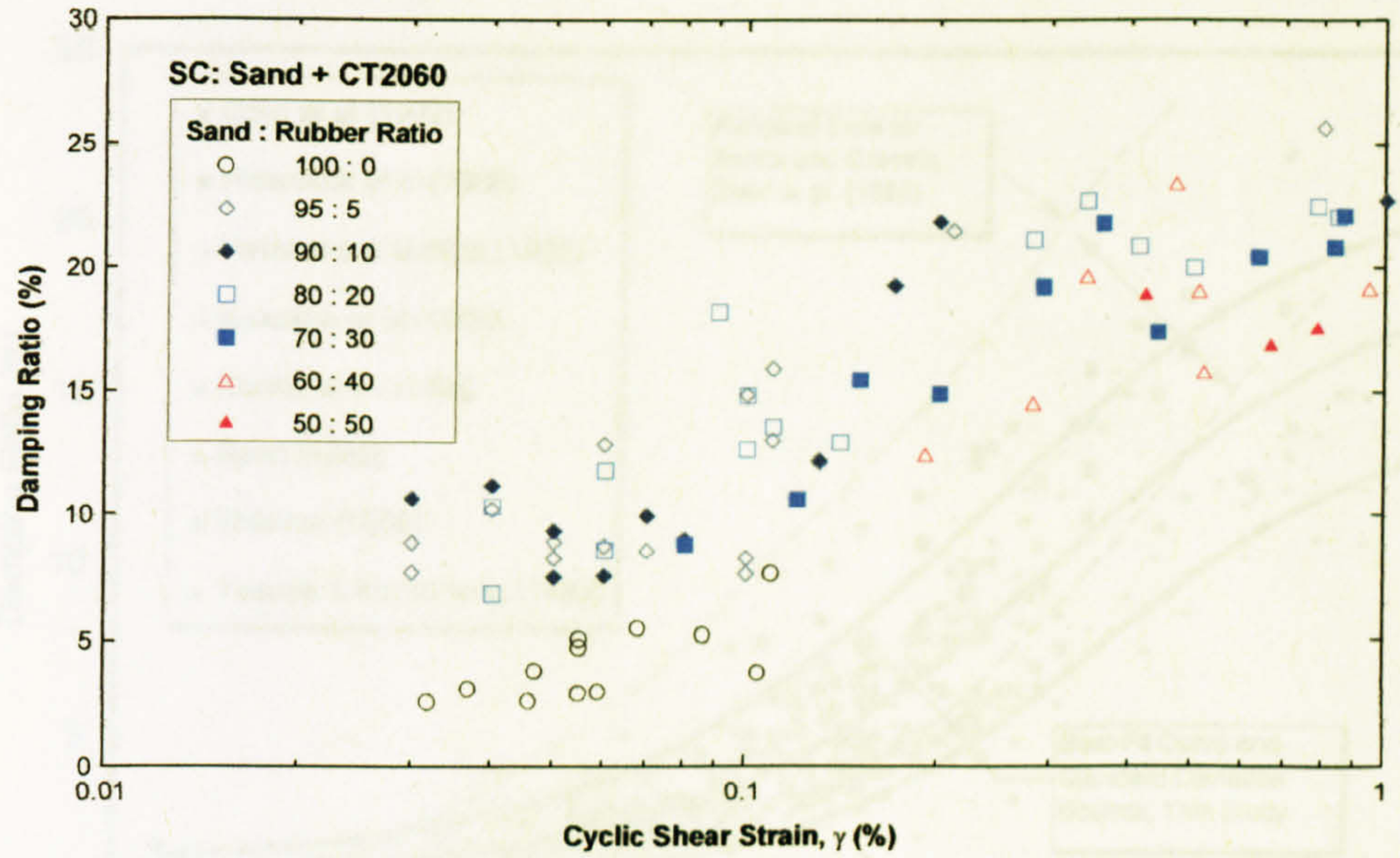

Figure 7. 63 Damping ratios mixtures SC

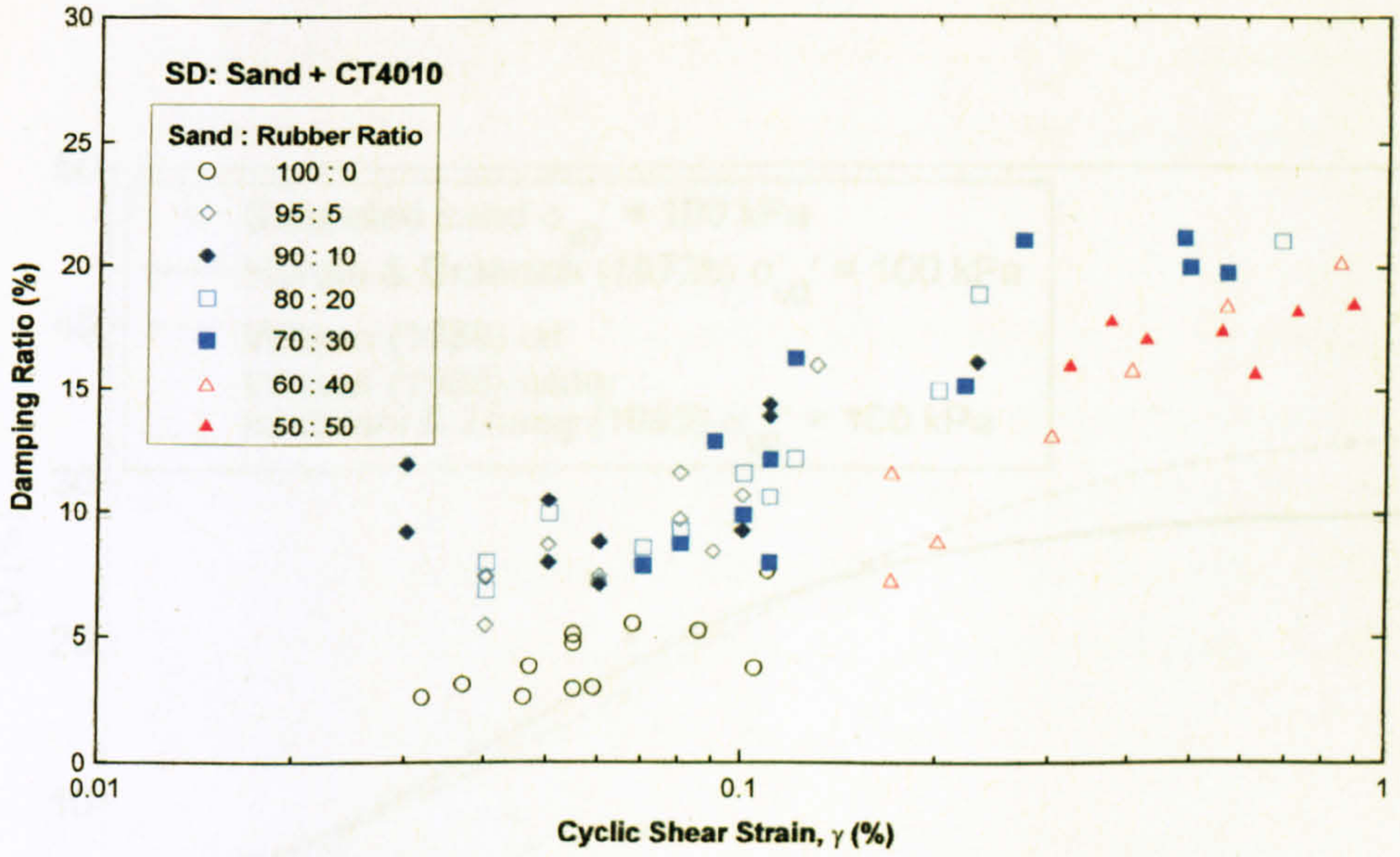

Figure 7. 64 Damping ratios mixtures SD

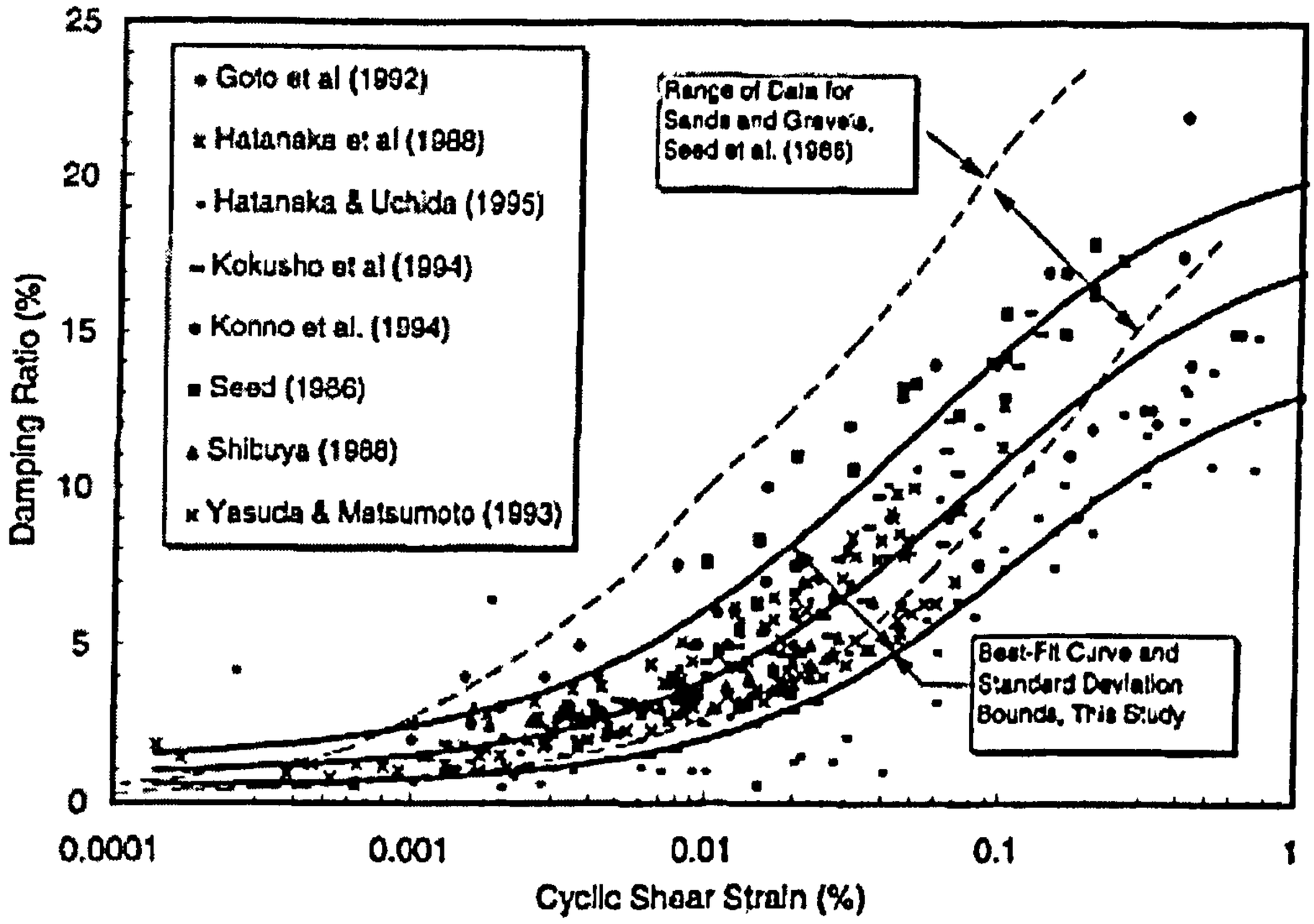

Figure 7. 65 Damping ratios for sand and gravel (after Rollins *et al.*, 1998)

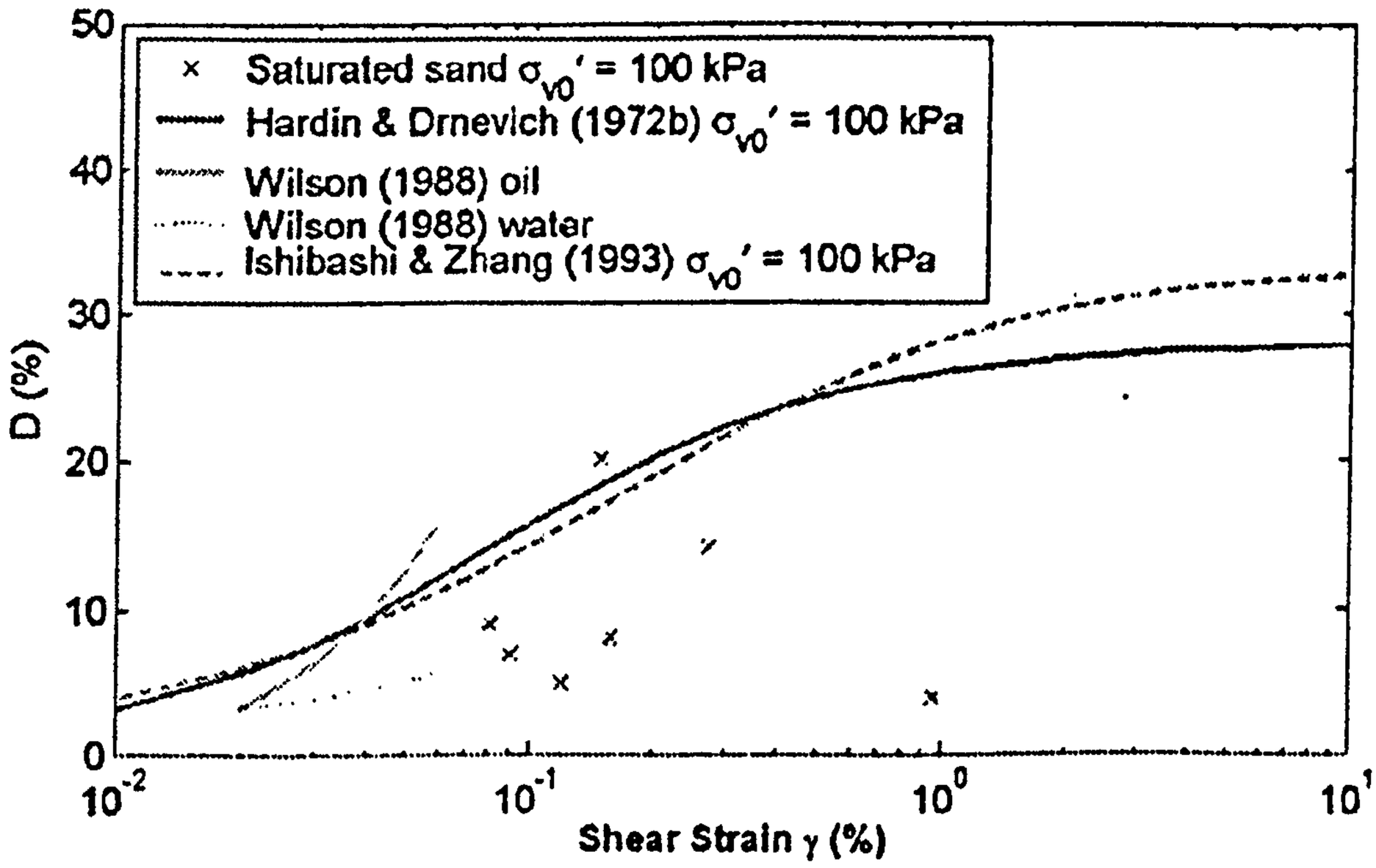

Figure 7. 66 Damping-shear strain for saturated sand, σ'_{vo} = 100 kPa (after Brennan *et al.*, 2005)

CHAPTER 8

SEISMIC RESPONSE ANALYSIS BY EQUIVALENT LINEAR MODEL

8.1 Introduction

When an earthquake strikes, the direct consequence is that the ground shakes with the possibility of structural damage depending on the level of shaking. For geotechnical engineers, however, landslides and soil liquefaction are of more concern. Before these problems can be examined, the characteristics of ground motion must be first appreciated. To be able to compute the ground motion as well as its consequences, both basic soil properties and an understanding of the behaviour of the soil under dynamic loading are needed.

The aim of this chapter is to demonstrate how to harness the test data obtained from the undrained cyclic triaxial tests and the bender element tests for analysing the ground response caused by an earthquake. A typical example of layered soil comprising sands and clays sitting on bedrock has been presented. This has then been modified by introducing the materials whose dynamic properties have been examined in this thesis tested, resulting in eight different scenarios.

The acceleration used for the seismic analysis was obtained from 1989 Loma Prieta earthquake. A computer program called Equivalent-linear Earthquake Response Analysis, EERA for short, was employed to analyse the ground response, giving resultant ground accelerations, shear strains, and shear stresses. The analysis of the liquefaction potential for all scenarios was also included.

8.2EERA program

EERA (Bardet *et al.*, 2000) is a computer program for the analysis of site response caused by earthquake shaking. It was developed at the University of Southern California in 1998 using a computer language FORTRAN 90; nonetheless, the input and output are fully integrated within the spread sheet software Excel.

Its basic concepts are the same as the well-known software SHAKE (Schnabel *et al.*, 1972) that has been the standard software for geotechnical earthquake engineering. As the name suggests, the concepts of an equivalent linear approach are implemented for the analysis. Note that the equivalent linear approach employs the stress-strain response of a soil based on a Kelvin-Voigt model at which the shear stress τ depends on two factors: (1) the shear strain γ and (2) the rate of shear strain $d\gamma/dt$. The full details of the equivalent linear model can be found in Kramer (1996) and Bardet *et al.* (2000).

8.3Examples of EERA Analysis

8.3.1 Earthquake Data

The acceleration used for the analysis was from within an example in EERA; it was obtained from the measurement at Diamond Heights during the 1989 Loma Prieta earthquake having a moment magnitude M_w of 6.9. The time step for the constant time interval separating the acceleration values defining the earthquake input motion was 0.02s. The recorded acceleration is illustrated by Figure 8.1(a). The peak acceleration recorded was -0.1129g; the time at which the acceleration peaked was 10.94s. The recorded acceleration was filtered using a cut-off frequency of 25Hz; the filtered acceleration is illustrated by Figure 8.1(b).

The compatible shear modulus and damping ratio were calculated using the shear strain ratio; which is the ratio of the equivalent uniform shear strain (effective shear strain as used in the program) to the maximum shear strain. The equivalent uniform shear strain can be calculated from the relationship (M-1)/10 where M is an earthquake magnitude. This relationship was suggested by AIJ (2001) and Orense (2005).

The reason for using the concept of the shear strain ratio for the analysis is based on the assumption that the onset of soil liquefaction is influenced by the number of load

cycles. The acceleration observed indeed shows the maximum acceleration that has nothing to do with the number of load cycles (Orense, 2005). Thus, it is necessary to convert the maximum shear strain to a uniform shear strain so that the analysis can be based on the repeated load cycles.

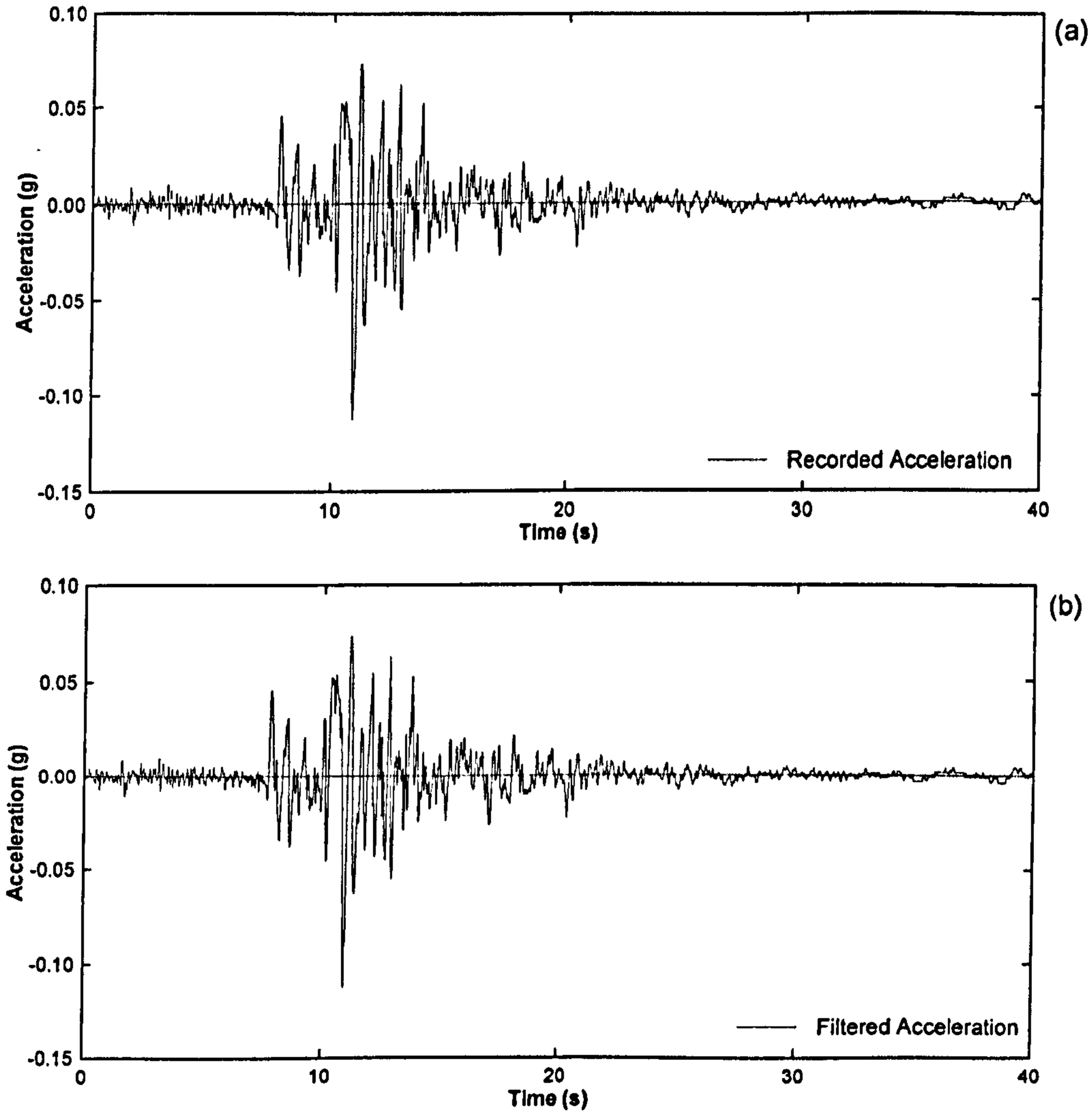

Figure 8. 1 Acceleration from the Loma Prieta Earthquake

8.3.2 Details of Layered-Soils

EERA provides an example of layered soils that was used for the following demonstration. The example comprises 17 layers, including two types of soil; sand and clay sitting on bedrock. Working from the top of the bedrock are layers of the sand, followed by four layers of clay; then the final four layers are the sand. The basic and dynamic soil properties as well as the layer thickness of the original example are illustrated by Figure 8.2.

The details of the layered soils from the clay downwards were kept unchanged. Layer 1 was further divided into two sub layers resulting in a total of 18 layers. The ground response analysis was done by replacing the top five layers of the example by the materials that had been tested in this research, namely Leighton Buzzard 16/30 sand, the mixture 50SD (50% sand + 50% tyre chips CT4010), and the mixture 95SD (95% sand + 5% tyre chips CT4010). This was because the dynamic properties were already available. The sand and the mixtures were altered within the top five layers, resulting in eight scenarios, as shown by Table 8.1. In addition, the water table level was assumed to be at the bottom of layer 2, depth -1.5m; and, these conditions were applied to all scenarios. This was intended to create a saturated soil below the water table in order that the liquefaction potential could be analysed.

The soil profile and properties used for EERA for scenario 1 are illustrated by Figures 8.3 and 8.4, respectively. For scenarios 2-8, they are illustrated by Figures 8.5 and 8.6, Figures 8.7 and 8.8, Figures 8.9 and 8.10, Figures 8.11 and 8.12, Figures 8.13 and 8.14, Figures 8.15 and 8.16, and Figures 8.17 and 8.18, respectively.

Apart from the properties shown in the soil profiles, two important dynamic properties are needed for the seismic response analysis, the shear modulus and the damping ratio. For the clay and the sand the typical values which come with the program were employed (see Figure 8.19(a) and (b), respectively).

For Leighton Buzzard 16/30 sand, the shear modulus employed was obtained from the undrained cyclic triaxial tests as well as the bender element tests as previously reported in Chapters 6 and 7, respectively. However, the damping ratio obtained from the cyclic test covered a very limited range of shear strains. Thus, for convenience and demonstration purposes, the damping curve for Leighton Buzzard 16/30 sand was determined by scaling typical sand provided by 60%. Nevertheless, this was based on the principle that the scaled values should be approximately similar to those of Leighton Buzzard 16/30 sand at the same shear strain obtained from the cyclic triaxial test. These were the same for the 50SD and 95SD mixtures, except that the damping ratio curve for the clay was scaled by 85% and 90%, respectively.

The shear modulus and damping ratio curves for Leighton Buzzard 16/30 sand as well as the mixtures 50SD and 95SD are illustrated by Figure 8.19(c), (d), and (e), respectively. For the bedrock the curves are illustrated by Figure 8.19(f).

Table 8. 1 Scenarios for layered soils for EERA analysis

Layer	Thickness (m)	Scenario 1	Scenario 2	Scenario 3	Scenario 4	Scenario 5	Scenario 6	Scenario 7	Scenario 8	Note
1	0.76	16/30 Sand	16/30 Sand	16/30 Sand	16/30 Sand	16/30 Sand	16/30 Sand	16/30 Sand	16/30 Sand	
2	0.76	16/30 Sand	16/30 Sand	16/30 Sand	16/30 Sand	16/30 Sand	16/30 Sand	16/30 Sand	16/30 Sand	Water Table
3	1.52	16/30 Sand	16/30 Sand	16/30 Sand	**50SD**	**50SD**	**50SD**	16/30 Sand	**95SD**	
4	3.05	16/30 Sand	16/30 Sand	**50SD**	16/30 Sand	**50SD**	**50SD**	16/30 Sand	**95SD**	
5	3.05	16/30 Sand	**50SD**	16/30 Sand	16/30 Sand	16/30 Sand	**50SD**	**95SD**	**95SD**	

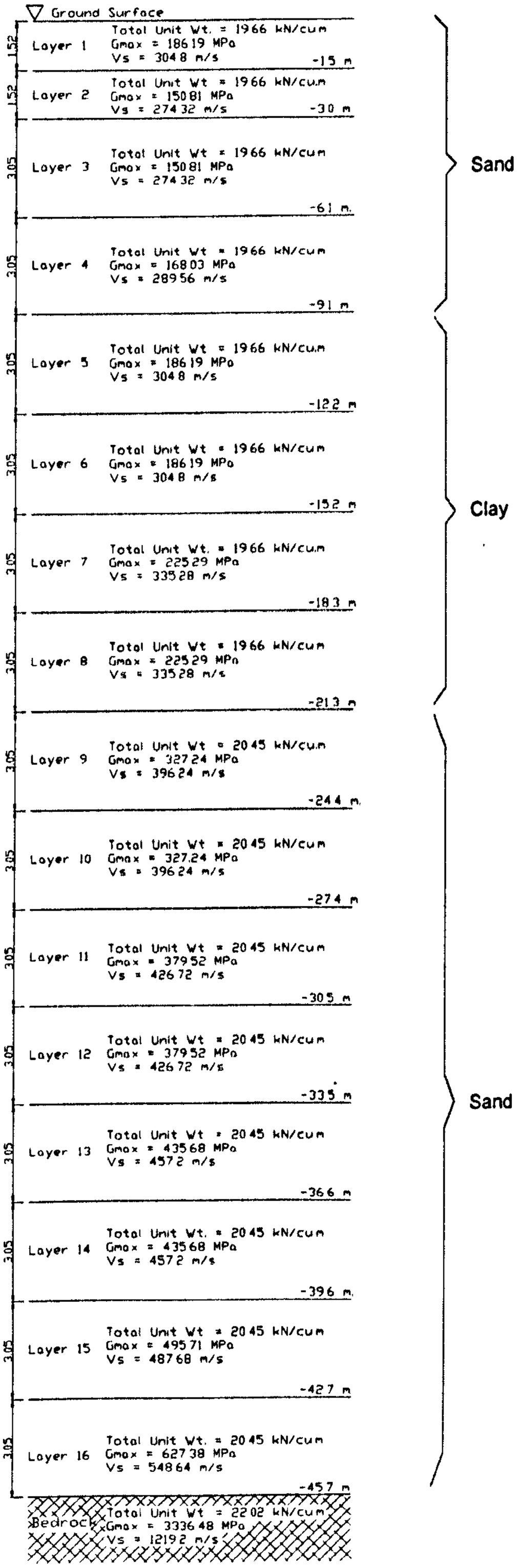

Figure 8. 2 Original soil profile

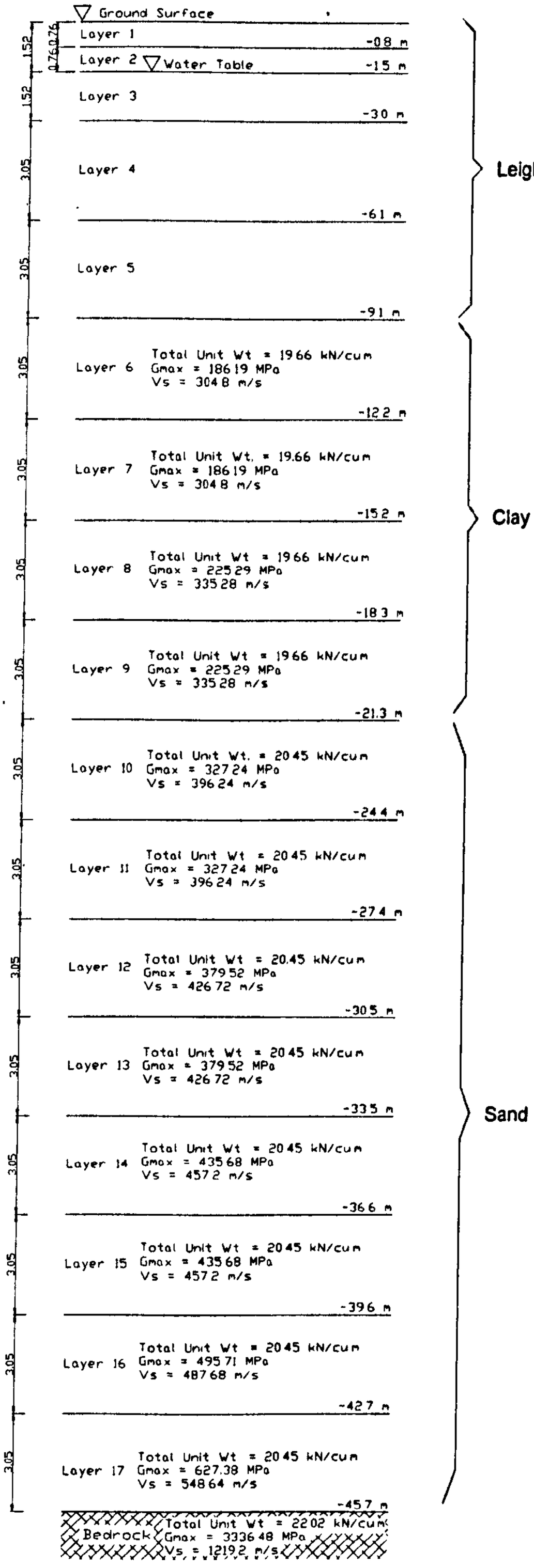

Figure 8. 3 Profile of layered-soils for scenario 1

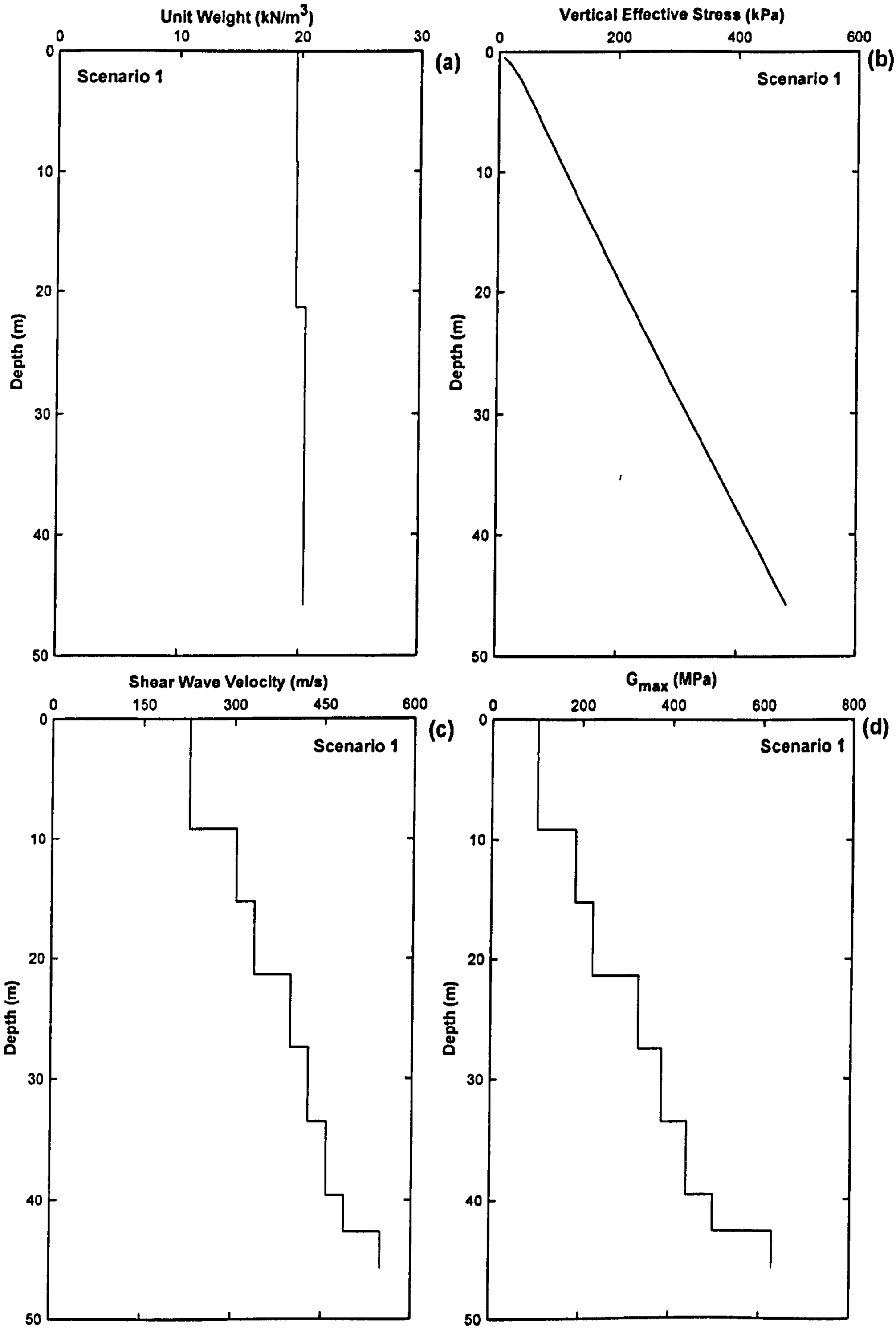

Figure 8. 4 Soil properties for scenario 1

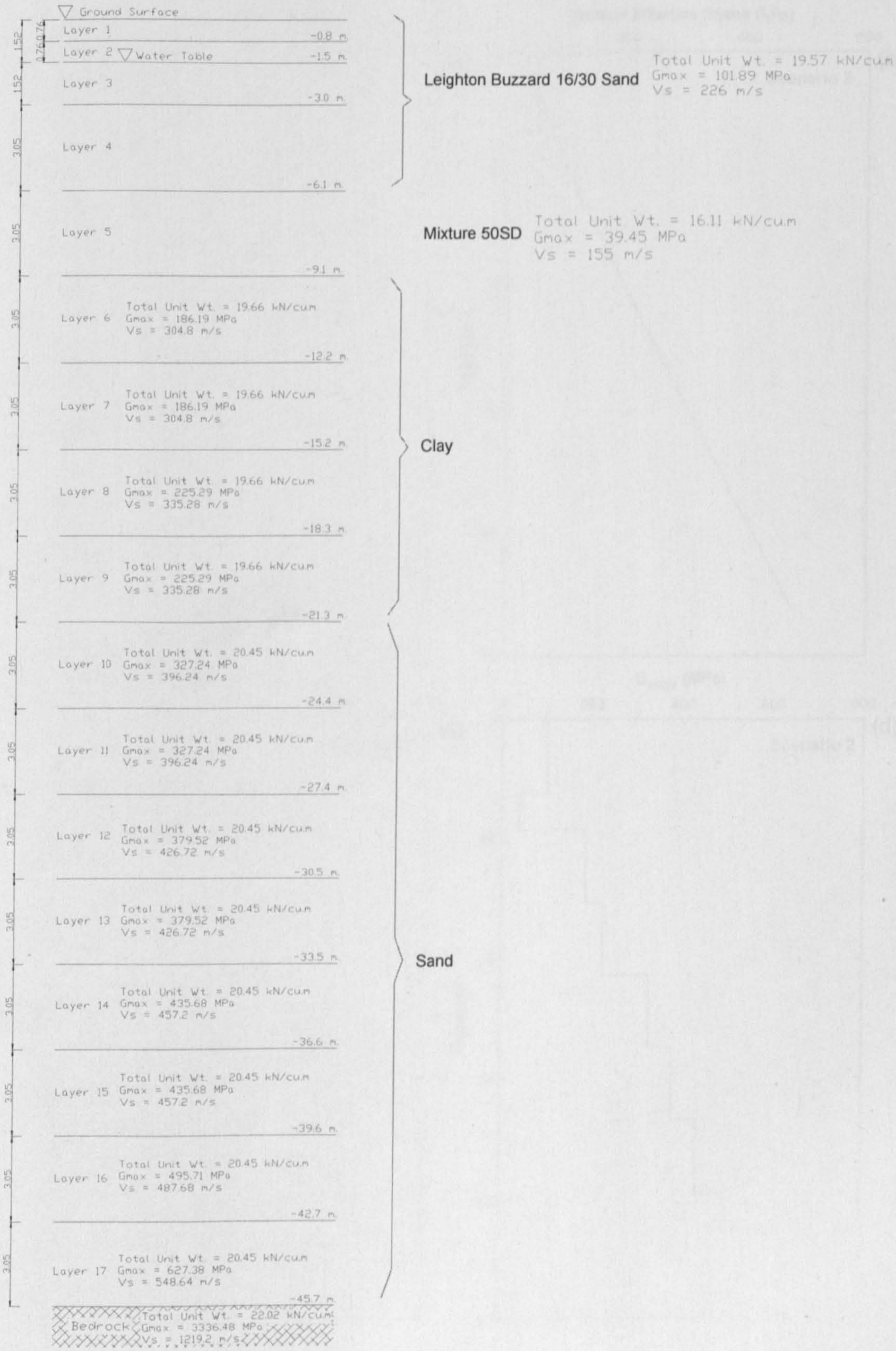

Figure 8. 5 Profile of layered-soils for scenario 2

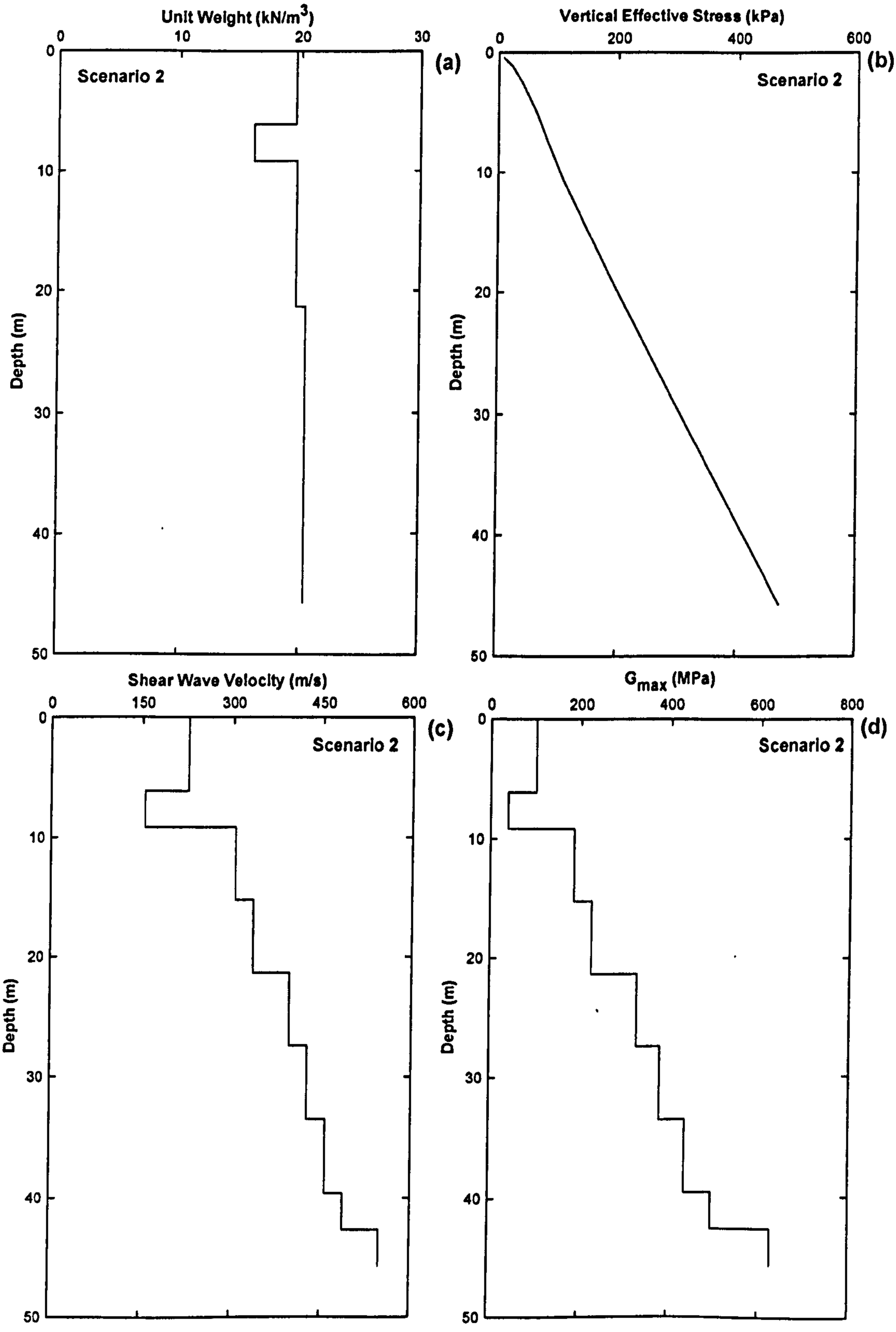

Figure 8. 6 Soil properties for scenario 2

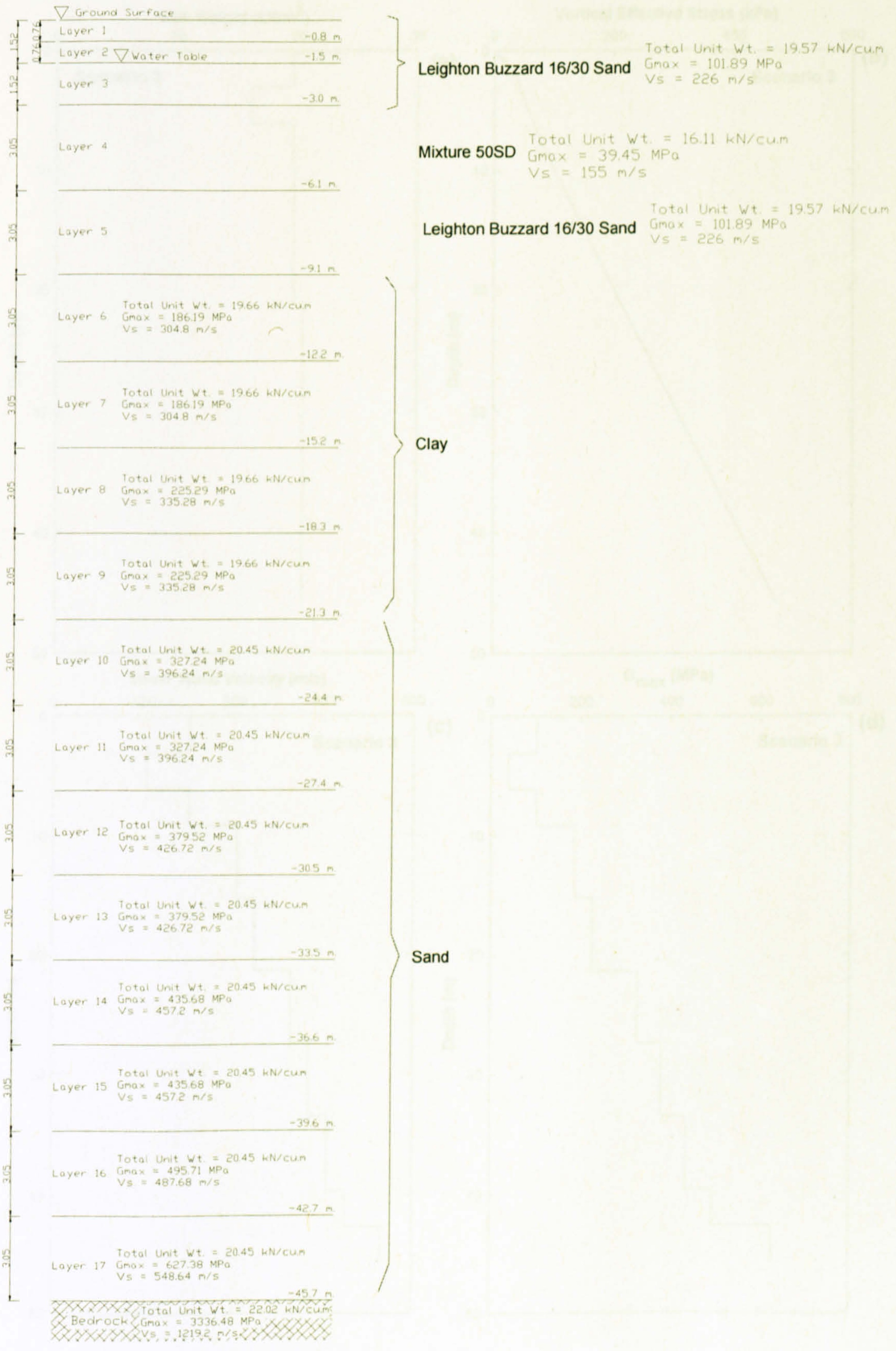

Figure 8. 7 Profile of layered-soils for scenario 3

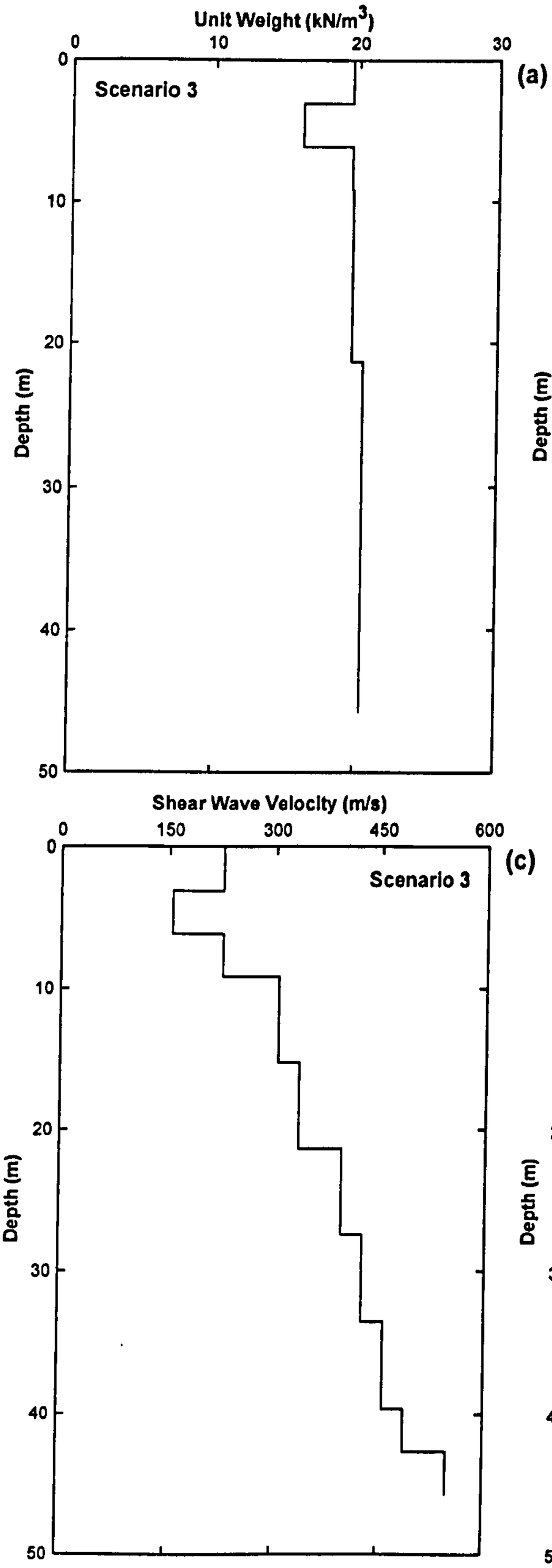

Figure 8. 8 Soil properties for scenario 3

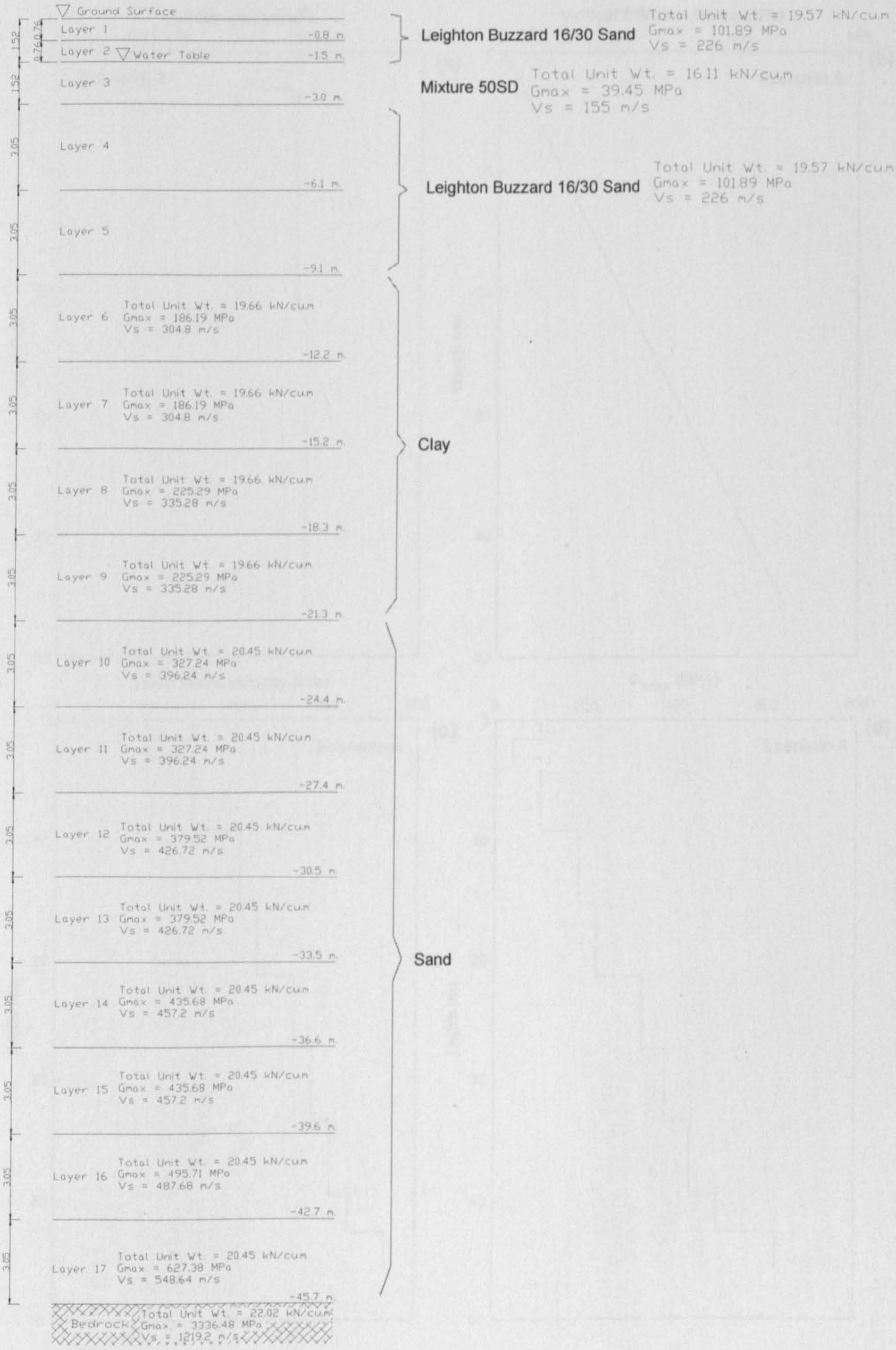

Figure 8. 9 Profile of layered-soils for scenario 4

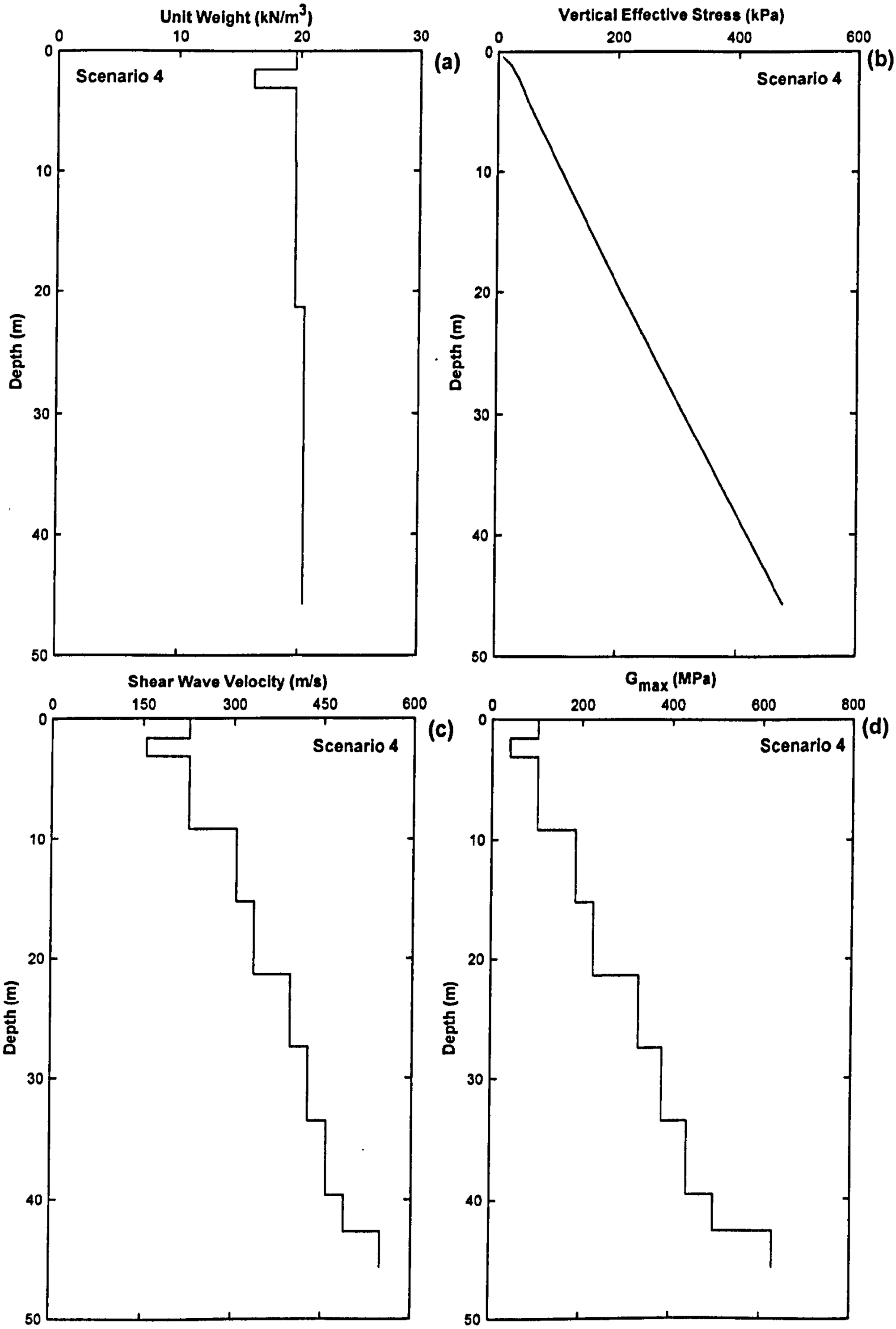

Figure 8. 10 Soil properties for scenario 4

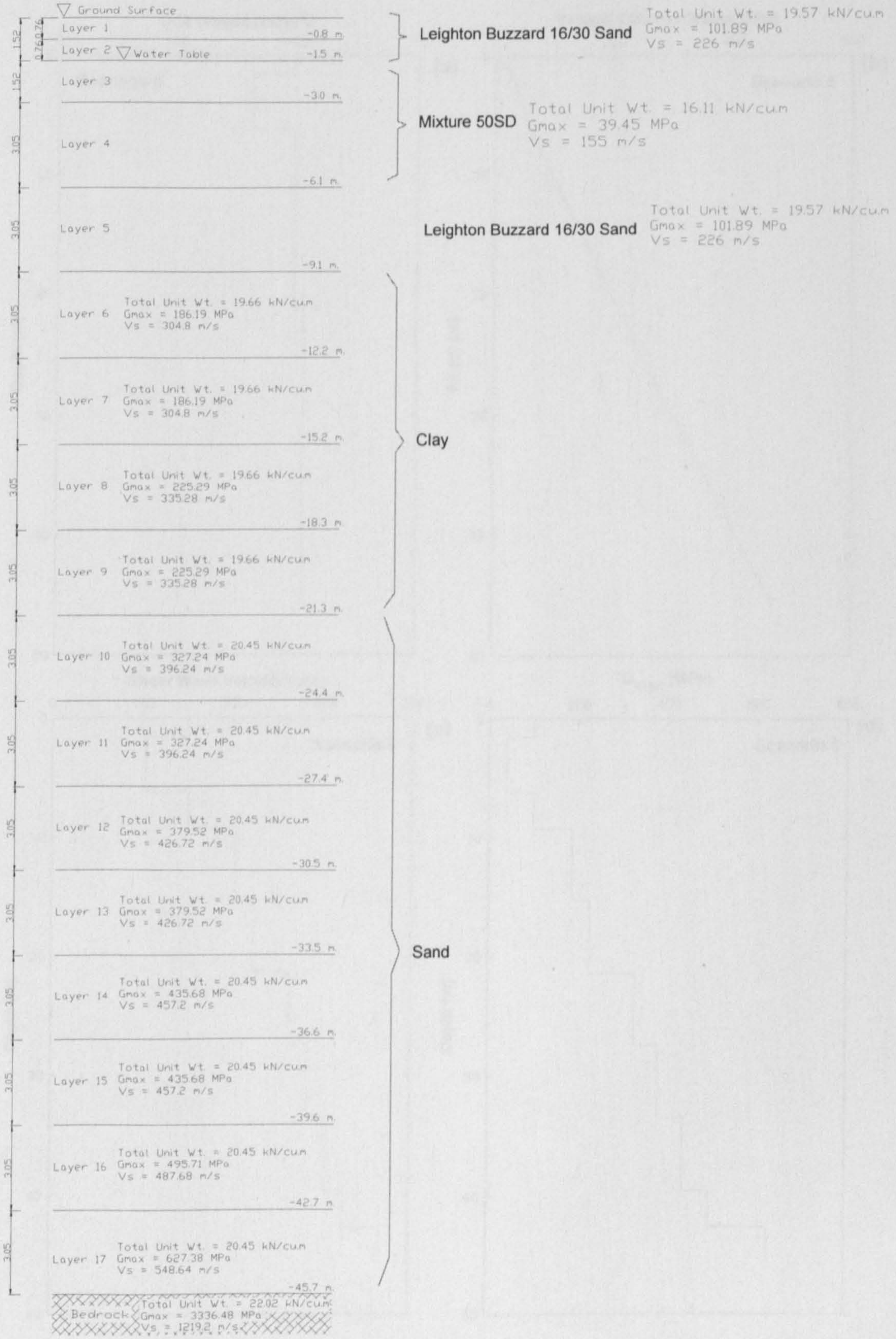

Figure 8. 11 Profile of layered-soils for scenario 5

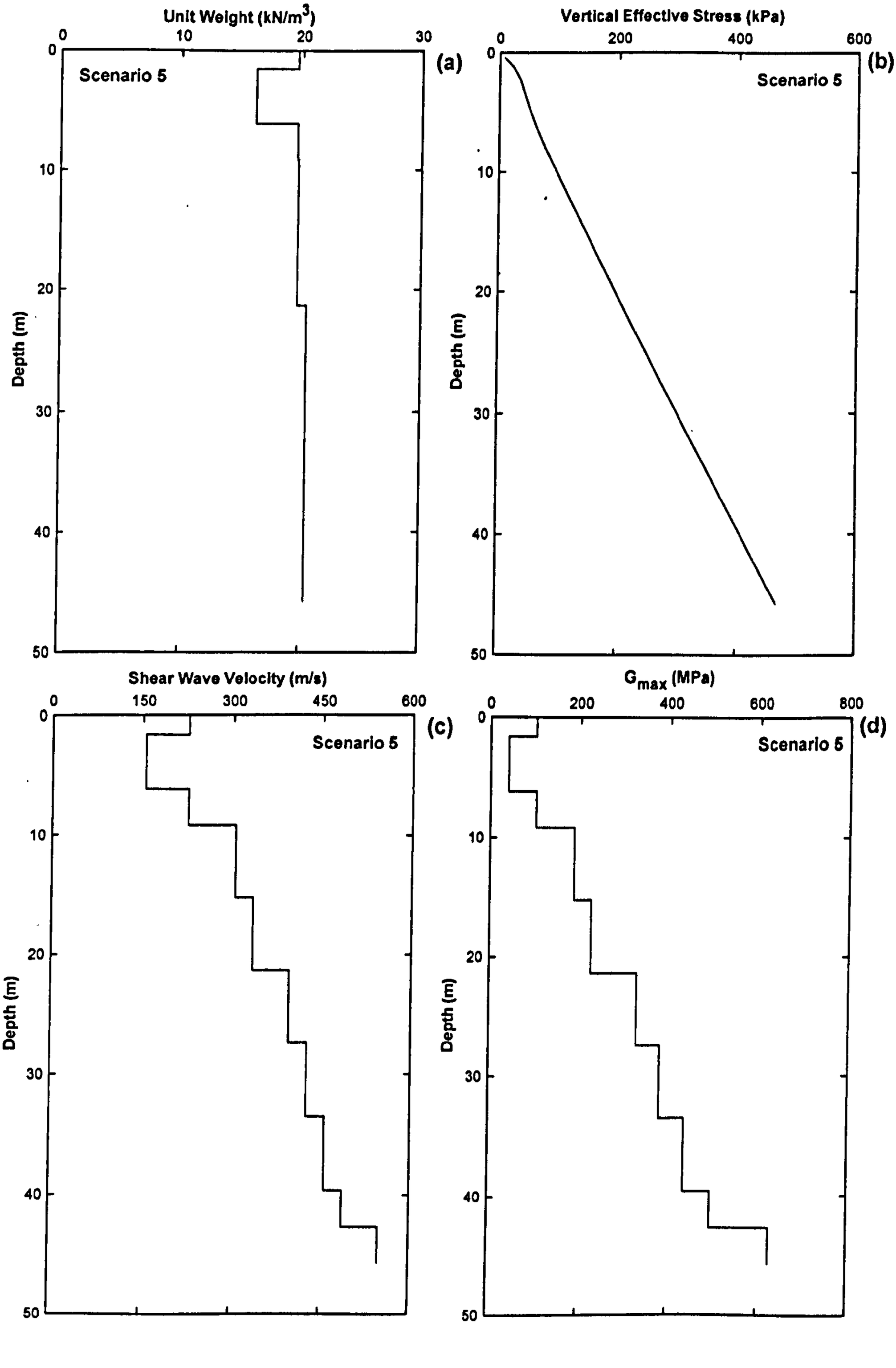

Figure 8. 12 Soil properties for scenario 5

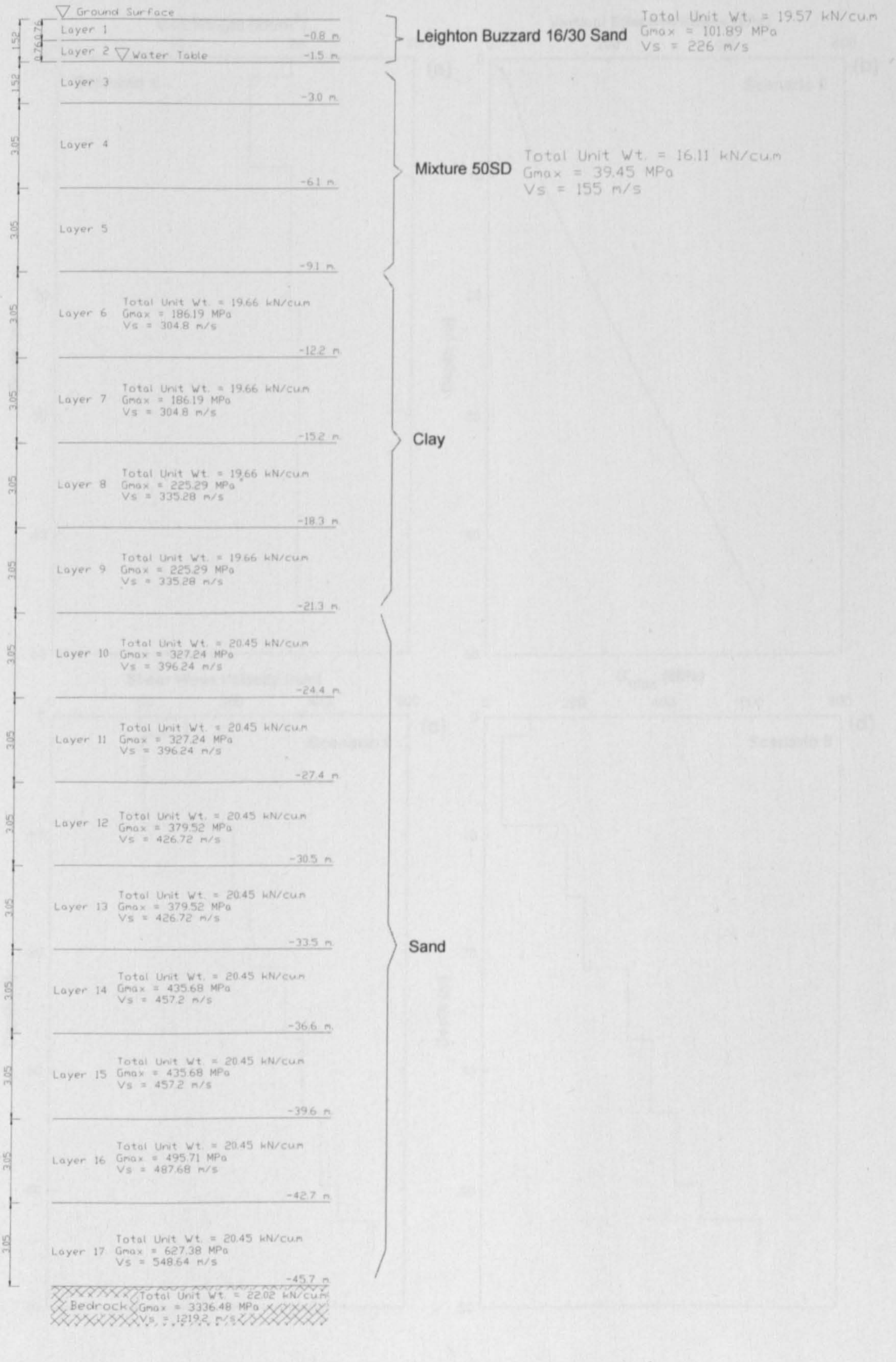

Figure 8. 13 Profile of layered-soils for scenario 6

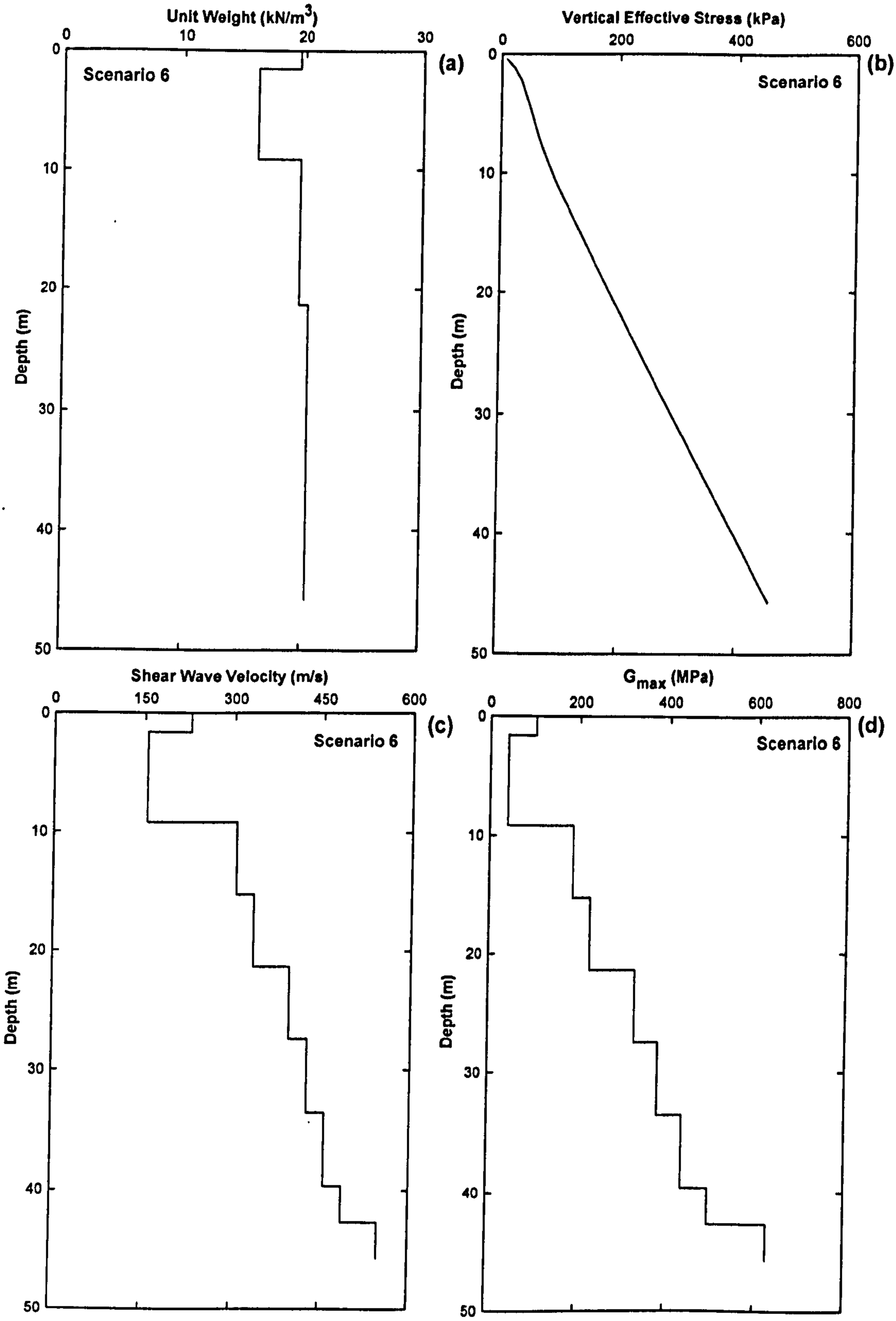

Figure 8. 14 Soil properties for scenario 6

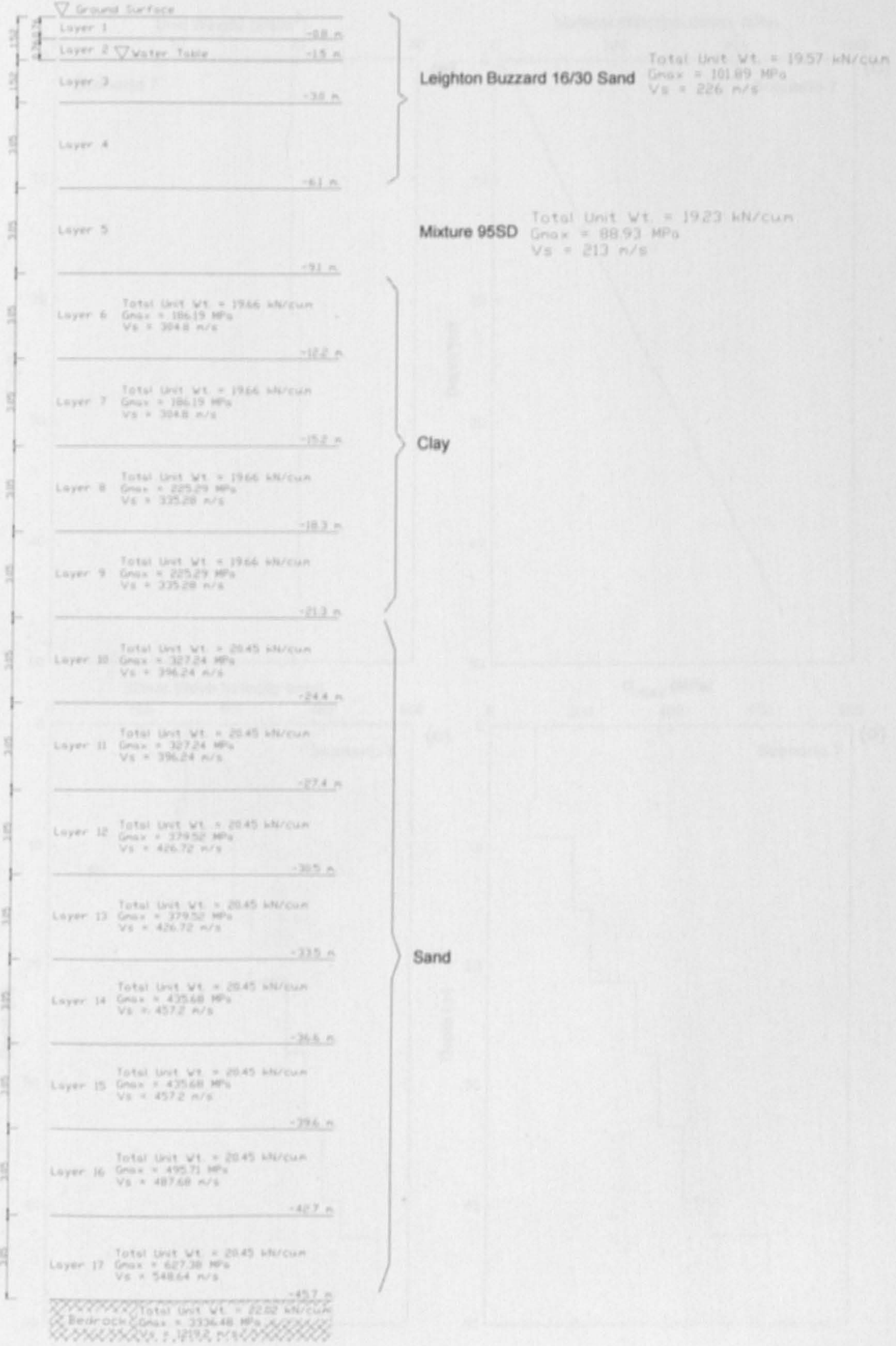

Figure 8. 15 Profile of layered-soils for scenario 7

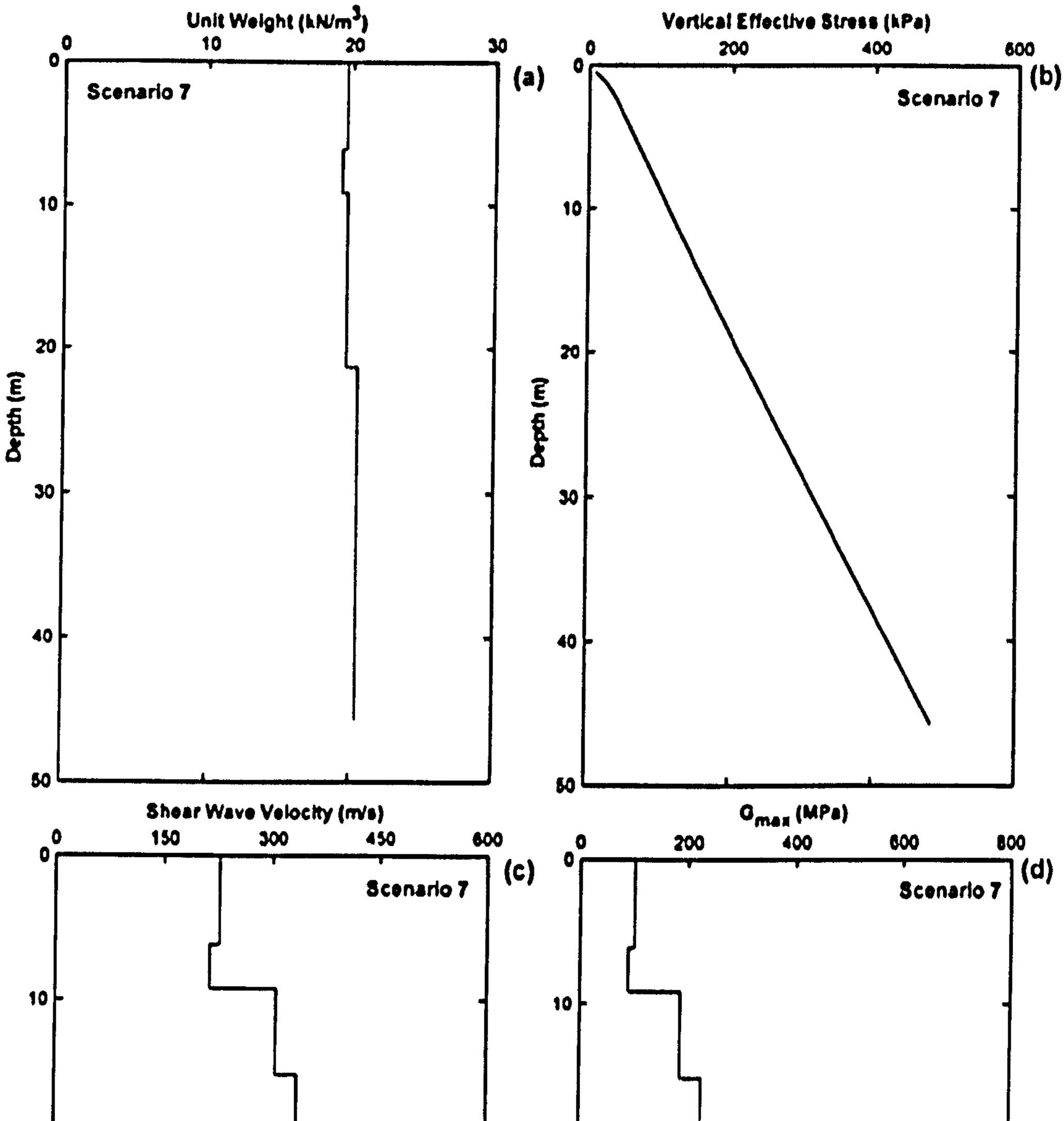

Figure 8. 16 Soil properties for scenario 7

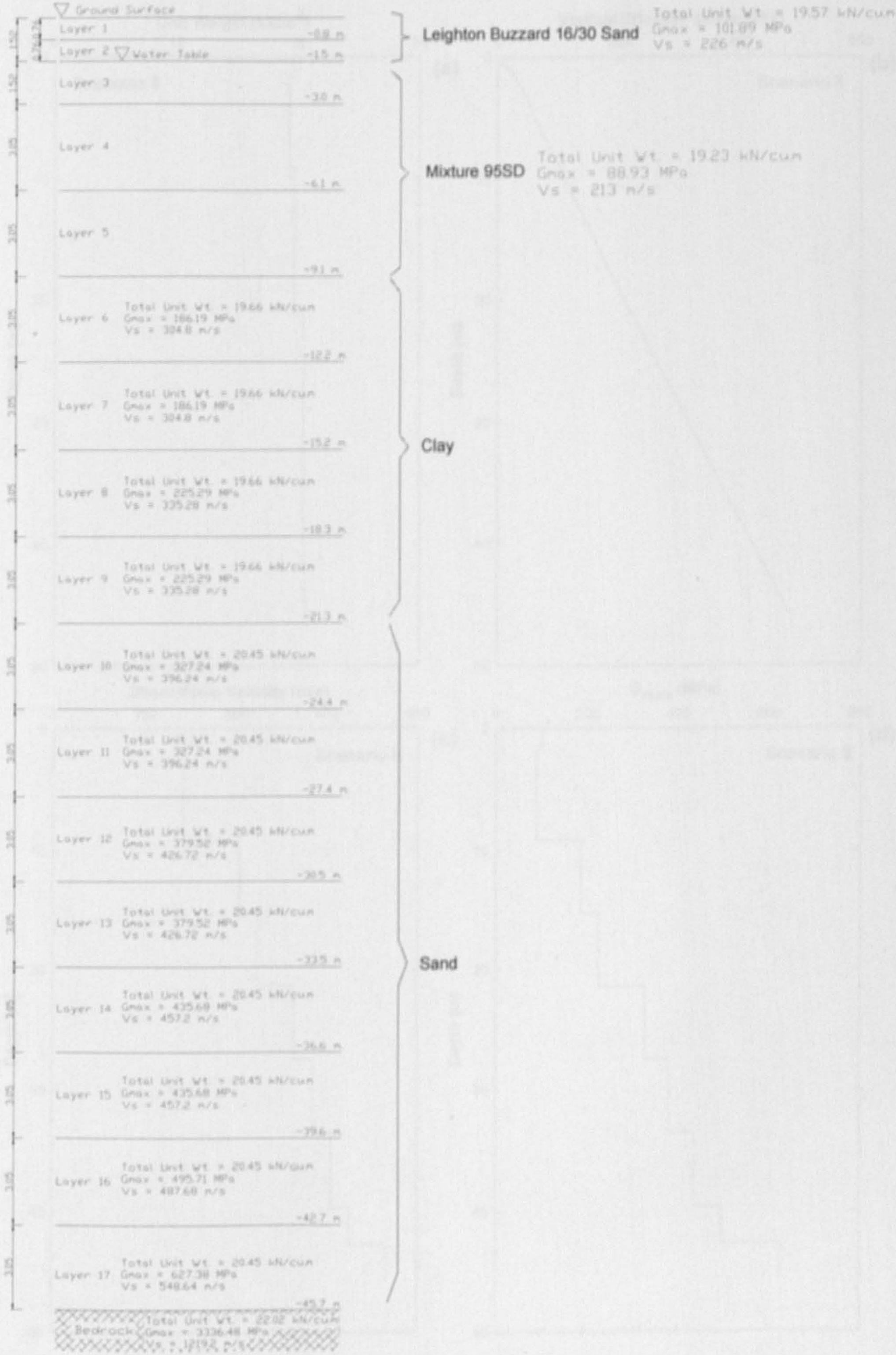

Figure 8. 17 Profile of layered-soils for scenario 8

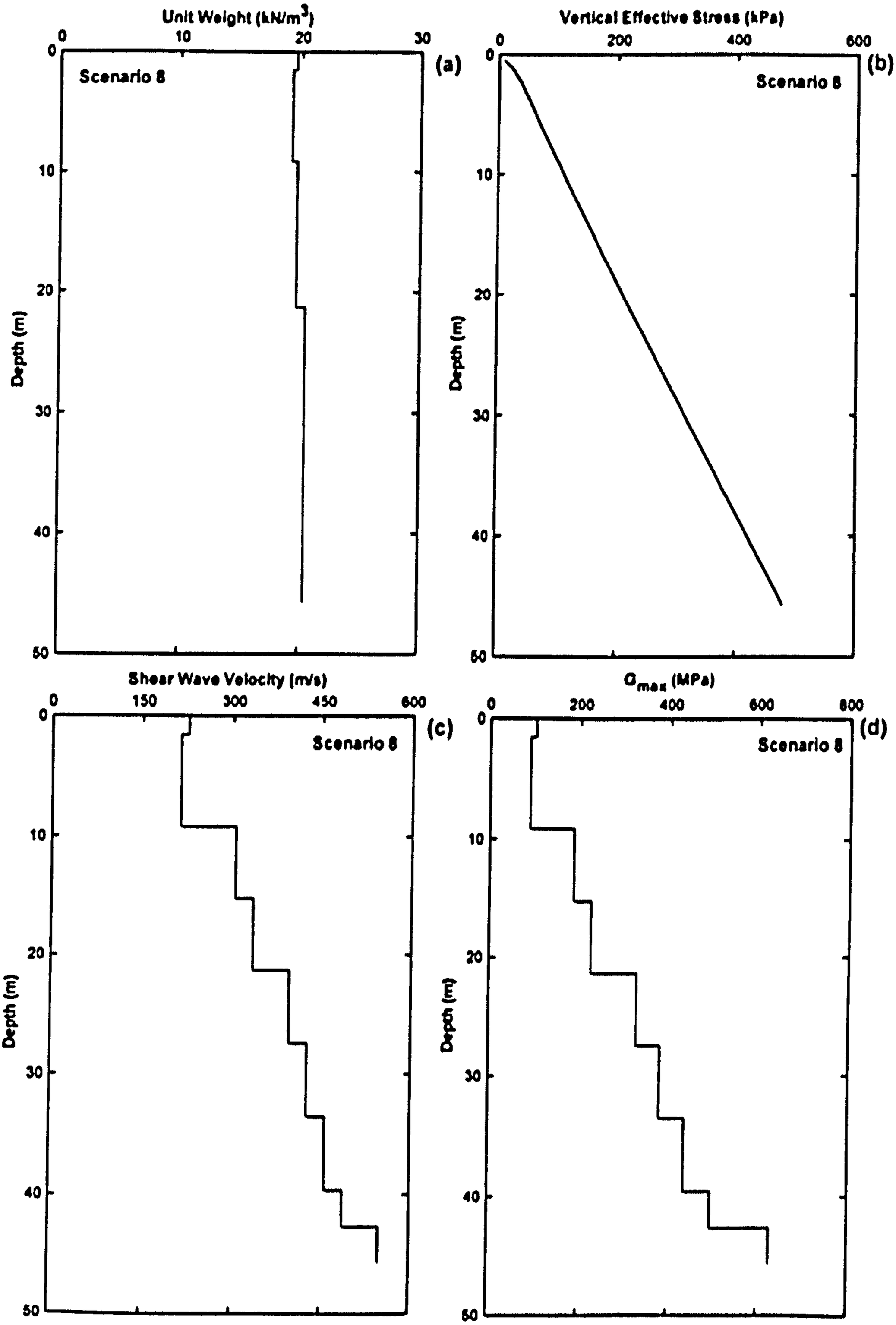

Figure 8. 18 Soil properties for scenario 8

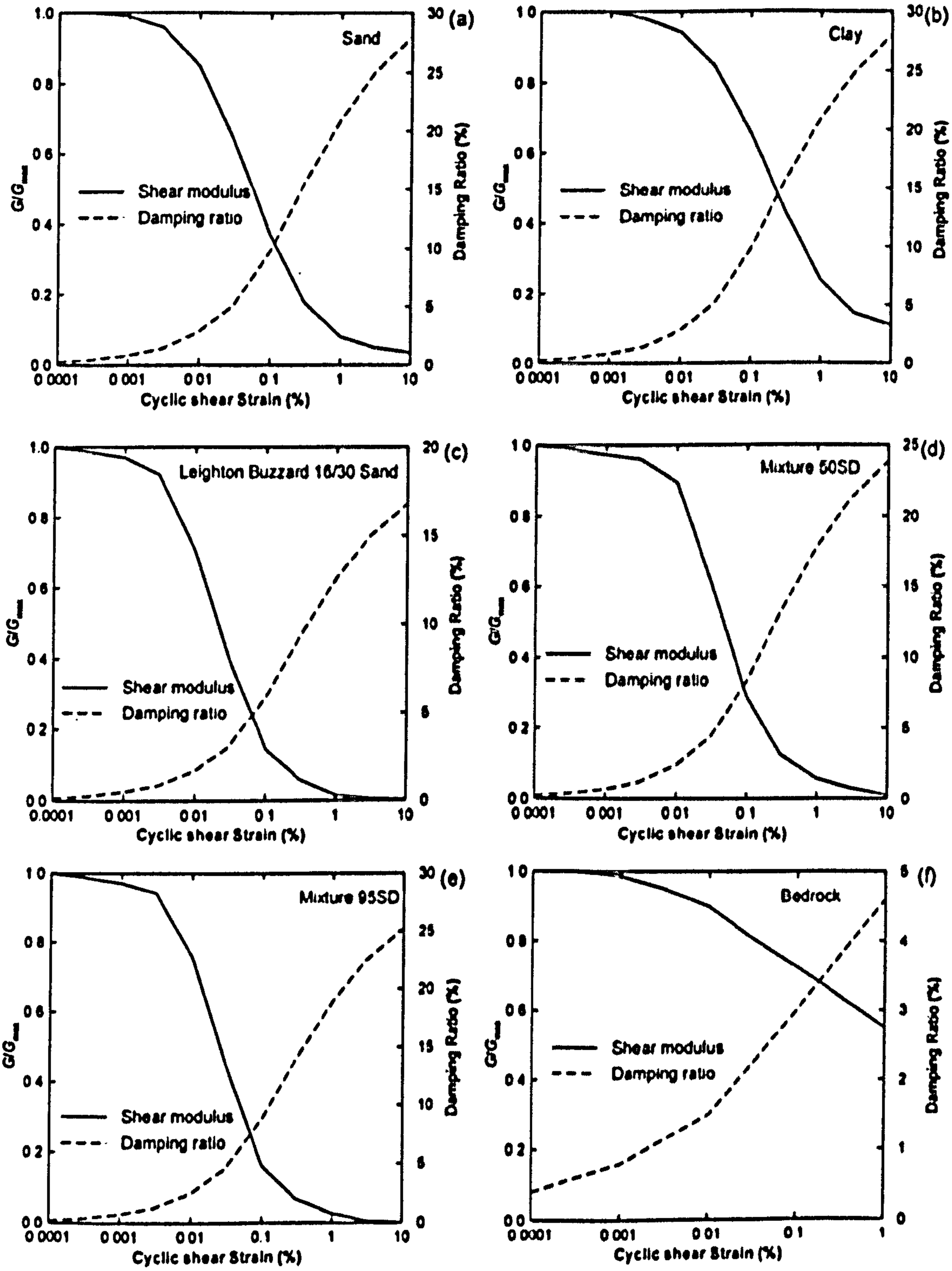

Figure 8. 19 Shear modull and damping ratios

8.4 Results

The EERA results for scenarios 1 - 8 are summarised in Tables 8.2 – 8.9, respectively, which present the details of the layered soils and the maximum values of acceleration a_{max}, shear strain γ_{max}, and shear stress τ_{max} for each layer. However, for the liquefaction analysis the maximum shear stress had to be factored by 0.65 in order to obtain the compatible uniform cyclic shear stress τ_{cyc}. Next, the cyclic stress ratio induced by the earthquake (induced *CSR*, M_w = 6.9) was computed by dividing τ_{cyc} by the vertical effective stress σ'_{vo}.

To determine the liquefaction potential the resistance to liquefaction of the materials must be known. Note that this was already obtained and reported in Chapter 6: The *CSR* values for the sand, mixtures 50SD and 95SD were 0.167, 0.220, and 0.196 respectively. However they were the *CSR* values obtained at 20 cycles of uniform cyclic stress corresponding to an earthquake with a magnitude of about 7.5 (Prakash, 1981). Thus, a factor was needed to multiply the *CSR* (M_w = 7.5) obtained so that they became the *CSR* (M_w = 6.9). This factor has been known as Magnitude Scaling Factor, or *MSF*; and, the following proposed by Andrus and Stokoe (2000) was employed:

$$MSF = \left(\frac{M_w}{7.5}\right)^{-2.56} \qquad \text{(Eq. 8. 1)}$$

Substitution of M_w of 6.9 into Eq. 8.1 resulted in an *MSF* of 1.238. Applying this factor to the *CSR* (M_w = 7.5), resulted in the *CSR* (M_w = 6.9). Now, the induced *CSR* and the *CSR* were for the same magnitude earthquake; and, the liquefaction potential was examined by comparing these two *CSRs*, as shown below:

$$FS_L = \frac{CSR}{Induced\ CSR} \qquad \text{(Eq. 8. 2)}$$

where FS_L is factor of safety against liquefaction. The liquefaction would occur if FS_L is lower than 1.0.

The maximum acceleration against depth for scenarios 1 – 8 is illustrated by Figure 8.20(a) – (h), respectively. In addition, the acceleration curves for scenarios 1 – 8 were plotted all together, and shown in Figure 8.21. For the maximum shear strain, the curves for each scenario are illustrated by Figure 8.22(a) – (h); and, they were plotted all together, and shown in Figure 8.23. The curves for the maximum shear stress and the

cyclic shear stress against depth for each scenario and for all scenarios are illustrated by Figure 8.24 and Figure 8.25, respectively.

Considering layer 1, it was observed that scenario 1 which employed the sand for all layers (1 to 5) produced the least acceleration; which was almost identical to that produced by scenario 8, but slightly greater. For scenario 6 that employed the mixture 50SD for layers 3 to 5, the acceleration was the greatest (see Figure 8.21 for comparison). This indicates that sand-rubber mixture when deposited according to scenario 6 in fact amplifies the ground acceleration. These findings can be confirmed when considering the ground acceleration for scenarios 2, 3, 4, 5, and 7 of which also employed the mixtures at a layer or layers: the acceleration generated by these scenarios was quite greater than that of scenario 1.

It has been recognised that softer soil amplifies the acceleration. This was evident in the 1985 earthquake in Mexico. The area affected by the earthquake can be divided into three zones with respect to different subsurface conditions: 1) Foothill Zone (shallow) comprising compact deposits of mostly granular, basalt, or volcanic tuff, 2) Lake Zone comprising thick deposits of very soft soils, and 3) Transition Zone comprising a thin layer of soft deposits interspersed with alluvial deposits. It was found that the acceleration recorded in the Foothill Zone was quite low, just 0.03 to 0.04g. The acceleration in the Transition Zone was slightly greater than that of the Foothill, but still quite low. However, the measurements at Lake Zone were five times greater than those at the Foothill (from Kramer, 1996).

The maximum shear strain for scenario 1 was observed to gradually increase for layer 1 to layer 5 from approximately zero to just over 0.03%. From layer 5 downwards and before the bedrock the maximum shear strain was quite consistent at about 0.03% (see Figure 8.22(a)). When the mixture 50SD was introduced at layer 5 (scenario 2, see Figure 8.22(b)) the shear strain from layers 1 to 4 was observed to be quite similar to that of scenario 1; but, it increased dramatically at layer 5. From layer 5 downwards, however, the behaviour of the shear strain was quite similar to that of scenario 1. This distinctive behaviour was also found for scenario 6 (see Figure 8.22(f)). For scenarios 3, 4, and 5 (see Figure 8.22(c), (d), and (e) respectively) the shear strains were observed to be very similar: the maximum values were observed at layer 4, regardless of where the mixture was deposited.

The maximum shear strains for scenarios 7 and 8 (see Figure 8.22(g) and (h) respectively) were observed to be quite similar to those for scenario 1, especially in the case of scenario 8. This may be because of the similarities of the dynamic properties between the sand and the 95SD mixture.

Unlike the maximum acceleration and the maximum shear strain, the behaviour of the maximum shear stress and the cyclic shear stress for all scenarios were observed to be quite similar, whether employing pure sand or the 50SD and 95SD mixtures.

Table 8. 2 EERA results for scenario 1

Layer	Type	Depth at Middle (m)	σ'_{vo} (kPa)	a_{max} (g)	γ_{max} (%)	τ_{max} (kPa)	τ_{eff} (kPa)	Induced CSR (M_w = 6.9)	CSR (M_w = 7.5)	CSR (M_w = 6.9)	FS_{Liq}	Liquefaction
1	16/30 sand	0.38	7.5	0.21155	0.00154	1.57	1.02	0.137	0.167	0.207	N/A	N/A
2	16/30 sand	1.14	22.4	0.21127	0.00471	4.71	3.06	0.137	0.167	0.207	N/A	N/A
3	16/30 sand	2.29	37.3	0.21043	0.00961	9.36	6.09	0.163	0.167	0.207	1.27	No
4	16/30 sand	4.57	59.6	0.20709	0.01974	18.50	12.03	0.202	0.167	0.207	1.02	No
5	16/30 sand	7.62	89.3	0.20072	0.03429	30.48	19.81	0.222	0.167	0.207	0.93	Yes
6	clay	10.67	119.2	0.18848	0.02497	41.82	27.18	0.228	N/A	N/A	N/A	N/A
7	clay	13.72	149.2	0.17710	0.03207	52.43	34.08	0.228	N/A	N/A	N/A	N/A
8	clay	16.76	179.3	0.15973	0.03129	62.05	40.33	0.225	N/A	N/A	N/A	N/A
9	clay	19.81	209.3	0.14059	0.03605	70.50	45.82	0.219	N/A	N/A	N/A	N/A
10	sand	22.86	240.5	0.11807	0.03400	77.71	50.51	0.210	N/A	N/A	N/A	N/A
11	sand	25.91	272.9	0.11062	0.03761	83.58	54.33	0.199	N/A	N/A	N/A	N/A
12	sand	28.96	305.3	0.10132	0.03283	87.86	57.11	0.187	N/A	N/A	N/A	N/A
13	sand	32.00	337.8	0.10157	0.03430	90.70	58.96	0.175	N/A	N/A	N/A	N/A
14	sand	35.05	370.2	0.09744	0.02949	93.22	60.60	0.164	N/A	N/A	N/A	N/A
15	sand	38.10	402.6	0.09321	0.03090	96.49	62.72	0.156	N/A	N/A	N/A	N/A
16	sand	41.15	435.0	0.08941	0.02687	99.03	64.37	0.148	N/A	N/A	N/A	N/A
17	sand	44.20	467.4	0.08697	0.02013	100.85	65.55	0.140	N/A	N/A	N/A	N/A
18	bedrock	45.72	483.7	0.08708	0.00308	102.87	66.86	0.138	N/A	N/A	N/A	N/A

Table 8. 3 EERA results for scenario 2

Layer	Type	Depth at Middle (m)	σ'_{vo} (kPa)	a_{max} (g)	γ_{max} (%)	τ_{max} (kPa)	τ_{eff} (kPa)	Induced CSR (M_w = 6.9)	CSR (M_w = 7.5)	CSR (M_w = 6.9)	FS_{Liq}	Liquefaction
1	16/30 sand	0.38	7.5	0.25518	0.00192	1.90	1.24	0.166	0.167	0.207	N/A	N/A
2	16/30 sand	1.14	22.4	0.25495	0.00591	5.70	3.71	0.166	0.167	0.207	N/A	N/A
3	16/30 sand	2.29	37.3	0.25423	0.01231	11.37	7.39	0.198	0.167	0.207	1.04	No
4	16/30 sand	4.57	59.6	0.25112	0.03055	22.46	14.60	0.245	0.167	0.207	0.84	Yes
5	50SD	7.62	84.0	0.23442	0.12834	34.67	22.54	0.268	0.220	0.272	1.02	No
6	clay	10.67	108.7	0.16475	0.02631	43.85	28.50	0.262	N/A	N/A	N/A	N/A
7	clay	13.72	138.7	0.14973	0.03239	52.91	34.39	0.248	N/A	N/A	N/A	N/A
8	clay	16.76	168.7	0.12830	0.03057	60.77	39.50	0.234	N/A	N/A	N/A	N/A
9	clay	19.81	198.7	0.11715	0.03427	67.36	43.78	0.220	N/A	N/A	N/A	N/A
10	sand	22.86	230.0	0.11184	0.03088	72.44	47.09	0.205	N/A	N/A	N/A	N/A
11	sand	25.91	262.4	0.11069	0.03314	76.27	49.58	0.189	N/A	N/A	N/A	N/A
12	sand	28.96	294.8	0.11146	0.02858	79.36	51.58	0.175	N/A	N/A	N/A	N/A
13	sand	32.00	327.2	0.10813	0.03055	83.35	54.18	0.166	N/A	N/A	N/A	N/A
14	sand	35.05	359.6	0.10047	0.02685	86.99	56.54	0.157	N/A	N/A	N/A	N/A
15	sand	38.10	392.1	0.09177	0.02806	89.87	58.41	0.149	N/A	N/A	N/A	N/A
16	sand	41.15	424.5	0.08751	0.02429	91.83	59.69	0.141	N/A	N/A	N/A	N/A
17	sand	44.20	456.9	0.08668	0.01808	92.92	60.40	0.132	N/A	N/A	N/A	N/A
18	bedrock	45.72	473.1	0.08602	0.00280	93.36	60.68	0.128	N/A	N/A	N/A	N/A

Table 8. 4 EERA results for scenario 3

Layer	Type	Depth at Middle (m)	σ'_m (kPa)	a_{max} (g)	γ_{max} (%)	τ_{max} (kPa)	τ_{av} (kPa)	Induced CSR (M_w = 6.9)	CSR (M_w = 7.5)	CSR (M_w = 6.9)	FS_{liq}	Liquefaction
1	16/30 sand	0.38	7.5	0.25375	0.00191	1.88	1.23	0.164	0.167	0.207	N/A	N/A
2	16/30 sand	1.14	22.4	0.25330	0.00586	5.65	3.68	0.164	0.167	0.207	N/A	N/A
3	16/30 sand	2.29	37.3	0.25195	0.01222	11.28	7.33	0.197	0.167	0.207	1.05	No
4	50SD	4.57	54.3	0.24766	0.06704	20.84	13.55	0.249	0.220	0.272	1.09	No
5	16/30 sand	7.62	78.8	0.20518	0.05532	32.05	20.83	0.264	0.167	0.207	0.78	Yes
6	clay	10.67	108.7	0.17542	0.02539	42.46	27.60	0.254	N/A	N/A	N/A	N/A
7	clay	13.72	138.7	0.16083	0.03168	51.86	33.71	0.243	N/A	N/A	N/A	N/A
8	clay	16.76	168.7	0.14233	0.03038	60.42	39.27	0.233	N/A	N/A	N/A	N/A
9	clay	19.81	198.7	0.12633	0.03457	67.89	44.13	0.222	N/A	N/A	N/A	N/A
10	sand	22.86	230.0	0.11323	0.03204	74.42	48.37	0.210	N/A	N/A	N/A	N/A
11	sand	25.91	262.4	0.10577	0.03534	79.91	51.94	0.198	N/A	N/A	N/A	N/A
12	sand	28.96	294.8	0.10096	0.03091	84.06	54.64	0.185	N/A	N/A	N/A	N/A
13	sand	32.00	327.2	0.09820	0.03237	86.94	56.51	0.173	N/A	N/A	N/A	N/A
14	sand	35.05	359.6	0.09397	0.02803	89.80	58.37	0.162	N/A	N/A	N/A	N/A
15	sand	38.10	392.1	0.09389	0.02938	92.97	60.43	0.154	N/A	N/A	N/A	N/A
16	sand	41.15	424.5	0.09126	0.02547	95.14	61.84	0.146	N/A	N/A	N/A	N/A
17	sand	44.20	456.9	0.09102	0.01897	96.39	62.65	0.137	N/A	N/A	N/A	N/A
18	bedrock	45.72	473.1	0.08908	0.00294	98.23	63.85	0.135	N/A	N/A	N/A	N/A

Table 8. 5 EERA results for scenario 4

Layer	Type	Depth at Middle (m)	σ'_m (kPa)	a_{max} (g)	γ_{max} (%)	τ_{max} (kPa)	τ_{av} (kPa)	Induced CSR (M_w = 6.9)	CSR (M_w = 7.5)	CSR (M_w = 6.9)	FS_{liq}	Liquefaction
1	16/30 sand	0.38	7.5	0.23479	0.00176	1.75	1.14	0.152	0.167	0.207	N/A	N/A
2	16/30 sand	1.14	22.4	0.23439	0.00539	5.22	3.39	0.152	0.167	0.207	N/A	N/A
3	50SD	2.29	34.6	0.23315	0.02747	9.66	6.28	0.181	0.220	0.272	1.50	No
4	16/30 sand	4.57	54.3	0.22067	0.02339	18.80	12.22	0.225	0.167	0.207	0.92	Yes
5	16/30 sand	7.62	84.0	0.21032	0.05258	31.21	20.29	0.241	0.167	0.207	0.86	Yes
6	clay	10.67	113.9	0.18425	0.02532	42.35	27.53	0.242	N/A	N/A	N/A	N/A
7	clay	13.72	144.0	0.17059	0.03214	52.54	34.15	0.237	N/A	N/A	N/A	N/A
8	clay	16.76	174.0	0.15227	0.03108	61.68	40.09	0.230	N/A	N/A	N/A	N/A
9	clay	19.81	204.0	0.13364	0.03559	69.69	45.30	0.222	N/A	N/A	N/A	N/A
10	sand	22.86	235.2	0.11737	0.03331	76.56	49.77	0.212	N/A	N/A	N/A	N/A
11	sand	25.91	267.6	0.10905	0.03675	82.20	53.43	0.200	N/A	N/A	N/A	N/A
12	sand	28.96	300.1	0.09972	0.03206	86.35	56.12	0.187	N/A	N/A	N/A	N/A
13	sand	32.00	332.5	0.09818	0.03348	89.12	57.93	0.174	N/A	N/A	N/A	N/A
14	sand	35.05	364.9	0.09273	0.02892	91.88	59.72	0.164	N/A	N/A	N/A	N/A
15	sand	38.10	397.3	0.08959	0.03036	95.23	61.90	0.156	N/A	N/A	N/A	N/A
16	sand	41.15	429.8	0.08758	0.02640	97.72	63.52	0.148	N/A	N/A	N/A	N/A
17	sand	44.20	462.2	0.08897	0.01968	99.13	64.43	0.139	N/A	N/A	N/A	N/A
18	bedrock	45.72	478.4	0.08883	0.00301	100.58	65.37	0.137	N/A	N/A	N/A	N/A

Table 8. 6 EERA results for scenario 5

Layer	Type	Depth at Middle (m)	σ'_{vo} (kPa)	a_{max} (g)	γ_{max} (%)	τ_{max} (kPa)	τ_{eq} (kPa)	Induced CSR (M_w = 6.9)	CSR (M_w = 7.5)	CSR (M_w = 6.9)	FS_{Liq}	Liquefaction
1	16/30 sand	0.38	7.5	0.26232	0.00197	1.95	1.27	0.170	0.167	0.207	N/A	N/A
2	16/30 sand	1.14	22.4	0.26183	0.00605	5.82	3.78	0.169	0.167	0.207	N/A	N/A
3	50SD	2.29	34.6	0.26033	0.03145	10.92	7.10	0.205	0.220	0.272	1.33	No
4	50SD	4.57	49.0	0.24670	0.06305	19.84	12.89	0.263	0.220	0.272	1.04	No
5	16/30 sand	7.62	73.5	0.20823	0.05202	31.02	20.16	0.274	0.167	0.207	0.75	Yes
6	clay	10.67	103.4	0.17532	0.02478	41.53	27.00	0.261	N/A	N/A	N/A	N/A
7	clay	13.72	133.4	0.16125	0.03117	51.11	33.22	0.249	N/A	N/A	N/A	N/A
8	clay	16.76	163.4	0.14466	0.03002	59.77	38.85	0.238	N/A	N/A	N/A	N/A
9	clay	19.81	193.5	0.12862	0.03433	67.47	43.85	0.227	N/A	N/A	N/A	N/A
10	sand	22.86	224.7	0.11445	0.03192	74.20	48.23	0.215	N/A	N/A	N/A	N/A
11	sand	25.91	257.1	0.10607	0.03532	79.87	51.92	0.202	N/A	N/A	N/A	N/A
12	sand	28.96	289.5	0.09881	0.03097	84.19	54.73	0.189	N/A	N/A	N/A	N/A
13	sand	32.00	321.9	0.09638	0.03252	87.25	56.71	0.176	N/A	N/A	N/A	N/A
14	sand	35.05	354.4	0.09368	0.02815	90.07	58.55	0.165	N/A	N/A	N/A	N/A
15	sand	38.10	386.8	0.09404	0.02934	92.87	60.37	0.156	N/A	N/A	N/A	N/A
16	sand	41.15	419.2	0.09163	0.02547	95.14	61.84	0.148	N/A	N/A	N/A	N/A
17	sand	44.20	451.6	0.09114	0.01910	96.91	62.99	0.139	N/A	N/A	N/A	N/A
18	bedrock	45.72	467.8	0.08926	0.00297	99.01	64.35	0.138	N/A	N/A	N/A	N/A

Table 8. 7 EERA results for scenario 6

Layer	Type	Depth at Middle (m)	σ'_{vo} (kPa)	a_{max} (g)	γ_{max} (%)	τ_{max} (kPa)	τ_{eq} (kPa)	Induced CSR (M_w = 6.9)	CSR (M_w = 7.5)	CSR (M_w = 6.9)	FS_{Liq}	Liquefaction
1	16/30 sand	0.38	7.5	0.30047	0.00227	2.24	1.46	0.195	0.167	0.207	N/A	N/A
2	16/30 sand	1.14	22.4	0.30000	0.00703	6.71	4.36	0.195	0.167	0.207	N/A	N/A
3	50SD	2.29	34.6	0.29854	0.03664	12.53	8.15	0.235	0.220	0.272	1.16	No
4	50SD	4.57	49.0	0.28346	0.07416	22.58	14.68	0.299	0.220	0.272	0.91	Yes
5	50SD	7.62	68.2	0.22881	0.12308	33.57	21.82	0.320	0.220	0.272	0.85	Yes
6	clay	10.67	92.8	0.15675	0.02539	42.45	27.59	0.297	N/A	N/A	N/A	N/A
7	clay	13.72	122.9	0.14446	0.03100	50.85	33.05	0.269	N/A	N/A	N/A	N/A
8	clay	16.76	152.9	0.12952	0.02921	58.31	37.90	0.248	N/A	N/A	N/A	N/A
9	clay	19.81	182.9	0.12269	0.03272	64.61	41.99	0.230	N/A	N/A	N/A	N/A
10	sand	22.86	214.1	0.11746	0.02916	69.45	45.14	0.211	N/A	N/A	N/A	N/A
11	sand	25.91	246.6	0.11373	0.03172	73.88	48.02	0.195	N/A	N/A	N/A	N/A
12	sand	28.96	279.0	0.10627	0.02801	78.19	50.82	0.182	N/A	N/A	N/A	N/A
13	sand	32.00	311.4	0.10285	0.02977	81.78	53.16	0.171	N/A	N/A	N/A	N/A
14	sand	35.05	343.8	0.09595	0.02611	85.18	55.37	0.161	N/A	N/A	N/A	N/A
15	sand	38.10	376.2	0.09074	0.02732	88.11	57.27	0.152	N/A	N/A	N/A	N/A
16	sand	41.15	408.7	0.08727	0.02369	90.14	58.59	0.143	N/A	N/A	N/A	N/A
17	sand	44.20	441.1	0.08540	0.01768	91.32	59.36	0.135	N/A	N/A	N/A	N/A
18	bedrock	45.72	457.3	0.08514	0.00283	94.42	61.37	0.134	N/A	N/A	N/A	N/A

Table 8. 8 EERA results for scenario 7

Layer	Type	Depth at Middle (m)	σ'_{vo} (kPa)	a_{max} (g)	γ_{max} (%)	τ_{max} (kPa)	τ_{eqv} (kPa)	Induced CSR (M_w = 6.9)	CSR (M_w = 7.5)	CSR (M_w = 6.9)	FS_{Liq}	Liquefaction
1	16/30 sand	0.38	7.5	0.22677	0.00171	1.69	1.10	0.147	0.167	0.207	N/A	N/A
2	16/30 sand	1.14	22.4	0.22646	0.00538	5.04	3.28	0.147	0.167	0.207	N/A	N/A
3	16/30 sand	2.29	37.3	0.22546	0.01243	10.01	6.51	0.175	0.167	0.207	1.18	No
4	16/30 sand	4.57	59.6	0.22086	0.03753	19.51	12.68	0.213	0.167	0.207	0.97	Yes
5	95SD	7.62	88.8	0.20212	0.03543	31.51	20.48	0.231	0.158	0.196	0.85	Yes
6	clay	10.67	118.2	0.18522	0.02543	42.53	27.64	0.234	N/A	N/A	N/A	N/A
7	clay	13.72	148.2	0.17182	0.03230	52.78	34.31	0.231	N/A	N/A	N/A	N/A
8	clay	16.76	178.2	0.15357	0.03126	62.00	40.30	0.226	N/A	N/A	N/A	N/A
9	clay	19.81	208.2	0.13481	0.03580	70.07	45.55	0.219	N/A	N/A	N/A	N/A
10	sand	22.86	239.5	0.11853	0.03358	77.00	50.05	0.209	N/A	N/A	N/A	N/A
11	sand	25.91	271.9	0.11024	0.03705	82.69	53.75	0.198	N/A	N/A	N/A	N/A
12	sand	28.96	304.3	0.09997	0.03234	86.89	56.48	0.186	N/A	N/A	N/A	N/A
13	sand	32.00	336.7	0.09820	0.03379	89.72	58.32	0.173	N/A	N/A	N/A	N/A
14	sand	35.05	369.1	0.09264	0.02909	92.29	59.99	0.163	N/A	N/A	N/A	N/A
15	sand	38.10	401.6	0.08919	0.03058	95.75	62.24	0.155	N/A	N/A	N/A	N/A
16	sand	41.15	434.0	0.08716	0.02660	98.26	63.87	0.147	N/A	N/A	N/A	N/A
17	sand	44.20	466.4	0.08866	0.01982	99.68	64.79	0.139	N/A	N/A	N/A	N/A
18	bedrock	45.72	482.6	0.08867	0.00301	101.01	65.66	0.136	N/A	N/A	N/A	N/A

Table 8. 9 EERA results for scenario 8

Layer	Type	Depth at Middle (m)	σ'_{vo} (kPa)	a_{max} (g)	γ_{max} (%)	τ_{max} (kPa)	τ_{eqv} (kPa)	Induced CSR (M_w = 6.9)	CSR (M_w = 7.5)	CSR (M_w = 6.9)	FS_{Liq}	Liquefaction
1	16/30 sand	0.38	7.5	0.21277	0.00160	1.58	1.03	0.138	0.167	0.207	N/A	N/A
2	16/30 sand	1.14	22.4	0.21249	0.00500	4.74	3.08	0.138	0.167	0.207	N/A	N/A
3	95SD	2.29	37.0	0.21161	0.01053	9.36	6.09	0.164	0.158	0.196	1.19	No
4	95SD	4.57	58.5	0.20804	0.02066	18.38	11.94	0.204	0.158	0.196	0.96	Yes
5	95SD	7.62	87.2	0.20134	0.03396	30.20	19.63	0.225	0.158	0.196	0.87	Yes
6	clay	10.67	116.6	0.18911	0.02474	41.48	26.96	0.231	N/A	N/A	N/A	N/A
7	clay	13.72	146.6	0.17774	0.03187	52.14	33.89	0.231	N/A	N/A	N/A	N/A
8	clay	16.76	176.7	0.16034	0.03115	61.79	40.17	0.227	N/A	N/A	N/A	N/A
9	clay	19.81	206.7	0.14114	0.03592	70.28	45.68	0.221	N/A	N/A	N/A	N/A
10	sand	22.86	237.9	0.11882	0.03389	77.53	50.39	0.212	N/A	N/A	N/A	N/A
11	sand	25.91	270.3	0.11111	0.03752	83.43	54.23	0.201	N/A	N/A	N/A	N/A
12	sand	28.96	302.8	0.10189	0.03277	87.74	57.03	0.188	N/A	N/A	N/A	N/A
13	sand	32.00	335.2	0.10142	0.03426	90.62	58.90	0.176	N/A	N/A	N/A	N/A
14	sand	35.05	367.6	0.09717	0.02948	93.21	60.59	0.165	N/A	N/A	N/A	N/A
15	sand	38.10	400.0	0.09278	0.03091	96.52	62.74	0.157	N/A	N/A	N/A	N/A
16	sand	41.15	432.4	0.08912	0.02689	99.08	64.40	0.149	N/A	N/A	N/A	N/A
17	sand	44.20	464.9	0.08705	0.02015	100.92	65.59	0.141	N/A	N/A	N/A	N/A
18	bedrock	45.72	481.1	0.08718	0.00308	102.92	66.90	0.139	N/A	N/A	N/A	N/A

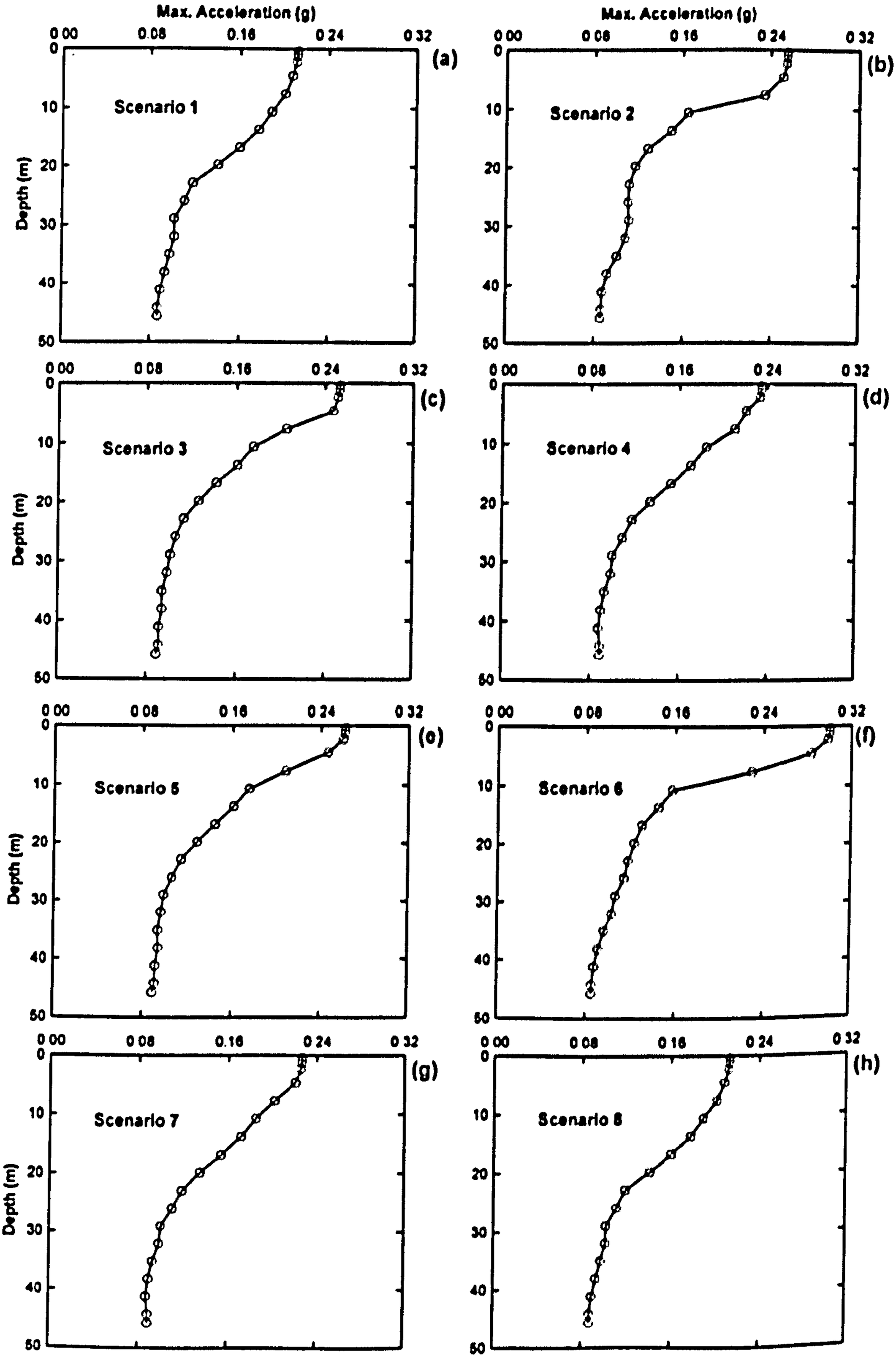

Figure 8. 20 Maximum acceleration for each scenario

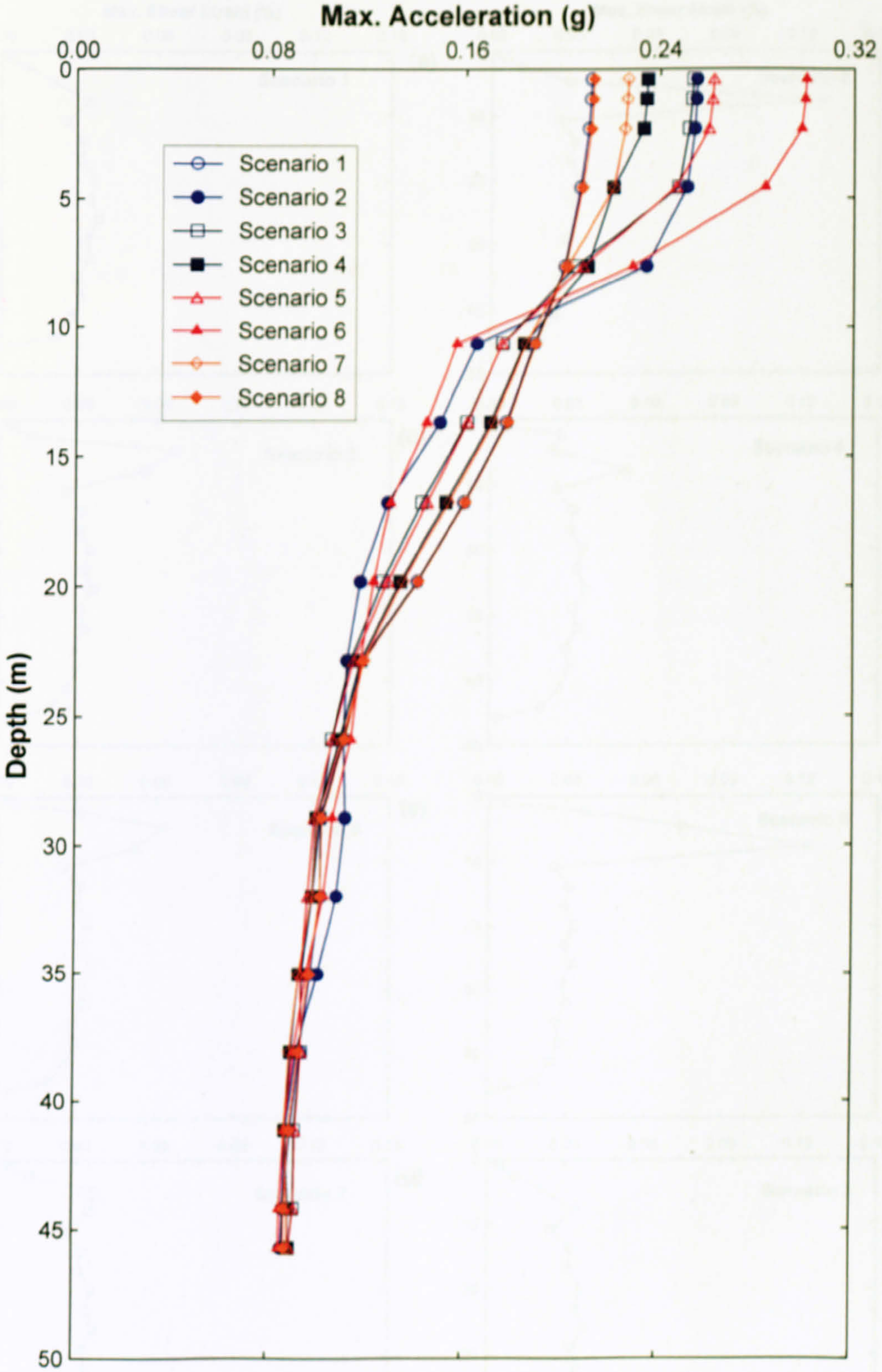

Figure 8. 21 Maximum acceleration for all scenarios

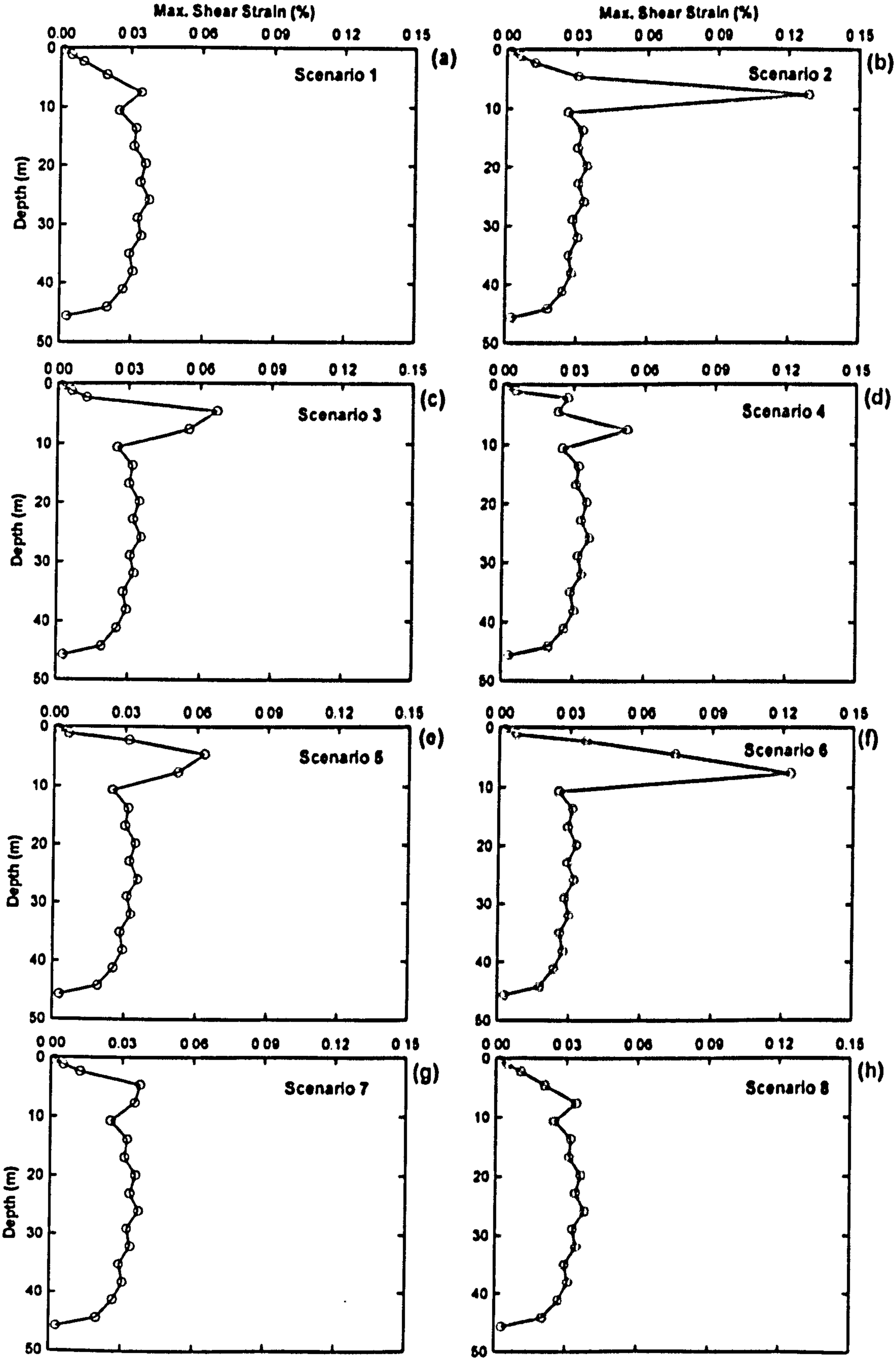

Figure 8. 22 Maximum shear strain for each scenario

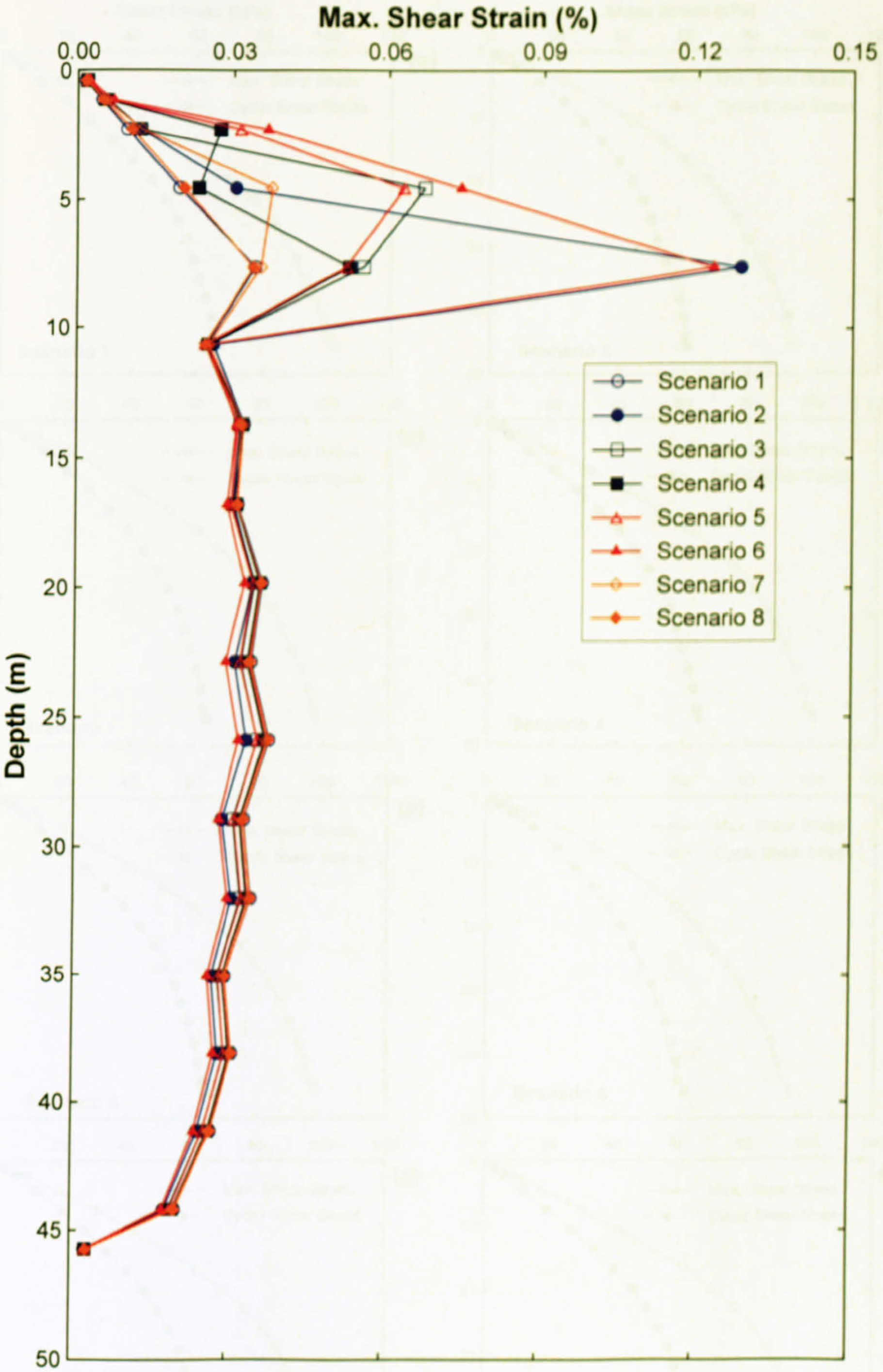

Figure 8. 23 Maximum shear strain for all scenarios

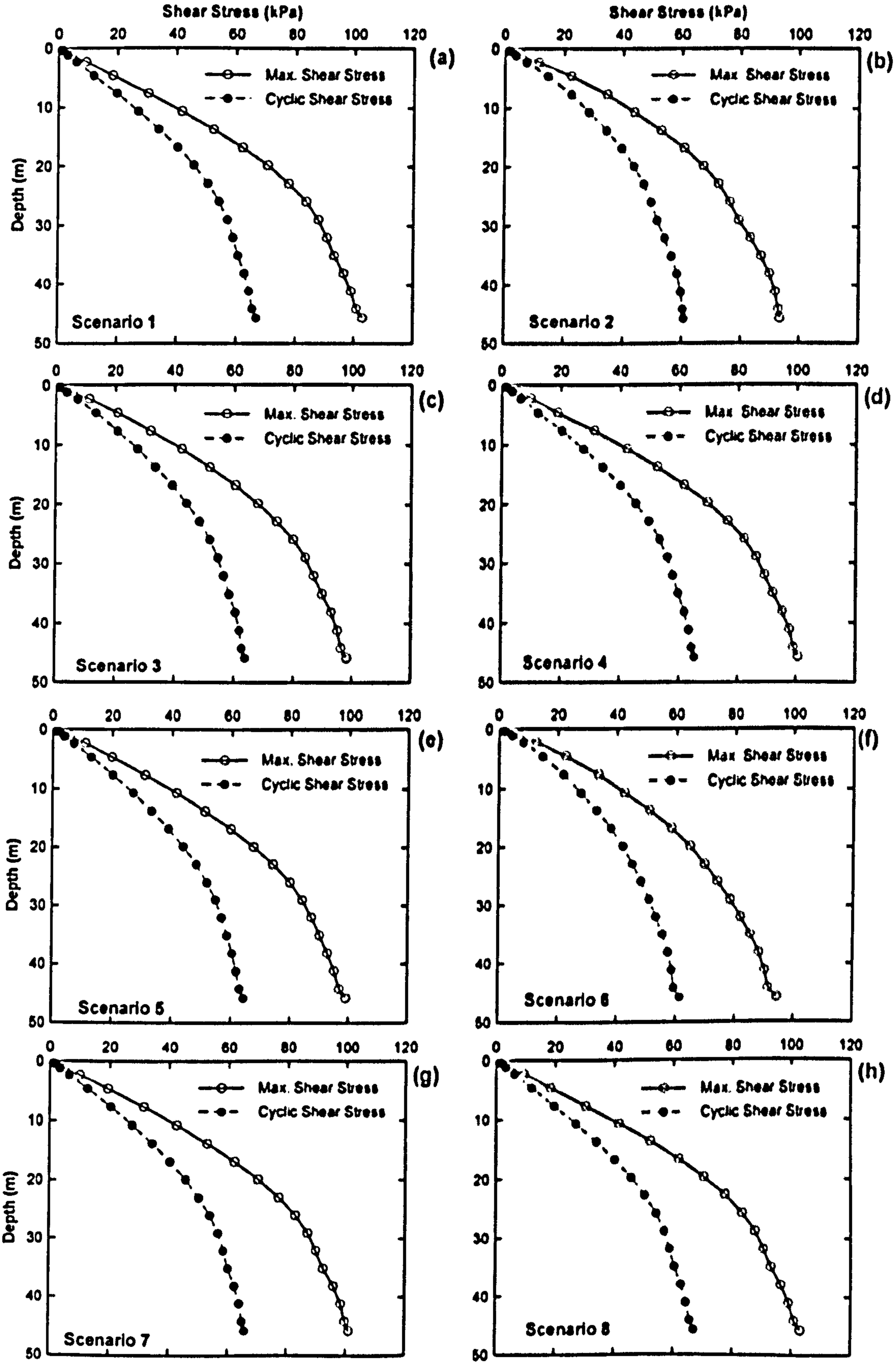

Figure 8. 24 Maximum shear stress and cyclic shear stress for each scenario

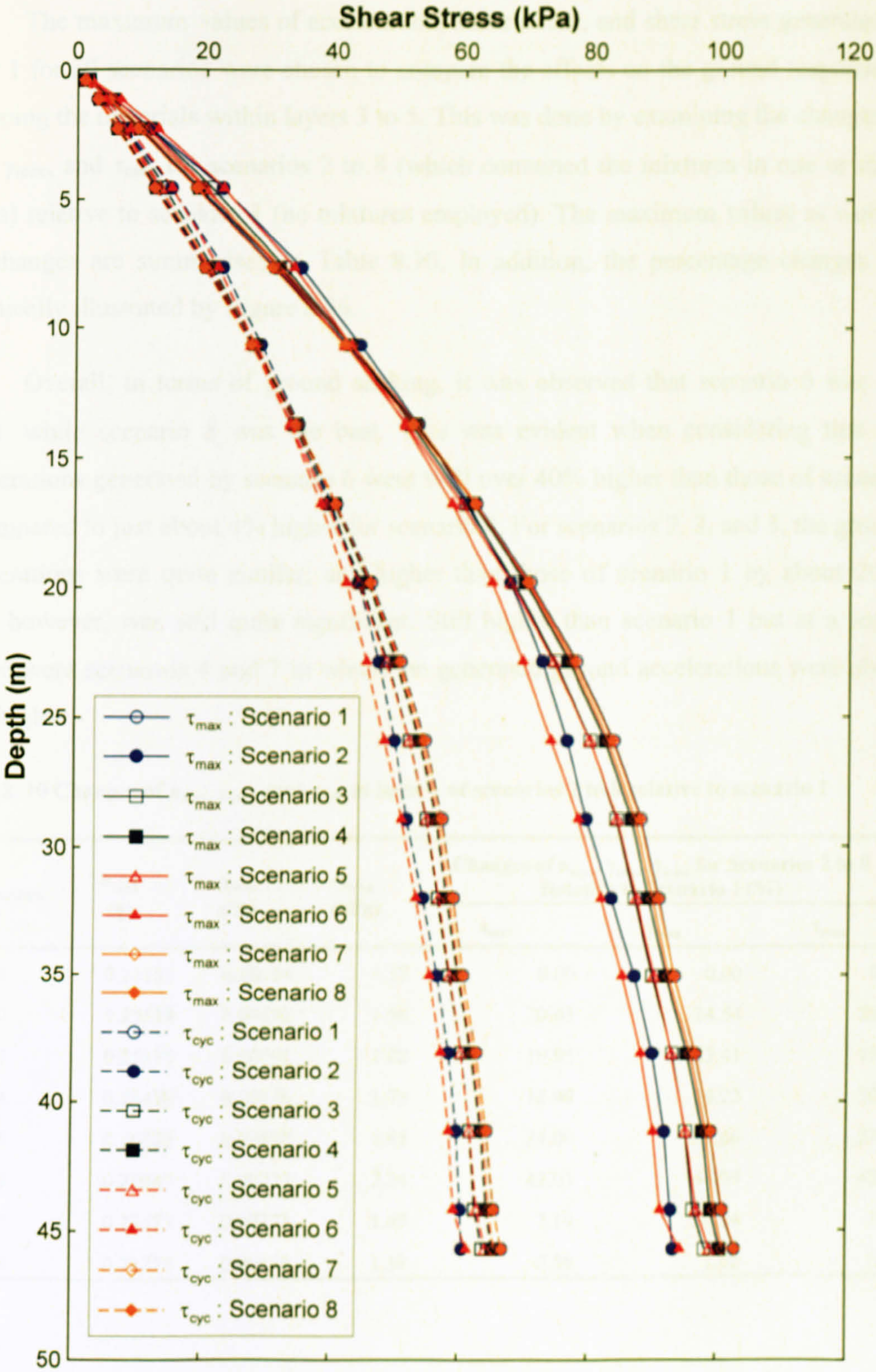

Figure 8. 25 Maximum shear stress and cyclic shear stress for all scenarios

The maximum values of acceleration, shear strain, and shear stress generated in layer 1 for all scenarios were chosen to compare the effects on the ground response of swapping the materials within layers 3 to 5. This was done by examining the changes of a_{max}, γ_{max}, and τ_{max} for scenarios 2 to 8 (which contained the mixtures in one or more layers) relative to scenario 1 (no mixtures employed). The maximum values as well as the changes are summarised in Table 8.10. In addition, the percentage changes are graphically illustrated by Figure 8.26.

Overall, in terms of ground shaking, it was observed that scenario 6 was the worst, while scenario 8 was the best. This was evident when considering that the accelerations generated by scenario 6 were well over 40% higher than those of scenario 1, compared to just about 4% higher for scenario 8. For scenarios 2, 3, and 5, the ground accelerations were quite similar; and higher than those of scenario 1 by about 20%. This, however, was still quite significant. Still higher than scenario 1 but at a lesser degree were scenarios 4 and 7 in which the generated ground accelerations were about 10% higher.

Table 8. 10 Changes of a_{max}, γ_{max}, and τ_{max} at layer 1 of scenarios 2 to 8 relative to scenario 1

Scenario	a_{max} (g)	γ_{max} (%)	τ_{max} (kPa)	Changes of a_{max}, γ_{max}, τ_{max} for Scenarios 2 to 8 Relative to Scenario 1 (%)		
				a_{max}	γ_{max}	τ_{max}
1	0.21155	0.00154	1.57	0.00	0.00	0.00
2	0.25518	0.00192	1.90	20.63	24.54	20.86
3	0.25375	0.00191	1.88	19.95	23.41	19.77
4	0.23479	0.00176	1.75	10.99	14.22	10.96
5	0.26232	0.00197	1.95	24.00	27.66	23.85
6	0.30047	0.00227	2.24	42.03	46.99	42.35
7	0.22677	0.00171	1.69	7.19	10.54	7.15
8	0.21277	0.00160	1.58	0.58	3.62	0.61

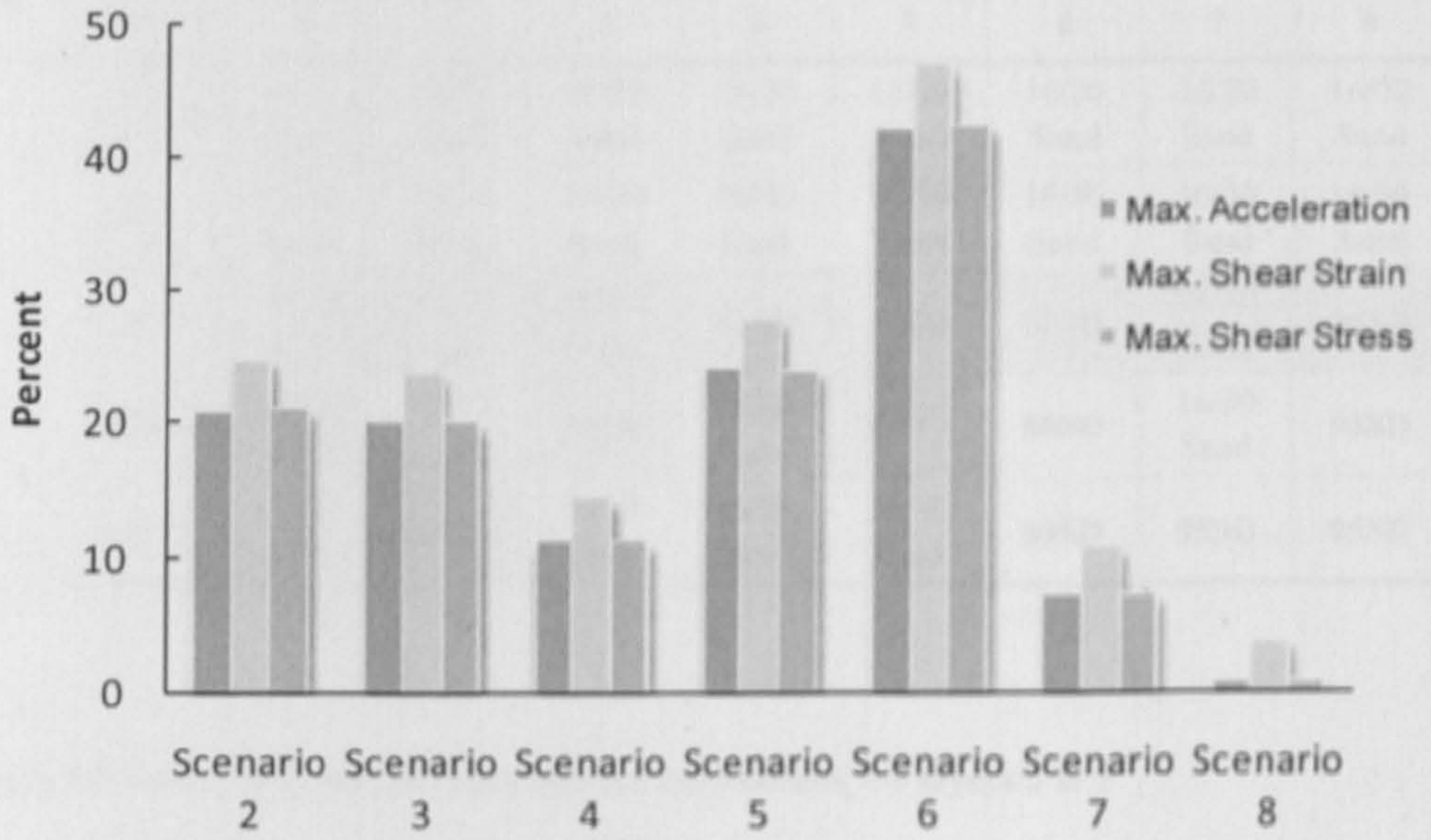

Figure 8. 26 Changes of a_{max}, γ_{max}, and τ_{max} at layer 1 of scenarios 2 to 8 relative to scenario 1

Referring to Tables 8.2 – 8.9 showing the EERA results, it was interesting to further analyse the effects of the mixtures on the occurrence of liquefaction. Note that the liquefaction was only analysed for layers 3 to 5. It was not done for layers 1 and 2 because they were not saturated. The layers that were not liquefied are illustrated by the shaded areas in Table 8.11.

For all scenarios it was observed that layer 3 was not liquefied, regardless of the material deposited. For layer 4, however, only scenarios 1, 3, and 5 did not liquefy. Scenario 2 was the only one where layer 5 was not liquefied. However, whether a layer liquefied or not may be inadequate in terms of ground response analysis; the factor of safety against the liquefaction should also be taken into account, as illustrated by Table 8.12 and Figure 8.27.

Overall, it may be suggested that scenario 5 was better than scenario 1 in terms of the resistance to liquefaction, as FS_{Lq} was generally greater. However, layer 5 was still liquefiable. For this circumstance, the still-liquefiable layer may be mitigated by other countermeasures such as replacement by better materials, densification of the layer, soil improvement, and dewatering.

Table 8. 11 Shaded area indicating the layer is non-liquefiable

Layer	Thickness (m)	Scenario 1	Scenario 2	Scenario 3	Scenario 4	Scenario 5	Scenario 6	Scenario 7	Scenario 8	Note
1	0.76	16/30 Sand	16/30 Sand	16/30 Sand	16/30 Sand	16/30 Sand	16/30 Sand	16/30 Sand	16/30 Sand	
2	0.76	16/30 Sand	16/30 Sand	16/30 Sand	16/30 Sand	16/30 Sand	16/30 Sand	16/30 Sand	16/30 Sand	Water Table
3	1.52	16/30 Sand	16/30 Sand	16/30 Sand	**50SD**	**50SD**	**50SD**	16/30 Sand	**95SD**	
4	3.05	16/30 Sand	16/30 Sand	**50SD**	16/30 Sand	**50SD**	**50SD**	16/30 Sand	**95SD**	
5	3.05	16/30 Sand	**50SD**	16/30 Sand	16/30 Sand	16/30 Sand	**50SD**	**95SD**	**95SD**	

Table 8. 12 Values of factor of safety against liquefaction for layers 3 to 5

Layer	Factor of Safety against Liquefaction, FS_{Lq}							
	Scenario 1	Scenario 2	Scenario 3	Scenario 4	Scenario 5	Scenario 6	Scenario 7	Scenario 8
3	1.27	1.04	1.05	1.50	1.33	1.16	1.18	1.19
4	1.02	0.84	1.09	0.92	1.04	0.91	0.97	0.96
5	0.93	1.02	0.78	0.86	0.75	0.85	0.85	0.87

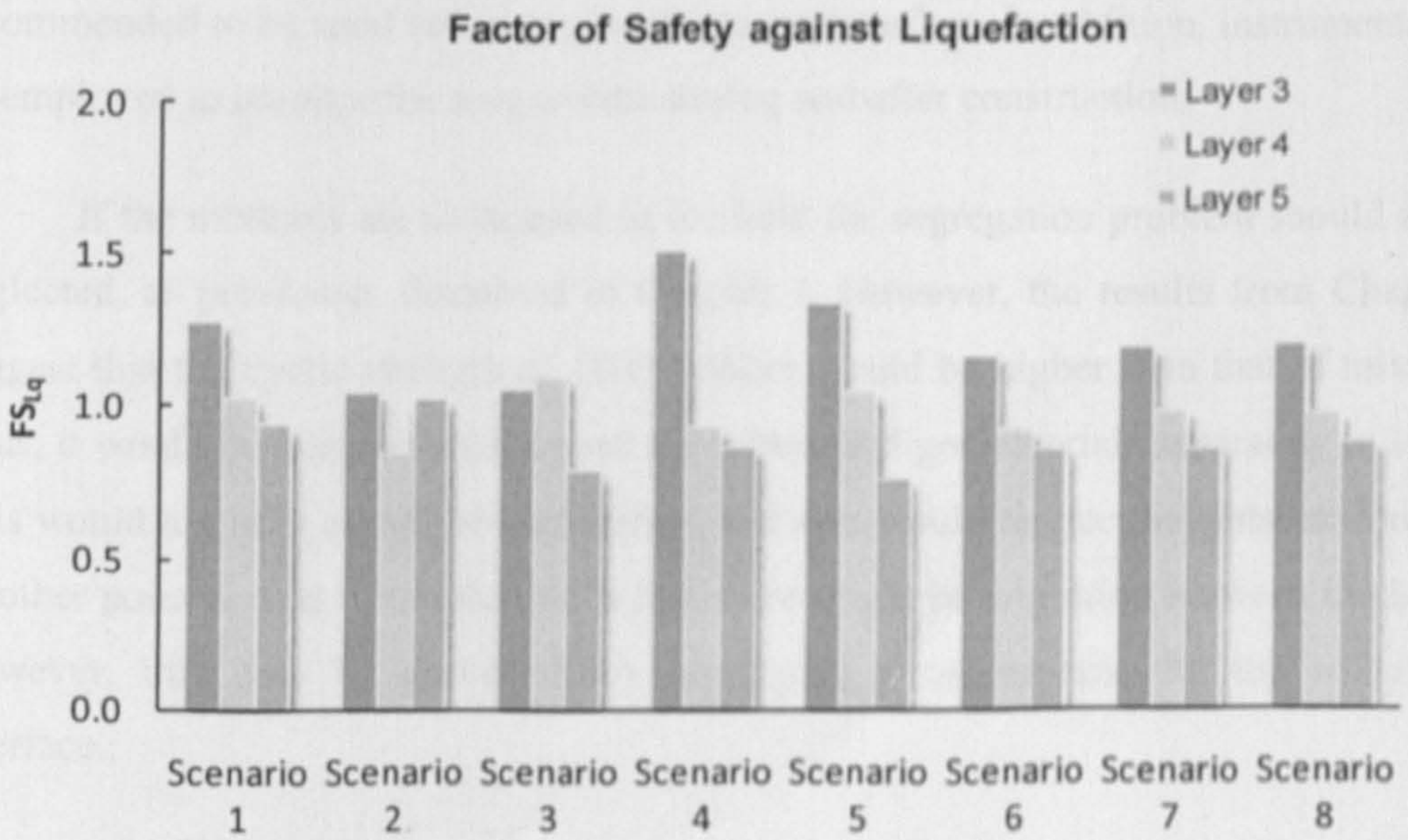

Figure 8. 27 Factor of safety against liquefaction for layers 3 to 5

It should be noted herein that EERA cannot compute the generated pore water pressure during earthquake shaking; thus, this limitation must be considered. The behaviour of sand-rubber matrix is very complex, especially when taking the pore water pressure into account. It is therefore recommended that other computer programs that can include the behaviour of pore water pressure should be employed for further investigation.

There have been concerns that utilising recycled rubber for construction projects may cause the environmental problems, especially to ground water. As a result, the water quality effects due to making use of recycled rubber have been investigated. For example, Humphrey (1998) reported that tyre shreds have a negligible impact on the quality of ground water; and concluded that they can be used for most civil engineering applications. This study, however, was based on the condition that the pH of the ground water is near neutral. As such, Humphrey (1998) suggested that the effects of tyre shreds on water quality for acidic or basic conditions should be further studied.

Another important problem should be considered is exothermic reactions which have occurred in Washington and Colorado. The reason is that waste tyres may catch fire as a result of the oxidation of the steel belts in combination with high temperature (Moo-Young *et al.*, 2003). If this happens, the consequences may be disastrous as the burnt tyres may contaminate ground water. Therefore, the recycle rubber has been recommended to be used not very near the ground surface. In addition, instruments may be employed to monitor the temperature during and after construction.

If the mixtures are to be used in the field the segregation problem should not be neglected, as previously discussed in Chapter 3. However, the results from Chapter 6 suggest that the cyclic strength of 100% rubber would be higher than that of mixtures. Thus, it would be pragmatic to deposit the rubber and geomaterials separately in layers. This would not only avoid the segregation, but also would reduce the construction cost. Another point should be considered is that there might be migration between the layers. However, this may be prevented by employing geomembranes at the soil-rubber interface.

CHAPTER 9

CONCLUSIONS

9.1 Introduction

Leighton Buzzard 16/30 sand (S) was mixed with tyre chips CT0515 (A), CT1030 (B), CT2060 (C), and CT4010 (D) to investigate the liquefaction characteristics, dynamic properties, and monotonic behaviour, under undrained conditions. The mean particle sizes with respect to S, A, B, C, and D were 0.7, 1.2, 2.3, 4.0, and 8.0mm, which correspond to the particle size ratios D_r/D_s of 1.7, 3.3, 5.7, and 11.4. The sand to rubber ratios by solid volume were 100:0, 95:5, 90:10, 80:20, 70:30, 60:40, and 50:50.

The liquefaction characteristics including cyclic strength, pore water pressure, and strain behaviour were studied by means of a computer-controlled cyclic triaxial testing system. The system was modified in order to house bender elements for the measurements of shear wave velocity, hence the small strain shear modulus. The monotonic stress-strain behaviour was obtained employing a conventional triaxial testing machine with pore water pressure measurements. Based on the experiences, test results, and analyses, the following conclusions have been drawn.

9.2 Test Materials and Sample Preparation

(1) The specific gravity of the sand and tyre chips were 2.66 and 1.15 respectively.

(2) Apart from the size of the materials, all particle size distribution curves for S, A, B, C, and D were similar.

(3) Even though the sizes were different, the minimum and maximum densities for tyre chips A, B, C, and D were very similar. However, the tyre chips having the smallest particle size, A, had the lowest minimum density.

(4) For sand mixed with tyre chips, the higher the percentage of rubber added the lower the minimum and maximum densities.

(5) For mixtures having a lower percentage of rubber such as 5 and 10%, there are only slight differences between the minimum and maximum densities. When the rubber is increased to 30% and higher, however, the differences are pronounced.

(6) The sand-tyre chip specimens cannot be prepared by means of underwater deposition as the tyre chips immediately float once deposited.

9.3 Monotonic Behaviour

(1) For S, an initial peak deviator stress occurs at very low strain for both TC and TE, followed by strain hardening and strain softening for TC and TE respectively. The peak deviator stress for both TC and TE occurs at about 8% axial strain.

(2) For SA with 5% rubber the stress-strain curves are quite similar to those of S, but the peak deviator stresses are smaller and occur at larger strains. When the rubber is increased to 10% and higher, there is no definite peak deviator stress.

(3) For SB with 5 and 50% rubber, the stress-strain curves resemble to those of SA with the same rubber content. However, for SB with rubber contents of 10, 20, 30, and 40%, the stress-strain curves exhibit a peak.

(4) The stress-strain curves for SC and SD are quite similar at the same rubber contents. The peak deviator stress occurs for the mixtures containing rubber contents of 5, 10, and 20%. When the rubber is increased to 30% and higher, some mixtures exhibit a peak deviator stress, but not necessarily marked.

(5) The q_f values under TC for SC and SD gradually decrease when the rubber is increased from 5 to 50%. However, for SA and SB, as the particle size is smaller, the q_f values also gradually decrease when the rubber is increased from 5 to 20%, but at much higher rate compared to SC and SD. It just slightly decreases when the rubber is increased to 30%. When the rubber is increased to 40 and 50%, q_f remains approximately constant.

(6) The q_f values under TE with respect to the increase of rubber contents have a pattern similar to those of TC. However, regardless of the size of the rubber, the q_f values for SA, SB, SC, and SD with 50% rubber are quite similar.

(7) The PT point for S under TC occurs at a very low strain level of less than 1%. For all mixtures, however, the higher the rubber content the larger the strain at which the PT point occurs. In addition, for all mixtures having 5% rubber content the PT points occur at a strain level similar to that of S, but slightly higher. This proportionate occurrence of the PT under TC is not the case for TE.

(8) The behaviour of Δu for S is typical of that for a dense or medium dense sand.

(9) The Δu for S under TC increases sharply to a maximum of about 26kPa at the beginning of shearing. It then decreases very rapidly at almost the same rate to a minimum of -254kPa. This behaviour is also the case for TE, except that the maximum is somewhat higher, and occurs at a larger strain.

(10) The behaviours of Δu for SA with 5% rubber, SB with 5 and 10% rubber, SC and SD with 5, 10, and 20% rubber, are similar to those of S, except that the maximum positive Δu for both TC and TE is greater.

(11) For SA, SB, SC, and SD, the higher the percentage of rubber, the greater is Δu at the end of shearing.

(12) The value of A_f for S under TC indicates that it was prepared in a medium to dense state. In addition, the difference between the A_f obtained from both TC and TE is quite high, indicating a high degree of anisotropy for the sand which occurs during sample preparation.

(13) For SA, SB, SC, and SD with 5% rubber, the values of A_f are similar to that of S. However, it tends to increase with rubber content from 10 to 50%.

(14) For S under TC, the $p' - q$ stress path at the beginning of shearing dilates slightly until the PT is met. It then exhibits a marked dilation until the failure occurs at the maximum p'. It then travels backwards to the end of shearing. Contrary to TC, the stress path for TE initially shows a marked contractile tendency. Then the stress path exhibits the dilative behaviour towards the end of shearing.

(15) For SA, SB, SC, and SD with 5% rubber and SC and SD with 10% rubber, the stress paths are comparable to those of S, except for SA and SB which initially exhibit slight contraction. For the rest, the initial contraction is apparent.

(16) For SA, SB, SC and SD with 5 and 10% rubber contents, where the stress path changes from contractive to dilative is also the PT point. At higher rubber contents, however, the PT points occur just slightly after the changes have taken place.

9.4 Cyclic Behaviour

(1) The stress-strain curve for S indicates brittle behaviour.

(2) For SA, SB, SC, and SD, the higher the percentage of rubber added the more ductile the behaviour.

(3) The cyclic strength for SA, SB, SC, and SD with 5, 10, and 20% rubber and SA, SB, and SD with 30% rubber is lower than that of S. The cyclic strength is the lowest for all at 20% rubber content.

(4) When the rubber is increased to 30, 40, and 50% for SC; 40 and 50% for SA, SB, and SD, the cyclic strength then is greater than that of S. The cyclic strengths are greatest at 50% rubber content.

(5) For S subjected to low to moderate q_{cyc}, Δu_p increases gradually during cyclic loading. At Δu_p equal to approximately to 0.6, it then increases rapidly after a few more cycles, leading to liquefaction. At greater applied q_{cyc}, however, Δu_p increases very quickly, and liquefies after only 3 cycles of loading.

(6) For SA, SB, SC, and SD with 5 and 10% rubber, the behaviour of Δu_p is similar to that of S, but the rate of increase is greater. When the rubber content is increased, Δu_p initially increases very rapidly, and then gradually increases towards liquefaction, particularly for the mixtures having 40 and 50% rubber contents.

(7) For S subjected to low to moderate q_{cyc}, $\varepsilon_{a,DA}$ remains virtually zero during cyclic loading until the last few cycles when it increases almost vertically to over 5%.

(8) For SA, SB, SC, and SD with 5, 10, and 20% rubber contents the behaviour of $\varepsilon_{a,DA}$ is similar to that of S. When the rubber is increased to 30%, $\varepsilon_{a,DA}$ then gradually increases, followed by a sudden increase towards liquefaction.

(9) For SA, SB, SC, and SD with 40 and 50% rubber contents, $\varepsilon_{a,DA}$ increases very rapidly towards liquefaction.

(10) The reason the mixtures had the lowest cyclic strength when containing 20% or rubber may be explained when considering the inter-rubber void ratio e_r against the rubber content. It was found that when the mixtures contained rubber contents from 5 to 10%, e_r decreased sharply. When the rubber was increased from 10 to 30%, then the rate of the decrease decreased. Subsequently, when the rubber was increased to 40% and above, the rate of the decrease was approximately constant. Therefore, it may be concluded that the cyclic behaviour of the mixtures containing rubber content of around 20% is transitional.

9.5 Dynamic Properties

(1) Of all the bender element interpretation methods, the results obtained by first major peak to peak method (PP) are the most consistent.

(2) The arrival of shear waves by first arrival technique (FA) is dependent on the input frequency. This, however, is not the case for PP and cross correlation (CC).

(3) Only SA with 5% rubber content has V_s and G_{max} slightly higher than those of S. For the rest, all have lower V_s and G_{max}.

(4) Regardless of the size of rubber added, the higher the percentage of rubber the lower the values of V_s and G_{max}.

(5) When the rubber is increased to 30% and higher, V_s and G_{max} depend on the particle size of rubber, i.e., the bigger the rubber size the greater the V_s and G_{max}.

(6) When the mixtures containing rubber contents of 30% and higher were subjected to input frequencies of 7kHz and greater, there was so much noise that the signals are un-interpretable.

(7) The G/G_{max} curve for S is comparable to the curve provided by Seed and Idriss (1970).

(8) For SA, SB, SC, and SD with 5% rubber content, the G/G_{max} curves are quite similar to that of S, suggesting there is only a very marginal effect on the stiffness when 5% of rubber is added to S.

(9) For SA, SB, SC, and SD with 50% rubber content, the G/G_{max} curves are shifted to the right significantly indicating a pronounced effect of rubber on the stiffness of sand-rubber mixtures.

(10) The damping ratio (D) for S at about 0.1% cyclic shear strain is approximately 5%, which is comparable with other studies.

(11) For SA with 5% rubber content, the D value is similar to that of S. For SB, SC, and SD with the same rubber content, however, their values are greater, compared to S.

(12) For SA, SB, SC, and SD with rubber contents of 10% and higher, D values are greater than that of S.

9.6 Response to Seismic Loading

(1) The sand-rubber mixtures in fact amplify the ground acceleration and generate higher shear strain, compared to pure sand. However, it seems the addition of rubber does not alter the generated shear stress.

(2) The sand-rubber mixtures improve the overall factor of safety against liquefaction, implying that they may be used to mitigate the hazard.

9.7 Recommendations for Further Work

(1) It is recommended to carry out undrained cyclic triaxial tests for sand mixed with tyre chips having higher proportions of rubber than used in this research, e.g., 60%, 80%, and 100%, providing a complete cyclic strength curve.

(2) It would be interesting to determine the liquefaction potential of soil mixed with recycled tyres having different particle size ratios D_r/D_s to those used in this research. For example, instead of sand, gravel should be used as a base material, with rubber having a smaller size than the gravel mixed in. This will result in a particle size ratio lower than 1.0.

(3) The maximum size of rubber used in this research was restricted by the condition that it must not be greater than 1/10 the diameter of a cylindrical triaxial specimen. In practice, using bigger size of rubber means that the cost of producing the recycled rubber is lower. Thus, it is important to carry out the cyclic triaxial test of sand mixed with tyre chips having bigger sizes of which

in turn a bigger specimen size is required, hence a bigger triaxial cell and an actuator with higher capacity and longer stroke.

(4) Instead of mixing the sand and the rubber, preparing them separately in layers may provide an interesting result. For such sample preparation, however, a shaking table may be more suitable than the cyclic triaxial test. Another possibility is a centrifuge test.

(5) Other kinds of test that could provide the shear modulus and damping ratios of the mixtures for cyclic shear strain ranges that this research did not cover should be studied, providing a complete curve without any interpolation, for example, cyclic simple shear and cyclic torsional shear tests.

(6) A computer package such as the discrete element method (DEM) should be used to study how stresses are transferred within sand-rubber matrices during cyclic loading in order to understand the interactions between sand, rubber and the pore water.

REFERENCES

Alarcon-Guzman, A., Leonards, G. A., and Chameau, J. L. (1988), Undrained monotonic and cyclic strength of sands, J. of Geotechnical Engineering, ASCE, Vol. 114, No. 10, 1089-1109.

Amini, F., and Chakravrty, A. (2004), Liquefaction testing of layered sand-gravel composites, Geotechnical Testing J., ASTM, Vol. 27, No. 1, 1-11.

Andrews, D. C. A., and Martin, G. R. (2000), Criteria for liquefaction of silty soils, 12th World Conference on Earthquake Engineering, Auckland, New Zealand.

Andrus, R. D., and Stokoe II, K. H. (2000), Liquefaction resistance of soils from shear-wave velocity, J. of Geotechnical and Geoenvironmental Engineering, ASCE, Vol. 126, No. 11, 1015-1025.

Architectural Institute of Japan (2001), Recommendations for design of building foundations (in Japanese).

Arulnathan, R., Boulanger, R. W., and Riemer, M. F. (1998), Analysis of bender element tests, Geotechnical Testing J., Vol. 21, No. 2, 120-131.

ASTM (1996a), Standard test method for consolidated undrained triaxial compression test for cohesive soils, ASTM D4767-95, W. Conshohocken, PA.

ASTM (1996b), Standard test method for load controlled cyclic triaxial strength of soil, ASTM D5311-92, W. Conshohocken, PA.

ASTM (1997), Laboratory determination of pulse velocities and ultrasonic elastic constants of rock, ASTM D2845-95, W. Conshohocken,

ASTM (1998), Standard practice for use of scrap tires in civil engineering, ASTM D6270-98, W. Conshohocken, PA.

Atkinson, J. H., and Bransby, P. L. (1978), The mechanics of soils: an introduction to critical state soil mechanics, McGraw-Hill, Maidenhead, Berkshire, England.

Bardet, J. P., Ichii, K., and Lin, C. H. (2000), EERA: A computer program for Equivalent-linear Earthquake site Response Analyses of Layered Soil Deposits, U of Southern California.

Belloti, R., Jamiolkowski, M., Lo Presti, D. C. F., and O'Neill, D. A. (1996), Anisotropy of small strain stiffness of Ticino sand, Geotechnique, Vol. 46, No. 1, 115-131.

Bergado, B.T., Youwai, S., and Rittirong, A. (2005), Strength and deformation characteristics of flat and cubical rubber tyre chip-sand mixtures, Geotechnique, Vol. 55, No. 8, 603-606.

Bishop, A. W., and Henkel, D. J. (1962), The measurement of soil properties in the triaxial test, Edward Arnold, London, UK.

Bishop, A. W., and Hight, D. W. (1977), The value of Poisson's ratio in saturated soils and rocks stressed under undrained conditions, Geotechnique, Vol. 27, No. 3, 369-384.

Blewett, J., Blewett, I. J., and Woodward, P. K. (2000), Phase and amplitude responses associated with the measurement of shear-wave velocity in sand by bender elements, Canadian Geotechnical J., Vol. 37, 1348-1357.

Brennan, A. J., Thusyanthan, N. I., and Madabhushi, S. P. G. (2005), Evaluation of shear modulus and damping in dynamic centrifuge tests, J. of Geotechnical and Geoenvironmetal Engineering, Vol. 131, No. 12, 1488-1497.

Brignoli, E., Gotti, M., and Stoke, K. H. (1996), Measu rement of shear waves in laboratory specimens by means of piezoelectric transducers , Geotechnical Testing J., Vol. 19, No. 4, 384-397.

BS 1377-2 (1990), Methods of test for soils for civil engineering purposes, British Standards Institution, London, UK.

BS 1377-7 (1990), Methods of test for soils for civil engineering purposes – Part 7: Shear strength tests (total stress), British Standard.

Casagrande, A. (1936), Characteristics of cohesionless soils affecting the stability of earth fills, Boston Society of Civil Engineers, Vol. 23, 257-276.

Casagrande, A. (1940), Characteristics of cohesion less soils affecting the stability of slopes and earth fills, Contributions to Soil Mechanics, 1924-1940, Boston Society of Civil Engineers, Boston, Massachusetts, 257-276.

Castro, G. (1969), Liquefaction of sand, Harvard Soil Mechanics Series, No. 81.

Chan, C. M. (2006), A laboratory investigation of shear wave velocity in stabilised soft soils, PhD Thesis, University of Sheffield, UK.

Chillarige, A. V., Robertson, P. K., Morgenstern, N. R., and Christian, H. A. (1997), Site investigations to evaluate flow liquefaction slides at Sand Heads, Fraser River delta, Canadian Geotechnical J., Vol. 34, 384-397.

Dano, C., Hareb, H., and Hicher, P. Y. (2003), Characterization of Loire River sand in the small strain domain using new bender-extender elements, 16th ASCE Engineering Mechanics Conference, U. of Washington, Seattle.

Drnevich, V. P., Hardin, B. O., and Shippy, D. J. (1978), Modulus and damping of soils by the resonant-column method, Dynamic Geotechnical Testing, ASTM STP 654, ASTM, 91-125.

Edil, T. B., and Bosscher, P. J. (1994), Engineering properties of tire chips and soil mixtures, Geotechnical Testing J., ASTM, Vol. 17, No. 4, 453-464.

Erten, D., and Maher, M. H. (1995), Cyclic undrained behavior of silty sand, Soil Dynamics and Earthquake Engineering, Vol. 14, 115-123.

Evans, M. D. (1992), Density changes during undrained loading-membrane compliance, J. of Geotechnical Engineering, ASCE, Vol. 118, No. 6, 1924-1936.

Evans, M. D., Seed, H. B., and Seed, R. B. (1992), Membrane compliance and liquefaction of sliced gravel specimens, J. of Geotechnical Engineering, ASCE, Vol. 118, No. 6, 856-872.

Evans, M. D., and Zhou, S. (1995), Liquefaction behavior of sand-gravel composites, J. of Geotechnical Engineering, ASCE, Vol. 121, No. 3, 287-298.

Feng, Z. Y., and Sutter, K. G. (2000), Dynamic properties of granulated rubber/sand mixtures, Geotechnical Testing J., ASTM, Vol. 23, No. 3, 338-344.

Foose, G. J., Benson, C. H., and Bosscher, P. J. (1996), Sand reinforced with shredded waste tires, J. of Geotechnical Engineering, ASCE, Vol. 122, No. 9, 760-767.

Ghazavi, M. (2004), Shear strength characteristics of sand-mixed with granular rubber, Geotechnical and Geological Engineering, Vol. 22, 401-416.

Ghazavi, M., and Sakhi, M. A. (2005), Influence of optimized tire shreds on shear strength parameters of sand, International J. of Geomechanics, ASCE, Vol. 5, No. 1, 58-65.

Grozic, J. L. H., Robertson, P. K., and Morgenstern, N. R. (2000), Cyclic liquefaction of loose gassy sand, Canadian Geotechnical J., Vol. 37, 843-856.

Hardin, B. O., and Black, W. L. (1968), Vibration modulus and damping in soils, J. of the Soil Mechanics and Foundations Division, ASCE, Vol. 94, No. SM2, 353-369.

Hausmann, M. R. (1990), Engineering principles of ground modification, McGraw-Hill, New York.

Head, K. H. (1986), Manual of soil laboratory testing: Volume 3 effective stress tests, Pentech Press, London.

Higuchi, T. (2001), Liquefaction and cyclic failure of low plasticity silt, PhD Thesis, University of Sheffield, UK.

Hird, C. C., and Hassona, F. A. K. (1990), Some factors affecting the liquefaction and flow of saturated sands in laboratory tests, Engineering Geology, Vol. 28, 149-170.

Hoar, R. J., and Stokoe, K. H., II. (1978), Generation and measurement of shear wave in site, Dynamic Geotechnical Testing, ASTM STP 654, ASTM, 3-29.

Hosono, Y., and Yoshimine, M. (2004), Liquefaction of sand in simple shear condition, International Conference on Cyclic Behaviour of Soils and Liquefaction Phenomena, Bochum, Germany, 129-136.

Huang, B., Yin, J. H., Wu, S. M., and Chen, Y. M. (2000), Dynamic testing of silt using bender element, An International Conference on Geotechnical & Geological Engineering, Melbourne, Australia.

Huang, Y. T., Huang, A. B., Kuo, Y. C., and Tsai, M. D. (2004), A laboratory study on the undrained strength of a silty sand from Central Western Taiwan, Soil Dynamics and Earthquake Engineering, Vol. 24, 733-743.

Humphrey, D. N. (1998), Civil engineering application of tire shreds, Rubber Recycling '98, Toronto, Ontario.

Hyde, A. F. L., and Higuchi, T. (2005), Post liquefaction characteristics of low plasticity silt, 16th International Conference on Soil Mechanics and Geotechnical Engineering, 2659-2662.

Hyodo, M., Aramaki, N., Itoh, M., and Hyde, A. F. L. (1996), Cyclic strength and deformation of crushable carbonate sand, Soil Dynamics and Earthquake Engineering, Vol. 15, 331-336.

Hyodo, M., Hyde, A. F. L., and Aramaki, N. (1998), Liquefaction of crushable soils, Geotechnique, Vol. 48, No. 4, 527-543.

Hyodo, M., Yamada, S., Orense, R. P., and Okamoto, M. (2008), Undrained cyclic shear properties of tire chip-sand mixtures, Scrap Tire Geomaterials-Opportunities and Challenges, Taylor & Francis, London, UK.

Ishihara, K. (1993), Liquefaction and flow failure during earthquakes, Geotechnique, Vol. 43, No. 3, 351-415.

Ishihara, K., Sodekawa, M., and Tanaka, Y. (1978), Effects of overconsolidation on liquefaction characteristics of sands containing fines, Dynamic Geotechnical Testing, ASTM STP 654, ASTM, 246-264.

Ishihara, K., Tatsuoka. F., and Yasuda, S. (1975), Undrained deformation and liquefaction of sand under cyclic stresses, Soils and Foundation, Vol. 15, 29-44.

Ismail, M. A., and Rammah, K. I. (2005), Shear-plate transducers as a possible alternative to bender elements for measuring Gmax, Geotechnique, Vol. 55, No. 5, 403-407.

JGS (1998), Remedial measures against soil liquefaction: From investigation and design to implementation, A. A. Balkema, Rotterdam, Netherlands.

Jovičić, V., Coop, M. R., and Simić, M. (1996), Objective criteria for determining Gmax from bender element tests, Geotechnique, Vol. 46, 357-362.

Khalid, H. A., and Artamendi, I. (2004), Mechanical properties of used-tyre rubber, Engineering Sustainability, Vol. 157, No. 1, 37-43.

Kim, H. K., and Santamarina, J. C. (2008), Sand-rubber mixtures (large rubber chips), Canadian Geotech. J., Vol. 45, 1457-1466.

Kramer, S. L. (1996), Geotechnical earthquake engineering, Prentice Hall, New Jersey.

Kramer, S. L., and Seed, H. B. (1988), Initiation of soil liquefaction under static loading conditions, J. of Geotechnical Engineering, ASCE, Vol. 114, No. 4, 412-430.

Krishnaswamy, N. R., and Isaac, N. T. (1995), Liquefaction analysis of saturated reinforced granular soils, J. of Geotechnical Engineering, ASCE, Vol. 121, No. 9, 645-651.

Lacasse, S., and Berre, T. (1988), Triaxial testing methods for soils, Advanced Triaxial Testing of Soil and Rock, ASTM STP 977, ASTM, 264-289.

Ladd, R.S., Chan, C.K. (1976), Cyclic triaxial strength of standard test sand, J. of the Soil Mechanics and Foundations Division, ASCE, Vol. 102, no. 5, 511-523.

Lambe, T. W., and Whitman, R. V. (1979), Soil Mechanics, SI Version, John Wiley & Sons, New York.

Lee, I. K., White, W., and Ingles, O. G. (1983), Geotechnical engineering, Pitman, Boston.

Lee, J. S., and Santamarina, J. C. (2005), Bender elements: performance and signal interpretation, J. of Geotechnical and Geoenvironmental Engineering, ASCE, Vol. 131, No. 9, 1063-1070.

Lee, J. H., Salgado, R., Bernal, A., and Lovell, C. W. (1999), Shredded tires and rubber-sand as lightweight backfill , J. of Geotechnical and Geoenvironmental Engineering, ASCE, Vol. 125, No. 2, 132-141.

Leong, E. C., Yeo, S. H., and Rahardjo, H. (2005), Measuring shear wave velocity using bender elements, Geotechnical Testing J., ASTM, Vol. 28, No. 5, 1-11.

Liao, S. S. C., and Whitman, R. V. (1986), Catalogue of liquefaction and non-liquefaction occurrences during earthquakes, Res. Rep., Department of Civil Engineering, M.I.T., Cambridge, Massachusetts.

Lings, M. L., and Greening, P. D. (2001), A novel bender/extender element for soil testing, Geotechnique, Vol. 51, No. 8, 713-717.

Meca, J. B. (2004), Rate effects of rapid loading in clay soils, PhD Thesis, University of Sheffield, UK.

Mitchell, J. K. (1993), Fundamentals of soil behavior, 2nd edition, John Wiley & Sons, New York.

Moo-Young, H., Sellasie, K., Zeroka, D., and Sabnis, G. (2003), Physical and chemical properties of recycled tire shreds for use in construction, J. of Environmental Engineering, ASCE, Vol. 129, No. 10, 921-929.

Mulilis, J. P., Townsend, F. C., and Horz, R.C. (1978), Triaxial testing techniques and sand liquefaction, Dynamic Geotechnical Testing, ASTM STP 654, ASTM, 265-279.

North Carolina Department of Environment and Natural Resources Web Site http://www.p2pays.org/

O'Reilly, M. P., and Brown, S. F. (eds) (1991), Cyclic loading of soils: from theory to design, Blackie and Son Ltd., Glasgow, UK.

Orense, R. P. (2005), Assessment of liquefaction potential based on peak ground motion parameters, Soil Dynamics and Earthquake Engineering, Vol. 25, 225-240.

Parkin, S., Fommer, F., and Uren, S. (2003), Sustainable development: understanding the concept and practical challenge, Engineering Sustainability, Vol. 156, No. 1, 19-26.

PIRI (1997), Handbook on liquefaction remediation of reclaimed land, A.A. Balkema, Rotterdam, Netherlands.

Poorooshasb, H. B. (1989), Description of flow of sand using state parameters, Computers and Geotechnics, Vol. 8, No. 3, 195-218.

Poulos, S. J. (1981), The steady state of deformation, J. of Geotechnical Engineering, ASCE, Vol. 107, No. 5, 553-562.

Poulos, S. J., Castro, G., and France, J. W. (1985), Liquefaction evaluation procedure, J. of Geotechnical Engineering, ASCE, Vol. 111, No. 6, 772-792.

Prakash, S. (1981), Soil dynamics, McGraw-Hill, New York.

Promputthangkoon, P., and Hyde, A F. L. (2008a), Compound soil with tyre chips as a sustainable fill in seismic zones, 8th ISOPE Pacific/Asia Offshore Mechanics Symposium, Bangkok, Thailand.

Promputthangkoon, P., and Hyde, A F. L. (2008b), Compressibility and liquefaction potential of rubber composite soils, Scrap Tire Derived Geomaterials-Opportunities and Challenges, Taylor & Francis, London, UK.

Rauch, A. F. (1997), EPOLLS: An empirical method for predicting surface displacements due to liquefaction-induced lateral spreading in earthquakes, PhD Thesis, Virginia Polytechnic Institute and State University.

Riemer, M. (2004), Emerging trends in cyclic triaxial testing, International Workshop on Uncertainties in Nonlinear Soil Properties and their Impact on Modelling Dynamic Soil Response, PEER Headquarter, UC Berkley, 1-7.

Robertson, P. K., and Wride, C. E. (1998), Evaluating cyclic liquefaction potential using the cone penetration test, Canadian Geotechnical J., Vol. 35, No. 3, 442-459.

Robertson, P. K., Woeller, D. J., and Finn, W. D. L. (1992), Seismic cone penetration test for evaluating liquefaction potential under cyclic loading, Canadian Geotechnical J., Vol. 29, 686-695.

Roesler, S. K. (1979), Anisotropic shear modulus due to stress anisotropy, J. of Geotechnical Engineering, ASCE, Vol. 105, No. 7, 871-880.

Rollins, K. M., Evans, M. D., Diehl, N. B., and Daily III, W. D. (1998), Shear modulus and damping relationships for gravels, J. of Geotechnical and Geoenvironmental Engineering, ASCE, Vol. 124, No. 5, 396-405.

Roscoe, K. H., Schofield, A. N., and Wroth, C. P. (1958), On the yielding of soils, Geotechnique, Vol. 9, 22-53.

Salinero, I. S., Roesset, J. M., and Stokoe, K. H. (1986), Analytical studies of body wave propagation and attenuation, Report GR 86-15, University of Texas at Austin.

Schnabel, P. B., Lysmer, J., and Seed, H. B. (1972), SHAKE: A computer program for earthquake response analysis of horizontally layered soils, Report No. UCB/EERC-72/12, EERC, U of California, Berkeley.

Schofield, A. N., and Wroth, C. P. (1968), Critical state soil mechanics, McGraw-Hill, London.

Seed, H. B. (1979), Soil liquefaction and cyclic mobility evaluation for level ground during earthquakes, J. of Geotechnical Engineering, ASCE, Vol. 105, No. 2, 201-255.

Seed, H. B., and Idriss, I. M. (1970), Soil moduli and damping factors for dynamic response analysis, Rep. No. EERC 70-10, Earthquake Engineering Research Center, Berkley, Calif.

Seed, H. B., and Idriss, I. M. (1971), Simplified procedure for evaluating soil liquefaction potential, J. of Geotechnical Engineering Division, ASCE, Vol. 97, No. 9, 1249-1273.

Seed, H. B., and Idriss, I. M. (1982), Ground motions and soil liquefaction during earthquakes, Earthquake Engineering Research Institute Monograph, Oakland, California.

Seed, H. B., and Lee, K. L. (1967), Undrained strength characteristics of cohesionless soils, J. of Soil Mechanics and Foundation Engineering, ASCE, Vol. 93, No. 6, 333-360.

Seed, R. B., Cetin, K. O., Moss, R. E. S., Kammerer, A. M., Wu, J., Pestana, J. M., Riemer, M. F., Sancio, R. B., Bray, J. D., Kayen, R. E., and Faris, A. (2003), Recent advances in soil liquefaction engineering: a unified and consistent framework, 26th Annual ASCE Los Angeles Geotechnical Spring Seminar, Keynote Presentation, H.M.S. Queen Mary, Long Beach, California.

Seed, H. B., Tokimatsu, K., Harder, L. F., and Chung, R. M. (1985), The influence of SPT procedures in soil liquefaction resistance evaluations, J. of Geotechnical Engineering, ASCE, Vol. 111, No. 12, 1425-1445.

Selig, E. T., and Chang, S. C. (1981), Soil failure modes in undrained cyclic loading, J. of Geotechnical Engineering, ASCE, Vol. 107, No. 5, 539-551.

Shirley, D. J. (1978), An improved shear wave transducer, J. of the Acoustical Society of America, Vol. 63, No. 5, 1643-1645.

Shirley, D. J., and Hampton, L. D. (1978), Shear-wave measurements in laboratory sediments, J. of the Acoustical Society of America, Vol. 63, No. 2, 607-613.

Silver, M. L., Wilson, J. H., Valera, J. E., Townsend, F. C., Tiedemann, D. A, Lee, K. L., Ladd, R. S., and Chan, C. K. (1976), Cyclic triaxial strength of a standard test sand, J. of Geotechnical Engineering, ASCE, 511-524.

Sitharam, T. G. (2003), Earthquake geotechnical engineering: An overview, Workshop on Current Practices and Future Trends in Earthquake Geotechnical Engineering, Golden Jubilee Seminar Hall, Civil Engineering Department, Indian Institute of Science, Bangalore, India.

Sitharam, T. G., Govindaraju, L., and Sridharan, A. (2004), Dynamic properties and liquefaction potential of soils, Current Science, Vol. 87, No. 10, 1370-1378.

Skempton, A. W. (1954), The pore-pressure coefficients A and B, Geotechnique, Vol. 4, 143-147.

Skempton, A. W. (1986), Standard penetration test procedures and the effects in sands of overburden pressure, Geotechnique, Vol. 36, No. 3, 425-447.

Song, B. W., Yosuhara, K., and Murakami, S. (2004), Direct simple shear testing for post-cyclic degradation in stiffness of nonplastic silt, Geotechnical Testing J., ASTM, Vol. 27, No. 6, 1-7.

Stephenson, R. W. (1978), Ultrasonic testing for determining dynamic soil moduli." Dynamic Geotechnical Testing, ASTM STP 654, ASTM, 179-195.

Stokoe, K. H., II, Lee, S. H. H., and Knox, D. P. (1985), Shear moduli measurements under true triaxial stresses, Proceeding, Advanced in the Art of Testing Soil under Cyclic Conditions, ASCE, 166-185.

Sykora, D. W. (1987), Creation of a data base of seismic shear wave velocities for correlation analysis, Geotechnical Laboratory Miscellaneous Paper GL-87-26, U.S. Army Engineer Waterways Experiment Station, Miss.

Tatsuoka, F., Toki, S., Minura, S., Kato, H., Okamoto, M., Yamada, S., Yasuda, S., and Tanizawa, F. (1986), Some factors affecting cyclic undrained triaxial strength of sand, Soils and Foundations, Vol. 26, No. 3, 99-116.

Terzaghi, K., and Peck, R. B. (1948), Soil mechanics and engineering practice, John Wiley & Sons, New York.

Thevanayagam, S. (1998), Effect of fines and confining stress on undrained shear strength of silty sands, J of Geotechnical and Geoenvironmental Engineering, Vol. 124, No. 6, 479-491.

Tsang, H. H. (2008), Seismic isolation by rubber-soil mixtures for developing countries, Earthquake Engineering and Structural Dynamics, Vol. 37, 283-303.

Uchihara, T., Chi, N. A., Nirmalan, S, Sato, T., Meidani, M., and Towhata, I. (2008), Shaking table tests on effect of tire chips and sand mixture in increasing liquefaction resistance and mitigating uplift of pipe, Scrap Tire Derived Geomaterials – Opportunities and Challenges, Taylor & Francis Group, London, 179-186.

UTM Hardware Reference (1998), UTM Manual, ELE Internaitonal, UK.

UTM for Windows (2006), Cyclic Triaxial Test: Software reference manual, IPC Global, Australia.

Vaid, Y. P., and Chern, J. C. (1985), Cyclic and monotonic undrained response of saturated sands, Advances in the art of testing soils under cyclic conditions, ASCE Annual Convention, Detroit, Mich, 120-147.

Vaid, Y. P., and Sivathayalan, S. (2000), Fundamental factors affecting liquefaction susceptibility of sands, Canadian Geotechnical J., Vol. 37, 592-606.

Vaid, Y. P., Stedman, J. D., and Sivathayalan, S. (2001), Confining stress and static shear effects in cyclic liquefaction, Canadian Geotechnical J., Vol. 38, 580-591.

Vercueil, D., Billet, P., and Cordary, D. (1997), Study of the liquefaction resistance of a saturated sand reinforced with geosynthetics, Soil Dynamics and Earthquake Engineering, Vol. 16, 417-425.

Viggiani, G., and Atkinson, J. H. (1995), Interpretation of bender element tests, Geotechnique, Vol. 45, No. 1, 149-154.

Wang, W. (1979), Some findings in soil liquefaction, Research Report, Water Conservancy and Hydrostatic Power Scientific Research Institute, Beijing.

Whitlow, R. (1995), Basic soil mechanics 3rd edition, Longman, Malaysia.

Wiegel, R. L. (ed) (1970), Earthquake engineering, Prentice-Hall, New Jersey.

Wu, W. Y., Benda, C. C., and Cauley, R. F. (1997), Triaxial determination of shear strength of tire chips, J. of Geotechnical and Geoenvironmental Engineering, ASCE, Vol. 123, No. 5, 479-482.

Xenaki, V. C., and Athanasopoulos, G. A. (2003), Liquefaction resistance of sand-silt mixtures: an experimental investigation of the effect of fines, Soil Dynamics and Earthquake Engineering, Vol. 23, 183-194.

Yamamuro, J. A., and Lade, P. V. (1997), Static liquefaction of very loose sands, Canadian Geotechnical J., Vol. 34, No. 6, 905-917.

Yamamuro, J. A., and Lade, P. V. (1998), Steady state concepts and static liquefaction of silty sands, J. of Geotechnical and Geoenvironmental Engineering, ASCE, Vol. 124, No. 9, 868-877.

Yamamuro, J. A., and Wood, F. M. (2003), Effect of depositional method on the undrained behavior and microstructure of sand with silt, U.S. - Taiwan Workshop on Soil Liquefaction, National Chiao Tung University, Hsin-Chu, Taiwan.

Yang, S., Lohnes, R. A., and Kjartanson, B. H. (2002), Mechanical properties of shredded tires, Geotechnical Testing J., ASTM, Vol. 25, No. 1, 44-52.

Yoshimine, M., and Ishihara, K., F. (1998), Flow potential of sand during liquefaction, Soils and Found., Vol. 15, 29-44.

Yoshimine, M., Robertson, P. K., and Wride, C. E. (1999), Undrained shear strength of clean sands to trigger flow liquefaction, Canadian Geotechnical J., Vol. 36, 891-906.

Youd, T. L., and Idriss, I. M. (2001), Liquefaction resistance of soils: summary report from the 1996 NCEER and 1998 NCEER/NSF workshops on evaluation of liquefaction resistance of soils, J. of Geotechnical and Geoenvironmental Engineering, ASCE, Vol. 127, No. 4, 297-313.

Youd, T. L., Idriss, I. M., Andrus, R. D., Arango, I., Castro, G., Christine, J. T., Dobry, R., Finn, W. D. L., Harder Jr., L. F., Hynes, M. E., Ishihara, K., Koester, J. P., Liao, S. S. C., Marcuson III, W. F., Martin, G. R., Mitchell, J. K., Moriwaki, Y., Power, M. S., Robertson, P. K., Seed, R. B., and Stoke II, K. H. (2001), Liquefaction resistance of soils: summary report from the 1996 NCEER and 1998 NCEER/NSF workshops on evaluation of liquefaction resistance of soils, J. of Geotechnical and Geoenvironmental Engineering, ASCE, Vol. 127, No. 10, 817-833.

Youwai, S., and Bergado, D. T. (2003), Strength and deformation characteristics of shreded rubber tire-sand mixtures, Canadian Geotechnical J., Vol. 40, 254-264.

Zeng, X., and Grolewski, B. (2005), Measurement of Gmax and estimated of Ko of saturated clay using bender elements in an oedometer, Geotechnical Testing J., ASTM, Vol. 28, No. 3, 1-11.

Zhang, H., and Garga, V. K. (1997), Quasi-steady state: a real behaviour?, Canadian Geotechnical J., Vol. 34, 749-761.

Zornberg, J. G., Cabral, A. R., and Varatjandr, C. (2004), Behaviour of tire shred-sand mixtures, Canadian Geotechnical J., Vol. 41, 227-241.

APPENDIX

SUMMARY OF BENDER ELEMENT TESTS

Table A. 1 BE test results for pure sand, mixtures 100:0.

Test No.	f_{in} (kHz)	First Arrival (FA)		Peak to Peak (PP)		Cross Correlation (CC)	
		V_s (m/s)	G_{max} (MPa)	V_s (m/s)	G_{max} (MPa)	V_s (m/s)	G_{max} (MPa)
BE100S430	2	228	104	234	109	199	79
	4	234	109	231	106	231	106
	7	234	109	231	106	231	106
	11	240	115	234	109	231	106
	16	246	121	234	109	234	109
BE100S370	2	220	97	231	106	-	-
	4	220	97	223	99	220	97
	7	223	99	220	97	220	97
	11	234	109	223	99	220	97
	16	237	112	231	106	220	97
BE100S320	2	220	96	231	106	217	94
	4	223	99	223	99	223	99
	7	231	106	223	99	220	96
	11	234	109	231	106	220	96
	16	240	114	231	106	220	96
BE100S290	2	207	86	219	96	198	79
	4	217	94	217	94	217	94
	7	219	96	217	94	217	94
	11	230	106	219	96	214	92
	16	233	108	219	96	212	90
BE100S250	2	219	96	230	106	213	90
	4	222	98	219	96	219	96
	7	227	103	225	101	219	96
	11	236	111	230	106	219	96
	16	245	120	233	108	219	96

Table A. 2 BE test results for SA, mixtures 95:5.

Test No.	f_{in} (kHz)	First Arrival (FA)		Peak to Peak (PP)		Cross Correlation (CC)	
		V_s (m/s)	G_{max} (MPa)	V_s (m/s)	G_{max} (MPa)	V_s (m/s)	G_{max} (MPa)
BE95SA365	2	234	106	227	100	228	101
	4	249	121	225	99	223	96
	7	237	109	225	99	218	92
	11	234	106	225	99	218	92
	16	237	109	227	100	214	89
BE95SA296	2	246	118	234	106	231	104
	4	249	121	231	104	227	100
	7	234	106	231	104	223	96
	11	234	106	227	100	218	92
	16	249	121	237	109	223	96
BE95SA240	2	235	107	235	107	224	97
	4	247	119	228	101	229	102
	7	238	110	232	104	226	99
	11	235	107	235	107	228	101
	16	259	130	238	110	221	95
BE95SA225	2	249	120	230	103	228	101
	4	263	134	233	106	225	98
	7	267	138	249	120	220	94
	11	233	106	230	103	220	94
	16	239	111	228	101	214	89
BE95SA205	2	249	121	234	106	226	100
	4	267	139	231	103	226	100
	7	249	121	231	103	226	100
	11	252	124	234	106	226	100
	16	267	139	237	109	222	96

Table A. 3 BE test results for SA, mixtures 90:10.

Test No.	f in (kHz)	First Arrival (FA)		Peak to Peak (PP)		Cross Correlation (CC)	
		V_s (m/s)	G_{max} (MPa)	V_s (m/s)	G_{max} (MPa)	V_s (m/s)	G_{max} (MPa)
BE90SA285	2	220	92	210	84	210	84
	4	222	94	215	88	205	80
	7	226	97	215	88	205	80
	11	233	104	222	94	207	82
	16	233	104	220	92	201	77
BE90SA220	2	207	81	209	83	212	85
	4	219	91	212	85	207	81
	7	233	103	219	91	202	78
	11	233	103	217	89	207	81
	16	248	117	233	103	205	80
BE90SA185	2	217	89	207	82	205	80
	4	220	92	207	82	201	77
	7	233	103	205	80	197	73
	11	249	118	210	84	192	70
	16	225	96	210	84	189	68
BE90SA165	2	207	82	207	82	203	78
	4	220	92	199	75	199	75
	7	207	82	199	75	197	73
	11	210	83	203	78	195	72
	16	212	85	205	80	189	67

Table A. 4 BE test results for SA, mixtures 80:20.

Test No.	f in (kHz)	First Arrival (FA)		Peak to Peak (PP)		Cross Correlation (CC)	
		V_s (m/s)	G_{max} (MPa)	V_s (m/s)	G_{max} (MPa)	V_s (m/s)	G_{max} (MPa)
BE80SA280	2	178	57	171	53	168	51
	4	187	63	174	55	167	50
	7	195	69	176	56	167	50
	11	197	70	180	59	164	49
	16	205	76	181	59	161	47
BE80SA230	2	176	56	171	53	171	53
	4	184	61	176	56	168	51
	7	194	68	177	57	163	48
	11	194	68	177	57	163	48
	16	196	70	177	57	165	49
BE80SA195	2	176	56	171	53	171	53
	4	186	63	176	56	168	51
	7	190	65	177	57	168	51
	11	194	68	183	60	166	50
	16	201	73	184	61	163	48
BE80SA160	2	176	56	171	53	170	52
	4	187	63	174	55	168	51
	7	193	67	178	57	168	51
	11	195	68	181	59	167	50
	16	195	68	181	59	161	47

Table A. 5 BE test results for SA, mixtures 70:30.

Test No.	f_{in} (kHz)	First Arrival (FA)		Peak to Peak (PP)		Cross Correlation (CC)	
		V_s (m/s)	G_{max} (MPa)	V_s (m/s)	G_{max} (MPa)	V_s (m/s)	G_{max} (MPa)
BE70SA350	2	172	51	152	40	140	34
	4	172	51	164	46	136	32
	7	-	-	-	-	-	-
	11	-	-	-	-	-	-
	16	-	-	-	-	-	-
BE70SA270	2	147	37	139	33	133	30
	4	158	43	144	35	136	32
	7	160	44	146	37	137	32
	11	-	-	-	-	-	-
	16	-	-	-	-	-	-
BE70SA245	2	158	43	142	34	133	31
	4	173	51	146	37	130	29
	7	173	51	149	38	129	28
	11	-	-	-	-	-	-
	16	-	-	-	-	-	-
BE70SA230	2	165	47	146	36	136	32
	4	173	52	165	47	130	29
	7	-	-	-	-	-	-
	11	-	-	-	-	-	-
	16	-	-	-	-	-	-

Table A. 6 BE test results for SA, mixtures 60:40.

Test No.	f_{in} (kHz)	First Arrival (FA)		Peak to Peak (PP)		Cross Correlation (CC)	
		V_s (m/s)	G_{max} (MPa)	V_s (m/s)	G_{max} (MPa)	V_s (m/s)	G_{max} (MPa)
BE60SA420	2	118	23	106	19	102	17
	4	118	23	106	19	103	17
	7	126	26	114	21	101	17
	11	-	-	-	-	-	-
	16	-	-	-	-	-	-
BE60SA370	2	122	24	108	19	102	17
	4	126	26	114	21	102	17
	7	-	-	-	-	-	-
	11	-	-	-	-	-	-
	16	-	-	-	-	-	-
BE60SA340	2	128	27	116	22	111	20
	4	131	28	119	23	113	21
	7	-	-	-	-	-	-
	11	-	-	-	-	-	-
	16	-	-	-	-	-	-
BE60SA310	2	123	25	112	21	104	18
	4	126	26	113	21	104	18
	7	-	-	-	-	-	-
	11	-	-	-	-	-	-
	16	-	-	-	-	-	-

Table A. 7 BE test results for SA, mixtures 50:50.

Test No.	f_{in} (kHz)	First Arrival (FA)		Peak to Peak (PP)		Cross Correlation (CC)	
		V_s (m/s)	G_{max} (MPa)	V_s (m/s)	G_{max} (MPa)	V_s (m/s)	G_{max} (MPa)
BE50SA515	2	109	19	92	13	85	11
	4	-	-	-	-	-	-
	7	-	-	-	-	-	-
	11	-	-	-	-	-	-
	16	-	-	-	-	-	-
BE50SA465	2	113	20	92	13	81	10
	4	-	-	-	-	-	-
	7	-	-	-	-	-	-
	11	-	-	-	-	-	-
	16	-	-	-	-	-	-
BE50SA420	2	106	17	90	12	82	10
	4	-	-	-	-	-	-
	7	-	-	-	-	-	-
	11	-	-	-	-	-	-
	16	-	-	-	-	-	-
BE50SA370	2	108	18	91	13	84	11
	4	105	17	95	14	86	12
	7	-	-	-	-	-	-
	11	-	-	-	-	-	-
	16	-	-	-	-	-	-

Table A. 8 BE test results for SB, mixtures 95:5.

Test No.	f_{in} (kHz)	First Arrival (FA)		Peak to Peak (PP)		Cross Correlation (CC)	
		V_s (m/s)	G_{max} (MPa)	V_s (m/s)	G_{max} (MPa)	V_s (m/s)	G_{max} (MPa)
BE95SB270	2	192	72	196	75	187	68
	4	205	82	196	75	196	75
	7	207	84	196	75	190	71
	11	207	84	196	75	188	69
	16	220	94	199	77	187	68
BE95SB245	2	196	75	201	78	199	77
	4	207	84	199	77	199	77
	7	212	88	205	82	196	75
	11	220	94	207	84	194	74
	16	220	94	207	84	194	74
BE95SB225	2	197	75	199	77	191	71
	4	208	84	199	77	199	77
	7	208	84	201	79	195	74
	11	214	89	203	80	195	74
	16	217	92	205	82	197	75
BE95SB210	2	197	75	205	82	185	67
	4	205	82	199	77	202	79
	7	205	82	203	80	199	77
	11	215	90	208	84	197	75
	16	220	94	205	82	197	75

Table A. 9 BE test results for SB, mixtures 90:10.

Test No.	f_{in} (kHz)	First Arrival (FA)		Peak to Peak (PP)		Cross Correlation (CC)	
		V_s (m/s)	G_{max} (MPa)	V_s (m/s)	G_{max} (MPa)	V_s (m/s)	G_{max} (MPa)
BE90SB260	2	186	66	181	63	171	56
	4	194	72	186	66	184	65
	7	205	80	192	70	181	63
	11	207	82	194	72	183	64
	16	214	88	196	73	181	63
BE90SB235	2	187	66	183	64	180	61
	4	197	74	187	66	185	65
	7	199	75	192	70	181	63
	11	208	82	195	72	181	63
	16	208	82	193	71	178	60
BE90SB213	2	181	62	176	59	171	56
	4	192	70	184	65	179	61
	7	196	73	186	66	179	61
	11	202	78	192	70	181	62
	16	207	82	191	70	181	62
BE90SB190	2	186	66	169	55	169	55
	4	196	73	186	66	184	65
	7	205	80	190	69	183	64
	11	207	82	196	73	183	64
	16	209	84	198	75	181	62

Table A. 10 BE test results for SB, mixtures 80:20.

Test No.	f_{in} (kHz)	First Arrival (FA)		Peak to Peak (PP)		Cross Correlation (CC)	
		V_s (m/s)	G_{max} (MPa)	V_s (m/s)	G_{max} (MPa)	V_s (m/s)	G_{max} (MPa)
BE80SB256	2	187	64	178	58	176	57
	4	197	71	182	60	176	57
	7	206	77	187	64	173	55
	11	206	77	193	68	173	55
	16	206	77	193	68	172	54
BE80SB217	2	185	63	176	57	172	54
	4	195	69	185	63	181	60
	7	206	77	187	64	180	59
	11	206	77	191	67	183	61
	16	206	77	191	67	178	58
BE80SB195	2	191	67	180	59	178	58
	4	206	77	184	61	178	58
	7	218	87	189	65	175	56
	11	218	87	189	65	177	57
	16	195	69	195	69	172	54
BE80SB170	2	206	78	187	64	184	62
	4	209	79	187	64	184	62
	7	216	85	197	71	180	59
	11	218	87	202	74	181	60
	16	218	87	209	79	180	59

Table A. 11 BE test results for SB, mixtures 70:30.

Test No.	f_{in} (kHz)	First Arrival (FA)		Peak to Peak (PP)		Cross Correlation (CC)	
		V_s (m/s)	G_{max} (MPa)	V_s (m/s)	G_{max} (MPa)	V_s (m/s)	G_{max} (MPa)
BE70SB340	2	160	45	148	38	145	37
	4	175	54	157	43	145	37
	7	187	61	160	45	147	38
	11	189	63	162	46	147	38
	16	-	-	-	-	-	-
BE70SB300	2	167	49	156	42	147	38
	4	184	59	161	45	149	39
	7	184	59	168	50	153	41
	11	-	-	-	-	-	-
	16	-	-	-	-	-	-
BE70SB260	2	167	49	151	40	142	36
	4	184	59	160	45	140	34
	7	-	-	-	-	-	-
	11	-	-	-	-	-	-
	16	-	-	-	-	-	-
BE70SB200	2	167	49	147	38	140	34
	4	175	53	157	43	139	34
	7	183	59	152	40	165	48
	11	-	-	-	-	-	-
	16	-	-	-	-	-	-

Table A. 12 BE test results for SB, mixtures 60:40.

Test No.	f_{in} (kHz)	First Arrival (FA)		Peak to Peak (PP)		Cross Correlation (CC)	
		V_s (m/s)	G_{max} (MPa)	V'_s (m/s)	G_{max} (MPa)	V'_s (m/s)	G_{max} (MPa)
BE60SB550	2	134	30	117	23	110	20
	4	-	-	-	-	-	-
	7	-	-	-	-	-	-
	11	-	-	-	-	-	-
	16	-	-	-	-	-	-
BE60SB435	2	135	30	117	23	110	20
	4	145	35	120	24	112	21
	7	-	-	-	-	-	-
	11	-	-	-	-	-	-
	16	-	-	-	-	-	-
BE60SB350	2	128	28	117	23	109	20
	4	143	35	120	24	108	20
	7	-	-	-	-	-	-
	11	-	-	-	-	-	-
	16	-	-	-	-	-	-
BE60SB310	2	135	30	118	23	112	21
	4	152	38	125	26	112	21
	7	-	-	-	-	-	-
	11	-	-	-	-	-	-
	16	-	-	-	-	-	-

Table A. 13 BE test results for SB, mixtures 50:50.

Test No.	f_{in} (kHz)	First Arrival (FA)		Peak to Peak (PP)		Cross Correlation (CC)	
		V_s (m/s)	G_{max} (MPa)	V_s (m/s)	G_{max} (MPa)	V_s (m/s)	G_{max} (MPa)
BE50SB540	2	126	25	99	15	91	13
	4	-	-	-	-	-	-
	7	-	-	-	-	-	-
	11	-	-	-	-	-	-
	16	-	-	-	-	-	-
BE50SB455	2	118	22	98	15	90	13
	4	118	22	107	18	90	13
	7	-	-	-	-	-	-
	11	-	-	-	-	-	-
	16	-	-	-	-	-	-
BE50SB445	2	122	23	107	18	95	14
	4	-	-	-	-	-	-
	7	-	-	-	-	-	-
	11	-	-	-	-	-	-
	16	-	-	-	-	-	-
BE50SB405	2	111	19	98	15	92	13
	4	-	-	-	-	-	-
	7	-	-	-	-	-	-
	11	-	-	-	-	-	-
	16	-	-	-	-	-	-
BE50SB350	2	118	22	104	17	95	14
	4	-	-	-	-	-	-
	7	-	-	-	-	-	-
	11	-	-	-	-	-	-
	16	-	-	-	-	-	-

Table A. 14 BE test results for SC, mixtures 95:5.

Test No.	f_{in} (kHz)	First Arrival (FA)		Peak to Peak (PP)		Cross Correlation (CC)	
		V_s (m/s)	G_{max} (MPa)	V_s (m/s)	G_{max} (MPa)	V_s (m/s)	G_{max} (MPa)
BE95SC380	2	217	93	220	95	205	83
	4	217	93	217	93	215	90
	7	222	97	217	93	212	88
	11	231	104	222	97	212	88
	16	234	107	220	95	210	86
BE95SC360	2	205	83	210	87	195	74
	4	205	83	203	81	202	80
	7	208	85	208	85	199	78
	11	212	89	210	87	199	78
	16	220	95	208	85	197	76
BE95SC300	2	201	79	205	83	195	74
	4	208	84	205	83	201	79
	7	215	90	208	84	201	79
	11	220	95	210	86	201	79
	16	227	101	210	86	197	76
BE95SC250	2	208	85	210	86	199	78
	4	208	85	205	83	208	85
	7	217	93	210	86	208	85
	11	220	95	210	86	205	83
	16	222	97	217	93	205	83
BE95SC230	2	206	83	211	87	195	75
	4	208	85	206	83	204	81
	7	211	87	206	83	202	79
	11	220	95	208	85	202	79
	16	220	95	211	87	199	78

Table A. 15 BE test results for SC, mixtures 90:10.

Test No.	f_{in} (kHz)	First Arrival (FA)		Peak to Peak (PP)		Cross Correlation (CC)	
		V_s (m/s)	G_{max} (MPa)	V_s (m/s)	G_{max} (MPa)	V_s (m/s)	G_{max} (MPa)
BE90SC365	2	197	75	193	72	185	66
	4	208	83	199	76	197	75
	7	210	85	203	80	197	75
	11	220	93	208	83	195	73
	16	220	93	208	83	199	76
BE90SC310	2	208	83	215	89	187	67
	4	217	91	210	85	210	85
	7	220	93	217	91	210	85
	11	222	95	220	93	212	87
	16	233	105	220	93	210	85
BE90SC260	2	203	80	191	70	187	68
	4	217	91	205	82	208	83
	7	234	106	208	83	202	79
	11	234	106	210	85	208	83
	16	-	-	-	-	-	-
BE90SC210	2	202	79	196	74	187	67
	4	207	83	202	79	199	76
	7	217	91	207	83	196	74
	11	210	85	205	81	196	74
	16	220	93	207	83	196	74

Table A. 16 BE test results for SC, mixtures 80:20.

Test No.	f_{in} (kHz)	First Arrival (FA)		Peak to Peak (PP)		Cross Correlation (CC)	
		V_s (m/s)	G_{max} (MPa)	V_s (m/s)	G_{max} (MPa)	V_s (m/s)	G_{max} (MPa)
BE80SC320	2	181	61	171	54	165	51
	4	196	71	183	62	179	60
	7	207	80	186	64	179	60
	11	207	80	191	68	183	62
	16	-	-	-	-	-	-
BE80SC300	2	178	59	173	56	171	55
	4	189	66	181	61	176	58
	7	197	72	183	62	176	58
	11	207	80	185	64	182	62
	16	197	72	191	68	173	56
BE80SC250	2	180	60	176	58	170	54
	4	195	70	181	61	178	59
	7	197	72	187	65	180	60
	11	207	80	191	67	178	59
	16	207	80	191	67	187	65
BE80SC230	2	178	59	174	57	170	54
	4	189	66	181	61	178	59
	7	197	72	185	64	178	59
	11	199	73	189	66	176	58
	16	207	80	189	66	176	58
BE80SC212	2	184	63	175	57	170	54
	4	195	71	186	64	180	61
	7	204	78	190	67	181	61
	11	206	79	193	70	184	63
	16	-	-	-	-	-	-

Table A. 17 BE test results for SC, mixtures 70:30.

Test No.	f_{in} (kHz)	First Arrival (FA)		Peak to Peak (PP)		Cross Correlation (CC)	
		V_s (m/s)	G_{max} (MPa)	V_s (m/s)	G_{max} (MPa)	V_s (m/s)	G_{max} (MPa)
BE70SC430	2	213	82	186	62	175	55
	4	219	85	196	68	170	52
	7	-	-	-	-	-	-
	11	-	-	-	-	-	-
	16	-	-	-	-	-	-
BE70SC350	2	196	69	177	56	165	49
	4	207	77	196	69	162	47
	7	-	-	-	-	-	-
	11	-	-	-	-	-	-
	16	-	-	-	-	-	-
BE70SC320	2	188	63	186	62	169	51
	4	-	-	-	-	-	-
	7	-	-	-	-	-	-
	11	-	-	-	-	-	-
	16	-	-	-	-	-	-
BE70SC280	2	216	84	177	56	170	52
	4	195	68	195	68	169	51
	7	-	-	-	-	-	-
	11	-	-	-	-	-	-
	16	-	-	-	-	-	-

Table A. 18 BE test results for SC, mixtures 60:40.

Test No.	f_{in} (kHz)	First Arrival (FA)		Peak to Peak (PP)		Cross Correlation (CC)	
		V'_s (m/s)	G_{max} (MPa)	V'_s (m/s)	G_{max} (MPa)	V'_s (m/s)	G_{max} (MPa)
BE60SC550	2	168	48	148	38	137	32
	4	176	53	165	47	142	35
	7	•	•	•	•	•	•
	11	•	•	•	•	•	•
	16	•	•	•	•	•	•
BE60SC440	2	176	53	148	38	137	32
	4	176	53	161	44	139	33
	7	•	•	•	•	•	•
	11	•	•	•	•	•	•
	16	•	•	•	•	•	•
BE60SC370	2	168	49	148	38	137	32
	4	185	59	161	44	141	34
	7	•	•	•	•	•	•
	11	•	•	•	•	•	•
	16	•	•	•	•	•	•
BE60SC300	2	176	53	147	37	137	32
	4	•	•	•	•	•	•
	7	•	•	•	•	•	•
	11	•	•	•	•	•	•
	16	•	•	•	•	•	•

Table A. 19 BE test results for SC, mixtures 50:50.

Test No.	f_{in} (kHz)	First Arrival (FA)		Peak to Peak (PP)		Cross Correlation (CC)	
		V'_s (m/s)	G_{max} (MPa)	V'_s (m/s)	G_{max} (MPa)	V'_s (m/s)	G_{max} (MPa)
BE50SC560	2	153	38	131	28	105	18
	4	-	-	-	-	-	-
	7	-	-	-	-	-	-
	11	-	-	-	-	-	-
	16	-	-	-	-	-	-
BE50SC495	2	143	33	124	25	110	20
	4	-	-	-	-	-	-
	7	-	-	-	-	-	-
	11	-	-	-	-	-	-
	16	-	-	-	-	-	-
BE50SC430	2	142	32	129	27	113	21
	4	-	-	-	-	-	-
	7	-	-	-	-	-	-
	11	-	-	-	-	-	-
	16	-	-	-	-	-	-
BE50SC345	2	153	38	122	24	106	18
	4	-	-	-	-	-	-
	7	-	-	-	-	-	-
	11	-	-	-	-	-	-
	16	-	-	-	-	-	-

Table A. 20 BE test results for SD, mixtures 95:5.

Test No.	f_{in} (kHz)	First Arrival (FA)		Peak to Peak (PP)		Cross Correlation (CC)	
		V_s (m/s)	G_{max} (MPa)	V_s (m/s)	G_{max} (MPa)	V_s (m/s)	G_{max} (MPa)
BE95SD350	2	205	83	210	87	199	78
	4	208	85	208	85	208	85
	7	217	93	210	87	208	85
	11	220	95	210	87	205	83
	16	222	97	210	87	203	81
BE95SD325	2	231	104	212	88	195	74
	4	215	90	208	85	208	85
	7	217	93	210	86	205	83
	11	225	99	210	86	208	85
	16	231	104	212	88	203	81
BE95SD280	2	208	85	215	91	201	79
	4	218	93	213	89	213	89
	7	223	97	218	93	210	87
	11	231	105	220	95	210	87
	16	234	107	223	97	210	87
BE95SD240	2	208	85	213	89	189	70
	4	215	91	210	87	208	85
	7	218	93	213	89	208	85
	11	225	100	218	93	208	85
	16	231	105	218	93	206	83

Table A. 21 BE test results for SD, mixtures 90:10.

Test No.	f_{in} (kHz)	First Arrival (FA)		Peak to Peak (PP)		Cross Correlation (CC)	
		V_s (m/s)	G_{max} (MPa)	V_s (m/s)	G_{max} (MPa)	V_s (m/s)	G_{max} (MPa)
BE90SD360	2	208	84	184	65	182	64
	4	218	92	210	86	206	82
	7	220	94	218	92	210	86
	11	231	103	218	92	210	86
	16	234	106	220	94	208	84
BE90SD305	2	197	75	199	77	185	67
	4	208	84	206	82	201	79
	7	213	88	208	84	201	79
	11	220	94	211	86	206	82
	16	226	99	211	86	197	75
BE90SD270	2	205	82	208	83	201	78
	4	210	85	208	83	205	82
	7	217	91	210	85	205	82
	11	220	93	212	87	205	82
	16	234	105	217	91	201	78
BE90SD225	2	197	75	197	75	183	65
	4	208	83	201	78	199	76
	7	220	93	205	81	197	75
	11	217	91	210	85	197	75
	16	220	93	208	83	191	70

Table A. 22 BE test results for SD, mixtures 80:20.

Test No.	f_{in} (kHz)	First Arrival (FA)		Peak to Peak (PP)		Cross Correlation (CC)	
		V_s (m/s)	G_{max} (MPa)	V_s (m/s)	G_{max} (MPa)	V_s (m/s)	G_{max} (MPa)
BE80SD322	2	183	62	170	54	165	51
	4	194	70	187	65	183	62
	7	196	72	192	69	185	64
	11	-	-	-	-	-	-
	16	-	-	-	-	-	-
BE80SD240	2	185	64	173	56	162	49
	4	205	78	196	72	190	68
	7	217	88	201	75	188	66
	11	-	-	-	-	-	-
	16	-	-	-	-	-	-
BE80SD220	2	185	64	175	57	170	54
	4	197	72	195	71	191	68
	7	217	88	205	79	193	69
	11	-	-	-	-	-	-
	16	-	-	-	-	-	-
BE80SD205	2	185	64	173	56	170	54
	4	197	72	193	69	185	64
	7	203	77	203	77	189	66
	11	-	-	-	-	-	-
	16	-	-	-	-	-	-

Table A. 23 BE test results for SD, mixtures 70:30.

Test No.	f_{in} (kHz)	First Arrival (FA)		Peak to Peak (PP)		Cross Correlation (CC)	
		V_s (m/s)	G_{max} (MPa)	V_s (m/s)	G_{max} (MPa)	V_s (m/s)	G_{max} (MPa)
BE70SD420	2	205	76	190	65	187	63
	4	220	87	196	69	190	65
	7	220	87	205	76	190	65
	11	-	-	-	-	-	-
	16	-	-	-	-	-	-
BE70SD330	2	219	86	196	69	186	62
	4	221	88	207	77	190	65
	7	221	88	207	77	200	72
	11	-	-	-	-	-	-
	16	-	-	-	-	-	-
BE70SD300	2	207	77	194	68	186	62
	4	216	84	204	75	188	64
	7	207	77	204	75	186	62
	11	-	-	-	-	-	-
	16	-	-	-	-	-	-
BE70SD250	2	206	77	196	69	186	62
	4	206	77	204	75	190	65
	7	216	84	204	75	194	68
	11	-	-	-	-	-	-
	16	-	-	-	-	-	-
BE70SD210	2	207	77	188	64	185	61
	4	207	77	201	72	190	65
	7	210	79	207	77	194	68
	11	-	-	-	-	-	-
	16	-	-	-	-	-	-

Table A. 24 BE test results for SD, mixtures 60:40.

Test No.	f_{in} (kHz)	First Arrival (FA)		Peak to Peak (PP)		Cross Correlation (CC)	
		V_s (m/s)	G_{max} (MPa)	V_s (m/s)	G_{max} (MPa)	V_s (m/s)	G_{max} (MPa)
BE60SD555	2	177	54	161	45	137	33
	4	195	66	180	56	135	32
	7	-	-	-	-	-	-
	11	-	-	-	-	-	-
	16	-	-	-	-	-	-
BE60SD445	2	177	54	169	49	137	32
	4	-	-	-	-	-	-
	7	-	-	-	-	-	-
	11	-	-	-	-	-	-
	16	-	-	-	-	-	-
BE60SD340	2	185	59	161	45	137	32
	4	-	-	-	-	-	-
	7	-	-	-	-	-	-
	11	-	-	-	-	-	-
	16	-	-	-	-	-	-
BE60SD305	2	176	54	154	41	136	32
	4	195	65	176	54	137	32
	7	-	-	-	-	-	-
	11	-	-	-	-	-	-
	16	-	-	-	-	-	-

Table A. 25 BE test results for SD, mixtures 50:50.

Test No.	f_{in} (kHz)	First Arrival (FA)		Peak to Peak (PP)		Cross Correlation (CC)	
		V_s (m/s)	G_{max} (MPa)	V_s (m/s)	G_{max} (MPa)	V_s (m/s)	G_{max} (MPa)
BE50SD550	2	168	46	149	37	-	-
	4	174	50	161	43	-	-
	7	176	51	168	46	-	-
	11	-	-	-	-	-	-
	16	-	-	-	-	-	-
BE50SD400	2	161	42	154	39	142	33
	4	176	51	161	42	149	36
	7	176	51	165	45	150	37
	11	-	-	-	-	-	-
	16	-	-	-	-	-	-
BE50SD365	2	162	43	146	35	138	31
	4	177	51	155	39	148	36
	7	177	51	156	40	146	35
	11	-	-	-	-	-	-
	16	-	-	-	-	-	-
BE50SD300	2	153	38	139	32	-	-
	4	164	44	153	38	-	-
	7	164	44	158	41	-	-
	11	-	-	-	-	-	-
	16	-	-	-	-	-	-